COLLECTED PAPERS

ON

NANO/ATOM PHOTONICS

Volume 12

September 1996—July 1997

Professor

Motoichi OHTSU

TOKYO INSTITUTE OF TECHNOLOGY

Interdisciplinary Graduate School of Science and Engineering

4259 Nagatsuta, Midori-ku, Yokohama, Kanagawa 226, JAPAN

TEL : +81—45—924—5455

FAX : +81—45—921—1204

E-mail : ohtsu @ ae. titech. ac. jp

PREFACE

In order to realize the ultimate status of light and matter, M. Ohtsu tries to control the spatial properties of light. The approach he has used is through the research of near-field optics and its application to nano-fabrication and atom manipulation. This will open up a new era of nano/atom photonics. It should be pointed out that the nano/atom photonics is closely related to quantum optics, atom optics, high density optical storage, bio-technology, and so on (see the figure on the next page). And by means of this relationship of near-field optics with a variety of fields, nano/atom photonics exhibits rapid progress. Further research will be done to realize novel nanometric materials and devices.

A "PHOTON CONTROL" project, Kanagawa Academy of Science and Technology(KAST)(*), directed by Ohtsu is also engaged in the research subject described above. Twelve research staffs including three visiting scientists from industries and one visiting STA fellow from Canada have obtained several results on nano/atom photonics. Their details are reviewed in this issue of the COLLECTED PAPERS.

August 1997

Motoichi OHTSU

大津　元一

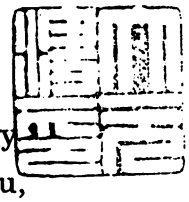

(*) Address: Photon Control Project,
Kanagawa Academy of Science and Technology
KSP East, Rm. 408, 3-2-1 Sakado, Takatsu-ku,
Kawasaki-shi, Kanagawa 213, JAPAN
Phone: +81-44-819-2071
Fax: +81-44-819-2072
E-mail: ohtsu@net.ksp.or.jp
〒２１３　神奈川県川崎市高津区坂戸３－２－１
ＫＳＰ東棟４０８号室
（財）神奈川科学技術アカデミー
フォトン制御プロジェクト

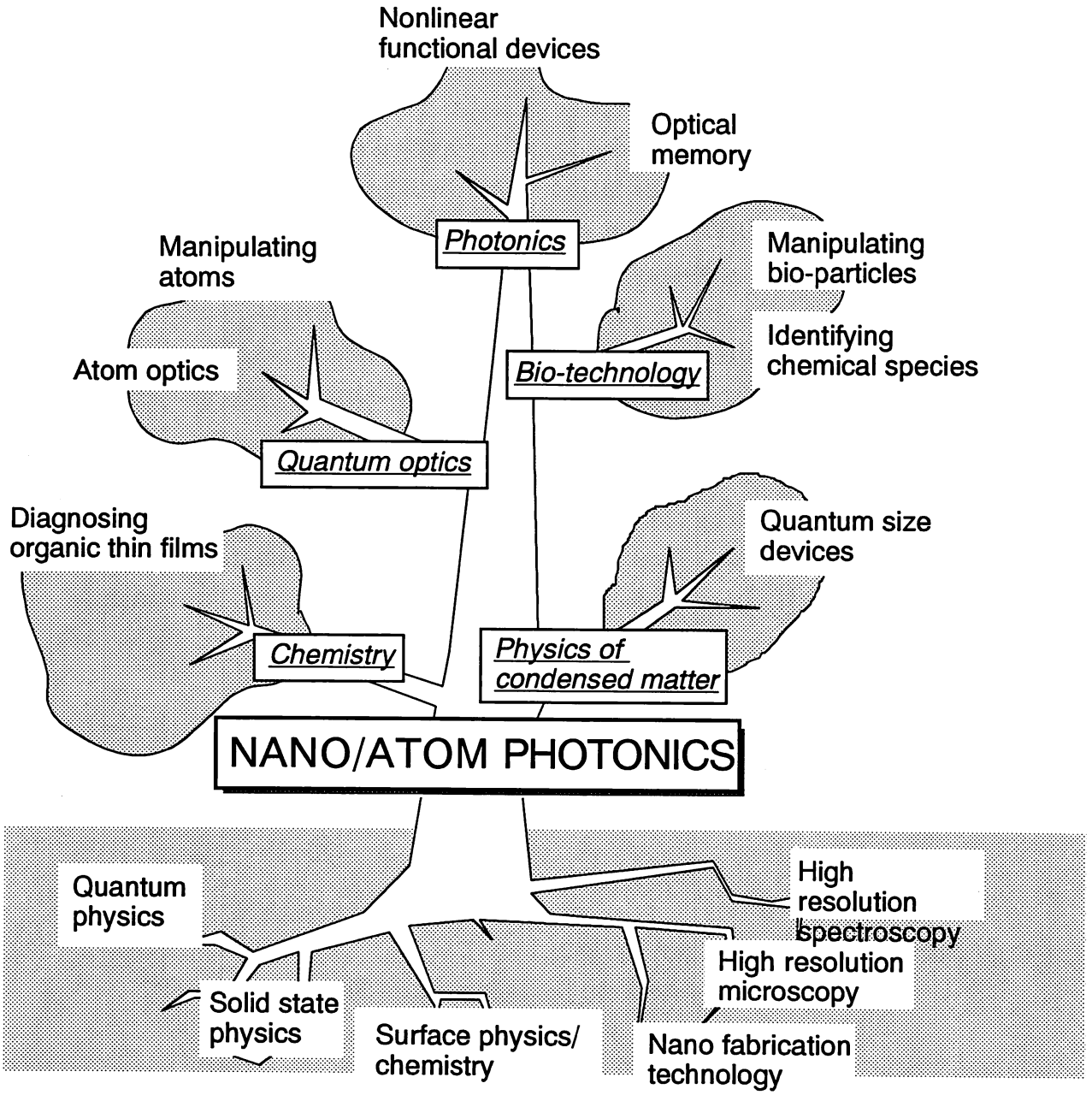

Nano/atom photonic tree with its roots and leaves covering a wide range of fields

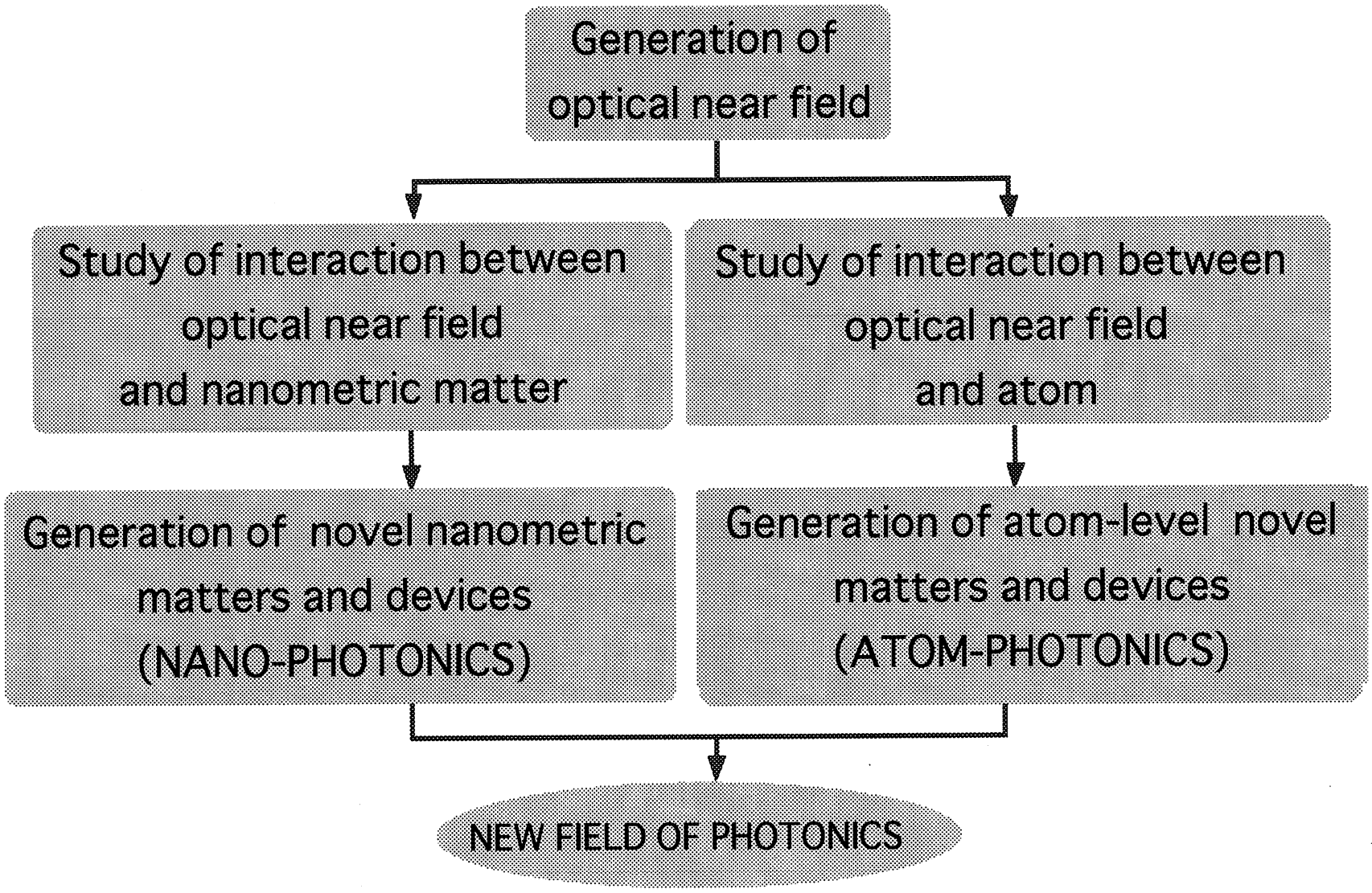
Generation of optical near field
Study of interaction between optical near field and nanometric matter
Study of interaction between optical near field and atom
Generation of novel nanometric matters and devices (NANO-PHOTONICS)
Generation of atom-level novel matters and devices (ATOM-PHOTONICS)
NEW FIELD OF PHOTONICS

MEMBERS

(From April 1, 1997)

[I] TOKYO INSTITUTE OF TECHNOLOGY

Professor

Motoichi OHTSU[a)]	(Dr. Eng.)

Research Associate

Motonobu KOUROGI[b)]	(Dr. Eng.)

Graduate Students (Doctor Candidates)

Andrei Vasilyevich ZVYAGIN	(M. Sci.)
Kazuhiro IMAI	(M. Eng.)
Keiji SAKAKI	(M. Eng.)
Takuya MATSUMOTO	(M. Eng.)
Vitali Vasilyevich POLONSKI	(M. Sci.)
Takashi YATSUI	(M. Eng.)
Bambang WIDIYATMOKO	(M. Eng.)

Graduate Students (Master Course)

Yoh YAMAMOTO	(B. Eng.)
Kazumi WATANABE	(B. Sci.)
Kouichi OTAKE	(B. Sci.)
Kouichi YAMAGUCHI	(B. Eng.)
Jia-Jun CHEN	(B. Eng.)

Undergraduate Students

Shigeru ISHIMURA
Tsutomu ICHIMURA
Akifumi TAKAMIZAWA

Visiting Scientists

Myung-Bok LEE[c)]	(Dr. Eng.)

Secretaries

Chikako ISHIDA
Kaoru OGURA

a) Also with Kanagawa Academy of Science and Technology
(Director, "Photon Control" Project)
b) Also with Kanagawa Academy of Science and Technology
(Part-time researcher, "Photon Control" Project)
c) Permanent affiliation: National Institute for Adcanced Interdisciplinary
Research, Ministry of Internatoinal Trade and Industry

[II] KANAGAWA ACADEMY OF SCIENCE AND TECHNOLOGY

Full-Time Researchers

Toshiharu SAIKI	(Dr. Eng.)
Shuji MONONOBE	(M. Eng.)
Haruhiko ITO[d]	(Dr. Sci.)
Kazuyoshi KURIHARA	(Dr. Sci.)
Makoto ASHINO	(Dr. Eng.)

Part-Time Researchers

Rajagopalan UMAMAHESWARI	(Dr. Eng.)
Motonobu KOUROGI[e]	(Dr. Eng.)
Hirofumi KADONO[f]	(Dr. Eng.)

Visiting Researchers

Hiroaki FUKUDA[g]	(M. Eng.)
Toshiyasu TADOKORO[h]	(B. Sci.)
Yoshihiko NARITA[h]	(M. Sci.)

STA Fellow

Johnathon David WHITE	(Ph.D.)

Secretary

Nobue Lucy WATANABE

d) Also with Precursory Research for Embryonic Science and Technology, Japan Science and Technology Corporatoin
e) Permanent affiliation: Tokyo Institute of Technology
f) Permanent affiliation: Saitama University
g) Permanent affiliation: RICOH Corporation
h) Permanent affiliation: JASCO Corporation

LIST OF PAPERS

[(pp.XX-XX; pages in this issue of the COLLECTED PAPERS]

[I] PAPERS IN NANO/ATOM PHOTONICS

[I-1] ATOM PHOTONICS

(a) Journal Papers

(b) International Conferences

Lasers and Electro-Optics (CLEO/Pacific Rim '97), paper number TuI5, 14-18 July, 1997, Makuhari, Japan, pp.29-30

(pp.17-18)

[4] H. Ito, K. Sakaki, and M. Ohtsu, "Evanescent light guiding in hollow optical fibers for atom deposition", Technical Digest, Quantum Electronics and Laser Science Conference (QELS'97), paper number QWH4, 18-23 May, 1997, Baltimore, USA, pp.126-127

(pp.19-20)

[5] M. Ohtsu, "Atom manipulation by optical near-field", Abstract, Scanning Microscopy 1997 Meeting, paper number Wed.5, 10-15 May, 1997, Chicago, USA **[Review presentation]**

(p.21)

[6] M. Ohtsu, H. Ito, and K. Sakaki, "Guiding atoms by optical near-field and manipulation for atomic-level deposition", Abstract, European Workshop on Microtechnology and Scanning Probe Microscopy, 7-9 April, 1997, Mainz, Germany **[Invited presentation]**

(pp.22-23)

[7] H. Ito, K. Sakaki, W. Jhe, and M. Ohtsu, "Atom guidance using evanescent waves in small hollow optical fibers and its applications", Proceedings, Atom Optics, SPIE, vol.2995, 10-12 February, 1997, San Jose, USA, pp.138-145

(pp.24-31)

[8] M. Ohtsu, "Atom guidance and manipulation by near field optics", Abstract, Tsukuba Workshop on Scanning Probe-based Nanoelectronics(SP-Nano'96), 19-20 December, 1996, Tsukuba, Japan, pp.13-14
[Invited presentation]

(pp.32-33)

[I-2] NANO PHOTONICS

(a) Journal Papers

[1] N. Saito, F. Sato, K. Takizawa, J. Kusano, H. Okumura, T. Aida, T. Saiki, and M. Ohtsu, "Spatially Resolved Detection of Electroluminescence from Lateral p-n Junctions on GaAs (111)A Patterned Substrates Using a Near-Field Scanning Optical Microscope", Jpn. J. Appl. Phys., vol.36, part 2, no.7B,

July 1997, pp.L896-L898

(pp.34-36)

[2] A. V. Zvyagin, J.D. White, and M. Ohtsu, "Near-field optical microscope image formation: a theoretical and experimental study", Opt. Lett., vol.22, no.13, July 1997, pp.955-957

(pp.37-39)

[3] S. Mononobe and M. Ohtsu, "A Model Based on Geometrical Construction in Designing a Pencil-Shaped Fiber Probe for Near-Field Optics", J. Lightwave Technol., vol.15, no.6, June 1997, pp.1051-1055

(pp.40-44)

[4] M. Naya, R. Micheletto, S. Mononobe, R. Uma Maheswari, and M. Ohtsu, "Near-field optical imaging of flagellar filaments of salmonella in water with optical feedback control", Appl. Opt., vol.36, no.7, March 1997, pp.1681-1683

(pp.45-47)

[5] S. Mononobe, M. Naya, T. Saiki, and M. Ohtsu, "Reproducible fabrication of a fiber probe with a nanometric protrusion for near-field optics", Appl. Opt., vol.36, no.7, 1 March 1997, pp.1496-1500

(pp.48-52)

[6] S.-K. Eah, W. Jhe, T. Saiki, and M. Ohtsu, "Near-field Photoluminescence of Si-doped GaAs", Opt. Rev., vol.3, no.6B, November 1996, pp.450-453

(pp.53-56)

[7] R. Uma Maheswari, S. Mononobe, H. Tatsumi, Y. Katayama, and M. Ohtsu, "Observation of Subcellular Structure of Neurons by an Illumination Mode Near-Field Optical Microscope under an Optical Feedback Control", Opt. Rev., vol.3, no.6B, November 1996, pp.463-467

(pp.57-61)

[8] A. Zvyagin and M. Ohtsu, "Near-field optical microscope for true surface topography: theoretical study", Opt. Commun., vol.133, 1997, pp.328-338

(pp.62-72)

[9] R. Uma Maheswari, S. Mononobe, and M. Ohtsu, "Deducing structural variations of the apex of probes used in near-field optical microscopy through simultaneous measurement of shear force and evanescent intensity", Appl. Opt., vol.35, no.34, December 1996, pp.6740-6743

(pp.73-76)

[10] R. Uma Maheswari, H. Kadono, and M. Ohtsu, "Power spectral analysis

for evaluating optical near-field images of 20 nm gold particles", Opt. Commun., vol.131, 1996, pp.133-142

(pp.77-86)

[11] T. Matsumoto and M. Ohtsu, "Fabrication of a Fiber Probe with a Nanometric Protrusion for Near-Field Optical Microscopy by a Novel Technique of Three-Dimensional Nanophotolithography", J. Lightwave Technol., vol.14, no.10, October 1996, pp.2224-2230

(pp.87-93)

[12] S. Mononobe and M. Ohtsu, "Fabrication of a Pencil-Shaped Fiber Probe for Near-Field Optics by Selective Chemical Etching", J. Lightwave Technol., vol.14, no.10, October 1996, pp.2231-2235

(pp.94-98)

(b) International Conferences

[1] T. Saiki, Y. Yokoyama, K. Nishi, and M. Ohtsu, "Near-field optical microscopy and imaging of single quantum dots", Technical Digest, The Pacific Rim Conference on Lasers and Electro-Optics (CLEO/Pacific Rim '97), paper number TuI2, 14-18 July, 1997, Makuhari, Japan, pp.27-28

(pp.99-100)

[2] T. Yatsui, M. Kourogi, and M. Ohtsu, "Enhancing throughput over 30 times by an asymmetric fiber probe for near-field optics", Technical Digest, The Pacific Rim Conference on Lasers and Electro-Optics (CLEO/Pacific Rim '97), paper number TuI3, 14-18 July, 1997, Makuhari, Japan, p.28

(p.101)

[3] M.B. Lee, T. Nakano, T. Yatsui, M. Kourogi, K. Tsutsui, N. Atoda, and M. Ohtsu, "Fabrication of Si planar apertured array for high speed near-field optical storage and readout", Technical Digest, The Pacific Rim Conference on Lasers and Electro-Optics (CLEO/Pacific Rim '97), paper number WL2, 14-18 July, 1997, Makuhari, Japan, pp. 91-92

(pp.102-103)

[4] K. Kurihara and M. Ohtsu, "Fabrication of functional probes for near-field optical microscopy", Technical Digest, The Pacific Rim Conference on Lasers and Electro-Optics (CLEO/Pacific Rim '97), paper number ThK3, 14-18 July, 1997, Makuhari, Japan, pp.148-149

(pp.104-105)

[5] S. Mononobe, T. Saiki, and M. Ohtsu, "Fabrication of a triple tapered fiber probe for near-field optical spectroscopy in an ultraviolet region by selective etching of a multistep index fiber", Technical Digest, The Pacific Rim Conference on Lasers and Electro-Optics (CLEO/Pacific Rim '97), paper number P29, 14-18 July, 1997, Makuhari, Japan, pp.169-170

(pp.106-107)

[6] J.D. White, A. Zvyagin, A. Uchida, S. Hisanaga, H. Tatsumi, Y. Katayama, and M. Ohtsu, "Application of the near-field optical microscope to the imaging of non-labelled microtubules and comparison with other techniques", Technical Digest, The Pacific Rim Conference on Lasers and Electro-Optics (CLEO/Pacific Rim '97), paper number ThR2, 14-18 July, 1997, Makuhari, Japan, pp.242-243

(pp.108-109)

[7] M. Ashino, Y. Yamamoto, and M. Ohtsu, "Direct observation of surface plasmon interference using a near-field optical microscope", Technical Digest, The Pacific Rim Conference on Lasers and Electro-Optics (CLEO/Pacific Rim '97), paper number FJ2, 14-18 July, 1997, Makuhari, Japan, p.272

(p.110)

[8] A. Zvyagin, J. D. White, and M. Ohtsu, "Near-field optical microscope image formation: theoretical and experimental study", Technical Digest, The Pacific Rim Conference on Lasers and Electro-Optics (CLEO/Pacific Rim '97), paper number FV2, 14-18 July, 1997, Makuhari, Japan, pp.305-306

(pp.111-112)

[9] R. Uma Maheswari, S. Takehara, S. Mononobe, G.H. Lee, M. Yoshimoto, H. Koinuma, and M. Ohtsu, "Near field optical imaging of an atomic sapphire step and nanometric lithium niobate crystals under the absence of shear force feedback", Technical Digest, The Pacific Rim Conference on Lasers and Electro-Optics (CLEO/Pacific Rim '97), paper number FV3, 14-18 July, 1997, Makuhari, Japan, p. 306

(p.113)

[10] M. Ohtsu, "Diagnosing Electronic/Photonic Devices and Materials by Near-field Optical Technique", Technical Digest, The 16th Electronic Materials Symposium (EMS'97), paper number H1, 9-11 July, 1997, Osaka, Japan, pp.193-196 **[Invited presentation]**

(pp.114-117)

[11] M. Ohtsu, "Near Field Optical Technology toward Nano/Atom

Photonics", Technical Digest, 1997 International Microprocesses and Nanotechnology Conference (MNC), paper number 8A-1-1, 7-10 July, 1997, Nagoya, Japan, pp.6-7 **[Invited presentation]**

(pp.118-119)

[12] M. Ohtsu, "Near-field Optical Technology for Nano/Atom Photonics", Abstracts, France-Japan Workshop; from Nano to Macroscale science and technology through Microsystems (N2M'97), paper number 2, 21-23 May, 1997, Tokyo, Japan **[Invited presentation]**

(pp.120-125)

[13] J.D. White, A. Zvyagin, M. Ohtsu, "Application of the near field optical microscope to the imaging of non-labelled microtubules", Abstract, The Third Hamamatsu International Symposium on Biophotonics: Molecular Communication in Cellular Physiology, poster paper, 19-21 February, 1997, Hamamatsu, Japan

(p.126)

[14] M. Ohtsu, T. Saiki, S. Mononobe, S. Koshihara, K. Ebihara, K. Obata, T. Miyazawa, M. Kira, M. Yoshimoto, T. Maeda, T. Ohnishi, K. Yoshida, and H. Koinuma, "Near-field ultraviolet photoluminescence study of one-dimensional electronic structures of polisilanes", European Workshop on Microtechnology and Scanning Probe Microscopy, 7-9 April, 1997, Mainz, Germany

(pp.127-128)

[15] M. Ohtsu, R. Uma Maheswari, R. Micheletto, S. Takehara, and S. Mononobe, "Near-field optical images of atomic step on an α-Al_2O_3 plate and nanometric $LiNbO_3$ crystals without shear force feedback", European Workshop on Microtechnology and Scanning Probe Microscopy, 7-9 April, 1997, Mainz, Germany

(pp.129-130)

[16] M. Ohtsu, T. Yatsui, M. Kourogi, S. Mononobe, T. Saiki, M.B. Lee., K. Tsutui, and N. Atoda, European Workshop on Microtechnology and Scanning Probe Microscopy, 7-9 April, 1997, Mainz, Germany

(pp.131-132)

[I-3] REVIEW PAPERS

[1] M. Ohtsu, "Present and future of near-field optical microscope", Science

and Machine, vol.49, no.5, May 1997, pp.529-535
【大津元一、「近接場光学顕微鏡の現状と将来」、機械の研究、第４９巻、第５号、１９９７年５月、pp.529-535】

(pp.133-139)

[2] T. Saiki and M. Ohtsu, "Diagnosing spectroscopic properties of semiconductor materials by near field optical microscopy", Molecular Electronics and Bioelectronics, vol.8, no.1, Februaray 1997, pp.17-27
【斎木敏治、大津元一、「近接場光学顕微鏡による半導体試料の分光観察」、応用物理学会、有機分子・バイオエレクトロニクス分科会　会誌、第８巻、第１号、１９９７年２月、pp.17-27】

(pp.140-150)

[3] H. Ito and M. Ohtsu, "Optical tunnel for guiding atoms - Control of atoms by evanescent light -", Chemistry Today, no.311, February 1997, pp.49-55
【伊藤治彦、大津元一、「原子を導く光のトンネル　－エバネッセント光による原子の制御－」、現代化学、通巻３１１号、１９９７年２月、pp.49-55】

(pp.151-157)

[4] M. Ohtsu, "Realizing Ultrahigh Resolution in a Near-field Optical Microscope", Journal of The Surface Science Society of Japan, vol.18, no.1, January 1997, pp.55-57
【大津元一、「近接場光学顕微鏡でどこまで高分解能が得られるか？（２）」、表面科学、第１８巻、第１号、１９９７年１月、pp.55-57】

(pp.158-160)

[5] M. Ohtsu, "Present status and future trends of near-field optical microscopy", Ultra Precision, vol.6, December 1996, pp.38-44
【大津元一、「近接場光学顕微鏡の現状と将来」、超精密、第６巻、１９９６年１２月、pp.38-44】

(pp.161-167)

[6] M. Ohtsu, "Realizing Ultrahigh Resolution in a Near-field Optical Microscope", Journal of The Surface Science Society of Japan, vol.17, no.12, December 1996, pp.771-774
【大津元一、「近接場光学顕微鏡でどこまで高分解能が得られるか？（１）」、表面科学、第１７巻、第１２号、１９９６年１２月、pp.771-774】

(pp.168-171)

[7] M. Ohtsu, "Ultra-High Density Optical Storage by Near-Field Optical Technique", The Journal of the Institute of Electronics, Information and Communication Engineers, vol.79, no.11, November 1996, pp.1160-1164

【大津元一、「近接場光学による超高密度光メモリ」、電子情報通信学会誌、第７９巻、第１１号、１９９６年１１月、pp.1160-1164】

(pp.172-176)

[II] PAPERS IN OTHER FIELDS

(a) Journal Papers

[1] S. Sayama and M. Ohtsu, "Tunable UV CW generation by frequency tripling of a Ti:sapphire laser", Opt. Commun., vol.137, 1997, pp.295-298

(pp.177-180)

[2] T. Fujii, T. Nayuki, K. Nemoto, M. Kozuma, M. Kourogi, and M. Ohtsu, "Accurate Frequency Control of External-Cavity Laser Diode by Sideband Locking Technique", Jpn. J. Appl. Phys., vol.35, part 1, no.12A, December 1996, pp.6090-6094

(pp.181-185)

[3] M. Kourogi, T. Enami, and M. Ohtsu, "A Coupled-Cavity Monolithic Optical Frequency Comb Generator", IEEE Photonics Technol. Lett., vol.8, no.12, December 1996, pp.1698-1700

(pp.186-188)

[4] T. Saitoh, M. Kourogi, and M. Ohtsu, "An Optical Frequency Synthesizer Using a Waveguide-Type Optical Frequency Comb Generator at 1.5-μ m Wavelength", IEEE Photonics Technol. Lett., vol.8, no.11, November 1996, pp.1543-1545

(pp.189-191)

[5] T. Saitoh, M. Kourogi, and M. Ohtsu, "Expansion of Span-Width of an Optical Frequency Comb Using a Higher Harmonic Wave Modulation", IEEE Photonics Technol. Lett., vol.8, no.10, October 1996, pp.1379-1381

(pp.192-194)

(b) International Conferences

[1] K. Imai, M. Kourogi, and M. Ohtsu, "47THz span optical frequency comb generation by self-phase modulation in an optical fiber", Technical Digest, The Pacific Rim Conference on Lasers and Electro-Optics (CLEO/Pacific Rim '97), paper number ThA1, 14-18 July, 1997, Makuhari, Japan, p.113

(p.195)

[III] PRESENTED PH.D THESIS

[1] M. Kozuma, "Observation and control of ultra-cold atomic de-Broglie wave dynamics in an optical lattice", January 1997

[I] PAPERS IN NANO/ATOM PHOTONICS

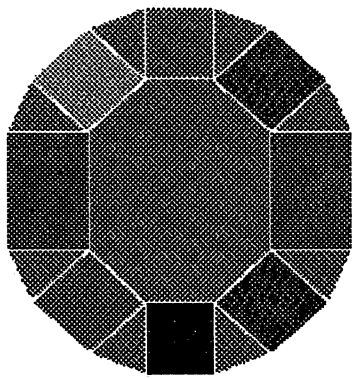

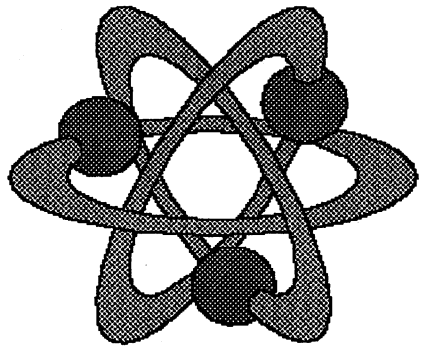

[I-1] ATOM PHOTONICS

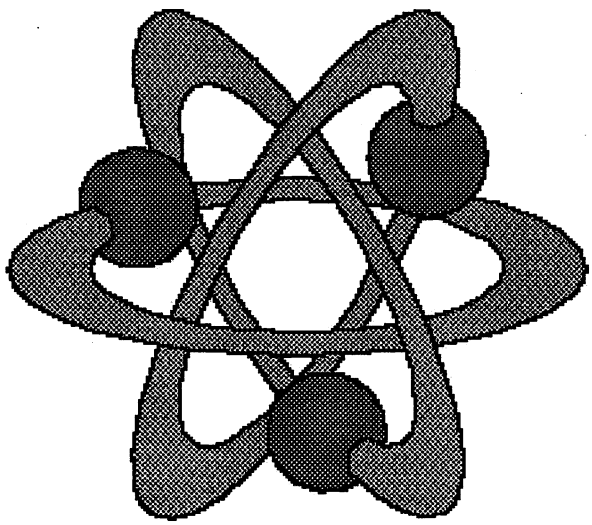

Atomic funnel with evanescent light

H. Ito,[1,2,*] K. Sakaki,[3] W. Jhe,[4] and M. Ohtsu[2,3]
[1]*PRESTO, Japan Science and Technology Corporation, Kawaguchi Center Building, 4-1-8 Honcho, Kawaguchi 332, Japan*
[2]*Kanagawa Academy of Science and Technology, KSP East, 3-2-1 Sakado, Takatsu-ku, Kawasaki 213, Japan*[†]
[3]*Interdisciplinary Graduate School of Science and Engineering, Tokyo Institute of Technology, 4259 Nagatsuta, Midori-ku, Yokohama 226, Japan*
[4]Department of Physics, Seoul National University, Seoul 151-742, Korea
(Received 6 December 1996)

We propose an atomic funnel composed of an evanescent-light mirror produced in a conical hollow prism. The funneling of cold Rb atoms released from a magneto-optical trap is simulated in the scheme of the evanescent-light-induced Sisyphus cooling for compensating the heating by gravity. A geometric method of the conversion of a Gaussian light beam into a doughnut-shaped light beam suitable for the atomic funnel is also experimentally demonstrated by means of a double-cone prism. Under the assumption of a proper optical intensity distribution over the inner surface of a specific conical hollow prism, the Monte Carlo simulation including the van der Waals interaction shows that a half of the released Rb atoms can be collected and the mean temperature of the collected atoms is low enough for the application to be guided with a bent hollow optical fiber. [S1050-2947(97)03007-2]

PACS number(s): 32.80.Pj, 42.50.Vk

I. INTRODUCTION

Cold atoms are expected to be applied to studies on quantum-mechanical or quantum-optical phenomena, for example, the atom laser [1], the Aharonov-Casher effect [2,3], and the cavity quantum-electrodynamic (QED) effect including the Casimir-Polder force [4–6]. Most of the interesting experiments require the precise control of atomic motion. For this purpose, we have recently demonstrated the guiding of thermal atoms through a micron-sized hollow optical fiber escorted by blue-detuned evanescent light [7]. A similar experiment has been made with a larger hollow glass capillary [8]. The evanescent light is an optical near field localized in the region below a wavelength from the surface. Moreover, in contrast to propagating light, the evanescent light has the advantage of not being affected by diffraction [9]. The atom-guidance technique with evanescent light, therefore, has the possibility of manipulating cold atoms in the subwavelength region, or even beyond the diffraction limit determined by the wavelength used. The atom-guidance technique will be improved more if a bent hollow fiber is used [10].

In our previous work [7], we introduced a collimated thermal atomic beam into a straight hollow fiber and obtained a high guiding efficiency. The scheme with a thermal atomic beam, however, is limited in the use of the bent hollow fiber because the minimum value of the radius of curvature at which atoms can be guided is determined by the repulsive optical potential produced in the hollow region against the transverse kinetic energy of atoms approaching the inner wall [11]. The use of cold atoms can considerably raise the limitation to the radius of curvature. Recently, atomic holography [12], lithography, and deposition [13–16] with methods of atom optics have attracted a lot of experimental attention. The evanescent-light guiding of cold atoms with bent hollow fibers will be useful as a form of optical atomic deposition or lithography in which arbitrary patterns can be produced with nanometric spatial accuracy. The advanced atom-guidance technique enables one to create atomic-level matter such as quantum dots under the precise control of the deposition rate [17].

A dense ensemble of cold atoms can be produced at the center of a magneto-optical trap (MOT) [18]. However, when the MOT is turned off, the cold atoms divergently fall according to each initial momentum. In addition, they are extremely accelerated by gravity from the fall within several millimeters. As a result, many cold atoms are lost in the coupling to the micron-sized hollow fiber placed below the MOT. In this paper, to overcome this difficulty, we present a scheme using an atomic funnel with blue-detuned evanescent light to efficiently collect cold atoms released from an MOT. In contrast to the wire funnel [19] or the two-dimensional (2D) MOT funnel [20], the one proposed here has a mechanism of recooling the accelerated atoms: the evanescent-light-induced Sisyphus cooling [21,22] arises inside the funnel with a weak pumping light so that the heating by gravity is compensated for well enough. This atomic funnel, therefore, converts a cold but spatially extended sample of atoms from an MOT to a well-collimated cold atomic beam. Thus, the attachment of the funnel to the hollow fiber greatly increases the coupling efficiency of the cold atoms.

The atomic funnel is based on the near-resonant dipole interaction between atoms and evanescent light. Because of the frequency-dispersion property, the dipole force and then the optical potential become repulsive when the frequency of the laser producing the evanescent light is higher than the atomic resonant frequency, which is called blue detuning. Figure 1 shows the schematic diagram of the atomic funnel composed of a conical hollow prism with a small hole at the bottom. In order to induce the evanescent-light atomic mirror [23,24] over the inner surface, we irradiate the hollow coni-

*Corresponding author.
[†]Corresponding address.

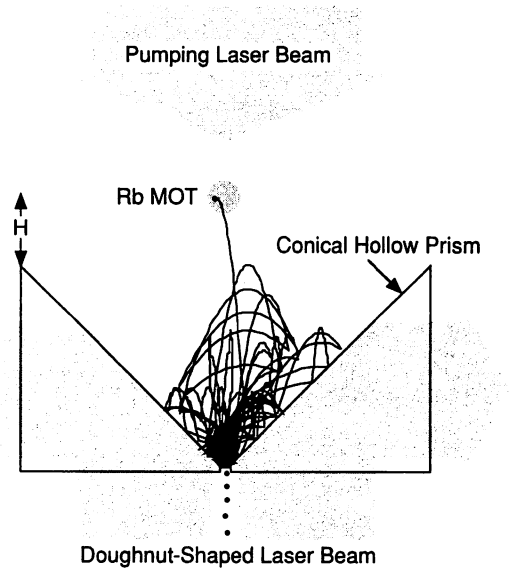

FIG. 1. Sketch of an atomic funnel to cellect cold atoms. A doughnut-shaped laser beam is shone upward to induce an evanescent-light mirror over the inner surface of a conical hollow prism, avoiding the heating of atorns coming out of the exit hole. An additional pumping laser beam is shone downward to recool the atoms accelerated by gravity. A cross-sectional trajectory of a ^{85}Rb atom randomly sampled from a Maxwell-Boltzmann distribution with a temperature of 10 μK is also shown, where H indicates the height of the center of an MOT measured above the open face of a conical hollow prism.

cal prism upwardly with a laser beam. Here, to avoid heating effects on the atoms coming out of the bottom, we use a doughnut-shaped light beam. Moreover, to compensate for the heating of the cold atoms by gravity, according to Ref. [21], we shine a weak pumping laser beam downward. If the potential barrier generated over the inner surface via total reflection of the doughnut-shaped laser beam exceeds the atomic kinetic energy, the atoms approaching the inner surface can be reflected without hitting the surface. Then the recooled atoms are sent out of the exit hole after bouncing off the optical potential many times.

In the next section, we introduce a geometric method of producing a doughnut-shaped laser beam with high efficiency in a simple way. In Sec. III, the total potential to reflect Rb atoms is presented including the van der Waals cavity potential. In Sec. IV, we perform Monte Carlo simulation on an atomic funnel assuming proper parameters. Finally, we discuss the collected fraction, the hit fraction, and the escaped fraction of the cold Rb atoms based on the results obtained from the simulation. In addition, to indicate the cooling effects, we estimate the mean momentum of the collected Rb atoms.

Figure 1 also shows a cross-sectional trajectory of a ^{85}Rb atom released from an MOT with a temperature of 10 μK, which is obtained from the 3D Monte Carlo simulation. Here, we assume a conical hollow prism with a height of 4 mm and an exit hole whose diameter is 0.1 mm. Note that the conical hollow prism is chosen such that the collection efficiency becomes high under feasible experimental conditions.

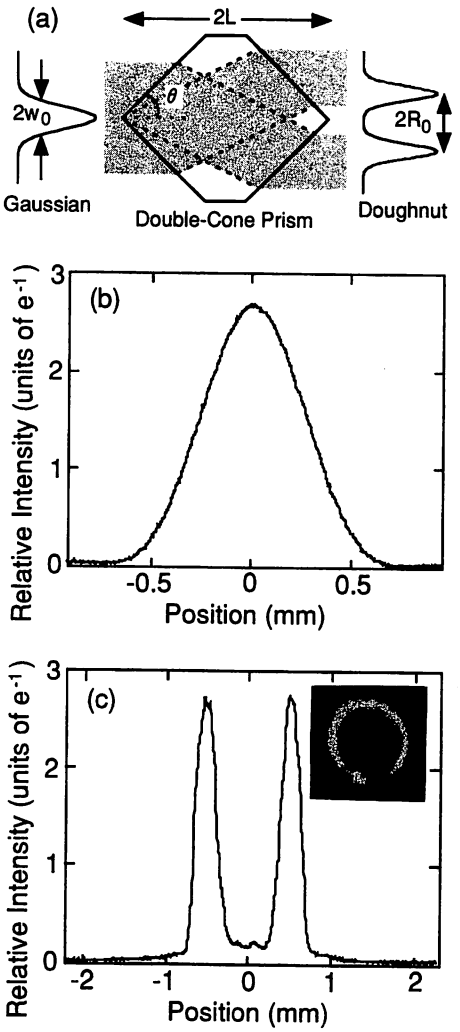

FIG. 2. (a) Conversion of a Gaussian light beam into a doughnut-shaped light beam with a double-cone prism. (b) Relative intensity profile of a Gaussian light beam with a waist $2w_0 = 0.7$ mm from a He-Ne laser. (c) Relative intensity profile of a doughnut-shaped light beam converted by means of a double-cone prism with a length $2L = 4.25$ mm and a full apex angle $2\theta = 90°$. The outer and inner diameters are 1.4 mm and 0.6 mm at a value e^{-1} times the maximum intensity, respectively. The inset picture shows a cross-sectional image of the doughnut-shaped light beam.

II. DOUGHNUT-BEAM CONVERSION

The conversion of a Gaussian light beam into a doughnut-shaped light beam has been made with holographic techniques [25,26]. In spite of the elaborate method, the conversion efficiency into the doughnut TEM_{01}^{*} mode [27] is not necessarily high because it is normally accompanied by higher modes. In this section, we study a geometric method using a double-cone prism. The conversion efficiency is approximately 100%. Moreover, the exact doughnut TEM_{01}^{*} mode is not necessary for the atomic funnel considered here. This simple method, therefore, is useful for generating an evanescent field that is intense enough to reflect atoms over a wide range of the inner surface under feasible experimental conditions. Figure 2(a) schematically explains the conversion mechanism through a double-cone prism: a Gaussian laser beam is divided into two paths by the first refraction at the

apex of the prism, and then a nondivergent doughnut-shaped laser beam appears from the other side after the second refraction.

The intensity $I_g(y,z)$ of a TEM_{00} Gaussian light beam with a power P_0, a waist $2w_0$, and a wavelength λ is written as [28]

$$I_g(y,z)=\frac{2P_0}{\pi w(z)^2}\exp\left\{-\frac{2y^2}{w(z)^2}\right\}, \tag{1}$$

where the z axis indicates the direction in which the light beam propagates and the y axis indicates the direction perpendicular to the z axis. The beam waist $2w(z)$ at a position z and the characteristic length z_0 are given by

$$w(z)=w_0\sqrt{1+\frac{z^2}{z_0^2}}, \tag{2}$$

$$z_0=\frac{\pi}{\lambda}w_0^2, \tag{3}$$

respectively.

Let us consider the conversion into a doughnut-shaped light beam through a double-cone prism with a length $2L$, a full apex angle 2θ, and a refractive index n. From the simple analysis with ray optics, the intensity $I_d(y,z)$ of the doughnut-shaped light beam can be approximately expressed as the sum of the intensities $I_{\pm}(y,z)$ of two modified Gaussian light beams:

$$I_d(y,z)=I_+(y,z)+I_-(y,z), \tag{4}$$

where

$$I_{\pm}(y,z)=\frac{P_0}{\pi w_{\pm}(y,z)^2}\exp\left\{-\frac{2(y\mp R_0)^2}{w_{\pm}(y,z)^2}\right\}. \tag{5}$$

The waists $2w_{\pm}(y,z)$ of the two modified Gaussian light beams at a coordinate (y,z) are given by

$$w_{\pm}(y,z)=w_0\sqrt{1+\frac{\{z+(y\mp R_0)/\tan\theta\}^2}{z_0^2}}. \tag{6}$$

In addition, the ring diameter $2R_0$, which is defined in Fig. 2(a), between the two peaks of the doughnut-shaped light beam is determined by the length L and the angle θ as

$$R_0=L\sin 2\theta\left(1-\frac{\sin\theta}{\sqrt{n^2-\cos^2\theta}}\right). \tag{7}$$

We have demonstrated the conversion by means of a double-cone prism with a length $2L=4.3$ mm and a full apex angle $2\theta=90$ °. Here, as the source of the Gaussian light beam, we use a He-Ne laser with a beam waist $2w_0=0.7$ mm, whose relative intensity profile is shown in Fig. 2(b). Fig. 2(c) shows the relative intensity profile and the cross-sectional image of a doughnut-shaped light beam converted from the Gaussian light beam. The inner and outer diameters of the doughnut-shaped light beam are 0.6 and 1.4 mm at a value e^{-1} times the maximum intensity, respectively. The ring diameter $2R_0=1.0$ mm is in good agreement with that obtained from Eq. (7). This conversion method will also be useful for experiments such as the dark MOT [29].

III. OPTICAL AND CAVITY POTENTIALS

The atomic states in the evanescent field can be described by the dressed-atom picture. We assume that the dipole interaction between a ^{85}Rb atom and a near-resonant evanescent light with a photon number N alters the two hyperfine ground states $|F=2, N\rangle$ and $|F=3, N\rangle$ into the two dressed states $|1, N-1\rangle$ and $|2, N-1\rangle$, respectively. In the dressed-atom picture, the optical potential is equal to the light shift of the ground state.

To compensate the heating of cold atoms released from an MOT by gravity, we apply the technique of evanescent-light-induced Sisyphus cooling [21,22] to the atomic funnel. If the frequency of the evanescent light is blue detuned for both of the $5S$ hyperfine ground states, the light shift of the $F=2$ lower ground state becomes larger than that of the $F=3$ upper ground state, because the light shift at a given light intensity is in inverse proportion to the detuning $\Delta=\omega_L-\omega_0$ between the laser frequency ω_L and the atomic resonant frequency ω_0. Here, we omit the small Doppler shift of cold atoms. When a ^{85}Rb atom in the lower ground dressed state $|1, N\rangle$ spontaneously decays into the upper ground dressed state $|2, N-1\rangle$ in the process of reflection, the atom loses its kinetic energy by the amount of the difference between the two light-shift energies. Soon after the reflection, the atom is repumped to the $F=2$ lower ground state by a weak pumping laser beam, so that the energy-loss process becomes a cooling cycle.

We consider the optical potential on the ^{85}Rb atom in the $5S$ ground state. At a distance r from the position x on the inner surface of a conical hollow prism with a refractive index n_p and a slope angle α, the evanescent light with the intensity $I_d(x,r)$ produces the optical potential $U_{opt}(x,r)$ approximately given by [21,22]

$$U_{opt}(x,r)=\frac{1}{12}\frac{\hbar\Gamma^2}{\Delta}\frac{I_d(x,r)}{I_s}\exp\left(-\frac{2r}{\eta}\right), \tag{8}$$

where Γ and I_s are the natural linewidth ($=2\pi\times5.9$ MHz) and the saturation intensity ($=1.6$ mW/cm^2) of the Rb D_2 line with the wavelength $\lambda=780$ nm, respectively. In addition, the decay length η of the evanescent light is given by [30]

$$\eta=\frac{\lambda}{2\pi\sqrt{n_p^2\sin^2\alpha-1}}=0.7\lambda. \tag{9}$$

On the other hand, the van der Waals interaction arises between a Rb atom and the dielectric wall in the vicinity of the inner surface [24,31]. The attractive cavity potential produced by the van der Waals force can be written in a simple form as [32]

$$U_{vdW}(r)=-\frac{3}{4f}\frac{n_p^2-1}{n_p^2+1}\frac{\hbar\Gamma}{(kr)^3}, \tag{10}$$

where f and k are the oscillator strength ($=0.67$) and the wave number of the Rb D_2 line, respectively. The total po-

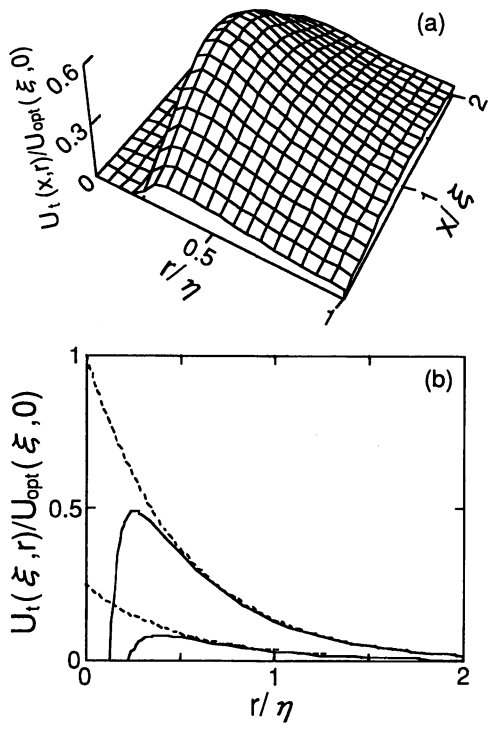

FIG. 3. Total potential $U_t(x,r)$ over the inner surface of a conical hollow prism with a height of 4 mm and an exit hole of 0.1 mm, where x is the distance from the center of the exit hole along the slope and r is the vertical distance from the inner surface: (a) map of the total potential $U_t(x,r)$ normalized to the maximum optical potential $U_{opt}(\xi,0)$ on the ^{85}Rb atoms in the lower ground state and (b) cross-sectional profile of the total potential $U_t(\xi,r)$ at the position $x=\xi$ normalized to $U_{opt}(\xi,0)$, where ξ indicates the position where the optical potential is maximum on the inner surface. In (b), the upper solid and broken curves show the total and optical potentials in the lower ground state, while the lower solid and broken curves show the total and optical potentials in the upper ground state, respectively. Here, the intensity distribution of the evanescent light is generated by a doughnut-shaped light beam with a ring diameter $2R_0=4$ mm in the case where the power P_0 is 1 W and the blue detuning Δ is +1 GHz measured from the lower ground state.

tential $U_t(x,r)$, therefore, is the sum of the repulsive optical potential $U_{opt}(x,r)$ and the attractive van der Waals cavity potential $U_{vdW}(r)$.

Now, in order to illustrate an atomic funnel with a high collection efficiency, we hereafter assume a specific doughnut-shaped light beam with a ring diameter $2R_0=4$ mm and the conical hollow prism mentioned at the end of Sec. I. The doughnut-shaped light beam can be generated from a Gaussian light beam with a waist $2w_0=4$ mm by means of a proper double-cone prism. We also assume that the conical hollow prism has a slope angle $\alpha=45°$ and a refractive index $n_p=1.45$.

Let us estimate the potential barrier in the case where the power P_0 is 1 W and the blue detuning Δ is +1 GHz measured from the $5S_{1/2}$, $F=2$ lower ground state. Figure 3(a) shows the map of the total potential $U_t(x,r)$ on the ^{85}Rb atoms in the $5S_{1/2}$, $F=2$ lower ground state. The total potential $U_t(x,r)$ is normalized to the maximum optical potential $U_{opt}(\xi,0)$ on the inner surface. Here, we use ξ to denote the position where the optical potential $U_{opt}(x,0)$ on the inner surface is maximum. As shown in Figure 3(a), the evanescent-light atomic mirror is induced over a distance of more than 2ξ along the slope. Moreover, we can estimate that the maximum of the potential barrier is 3.3 mK in terms of temperature.

Figure 3(b), on the other hand, shows the cross-sectional profile of the total potential $U_t(\xi,r)$ and the pure optical potential $U_{opt}(\xi,r)$ on the ^{85}Rb atoms. The upper solid and broken curves show the total and optical potentials in the $5S_{1/2}$, $F=2$ lower ground state, while the lower solid and broken curves show the total and optical potentials in the $5S_{1/2}$, $F=3$ upper ground state, respectively. These potentials are normalized to the maximum optical potential $U_{opt}(\xi,0)$ on the ^{85}Rb atoms in the $5S_{1/2}$, $F=2$ lower ground state. In Figure 3(b), we can see that the attractive van der Waals cavity potential greatly reduces the repulsive optical potential in the vicinity of the inner surface. If the kinetic energy of a ^{85}Rb atom approaching the inner surface is larger than the maximum of the total potential, the atom will cross the potential barrier so that it will hit the surface and then stick there with high probability.

IV. MONTE CARLO SIMULATION

There are some factors in determining the collecting efficiency of the atomic funnel: blue detuning, laser power, the intensity distribution of the evanescent light, the initial temperature of the atomic ensemble, and the release height of cold atoms. In order to examine the dependence of the atomic funnel on these parameters, we have made the Monte Carlo simulation by modifying the procedure given in Ref. [21]. In particular, as mentioned in Sec. III, we introduce the specific doughnut-shaped light beam to induce an evanescent-light mirror suitable for efficiently collecting cold Rb atoms. Furthermore, we take into account the van der Waals cavity potential in the Monte Carlo simulation to estimate the collected fraction, the hit fraction, the escaped fraction, and the mean momentum of collected atoms.

In the process of reflection, two kinds of spontaneous decay, $|1,N\rangle\rightarrow|1,N-1\rangle$ and $|1,N\rangle\rightarrow|2,N-1\rangle$, can occur with the transition probabilities of $\alpha P(v_r)$ and $(1-\alpha)P(v_r)$, respectively. According to Ref. [21], the branching ratio α is 0.74 for the ^{85}Rb D_2 line. We also neglect a transition to the excited dressed-state with a very small probability. For an atom with a mass m and a velocity v_r perpendicular to the inner surface, the probability $P(v_r)$ of the spontaneous emission is given by [33]

$$P(v_r)=1-\exp\left(-\frac{mv_r\eta\Gamma}{\hbar\Delta}\right). \tag{11}$$

To determine which transition takes place in the process of reflection, we first generate a random number having a value between 0 and 1, and then compare it with each transition probability. If the first transition $|1,N\rangle\rightarrow|1,N-1\rangle$ occurs, the small heating energy $(n_p^2+1)E_{re}$ due to the scattering of an evanescent photon is only added to the kinetic energy of the atom, where $E_{re}=(\hbar k)^2/2m$ is the recoil energy. On the other hand, if the second transition $|1,N\rangle\rightarrow|2,N-1\rangle$ occurs, the energy loss ΔK is subtracted

from the kinetic energy, while the small heating energy is added. According to Eqs. (7), (8), and (9) given in Ref. [21], the mean energy loss ΔK per reflection can be estimated from the amount of the difference between the total potentials in the two ground dressed states as

$$\Delta K = -\frac{2}{3}\frac{\delta}{\Delta+\delta}K_r, \tag{12}$$

where K_r and δ are the kinetic energy perpendicular to the inner surface and the hyperfine splitting ($=2\pi\times 3036$ MHz) between the $5S_{1/2}$, $F=2$, and $F=3$ ground states of ^{85}Rb, respectively.

The atom which fell to the upper dressed state $|2, N\rangle$, soon after the reflection, is transferred back to the lower dressed state $|1, N\rangle$ by the weak pumping light tuned to the transition from the $5S_{1/2}$, $F=3$ upper ground state. In this case, since the pumping light beam is shone downward, the additional cooling due to the scattering of the photons of the pumping light occurs to the atom moving upward with a velocity v_z. As a result, the energy change $(-q\hbar k v_z + 2q^2 E_{re})$ is also added to the kinetic energy of the atom, where q ($=1.7$) is the mean number of photons scattered by the ^{85}Rb atom [21].

According to the above procedure, we have simulated the number of the ^{85}Rb atoms coming out of the exit hole with an ensemble of 10^4 atoms which follows a Maxwell-Boltzmann distribution with a mean temperature of 10 μK. We also assume that the center of the MOT is placed at a position $H=1$ mm above the open face of the atomic funnel. Figure 4 shows the collected fraction of the ^{85}Rb atoms released from the MOT with a diameter of 1 mm as a function of time t after the release. The filled circles and the solid curve show the data obtained from the Monte Carlo simulation and the fitting, in the case where the van der Waals cavity potential is taken into account, respectively. From this, we can see that the collected fraction approaches a constant value of 50%. In addition, the distribution area of the cold atomic sample is effectively reduced to 0.01 times as large as that of the MOT. Therefore, if the atomic funnel is applied to the hollow fiber, the efficiency in the loading of the hollow fiber with cold atoms is estimated to be more than 50 times as large as the efficiency without the atomic funnel. The open circles and the broken curve, on the other hand, show the data and the fitting without the van der Waals cavity potential, respectively; the collected fraction reaches 78% at $t=20$ s.

V. DISCUSSIONS

The fitting curves in Fig. 4 are expressed as $C_1\{1-\exp(-C_2 t)\}$, where C_1 and C_2 are constants. In this case, if a multiple loading of the atomic funnel is made, the collection rate can be defined by the asymptotic value C_1 of the collected fraction. For example, the collection rate is estimated to be 0.5Φ atom/s from the solid curve in Fig. 4, where Φ is the number of atoms released from the MOT per second. Thus, the flux of the collected cold atoms results from the multiple loading of the funnel.

Because of large gravitational acceleration, the collecting efficiency of the atomic funnel depends greatly on the release

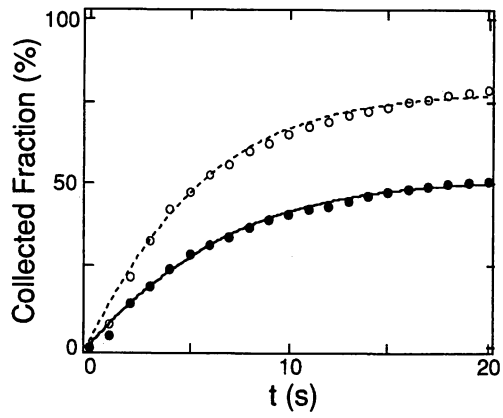

FIG. 4. Temporal change of the collected fraction of the ^{85}Rb atoms released from an MOT with a mean temperature of 10 μK. The Monte Carlo simulation is made with an ensemble of 10^4 atoms under the conditions given in Fig. 3. The filled circles and the solid curve show the data and the fitting in the case where the van der Waals cavity potential is taken into account. The open circles and the broken curve indicate the data and the fitting in the case without the van der Waals cavity potential.

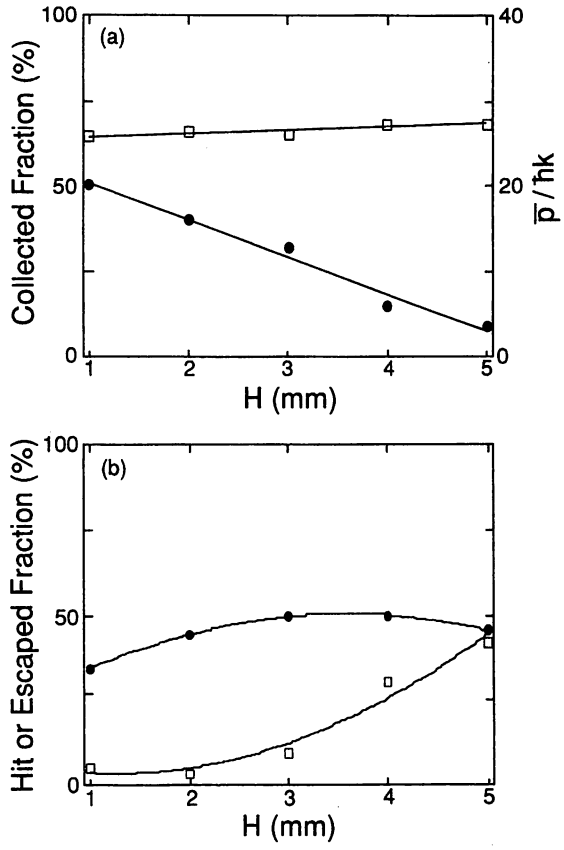

FIG. 5. Dependence of the atomic funnel on the height H: (a) collected fraction (filled circles) and mean momentum (open squares) of the collected ^{85}Rb atoms and (b) hit fraction (filled circles) and escaped fraction (open squares). The mean momentum $\bar{p}$ is normalized to the recoil momentum $\hbar k$. The Monte Carlo simulation is made with an ensemble of 10^4 atoms having a mean temperature of 10 μK.

height of cold atoms. To examine this dependence, we have made a Monte Carlo simulation with an ensemble of 10^4 atoms by changing the height of the MOT. Figure 5(a). shows the results obtained at $t=20$ s as a function of the height H. The filled circles and the open squares show the collected fraction and the mean momentum $\bar{p}$ of the collected ^{85}Rb atoms normalized to the recoil momentum $\hbar k$, respectively. In Fig. 5(a), while the collected fraction decreases from 50% at $H=1$ mm to 9% at $H=5$ mm, the mean momentum is almost constant. When atoms are recooled below a temperature that is specific to the atomic funnel used, they reach the bottom and go out of the funnel. This is the reason why the mean momentum of the collected atoms is almost unchanging. The mean momentum is estimated to be 26 times as large as the recoil momentum $\hbar k$, which corresponds to 80 μK in terms of temperature. Due to a few atoms dropping straight from the MOT, the mean momentum slightly increases with the height H.

A part of the released atoms are lost due to the adherence to the inner surface or the escape from the open face of the funnel. To check whether an atom hits the inner surface in the reflection, we compare the kinetic energy of the atom with the height of the potential barrier when the atom is approaching the inner surface. In the simulation, we assume that, if the kinetic energy is larger than the potential barrier, the atom hits the inner surface without being reflected and then sticks there. The hitting can occur in cases where an atom is in an area where the potential barrier is low or the cooling is not sufficient. In addition, if an atom is transferred to the upper ground state before reflection, the possibility of hitting the inner surface increases because the potential barrier in the upper ground state is poorer than that in the lower ground state as shown in Fig. 3(b). On the other hand, the escape of atoms from the open face shows a tendency to take place at the beginning of the funneling process before the cooling mechanism works. Figure 5(b) shows the hit fraction (filled circles) and the escaped fraction (open squares) obtained at $t=20$ s as a function of the height H. The hit fraction gradually increases with the height up to $H=3$ mm but then begins to decrease. This is because the escaped fraction increases with the height H as shown in Fig. 5(b); in other words, because the number itself of atoms in the funnel decreases with the height H.

As was expected, it follows that as the height where cold atoms are released becomes lower, the collected fraction increases. One of the authors (W.J.) has recently demonstrated that atoms can be trapped inside a pyramidal hollow prism or a conical hollow prism with a single circularly polarized light beam [34]. If an MOT is made inside the atomic funnel with such a technique, the collecting efficiency will be greatly enhanced.

VI. CONCLUSIONS

We have shown the feasibility of an atomic funnel composed of an evanescent-light mirror by Monte Carlo simulations including the van der Waals interaction. Assuming a specific conical hollow prism and a proper optical intensity distribution over the inner surface, we see that half of the ^{85}Rb atoms released from an MOT can be collected under feasible experimental conditions. This indicates that the loading efficiency of the hollow fiber is greatly enhanced. Moreover, in the scheme of the evanescent-light-induced Sisyphus cooling, the temperature of the collected ^{85}Rb atoms is estimated to be low enough that the atoms can be guided in a bent hollow fiber with a radius of curvature of less than 1 cm. The multiple loading of the atomic funnel will give rise to an enhancement of the flux of the collected cold atoms.

The atom-guidance technique using the hollow optical fiber combined with an atomic funnel will be applied to the control of atomic motion with pinpoint accuracy. For example, cold atoms can be guided to a sharpened optical fiber with a nanometric tip [35] and caught by an evanescent field induced on the tip [9]. This opens the possibility of performing a single-atom manipulation, so that the atom-by-atom crystal growth can be realized.

ACKNOWLEDGMENTS

We acknowledge the MATSUO Foundation of Japan for financial support. W.J. is also grateful to the STEPI of Korea for financial support.

[1] M. Holland, K. Burnett, C. Gardiner, J. I. Cirac, and P. Zoller, Phys. Rev. A **54**, R1757 (1996).

[2] Y. Aharonov and A. Casher, Phys. Rev. Lett. **53**, 319 (1984).

[3] K. Sangster, E. A. Hinds, S. M. Barnett, and E. Riis, Phys. Rev. Lett. **71**, 3641 (1993).

[4] H. B. G. Casimir and D. Polder, Phys. Rev. **73**, 360 (1948).

[5] C. I. Sukenic, M. G. Boshier, D. Cho, V. Sandoghdar, and E. A. Hinds, Phys. Rev. Lett. **70**, 560 (1993).

[6] S. K. Lamoreaux, Phys. Rev. Lett. **78**, 5 (1997).

[7] H. Ito, T. Nakata, K. Sakaki, M. Ohtsu, K. I. Lee, and W. Jhe, Phys. Rev. Lett. **76**, 4500 (1996).

[8] M. J. Renn, E. A. Donley, E. A. Cornell, C. E. Wieman, and D. Z. Anderson, Phys. Rev. A **53**, R648 (1996).

[9] M. Ohtsu, S. Jiang, T. Pangaribuan, and M. Kozuma, in *Near Field Optics*, edited by D. W. Pohl and D. Courjon (Kluwer, Dordrecht, 1993), pp. 131–140; M. Ohtsu, J. Lightwave Technol. **13**, 1200 (1995).

[10] M. J. Renn, D. Montgomery, O. Vdovin, D. Z. Anderson, C. E. Wieman, and E. A. Cornell, Phys. Rev. Lett. **75**, 3253 (1995).

[11] M. A. Ol'Shanii, Yu. B. Ovchinnikov, and V. S. Letokhov, Opt. Commun. **98**, 77 (1993).

[12] J. Fujita, M. Morinaga, T. Kishimoto, M. Yasuda, S. Matsui, and F. Shimizu, Nature (London) **380**, 691 (1996); M. Morinaga, M. Yasuda, T. Kishimoto, F. Shimizu, J. Fujita, and S. Matsui, Phys. Rev. Lett. **77**, 802 (1996).

[13] G. Timp, R. E. Behringer, D. M. Tennant, J. E. Cunningham, M. Prentiss, and K. K. Berggren, Phys. Rev. Lett. **69**, 1636 (1992).

[14] J. J. McClelland, R. E. Scholten, E. C. Palm, and R. J. Celotta, Science **262**, 877 (1993).

[15] R. Gupta, J. J. McClelland, Z. J. Jabbour, and R. J. Celotta, Appl. Phys. Lett. **67**, 1378 (1995).

[16] R. W. McGowan, D. M. Giltner, and S. A. Lee, Opt. Lett. **20**, 2535 (1995).

[17] H. Ito, K. Sakaki, M. Ohtsu, and W. Jhe, Appl. Phys. Lett. **70**, 2496 (1997).

[18] E. L. Raab, M. Prentiss, A. Cable, S. Chu, and D. E. Pritchard, Phys. Rev. Lett. **59**, 2631 (1987).

[19] T. B. Swanson, N. J. Silva, S. K. Mayer, J. J. Maki, and D. H. McIntyre, J. Opt. Soc. Am. B **13**, 1833 (1996).

[20] J. Yu, J. Djemaa, P. Nosbaum, and P. Pillet, Opt. Commun. **12**, 136 (1994).

[21] J. Söding, R. Grimm, and Yu. B. Ovchinnikov, Opt. Commun. **119**, 652 (1995).

[22] P. Desbiolles, M. Arndt, P. Szriftgiser, and J. Dalibard, Phys. Rev. A **54**, 4292 (1996).

[23] C. G. Aminoff, A. M. Steane, P. Bouyer, P. Desbiolles, J. Dalibard, and C. Cohen-Tannoudji, Phys. Rev. Lett. **71**, 3083 (1993).

[24] A. Landragin, J.-Y. Courtois, G. Labeyrie, N. Vansteenkiste, C. I. Westbrook, and A. Aspect, Phys. Rev. Lett. **77**, 1464 (1996); A. Landragin, G. Labeyrie, C. Henkel, R. Kaiser, N. Vansteenkiste, C. I. Westbrook, and A. Aspect, Opt. Lett. **21**, 1591 (1996).

[25] H. S. Lee, B. W. Stewart, K. Choi, and H. Fenichel, Phys. Rev. A **49**, 4922 (1994).

[26] K. T. Gahagan and G. A. Swartzlander, Jr., Opt. Lett. **21**, 827 (1996).

[27] G. M. Gallatin and P. L. Gould, J. Opt. Soc. Am. B **8**, 502 (1991).

[28] A. Yariv, *Optical Electronics* (Holt, New York, 1985).

[29] W. Ketterle, K. B. Davis, M. A. Joffe, A. Martin, and D. E. Pritchard, Phys. Rev. Lett. **70**, 2253 (1993).

[30] S. Feron, J. Reinhardt, M. Ducloy, O. Gorceix, S. Nic Chormaic, Ch. Miniatura, J. Robert, J. Baudon, V. Lorent, and H. Haberland, Phys. Rev. A **49**, 4733 (1994).

[31] V. Sandoghdar, C. I. Sukenik, E. A. Hinds, and S. Haroche, Phys. Rev. Lett. **68**, 3432 (1992).

[32] J.-Y. Courtois, J.-M. Courty, and J. Mertz, Phys. Rev. A **53**, 1862 (1996).

[33] M. A. Kasevich, D. S. Weiss, and S. Chu, Opt. Lett. **15**, 607 (1990).

[34] K. I. Lee, J. A. Kim, H. R. Noh, and W. Jhe, Opt. Lett. **21**, 1177 (1996); J. A. Kim, K. I. Lee, H. R. Noh, W. Jhe, and M. Ohtsu, *ibid.* **22**, 117 (1997).

[35] S. Mononobe and M. Ohtsu, J. Lightwave Technol. **14**, 2231 (1996).

Evanescent-light guiding of atoms through hollow optical fiber for optically controlled atomic deposition

H. Ito[b)]
PRESTO, Japan Science and Technology Corporation, Kawaguchi 332, Japan

K. Sakaki and M. Ohtsu[a)]
Interdisciplinary Graduate School of Science and Engineering, Tokyo Institute of Technology, 4259, Nagatsuta, Midori-ku, Yokohama 226, Japan

W. Jhe
Department of Physics, Seoul National University, Seoul 151-742, Korea

(Received 12 December 1996; accepted for publication 14 March 1997)

This work demonstrates that the technique of guiding atoms through hollow optical fiber escorted by evanescent light is useful as a novel scheme of optical atom deposition. To show the feasibility of fabricating micron-sized structures with nanometric depth on a substrate, we measure the spatial distribution of the guided atom flux with a hot-wire detector. Moreover, precise control of the deposition rate is illustrated with a 1.4-μm-hollow fiber via photoionization spectroscopy. The ratio of the guided atom flux relative to the background transmission is enhanced up to 80-fold with a slightly tilted hollow fiber. © *1997 American Institute of Physics.* [S0003-6951(97)03219-1]

Fabrication of submicron-scale structures by means of irradiation of a substrate with atomic vapor flows has been attracting much experimental interest.[1] In particular, optical control of an atomic beam is fascinating for the creation of nanometric matters. For example, it has been demonstrated to form a pattern of parallel lines with a method of atom optics.[2] The optical deposition or lithography with propagating light, however, is limited in spatial accuracy of manipulating atoms, which is determined by the wavelength used, due to the diffraction. In order to create smaller three-dimensional structures such as quantum dots, the precise control of a small number of atoms beyond the diffraction limit is required in the optical deposition or lithography.

Recently, we have shown that atoms could be sent down micron-sized hollow optical fibers escorted by the blue-detuned evanescent light.[3] A similar experiment with a larger glass capillary has been made independently of us.[4] The evanescent light has the advantage of not being affected by the diffraction. This technique, therefore, overcoming the diffraction limit, has the possibility of forming arbitrary patterns and making atomic-level matters. To this goal, we demonstrate here that the guiding of atoms through the small hollow fiber is useful for creating dot-shaped structures with nanometric depth and fine control of the number of atoms.

The guiding scheme is based on the near-resonant dipole interaction between atoms and evanescent light.[5,6] The dipole force becomes repulsive when the frequency ω_L of a guide laser supporting the evanescent light is higher than the atomic resonant frequency, which is called blue detuning. Figure 1 schematically explains the method of guiding atoms in a hollow optical fiber. When the blue-detuned laser beam is coupled to the core transmitting light via the total internal reflection, the evanescent light leaks to the hollow region so that a repulsive optical potential[7] is produced on the inner wall. Provided that the potential barrier exceeds the atomic transverse kinetic energy, the atoms approaching the inner wall can be reflected without hitting the surface. Then the atoms are guided through a long distance without much loss by bouncing off the optical potential many times.

We have measured a flux density of the guided Rb atoms. The experimental setup is similar to that employed in our previous work,[3] except for the detection scheme. A collimated thermal atomic beam containing two stable isotopes ^{85}Rb and ^{87}Rb is introduced into a hollow fiber with a hollow diameter $2a$ of 7 μm. The atoms not entering the hollow region are completely blocked by a pinhole plate placed in front of the fiber such that they are not observed downstream. A guide-light beam from a Ti:sapphire laser (780 nm) is coupled to the 4-μm-thick core around the hollow region. The guided Rb atoms are detected by a channel electron multiplier (CEM) via the surface ionization with a fine hot wire.

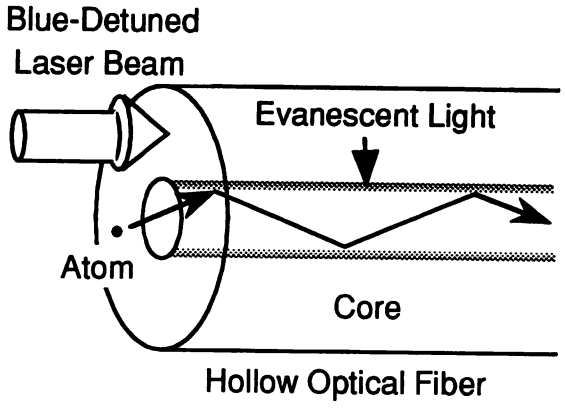

FIG. 1. Sketch of the evanescent-light guiding of atoms in a hollow optical fiber. The guide-laser beam supporting the evanescent light is coupled to the core around the hollow region. Under the blue-detuning condition, the repulsive dipole force from the evanescent light reflects atoms approaching the inner wall.

[a)]Also with Kanagawa Academy of Science and Technology, KSP East, 3-2-1 Sakado, Takatsu-ku, Kawasaki 213, Japan.
[b)]Corresponding author. Electronic mail: haruhiko@net.ksp.or.jp

 0003-6951/97/70(19)/2496/3/$10.00

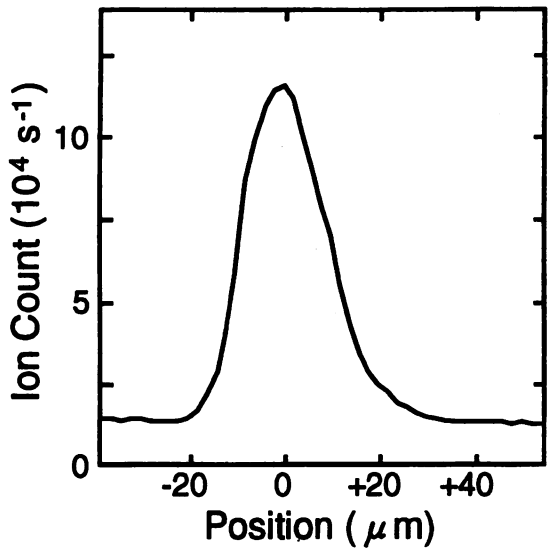

FIG. 2. Spatial distribution of the Rb beam guided through a 7-μm- hollow fiber with a length of 3 cm. The surface-ionization signal is obtained from the scan of the cross section at 12 mm downstream with a 10-μm-wide Pt hot wire. The guide-laser frequency is blue detuned at +3 GHz above the $5S_{1/2}$, $F=3$ upper-ground state of ^{85}Rb.

Figure 2 shows the surface-ionization signal on the spatial distribution of the Rb flux guided over a distance of 3 cm. Here we scan a range over 100 μm at a distance of 12 mm downstream from the exit facet with a Pt hot wire having a diameter of 10 μm. The guide-laser frequency is blue detuned at the optimal value of +3 GHz, which is measured in respect to the $5S_{1/2}$, $F=3$ upper ground state of ^{85}Rb. Note that the ^{85}Rb atoms in the upper ground state are dominant in the atomic beam. From Fig. 2, we obtain the spatial distribution of 20 μm at FWHM. Moreover, taking into account the quantum efficiency of 0.9 on the CEM biased at a voltage of -3 kV and the cross section of the hot wire, we get the guided Rb flux Φ of 1.7×10^5 atom/s measured above the background level.

The mean transverse velocity of the incident Rb beam is estimated to be 20 cm/s in the collimation scheme. On the other hand, considering the detecting position of 12 mm downstream and the mean-longitudinal velocity of 360 m/s, from the spatial distribution, we figure the divergence 2θ of the guided Rb beam to be 1.1 mrad, which leads to the transverse velocity of 19 cm/s. The result implies that the transverse velocity is not changed through the guidance. This is because the dipole-force guiding of atoms is energy conservative when the frequency detuning is large enough that the spontaneous emission per bounce is negligible.

Let us estimate the deposition rate. At a position of x (in units of mm) downstream, the flux density $d(\Phi,x)$ (in units of atom/s μm^2) is given by $d(\Phi,x)=\Phi/\pi(x\theta+a)^2$. From this, assuming the density of 1.53 g/cm^3 for Rb metal, we get the supply rate $\eta(\Phi,x)$ (in units of nm/s) as follows: $\eta(\Phi,x)=3.2\times10^{-7}\cdot\Phi/(x+6.5)^2$. Consequently, in case a substrate is placed at $x=1$ mm, the inverse rate η^{-1} is equal to 17 min/nm. Since the number of Rb atoms not fixed to a substrate can be much reduced by cooling the substrate or processing it with selective etching, the supply rate η can be regarded as the deposition rate.

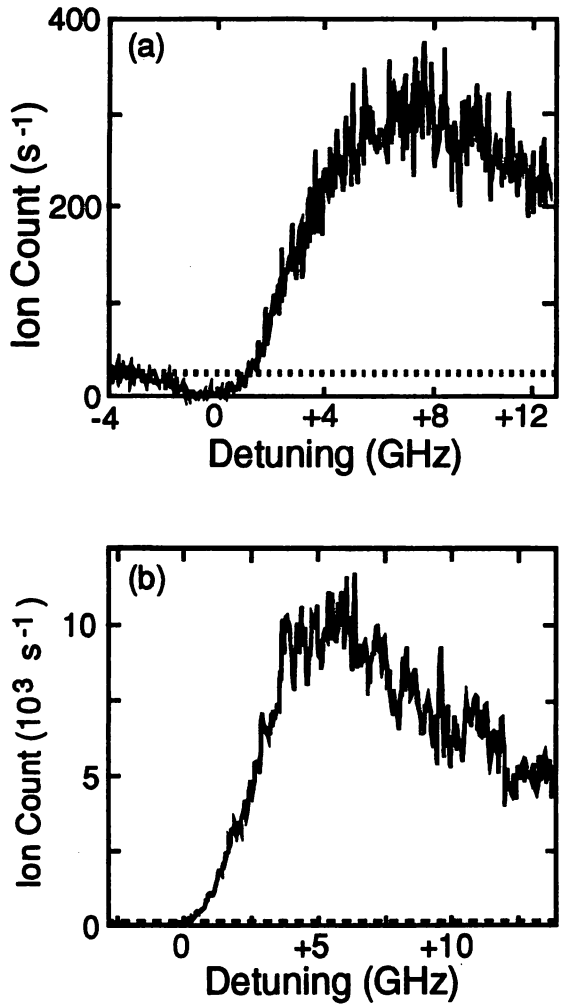

FIG. 3. Two-step photoionization spectra of the guided ^{87}Rb atoms in the $5S_{1/2}$, $F=2$ upper-ground state as a function of the blue detuning not including the Doppler shift: (a) precise control of the guided atom flux with a 1.4-μm-hollow fiber at a lower oven temperature, and (b) 80-fold enhancement of the guided atom flux relative to the background transmission through a 2-μm-hollow fiber tilted slightly. The broken lines show the background flux without the guide light.

The guided atom flux Φ, or the deposition rate η, depends on oven temperature, hollow diameter, guide-laser intensity, and blue detuning. In particular, by changing the blue detuning, one can accurately control the deposition rate. In order to illustrate this, we have made the laser spectroscopy on the guided Rb flux by using the Doppler-free two-step photoionization (PI) with a diode laser tuned to the D_2 line and an Ar-ion laser with a wavelength of 476.5 nm.[3] Figure 3(a) shows the PI spectrum on the ^{87}Rb atoms in the $5S_{1/2}$, $F=2$ upper ground state guided through a minute-hollow fiber with a hollow diameter of 1.4 μm, where the ionized ^{87}Rb flux is plotted as a function of the blue detuning measured from the upper ground state. Here, the oven temperature is low enough that the incident flux is limited to a rather low level. Note that the state-selective PI detection enables one to observe a small number of the guided atoms without background noise. From the rising part of the curve in Fig. 3(a), we can estimate the ratio of the flux change $\Delta\Phi$ to the frequency change $\Delta\omega_L$, namely $\Delta\Phi/\Delta\omega_L$, to be about 50 s^{-1}/GHz.

In Fig. 3(a), the broken line shows the background transmission of ^{87}Rb atoms without the guide light. Since the background transmission falls at zero level when the atomic beam is turned off with a mechanical shutter, the background transmission must be due to the atoms flying ballistically through the hollow region. For the precise control of the deposition rate, the ballistic transmission should be suppressed. For this purpose, we have made the PI spectroscopy by slightly tilting a hollow fiber from the axis of the atomic beam such that the background level becomes very low. Figure 3(b) shows the result on the ^{87}Rb atoms in the $5S_{1/2}$, $F=2$ upper ground state guided through a 2-μm-hollow fiber. Comparing the maximum guided flux at a blue detuning of +7 GHz with the background level shown by the broken line, we get a high enhancement factor of 80.

This type of atom deposition is advantageous with respect to purity, which is important for the atomic-level crystal growth, thanks to the species- and state-selective guidance based on the frequency-dispersion property. On the other hand, the use of bent hollow optical fiber enables one to carry the guided atoms aiming at any point on a substrate. In this connection, the guiding of laser-cooled atoms is considered for atom-by-atom crystal growth.[8] Furthermore, if a sharpened optical fiber[9] with evanescent field excited on the nanometric tip is utilized together with the atom-guidance technique, the cold atoms guided through a hollow fiber can be manipulated with nanometric accuracy well beyond the diffraction limit of the light used.[10] In this case, the manipulation accuracy will depend on the diffraction limit of the atomic de Broglie waves.

In summary, we have demonstrated the possible use of the evanescent-light guiding for a novel form of optical atom deposition with convenient control and high purity. Under the optimal experimental conditions, within uncertainty as to the surface-ionization efficiency, the deposition rate is estimated to be large enough that a micron-sized dot pattern with nanometric depth is created. Moreover, the deposition rate is accurately controlled with the frequency detuning so that the relative resolution of less than 10 atoms can be achieved. Besides, tilting the hollow fiber highly enhances the ratio of the number of atoms transmitted with the guide light relative to the background transmission without the guide light. The guiding of atoms in the subwavelength region beyond the diffraction limit is now in progress by means of a 300-nm-hollow fiber.

The authors acknowledge Dr. S. Sudo and Dr. Y. Sakai of NTT Opto-Electronic Laboratory for useful discussion on micron-sized hollow optical fibers.[11] This work was supported by the MATSUO Foundation of Japan. One author (W. J.) is also grateful to the Ministry of Education and the STEPI of Korea for its support.

[1] K. S. Johnson, K. K. Berggren, A. Black, C. T. Black, A. P. Chu, N. H. Dekker, D. C. Ralph, J. H. Thywissen, R. Younkin, M. Tinkham, M. Prentiss, and G. M. Whitesides, Appl. Phys. Lett. **69**, 2773 (1996).
[2] R. W. McGowan, D. M. Giltner, and S. A. Lee, Opt. Lett. **20**, 2535 (1995).
[3] H. Ito, T. Nakata, K. Sakaki, M. Ohtsu, K. I. Lee, and W. Jhe, Phys. Rev. Lett. **76**, 4500 (1996).
[4] M. J. Renn, E. A. Donley, E. A. Cornell, C. E. Wieman, and D. Z. Anderson, Phys. Rev. A **53**, R648 (1996).
[5] S. Marksteiner, C. M. Savage, P. Zoller, and S. L. Rolston, Phys. Rev. A **50**, 2680 (1994).
[6] H. Ito, K. Sakaki, T. Nakata, W. Jhe, and M. Ohtsu, Opt. Commun. **115**, 57 (1995): *ibid.* Ultramicroscopy **61**, 91 (1995).
[7] V. I. Balykin, V. S. Letokhov, Yu. B. Ovchinnikov, and A. I. Sidorov, Phys. Rev. Lett. **60**, 2137 (1988).
[8] H. Ito, K. Sakaki, W. Jhe, and M. Ohtsu, in *Quantum Electronics and Laser Science Conference,* Vol. 10, OSA Tech. Dig. Ser., pp. 91–92 (OSA, 1996).
[9] S. Mononobe and M. Ohtsu, J. Lightwave Technol. **14**, 2231 (1996).
[10] M. Ohtsu, J. Lightwave Technol. **13**, 1200 (1995); W. Jhe and M. Ohtsu, *Laser Spectroscopy XII* (World Scientific, Singapore, 1996), p. 440.
[11] S. Sudo, I. Yokohama, H. Yasaka, Y. Sakai, and T. Ikegami, IEEE Photonics Technol. Lett. **2**, 128 (1990).

Atom trap in an axicon mirror

J. A. Kim, K. I. Lee, H. R. Noh, and W. Jhe

Department of Physics and Condensed Matter Research Institute, Seoul National University, Seoul 151-742, Korea

M. Ohtsu*

Interdisciplinary Graduate School, Tokyo Institute of Technology, Yokohama 226, Japan

Received September 10, 1996

We have realized a novel atom trap in an axicon (conical hollow) mirror, using a frequency-modulated, single-diode laser. Different spatial distributions of trapped atoms such as a ball and a ring are observed. We show that our numerical simulations are consistent with experimental results. In particular, the ring diameter is found to be approximately the separation between the mirror axis and the magnetic field axis. The axicon trap may be useful as a precooled atom source for cold atomic beams, atom funnels, and atom waveguides.

Laser cooling and trapping of neutral atoms has been a subject of much interest and wide application. One efficient and simple atom trap is the magneto-optical trap[1,2] (MOT). Use of the MOT has made possible many advances in studies of cold collision, high-resolution spectroscopy, nonlinear optics, and atom optics. In particular, MOT is useful as a precooled atom source for other interesting experiments with Bose–Einstein condensation,[3] atom guides,[4] atom funnels, and cold atomic beams.[5]

Therefore it is desirable to realize even simpler MOT configurations suitable for applications such as those mentioned above. Recently, a simple single-beam atom trap was realized in a pyramidal hollow mirror by use of a microwave-modulated diode laser.[6] Although the possibility of developing a MOT in a conical hollow system by use of roughly machined, cone-shaped aluminum block was indicated in Ref. 6, it is important for researchers to realize a real conical mirror trap, in particular because of its interesting configuration and promising applications.

In this Letter we report an experimental realization of a novel axicon-mirror atom trap. Detailed trap properties of spatial distribution and optical forces as well as numerical analysis are also presented. Our axicon-mirror atom trap (Fig. 1) consists of a rubidium vapor cell, a quadrupole magnetic field, and a single-diode laser beam,[7] as in the pyramidal trap.[6] The incident laser has a circular polarization and is retroreflected by double reflections on the mirror surfaces. As a result, three pairs of counterpropagating beams with the same polarization configuration as in the conventional six-beam MOT are automatically produced inside the conical hollow region. Note that, unlike in the pyramidal case, there exist infinite pairs of concentric, counterpropagating beams in the planes perpendicular to the mirror axis. The differences in trap dynamics between axicon and conventional MOT's are discussed below.

The axicon mirror is made up of a glass substrate whose surfaces are polished to an optical flat within a wavelength. A thick layer of aluminum is then deposited upon the hollow surface to fabricate a mirror. Unlike in the pyramidal case, the axicon mirror has a hole (diameter 2 mm) at the apex (although it can be made smaller, the hole is practically unavoidable, mainly owing to a difficulty in machining a sharp edge, but the hole will be useful for extracting a cold atomic beam[5]). Consequently, when we operate the system as an atom trap that requires retroreflected beams in the hollow region, we need to insert a quarter-wave plate and a backreflecting mirror into the opposite side of the axicon mirror outside the vacuum cell.

For cooling and trapping of ^{85}Rb atoms, we used the same frequency-modulated and frequency-stabilized diode laser[7] with a beam diameter of 2.5 cm. The magnetic field is produced by an anti-Helmholtz coil

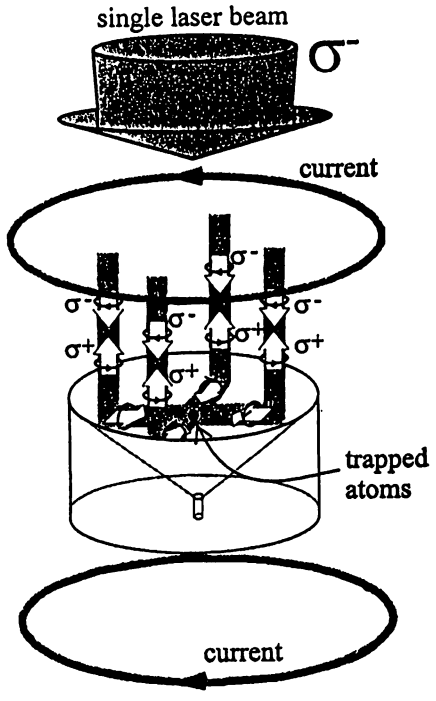

Fig. 1. Schematics of the experimental setup and the polarization configuration in an axicon-mirror atom trap.

0146-9592/97/020117-03$10.00/0

(4 cm in diameter and separation) placed along the mirror axis outside the glass cell and mounted upon an $x-y$ translator so that the minimum field ($B = 0$) position can be easily moved within the hollow.

When the incident laser is well aligned (or retroreflected) such that all the converging beams in the transverse plane cross the $B = 0$ point (i.e., when the magnetic field axis and the mirror axis overlap), the spatial distribution of the trap cloud is found to be a spherical ball with a diameter of ~0.5 mm [Fig. 2(a)]. When the $B = 0$ point is displaced with respect to the mirror axis, on the other hand, a ring-shaped cloud is observed as shown in Fig. 2(b). Moreover, the ring diameter is found to be approximately equal to the separation between the two axes, as shown in Fig. 3, in which the measured ring diameter is plotted as a function of the separation (note that the three points within ±0.5 mm near the origin represent ball-shaped clouds).

Note that when the trapping beams are slightly misaligned in the conventional MOT such that they form a racetrack configuration in a plane, a similar ring shape could also be observed.[8] However, this case was due to the fact that the Gaussian-profile laser beam produces a vortex force when it is slightly misaligned.[8]

In our case, on the other hand, because neither beam misalignment nor Gaussian intensity profile is involved, a different force mechanism is responsible for the ring-shaped cloud. Let us first consider an atom in the conical hollow region, where the coil axis (chosen as the z axis) is displaced by x_0 from the mirror axis that crosses the origin. Then the magnetic field can be written as $\mathbf{B}(\mathbf{r}) = bz\hat{z} - (b/2)[(x - x_0)\hat{x} + y\hat{y}]$. Because the optical scattering force in the x (or y) – z plane in the hollow region is identical to that of a conventional MOT, we will concentrate, without loss of generality, on the atomic motion in only the $x-y$ plane.

Let us consider that a pair of counterpropagating beams with $\sigma^{\pm}$ polarizations travel in the $x-y$ plane along the $\pm\eta$ axis, respectively, which intersects the x axis at the origin at an angle α. We also assume the quantization axis ζ is parallel to the local magnetic field direction (note that the $B = 0$ point is moved to $x = x_0$ and $y = 0$). If the magnetic field makes an angle β with the x axis, the beam propagation vector then crosses the quantization axis with an angle $\theta = \beta - \alpha$. Therefore each polarization vector can be written as

$$\begin{aligned}\hat{\sigma}_+ &= \frac{1}{\sqrt{2}}\sin\theta\hat{\epsilon}_0 + \frac{1}{2}(1 - \cos\theta)\hat{\epsilon}_- \\ &\quad + \frac{1}{2}(1 + \cos\theta)\hat{\epsilon}_+, \\ \hat{\sigma}_- &= \frac{1}{\sqrt{2}}\sin\theta\hat{\epsilon}_0 + \frac{1}{2}(1 + \cos\theta)\hat{\epsilon}_- \\ &\quad + \frac{1}{2}(1 - \cos\theta)\hat{\epsilon}_+, \end{aligned} \tag{1}$$

where $\hat{\epsilon}_{\pm}$ and $\hat{\epsilon}_0$ represent the unit vectors associated with the quantization axis ζ. As a result, the $\sigma^{\pm}$ beams along $\pm\eta$ induce $\Delta M_j = +1, -1, 0$ transitions with the respective probabilities given by

$$P_{0\to+1}^{\sigma^{\pm}} = \frac{1}{4}(1 \pm \cos\theta)^2, \qquad P_{0\to-1}^{\sigma^{\pm}} = \frac{1}{4}(1 \mp \cos\theta)^2,$$

$$P_{0\to0}^{\sigma^{\pm}} = \frac{1}{2}\sin^2\theta. \tag{2}$$

For a two-level atom, the force is approximately the sum of spontaneous forces:

$$\begin{aligned}\mathbf{F} &= \mathbf{F}_{\sigma-} - \mathbf{F}_{\sigma+} \\ &= P_{0\to-1}^{\sigma^-}\mathbf{f}(\Delta - \delta_B - \mathbf{k}\cdot\mathbf{v}) + P_{0\to0}^{\sigma^-}\mathbf{f}(\Delta - \mathbf{k}\cdot\mathbf{v}) \\ &\quad + P_{0\to+1}^{\sigma^-}\mathbf{f}(\Delta + \delta_B - \mathbf{k}\cdot\mathbf{v}) \\ &\quad - P_{0\to+1}^{\sigma^+}\mathbf{f}(\Delta + \delta_B + \mathbf{k}\cdot\mathbf{v}) - P_{0\to0}^{\sigma^+}\mathbf{f}(\Delta + \mathbf{k}\cdot\mathbf{v}) \\ &\quad - P_{0\to-1}^{\sigma^+}\mathbf{f}(\Delta - \delta_B + \mathbf{k}\cdot\mathbf{v}), \end{aligned} \tag{3}$$

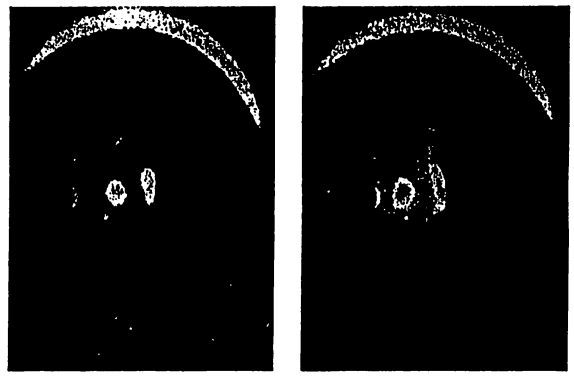

(a) (b)

Fig. 2. CCD images of the spatial distributions of trapped rubidium atoms in the axicon mirror, showing (a) spherical and (b) ring-shaped clouds. Their mirror images are also shown on the right-hand side of each cloud image.

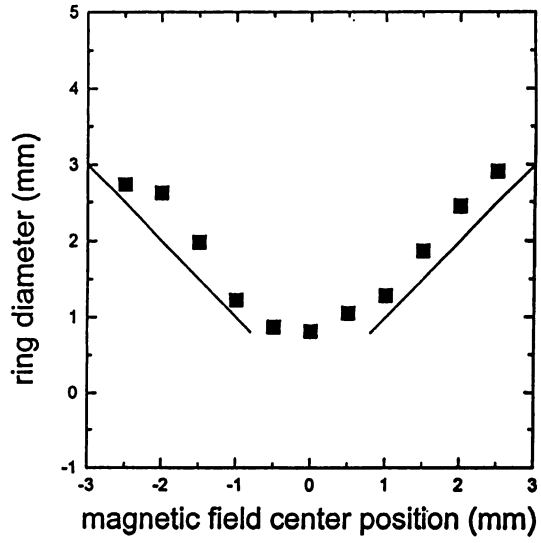

Fig. 3. Measured ring diameter as a function of the separation between the magnetic field axis and the mirror axis (or the origin). The data are in good agreement with the unit-slope lines of ring diameter that are equal to separation (see text for details). Note that the three squares near the origin correspond to ball-shaped clouds.

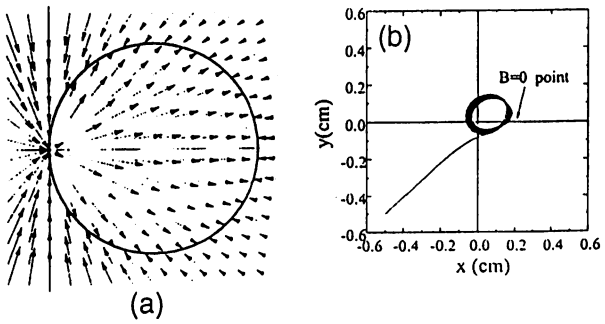

Fig. 4. (a) Optical force fields acting on atoms at rest. The resulting force-free contour is obtained as a circle. (b) Typical atomic trajectory in the axicon mirror trap. The atom's initial position is $x = y = -0.5$ cm, and its initial velocity is $v_x = 8$ m/s, $v_y = 7.5$ m/s.

where

$$\mathbf{f}(\delta) = \frac{I/I_s}{1 + I/I_s + 4(\delta/\Gamma)^2} \frac{\hbar \mathbf{k} \Gamma}{2}. \quad (4)$$

Here $\Delta = \omega - \omega_0$ is the frequency detuning, $\mathbf{k}$ is the laser wave vector (along η axis), $\mathbf{v}$ is the atomic velocity, I_s is the saturation intensity, Γ is the $5P_{3/2}$ decay rate, and δ_B is the local Zeeman shift.

Let us first consider atoms at rest, for simplicity. Then, using Eqs. (3) and (4), we can easily show that the region in which the radiation-trapping forces vanish for stationary atoms corresponds to a circle whose diameter is given by the separation between the origin (mirror axis) and the $B = 0$ point (coil axis). The circular contour of force-free fields is also shown in Fig. 4(a).

Now, the two-dimensional atomic motion in the axicon trap is obtained by numerical solution of the equation $m(\mathrm{d}^2\mathbf{r}/\mathrm{d}t^2) = \mathbf{F}(\mathbf{r})$, where $\mathbf{F}(\mathbf{r}) = F_x\hat{x} + F_y\hat{y}$ and $\mathbf{r} = (x, y)$. The Runge–Kutta simulation provides a typical atomic trajectory as shown in Fig. 4(b). It is clearly observed that atoms are cooled and trapped in a ring-shaped cloud. However, note that, for slowly moving atoms, the circle in Fig. 4(a) becomes slightly distorted and shifted in the direction opposite the $B = 0$ point. In fact, this is why the measured average diameter in Fig. 3 is slightly larger than the separation. We also have found that as the atomic velocity is decreased with time, it reaches a steady-state value independently of the initial conditions.

It is also observed that when the detuning or the magnetic field gradient is changed, the spatial distributions can be slightly distorted. We could even obtain a cloud shape with a ring around a ball or with two rings as we move the coil axis near the edge of the axicon mirror. We found that such an irregular distribution was caused by the imperfect fabrication of the apex edge of the mirror, which resulted in an annular dark region in which no backreflection exists.

We measured the number of trapped atoms by detecting the trap fluorescence with a photomultiplier tube. Under our experimental conditions of 7 G/cm field gradient and 13-MHz red detuning for a laser intensity of 1.6 mW/cm^2 (sideband intensity is 0.6% of the carrier), a simple estimate shows that the number of trapped atoms is as much as 10^7 in a spherical cloud but is slightly less in the case of ring-shaped cloud. Therefore the loading efficiency of the axicon MOT is comparable with that of the typical, or pyramidal, MOT. Moreover, the trap-loading time was found to be independent of ring diameter.

In the axicon trap atoms experience only radial forces in the x–y plane, which is the main difference between this trap and the typical MOT. However, when the mirror axis and the magnetic field axis overlap, in the limit of low velocity, our numerical analysis shows that the optical force fields in the axicon trap are similar to those of the typical MOT in the x–y plane. Therefore the optimum values of laser detuning and magnetic field gradient of the axicon trap are expected to be similar to those of the typical MOT, and our experimental results are in good agreement with the simulation results.

Because of its simplicity, easy control, and versatility, the single-beam atom trap realized in the axicon mirror can be useful as a precooled, funneled atom source for other ongoing elaborate experiments such as atom waveguides,[4] gravitational atom traps, cold atomic beams,[5] atom lithography, and the study of quantum statistical properties.

This study was supported by the Korea Science and Engineering Foundation and the Korean Ministry of Education (BSRI 96-2421).

*Also with the Kanagawa Academy of Science and Technology, Kawasaki 213, Japan.

References

1. E. L. Raab, M. Prentiss, A. Cable, S. Chu, and D. Pritchard, Phys. Rev. Lett. **59**, 2631 (1987).
2. F. Shimizu, K. Shimizu, and H. Takuma, Opt. Lett. **16**, 339 (1991); C. Chesman, E. G. Lima, F. A. M. de Oliveira, S. S. Vianna, and J. W. R. Tabosa, Opt. Lett. **19**, 1237 (1994).
3. M. H. Anderson, J. R. Ensher, M. R. Matthews, C. E. Wieman, and E. A. Cornell, Science **269**, 198 (1995).
4. H. Ito, T. Nakata, K. Sakaki, M. Ohtsu, K. I. Lee, and W. Jhe, Phys. Rev. Lett. **76**, 4500 (1996).
5. Z. T. Lu, K. L. Corwin, M. J. Renn, M. H. Anderson, E. A. Cornell, and C. E. Wieman, Phys. Rev. Lett. **77**, 3331 (1996).
6. K. I. Lee, J. A. Kim, H. R. Noh, and W. Jhe, Opt. Lett. **21**, 1177 (1996).
7. H. R. Noh, J. O. Kim, D. S. Nam, and W. Jhe, Rev. Sci. Instrum. **67**, 1431 (1996).
8. T. Walker, D. Sesko, and C. Wieman, Phys. Rev. Lett. **64**, 408 (1990); T. Walker, D. Hoffman, P. Feng, and R. S. Williamson III, Phys. Lett. A **163**, 309 (1992).

Plenary 5: M. Ohtsu

ATOM GUIDANCEAND MANIPULATION BY OPTICAL NEAR FIELD FOR FUTUREATOMIC-LEVEL DEPOSITION

M. OHTSU
Tokyo Institute of Technology
4259 Nagatsuta, Midori-ku, Yokohama 226, JAPAN

For a future application of near field optics, we review our recent experimental results on atomic quantum wire, i.e., guiding atoms by a dipole force of a cylindrical optical near field on the inner surface of a hollow fiber. Magnitude of cavity potential on the surface is estimated by guiding rubidium atoms, and in-line isotope separation is demonstrated. To present the capability of atomic-level deposition, deposition time for one nanometer thick layer and the coeffficient of discriminating the number of guided atoms per unit change of optical frequency are estimated. To carry atoms to the desired position, atomic funnel is proposed to couple cold atoms to a bent hollow fiber. Further, possibility of forming an atomic quantum dot, i.e., trapping a single atom by the optical near field on the top of a metal coated nanometric protruded fiber probe tip, is discussed.

TuC2 930

Evanescent-field atom guidance in the sub-wavelength region beyond the diffraction limit

Haruhiko Ito,* Keiji Sakaki,** Motoichi Ohtsu,** *Kanagawa Academy of Science and Technology, KSP East, 3-2-1 Sakado, Takatsu-ku, Kawasaki 213, JAPAN*

The hollow optical fiber supported by the blue-detuned evanescent light can transport atoms with high spatial accuracy without much loss over the long distance. In our previous work,[1] we have performed the atom-guidance experiment in 7- and 2-μm-hollow fibers.[2] Since the evanescent light is localized in the region below a wavelength, it can be applied to manipulating atoms beyond the diffraction limit. Here we have first demonstrated the guiding in the sub-wavelength region: the Rb atoms are guided in a hollow fiber with a core of 300 nm less than a half of a wavelength. The result indicates that the atomic motion was controlled beyond the diffraction limit by the evanescent field having less wave character, namely by the optical near-field. The combination of the "near-field atom fiber" with the sharpened optical fiber will lead to the nanometric atom manipulation, even the single-atom manipulation.[3]

Figure 1 shows the experimental setup. The collimated Rb beam from the oven with a typical temperature of 500 K is introduced into the straight hollow fiber with a 3.5-cm-length. The mean longitudinal atomic velocity along the fiber is 350 m/s while the mean transverse one is estimated to be 0.2 m/s. The guide-light beam from a Ti:Sapphire laser is coupled to the cylindrical optical-core with a 2-μm-thickness around the hollow region. For the wavelength of 780 nm to guide Rb atoms, the hollow fiber becomes single-mode: the LP_{01} mode.[4]

The guided atoms are detected by a channel electron multiplier under a bias of −3 kV via the two-step photoionization with a diode laser tuned to the Rb D_2-line and an Ar-ion laser (476.5 nm). Figure 2 shows the Doppler-free photoionization spectrum on the ^{85}Rb atoms in the $5S_{1/2}$, $F = 3$ upper ground state as a function of the frequency detuning. Compared to the background ballistic transmission (1300 atom/s) without the guide-laser beam, the enhancement on the guided flux is up to 80 times at the optimal detuning of +4 GHz.

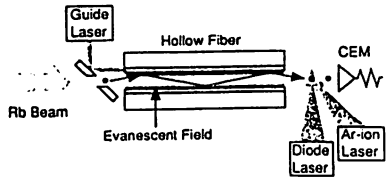

TuC2 Fig. 1. Sketch of the experimental setup. The Rb atomic beam is introduced into the hollow optical fiber with a core diameter of 300 nm and a length of 3.5 cm. The guided atoms are detected by a channel electron multiplier (CEM) through the two-step photoionization with a diode laser and an Ar-ion laser.

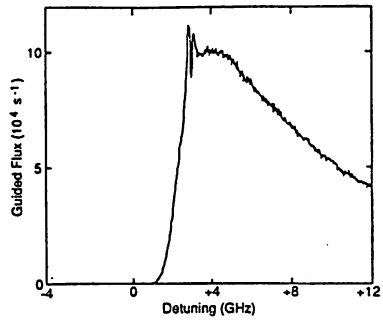

TuC2 Fig. 2. State-selective laser-photoionization spectrum on the guided ^{85}Rb atoms under the excitation of the LP_{01} evanescent field with a power of 250 mW. The two peaks near the maximum flux correspond to the increase due to the pumping from the $5S_{1/2}$, $F = 2$ state to the $5S_{1/2}$, $F = 3$ state.

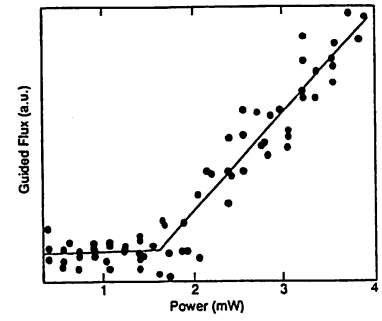

TuC2 Fig. 3. Measurement of the threshold on the atom guidance. The guided ^{87}Rb atom flux in the $5S_{1/2}$, $F = 2$ upper ground state is plotted as a function of the guide-laser power coupled to the 300-nm-hollow fiber under a blue detuning of +4 GHz.

The minute-hollow fiber is most useful for the study of the cavity QED effect in a cylindrical dielectric. Figure 3 shows the change of the guided ^{87}Rb flux in the $5S_{1/2}$, $F = 2$ upper ground state under a blue detuning of 4 GHz when the coupled power of the guide-laser beam is scanned in the low-intensity region. The threshold indicating the cancellation of the optical potential by the cavity one is observed at 1.6 mW.

We will also present the experimental results on the guiding of the Rb atoms in the $5S_{1/2}$ lower ground states, including the consideration of the optical pumping effect.

*PRESTO, Japan Science and Technology Corporation Kanagawa Academy of Science and Technology, KSP East, 3-2-1 Sakado, Takatsu-ku, Kawasaki 213, JAPAN
**Interdisciplinary Graduate School of Science and Engineering, Tokyo Institute of Technology, 4259, Nagatsuta, Midori-ku, Yokohama 226, JAPAN

1. H. Ito, T. Nakata, K. Sakaki, M. Ohtsu, K. I. Lee, W. Jhe, Phys. Rev. Lett. 76, 4500 (1996).
2. S. Sudo, I. Yokohama, H. Yasaka, Y.

Sakai, T. Ikegami, IEEE Photon. Technol. Lett. **2**, 128 (1990).
3. M. Ohtsu, S. Jiang, T. Pangaribuan, M. Kozuma, in *Near-Field Optics*, 131–139 (Kluwer, 1993).
4. H. Ito, K. Sakaki, T. Nakata, W. Jhe, M. Ohtsu, Opt. Commun. **115**, 57 (1995); *ibid.* Ultramicroscopy **61**, 91 (1995).

Tul5 Fig. 2. Microscope image of the 45°-ground facet of a hollow optical fiber with a hollow diameter of 2 μm. The thickness of the cylindrical core in which the guide-laser beam propagates in 4 μm and the outer diameter of the fiber is 125 mm.

Tul5 1215

Lateral light-coupling for evanescent-field guiding of cold atoms

Keiji Sakaki, Haruhiko Ito,*** Motoichi Ohtsu,** *Interdisciplinary Graduate School of Science and Engineering, Tokyo Institute of Technology, 4259, Nagatsuta, Midori-ku, Yokohama 226, JAPAN*

One-dimensional guiding of atoms by the blue-detuned evanescent light has been performed in micron-sized hollow optical fibers.[1] This technique can be applied as the manipulator to a novel form of the optical atom-deposition beyond the optical diffraction limit. Further, the use of cold atoms will be useful for the atomic level crystal growth. Recently, we have proposed the atomic funnel supported by the evanescent light in order to couple efficiently cold atoms to the hollow optical fiber.[2]

In our previous work, the guide-laser beam that excites the evanescent field in the hollow region was irradiated to the flat facet of the hollow optical fiber by a hollow mirror placed upstream. However, this scheme is sometimes inconvenient when combined with the atomic funnel. In order to overcome this difficulty, here we propose and demonstrate a new atom-guidance scheme with lateral coupling of the guide-laser beam.

The experimental setup of atom guidance is shown in Fig. 1. Figure 2 shows a microscope image of a fabricated 2 μm-hollow-core optical fiber with a facet ground at an angle of 45°. Under forming the 45°-slant facet at the edge of the fiber, the guide-laser beam from a Ti:Sapphire laser is laterally coupled to the core. A coupling efficiency as high as 40% was obtained. The frequency ω of the guide laser is scanned through 16GHz around the resonance frequency ω_0 of the Rb D_2-line. A collimated thermal Rb atomic beam is introduced into a 4-cm-long hollow optical fiber with a hollow diameter of 2 μm. The guided Rb atoms are detected by a channel electron multiplier (CEM) via the two-step photoionization.

The guiding of atoms is based on the repulsive dipole force from the blue-detuned evanescent light. Figure 3 shows

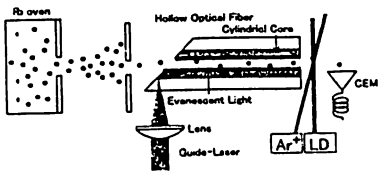

Tul5 Fig. 1. Sketch of the experimental setup. A guide-laser beam is coupled to the core from the lateral direction of the fiber by total internal reflection at the slant facet with an efficiency of 38%. The guided Rb atoms are detected by a channel electron multiplier (CEM) via the Doppler-free two-step photoionization with a diode laser and a high power Ar-ion laser.

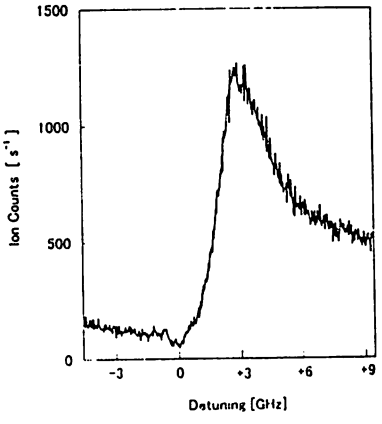

Tul5 Fig. 3. Ionization signal of the Rb atom flux guided in a 4-cm-long hollow fiber as a function of the frequency detuning. State-selective photoionization spectrum of the guided ^{85}Rb atoms in the $5S_{1/2}$, $F = 3$ upper ground state. The guided flux is measured above the background level.

the guided Rb atom flux plotted as a function of the frequency detuning $\delta = \omega - \omega_{a}$, not including the Doppler shift. The blue-detuning is measured with respect to the transition frequency of the ^{85}Rb atom in the $F = 3$ upper ground state. The increase of the guided atoms is clearly observed in the blue-detuning region. We find that the peak position of the guided Rb flux appears at the blue-detuning of about 3GHz. It may be due to the optical pumping of the dominant ^{85}Rb atoms in the guidance from the $F = 2$ lower ground state to the $F = 3$ upper one as a result of absorbing evanescent photons inside the hollow fiber or scattered photons near the entrance. The ^{85}Rb atoms pumped to the upper ground state feel the stronger repulsive force so that the number of the guided atoms is increased.

We will describe the detail on making of the slant facet and report the improvement of the coupling efficiency. The complementary detection with the two-step photoionization and the surface-ionization will also be presented.

*PRESTO, Japan Science and Technology Corporation

**Kanagawa Academy of Science and Technology, KSP East, 3-2-1 Sakado, Takatsu-ku, Kawasaki 213, JAPAN

1. H. Ito, K. Sakaki, M. Ohtsu, K. I. Lee, W. Jhe, Phys. Rev. Lett. 76, 4500 (1996).
2. H. Ito, K. Sakaki, W. Jhe, M. Ohtsu, Quantum Electronics and Laser Science Conference, 1996 Technical Digest Series, 10, 91 (OSA, 1996).

QWH4 5:45 pm

Evanescent light guiding in hollow optical fibers for atom deposition

Haruhiko Ito, Keiji Sakaki, Motoichi Ohtsu,*
Japan Science and Technology Corporation, Kanagawa Academy of Science and Technology, KSP East, 3-2-1 Sakado, Takatsu-ku, Kawasaki 213, Japan

In our previous works we have shown that the blue-detuned evanescent light excited in a micron-sized hollow optical fiber could send neutral atoms down the fiber through a long distance.[1,2] Such an atom guidance technique is expected to be applied to a new form of deposition and lithography. In this work we report the experimental progress for realization of the atom-by-atom deposition.

The experiments guiding an atomic beam have been performed by use of 7- and 2-μm-wide hollow optical fibers (See Ref. 3 about the 2-μm fiber). For further improvement in the atom manipulation accuracy, we use 1.4- and 0.8-μm-wide fibers. Figure 1 shows a laser photoionization spectrum on the ^{87}Rb atoms in the $5S_{1/2}$, F = 2 upper ground state guided in a 1.4-μm-wide hollow fiber. The frequency detuning is measured from the resonant frequency of the ^{87}Rb vapor. The two-step photoionization is carried out by overlapping a diode-laser beam tuned to the $5S_{1/2}$, F = 2 → $5P_{3/2}$, F = 3 transition and a high power Ar^+ laser beam with a wavelength of 476.5 nm. The ionized atoms are detected by a channeltron electron multiplier. As shown in Fig. 1, the guided atoms appear in the blue-detuning region. By adjusting the fiber axis, we get a large enhancement factor of 50 compared with a background level without evanescent light expressing the number of ballistic atoms.

To examine the spatial distribution of the guided atoms, the hot-wire scan is employed. Figure 2 shows a result in the case of the 3-cm-long guidance in a 7-μm-wide hollow fiber. A Pt hot-wire with a diameter of 10 μm is placed at a distance of 12 mm behind the fiber. The distribution width is 20 μm at FWHM. The Rb beam introduced into the

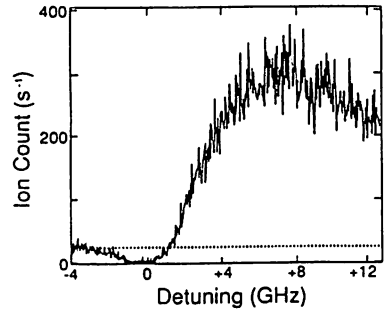

QWH4 Fig. 1 Two-step photoionization spectrum on the guided ^{87}Rb atoms in a 1.4-μm-wide hollow fiber through a distance of 3 cm. The ionized atom flux is plotted as a function of the frequency detuning of a guide laser. The dashed line shows a background level without the guide laser.

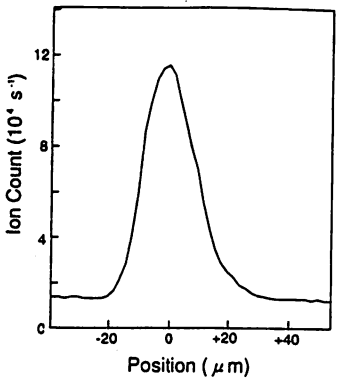

QWH4 Fig. 2 Measurement of the spatial distribution of the guided Rb atoms in a 7-μm-wide hollow fiber. The surface ionization is performed by use of a Pt hot-wire with a diameter of 10 μm.

hollow fiber has a most probable longitudinal velocity of 320 m/s and a transverse one of 0.2 m/s. On the other hand, the directivity of the guided Rb beam is estimated to be 0.54 mrad, which leads to a transverse velocity of 0.17 m/s. This shows that almost half of the incident flux can be transported through the fiber. In fact, we obtain a guidance efficiency of more than 50% from the ratio of the detected flux to the incident one. In this case, the density of the guided flux becomes 10^3 atom/s · μm^2. Considering the deposition on a substrate placed near the back of the fiber, we get a deposition time rate of 2.8 h/nm.

We will also report the guiding experiments using a convenient scheme of the side coupling of a guide laser beam to a hollow fiber with a slant polished edge. This scheme enables one to attach an atomic funnel to collect laser-cooled atoms.[4]

We thank W. Jhe of Seoul National University and S. Sudo and Y. Sakai of NTT Opto-electron. Lab. for their useful discussions.

Interdisciplinary Graduate School of Science and Engineering, Tokyo Institute of Technology, 4259, Nagatsuta, Midori-ku, Yokohama 226, Japan

1. H. Ito, T. Nakata, K. Sakaki, M. Ohtsu, K. I. Lee, W. Jhe, Phys. Rev. Lett. 76, 4500 (1996).
2. H. Ito, T. Nakata, K. Sakaki, W. Jhe, M. Ohtsu, IQEC 1996 Technical Digest Series, 2 (1996).
3. S. Sudo, I. Yokohama, H. Yasaka, Y. Sakai, T. Ikegami, IEEE Photon. Technol. Lett. 2, 128 (1990).
4. H. Ito, K. Sakaki, T. Nakata, W. Jhe, M. Ohtsu in *Quantum Electronics and Laser Science Conference*, Vol. 10, 1996 OSA Technical Digest Series p, 91.

ATOM MANIPULATION BY OPTICAL NEAR-FIELD

Motoichi OHTSU

Interdisciplinary Graduate School of Science and Engineering,
Tokyo Institute of Technology
4259 Nagatsuta, Midori-ku, Yokohama 226, JAPAN

We propose the method of trapping a single atom by the optical near field on the top of a nanometric fiber probe tip to form an atomic quantum dot. We also review our experimental results on atomic quantum wire, i.e., guiding atoms by the cylindrical optical near field on the inner surface of a subwavelength hollow fiber. Magnitude of cavity potential is estimated. Possibility of atomic-level deposition is also discussed.

GUIDING ATOMS BY OPTICAL NEAR-FIELD AND MANIPULATION FOR ATOMIC-LEVEL DEPOSITION

M. Ohtsu[1,2], H. Ito[2,3] and K. Sakaki[1]

1) Graduate School, Tokyo Inst. of Tech., 4259 Nagatsuta, Midori-ku, Yokohama 226, JAPAN 2) Kanagawa Academy of Sci. and Tech. 3) Japan Sci. and Tech. Corp.

We have previously proposed the method of trapping a single atom by the evanescent field on the top of a nanometric sharpened fiber probe tip, which can be applied for forming an atomic quantum dot[1]. Further, we have succeeded in realizing atomic quantum wire, i.e., guiding atoms by the cylindrical evanescent field on the inner surface of a hollow optical fiber[2]. Further developments of atom guidance experiments are reported and possibility of atomic-level deposition is presented in this paper.

Figure 1 shows an experimental setup. The LP_{01} mode was guided through the doughnut-core of the hollow fiber in order to generate an evanescent field on its inner surface. A thermal rubidium(Rb) atomic beam was injected into the hollow of the fiber. The atoms receive a repulsive dipole force from the blue-detuned evanescent field in the process of transition between the ground state and first-excited states. If this repulsive force is larger than the attractive van der Waals force, i.e., the force due to the cavity potential, the atoms can transmit through the fiber without being adsorbed onto the inner wall. Atomic beam of 1 x 10^6 s^{-1} flux was injected into the hollow from an atomic beam source at 473K. A frequency-controlled Ti:Al_2O_3 laser (780 nm wavelength) was used to generate the LP_{01} mode. Three kinds of fibers were used, which had the hollow diameters of 7, 2, and 1.4 μ m (, width of the doughnut core of 3.8, 4.3, and 2.0 μ m), respectively. Their lengths were 3 cm. Two-step photo-ionization by using laser diode and high power Ar laser, and surface-ionization by a hot-wire made of Pt was employed for measuring the number of guided atoms.

Figure 2 shows the relation between the Ti:Al_2O_3 laser frequency detuning and number of atoms transmitted through the 1.4-μ m hollow fiber. Increase in the atom counts for the blue-detuning represents the effect of guidance. The dispersive profile of the curve agrees with the theoretical prediction. Dependence of the number of guided atoms on the light power is given by Fig. 3, where the horizontal axis represents the power of the guided LP_{01} mode. Existence of the threshold on the curve is due to the attractive van der Waals force, which confirmed for the first time the existence of the cavity QED effect on a cylindrical surface.

The guidance efficiency as high as 56 % was obtained at a guiding mode power of 230 mW for the 7-μ m hollow fiber. By using these values, the time taken for depositing a layer of 1 nm of the transmitted Rb atoms on the crystal substrate was estimated to be 2.8 hours, i.e., deposition time is 2.8 hr/nm. Although this rate is slower than the conventional chemical process utilizing thermal equilibrium, e.g., molecular beam epitaxy, the present physical deposition process has several outstanding advantages. They are: (1) manipulation of small number of atoms is possible for realization of a single atomic-level deposition, (2) selectivity of atomic species is much higher, and (3) change of deposition rate is much easier. Thus, the present technique is compatible with the future fabrication process of nanometric/atomic materials and devices.

For further improvements in spatial accuracy of deposition, the following

two methods can be applied: (1) Injecting slower atoms for transmitting through a bent hollow fiber. Atomic funnel for the laser-cooled atom can be applied for this injection[3]. (2) Deflecting transmitted atoms by the evanescent field on the top of the sharpened fiber probe tip. Details of these method will be explained at the session. The present method of manipulation and deposition can be applied for a variety of atoms by preparing the coherent light resonant to the atoms. For silicon atoms, we have succeeded in generating a frequency -tunable coherent UV light of 252 nm wavelength using the third-harmonics generation technique[4].

The authors thank to Prof. W. Jhe (Seoul National Univ.) , Drs. S. Sudo and Y.Sakai (NTT Opto-electron. Lab.) for their intensive discussions.

References

1) M. Ohtsu, et al., in *Near Field Optics,* ed.by D. W. Pohl and D. Courjon, p.131
2) H. Ito, et al., Phys. Rev. Lett., 76 (1996) 450
3) H. Ito, et al., QELS'96 Tech. Digest, vol.10 (1996) 91
4) S. Sayama, et al., Opt. Commun., to be published

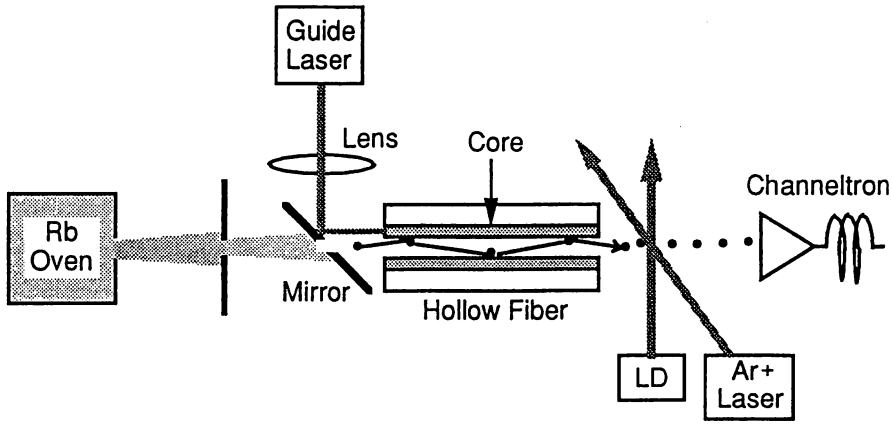

Fig. 1

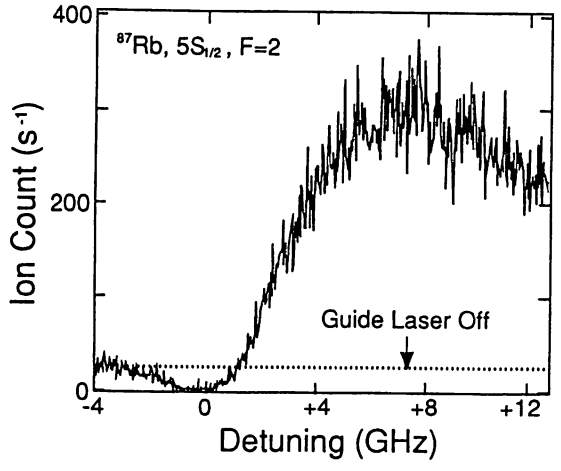

Fig. 2

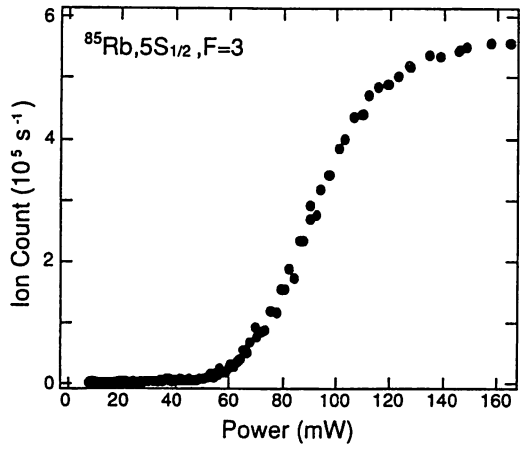

Fig. 3

Atom guidance using evanescent waves in small hollow optical fibers and its applications

Haruhiko Ito[a,b], Keiji Sakaki[c], Wonho Jhe[d], and Motoichi Ohtsu[b,c]

[a]PRESTO, Japan Science and Technology Corporation
[b]Kanagawa Academy of Science and Technology,
KSP East, 3-2-1 Sakado, Takatsu-ku, Kawasaki 213, Japan
[c]Interdisciplinary Graduate School of Science and Engineering,
Tokyo Institute of Technology,
4259 Nagatsuta, Midori-ku, Yokohama 226, Japan
[d]Department of Physics, Seoul National University,
Seoul 151-742, Korea

ABSTRACT

We report the recent progress of the experiments on guiding atoms by evanescent waves in micron-sized hollow optical fibers. The lateral manipulation accuracy is enhanced up to 1 micron with a large increase of more than 50 times on the guided atom flux. Moreover, the frequency tuning eanbles the fine control of the guided flux with a numerical accuracy of 10 atom/s. The atom-guidance scheme is applied to in-line isotope separation on rubidium atoms and measurement of the cavity quantum electrodynamic effect in a cylindrical dielectric. In addition, the feasibility of fabricating micron-sized structures with nanometric depth is discussed including the manipulation of a small number of laser-cooled atoms.

Keywords: evanescent waves, atom guidance, hollow optical fibers, isotope separation, cavity QED effects, atom deposition, atomic funnel

1. INTRODUCTION

The evanescent wave is an optical near-field whose intensity exponentially decays in a region below a wavelength in the vicinity of a dielectric-vacuum interface. The application of the localized evanescent field is expected to develop novel optical techniques much beyond the traditional ones with propagating light. From this point of view, we have been studying the manipulation of atoms with high accuracy by using the evanescent wave. In this paper, we report the progress of the evanescent-wave induced atom-guidance in micron-sized hollow optical fibers.[1-3] This technique can be useful for the studies on quantum mechanical[4] and quantum optical[5] phenomena. Accordingly, for the applications of the atom guidance, we present the experimental results on the isotope separation[1] and the measurement of the cavity quantum electrodynamic (QED) effect[6]. On the other hand, the atom deposition and lithography using the techniques of atom optics have been recently attracting much experimental attentions.[7] We also touch the new form of the optically-controlled atom deposition with the atom-guidance technique.[8]

SPIE Vol. 2995 • 0277-786X/97/$10.00

2. EVANESCENT-WAVE INDUCED ATOM GUIDANCE

The atom-guidance scheme is based on the near-resonant dipole interaction between atoms and evanescent waves. When a guide-laser beam is coupled to a thin core of a hollow optical fiber, the evanescent wave leaks to the hollow region via total reflection on the inner boundary. In the case that the guide-laser frequency is higher than the atomic resonance one (blue detuning), the evanescent wave produces the repulsive optical potential.[9] If the evanescent field is sufficiently intense, the atoms approaching the inner wall can be reflected without hitting the surface. Note that the atoms striking the inner wall will stick there with a high probability.

In the experiments, we use hollow optical fibers with small hollow diameters; 7 μ m, 2 μ m and 1.4 μ m.[10] Each hollow fiber has a cylindrical-core with a thickness of 4 μ m or 2 μ m around the hollow region. The guide-laser power is concentrated in the narrow core so that the intense evanescent wave can be efficiently excited under a feasible experimental condition. For the wavelength 780 nm of the rubidium (Rb) D_2-line, the 7- and 2-μ m-wide hollow fibers become multimode on the light-propagation modes while the 1.4-μ m-wide hollow fiber becomes single-mode.[2,3] The difference of the refractive indices between the core and the cladding is very small as the result that the light propagation can be described by the linearly-polarized (LP) modes in good approximation.[2,3] The fundamental mode is the LP_{01} mode[2,3] which is suitable for guiding atoms because of its round intensity profile.

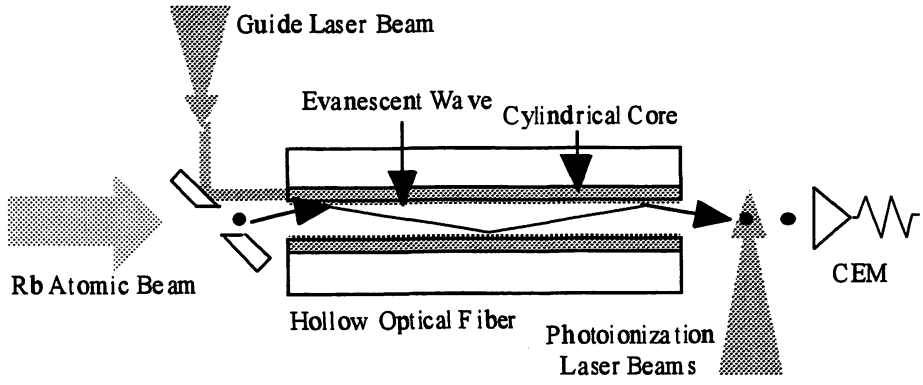

Fig. 1 Experimental Setup

Figure 1 schematically shows the experimental setup. A collimated thermal Rb atomic beam is introduced to a hollow optical fiber with a length of up to 4 cm. A guide-light beam from a Ti:Sapphire laser supporting the evanescent wave is coupled to the cylindrical-core through a mirror with a hole to pass the atomic beam. We selectively excite the LP_{01} mode by adjusting the incidence angle of the guide-laser beam, while monitoring the mode pattern on the exit facet of the hollow fiber by a CCD camera. The guided Rb atoms are detected by a channel electron multiplier (CEM) via their ionization. The atoms not entering the hollow region are completely blocked by a plate with a small hole placed just in front of the facet such that they are not detected downstream. Here, we use the two-step photoionization with a diode laser tuned to the Rb D_2-line and a high-power Ar-ion laser with a wavelength of 476.5 nm. Taking into account the quantum efficiency of 0.9 on the CEM under a negative bias of -3 kV, the detection efficiency is estimated to be up to 60 % in the case of the Ar-ion laser intensity of 0.4 GW/m^2.

Figure 2 shows the Doppler-free laser-photoionization spectrum on the ^{87}Rb atoms in the $5S_{1/2}$, F=2 upper ground state guided in a hollow optical fiber with a hollow diameter of 1.4 μ m over a distance of 3 cm as a function of the blue detuning. The photoionization is performed with two steps: the diode laser selectively excites the ^{87}Rb atoms in the $5S_{1/2}$, F=2 upper ground state to the $5P_{3/2}$, F=3 excited state, and then the Ar-ion laser excites them to the ionization level at 4.177 eV above the $5S_{1/2}$ ground state. The blue detuning is measured from the $5S_{1/2}$, F=2 upper ground state of the ^{87}Rb atoms. Note that the Doppler shift due to the longitudinal atomic velocity is not included here. As shown in Fig. 2, the increase of the guided atoms occurs in the blue-detuning region over 20 GHz. Comparing the maximum flux at a blue-detuning of +7 GHz with the background level that indicates the flux of the ballistic atoms without the guide-laser beam, we get an enhancement factor of 12. From the similar experiment in a hollow fiber with a hollow diameter of 2 μ m, a large enhancement factor of more than 50 is obtained by adjusting the fiber configuration. In the red-detuning region, the decrease of the guided atoms is observed. It is principally due to the adherence of the atoms to the inner wall as a result of the attractive dipole interaction.

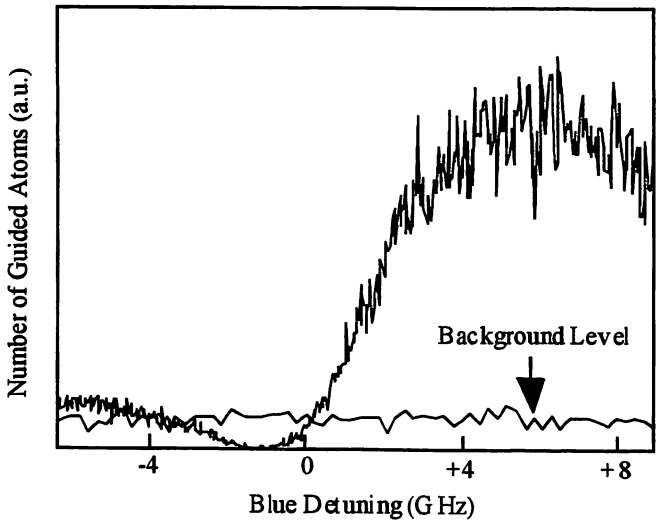

Fig. 2 Two-Step Photoionization Spectrum

3. ISOTOPE SEPARATION

The dipole interaction between atoms and evanescent waves is dispersive in respect of the atomic resonance frequency. Under the frequency-dispersion property, one can perform isotope separation by adjusting the frequency of the guide-laser beam. The Rb atomic beam employed in the experiments includes two stable isotopes with mass numbers 85 and 87 in the natural abundance ratio of 7 to 3. We have demonstrated the separation between the two isotopes by utilizing the isotope energy-shift on their hyperfine ground states.

Provided that the guide-laser frequency is blue-detuned for one isotope but red-detuned for the other, only the former can be selectively transported through the hollow fiber. Figure 3 shows the in-line change of the phtoionization signals on the Rb atom flux guided in a 3-cm-long hollow fiber with a diameter of 7 μ m when the frequency of the diode laser for the state-selective photoionization is scanned in a range involving resonance ones of the two isotopes. In the curve A, the guide-laser frequency is blue-detuned for both isotopes so that they are guided together. In the curve B, on the other hand,

the guide-laser beam is blue-detuned for the mass number 87 but red-detuned for the mass number 85 so that the former is guided while the latter is suppressed except small amounts of the ballistic atoms. This result indicates that the hollow optical fiber supported by the evanescent wave works as an atomic filter with species- and sate-selectivity.

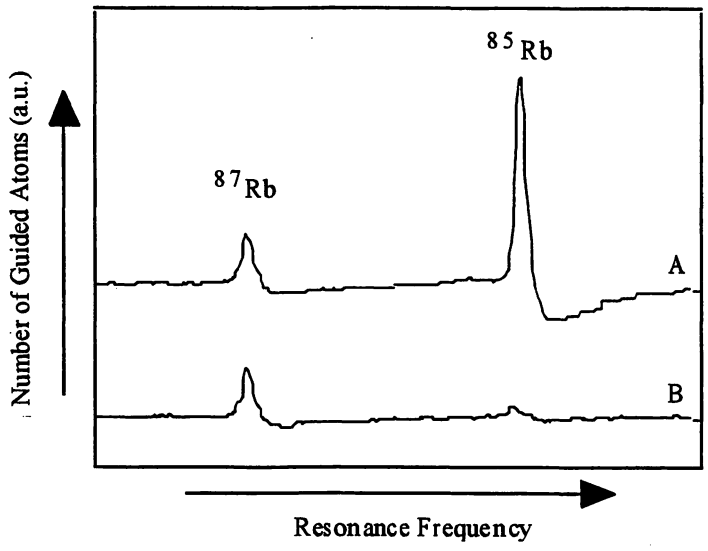

Fig. 3 In- Line Isotope Separation

4. MEASUREMENT OF CAVITY QED ENERGY SHIFTS

The use of such minute-hollow optical fibers enables one not only to enhance the atom-manipulation accuracy but also to apply the atom-guidance technique to the studies on quantem-mechanical and quantum-optical phenomena. In the vicinity of the dielectric wall of the hollow fiber supported by the blue-detuned evanescent wave, the atoms feel the attractive cavity potential as well as the repulsive optical potential. The former is due to the cavity QED effect involving the van der Waals force and the Casimir-Polder one while the latter is due to the dipole force from the evanescent wave. At a given blue-detuning, the repulsive optical potential is in proportion to the intensity of the evanescent wave. On the other hand, the attractive cavity potential becomes larger as the hollow diameter becomes smaller. Therefore, under the weak excitation of the evanescent wave in a small hollow fiber, the attractive cavity potential may exceed the repulsive optical potential as the result that the guiding of atoms is suppressed. We have studied the cavity QED energy-shift on the guided atoms in a hollow optical fiber with a hollow diameter of 1.4 μ m: it is only 1.8 times as the wavelengths of the Rb D-lines so that the cavity potential can be comparable to the optical one.

Figure 4 shows the change of the guided ^{87}Rb atom flux as a function of the optical potential U_{op} on the inner wall, which is in proportion to the guide-laser power. The two-step photoionization scheme selectively detects the ^{87}Rb atoms in the $5S_{1/2}$, F=2 upper ground state under tuning of the diode laser to the $5S_{1/2}$, F=2→$5P_{3/2}$, F=3 transition. The guide laser supporting the evanescent wave is blue-detuned at +3 GHz by locking its frequency to the transition line of the ^{85}Rb atoms in the $5S_{1/2}$, F=2 lower ground state. The optical potential is normalized to the transverse kinetic energy K_t. The threshold on the increase of the guided Rb atom flux can be clearly observed in Fig. 4.

Recently, the theoretical result for the cavity QED effect in a cylindrical dielectric has been obtained.[5] However, it requires much long computational time to analysis the experimental result. Therefore, instead of the exact solution, we derive the experimental formula from the simple form of the cavity potential in parallel conductor planes[11] by introducing a dielectric factor and a geometric one. From the result in Fig. 4, we get a geometrc factor of about 3.4,[6] which is in good agreement with the value estimated by the numerical analyses in a hollow spherical conductor[12] and parallel dielectric planes[13].

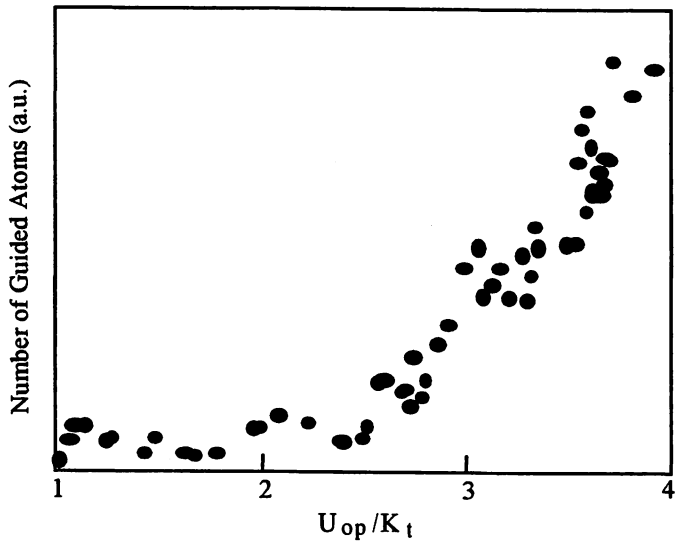

Fig. 4 Power Change of Guidance

5. FOR OPTICALLY-CONTROLLED ATOM DEPOSITION

The atom deposition with the techniques of atom optics has been demonstrated to form parallel-lines pattern within light-diffraction limit.[7] The atom-guidance scheme is useful in a novel form of the optical atom deposition beyond the diffraction limit. Because of the dot-shaped pattern on the guided atom flux, it may fabricate an arbitrary pattern with nanometer-scale depth, for example, quantum dots. In addition, since the fiber can be bent, one can carry the guided atoms aiming at any point on a substrate.

Figure 5 shows the spatial distribution of the Rb atom flux guided in a hollow optical fiber with a hollow diameter of 7 μ m. The distribution is measured by scanning a Pt hot-wire with a diameter of 10 μ m under a blue-detuning of +3 GHz above the $5S_{1/2}$, F=3 upper ground state of the ^{85}Rb atoms. The surface-ionization signal indicates that the spatial distribution becomes 20 μ m at FWHM measured from the background level. The estimated transverse velocity is in good agreement with the average transverse velocity 20 cm/s of the incidence atoms in our collimation scheme. From the measured flux in Fig. 5, the deposition time per 1 nm is estimated to be up to 1 hour. The deposition rate can be controlled by adjusting the blue-detuning. In the low-temperature experiment under suppressing the incidence atom flux, we get a flux change of about 10 atom/s for a frequency change of 1 GHz.

The use of cold atoms is considered for the atomic-level crystal growth. The attachment of the atomic funnel is effective to collect cold atoms and couple them to the hollow fiber.[14,15] In particular, it enables one to guide them in a bent fiber

scheme so that it will much enhance the manipulation accuracy. Moreover, if a sharpened optical fiber[16] with the evanescent wave excited on a nanometrc tip is combined together, the guided cold atoms can be manipulated with a nanometer accuracy,[17,18] which leads to the atom-by-atom deposition. For attaching the atomic funnel upstream the hollow fiber, the lateral light-coupling scheme will be useful.[19]

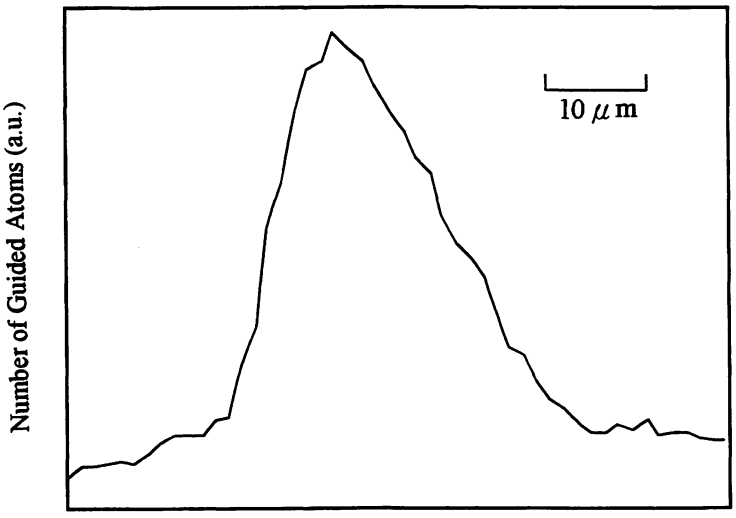

Fig 5 Surface Ionization Scan

Figure 6 shows the atomic funnel supported by the blue-detuned evanescent wave. The funnel is made up of a hollow conical prism with a height of 4 mm and a full apex angle of 90 degree. In order to avoid extra heating effect on the funneled atoms, the doughnut-shaped laser beam is irradiated upward. The potential barrier to reflect cold atoms dropped from a magneto-optical trap (MOT) is produced in the vicinity of the inner wall via the total reflection of the doughnut-shaped light beam. Since the gravitational acceleration is large, cooling mechanism is required to compensate the acceleration of the cold atoms. This can be carried out by adding a weak pumping beam downward based on the evanescent-wave cooling.[20] In Fig. 6, the cross-sectional trajectory of a ^{85}Rb atom randomly sampled from an MOT with a Maxwell-Boltzmann distribution at a temperature of 10 μ K is drawn by the 3-D Monte-Carlo simulation with an ensemble of 10^4 atoms. The Monte-Carlo simulation shows that, under a laser power of 1 W and a blue detuning of 1 GHz, about a half of the ^{85}Rb atoms released from the MOT prepared at 1 mm above the open face of the funnel can be sent through an exit hole with a diameter of 100 μ m at the bottom of the prism.[21]

6. SUMMARY

We have performed the atom-guidance experiment in three kinds of hollow optical fiber: their hollow diameters are 7 μ m, 2 μ m and 1.4 μ m. The Doppler-free photoionization spectrum shows that the blue-detuned evanescent wave can transport the thermal atoms down the hollow fibers through a long distance with high efficiency. Based on the frequency-dispersion property, the isotope separation between ^{85}Rb and ^{87}Rb atoms is carried out. Furthermore, by using a 1.4-μ m-hollow-core fiber, the atomic energy-shift due to the cavity QED effect is first measured in a cylindrical dielectric. The atom-guidance technique will lead to a new form of the optical atom deposition with high spatial accuracy and precise controll of the deposition rate.

The combination of the near-field atom optical methods with the evanescent wave such as the atom-guidance, the atomic funnel, and the sharpened optical fiber will realize the atom manipulation with nanometer accuracy.

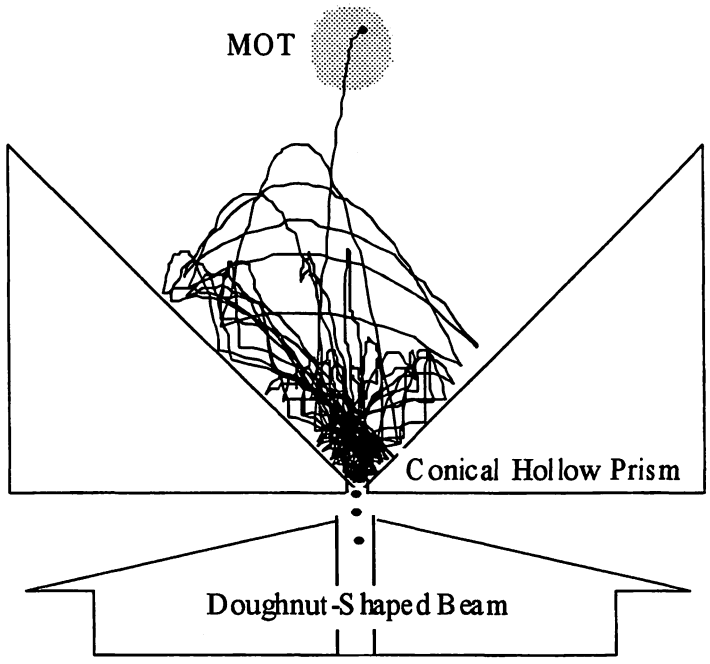

Fig. 6 Atomic Funnel

ACKNOWLEDGEMENTS

We thank Drs. S. Sudo and Y. Sakai of NTT Opto-Electronics Laboratories for their useful discussions on micron-sized hollow optical fibers. This work was supported by the MATSUO FOUNDATION of Japan. WJ is also grateful to the STEPI of Korea for its financial supports.

REFERENCES

1. H. Ito, T. Nakata, K. Sakaki, M. Ohtsu, K. I. Lee, and W. Jhe, "Laser spectroscopy of atoms by evanescent waves in micron-sized hollow optical fibers", Phys. Rev. Lett. **76**, pp. 4500-4503, 1996.
2. H. Ito, K. Sakaki, T. Nakata, W. Jhe, and M. Ohtsu, "Optical potential for atom guidance in a cylindrical-core hollow fiber", Opt. Commun. **115**, pp. 57-64, 1995.
3. H. Ito, K. Sakaki, T. Nakata, W. Jhe, and M. Ohtsu, "Optical guidance of neutral atoms using evanescent waves in a cylindrical-core hollow fiber: theoretical approach", Ultramicroscopy **61**, pp. 91-97, 1995.
4. D. J. Harris and C. M. Savage, Phys. Rev. A **51**, pp. 3967-3971, 1995.
5. H. Nha and W. Jhe, "Cavity quantum electrodynamics for a cylinder: inside a hollow dielectric and near a solid dielectric cylinder", submitted.
6. H. Ito, K. Sakaki, M. Ohtsu, H. Nha, and W. Jhe, "Measurement of atomic energy shifts in a hollow optical fiber", submitted.

7. R. W. McGowan, D. M. Giltner, and S. A. Lee, Opt. Lett. **20**, pp. 2535-2537, 1995.
8. H. Ito, K. Sakaki, M. Ohtsu, and W. Jhe, "Evanescent-light guiding for optically-controlled atom deposition", submitted.
9. V. I. Balykin, V. S. Letokov, Yu. B. Ovchinnikov, and A. I. Sidorov, "Quantum-state-selective mirror reflection of atoms by laser light", Phys. Rev. Lett. **60**, pp. 2137-2140, 1988.
10. S. Sudo, I. Yokoyama, H. Yasaka, Y. Sakai, and T. Ikegami, "Optical fiber with sharp optical absorption by vibrational-rotational absorption of C_2H_2 molecules", IEEE Photon. Technol. Lett. **2**, pp. 128-131, 1990.
11. G. Barton, "Quantum-electrodynamic level shifts between parallel mirrors: analysis", Proc. R. Soc. Lond. A **410**, pp. 141-174, 1987.
12. W. Jhe and K. Jang, "Cavity quantum electrodynamics inside a hollow apherical cavity", Phys. Rev. A **53**, pp. 1126-1129, 1996.
13. H. Nha and W. Jhe, "Cavity quantum electrodynamics between parallel dielectric surfaces", Phys. Rev. A **54**, pp. 3505-3513, 1996.
14. H. Ito, K. Sakaki, W. Jhe, and M. Ohtsu, "Atomic funnel with evanescent waves" in *Quantum Electronics and Laser Science Conference*, Vol. 10, 1996 OSA Technical Digest Series, pp. 91-92, OSA, Washington, D.C., 1996.
15. K. I. Lee, J. A. Kim, H. R. Noh, and W. Jhe, "Single-beam atom trap in a pyramidal and conical hollow mirror", Opt. Lett. **21**, pp. 1177-1179, 1996.
16. S. Mononobe and M. Ohtsu, "Fabrication of a pencil-shaped fiber probe for near-field optics by selective chemical etching", J. Lightwave Technol. **14**, pp. 2231-2235, 1996.
17. M. Ohtsu, S. Jiang, T. Pangaribuan, and M. Kozuma, "Nanometer resolution photon STM and single atom manipulation", in *Near-Field Optics*, edited by D. W. Pohl and D. Courjon, pp. 131-139, Kluwer, Dordrecht, 1993.
18. M. Ohtsu, "Progress of high-resolution photon scanning tunneling microscope due to a nanometric fiber probe", J. Lightwave Technol. **13**, pp. 1200-1221, 1995.
19. H. Ito, K. Sakaki, M. Ohtsu, and W. Jhe, "Atom guidance in a hollow optical fiber with light coupled sideways", submitted.
20. J. Söding, R. Grimm, and Yu. B. Ovchinnikov, "Gravitational laser trap for atoms with evanescent-wave cooling", Opt. Commun. **119**, pp. 652-662, 1995.
21. H. Ito, K. Sakaki, M. Ohtsu, and W. Jhe, "Atomic funnel with evanescent light", submitted.

Further author information -

H.I. (correspondence): Email: haruhiko@net.ksp.or.jp; Telephone: +81-44-819-2071; Fax: +81-44-819-2072

K.S.: Email: ksakaki@net.ksp.or.jp

W.J.: Email: whjhe@phya.snu.ac.kr; Telephone: +82-2-880-6600; Fax: +82-2-884-3002

M.O.: Email: ohtsu@ae.titech.ac.jp; Telephone: +81-45-924-5455; Fax: +81-45-921-1204

ATOM GUIDANCE AND MANIPULATION BY NEAR FIELD OPTICS

Motoichi OHTSU

(1) Interdisciplinary Graduate School of Science and Engineering, Tokyo Institute of Technology, 4259 Nagatsuta, Midori-ku, Yokohama 226, JAPAN

(2) Photon Control Project, Kanagawa Academy of Science and Technology, KSP East Rm.408, 3-2-1 Sakado, Takatsu-ku, Kawasaki, Kanagawa 213, JAPAN

In addition to utilizing the short-range optical resonant interaction with matter, sized-dependent localization of optical near-field can realize versatile and local processes for nano/atom lithography and deposition. This paper reviews recent progress of my works listed below and gives future overlook. The main part of this talk will be [Ⅳ].

[Ⅰ] ***Probe fabrication:*** Through developing reproducible chemical etching processes, we have realized a fiber probe with apex diameter < 3nm for high-resolution imaging(**Fig.1**). An axially asymmetric fiber probe has also been developed to excite HE plasmon mode so that the throughput was enhanced over 100 times for high S/N imaging(**Fig.2**).

[Ⅱ] ***Imaging and spectroscopy:*** Spatial Fourier analysis of our imaging experimental results showed the -3dB high-cut off spatial frequency of 1/0.8 nm^{-1}, from which a measure of spatial resolution was estimated to be 0.8 nm. Nanometric $LiNbO_3$ particles(**Fig.3**) and atomic-steps on sapphire substrate(**Fig.4**) were imaged, for which shear-force technique was not used for probe position control in order to avoid topographical artifacts. Spatially resolved photoluminescence spectroscopy of semiconductor quantum dots was carried out at Liq.-He temperature, by which inhomogeneous spectral broadening was removed. PL spectroscopy of one-dimensional electronic structures of polysilanes(**Fig.5**) was also carried out at UV region with a spatial resolution of < 20 nm(**Fig.6**).

[Ⅲ] ***High density optical storage:*** Photon-mode optical storage was carried out on a photochromic LB film with a pit diameter of < 100 nm(**Fig.7**). For high speed storage and read-out (≒100Mb/s@ shot noise limit), silicon planar micro-fabrication is now in progress to fabricate a 2-D planar array of flying head for high-speed near-field optical probe. Their details will be reviewed at the meeting.

[Ⅳ] ***Atom technology:*** We have previously proposed the method of trapping a single atom by evanescent field on the top of a nanometric sharpened fiber probe tip, which can be applied for forming an atomic quantum dot. Further, we have realized atomic quantum wire, i.e., guiding Rb atoms by the cylindrical evanescent field on the inner surface of a hollow optical fiber(**Fig.8**). Three kinds of hollow fibers of 3-cm length were used, which had the hollow diameters of 7-, 2-, and 1.4- μ m(**Fig.9**). Existence of the threshold on guidance efficiency, due to the attractive van der Waals force, was observed(**Fig.10**). The guidance efficiency as high as 56 % was obtained. By using these results, the time taken for depositing a 1-nm thick layer of the transmitted Rb atoms on the crystal substrate was estimated to be 2.8 hours, i.e., deposition time is 2.8hr/nm. Although this rate is slower than the conventional chemical process, the present physical deposition process can manipulate small number of atoms for a single atomic-level depositon. Outlook for further improvements of this process will be proposed at the meeting.

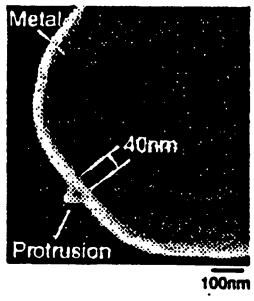

Fig.1

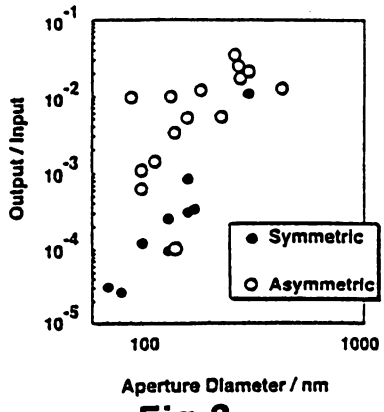

Fig.2

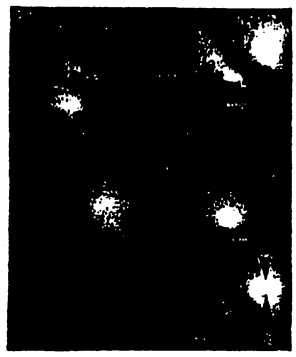

Fig.3

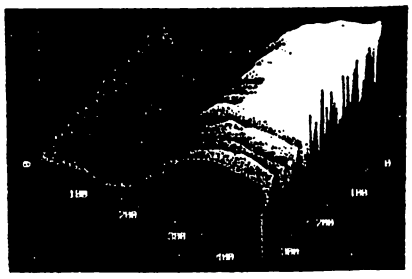

Fig.4

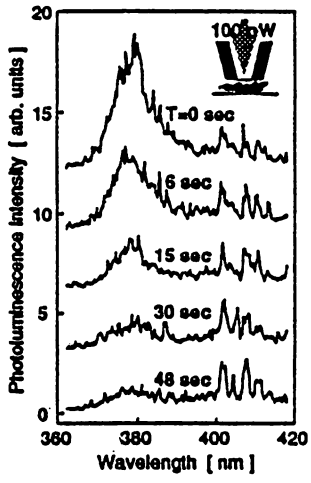

Fig.5

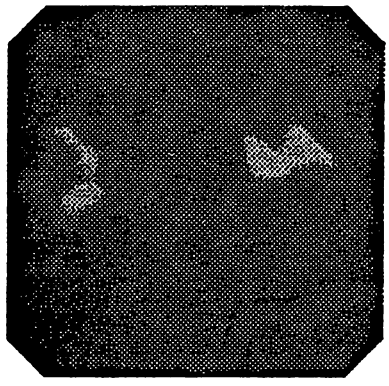

Fig.6

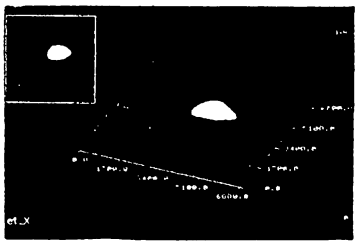

Fig.7

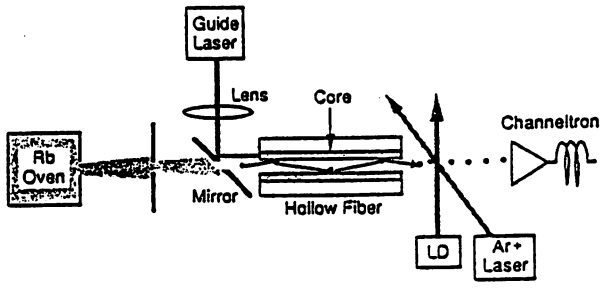

Fig.8

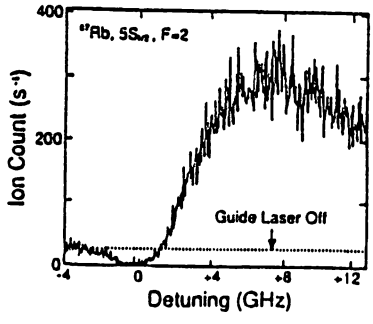

Fig.9

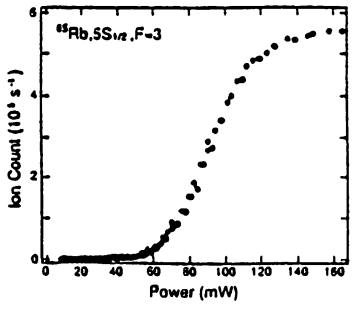

Fig.10

[I-2] NANO PHOTONICS

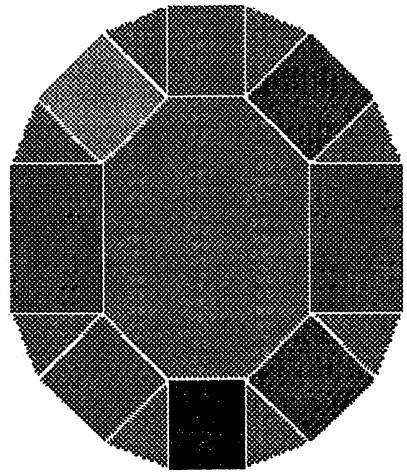

Jpn. J. Appl. Phys. Vol. 36 (1997) pp. L 896–L 898
Part 2, No. 7B, 15 July 1997

Spatially Resolved Detection of Electroluminescence from Lateral p-n Junctions on GaAs (111)A Patterned Substrates Using a Near-Field Scanning Optical Microscope

Nobuo SAITO, Fumio SATO, Kuniharu TAKIZAWA, Jun-ichi KUSANO, Hideyo OKUMURA, Tahito AIDA, Toshiharu SAIKI[1] and Motoichi OHTSU[1,2]

NHK Science and Technical Research Laboratories, Kinuta, Setagaya, Tokyo 157, Japan
[1] *Kanagawa Academy of Science and Technology, Takatsu-ku, Kawasaki, Kanagawa 213, Japan*
[2] *Tokyo Institute of Technology, Midori-ku, Yokohama, Kanagawa 226, Japan*

(Received May 19, 1997; accepted for publication June 13, 1997)

Lateral p-n junctions on GaAs (111)A patterned substrates are characterized through the spatially resolved detection of light emission by current injection using a collection-mode near-field scanning optical microscope. The junctions are one-step grown at the upper and the lower end of the slope, taking advantage of the amphoteric nature of Si in GaAs. Although the width of the transition region determined from spatially resolved photoluminescence measurements is much wider in the lower junction than in the upper one, the broadness of the junction, which is observed for the first time owing to the high resolution of the detection system, is the same for both junctions.

KEYWORDS: lateral p-n junction, GaAs (111)A, MBE, patterned substrate, near-field scanning optical microscope

One-step formation of lateral p-n junctions on a patterned substrate is a promising process for the fabrication of novel optical devices.[1–4] This is because the process causes less damage to the devices than a conventional fabrication one which consists of etching and overgrowth procedures. The junctions can be used not only as current confinement structures of light-emitting devices,[2,3] but also as active regions in lasers.

The process utilizes the amphoteric nature of Si in GaAs. Si can occupy the Ga site or the As site depending on the growth conditions.[5,6] For example, the conduction type of Si-doped GaAs changes as the orientation of the substrate changes: Si acts as a donor on (100) and (111)B substrates, while it acts mainly as an acceptor on (111)A substrates. The type also depends on the growth temperature on (110) and (311) A substrates, that is, it is p-type when the growth temperature is high and n-type when it is low. Hence, if we prepare patterned substrates which have two kinds of surfaces, n- and p-type regions are formed simultaneously.

Since the incorporation behavior of Si on a patterned substrate determines the switching of the conduction type on one surface to that on another surface, it has been studied extensively by various methods, such as cathodoluminescence (CL),[7,8] spatially resolved photoluminescence (PL),[9] and micro-Raman measurements.[10] Spatially resolved PL measurement using a near-field scanning optical microscope (NSOM) has been shown to be especially useful for the investigation of lateral p-n junctions, because its spatial resolution is beyond the diffraction limit of light and therefore higher than that of CL measurement ($\sim\mu$m).

Moreover, NSOM has the ability to simultaneously record both the optical properties and the topography through shear-force measurements. This enables us to determine precisely where the light emission occurs on the mesa structure, which is necessary for the design of the active region in a transverse junction stripe (TJS) laser.[11]

In this work, we have studied lateral p-n junctions through the spatially resolved detection of electroluminescence (EL) by current injection using a collection-mode NSOM in combination with a spatially resolved photoluminescence (PL) study[9] in which an illumination-mode NSOM is used.

The samples were prepared on a semi-insulating (111)A on-axis substrate. Patterned substrates with (311)A slopes of about 5 μm depth were fabricated by conventional photolithography and wet-chemical etching techniques. A solution of H_3PO_4:H_2O_2:H_2O (3:1:50) was used. Si-doped GaAs layers 1 μm thick were grown by molecular beam epitaxy (MBE) at a substrate temperature of 600°C and a growth rate of 1.3 μm/h with an As_4/Ga flux ratio of 2. Silicon concentration of the layer was 1×10^{18} cm^{-3}.

A schematic diagram of collection-mode detection of EL is shown in Fig. 1(a). The light was collected by a fiber probe and introduced to an avalanche photodi-

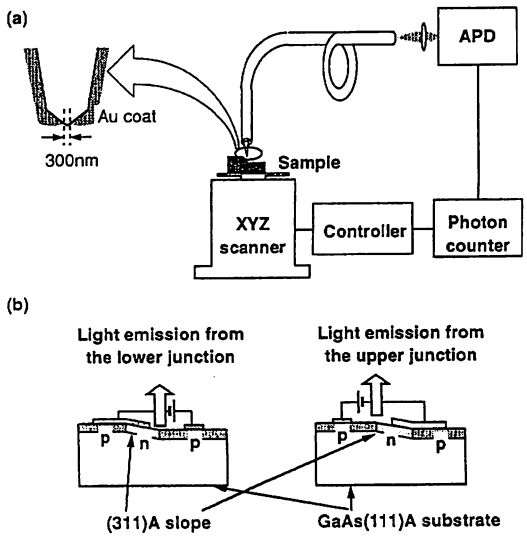

Fig. 1. (a) Schematic setup of a near-field scanning optical microscope in collection mode for spatially resolved detection of electroluminescence, and (b) two types of electrodes used for the detection of the emission from each of the lower junction and the upper one.

ode (APD). The shear force from the sample surface to the fiber tip[12] was detected as the change in its amplitude of oscillation, using a 1.5 μm laser diode to keep the distance between the tip and the surface constant at 10 nm. To study a sample with steps using a fiber probe, it is necessary to lengthen the tip to avoid the contact of the probe with the sample, while maintaining high transmission efficiency at the same time. To meet these requirements, we used a fiber probe whose tip has a stepped cone angle (inset of Fig. 1(a)).[13] After coating with gold, the topmost part of the tip was etched to obtain an aperture of 300 nm in diameter. Since the detection region in the collection mode is expected to be almost the same as the diameter of the aperture, the lateral resolution of this experiment is estimated as 300 nm.

The lateral p-n junctions are formed on both the upper and the lower ends of the slope. Two types of electrodes (Fig. 1(b)) were deposited to detect the light from each junction independently.

In Fig. 2, the EL image of the lower junction is shown with its topographic image. The light emission was observed at the foot of the slope in a straight line. The change of the intensity which was measured in the direction along a line perpendicular to the junction, is shown for the lower junction (Fig. 3(a)) and for the upper one (Fig. 3(b)), with the height of the surface (Fig. 3(c)). Also shown (Fig. 3(d)) is the PL peak wavelength as a function of position, obtained by spatially resolved PL spectroscopy measurement.[9] The transition region in which the PL peak wavelength shifted from the value of p-type (870 nm) to that of n-type (855 nm) is clearly seen. The peak of the EL from each junction is located in the p-type side of the corresponding transition region.

The conduction type and carrier concentration of the layer grown on (111)A substrates depend on the misorientation angle of the substrate from the (111)A direction under a given growth condition.[14] Under our etching condition, a clear edge was formed between the (111)A surface and the (311)A slope at the upper end of the slope, while at the lower end, the (311)A slope gradually changed into the (111)A surface. This can be clearly seen in Fig. 3. Hence, the gradual change in the orientation at the lower part of the slope causes the gradual change in the carrier concentration, which leads to the wide transition region. On the other hand, in the upper junction, the fact that the conduction type and carrier concentration change in a narrow region corresponds to the observation that the substrate changes abruptly from the (111)A surface into the (311)A slope.

The difference in the incorporation behavior of Si in GaAs on different surfaces can be understood in terms of surface bonds. On the (111)A surface, there are only single dangling-bond sites, while the (311)A surface consists of one double dangling-bond site alternating with one single dangling-bond site,[15] which are (100)-like and (111)A-like bond sites, respectively. Under a

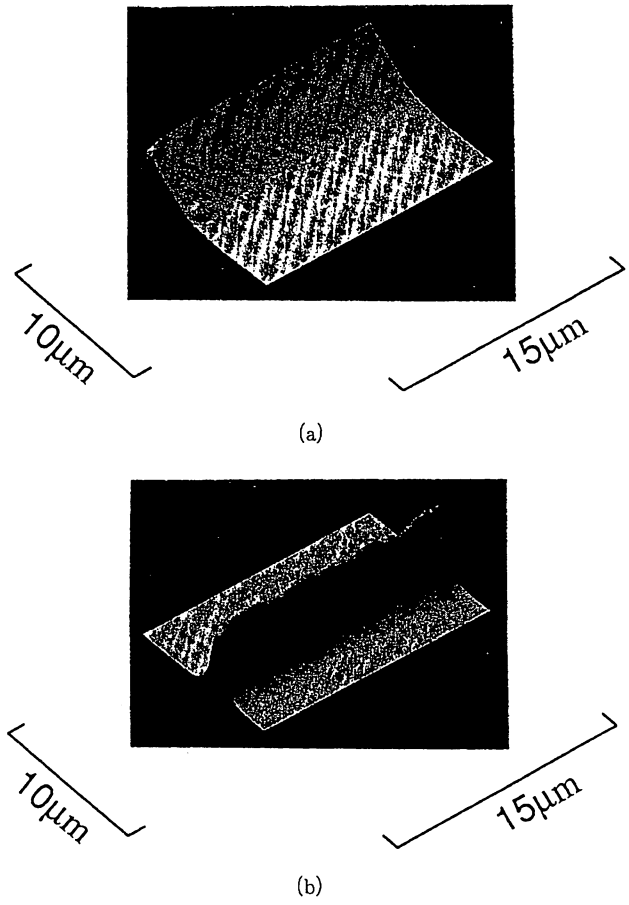

Fig. 2. Two-dimensional distribution of (a) the height of the surface and (b) the intensity of the electroluminescence.

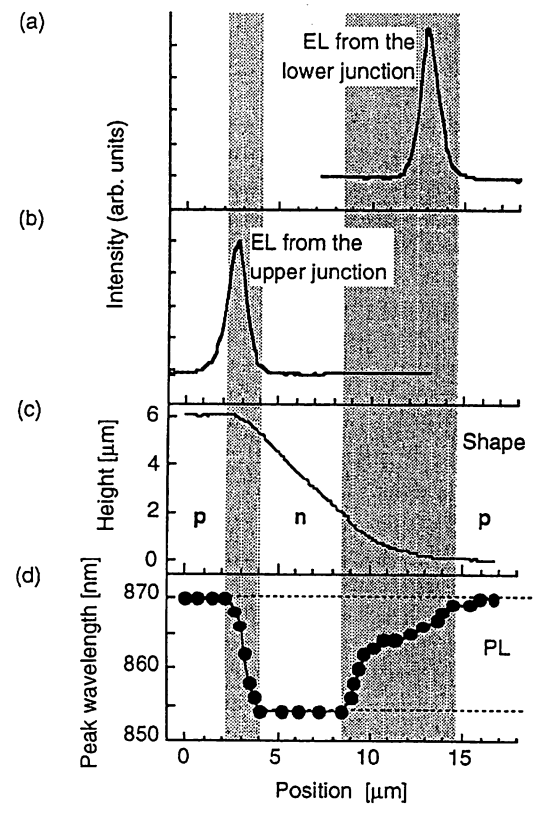

Fig. 3. Variation along a line perpendicular to the lateral p-n junctions of (a) intensity of electroluminescence from the lower junction, and (b) that from the upper one, (c) height of the sample, and (d) peak wavelength of photoluminescence.

given growth condition, Si is more likely to become an acceptor with (111)A-like bonds rather than (100)-like bonds. This can be explained by considering that As_4 with (111)A-like bonds is more difficult to decompose and hence the probability of the incorporation of Si into the As site becomes higher.[14] Therefore the conduction type is governed by the competition of the Si incorporation mechanisms between the (111)-A and the (100) type, in which Si occupies the Ga site or the As site, respectively, and the lateral p-n junction is formed at the boundary of the two regions. In other words, the position of the junction corresponds to the place where switching occurs between the two types of incorporation mechanisms. The result that the lower junction was formed on the nearly (111)A surface shows that the incorporation of Si in the Ga site is much more dominant on the non-(111)A surface, although almost all the Si is incorporated in As sites once the (111)A surface is attained. This is consistent with the result in ref. 14 that as the misorientation angle increases on substrates misoriented from (111)A, the number of donor sites for Si increases much more rapidly than the ratio of (100)-like bonding to (111)A-like bonding. Our result has directly shown the switching, for the first time, owing to both the high spatial resolution of the detection system and the gradual change of the surface orientation.

Moreover, since the width of the emission region for both junctions was the same as 1.1 μm (FWHM), competition between the two incorporation mechanisms takes place at the upper junction in the same manner as at the lower junction, in spite of the large difference in the widths of the transition region obtained from the PL measurement, 1.8 μm in the upper junction and 5.5 μm in the lower one.

Furthermore, from the viewpoint of designing laser, the lower junction is more suitable for a TJS laser, because it is formed on a more planar surface than the upper one. Mirrors for the cavity in surface-emitting configuration are expected to be fabricated more easily.

In conclusion, we have investigated the lateral p-n junctions grown on GaAs (111)A patterned substrates using a near-field scanning optical microscope. The position of light emission in lateral p-n junctions is directly determined through spatially resolved detection of electroluminescence by current injection with a spatial resolution of 300 nm. In combination with the spatially resolved PL measurements, which enabled the determination of the width and the position of the transition region, local characterization with a near-field scanning microscope is shown to be useful in the analysis of optical devices.

The authors would like to acknowledge Dr. I. Fujimoto for his useful discussion and M. Yamaga for his help in preparing the samples.

1) D. L. Miller: Appl. Phys. Lett. **47** (1985) 1309.
2) H. Jaeckel, H. P. Meier, G. L. Bona, W. Walter, D. J. Webb and E. Van Gieson: Appl. Phys. Lett. **55** (1989) 1059.
3) T. Takamori, Y. K. Sin, K. Watanabe and T. Kamijoh: Appl. Phys. Lett. **61** (1992) 2266.
4) M. Inai, T. Yamamoto, T. Takebe and T. Watanabe: Jpn. J. Appl. Phys. **32** (1993) L1718.
5) J. M. Ballingal and C. E. C. Wood: Appl. Phys. Lett. **41** (1982) 947.
6) W. I. Wang, E. E. Mendez, T. S. Kuan and L. Esaki: Appl. Phys. Lett. **47** (1985) 826.
7) M. Fujii, T. Yamamoto, M. Shigeta, T. Takebe, K. Kobayashi, S. Hiyamizu and I. Fujimoto: Surf. Sci. **267** (1992) 26.
8) N. Saito, M. Yamaga, F. Sato, I. Fujimoto, M. Inai, T. Yamamoto and T. Watanabe: *Proc. Int. Symp. GaAs and Related Compounds, Freiburg, 1993*, Inst. Phys. Conf. Ser. **136** (IOP Publishing Ltd., Bristol, 1994) p. 601.
9) T. Saiki, S. Mononobe, M. Ohtsu, N. Saito and J. Kusano: Appl. Phys. Lett. **67** (1995) 2191.
10) J. Gerster, J. M. Schneider, C. Ehret, W. Limmer, R. Sauer and H. Heinecke: Appl. Phys. Lett. **70** (1997) 69.
11) H. Namizaki: IEEE J. Quantum Electron. **QE-11** (1975) 427.
12) E. Betzig, P. L. Finn and J. S. Weiner: Appl. Phys. Lett. **60** (1992) 2484.
13) T. Saiki, S. Mononobe, M. Ohtsu, N. Saito and J. Kusano: Appl. Phys. Lett. **68** (1996) 2612.
14) Y. Okano, M. Shigeta, H. Seto. H. Katahama, S. Nishine and I. Fujimoto: Jpn. J. Appl. Phys. **29** (1990) L1357.
15) W. Q. Li, P. K. Bhattacharya, S. H. Kwok and R. Merlin: J. Appl. Phys. **72** (1992) 3129.

Near-field optical microscope image formation: a theoretical and experimental study

A. V. Zvyagin

Tokyo Institute of Technology, Nagatsuta 4259, Yokohama 227, Japan

J. D. White

Kanagawa Academy of Science and Technology, Kawasaki, 213, Japan

M. Ohtsu

Tokyo Institute of Technology, Nagatsuta 4259, Yokohama 227, Japan, and Kanagawa Academy of Science and Technology, Kawasaki, 213, Japan

Received March 3, 1997

A quantitative comparison between theory and experiment has been carried out for a collection-mode near-field optical microscope. A 30-nm (lateral dimension) cylindrical dielectric sample was imaged. This image was compared with the result of theoretical calculations that used a classical macroscopic nonglobal model based on the excitation theorem. Good agreement was obtained, with image inversion, edge enhancement, and edge asymmetry correctly predicted. © 1997 Optical Society of America

The near-field optical microscope (NOM), a member of the family of scanning probe microscopes that includes the scanning tunneling microscope and the atomic force microscope, is different from other optical microscopes in that it exploits the unique properties of the optical near field to yield subwavelength resolution. As it does not harm the sample, it has found application in such diverse fields as biology, spectroscopy, and optical storage.[1] To gain insight into the NOM image-formation mechanism and to clarify the often puzzling relationship between NOM images and real topography that is encountered in experiments, it is important to specify inherent NOM phenomena to be studied both experimentally and theoretically. Such effects as spatial localization,[2,3] polarization-directional dependence,[4,5] and image inversion[2,6] can be attributed to these purely near-field effects. These effects are dominant in samples characterized by $kd \ll 1$ and $kh \ll 1$, where d is the width of the sample, h is the maximum height of the sample above the planar substrate, and k is the wave number of the light used in observing the specimen. (In the case of illumination with the commonly used red laser, $d, h \ll 100$ nm.) Samples that satisfy these criteria can be reasonably denoted near-field objects.[7] In the most recent of several initial attempts[8–10] to carry out both experimental and theoretical NOM image study, Weeber *et al.*[10] imaged a sample [$d = 100$ nm ($kd \sim 1$), $h = 70$ nm ($kh \sim 0.7$)] and found qualitative agreement with their microscopic theory.[2] In the present study we quantitatively compare experimental results with theoretical calculations based on a classical macroscopic nonglobal model, using a well-defined nanometric- [$d \sim 30$ nm ($kd \sim 0.3$), $h \sim 16$ nm ($kh \sim 0.15$)] sized dielectric sample.

Whereas the NOM can be operated in a number of different modes, we have chosen the collection-mode NOM (c-mode NOM) for this image-formation study because the polarization state of the incident light can be accurately controlled. In this configuration the sample is illuminated under the total-internal-reflection condition (Fig. 1) and the optical field probed by a sharpened fiber tip. An image is formed by detection of the changes in optical field intensity as the fiber is scanned laterally.

For modeling purposes the fiber tip apex is represented as a nanometer-sized dielectric sphere. As the probe and the sample interact weakly,[5] the intensity picked up by the probe is proportional to the near-field intensity. The problem is thus reduced to the solution of Maxwell's equations, subject to a nonlocal boundary condition. Under the assumption that the dielectric medium is linear, homogeneous, and isotropic, Maxwell's equations reduce to the Helmholtz equation

$$(\nabla^2 + K^2)\mathbf{E}(\mathbf{r}) = 0, \qquad K = \begin{cases} \omega/c & \text{in air} \\ n_{\text{glass}}\omega/c & \text{in glass} \end{cases}, \tag{1}$$

where $\mathbf{E}(\mathbf{r})$ is the total electric field, K is the wave-vector amplitude, ω is the angular frequency of the incident light, c is the speed of light in air, and n_{glass} is the refractive index of the glass substrate and the sample (for simplicity and in view of the dominant influence of topographic features,[11] the refractive index of the sample is assumed to be equal to that of the glass substrate). This equation must be solved subject to the nonlocal boundary condition that

$$\mathbf{E}^i(r) + \frac{c}{4\pi\omega n_{\text{glass}}}\nabla\times\nabla \times \int_S \left[\mathbf{E}(\mathbf{r}')\frac{\partial G(\mathbf{r}|\mathbf{r}')}{\partial \hat{n}'} - G(\mathbf{r}|\mathbf{r}')\frac{\partial \mathbf{E}(\mathbf{r}')}{\partial \hat{n}'}\right] dS' = 0, \tag{2}$$

$r \in$ air, where $\mathbf{E}^i(r)$ is the electric field in glass, G is Green's function, and $\hat{n}$ is a unit vector normal to the surface S. This is also known as the optical extinction theorem.[12] The theorem formally expresses

0146-9592/97/130955-03$10.00/0

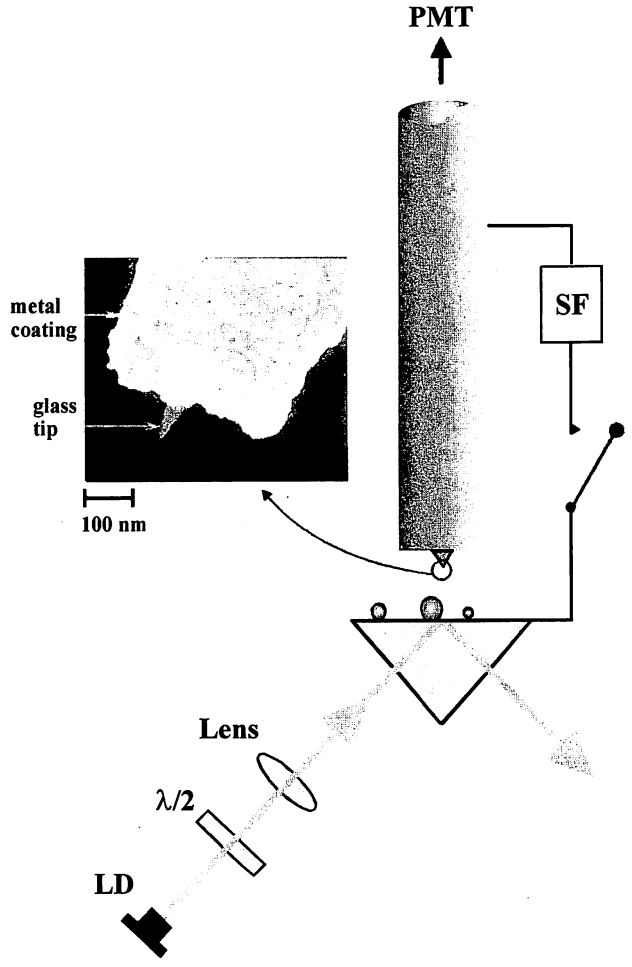

Fig. 1. Schematic diagram of the c-mode NOM experimental setup: LD, laser diode; $\lambda/2$, half-wavelength plate; PMT, photomultiplier tube; SF, shear-force control servo loop. When the shear-force control servo loop is locked the NOM setup runs in constant separation mode; otherwise it runs in constant-height mode. Inset: scanning electron microscope photograph of the fiber tip.

that if an electromagnetic wave electric vector $\mathbf{E}^i(r)$ is incident from glass upon air separated by a sample surface (S), it is canceled (extinguished) in the latter medium, giving rise to a new wave $[\mathbf{E}(\mathbf{r})]$. The electric field, Green's function, and their normal derivatives $(\partial/\partial n)$ are evaluated on the surface $(\mathbf{r}' \in S)$. When the sample height (h) is much less than the wavelength λ (the only case of practical interest), the electric field, Green's function, and their normal derivatives can be expressed as a power series of the sample height, allowing the problem to be solved in the small-perturbation limit by use of the field's angular spectrum representation (Rayleigh hypothesis). Under these assumptions, the near field is a vector sum of a large background field and a term containing the surface information filtered by propagation, translation, and diffraction factors. In the c-mode NOM operated in a constant-height mode (CHM) this model predicts both image inversion and edge enhancement.[6]

A biological specimen, a microtubule, was chosen as the subject of experimental investigation because of its well-identified nanometric size (with associated proteins, 25–30 nm in diameter and micrometers in length) and importance biologically. Its cylindrical shape allows for the investigation of directional and polarization effects, as the illumination direction can be varied with respect to the axis of the microtubule.

A schematic view of the experimental system is shown in Fig. 1. Focused light (linearly polarized) from a laser diode (λ = 680 nm) is incident upon the sample placed upon a glass prism. The polarization angle is controlled by means of a half-wave plate. A sharpened optical fiber is used to probe the evanescent field above the sample. This probe, fabricated by the two-step selective chemical etching method, was coated with a 200-nm gold film, which was subsequently etched away at the fiber tip to create a 30-nm aperture out of which the glass fiber protrudes.[1,13] (Fig. 1, inset). The light transmitted through the fiber is detected by a photomultiplier tube. Two coaxial peizo tubes are used. The outer tube supports a wagon upon which the prism and the sample are mounted and is used for both lateral scanning and Z positioning. For coarse vertical positioning it operates as a motor for a vertical piezoelectric inertial slider (slip–stick motion).[14] The inner tube holds and dithers the fiber when shear-force distance regulation is employed. A 1.3-μm laser diode–photodiode combination is used to monitor the fiber's vibration amplitude. To suppress air currents, the kinematic part of the system is enclosed in a case. All components are placed upon a vibration-damping stage.

The topographical layout of the sample was first determined by the shear-force technique to maintain a constant separation (~5 nm) between the fiber tip and the sample. In the shear-force (noncontact atomic force) image shown in Fig. 2(a) a microtubule with a height of 16 nm and an apparent width (FWHM) of 60–70 nm extends across the field of view. Having deter-

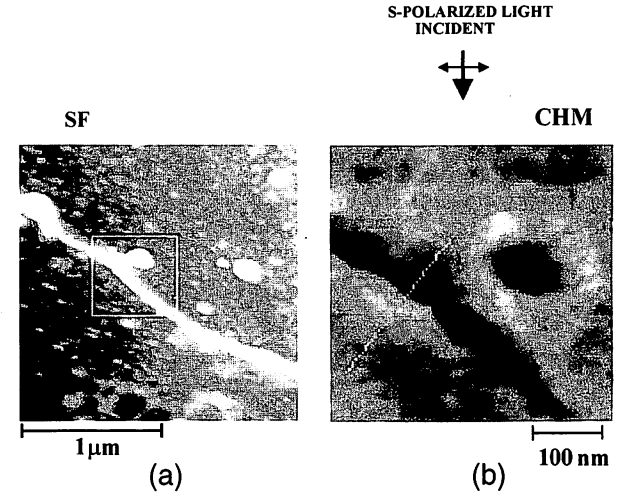

Fig. 2. Image of a microtubule (long and narrow) and a protein aggregate (round). (a) Topography of the 2 μm × 2 μm scan area obtained in shear-force mode. The microtubule and the aggregate are white. (b) Magnified optical image of the region highlighted in (a) taken in the CHM. Note the inversion of the optical image (dark) and the edge-enhancement effect in the images of both the microtubule and the protein aggregate. SF, shear force.

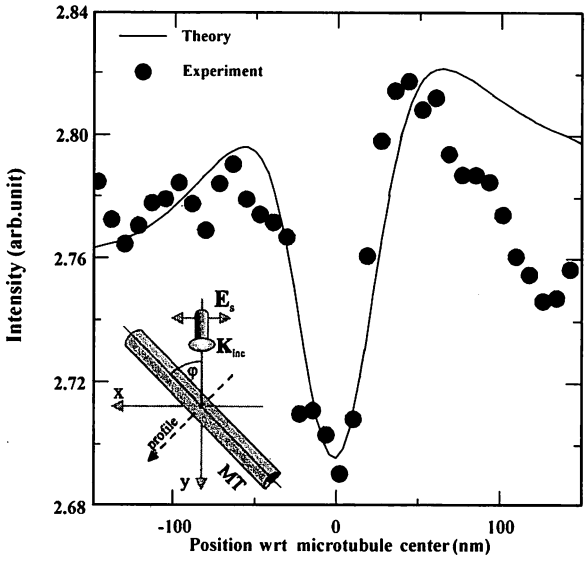

Fig. 3. Comparison of light intensity observed in passing over a microtubule in the CHM with theoretical calculations based on the optical extinction theorem. Inset: the geometry used in calculations based on the classical nonglobal model incorporating the optical extinction theorem. The refractive index of the microtubule is set equal to that of the glass substrate (1.5); $\varphi = 45°$ is an angle between the plane of the incident light and the microtubule's axis. wrt, With respect to.

mined the overall layout of the sample, we zero in on an isolated microtubule for a higher-resolution optical scan in the CHM to facilitate comparison with theory. (In the CHM the shear-force feedback loop is unlocked and the probe is kept at a constant height of ~30 nm from the surface of the prism.) Figure 2(b) shows the optical image of the area highlighted in Fig. 2(a) when *s*-polarized light was used for illumination of the sample with the direction of incidence shown in the figure. Comparing Figs. 2(a) and 2(b), we see that the optical image appears to be inverted and exhibits an edge-enhancement effect for both the microtubule and the nearby protein aggregate (round), in agreement with the qualitative predictions of the optical extinction theorem. As we have no independent determination of the size of the round protein aggregate that appears vividly in the center of the image, we limit our further quantitative discussion to the microtubule itself. A quantitative comparison is shown in Fig. 3. Here the observed light intensity (filled circles) is compared with the optical extinction theorem–based calculations (curve). Experimental data are taken along the line shown in Fig. 2(b). As illustrated in Fig. 3 (inset), for the purpose of calculation the microtubule is represented by a 30-nm-diameter half-cylinder with a refractive index of 1.5 placed upon a flat substrate of the same index. An *s*-polarized plane wave is incident upon the sample under total-internal-reflection conditions from below. The theoretical curve is obtained along the path depicted in Fig. 3 (inset) at a constant height from the substrate. We obtained the theoretical curve by adjusting the background level and the scan height, where the latter appears to be ~40 nm. The calculations seem to account accurately for the experimental results both for the apparent microtubule diameter (~40–50 nm) and in the observed asymmetry of the edge effect (the intensity is lower in the direction closest to the light source). It is interesting to note that such effects as image inversion and edge enhancement can be qualitatively understood with the aid of a simple quasi-electrostatic model (nonretardation limit).[6] Conversely, the effect of the edge asymmetry with respect to the direction of illumination requires the inclusion of the retarded Green function and thus indicates the limit where the electrostatic approach breaks down.

In summary, a detailed theoretical and experimental study of the imaging of a nanometer-sized dielectric sample by a c-mode NOM has been carried out and good quantitative agreement obtained. Application of nonglobal macroscopic theory to study the NOM image-formation mechanism for a small dielectric sample with a protruding fiber probe has proved to be a valid approach. In the future we expect to present a detailed comparison between theoretical calculations and experimental images for arbitrary polarization and direction of incident light.

We gratefully acknowledge the assistance of Shinichi Hisanaga of the Tokyo Institute of Technology and Hitoshi Tatsumi of Tokyo Medical and Dental University with the biological aspects of this research.

In Jesus' name.

References

1. See, for example, D. W. Pohl and D. Courjon, *Near Field Optics* (Kluwer, Dordrecht, The Netherlands, 1993); M. Ohtsu, J. Lightwave Technol. **13,** 1200 (1995).
2. O. J. F. Martin, C. Girard, and A. Dereux, Phys. Rev. Lett. **74,** 526 (1995).
3. K. Jang and W. Jhe, Opt. Lett. **21,** 236 (1996).
4. L. Novotny, D. W. Pohl, and P. Regli, J. Opt. Soc. Am. A **11,** 1768 (1994).
5. D. van Labeke and D. Barchiesi, J. Opt. Soc. Am. A **10,** 2193 (1993).
6. A. Zvyagin and M. Ohtsu, Opt. Commun. **133,** 328 (1997).
7. J. D. Jackson, *Classical Electrodynamics* (Wiley, New York, 1962), Chap. 16.
8. J. Cites, M. F. M. Sanghadasa, C. C. Sung, R. C. Reddick, R. J. Warmack, and T. L. Ferrell, J. Appl. Phys. **71,** 7 (1992).
9. J. C. Weeber, F. de Fornel, L. Salomon, E. Bourillot, P. Adam, and J. P. Goudonnet, Opt. Commun. **119,** 23 (1995).
10. J. C. Weeber, E. Bourillot, A. Dereux, J. P. Goudonnet, Y. Chen, and C. Girard, Phys. Rev. Lett. **77,** 5332 (1996).
11. O. J. F. Martin, C. Girard, and A. Dereux, J. Opt. Soc. Am. A **13,** 1801 (1996).
12. G. S. Agarwal, Phys. Rev. B **15,** 2371 (1977).
13. S. Mononobe, M. Naya, T. Saiki, and M. Ohtsu, Appl. Opt. **36,** 1496 (1997).
14. Ch. Renner, Ph. Niedermann, A. D. Kent, and Ø. Fisher, Rev. Sci. Instrum. **61,** 965 (1990).

A Model Based on Geometrical Construction in Designing a Pencil-Shaped Fiber Probe for Near-Field Optics

Shuji Mononobe and Motoichi Ohtsu, *Senior Member, IEEE*

***Abstract*— We propose a model based on geometrical considerations to determine the etching times required in fabricating a pencil-shaped fiber probe. In this model, we introduce a minimum etching time which is defined as the time required for having a zero apex diameter. Based on its value, the total etching times required in fabricating the pencil-shaped probe could be determined. We have found that the theoretically determined minimum etching time of 2.1 min agrees very well with our experimental value of 2 min.**

***Index Terms*— Etching, microscopy, near-field optics, optical fibers, optical fiber (device) fabrication, optical fiber measurement applications.**

I. Introduction

NEAR-FIELD optical microscopy (NOM) [1]–[4] has been developed to achieve nanometric resolution in optical imaging of for example, nanometric biological specimens [5], [6] and semiconductor devices [7], [8]. In NOM employing a probe tip, the apex size of the probe tip is one of the main factors deciding the resolution of the imaging. We succeeded in obtaining subwavelength images of salmonella flagellar filaments [5] and neurons [6] with a collection mode NOM[1] (or PSTM[2]) employing a fiber probe having a protruding tip [9], [10] with an apex diameter of less than 10 nm. For details of the probe tip, refer to [9].

Earlier, we proposed a method to fabricate a tapered fiber probe called a pencil-shaped probe having an apex diameter less than 10 nm for NOM by utilizing selective chemical etching [11]–[14]. In order to fabricate such pencil shaped fiber probes, the etching times have to be optimized for the probe having a zero apex diameter. For details of experimental results of the pencil-shaped probe, refer to [11].

In this paper, we propose a model based on pure geometrical considerations in order to find optimized etching times. In this model, we introduce a minimum etching time which is defined as the time required for having a zero apex diameter. The total etching times are determined by the minimum etching time. In Section II, the geometrical model is described and in Section III, results and discussion are given. Section IV gives a summary.

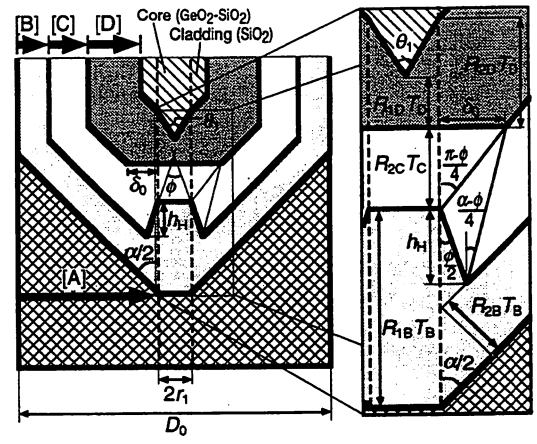

Fig. 1. Geometrical illustrations of an original fiber shape and the etched fiber shapes in the method shown in [11, Fig. 1]. Here, the region of a grid pattern, the bright shade, the white region, the dark shade, and the hatched region show the original fiber shape and the shapes etched by steps [A]–[D], respectively. R_1 and R_2 are the dissolution rates of the core and the cladding, respectively. R_1 in step [B] is denoted as R_{1B}. α is the taper angle, θ_1 is the cone angle [defined by (10)]. The radial thickness of the flat cladding δ_0 is equal to $R_{2Dh}\tau_1$ where R_{2Dh} and τ_1 are defined by (11) and (13), respectively. h_H [defined by (5)] is the depth of the hollow.

II. Geometrical Model

Fig. 1 shows the cross-sectional profile of an GeO_2 doped fiber and the etched fibers in steps [A]–[D] shown in [11, Fig. 1]. Here, α is the taper angle, ϕ is the cone angle of the hollow, r_1 is the radius of the core, and D_0 is the diameter of the cladding. R_1 and R_2 are the dissolution rates of the core and the cladding, respectively. In this paper, we denote the etching rate R_2 in step [B] as R_{2B}. T_A, T_B, T_C, and T_D are defined as the etching times in steps [A]–[D].

By the etching of step [A], the cladding of the fiber is tapered with a taper angle α while the end of the fiber remains flat with a radius r_1 as shown by the bright shade. Step [A] based on meniscus etching [15] is performed in HF acid with a surface layer of oil. Using the dissolution rates of R_{1A} and R_{2A} of the core and the cladding in HF acid, the etching time

Manuscript received July 22, 1996; revised February 10, 1997.

S. Mononobe is with the Kanagawa Academy of Science and Technology, Kawasaki 213, Japan.

M. Ohtsu is with the Tokyo Institute of Technology, Yokohama 226, Japan. He is also with the the Kanagawa Academy of Science and Technology, Kawasaki 213, Japan.

Publisher Item Identifier S 0733-8724(97)04336-3.

[1] In the collection mode NOM, the sample is illuminated under total internal reflection and a nanometric probe tip is used as a scatterer of the evanescent field over the sample and the scattered field is detected.

[2] For acronyms appearing here, refer to Pohl in [1].

T_A in step [A] is represented by

$$T_A = \frac{(D_0/2) - r_1}{R_{2A}} + \frac{r_1}{R_{1A}}. \quad (1)$$

The tapered fiber is hollowed by step [B] as shown by the white region and has two peaks on either side of the end with the angle of $[\alpha/2 + \phi/2]$ in the cladding region. To perform this process, the etching rate R_{1B} of the core has to be larger than the value R_{2Bv} which is defined as

$$R_{2Bv} = \frac{1}{\sin(\alpha/2)} R_{2B}. \quad (2)$$

Here, we assume that the hollow has the conical shape having the cone angle ϕ determined by

$$\sin(\phi/2) = \frac{R_{2B}}{R_{1B}} \quad (3)$$

and the truncated plane with a radius of r_1. By representing the depth of the hollow by h_H, it is straightforward to show that

$$h_H + = \frac{h_H \tan(\phi/2)}{\tan(\alpha/2)} = (R_{1B} - R_{2Bv}) T_B. \quad (4)$$

From (2) to (4), one obtains

$$h_H = \left[\frac{\sin(\alpha/2) - \sin(\phi/2)}{\sin(\alpha/2)\sin(\phi/2)}\right] \cdot \left[\frac{\tan(\alpha/2)}{\tan(\alpha/2) + \tan(\phi/2)}\right] R_{2B} T_B. \quad (5)$$

In step [C], the end of the fiber having the peaks with the angle of $[\alpha/2 + \phi/2]$ is flattened as shown by the dark shade in Fig. 1. As a result, the fiber has the flat end with a radius of $[r_1 + \delta_0]$ where δ_0 is the radial thickness of the cladding. Assuming that R_{1C} $(= R_{2C})$ is constant inside the hollow region and the surface anywhere which is exposed to the etching solution, we obtain the relation

$$h_H \tan\left(\frac{\phi}{2}\right) + \left[(h_H + R_{2C} T_C) \tan\left(\frac{\alpha - \phi}{4}\right)\right] = R_{2C} T_C \tan\left(\frac{\pi - \phi}{4}\right) (= \delta_0). \quad (6)$$

Therefore, the etching time T_C in step [C] and the radial thickness δ_0 of the flat cladding are expressed as

$$T_C = A(R_{2B}/R_{2C}) T_B \quad (7)$$

where

$$A = \left[\frac{\sin\left(\frac{\alpha}{2}\right) - \sin\left(\frac{\phi}{2}\right)}{\sin\left(\frac{\alpha}{2}\right)\sin\left(\frac{\phi}{2}\right)}\right] \left[\frac{\tan\left(\frac{\alpha}{2}\right)}{\tan\left(\frac{\alpha}{2}\right) + \tan\left(\frac{\phi}{2}\right)}\right] \cdot \left[\frac{\tan\left(\frac{\phi}{2}\right) + \tan\left(\frac{\alpha - \phi}{4}\right)}{\tan\left(\frac{\pi - \phi}{4}\right) - \tan\left(\frac{\alpha - \phi}{4}\right)}\right] \quad (8)$$

and

$$\delta_0 = A \tan\left(\frac{\pi - \phi}{4}\right) R_{2B} T_B \quad (9)$$

respectively. These equations show that T_C and δ_0 are proportional to T_B.

In step [D], the core is sharpened with the cone angle θ_1 represented by

$$\sin(\theta_1/2) = \frac{R_{1D}}{R_{2D}} \quad (10)$$

as in [11, eq. (A2)]. The radial thickness δ of the flat cladding is decreased with the etching rate R_{2Dh} which is expressed as

$$R_{2Dh} = \left[\frac{1}{\cos(\alpha/2)} - \tan(\alpha/2)\right] R_{2D}. \quad (11)$$

If the relations

$$\delta_0 = R_{2Dh} \tau_1 \quad (12)$$

and

$$\tau_1 = \left[\frac{\cos(\theta_1/2)}{\sin(\theta_1/2)\{1 - \sin(\theta_1/2)\}}\right] \left(\frac{r_1}{R_{2D}}\right) \quad (13)$$

are satisfied, by the etching for duration of $T_D = \tau_1$, the fiber becomes the pencil-shaped probe with the cone angle θ_1 and apex diameter $d = 0$ as shown by the hatched region. Here, (13) was derived from [11, eqs. (A2) and (A4)]. Then, we can define the minimum etching time T_{Bmin} in step [B] to obtain the pencil-shaped probe. T_{Bmin} is derived from (9), (11), (12), and (13) and then, is expressed as

$$T_{Bmin} = B(r_1/R_{2B}). \quad (14)$$

Here

$$B = \left[A \tan\left(\frac{\pi - \phi}{4}\right)\right]^{-1} \left[\frac{\left\{\cos\left(\frac{\alpha}{2}\right)\right\}^{-1} - \tan\left(\frac{\alpha}{2}\right)}{\tan\left(\frac{\theta_1}{2}\right)\left\{1 - \sin\left(\frac{\theta_1}{2}\right)\right\}}\right] \quad (15)$$

where A has been given by (8). Substituting T_{Bmin} of (14) into (7), the etching time T_C is given by $T_C = AB(r_1/R_{2C})$ and by using τ_1 given by (13), it is also reduced to

$$T_C = C(R_{2D}/R_{2C}) \tau_1 \quad (16)$$

where

$$C = \left[\tan\left(\frac{\pi - \phi}{4}\right)\right]^{-1} \left[\frac{1}{\cos(\alpha/2)} - \tan(\alpha/2)\right]. \quad (17)$$

On the other hand, in the case of $\delta_0 > R_{2Dh}\tau_1$, the shape of the probe can be controlled by varying the etching time in step [D]. Refer to Appendix A.

When the same etching solution is used in steps [C] and [D], the relations

$$R_{2C} = R_{2D} \quad (18)$$

and $R_{1C} = R_{2C} \sin(\theta_1/2)$ are satisfied. By this etching, both flattening and sharpening are performed in the cladding and the core, respectively. Sharpening the core is performed at the etching time T_{CD} represented by

$$T_{CD} = \tau_1 \quad (19)$$

where τ_1 is given by (13). If R_{1C} and R_{2C} were equal to R_{2D} $(= \sin(\theta_1/2)/R_{1D})$, the etching times $T_B = T_{Bmin}, T_C = C\tau_1$ given by substituting (18) into (16), and $T_D = \tau_1$ should be required for fabricating the pencil-shaped probe. In the case of using the same etching solution in steps [C] and [D], a minimum etching time T_{Bmin} is $[\tau_1/(T_C+T_D)]$ times that given by (14) and is represented by

$$T_{Bmin} = \frac{B}{C+1}\left(\frac{\tau_1}{R_{2B}}\right) \tag{20}$$

where B and C have been given by in (15) and (17).

III. Results and Discussion

In the fabrication of the pencil-shaped probe having a taper angle $\alpha = 20°$ and a cone angle $\theta_1 = 20°$, the apex diameter is less than 10 nm in an etching time $T_B = 2$ min of step [B] as shown by [11, Fig. 4]. Here, etching solutions used in steps [A] and [B] are 50 wt% HF acid with a surface layer of dimethylsilicone oil and 50 wt% HF acid, respectively. In steps [C] and [D], it is buffered HF solution (BHF) consisting of NH_4F solution (40 wt%), HF acid (50 wt%) and H_2O with a volume ratio of 10:1:1. From now onwards, we denoted BHF as 10:1:1. All etching is performed at 25 °C. Used fiber has the high GeO_2 doped core with a diameter of 2 μm, the pure silica cladding with a diameter of 125 μm, and an index difference of 2.5% [3]. This fiber was originally developed as a dispersion compensating fiber (DCF). For DCF, refer to [16]. In HF acid and 10:1:1, the dissolution rates of the cladding are 170 and 6 μm/h, respectively. The fiber was hollowed with a cone angle ϕ of 10° in step [B]. An etching time of step [A] is 22 min.

From (20), one derives the minimum etching time T_{Bmin} to be 2.1 min in the case of $r_1 = 1$ μm, $R_{2B} = 170$ μm, $R_{2C} = R_{2D} = 6$ μm/h, $\alpha = 20°, \theta_1 = 20°$, and $\phi = 10°$. This result agrees with the experimental value of 2 min obtained in [11, Fig. 1]. The model can be used for the design of the pencil-shaped probe. In using BHF of X:1:1 (where $X > 1.7$) in steps [C] and [D], the cone angle θ_1 is determined by X as shown in [11, Fig. 3]. Then, the dissolution rate R_{2D} $(= R_{2C})$ of the pure silica cladding is approximately expressed by

$$R_{2D} = 58X^{-0.94[\mu m/h]}. \tag{21}$$

Using the cone angle θ_1 and the dissolution rate R_{2D} given by (21), we obtained the minimum etching time and the etching time in steps [C] and [D] from (20) and (19), respectively. Fig. 2 shows the dependencies of the minimum etching time T_{Bmin}, the etching time T_{CD} in steps [C] and [D], the cone angle on X. Here, the broken and the solid curves represent the minimum etching time T_{Bmin} and the etching time T_{CD}, respectively. The dotted curve represents the cone angle θ_1. The closed triangles and the closed circles represent experimental results of T_{Bmin} and T_{CD}, respectively. The experimental results agrees to the theoretical results well. We found the total etching times of T_A, T_B, and T_{CD} for the high GeO_2 doped fiber in fabricating the pencil-shaped probe having the cone angle in a region of 20–120°.

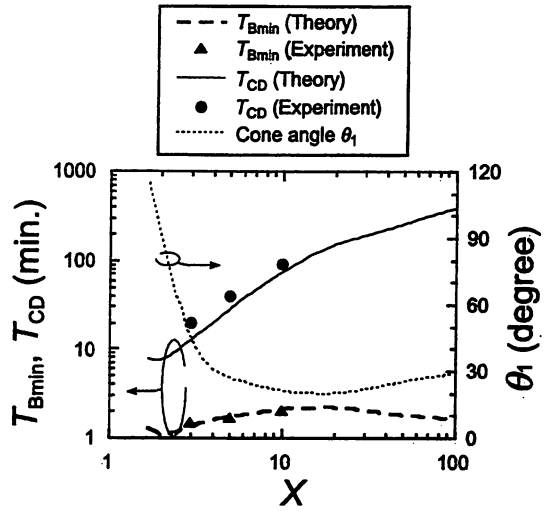

Fig. 2. Dependencies of the minimum etching time T_{Bmin}, the etching time T_{CD} in steps [C] and [D], and the cone angle θ_1 on a volume ratio X in steps [C] and [D]. Here, the broken curve is T_{Bmin} given by (20), the solid curve is T_{CD} given by (19), and the dotted curve represents experimental results of θ_1 obtained in [11]. Closed triangles and closed circles represent experimental results of T_{Bmin} and T_{CD}, respectively.

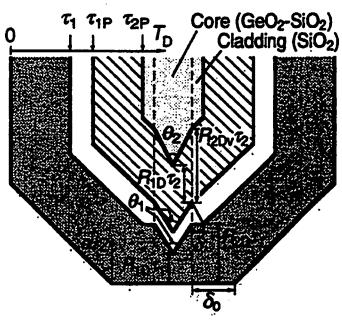

Fig. 3. Variation of the probe shape in step [D]. In the original shape shown the dark shade, the flat cladding δ_0 is larger than $R_{2Dh}\tau_{1P}$. Other symbols are defined as of Fig. 1. $R_{2Dv} = R_{2D}/\sin(\alpha/2)$. $\tau_{1P} = \delta_0/R_{2Dh}$. $\tau_{2P} = \delta_0/R_{2Dh} + \tau_2$. τ_2 is defined by (A2). The white shade, the dark shade, the hatched region, and bright shade are etched shapes at τ_1, τ_{1P}, and τ_{2P}, respectively. The white shade shows the shoulder-shaped probe having the flat cladding with δ and the sharpened core with the cone angle θ_1 [defined by Eq. 10] in the end of the taper. The hatched region and the bright shade show the pencil-shaped probes having different cone angles θ_1 and θ_2 [defined by (A3)], respectively.

IV. Summary

We developed a model based on pure geometrical considerations to determine the total etching times required in fabricating the pencil-shaped fiber probe having a zero apex diameter. In this model, we introduced a minimum etching time to determine the total etching times. In fabricating the probe having a cone angle of 20°, we have found that the theoretically determined minimum etching time of 2.1 min agrees very well with our experiment value of 2 min. Using this model, we determined total etching times for a high GeO_2 doped fiber in fabricating the probe having the cone angle in a region of 20–120°.

Appendix A
Variation of the Probe Shape in Step [D]

In the case of $\delta_0 > R_{2Dh}\tau_1$ at the start of step [D] as shown in Fig. 3, by the etching at a duration of T_D, the fiber can

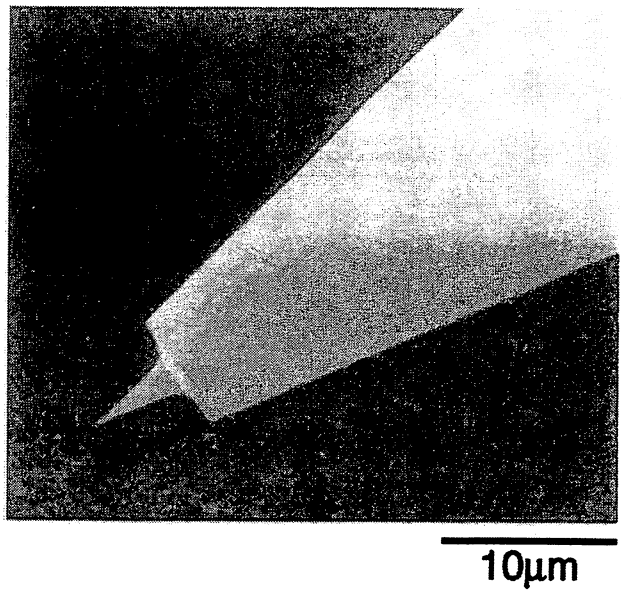

(a)

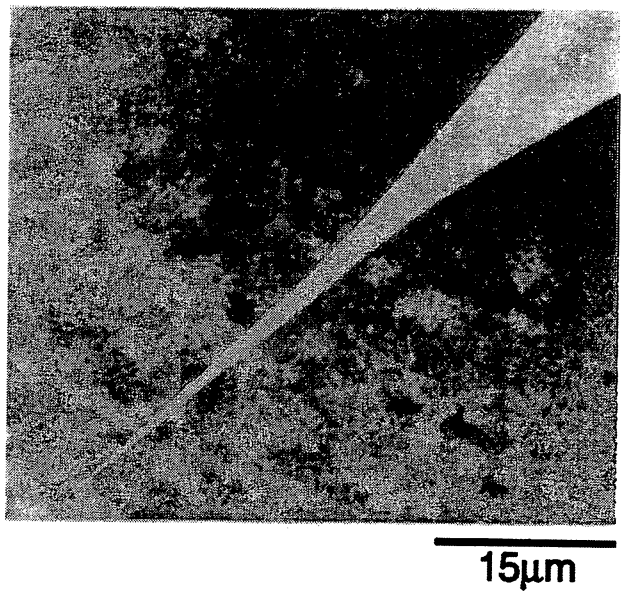

(b)

Fig. 4. Scanning electron micrographs of magnified views of (a) the shapened core of the shoulder-shaped probe having the tapered cladding with a taper angle of $\alpha = 20°$, a radial thickness of $\delta = 2$ μm, and a cone angle of $\theta_1 = 20°$ (b) the sharpened core of the pencil-shaped probe with a cone angle of $\theta_2 = 4°$.

have various shapes at the end of the taper with the angle α. Here, δ_0, and R_{2Dh}, and τ_1 are given by (9), (11), and (13), respectively. For $\tau_1 \leq T_D < \tau_{1P}$ $(= \delta_0/R_{2Dh})$ the fiber has the sharpened core with the cone angle θ_1, and the flat cladding end having the radial thickness δ as shown by the white region. This fiber having the flat cladding and the sharpened core is called the shoulder-shaped probe. At $T_D = \tau_{1P}$, we obtain the pencil-shaped probe with θ_1 as shown by the hatched region. In $T_D > \tau_{1P}$, the etching rate of the cladding for the sharpening the core is not R_{2D} but R_{2Dv} represented by

$$R_{2Dv} = R_{2D}/\sin(\alpha/2). \tag{A1}$$

TABLE I
CONDITIONS FOR FABRICATING THE SHOULDER-SHAPED PROBE WITH THE TAPERED CLADDING

Step	Etching solution [a]	Etching time
[A]	Dimethylsilicone oil [b] / HF acid (50wt%)	22 min
[B]	HF acid (50wt%)	3 min
[C] and [D]	NH_4F sol. (40wt%):HF acid (50wt%):H_2O = 10:1:1	90 min

[a] 25°C (±0.2°C).
[b] Density of oil is 0.935 g/cm^3.

Therefore, at $T_D \geq \tau_{2P}$ $(= \delta_0/R_{2Dh} + \tau_2)$ where τ_2 is expressed as

$$\tau_2 = (r_1/R_{1D})\sqrt{(R_{1D} + R_{2Dv})/(R_{2Dv} - R_{1D})} \tag{A2}$$

the pencil-shaped probe has the sharpened core with different cone angle θ_2 as shown by the bright shade. The cone angle θ_2 is represented by

$$\sin(\theta_2/2) = \sin(\theta_1/2)\sin(\alpha/2) \tag{A3}$$

and is smaller than θ_1 in the same X.

To fabricate the shoulder-shaped probe, the method shown in Fig. 1 of Ref. 11 was done by using conditions shown in Table I. The used fiber had the GeO_2 doped core, a core diameter of 2 μm, and an index difference of 2.5%. Fig. 4(a) shows a scanning electron micrograph of the sharpened core of the shoulder-shaped probe. The probe has a taper angle $\alpha = 20°$, a radial thickness of $\delta = 2$ μm, and a cone angle $\theta_1 = 20°$. Further, the pencil-shaped probe is fabricated for an etching time of 180 min in step [C] and [D]. Fig. 4(b) shows a SEM micrograph of the sharpened core of the fabricated probe. The probe has a taper angle of $\alpha = 20°$ and a cone angle of $\theta_2 = 4°$. The cone angle agrees with an estimated value of $\theta_2 = 3.5°$ obtained by substituting $\alpha = 20°$ and $\theta_1 = 20°$ into (A3).

APPENDIX B
SYMBOLS USED IN THIS PAPER

h_H: Depth [defined by (5)] of the truncated conical hollow.
A: Coefficient given by (8).
B: Coefficient given by (15).
C: Coefficient given by (17).
d: Apex diameter of a pencil-shaped fiber probe.
r_1: Radius of the core of a fiber.
R_1: Dissolution rate of the core.
R_{1A}: Dissolution rate of the core in step [A].
R_{1B}: Dissolution rate of the core in step [B].
R_{1C}: Dissolution rate of the core in step [C].
R_{1D}: Dissolution rate of the core in step [D].
R_2: Dissolution rate of the cladding.
R_{2A}: Dissolution rate of the cladding in step [A].
R_{2B}: Dissolution rate of the cladding in step [B].
R_{2C}: Dissolution rate of the cladding in step [C].
R_{2D}: Dissolution rate of the cladding in step [D].
R_{2Dh}: Etching rate [defined by (11)] of the cladding.
R_{2Dv}: Etching rate [defined by (A1)] of the cladding

T_A: Etching time in step [A] of the method.
T_B: Etching time in step [B] of the method.
T_{Bmin}: Minimum etching time required in step [B] for fabrication of a pencil-shaped probe having a zero apex diameter.
T_C: Etching time in step [C] of the method.
T_D: Etching time in step [D] of the method.
T_{CD}: Etching time in steps [C] and [D] of the method in which the etching solution in step [C] is the same as that in step [D].
X: Volume ratio of NH_4F solution in buffered HF solution of NH_4F solution (40 wt%), HF acid (about 50 wt%), and H_2O with a volume ratio of X:1:1
α: Taper angle of the tapered cladding.
δ: Radial thickness of the flat cladding of a shoulder-shaped probe.
δ_0: Radial thickness of the cladding flattened in step [C] of the method shown in Fig. 1.
ϕ: Cone angle [defined by (3)] of a truncated conical hollow in a fiber.
θ_1: Cone angle [defined by (10)] of the sharpened core.
θ_2: Cone angle [defined by (A3)] of the sharpened core.
τ_1: Etching time [defined by (13)] required for making apex diameter zero in the process of sharpening the core with the cone angle θ_1.
τ_{1P}: Etching time required for producing the pencil-shaped probe with the cone angle θ_1 in step [D].
τ_2: Etching time [defined by (A2)] required for making apex diameter zero in the process of sharpening the core with the cone angle θ_2.
τ_{2P}: Minimum etching time required for producing the pencil-shaped probe with the cone angle θ_2 in step [D].

ACKNOWLEDGMENT

The authors would like to thank Dr. R. U. Maheswari of Kanagawa Academy of Science and Technology for critically reading and commenting on the manuscript.

REFERENCES

[1] D. W. Pohl and D. Courjon, Eds., *Near-Field Optics*. Norwell, MA: Kluwer Academic, NATO ASI Series E, 1993, vol. 242.
[2] E. Betzig and J. K. Trautman, "Near-field optics: Microscopy, spectroscopy and surface modification beyond the diffraction limit," *Science*, vol. 257, pp. 189–195, 1992.
[3] M. Ohtsu, "Progress of high-resolution photon scanning tunneling microscopy due to a nanometric fiber probe," *J. Lightwave Technol.*, vol. 13, pp. 1200–1221, 1995.
[4] M. Paesler and N. van Hulst, Eds., *NFO-3, Ultramicroscopy*, vol. 61, nos. 1–4, 1995.
[5] M. Naya, S. Mononobe, R. Uma Maheswari, T. Saiki, and M. Ohtsu, "Imaging of biological samples by a collection-mode photon scanning tunneling microscope," *Opt. Commun.* vol. 124, pp. 9–15, 1996; also M. Naya, R. Micheletto, S. Mononobe, R. Uma Maheswari, and M. Ohtsu, "Near-field optical imaging of flagellar filaments of salmonella in water with optical feedback control," *Appl. Opt.*, vol. 36, no. 10, pp. 1681–1683, 1997.
[6] R. U. Maheswari, S. Mononobe, H. Tatsumi, Y. Katayama, and M. Ohtsu, "Observation of subcellular structure of neurons by an illumination mode near-field optical microscope under an optical feedback control," *Optic. Rev.*, vol. 6B, pp. 463–467, 1996.
[7] R. D. Grober, T. D. Harris, J. K. Trautman, E. Bezig, W. Wegscheider, L. Pfeiffer, and K. West, "Optical spectroscopy of a GaAs/AlGaAs quantum wire structure using near-field scanning optical microscopy," *Appl. Phys. Lett.*, vol. 64, pp. 1421–1423, 1994.
[8] T. Saiki, S. Mononobe, M. Ohtsu, N. Saito, and J. Kusano, "Spatially resolved photoluminescence spectroscopy of lateral *p-n* junctions prepared by Si-doped GaAs using a photon scanning tunneling microscope," *Appl. Phys. Lett.*, vol. 67, pp. 2191–2193, 1995; also T. Saiki, N. Saito, J. Kusano, and M. Ohtsu, "Determination of slant angle of *p-n* interface by multiwavelength near-field photocurrent measurement," *Appl. Phys. Lett.*, vol. 69, pp. 644–646, 1996.
[9] S. Mononobe, M. Naya, T. Saiki, and M. Ohtsu, "Reproducible fabrication of a fiber probe with a nanometric protrusion for near-field optics," *Appl. Opt.*, vol. 36, pp. 1496–1500, 1997.
[10] S. Mononobe, R. Uma Maheswari, T. Saiki, M. Naya, and M. Ohtsu, in *Near Field Optics-3, European Optic. Soc. Topic. Meeting*, Brno, Czech Republic, May 1995, vol. 8, pp. 105–106.
[11] S. Mononobe and M. Ohtsu, "Fabrication of a pencil-shaped fiber probe for near-field optics by selective chemical etching," *J. Lightwave Technol.*, vol. 14, pp. 2231–2235, Oct. 1996; Correspondence in *J. Lightwave Technol.*, vol. 15, pp. 162, Jan. 1997.
[12] T. Pangaribuan, S. Jiang, and M. Ohtsu, "High controllable fabrication of fiber probe for photon scanning tunneling microscope," *Scanning*, vol. 16, 362–367, 1994.
[13] M. Kawachi, T. Edahiro, and H. Toba, "Microlens formation on VAD single-mode fiber ends," *Electron. Lett.*, vol. 18, pp. 71–72, 1982.
[14] G. A. C. M. Spierings, "Wet chemical etching of silicate glasses in hydrofluoric acid based solutions," *J. Materials Science*, vol. 28, pp. 6261–6273, 1993.
[15] K. M. Takahashi, "Meniscus shapes on small diameter fibers," *J. Colloid Interface Sci.*, vol. 134, pp. 181–187, 1990.
[16] M. Onishi, Y. Koyano, M. Shigematsu, H. Kanamori, and M. Nishimura, "Dispersion compensating fiber with a high figure of merit of 250 ps/nm/dB," *Electron. Lett.*, vol. 30, pp. 161–162, 1994.

Shuji Mononobe was born in Osaka, Japan, 1967. He received the B.S. and M.S. degrees from Osaka Prefecture University, Sakai, Japan, in 1991 and 1993, respectively.

Since April 1993, he has been with the Kanagawa Academy of Science and Technology, Kawasaki, Japan, as a Researcher. His current research interests are near-field optics, optical fibers, etching of silicate glass, and plating.

Mr. Mononobe is a member of the Japan Society of Applied Physics, the Surface Finishing Society of Japan, and the Optical Society of America.

Motoichi Ohtsu (M'88–SM'90) was born in Kanagawa, Japan, on October 5, 1950. He received the B.E., M.E., and D.E. degrees in electronics engineering from Tokyo Institute of Technology, Tokyo, Japan, in 1973, 1975, and 1978, respectively.

In 1978, he was appointed to Research Associate and in 1982, he became Associate Professor at the Tokyo Institute of Technology. From 1986 to 1987, while on leave from Tokyo Institute of Technology, he joined the Crawford Hill Laboratory, AT&T Bell Laboratories, Holdmel, NJ. In 1991, he became a Professor at the Tokyo Institute of Technology. Since April 1993, he has been concurrently the leader of "PHOTON CONTROL" Project of Kanagawa Academy of Science and Technology, Kawasaki, Japan. His main fields of interest are near-field optical microscopy and its applications to nanoscale photonics and quantum optics, and laser frequency control. He has written over 130 papers and has received a number of patents. He is the author and coauthor of 13 books including two in English: *Highly Coherent Semiconductor Lasers* (Boston, MA: Artech House, 1992) and *Coherent Quantum Optics and Technology* (Norwell, MA: Kluwer Academic, 1993).

Dr. Ohtsu has been awarded eight prizes from academic institutions including Issac Koga Gold medal of URSI in 1984, Japan IBM Science Award in 1988, and two awards of the Japan Society of Applied Physics in 1982 and 1990. He is a member of the Institute of Electronics, Information and Communications Engineering (IEICE) of Japan, the Institute of Electrical Engineering of Japan, the Japan Society of Applied physics, and the Optical Society of America.

TECHNICAL NOTE

Near-field optical imaging of flagellar filaments of salmonella in water with optical feedback control

M. Naya, R. Micheletto, S. Mononobe, R. Uma Maheswari, and M. Ohtsu

We report on the high-resolution observation of biological samples in water with a collection-mode near-field optical microscope (c-mode NOM) operating under optical feedback control. With rapidly decreasing evanescent field power used as the feedback signal, for the first time to our knowledge, an image of straight-type flagellar filaments of salmonella in water has been obtained. The estimated diameter of a single filament is around 55 nm with a pixel size of 10 nm. A comparison with its nominal value of 25 nm obtained from electron microscope observations under high vacuum confirms that our c-mode NOM performs high-resolution imaging in water. © 1997 Optical Society of America

Key words: Near-field optical microscope, collection mode, optical feedback, evanescent field, biological samples in water.

For a real understanding of biological specimens, it is necessary to conduct *in vivo* observations in the natural environment of the specimens, i.e., in water or liquids. Although it is possible to conduct such observations with conventional optical microscopes, their resolutions are limited by wavelength. A near-field optical microscope (NOM) that surpasses this limit, has been receiving a lot of attention.[1,2] In one form of this microscope, called here the collection-mode (c-mode) NOM,[3] which is also known as a photon scanning tunneling microscope, the sample is illuminated under total internal reflection and the evanescent field generated on the sample is picked up by a sharpened protruding tip of nanometric size kept at a nanometric distance.[4] The main advantage of this c-mode NOM is that the exponential variation of the evanescent-field power can be profitably used as a control signal to regulate the sample–probe separation precisely. This is essential for obtaining high-resolution images. On the other hand, in an illumination-mode NOM, an auxiliary control signal is needed for sample–probe regulation and shear force is commonly used for this purpose.[5] Muramatsu *et al.* using an i-mode NOM operating in coordination with an atomic force microscope in the noncontact mode, obtained a resolution of 100 nm.[6]

The use of shear force in water has several problems: (1) The strong viscous drag of liquid arising from dithering the probe reduces the detection sensitivity of the sample–probe separation. (2) Dithering may scratch and injure soft biological samples. (3) With shear force or atomic force as the feedback control signal, the equiforce contour on the sample surface is mapped and is not necessarily and always equal to the equipower contour of the evanescent field, making interpretation of the near-field optical image rather complex.

We can solve these problems by advantageously using the evanescent signal for the feedback control of the c-mode NOM. That is, during imaging, the evanescent-field power on the sample surface is monitored for detecting the sample–probe separation, and the scanning is performed so as to keep the power constant. Because of the intrinsic feature of size-dependent localization of the evanescent-field power and size-dependent resonance between the sample and the probe,[7,8] the high detection sensitivity of the sample–probe separation is expected when the probe size is as small as the sample size. Moreover this monitoring technique is almost free from the strong viscous drag of water and hence from injuring the surface of the soft sample.

In this study, we present results of the high-resolution observation of straight-type flagellar filaments of salmonella (FFS) in water. To our

When this research was done, the authors were with Kanagawa Academy of Science and Technology, KSP East Rm 408, 3-2-1, Sakato, Takatsu-ku, Kawasaki-shi, Kanagawa, 213 Japan. M. Naya is now with Miyanodai Technology Development Center, Fuji Photo Film Company, Ltd., 798, Miyanodai, Kaisei-machi, Ashigarakami-gun, Kanagawa, 258 Japan.

Received 26 March 1996; revised manuscript received 12 November 1996.

0003-6935/97/071681-03$10.00/0

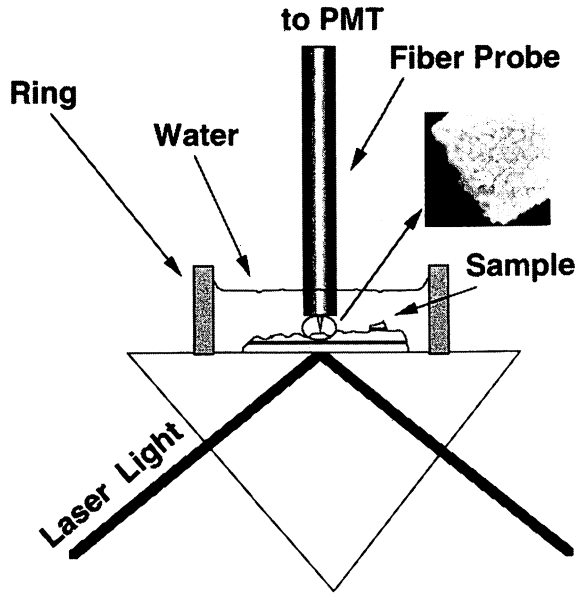

Fig. 1. Simplified schematic view of the experimental setup. The acrylic ring makes the surface tension of the water uniform, allowing the probe tip to be immersed in water without bending. Inset: Electron micrograph of the probe. The cone angle of the sharpened core is 14 deg, and the diameter at the foot of the protrusion with a metal coating is 30 nm.

knowledge, this is the first report on undertaking such an observation with the c-mode NOM.

Figure 1 shows a simplified schematic view of the experimental setup of the c-mode NOM, which is nearly the same as that used in our previous imaging experiment of FFS in air.[9] In this experiment, a diode laser of 685-nm wavelength was used as a light source with a wide-band modulation capability. A half-wavelength plate was used to control the polarization of the incident light, which illuminates the glass prism at an incident angle of 63 deg to satisfy the condition of total internal reflection. A thin glass plate was used as the sample substrate and was fixed on the prism with the index-matching oil sandwiched between.

The probe used here is the same as that used in Ref. 9, and its fabrication involves selective chemical etching,[10] metal film coating, and preferential removal of metal from the apex region of the sharpened tip.[11,12] The inset in Fig. 1 shows an electron micrograph of the probe with a protrusion core emerging from the metal film. The cone angle of the sharpened core is 14 deg. The apex diameter is smaller than 10 nm, and it makes the main contribution in the realization of high resolution by picking up high-spatial-frequency components in the evanescent field. The diameter at the foot of the protrusion with the metal coating is 30 nm, and this determines the cutoff of lower-spatial-frequency components. The sample was fixed on a tube-type piezoelectric transducer actuator to scan three dimensionally. We used a photomultiplier and a lockin amplifier for phase-sensitive detection by modulating the injection current of the diode laser. A commercial atomic force microscope controller (Seiko Instruments Inc., SPA 3700) was used for scanning and imaging. The sample–probe separation was controlled to keep the detected evanescent-field power constant.

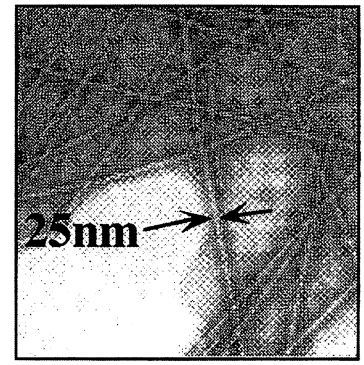

Fig. 2. Transmission electron micrograph of FFS obtained in vacuum.

The straight-type FFS can be advantageously used as a reference sample because their diameters are well calibrated by electron microscope observations to be 25 nm [see the transmission electron micrograph (TEM) in Fig. 2]. In this experiment, the FFS were preserved in water after being fixed on a hydrophilized glass plate. The samples prepared in the same conditions as in our experiment were observed with a dark-field microscope, and that observation confirmed the presence of FFS on the sample substrate. An acrylic ring was attached for conducting observations in water. The ring makes the surface of the water flat. The probe was inserted in the water at a contact angle of 90 deg, allowing the probe tip to be immersed without bending. The acrylic ring has an inner diameter of 10 mm and a height of 2 mm and was filled with water during the scanning.

Figure 3 shows the image of FFS obtained in water. The scan area is 600 nm × 600 nm with the corresponding pixel size 10 nm × 10 nm. During this scan the sample–probe separation was fixed at less than 30 nm. This value was estimated from the rapid decay of the evanescent power with respect to sample–probe separation. The decay length of the evanescent field, i.e., the position at which the field power is e^{-1} times the maximum, in water is estimated to be 284 nm, whereas that in air is around 60 nm. While we were acquiring this image, the probe was scanned at a sufficiently low speed (0.3 nm/s) to reduce the effect of the viscous drag of water. The arrows in Fig. 3 represent the directions of the wave vector of the incident light and the electric-field vector (*s* polarized). The bright segments in this figure represent fragments of FFS. Actually, five fragments of FFS lying at different orientations could be seen. Figure 4 shows a cross-sectional profile of the detected signal intensity for the part indicated by white bars in Fig. 2. The full width at half-maximum (FWHM) is 55 nm as indicated by the arrows in Fig. 3. When this is compared with its nominal value of 25 nm evaluated from TEM obser-

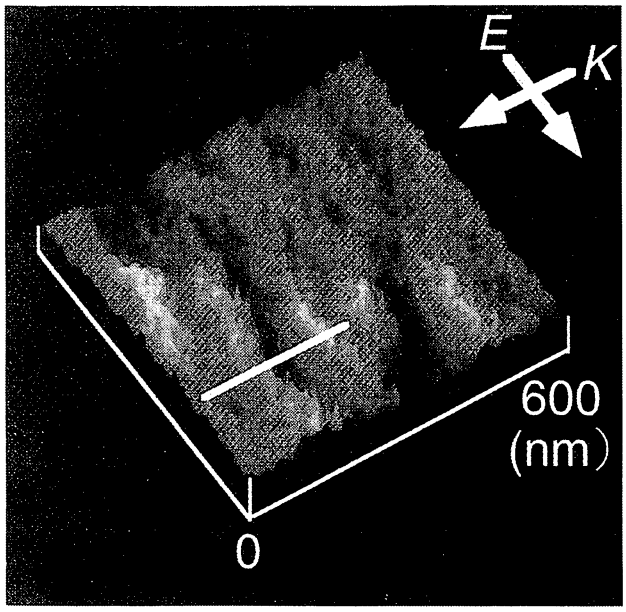

Fig. 3. Three-dimensional view image of FFS in water obtained by the collection-mode NOM. The arrows represent the directions of wave-vector **k** of the incident light and electric-field vector **E**.

vations in vacuum (Fig. 2), the difference is only around 30 nm in which the pixel size of 10 nm is also included. To our knowledge, this is the first type of observation of FFS in water with a resolution comparable with that of an electron microscope.

One of the origins of the difference between the observed diameter of the filament and its estimated diameter from the TEM is thought to be due to the effect of convolution between the aperture and the sample. When this effect of convolution of the aperture with the sample is considered, the value of the FWHM of 55 nm of our observed filament seems to be reasonable, because the aperture diameter is around 30 nm and the single flagellar filament diameter is 25 nm.[2,9] Note that in our previous report on the observation of FFS in air,[9] the diameter was estimated to be 50 nm, comparable with our current observation

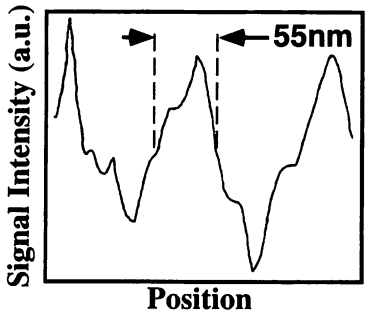

Fig. 4. Cross-sectional profile of the detected signal intensity for the part identified by a white bar in Fig. 3. The FWHM of the bright region is 55 nm.

result. Furthermore, note that during actual scans, Brownian motion, capillary forces, etc. that arise because of water did not affect the operation of the c-mode NOM in the realization of high resolution. Although the c-mode NOM can be applied only when the substrate is not strongly absorbing, the substrate for most of the biological nanometric samples meet this requirement. This means that the current monitoring technique can become a general method for imaging biological samples.

In summary, this study demonstrates the capability of stable operation of the c-mode NOM in water by controlling the sample–probe separation optically, i.e., by monitoring the rapid decay of the evanescent-field power from the sample surface. An image of FFS was obtained for the first time in water. The diameter estimated from a single strand of an image of FFS was around 55 nm with a pixel size of 10 nm, and this value is comparable with that estimated from the TEM.

The authors thank S. Aizawa, Teikyo University, for providing the flagellar filaments of salmonella.

References and Notes

1. D. W. Pohl and D. Courjon, eds., *Near Field Optics*, Vol. 242 of NATO ASI series E (Kluwer, Dordrecht, The Netherlands, 1993).
2. M. Ohtsu, "Progress of high-resolution photon scanning tunneling microscopy due to a nanometric fiber probe," J. Ligtwave Technol. **13,** 1200–1221 (1995).
3. The other generally used mode of operation is the illumination-mode NOM in which light from a nanometric aperture illuminates the sample and the scattered light is collected. Other terms used are SNOM or NSOM. For the acronyms appearing here, refer to the list compiled by Pohl and Courjon.[1]
4. D. Courjon, K. Sarayaddine, and M. Spajer, "Scanning tunneling optical microscope," Opt. Commun. **71,** 23–28 (1989).
5. E. Bezig and J. K. Trautman, "Near-field optics: microscopy, spectroscopy, and surface modification beyond the diffraction limit," Science **257,** 189–195 (1992).
6. H. Muramatsu, N. Chiba, K. Homma, K. Nakajima, T. Ataka, S. Ohta, A. Kusumi, and M. Fujihira, "Near-field optical microscopy in liquid," Appl. Phys. Lett. **12,** 3245–3247 (1995).
7. K. Jang and W. Jhe, "Nonglobal model for a near-field scanning optical microscope using diffraction of the optical near field," Opt. Lett. **21,** 236–238 (1996).
8. T. Saiki, M. Ohtsu, K. Jang, and W. Jhe, "Direct observation of the size-dependent feature of the optical near field on a subwavelength spherical surface," Opt. Lett. **21,** 674–676 (1996).
9. M. Naya, S. Mononobe, R. Uma Maheswari, T. Saiki, and M. Ohtsu, "Imaging of biosamples by a collection mode photon scanning tunneling microscope with an apertured probe," Opt. Commun. **124,** 9–15 (1996).
10. T. Pangaribuan, S. Jiang, and M. Ohtsu, "Highly controllable fabrication of fiber probe for photon scanning tunneling microscope," Scanning **16,** 362–367 (1993).
11. S. Mononobe and M. Ohtsu, "Fabrication of a pencil-shaped fiber probe for near-field optics by selective chemical etching," J. Lightwave. Technol. **14,** 2231–2235 (1996).
12. S. Mononobe, M. Naya, S. Saiki, and M. Ohtsu, "Reproducible fabrication of a fiber probe with a nanometric protrusion for near-field optics," Appl. Opt. **36,** 1496–1500 (1997).

TECHNICAL NOTE

Reproducible fabrication of a fiber probe with a nanometric protrusion for near-field optics

Shuji Mononobe, Masayuki Naya, Toshiharu Saiki, and Motoichi Ohtsu

We propose a new type of fiber probe with a nanometric protruding tip emerging from a metal film and describe a novel method, called the selective resin-coating method, for fabricating such probes. It is a reproducible etching process consisting of four steps and can be applied to silica fibers sharpened by selective chemical etching. With this method, we obtained tips with the apex diameter and the foot diameter of the protrusion being less than 10 and 30 nm, respectively, when the gold film was ~120 nm thick.

Key words: Near-field optics, probe, optical fiber, dip-coating, etching, scanning, feedback, evanescent light, dispersion-compensating fiber.

Recently, the nanometric probing technique of near-field optics[1,2] has been applied to high-density optical storage,[3] optical imaging of biological samples,[4–7] detection of fluorescent single molecules,[8] and spectroscopy of semiconductor devices.[9–11] With this optical probing technique, the process of energy transfer between the sample and the probe can be considered as a short-range dipole–dipole interaction occurring between the probe and the sample.[2,12] For the interaction to be most effective, the size of the probe must be equal to that of the sample.[13,14] Moreover the sample–probe separation must be shorter than the size of the sample. When a sharpened fiber with a nanometric tip as the probe is used,[4] the main factor determining the resolution of the near-field optical imaging is the apex size of the probe. However, to suppress scattering or the generation of low-spatial-frequency components of the near field, the sharpened fiber must be coated with metal except for the apex region.

In this paper, to improve the resolution of near-field optical microscopy (NOM), we propose a new probe that has a dielectric conical tip protruding from the metal film as shown schematically in Fig. 1(a). Here θ_1, d, d_F, and t_M represent the cone angle, the apex diameter, the foot diameter, and the metal thickness, respectively. This protruding probe rejects spatial-frequency components of less than $(1/d_F)$ and can transfer until $(1/d)$ of the protrusion is reached. In the region between $(1/d_F)$ and $(1/d)$, the protrusion is able to enhance the optical near field through its size-dependent effect[12–14] with the sample.

To realize such a probe as in Fig. 1(a), we propose a simple etching technique called selective resin coating (SRC). This method can be applied to a selectively etched fiber[15,16] called a shoulder-shaped fiber that has a sharpened core with a cone angle θ_1 and a flat cladding end with a diameter D. Here, using the radius r_1 of the core, we express the height of the sharpened core is as

$$h_{SC} = r_1/\tan(\theta_1/2). \quad (1)$$

Figure 1(b) shows a schematic diagram of the SRC method consisting of four steps: (I) metal coating, (II) resin coating, (III) preferential etching of metal from the apex region, (IV) resin removal. Figures 2(a) and 2(b) show, respectively, the scanning electron micrographs of the shoulder-shaped probe with a sharpened core and a magnified view of the protruding tip region of the sharpened core. For this case the protruding tip has $d < 10$ nm, $d_F = 30$ nm, $\theta_1 = 20°$, and $t_M = 120$ nm. In the following the SRC method is described for this shoulder-shaped fiber.

Before the process of applying the SRC, we fabricated the shoulder-shaped sharpened fiber by etching selectively a fiber with high GeO_2 doping in the core, and it has a cone angle of $\theta_1 = 20°$, height $h_{SC} = 5.7$

The authors are with the Kanagawa Academy of Science and Technology, KSP E-408, 3-2-1 Sakado, Takatsu-ku, Kawasaki 213, Japan. M. Ohtsu is also with the Tokyo Institute of Technology, Yokohama 226, Japan.

Received 4 March 1996; revised manuscript received 17 October 1996.

0003-6935/97/071496-05$10.00/0

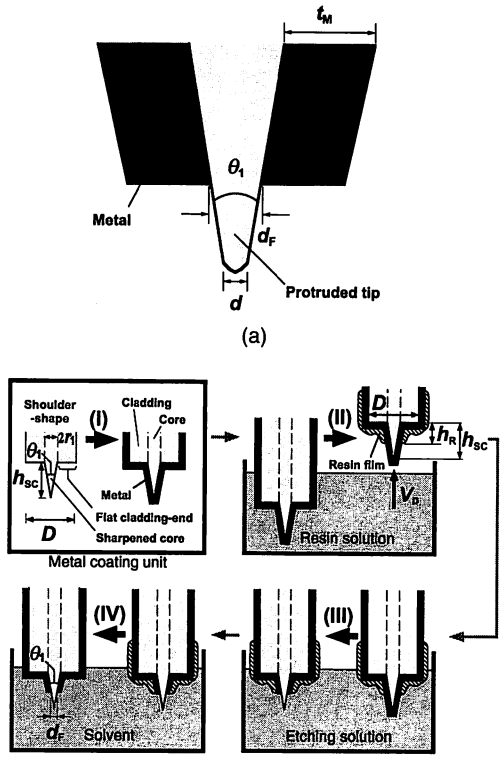

Fig. 1. (a) Schematic diagrams of a probe with protrusion: θ_1, d, d_F, and t_M represent the cone angle, the apex diameter, the foot diameter, and the thickness of the metal film, respectively. (b) Schematic illustration of the selective resin-coating method with (I) the coating metal, (II) the resin coating performed by dipping the film in the resin solution and pulling up with the withdrawal speed V_D in the air, (III) etching in the solution, and (IV) removal of resin by dipping the film into a solvent. The shoulder-shaped sharpened fiber has the flat cladding end with a diameter D and sharpened core with a cone angle of θ_1; r_1, h_{SC}, h_R, and d_F are the core radius, the height of the sharpened core, the resin height, and the protrusion foot diameter, respectively.

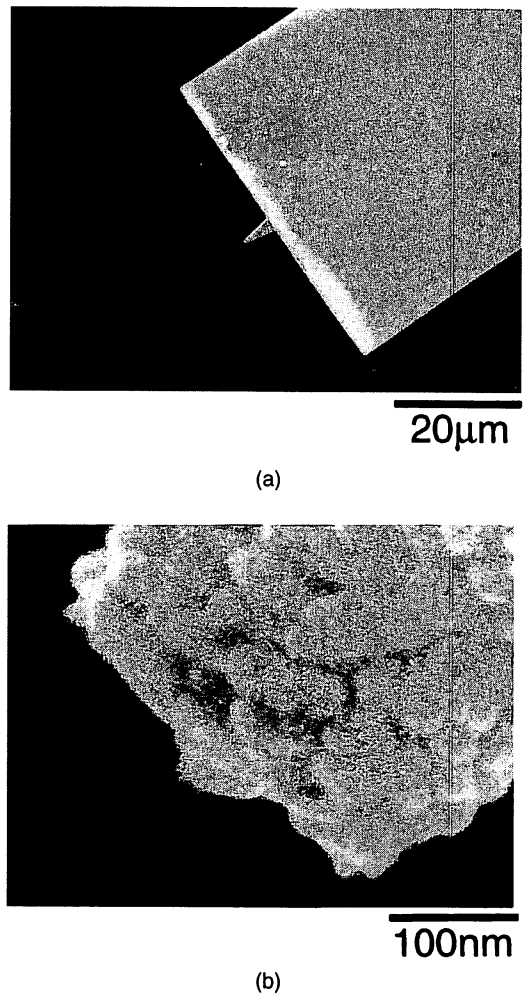

Fig. 2. Scanning electron micrographs of (a) the shoulder-shaped fiber probe obtained by the SRC method, (b) its protruding tip. The probe has a diameter D = 45 μm of the cladding end, a foot diameter d_F = 30 nm, a cone angle θ_1 = 20°, and an apex diameter d = 10 nm.

μm, and diameter D = 45 μm of the flat cladding end. The fiber was originally developed as a dispersion-compensating fiber (DCF) of the matched cladding type.[17] Thus it had a small core diameter of ~2 μm and a large index difference of ~2.5%. The fiber is consecutively etched for 50 and 90 min in solutions with volume ratios of NH_4F (40 wt. %): HF (50 wt. %): H_2O = 1.7:1:1 and 10:1:1 at 25 °C.[15] After the etching is done, we clean the sharpened fiber by dipping it in water. In step (I) the shoulder-shaped fiber was laid on the stage of a magnetron sputtering unit (Hitachi E-1030) in which the electric field applied between the metal target and the stage is perpendicular to the fiber. The target diameter was 6 cm, and the distance between the target and the stage was ~2 cm. The front and rear sides of the fiber were coated in the argon atmosphere at a pressure of ~6 Pa.

In step (II) the fiber was dipped in an acrylic resin solution and was drawn up with a withdrawal speed V_D of ~5 cm/s. The acrylic resin solution has a viscosity coefficient of 11 cP and a density of 0.85 g/cm^3 at 25 °C and is a commercial product (Gunze sangyo) used originally as a primer for painting metal etc. On withdrawal of the fiber from the acrylic resin solution, a submicrometer top region of the sharpened core is exposed from the resin film. Here the physical mechanism behind this selective resin coating in which the wettability of the resin solution is zero in a region of less than submicrometer size is complex and not well known. However, we have found that there is a size-dependent effect of the wettability. Although other resin solutions can be used instead of the acrylic resin solution, it must be corrosion-resistant against the etching solution in step (III) and must be easily removable by solvents in step (IV).

In step (III) the metal-coated sharpened core exposed from the resin film was etched for 2 min in a KI-I_2 solution diluted 50× with a KI:I_2:H_2O = 20:1:400 weight ratio. The etching time had to be controled according to the thickness of the metal coated in step (I). For a typical coating thickness of 100–

150 nm, the etching time varies around 2–3 min. In step (IV), we removed the acrylic resin film by dipping it into a solvent such as acetone.

To obtain a protruding probe with a foot diameter of more than 30 nm, we must control the thickness profile of the resin film formed on the flat cladding end and the sharpened core in step (II). Let us define a resin height h_R from the cladding end to the foot of the exposed region as shown schematically in Fig. 1(b). To fabricate the protruded probe, h_R must be smaller than the length h_{SC} of the sharpened core. Assuming that the apex diameter d of the shoulder-shaped fiber is equal to zero, a protruded tip fabricated by this method can have the foot diameter expressed as

$$d_F = 2(h_{SC} - h_R)\tan(\theta_1/2) \qquad h_R < h_{SC}. \qquad (2)$$

In case θ_1 and h_{SC} are fixed, d_F is determined by the height h_R of the resin film. When the metal-coated fiber is withdrawn from the acrylic resin solution in step (II), a liquid film of the resin solution adheres to the fiber with submicrometer thickness owing to the finite wettability of the solution and soon becomes a dried resin film. Hence the thickness of the resin film covering the side of the cladding is determined by the kinematic viscosity ν and the withdrawal speed V_D as is known from dip coating a flat substrate.[18] Here the kinematic viscosity ν is a ratio of the viscosity coefficient η to the density ρ and can be simply controlled by varying the concentration of the resin solution. Owing to the surface tension of the solution on the flat cladding end and the sharpened core, the thickness profile of the resin film is nonuniform; i.e., the resin film follows the contour of the sharpened core [see Fig. 1(b)]. Therefore the thickness profile and the resin height h_R depend not only on η, ρ, and V_D but also on the fiber shape, such as cladding diameter D, the cone angle of θ_1, and length h_{SC}. The foot diameter d_F can be controlled by varying the parameters of η, ρ, V_D, D, θ_1, and h_{SC}. In our actual conditions of $\theta_1 = 20°$, $h_{SC} = 5.7$ μm, $\eta = 11$ cP, and $\rho = 0.85$ g/cm^3, we varied the foot diameter d_F of the protrusion by controlling the diameter D of the flat cladding end and the withdrawal speed V_D. Figure 3(a) shows the dependence of d_F on D (for $V_D = 5$ cm/s). It can be seen that d_F decreases with increasing D and converges to a constant value at $D = 40$–45 μm. Figure 3(b) shows the variation of the foot diameter d_F of the protrusion with respect to the withdrawal speed V_D (at $D = 40$ μm). As seen, d_F decreases with increasing V_D and converges to a constant value at around 2–5 cm/s. In case θ_1 and/or h_{SC} is varied, we can satisfy the condition $h_R < h_{SC}$ by varying the concentration of the acrylic resin solution. Then d_F can be controlled by varying D and V_D.

To determine the reproducibility of the method of fabricating protruding-type probes, we fabricated 14 probes in the identical conditions of a viscosity coefficient of 11 cP, a density of 0.85 g/cm^3, and a withdrawal speed of 5(±0.5) cm/s. All the probes had a

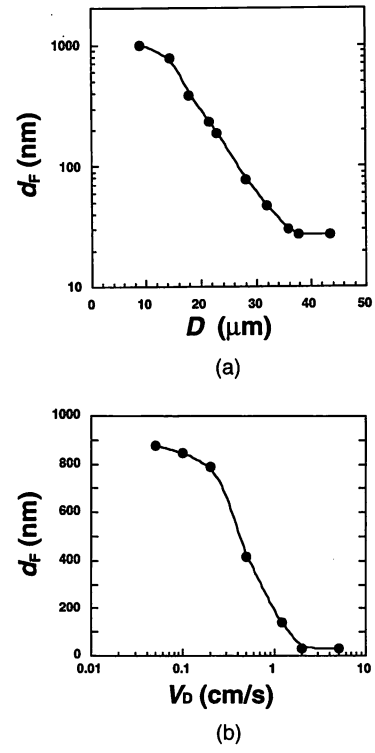

Fig. 3. Dependence of the foot diameter d_F (a) on the cladding diameter D for a withdrawal speed V_D of 5 cm/s and (b) on the withdrawal speed V_D at $D = 40$ μm.

cladding diameter of 33 ± 0.5 μm and an apex diameter of less than 10 nm. It has been found that the foot diameter of the fabricated protruding tips had an average of 45 nm and a standard deviation of 12 nm.

Although the results of the above process, (I)–(IV), have been presented for a tip with $\theta_1 = 20°$, it is possible to fabricate shoulder-shaped probes with different cone angles. The cone angle of the shoulder-shaped fiber can be controlled by varying the compositions of etching solutions in the sharpening process.[15]

To characterize throughput, we define a transmission coefficient given by the ratio of the detected intensity to the input intensity. The transmission coefficient depends on the foot diameter and the cone angle. We produced protruding probes with a cone angle θ_1 of 20° and foot diameters[19] d_F in the 80–900-nm region by the SRC method and evaluated the transmission coefficients of them[20] with a 0.4 N.A. objective lens. For details, see Saiki *et al.*[20] The protruding probe with $d_F = 100$ nm and $\theta_1 = 20°$ had a typical transmission coefficient[21] of approximately 1×10^{-4}. This value of the transmission coefficient is nearly twice that of an aperture fabricated by a micropipet puller and a metal coating[22] with an aperture diameter of 100 nm and a cone angle of 40°.

Furthermore, to improve the transmission coefficient, we fabricated protruding probes with a wide cone angle of 50° by the proposed method. For the protruding probe with a foot diameter d_F of 200 nm and $\theta_1 = 50°$, the transmission coefficient is large and

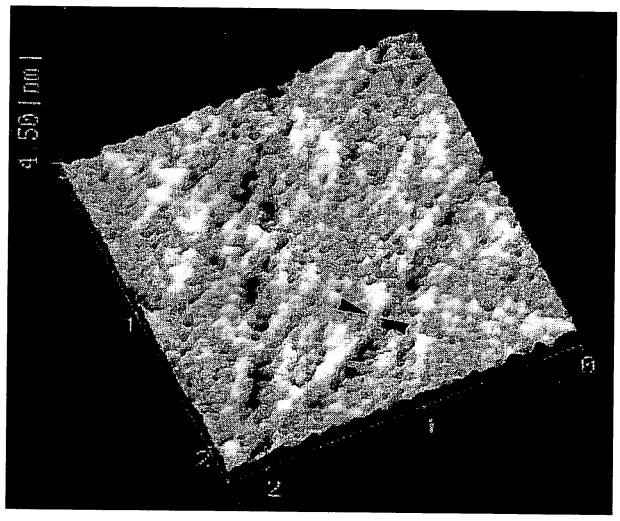

Fig. 4. Image of salmonella filaments obtained with the collection mode of a NOM employing the protruded tip as shown in Fig. 3(b). Here the sample is composed of straight-type flagellar filaments of salmonella with a diameter of 25 nm. The scan area is 2.2 μm × 2.2 μm. The incident light illuminating the sample is *s*-polarized. The minimum width of the filament as indicated by the arrow heads is around 50 nm.

approximately 1×10^{-3} (evaluated with a 0.4 N.A. objective lens). The protruding probes with cone angles of 30–50° and a foot diameter of 200 nm were used for spectroscopic studies of semiconductor devices such as lateral *p–n* junctions[10] and quantum dots.[11] Here, to avoid the sample damage caused by thermal excitation in the sample, the power coupled into the fiber probe was kept to less than 300 μW. (The coupling efficiency was approximately 60%.)

Finally, to demonstrate the imaging capability of the protruding-type probe, we performed the observation of flagellar filaments of salmonella bacteria by a collection mode NOM (Ref. 23) or PSTM (for acronyms appearing here, refer to Pohl in Ref. 1). A single filament has a width of 25 nm as estimated with an electron microscope. Figure 4 shows the image obtained. The width of the filament as indicated by the arrow heads is 50 nm, which is comparable with that obtained with the electron microscope. In that experiment, the evanescent signal power was used for feedback control of the sample–probe separation. This optical feedback cannot operate in a stable fashion with an uncoated probe[15] or a metalized probe with no protruding region[24] because of its poor signal-to-noise ratio. For details on this high-resolution imaging of salmonella by NOM, see Naya *et al.*[6]

In conclusion, for the near-field optical microscopy, we proposed a nanometric probe with a dielectric tip protruding from the metal film. We developed a new etching method called the SRC method for fabricating protruding-type probes. It was confirmed that the SRC method is a reproducible technique. The probe obtained had an apex diameter of less than 10 nm, a foot diameter of 30 nm, and a cone angle of 20°. Furthermore the foot diameter can be varied by controlling the diameter of the cladding end, the withdrawal speed of the probe from the resin, and the kinematic viscosity of the resin solution.

The authors thank S. Miyamoto (Fujikura Ltd.) for his discussion on fibers and especially R. Uma Maheswari (Kanagawa Academy of Science and Technology) for critical reading and comments.

References

1. D. W. Pohl and D. Courjon, eds., *Near Field Optics*, Vol. 242 of NATO ASI Series E (Kluwer, Dordrecht, The Netherlands, 1993).
2. M. Ohtsu, "Progress of high-resolution photon scanning tunneling microscopy due to a nanometric fiber probe," J. Lightwave Technol. **13,** 1200–1221 (1995).
3. E. Betzig, J. K. Trautman, R. Wolfe, E. M. Gyorgy, P. L. Fynn, M. H. Kryder, and C.-H. Chang, "Near-field magneto-optics and high density data storage," Appl. Phys. Lett. **61,** 142–144 (1992).
4. S. Jiang, H. Ohsawa, K. Yamada, T. Pangaribuan, M. Ohtsu, K. Imai, and A. Ikai, "Nanometric scale biosample observation using a photon scanning tunneling microscope," Jpn. J. Appl. Phys. **31,** 2282–2287 (1992).
5. R. Uma Maheswari, H. Tatsumi, Y. Katayama, and M. Ohtsu, "Observation of subcellular nanostructure of single neurones with an illumination mode photon scanning tunneling microscope," Opt. Commun. **120,** 325–334 (1995).
6. M. Naya, S. Mononobe, R. Uma Maheswari, T. Saiki, and M. Ohtsu, "Imaging of biological samples by a collection-mode photon scanning tunneling microscope," Opt. Commun. **124,** 9–15 (1996).
7. R. Uma Maheswari, S. Mononobe, H. Tatsumi, Y. Katayama, and M. Ohtsu, "Observation of subcellular structures of neurons by an illumination mode near-field optical microscope under an optical feedback control," Opt. Rev. **3,** 463–467 (1996).
8. E. Betzig and R. J. Chichester, "Single molecules observed by near-field scanning optical microscopy," Science **262,** 1422–1425 (1993).
9. R. D. Grober, T. D. Harris, J. K. Trautman, E. Bezig, W. Wegscheider, L. Pfeiffer, and K. West, "Optical spectroscopy of a GaAs/AlGaAs quantum wire structure using near-field scanning optical microscopy," Appl. Phys. Lett. **64,** 1421–1423 (1994).
10. T. Saiki, S. Mononobe, M. Ohtsu, N. Saito, and J. Kusano, "Spatially resolved photoluminescence spectroscopy of lateral *p–n* junctions prepared by Si-doped GaAs using a photon scanning tunneling microscope," Appl. Phys. Lett. **67,** 2191–2193 (1995).
11. Y. Toda, M. Kourogi, M. Ohtsu, Y. Nagamune, and Y. Arakawa, "Spatially and spectrally resolved imaging of GaAs quantum-dot structures using near-field optical technique," Appl. Phys. Lett. **69,** 827–829 (1996).
12. H. Hori, "Quantum optical picture of photon STM and proposal of single atom manipulation," in Ref. 1, pp. 105–114.
13. K. Jang and W. Jhe, "Nonglobal model for near-field scanning optical microscope using diffraction of the optical near field," Opt. Lett. **21,** 1–3 (1996).
14. T. Saiki, M. Ohtsu, K. Jang, and W. Jhe, "Direct observation of size-dependent features of the optical near field on a subwavelength spherical surface," Opt. Lett. **21,** 674–676 (1996).
15. T. Pangaribuan, S. Jiang, and M. Ohtsu, "Highly controllable fabrication of fiber probe for photon scanning tunneling microscope," Scanning **16,** 362–367 (1994).
16. S. Mononobe and M. Ohtsu, "Fabrication of a pencil-shaped fiber probe for near-field optics by selective chemical etching,"

J. Lightwave Technol. **14,** 2231–2235 (1996); Erratum, J. Lightwave Technol. **15,** 162 (1997).
17. For example, see M. Onishi, Y. Koyano, M. Shigematsu, H. Kanamori, and M. Nishimura, "Dispersion compensating fiber with a high figure of merit of 250 ps/nm/dB," Electron. Lett. **30,** 161–162 (1994).
18. For example, see C.-C. Yang, J. Y. Josefowicz, and L. Alexandru, "Deposition of ultrathin films by a withdrawal method," Thin Solid Films **74,** 117–127 (1980).
19. The aperture diameter is as in Ref. 20.
20. T. Saiki, S. Mononobe, M. Ohtsu, N. Saito, and J. Kusano, "Tailoring a high-transmission fiber probe for a photon scanning tunneling microscope," Appl. Phys. Lett. **68,** 2612–2614 (1996).
21. In this measurement, actually an objective lens of N.A. 0.4 was used, and for comparison a value of a transmission coefficient has been corrected to a lens of N.A. 1.
22. G. A. Valaskovic, M. Holton, and G. H. Morrison, "Parameter control, characterization, and optimization in the fabrication of optical fiber near-field probes," Appl. Opt. **34,** 1215–1228 (1995).
23. In the collection mode NOM, the sample is illuminated under total internal reflection, a nanometric probe tip is used as a scatterer of the evanescent field over the sample, and the scattered field is detected.
24. R. Uma Maheswari, S. Mononobe, and M. Ohtsu, "Control of apex shape of the fiber probe employed in photon scanning tunneling microscope by a multistep etching method," J. Lightwave Technol. **13,** 2308–2313 (1995).

OPTICAL REVIEW Vol. 3, No. 6B (1996) 450-453

Near-Field Photoluminescence of Si-doped GaAs*

Sang-Kee EAH,[1] Wonho JHE,[1] Toshiharu SAIKI[2] and Motoichi OHTSU[2,3]

[1]*Department of Physics, Seoul National University, Seoul 151-742, Korea,* [2]*Kanagawa Academy of Science and Technology KSP East 408, 3-2-1, Sakado Takatsu-ku, Kawasaki, 213 Japan*

(Received August 17, 1996; Accepted August 30, 1996)

We have measured surface photoluminescence properties of Si-doped bulk GaAs using a near-field scanning optical microscope. An apertured fiber probe tip is used as an emitter of excitation laser as well as a collector of luminescence from GaAs. Due to the Fabry-Perot etalon effect, the excitation laser is reflected or transmitted with an oscillation period of $\lambda_{He\text{-}Ne}/2$ as the gap between the tip and the GaAs surface varies. The luminescence from GaAs also varies with an oscillation period of $\lambda_{GaAs}/2$ due to the same etalon effect. Therefore, the intensity of luminescence light collected by the probe tip shows a beating between two oscillations of different periods. When the probe approaches the GaAs surface, the collected luminescence intensity increases due to tunneling of evanescent wave. On the other hand, when we collect the luminescence using a lens, the intensity also increases due to similar coupling of evanescent wave into propagating wave in spite of a shadowing effect of the wide metal coating.

Key words: near-field scanning optical microscopy, photoluminescence, GaAs, Fabry-Perot effect

1. Introduction

Near-field scanning optical microscopy (NSOM) has recently been the subject of very active research. It not only has the high resolution of scanning probe microscopy well beyond the diffraction limit of conventional optical microscopy which is about $\lambda/2$, but still retains all the capabilities of conventional optical microscopy.[1-3] Therefore, it is very useful to investigate semiconductor optical devices having novel structures such as quantum dots or quantum wires. This technique combined with conventional spectroscopic techniques has been successfully implemented in the study of luminescence spectroscopy of quantum structures at low temperatures,[4] fine-structure splitting of single quantum dots,[5] and spatially-resolved luminescence of magnetic heterostructures and p-n junctions.[6,7]

Since a semiconductor is opaque, reflection mode NSOM is needed. To obtain nanometric local excitation of sample, one has to transmit an excitation laser through a small aperture at the fiber probe tip. Consequently, it is desirable to use the configuration of simultaneous laser-excitation and luminescence-collection through the same apertured fiber probe. But in this case, the probe-tip geometry is rather complicated and there exist interferences both in transmission and reflection of the excitation laser and in transmission of luminescence from the sample.[8,9] In this paper, we report a quantitative study of near- field photoluminescence properties of Si-dope GaAs sample, taking into account interference effects as well as geometrical effects.

2. Experimental

Figure 1 shows a schematic of our experiment. We used Si-doped bulk GaAs sample grown by molecular beam epitaxy at room temperature. We measured intensity variations as the gap distance between the fiber tip and GaAs sample changes. We have checked the far-field optical spectrum of luminescence from GaAs and the distribution peaked around λ_{GaAs}=870 nm. The optical fiber probe tip was fabricated using an improved chemical etching method for high transmission and collection efficiency.[10] One particular probe tip had a total diameter of 1390 nm including both the metal coating and the core of Ge-doped SiO_2. The aperture diameter was 430 nm. Figure 1 also shows a scanning electron microscope (SEM) picture of the tip. As can be seen, there exists a 50 nm-high dielectric mountain protruding above the metal coating at the center of the core, which enables shear-force distance regulation.[11,12] In other words, all the metal coatings are lower than the core mountain which guarantees proper operation of shear-force feedback. Once the tip approaches the sample, we set a reference voltage above the saturation value of the shear-force signal. Then the tip moves away at a constant speed because our feedback circuit is type I, which includes only one integrator. We also determined the contact point when the shear-force signal becomes zero.

As shown, we used the configuration of simultaneous laser excitation and collection of luminescence from GaAs through the same fiber probe. We also collected the reflected excitation laser light through the same probe. Figure 2(a) shows reflection of the excitation laser source. There are two reflections: one is from the fiber glass-air interface and the other is from the air-GaAs interface. The tip-air-GaAs interface makes a Fabry-Perot etalon and

[1]Also with Interdisciplinary Graduate School of Science and Engineering, Tokyo Institute of Technology, Midori-ku, Yokohama, 226 Japan.

*This paper was originally presented at the first Asia-Pacific Workshop on Near Field Optics, which was held on August 17 and 18, 1996 at Seoul Education and Culture Center, Seoul, Korea, organized by Condensed Matter Research Institute, Seoul National University.

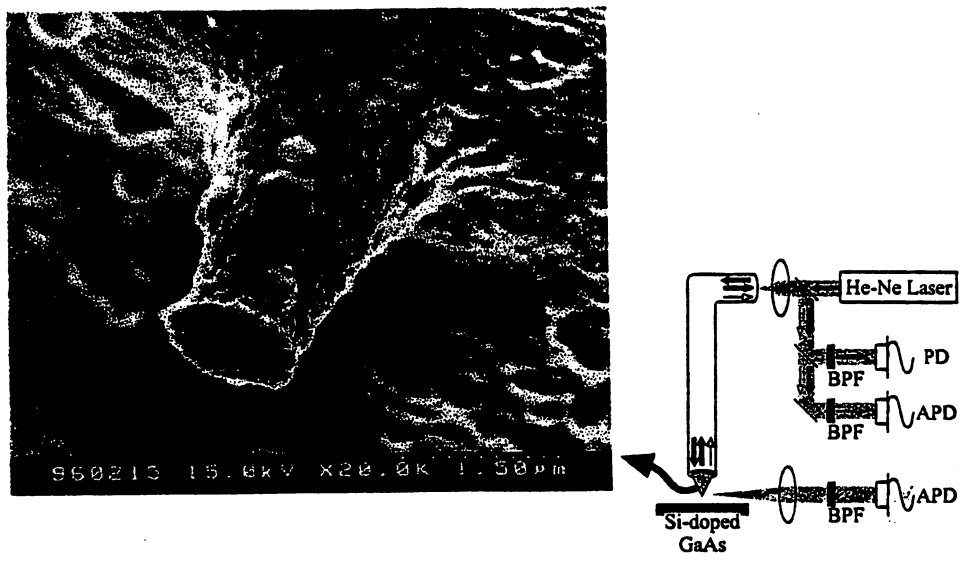

Fig. 1. Experimental setup. A He-Ne laser (632.8 nm) is used as excitation source, which is transmitted to GaAs through the optical fiber probe and the excitation laser light reflected through the same probe is detected by photodiode. Luminescence from GaAs (870 nm) is collected by the probe and lens and detected by two avalanche photodiodes. A SEM picture of the fiber probe tip used is also shown.

shows interference oscillations with a period of half the excitation laser wavelength; the excitation laser is thus strongly transmitted into the GaAs sample when the reflection is low and vice versa. We carefully isolates these reflections from the reflection at the air-glass interface at the fiber's input face near an optical fiber coupler. We used a He-Ne laser whose wavelength $\lambda_{He\text{-}Ne}$ is 632.8 nm. When the gap distance is an integral multiple of $\lambda_{He\text{-}Ne}/2$, the reflection is low and transmissivity is high, while when the distance is half-integer multiple of $\lambda_{He\text{-}Ne}/2$ the reflection is high and transmissivity is low. Here, the contact point is the same as the minimum reflection point.

We observed that the contact point can be different from the reflection minimum point when a smaller aperture probe is used. It was reported that the relation between contact point and minimum reflection point strongly depends on the dielectric constant ε of the sample surface.[8] According to our observation, however, the relation also depends strongly on the aperture size. We believe that the reflection point of glass-air interface is closely related to the cutoff radius of the subwavelength-sized aperture probe. If we could know the contact point from this reflection signal, we might even use this oscillation of reflection through the fiber probe as a feedback signal without depending on shear-force or additional collection of reflection.[9] As the gap between the probe tip and the GaAs surface increases, the interference visibility decreases since the reflection from the air-GaAs interface decreases whereas the reflection from the glass-air interface is constant. We also checked that the excitation laser light, transmitted from the probe and reflected from the GaAs surface, shows interference oscillations at far-field regime but decreases due to a shadowing effect of the relatively wide metal coating at proximity regime.[9]

This Si-doped GaAs has 200 nm penetration depth when

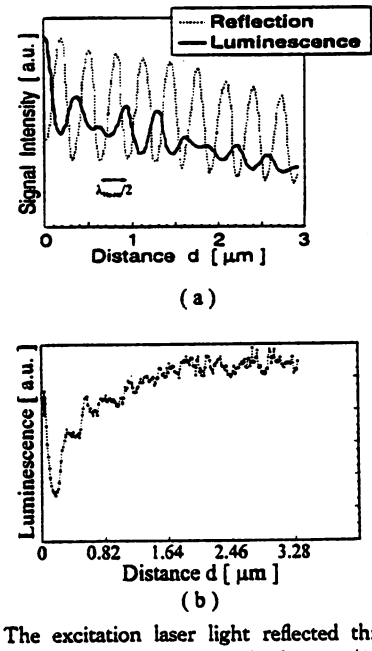

Fig. 2. (a) The excitation laser light reflected through the fiber probe shows oscillations with a period of $\lambda_{He\text{-}Ne}/2$. Luminescence from GaAs collected by the fiber probe shows beating oscillations because of the two different oscillations. (b) Luminescence from GaAs collected by a lens increases at close proximity even though there is a shadowing effect caused by the large metal coating.

the excitation laser has a wavelength of $\lambda_{He\text{-}Ne}$=632.8 nm, so the excitation laser light is almost absorbed at 200 nm below the surface. But due to the diffusion of photo-generated free carriers, the volume of radiative recombination centers becomes larger. At room temperature, the diffusion length is about 3 μm.[11] Therefore, the luminescence lights generated inside the bulk GaAs suffer from two loss mechanisms: one is due to refraction at the interface and

the other is due to total internal reflection. GaAs has a large index of refraction $n_{GaAs}=3.6$, so the maximum angle for escape of luminescence generated below the surface is only 16.1° and is responsible for low external quantum efficiency of light emitting diode.

We collected the luminescence from the GaAs sample in two ways: one through the fiber probe (Fig. 2(a)) and the other through an objective lens (×20, 0.4 N.A.) located nearly parallel to the GaAs sample surface (Fig. 2(b)). As shown in Fig. 1, the reflected excitation light and the luminescence from GaAs through the fiber probe trace the same optical path. After splitting the mixed light into two beams, we used a band-pass filter to prevent the reflected He-Ne laser from entering the Si avalanche photodiode. Figure 2(a) shows the luminescence collected through the fiber probe tip. When the luminescence light transmits the GaAs-air-glass interface, it also exhibits interference oscillations with a period of $\lambda_{GaAs}/2$. The excitation and the luminescence oscillate with different periods, so that the resulting signal shows beating oscillations. Due to the beating, the distances between local minima are not constant and the distance from the 2nd to the 3rd minimum is particularly short. In contrast to the case of excitation, evanescent wave tunneling can also occur at proximity regime. The possible angle for evanescent wave tunneling is from $\theta_{air}=\arcsin(n_{air}/n_{GaAs})=16.1°$ to $\theta_{glass}=\arcsin(n_{glass}/n_{GaAs})=24.6°$. At contact, the intensity increases quickly due to the tunneling evanescent components as in Fig. 2(a) and Fig. 3(a).

Just above the GaAs surface there is an intense evanescent wave which is generated by total internal reflection of radiations whose propagation angle inside GaAs is from 16.1° to 90°. In this case, we observed the coupling of evanescent wave into propagating wave when the luminescence was collected by an objective lens. The relatively-wide metal coating also has shadowing effects, which decrease the luminescence collected by a lens as well as the reflection of excitation laser collected by a lens. As shown in Fig. 2(b), the intensity decreases with oscillations due to shadowing effect and then increases again as the tip approaches the contact, as a result of coupling of evanescent wave into propagating wave by the probe tip.

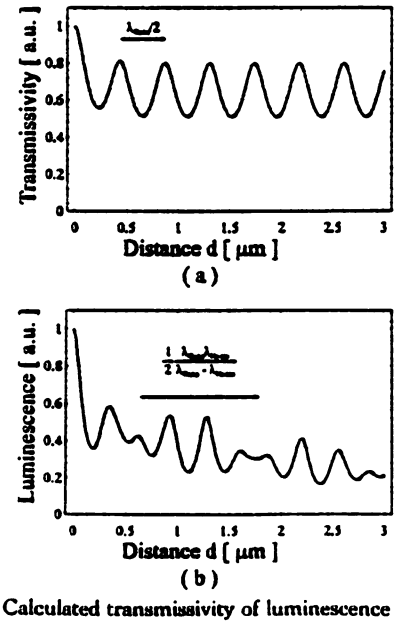

Fig. 3. (a) Calculated transmissivity of luminescence from GaAs to optical fiber. At proximity the transmissivity is large due to evanescent wave tunneling and oscillates with a period of $\lambda_{GaAs}/2$ at the far-field regime due to Fabry-Perot etalon effect. (b) Calculated luminescence collected through the fiber probe of Fig. 2(a).

To simulate these results numerically, we made a simple model. The formula for the luminescence intensity collected through the fiber probe can be written as a multiplication of the excitation and luminescence parts:

$$I(d)=E(d)L(d) \tag{1}$$

where d is the gap distance from the probe tip and GaAs surface.

For the excitation, we used the Fresnel coefficients of Fabry-Perot etalon when angle θ is zero. Because the beam from the aperture is not collimated but divergent, we considered a divergence term. Then, the excitation part becomes

$$E(d)=T(\theta=0,\lambda_{He\text{-}Ne},d)\frac{d_0^2}{(d+d_0)^2} \tag{2}$$

where T (θ, λ, d) is the Fresnel coefficient. The fitting parameter d_0 and aperture radius r determines the divergence angle as $\arctan(r/d_0)$.

The luminescence part can be represented by a summation of evanescent wave tunneling and transmissivity at zero angle:

$$L(d)=\int_{\rho_{air}}^{\rho_{glass}}\rho T(\arctan(\rho),\lambda_{GaAs},d)d\rho+wT(\theta=0,\lambda_{GaAs},d) \tag{3}$$

where ρ_{air} and ρ_{glass} denote $\tan(\theta_{air})$ and $\tan(\theta_{glass})$, respectively, and w is the fitting parameter.

Figure 3(a) of $L(d)$ versus d shows interference oscillations of luminescence transmissivity with a period of $\lambda_{GaAs}/2$ when $w=0.23$. Due to evanescent wave tunneling, $L(d)$ is enhanced until $d\sim\lambda_{He\text{-}Ne}/4$ and the ratio of evanescent wave to propagating wave at $d=0$ is 25%. Figure 3(b) shows a fitting curve for Fig. 2(a) and the corresponding fitting parameters are $d_0=6$ and $w=0.23$. As can be seen in Fig. 2(a) and Fig. 3(b), these simulations are in good agreement with experimental results both in the beating shape of oscillation and in the decrease of intensity with increasing d. The beating has a slow envelope of fast oscillations. At $d=0$, the height of the envelope is high. The period of the envelope, $\lambda_{GaAs}\lambda_{He\text{-}Ne}/(\lambda_{GaAs}-\lambda_{He\text{-}Ne})/2$, is 1.16 μm.

3. Conclusions

In conclusion, we made a quantitative study of photoluminescence properties of Si-doped GaAs using NSOM. We observed various kinds of oscillations: reflection of excitation with a period of $\lambda_{He\text{-}Ne}/2$, oscillations of luminescence through a lens, and beating oscillations of luminescence through the fiber due to two different periods of $\lambda_{He\text{-}Ne}/2$ and $\lambda_{GaAs}/2$. We also saw the coupling of evanescent wave into propagating wave, which enhances trans-

missivity of luminescence at the near contact region and overcomes the shadowing effects of metal coating. The metal coating may change decay rates of the free carrier pair's radiative recombinations.[13,14,15] However, note that in this experiment the radiation centers exist continuously in the d direction over the diffusion length. We also calculated the variations of decay rates due to the presence of the metal boundary of the tip and found the variation to be less than 0.5% after integration over the whole range. Quantum optical study of near-field photoluminescence properties can be done with a quantum well structure instead of a bulk sample, since the radiation centers have a well-defined distance from the metal coating. In that case the collected luminescence will be modulated due to the additional change of decay rates; this is now under investigation.

Acknowledgments

This work was supported in part by the Korea Science and Engineering Foundation (KOSEF) and the Inter-University Semiconductor Research Center (ISRC, 96-E-3208).

References

1) *Near Field Optics*, eds. D.W. Pohl and D. Courjon (Kluwer Academic, Dordrecht, 1993).
2) K. Jang and W. Jhe: Opt. Lett. 21 (1996) 236.
3) T. Saiki, M. Ohtsu, K. Jang and W. Jhe: Opt. Lett. 21 (1996) 674.
4) T.D. Harris, D. Gershoni, R.D. Grober, L. Pfeiffer, K. West and N. Chand: Appl. Phys. Lett. 68 (1996) 988.
5) D. Gammon, E.S. Snow, B.V. Shanabrook, D.S. Katzer and D. Park: Phys. Rev. Lett. 76 (1996) 3005.
6) J. Levy, V, Nikitin, J.M. Kikkawa, A. Cohen, N. Samarth, R. Garcia and D.D. Awschalom: Phys. Rev. Lett. 76 (1996) 1948.
7) T. Saiki, S. Mononobe, M. Ohtsu, N. Saito and J. Kusano: Appl. Phys. Lett. 68 (1996) 2191.
8) D.W. Pohl: *Scanning Tunneling Microscopy 2*, eds. R. Wiesendanger and H.-J. Güntherodt (Springer-Verlag, Berlin, 1992) Chap. 7, p. 253.
9) G. Guttroff, J.M. Keto, C.K. Shih, A. Anselm and B.G. Streetman: Appl. Phys. Lett. 68 (1996) 3620.
10) T. Saiki, S. Mononobe, M. Ohtsu, N. Saito and J. Kusano: Appl. Phys. Lett. 68 (1996) 2612.
11) E. Betzig, P.L. Finn and J.S. Weiner: Appl. Phys. Lett. 60 (1992) 2482.
12) M. Vae-Iravani and R. Toledo-Crow: Appl. Phys. Lett. 62 (1993) 1044.
13) J. Vilms and W.E. Spicer: J. Appl. Phys. 36 (1965) 2815.
14) X.S. Xie and R.C. Dunn: Science 265 (1994) 361.
15) R.X. Bian, R.C. Dunn, X.S. Xie and P.T. Leung: Phys. Rev. Lett. 75 (1995) 4772.

OPTICAL REVIEW Vol. 3, No. 6B (1996) 463-467

Observation of Subcellular Structures of Neurons by an Illumination Mode Near-Field Optical Microscope under an Optical Feedback Control*

Rajagopalan UMA MAHESWARI,[1] Shuji MONONOBE,[2] Hitoshi TATSUMI,[2,3] Yoshifumi KATAYAMA[2] and Motoichi OHTSU[1,4]

[1]*Kanagawa Academy of Science and Technology KSP East 408, 3-2-1, Sakado, Takatsu-ku, Kawasaki, Kanagawa, 213 Japan,* [2]*Department of Autonomic Physiology, Medical Research Institute, Tokyo Medical and Dental University, Chiyoda-ku, Tokyo, 101 Japan,* [3]*"The Intelligence and its Origin," PRESTO, Japan Science and Technology Corporation, Japan,* [4]*Interdisciplinary Graduate School of Science and Engineering, Tokyo Institute of Technology, 4259, Nagatsuda, Midori-ku, Yokohama, Kanagawa 226 Japan*

(Received August 17, 1996; Accepted September 3, 1996)

We propose an illumination mode near-field optical microscope operated under an optical feedback for imaging biological specimens in their natural environment. For feedback control, rapidly varying evanescent signal has been generated over the sample surface. It has been found that evanescent signal can be profitably used as a control signal by utilizing its sample feature dependent discrimination sensitivity. Neurons have been successfully observed both in air and in liquid with a resolution well beyond the diffraction limit.

Key words: near-field optical microscope, illumination mode, evanescent feedback, sample feature dependent discrimination sensitivity, nanometric protruding tip

1. Introduction

Dynamic observations of biological specimens *in vivo* are usually conducted by a conventional optical microscope which provides only a diffraction limited resolution to the order of the wavelength of light. For conducting observations of fine structures, an electron microscope is usually used and it could see only dried specially prepared samples. However, with the current rapid development of near-field optical microscope (NOM),[1,2] it is possible to conduct observations in liquid.[3-5] We reported earlier about the observation of microtubules present in the neural process of neurons with an illumination mode NOM* (i-mode NOM) operated along with shear force sample-probe separation control with a resolution comparable to that of the electron microscope.[6] However, the use of shear force technique leads to the following problems:

(1) Dithering of the probe in sensing the shear force introduces damages in the sample;

(2) Under small sample-probe separations, the dithering motion of the probe leads to cross-talk problems between the shear force topographic image and the near-field optical image;

(3) Under the implementation of shear force for sample-probe separation control, the probe/sample is moved to map the contours of equiforce and hence it becomes difficult to interpret the images;

(4) Implementation of shear force technique introduces some difficulties for extending the observation in liquid due to the presence of large capillary forces.

In the current study, we propose an i-mode NOM that uses the rapid decay of the evanescent signal for controlling the sample-probe separation. The proposed method of optically controlling the sample-probe separation has the following advantages:

(i) No mechanical dithering is involved;

(ii) Maps equipower contour of the evanescent field and hence the interpretation of the i-mode image is made easier; Here, the proper choice of wavelength away from the absorption of the sample and sample feature dependent characteristic decay length of the evanescent field[7,8] will reduce cross-talk problems between the evanescent topographic image and the illumination mode image;

(iii) Easier to implement the system for conducting observation in liquid which is very essential for biological specimens.

With the proposed system, we have imaged subcellular structures of neurons with high resolution under optical feedback. We will show that the system under optical feedback works as good as that under shear force feedback with the obtained images showing remarkable similarities. In Sect. 2, we describe the experimental details with a brief description on the probe fabrication and sample preparation. Section 3 presents some images of neurons obtained in air under different feedback controls and in liquid. Finally, Sect. 4 gives a summary.

2. Experiments

In this section, we describe about the fabrication of the probe, sample preparation and experimental system.

*This paper was originally presented at the first Asia-Pacific Workshop on Near Field Optics, which was held on August 17 and 18, 1996 at Seoul Education and Culture Center, Seoul, Korea, organized by Condensed Matter Research Institute, Seoul National University.

*In illumination mode (i-mode) NOM, light from a nanometric aperture illuminates the sample and the light scattered by the sample is detected. In a collection mode (c-mode) NOM, the sample is illuminated under total internal reflection and a nanometric tip is used as a scatterer of the evanescent field over the sample and the scattered field is detected.

2.1 Probe Fabrication

In order to facilitate the operation of an i-mode NOM under evanescent intensity feedback, we need probes that should work as (A) a nanometric aperture acting as an illuminating source and (B) at the same time an efficient nanometric scattering center and a collector for picking up the evanescent field. Therefore, with probes fabricated by pulling and metal coating, it is difficult to attain enough signal to noise ratio for picking up the evanescent field although it can work as an efficient illuminating source. For this purpose, we use probes with a nanometric dielectric protrusion as shown in the scanning electron micrograph (SEM) of Fig. 1. The foot and the apex diameters of the protruded region being less than 40 nm and 10 nm, respectively. The fabrication of such fiber probe involves first sharpening an optical fiber by a two-step selective chemical etching method[9] followed by coating of these fibers with a gold film of thickness around 200 nm in a sputtering unit. Next, these metallized fibers are coated with a resin film so as to have the apex part devoid of resin and finally, gold from the apex part is removed by etching in a solution of potassium iodide and iodine. For details about fabricating the nanometric protruding tip, refer to Ref. 10).

2.2 Sample Preparation

Neurons isolated from the brain cortex of a Wistar rat plated and cultured on a microscopic cover glass were cultured for 14 days. The chemical fixation was done with 4% parapharmaldehyde for 30 minutes followed by washing three times in phosphate buffered solution (PBS). Prepared samples were stored in PBS at 4°C to prevent the deterioration of the cells. During the actual measurement in aqueous environment, PBS has been used.

In order to get a basic idea about the typical structure of neuron,[11] a schematic drawing is shown in Fig. 2. A neuron consists of soma and many branches called as neural processes. Inside a single neural process, there are many tubulin[12,13] filaments forming a network and they are responsible for transporting nutrients to distal part of the cells. A single tubulin filament has got a diameter of 25 nm as estimated using transmission electron microscope.

2.3 Experimental System

The experimental system of an i-mode NOM operated under optical feedback is shown in Fig. 3. Light from an Ar^+ laser is coupled into the probe having the nanometric protruding tip to illuminate the neuron sample. In order to generate the rapidly decaying evanescent light for the feedback control, a small right angled prism ($1\times1\times2$ mm^3) was optically bonded to a parallel plate and light from an LD (wavelength 685 nm) was made to incident the prism at the angle of total reflection. The light is guided inside the parallel plate like in a waveguide. The sample substrate was mounted on the parallel plate with a sandwich of index matching oil. The evanescent field generated on the sample surface is picked up by the same probe and detected through a photomultiplier tube. To have a better S/N ratio, phase-sensitive detection has been employed in both the detection of the evanescent field and the scattered Ar^+ light. In this experiment, to reduce the background signal, proper filters have been installed in front of the detectors. Further, a shear force detection scheme[14,15] has been included to make a qualitative comparison of the images obtained under evanescent feedback. For this purpose, the probe has been mounted on a dithering piezo device and the vibrations of the probe have been detected with a He-Ne laser and a photodetector.

Figure 4 shows the variation of the evanescent signal intensity and the dithering amplitude as a function of the sample-probe separation. Here, the solid line of curve A corresponds to evanescent intensity variation and the dashed line of curve B corresponds to the variation of the dithering amplitude. It can be seen that with decreasing sample to probe separation, the dithering amplitude decreases while the evanescent intensity increases. Moreover, it can be noted that the rise of the evanescent intensity is as steep as the of fall the dithering amplitude and the transition points in both the curves occur at almost the same sample-probe separation. Hence, the evanescent signal can be profitably used for sample-probe separation feedback control with high sensitivity. We also found this

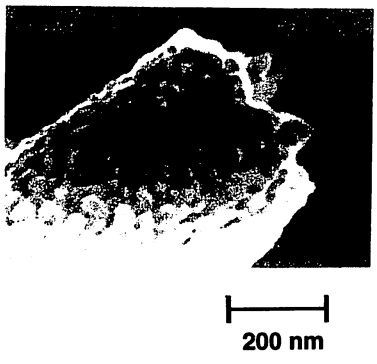

Fig. 1. A SEM image of the nanometric protruding probe used in i-mode NOM under evanescent intensity feedback control.

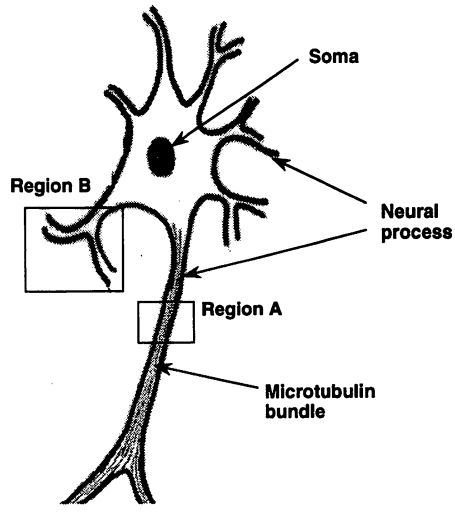

Fig. 2. An illustrative sketch showing the structure of the neuron. Regions indicated by A and B were imaged and shown in Figs. 5-7, respectively.

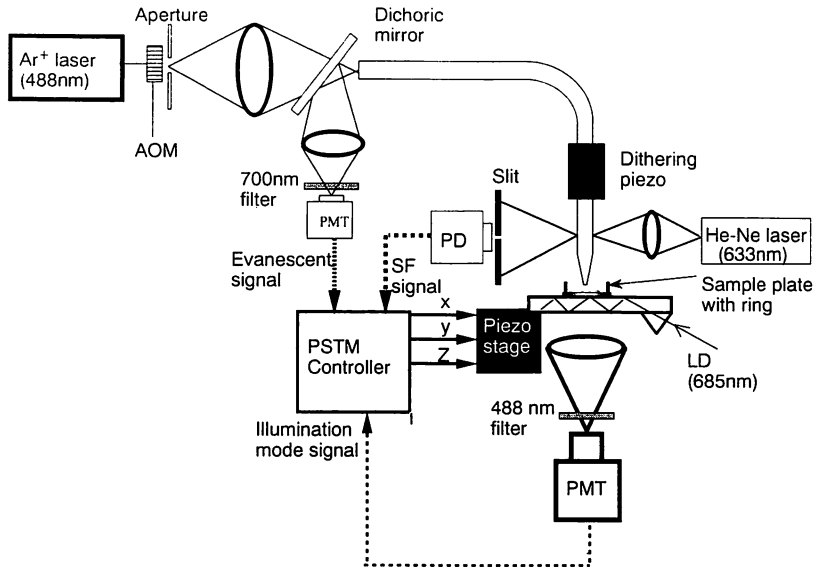

Fig. 3. A schematic sketch of the experimental system of i-mode NOM under evanescent feedback.

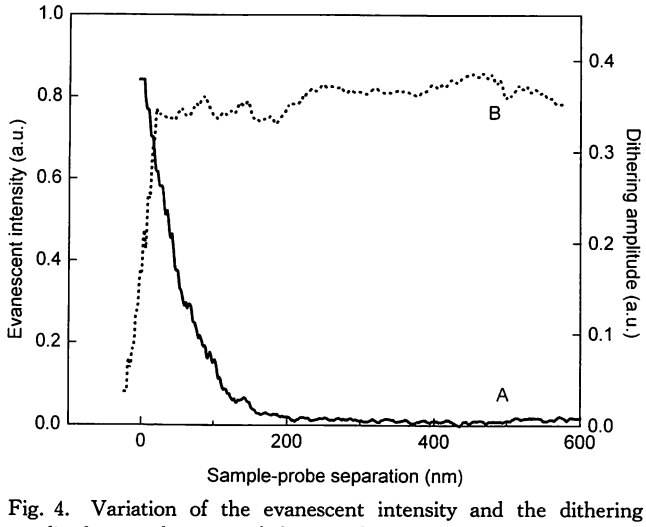

Fig. 4. Variation of the evanescent intensity and the dithering amplitude as a function of the sample-probe separation. Here, the solid line of curve A represents the evanescent intensity while the dashed line of curve B corresponds to the dithering amplitude.

simultaneous monitoring of evanescent intensity and dithering amplitude could be used as a error signal in detecting probe irregularities during actual scanning operation. This is because, when some dirt/dust gets attached to the probe, the separation at which the evanescent intensity first rises is different from that of the fall in the dithering amplitude.[16]

3. Results and Discussion

In this section, we give a qualitative comparison between the images of neurons obtained under evanescent and shear force feedback control and the image of neuron obtained in liquid environment.

3.1 A Qualitative Comparison

In order to compare the images under two different feedback controls, namely, the evanescent and the shear force, first a scanning area is selected. Next, the variations of the evanescent signal intensity and the dithering amplitude are obtained as a function of sample-probe separation at a point which is supposed to be the center of the scanning area selected. Finally, scanning is performed at a constant sample-probe separation corresponding to a position selected from the linear slope regions of curve B and curve A of Fig. 4 to obtain respectively, the image under constant shear force and constant evanescent signal intensity. In all the scanning results presented here, the sample-probe separation was kept to be less than 20 nm.

Figure 5 shows the i-mode image of a section of the neural process corresponding to area A in Fig. 2 under shear force feedback control. Inside the neural process, bundles of tubulin filaments (or neurofilaments) as indicated by arrow heads could be seen. Figures 6(a) and (b) show a magnified view of the area indicated by a square of Fig. 5 under shear force and evanescent feedback, respectively. As seen on left corner of both Figs. 6(a) and (b) as indicated by arrow heads, a large bundle of tubulin (or bundle of neurofilament) appearing dark could be seen. Also on the right lower corner dark fringe like structures as indicated by the arrow heads could be seen. These are persumed to be bundles of tubulin (or neurofilaments). Further, conducting observation of these neurons stained with monoclonal antibody of tubulin by a confocal microscope suggests that the neural processes contain tubulin filaments.

Our results show that under evanescent feedback control, it is possible to obtain the topographical variations almost the same as that under shear force. However, apart from the existence of similar features in Figs. 6(a) and (b), apparently there exist also some differences such as the minute features as indicated by the small arrows in Fig. 6(b). This indicates that under evanescent feedback control, the i-mode image contains not only features corre-

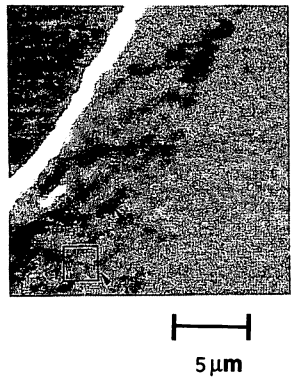

Fig. 5. i-mode NOM image of a neural process under shear force feedback control. Arrows indicate bundles of tubulin filament (or neurofilament). Scan area is 20×20 μm^2 with the pixel size being 78×78 nm^2.

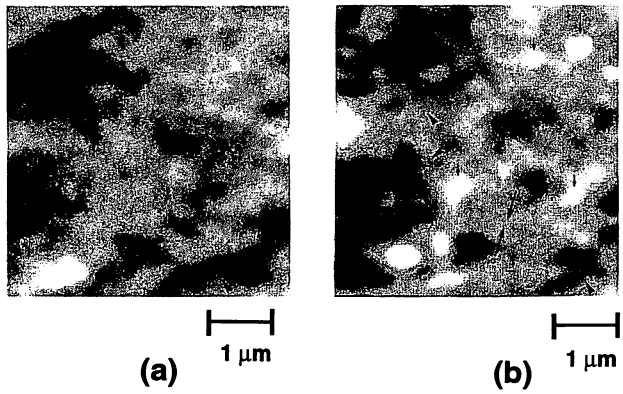

Fig. 6. i-mode NOM image of a magnified view of the region indicated by a square in Fig. 5 obtained under (a) shear force feedback and (b) evanescent intensity feedback. Scan area is 5×5 μm^2 with the pixel size being 39×39 nm^2. Arrow heads indicate bundles of tubulin (or neurofilament) present within the neural process. Small arrows indicate the differing minute features present in the image of Fig. 6(b). The full width of the narrowest bundle as indicated by the arrows in Fig. 6(b) is around 70 nm.

sponding to the topography of the scanned region but also features containing different information of the sample. This difference is believed to be originating from the changes in the absorption properties and refractive index changes during the scan by maintaining the detected evanescent intensity constant. In order to make an actual quantitative comparison, a well characterized sample such as nanometer sized gold particles could be used. Earlier, we have successfully imaged and performed Fourier analysis of the near-field images of 20 nm sized gold particles with i-mode NOM under shear force feedback.[17] Further, the full width of the narrowest bundle as indicated by the arrows in the image of Fig. 6(b) is estimated to be less than 70 nm. This indicates that the proposed system with evanescent signal intensity for feedback control has got the potential for attaining resolutions as high as that of the electron microscope.

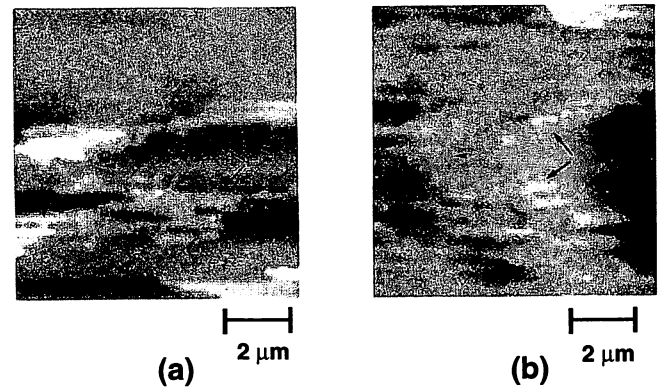

Fig. 7. Image showing the junction of two neural processes extending from the cell obtained under evanescent intensity feedback in liquid with (a) being the evanescent topography and (b) being the corresponding i-mode image. Scan area is 10×10 μm^2 with the pixel size being 78×78 nm^2. Arrows represent the neural process and arrow head indicates the junction.

3.2. Imaging in Liquid Environment

To conduct imaging in liquid, the sample plate was attached with a plastic ring so as to hold the liquid. The ring also makes the surface tension to be uniform all over the liquid surface. The ring attached sample plate is placed over the parallel plate with a sandwich of index matching oil. Next, scanning is performed at a constant sample-probe separation by keeping the intensity of the evanescent signal constant.

Figures 7(a) and (b) show respectively, the evanescent topographic and the i-mode images obtained on scanning a region B, corresponding to the junction of neural processes extending from the cell of Fig. 2. Here, scanning area is 10×10 μm^2 with the corresponding pixel size being 78×78 nm^2. As seen from Fig. 7, in both the evanescent topography and the i-mode image, as indicated by arrows two neural processes could be seen. Further, the junction between two neural processes as indicated by the arrow heads could also be seen in both Figs. 7(a) and (b). Moreover, in the i-mode image, some subcellular features within the region of the neural process could also be observed. These preliminary results demonstrate that it is possible to operate an i-mode NOM under evanescent signal intensity feedback control for operation in liquid.

4. Summary

In this paper, we proposed an i-mode NOM which uses the rapid decay of the evanescent signal intensity for controlling the sample-probe separation. We have found that the evanescent intensity feedback works as good as the popularly used shear force feedback. Preliminary results based on imaging neurons in air have shown that the images obtained under evanescent and shear force feedback show good similarity. The proposed NOM system has the potential for attaining resolution comparable to that of the electron microscope. Further, some preliminary results on imaging neuron in liquid have also been presented.

References

1) D.W. Pohl and D. Courjon eds.: Near-Field Optics, NATO ASI series E 242 (Kluwer, Dordrecht, The Netherlands, 1993).
2) M. Ohtsu: J. Lightwave Technol. 13 (1995) 1200.
3) M. Naya, R. Micheletto, S. Mononobe, R. Uma Maheswari and M. Ohtsu: submitted to Appl. Opt.
4) H. Muramatsu, N. Chiba, K. Homma, K. Nakajima, T. Ataka, S. Ohta, A. Kusumi and M. Fujihira: Appl. Phys. Lett. 66 (1995) 3245.
5) P.J. Moyer and S.B. Kammer: Appl. Phys. Lett. 68 (1996) 3380.
6) R. Uma Maheswari, H. Tatsumi, Y. Katayama and M. Ohtsu: Opt. Commun. 120 (1995) 325.
7) K. Jang and W. Jhe: Opt. Lett. 21 (1996) 1.
8) T. Saiki, M. Ohtsu, K. Jang and W. Jhe: Opt. Lett. 21 (1996) 674.
9) T. Pangaribuan, S. Jiang and M. Ohtsu: Electron. Lett. 29 (1993) 1978.
10) S. Mononobe, M. Naya, R. Uma Maheswari, T. Saiki and M. Ohtsu: submitted to Appl. Opt.
11) B. Alberts, D.Bray, J. Lewis, M. Raff, K. Roberts and J.D. Watson: *Molecular Biology of the Cell* (Garland Publishing Inc., New York, 1983).
12) E.M. Mandelkow and E. Mandelkow: J. Mol. Biol. 181 (1985) 123.
13) W. Yu, M.J. Schwei and P.W. Baas: J. Cell Biol. 133 (1996) 151.
14) E. Betzig, P.L Finn and J.S. Weiner: Appl. Phys. Lett. 60 (1992) 2484.
15) M. Vaez-Iravani, R. Toledo-Crow and Y. Chen: J. Vac. Sci. Technol. A 11 (1993) 742.
16) R. Uma Maheswari, S. Mononobe and M. Ohtsu: Appl. Opt. (in press)
17) R. Uma Maheswari, H. Kadono and M. Ohtsu: Opt. Commun. (in press).

ELSEVIER

1 January 1997

Optics Communications 133 (1997) 328–338

OPTICS COMMUNICATIONS

Full length article

Near-field optical microscope for true surface topography: theoretical study

A. Zvyagin [a], M. Ohtsu [a,b]

[a] *Interdisciplinary Graduate School of Science and Engineering, Tokyo Institute of Technology, 4259, Nagatsuta-cho, Midori-ku, Yokohama 226, Japan*

[b] *Kanagawa Academy of Science and Technology, KSP East 408, 3-2-1 Sakado, Takatsu-ku, Kawasaki 213, Japan*

Received 9 April 1996; revised version received 1 July 1996; accepted 5 July 1996

Abstract

We demonstrate an application of the perturbation theory based on the optical extinction theorem for the calculation of the near-field generated over a sample on a flat surface illuminated by a plane wave under total internal reflection angle. It is closely related to the theoretical modelling of a collection-mode near-field optical microscope (c-mode NOM). As an example, we calculated the near-field intensity over a semi-sphere on the flat surface. The main features of the calculated near-field are also discussed qualitatively in connection with a simple quasi-electrostatic model. On the basis of our analytical and numerical results we propose a c-mode NOM configuration which is advantageous for obtaining true surface topography.

1. Introduction

Recent progress in near-field optical microscopy (NOM) [1] not only increased resolution far beyond the diffraction limit, but shed light on the short-range interaction of matter and electromagnetic (EM) field. A number of experimental NOM results presently available require an appropriate theoretical interpretation. However, the theoretical model of an entire NOM system is complicated and can be met only by extended numerical simulations [2]. Besides, a variety of NOM operation modes require a specific theoretical modelling. Among these, the following two NOM modes are of wide usage: an illumination mode NOM (i-mode NOM) [3,4] and a collection mode NOM (c-mode NOM) [5,6]. In the i-mode NOM, light is commonly delivered from an external source through an optical fiber to its sharpened tip, which represents itself either: (a) a protruded tip apex (can be coated by metal except at the very end) [5,7,8]; or (b) a nanometer radius aperture in a metal coated tip [3,9]. In both cases the tip is a tiny light source generously emanating evanescent light *with high spatial frequencies*, which creates a strongly localized field at the apex (aperture) due to the non-propagating nature of evanescent light. Illumination of a small sample by this source from the nanometer-scale vicinity actuates the evanescent light scattering. As a result, thus created propagating light transfers the information on subwavelength details of the sample to the far-field zone. The c-mode NOM set up usually consists of a small sample placed on a glass prism and illuminated under the total internal reflection (TIR) angle. The probe tip (either of the

PII S0030-4018(96)00452-X

two kinds described above) is used in its reversed mode, i.e. being immersed into an evanescent wave continuum generated over the sample it picks up this light via a scattering process, and guides it into a detector. Again, the intensity of the evanescent waves with high spatial frequencies localized in the vicinity of the sample and carrying information about the small details of the sample can be detected. Both modes provide approximately equal lateral resolution ($\sim$ 20 nm [3,4,10]). Nevertheless, c-mode NOM better suits for the image interpretation purpose because the incident light polarization state, which crucially affects the optical near-field, can be precisely controlled. C-mode NOM can be theoretically modelled in a simple manner:

(i) A sample on the flat surface illuminated under TIR condition generates an optical field which can be represented as a spectrum of plane homogeneous (propagating) and inhomogeneous (evanescent) waves. If the sample is small the evanescent waves greatly dominate creating a non-propagating near-field localized above the surface.

(ii) This near-field can be *adequately* probed by a protruded probe tip closely brought to the surface by means of scattering the plane evanescent waves constituting the near-field, provided:

(a) the probe can be modelled by a small sphere;

(b) the small sphere scatters these evanescent waves as an electric point-like dipole;

(c) the system "probe–sample" is *almost uncoupled*, i.e. the probe and the sample interact (via multiple reflections) weakly. It may be therefore said, that the probe in our model is a "probe" but not an "interactor", and from now onward we will call it "ideal probe". The intensity scattered into all angles by such an ideal probe is known to be proportional to the square modulus of the electric field amplitude in the near-field zone. Thus, the intensity detection in the far-field zone versus lateral position of the probe enables one to obtain true EM near-field intensity surface mapping, which is believed to correlate with the surface topography. Rigorously speaking concerning assumption (c), the scattering process must be treated self-consistently. Yet, it is of interest to use weak coupling limit, not only because it lends significant simplification of the theoretical model but has its own range of application as well. For example, if the radius of the scattering sphere is as small as 10 nm and its centre is placed twice the radius from the planar surface (20 nm) it is already a weak coupling system [11].

The model can be classified as macroscopic and non-global. The advantage of this model is obvious: it permits to consider the EM near-field over the sample and the scattering process separately. It has received much attention recently in a series of publications [12–15]. In this paper, we further pursue the macroscopic non-global approach, performing an analytical and numerical study of the near-field over a small sample via the optical extinction theorem (ET) [16] written for the case of two dielectric media. In the non-global NOM theory development, we avoid embarking on the assumption of the Rayleigh hypothesis from the beginning as it was done in Refs. [12–15]. Instead, we solve the ET based boundary-valued problem in the small sample height limit, which may allow one to handle arbitrary media-constitutive scattering objects as well as the general geometry of the scattering surfaces (particularly, surfaces possessing cylindrical and spherical symmetry). And only then we apply angular spectrum representation. In addition, as it was recently demonstrated [17] for the two-dimensional case, the ET application makes it possible to develop a global macroscopic theory of NOM, i.e. where the tip and the sample are considered self-consistently. We also discuss an intuitive quasi-electrostatic model as a limiting case of our EM theory in order to gain insight into the surface–sample interaction problem in the near-field zone.

The objective of this paper is a theoretical study of the c-mode NOM as a device providing *true surface topography*, and on the basis of the described model we will demonstrate such a c-mode NOM configuration which is capable to reproduce a real surface profile, and can be realised experimentally.

2. Theory

We state the c-mode NOM related EM boundary-valued problem as follows. Let us consider a dielectric occupying the volume bounded by the surface S and embedded into another dielectric filling the rest of the space. Both dielectrics are assumed to be

linear homogeneous and isotropic. Let an EM wave $E^{i}(r)$ (harmonic time dependence $\exp(-i\omega t)$ will be assumed throughout the paper) be incident from the first dielectric (glass substrate with dielectric constant $\varepsilon_{glass} = \varepsilon$) on the second one (air, $\varepsilon_{air} \cong 1$), as shown in Fig. 1. Because of the assumed character of the media the electric field vector obeys the homogeneous Helmholtz equation everywhere in space such as

$$(\nabla^2 + K^2)E(r) = 0, \quad K = \begin{cases} k, & \text{in glass} \\ k_0, & \text{in air} \end{cases}$$

$$k = k_0\sqrt{\varepsilon}, \quad k_0 = \omega/c, \tag{1}$$

with the associated Green's function written for the unbounded space,

$$G(r\,|\,r') = \frac{\exp(ik\,|\,r - r'\,|)}{|\,r - r'\,|}. \tag{2}$$

The Helmholtz equation (1) is subject to a non-local boundary condition:

$$E^{i}(r) + \frac{1}{4\pi k}\nabla \times \nabla \times \int_S \left\{ E(r')\frac{\partial G(r\,|\,r')}{\partial n'} - G(r\,|\,r')\frac{\partial E(r')}{\partial n'} \right\} dS' = 0, \tag{3}$$

where $r \in$ air. This equation is known as the Ewald-Oseen optical extinction theorem. In this paper context, it reads that the electric field vector $E^{i}(r)$ originated in glass medium is cancelled (extinguished) in air. It is formally expressed in terms of $E(r')$ propagating in the latter medium, and its normal derivative $\partial E(r')/\partial n'$. Both are evaluated on the boundary S with the unit normal vector n pointed outward. It is interesting to note, that ET was originally derived from the microscopic theory [16], and actually is a product of two different branches of theoretical physics.

Since the aim of NOM is the study of subwavelength objects, the theoretical model can be further simplified. We will treat our scattering problem in the small surface roughness limit. A related perturbation theory via ET has been reported by Agarwal [18] and hence in what follows we will mainly keep within his systematic development. However, since we have written the non-local boundary condition for the two dielectric media case it is then necessary to

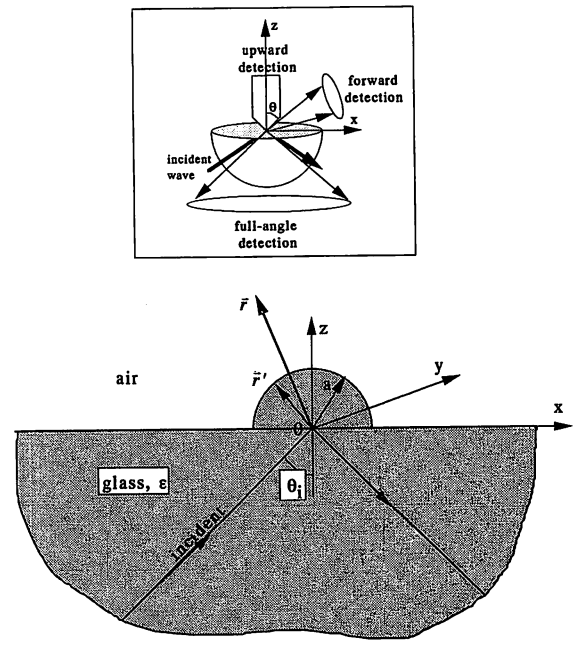

Fig. 1. An electromagnetic wave is incident from glass with dielectric constant ε on air under the total internal reflection angle θ_i. The interface between the two media consists of a planar surface $z = 0$ and the sample, a semi-sphere of radius a with its centre at the origin. The inset shows the schematic of three c-mode NOM configurations: "upward detection" by means of a fiber with cone angle θ; "full-angles detection" by means of a lens with large numerical aperture; "forward detection" (can be equivalently "backward detection") by means of a collection lens with its focal plane in the $x-z$ plane.

trace the main steps of the appropriate perturbation theory via ET. Let the perturbed surface separating glass and air be plane everywhere except at the points where a glass sample resides. We describe our sample by $z - af(x, y) = 0$ $(0 \le f(x, y) \le 1)$, where a is a perturbation parameter ($a \ll 2\pi/k$). First, the electric field vector, Green's function, their normal derivatives, and the unit normal to the surface are to be expanded in powers of a. We retain only the 1st order perturbative term in the expansion: $E = E^{(0)} + aE^{(1)} + \ldots$ for the field, $G = G^{(0)} + aG^{(1)} + \ldots$ for the Green function. Second, all of these quantities are to be evaluated on the surface using Taylor's series expansion, again retaining only terms up to the 1st order:

$$E(x', y', z')|_{z'=af} = E^{(0)}(x', y', 0)$$

$$+af(x', y')\frac{\partial E^{(0)}(x', y', 0)}{\partial z'} + aE^{(1)}(x', y', 0) + \ldots, \quad (4)$$

which implies that the electric field vector evaluated on the perturbed surface is expanded in terms of the fields and their normal derivatives evaluated on the plane (unperturbed) surface. Similarly, this can be done for the Green function. The next step is substituting the thus expanded electric field vector, Green's function, their normal derivatives into (3) and equating terms with the same powers of a. It leads to the following set of coupled equations,

$$\nabla\times\nabla\times\left\{E^{i}(r) - \frac{1}{4\pi k}\times\int\int dx'\,dy'\,E^{(0)}(x', y', 0)\times\frac{\partial G^{(0)}(r\,|\,x', y', 0)}{\partial z'} - G^{(0)}(r\,|\,x', y', 0)\frac{\partial E^{(0)}(x', y', 0)}{\partial z'}\right\}dx'\,dy' = 0 \quad (5)$$

for the 0th order, and for the 1st order:

$$\nabla\times\nabla\times\iint_{z'=0}\left\{k_0^2(\varepsilon-1)f(x', y')\times G^{(0)}(r\,|\,x', y', 0)E^{(0)}(x', y', 0) + G^{(0)}(r\,|\,x', y', 0)\frac{\partial E^{(1)}(x', y', 0)}{\partial z'} - E^{(1)}(x', y', 0)\frac{\partial G^{(0)}(r\,|\,x', y', 0)}{\partial z'}\right\} = 0. \quad (6)$$

Note that the curl operator acts with respect to r.

Since both the incident and the transmitted waves ($E^{i}(r)$ and $E(r)$, respectively) satisfy the Helmhotz equation, they can be written in angular spectrum representation:

$$E(r) = \int\int \mathscr{E}(u, v)\exp(iux + ivy + iWz)\,du\,dv,$$

$$E^{i}(r) = \int\int \mathscr{E}^{i}(u, v)\times\exp(iux + ivy + iW_0 z)\,du\,dv, \quad (7)$$

where $\mathscr{E}^{i}$ and $\mathscr{E}$ are angular spectral amplitudes of the incident and the transmitted waves respectively. The integrals run over all angular plane (u, v) parallel to the unperturbed surface $z = 0$. Every plane wave of the angular spectrum propagates with wave vector $\boldsymbol{K}$ in air and with $\boldsymbol{K}_0$ in glass. The wave vectors are defined as

$$\boldsymbol{K} = (u, v, W),$$

$$W = \sqrt{k_0^2 - u^2 - v^2}, \quad \text{if } |(u, v)| \le k_0,$$

$$= i\sqrt{u^2 + v^2 - k_0^2}, \quad \text{if } |(u, v)| > k_0,$$

$$\boldsymbol{K}_0 = (u, v, W_0),$$

$$W_0 = \sqrt{k_0^2\varepsilon - u^2 - v^2}, \quad \text{if } |(u, v)| \le k_0\sqrt{\varepsilon},$$

$$= i\sqrt{u^2 + v^2 - k_0^2\varepsilon}, \quad \text{if } |(u, v)| > k_0\sqrt{\varepsilon}. \quad (8)$$

From these equations one can see that W and W_0 can be either real or pure imaginary. Referring to Eq. (7) it is easy to see that in the former case the corresponding plane wave will be homogeneous and propagating, and in the latter case it will be inhomogeneous and evanescent with attenuation from the surface along the z-axis. The Maxwell equations for the incident and the transmitted electric field vectors in our sourceless media ($\nabla\cdot\boldsymbol{E}^{i} = 0$ and $\nabla\cdot\boldsymbol{E} = 0$, respectively) lead to the orthogonality relations written in terms of the angular spectral amplitudes:

$$\mathscr{E}(u, v)\cdot\boldsymbol{K} = 0, \quad \mathscr{E}^{i}(u, v)\cdot\boldsymbol{K}_0 = 0. \quad (9)$$

The Green function can be represented as

$$G(r\,|\,r') = \frac{i}{2\pi}\int\int\frac{1}{W_0}\exp[iu(x - x') + iv(y - y') + iW_0\,|\,z - z'\,|]\,du\,dv. \quad (10)$$

Substituting (7) and (10) into (5) and (6), and simplificating, we obtain the following expression for the 0th-order angular amplitude $\mathscr{E}^{(0)}$,

$$\mathscr{E}^{(0)}(u^{(0)}, v^{(0)}) = \frac{2W_0^{(0)}\mathscr{E}^{(i)}(u^{(0)}, v^{(0)})}{W^{(0)} + W_0^{(0)}} - \frac{2W_0^{(0)}(\boldsymbol{K}^{(0)}\mathscr{E}^{(i)}(u^{(0)}, v^{(0)}))\boldsymbol{K}_0^{(0)}}{k_0^2(W_0^{(0)} + W^{(0)}\varepsilon)}. \quad (11)$$

Note, that it is written in terms of the incident wave amplitude $\mathscr{E}^{(i)}$. It should be kept in mind that $W^{(0)}$, $W_0^{(0)}$ are functions of $(u^{(0)}, v^{(0)})$ and obtained from the corresponding W, W_0 by $(u, v) \rightarrow (u^{(0)}, v^{(0)})$. The 1st-order electric field vector angular amplitude $\mathscr{E}^{(1)}$ is likewise expressed in terms of the 0th-order as

$$\mathscr{E}^{(1)}(u, v) = \mathrm{i}(\varepsilon - 1) F(u - u^{(0)}, v - v^{(0)}) \times \left\{ \frac{k_0^2 \mathscr{E}^{(0)}(u^{(0)}, v^{(0)})}{W + W_0} - \frac{(\boldsymbol{K}\mathscr{E}^{(0)}(u^{(0)}, v^{(0)}))\boldsymbol{K}_0}{W_0 + W\varepsilon} \right\}, \quad (12)$$

where $F(u, v)$ is the Fourier transform of the surface profile function,

$$F(u, v) = \frac{1}{4\pi^2} \int\int f(x, y) \exp(\mathrm{i}ux + \mathrm{i}vy)\, \mathrm{d}x\, \mathrm{d}y. \quad (13)$$

We have assumed the incident wave to be plane in (11) and (12). However Eqs. (5)–(9) are general enough to treat an incident wave with an arbitrary angular spectrum.

From now on we assume,

(i) the incident wave is either s-polarized (electric vector lies perpendicular to the plane of incidence),
(ii) or p-polarized (electric vector lies in the plane of incidence);
(iii) plane of incidence is the x–z plane;
(iv) the wave is incident under the TIR angle;
(v) the sample is a semi-sphere of radius a with its surface profile function and Fourier transform given respectively as

$$af(x, y) = \sqrt{a^2 - x^2 - y^2},$$

$$aF(u, v) = \frac{a^2 j_1\left(a\sqrt{u^2 + v^2}\right)}{2\pi(u^2 + v^2)^{3/2}}; \quad (14)$$

j_1 is the 1st-order spherical Bessel function. It is straithforward to substitute Eqs. (12) and (11) into Eq. (7) and simplify the latter taking into account specifications (i)–(v). After some algebra we obtain

$$E_\xi(r) = \mathscr{E}_{\chi\xi}^{(0)}(u^{(0)}, 0) \left\{ \exp(\mathrm{i}u^{(0)}x - |W^{(0)}|z) + \mathrm{i}(\varepsilon - 1) \int\int F(u - u^{(0)}, v)\, D_{\chi\xi}(u, v) \times \exp(\mathrm{i}\boldsymbol{K}\cdot r)\, \mathrm{d}u\, \mathrm{d}v \right\}, \quad (15)$$

where ξ stands for the projection onto the corresponding coordinate axis, χ indicates the state of polarization of the incident wave (s or p); $\boldsymbol{K}$ denotes the wave vector, generally complex, of the corresponding spectral amplitude and is defined in (8). $\mathscr{E}_{\chi\xi}^{(0)}$ is simply the *Fresnel coefficient* ξ-component. They are written as

$$\mathscr{E}_{sy}^{(0)}(u^{(0)}, 0) = \frac{2W_0^{(0)}}{W^{(0)} + W_0^{(0)}} \mathscr{E}_s^i,$$

s-incident wave; (16a)

$$\mathscr{E}_{px}^{(0)}(u^{(0)}, 0) = -\frac{2\varepsilon W^{(0)} \mathscr{E}_p^i}{W_0^{(0)} + W^{(0)}\varepsilon} \cos\theta_i$$

$$\mathscr{E}_{pz}^{(0)}(u^{(0)}, 0) = \frac{2\varepsilon W_0^{(0)} \mathscr{E}_p^i}{W_0^{(0)} + W^{(0)}\varepsilon} \sin\theta_i, \quad (16b)$$

p-incident wave,

with θ_i denoting incident angle. The components of $D_{\chi\xi}$ are listed below:

$$D_{sy}(u, v) = \frac{k_0^2}{W + W_0} - \frac{v^2}{W_0 + W\varepsilon}$$

s-incident wave, (17a)

$$D_{px}(u, v) = \frac{WW_0 + v^2 + Wuu^{(0)}/W^{(0)}}{W_0 + W\varepsilon}$$

$$D_{pz}(u, v) = \frac{u^2 + v^2 + W_0 uW^{(0)}/u^{(0)}}{W_0 + W\varepsilon} \quad (17b)$$

p-incident wave,

The linkage between the analytical structure of Eq. (15) and the c-mode NOM characteristics ex-

pressed in terms of Fourier optics can be established by the following schematic equation:

$$\begin{bmatrix}\text{measured}\\ \text{near-field}\end{bmatrix} = \begin{bmatrix}\text{coupling}\\ \text{factor}\end{bmatrix} \times \left\{ \textit{background} + \begin{bmatrix}\textit{structure}\\ \textit{function}\end{bmatrix} \times \textit{filter} \begin{pmatrix}\textit{propagation}\\ \textit{translation}\\ \textit{diffraction}\end{pmatrix} \right\}. \quad (18)$$

The "background" term is due to the 0th-order scattered field, i.e. if there were no samples on the surface. As it is easy to see, it is of dominating order and therefore causes a serious drawback in achieving the ultimate resolution of NOM. The second term in the figure brackets stems from the 1st-order transmitted (scattered) field and is due to the scattering by the sample. It contains information on the structure profile via the Fourier transform of the sample surface profile, modulated (filtered) by three factors. The first one, "propagation" filtering, is very well known in Fourier optics (see for example, Ref. [19]). In Eq. (15) it takes the form $\exp(-|W|z)$, provided W is pure imaginary, which is the case when the spectral frequencies (u, v) are high: $|(u, v)| > k_0$. It tells us that in order to reproduce small details of the sample profile one must accumulate a large number of high-frequency components of the corresponding Fourier spectrum. At the same time, the higher the spatial frequency, the faster the corresponding evanescent wave attenuates propagating from the surface. It urges someone to probe the near-field in the vicinity of the sample. The second factor, "translation" filtering [15], affects the true surface profile reproduction in such a way that the Fourier transform function in the present context comes out in the form $F(u - u^{(0)}, v)$, not in $F(u, v)$. It induces translation asymmetry in the near-field with respect to the plane of incidence. The third factor, "diffraction" filtering $D_{\chi\xi}$ [12], accounts for the vector nature of the optical field and depends on angular frequency, incident field polarization, and the plane of incidence and the sample mutual orientation. It is worth to note that our diffraction factors calculated via ET agree with those calculated by van Labeke and Barchiesi [14].

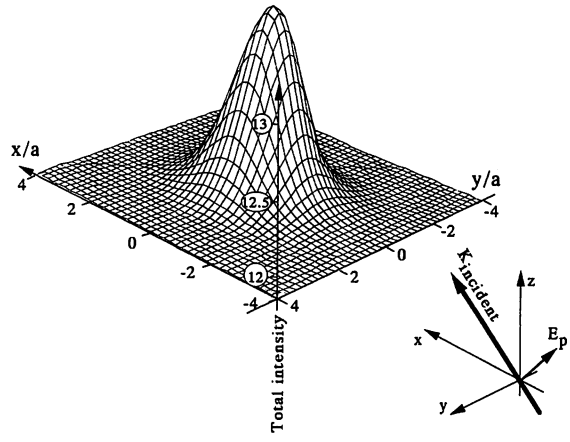

Fig. 2. Surface plot of the near-field total intensity calculated for a semi-sphere of radius $a = 20$ nm and its centre at the origin on the planar surface, provided a plane p-polarized wave (electric vector lies in the $x-z$ plane) is incident on it. The other parameters of the numerical calculation are: the scan height $h = 30$ nm; illumination light wavelength $\lambda_{air} = 680$ nm; glass dielectric constant $\varepsilon = 2.25$; angle of incidence 45°. The total intensity is given in arbitrary units, although proportionality between p- and s-incident wave cases (cf. Fig. 3) is kept.

The "coupling factor" can be appreciated if we integrate Eq. (15) over a finite solid angle. In this case it will depend on: first, the Fresnel coefficient

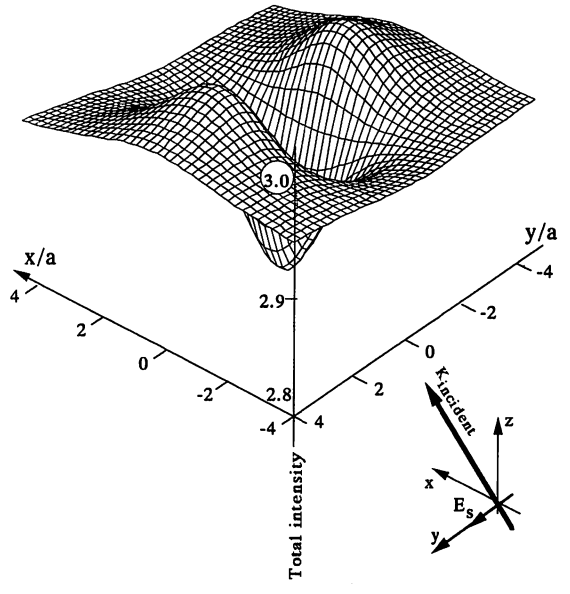

Fig. 3. The same as in Fig. 2 with the s-polarized wave (electric vector vibrates along the y-axis).

written for each electric near-field projection onto the corresponding coordinate axis $\mathscr{E}^{(0)}_{x\xi}$ which is a function of the incident wave polarization, angle of incidence, and relative refractive indices of the media. Second, the "coupling factor" depends on the direction angle of the integration, or in other words, how the light scattered by the ideal probe is detected.

3. Numerical results and discussion

The total near-field intensity over a semi-spherical sample is plotted on the x–y plane at $z = \text{const}$; it corresponds to the so-called "constant height scan" (see Figs. 2 and 3). Fig. 2 exhibits a strong near-field localization around the sample if it is illuminated by the p-polarized plane wave. It is almost symmetric with respect to the z-axis except slightly prolonged in the x-direction. On the other hand, if the s-wave is incident on it the near-field behaviour changes drastically: First, the near-field intensity plot shows negative resonance behaviour right over the sample top, or in other words, the sample image is inverted. Second, note the strong field anisotropy with respect to the plane of incidence: the near-field is weakly confined in the direction of incidence, unlike in the transverse direction. A cross-sectional view taken in the transverse direction would clearly display a double-peak image structure. It can be also viewed as the so-called "edge enhancement effect".

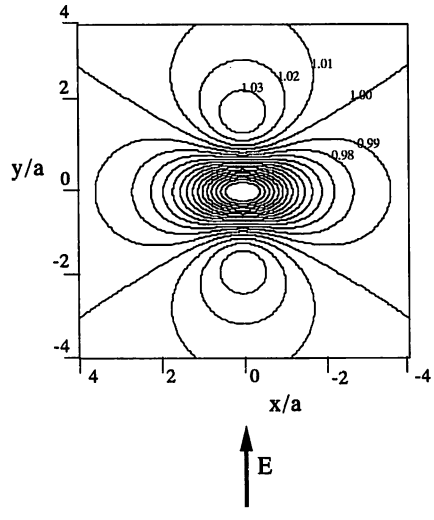

Fig. 4. Contour plot of the electrostatic field intensity calculation: a dielectric sphere in a uniform external field with its centre at the origin. The plot is taken in the $z = h$ plane with the electric field E_0 set to be 1 and directed along the y-axis. a, ε, h are the same as those for Fig. 2.

The following simple qualitative model elucidates this behaviour. It exploits the quasi-electrostatic approximation due to the slow variation of the electromagnetic fields in the region of interest. To begin with an s-polarized incident wave, let us consider a dielectric sphere of radius a with dielectric constant ε placed in a uniform constant electric field which is directed along the y-axis and has magnitude E_0 at large distances from the sphere [20]. Outside the sphere, the electrical field $\boldsymbol{E}$ is known to be equivalent to the applied field $\boldsymbol{E}_0$ plus the field of an electric dipole at the origin. The calculation of the total field intensity I_{total} over the sphere on the plane $z = \text{const}$ leads to the following result:

$$I_{\text{total}}(x, y, z = \text{const}) \propto \frac{E^2(x, y, z = \text{const})}{E_0^2} = \left(1 - \frac{\varepsilon - 1}{\varepsilon + 2}\frac{a^3}{r^3}\right)^2 + \frac{\varepsilon - 1}{\varepsilon + 2}\frac{3\xi^2 a^3}{r^5}\left(2 + \frac{\varepsilon - 1}{\varepsilon + 2}\frac{a^3}{r^3}\right), \tag{19}$$

where $r = \sqrt{x^2 + y^2 + z^2}$, and ξ stands for the coordinate of the axis along which the external field is directed. Fig. 4 presents the contour plot of the total electric field calculated using Eq. (19) with $\xi = y$ and parameters as listed in the caption of Fig. 2. One can see that it much resembles the near-field intensity plot of Fig. 3 for the s-polarized incident wave, that is, if the electric field vector of the incident wave vibrates along the y-axis. The contour plot similarly exhibits a double peak structure along the y-axis with the intensity drop right over the sphere top. Physically, it can be understood in terms of polarization surface charge which is induced by the external (incident) field and distributed on the sphere surface falling off gradually from the maximum at the poles at $(0, \pm a, 0)$ to zero on the equator. On the other hand, if the external field is directed along

the z-axis ($\xi = z$), (i.e. the observation plane is perpendicular to the external electric field direction) the total field will exhibit a single resonance peak with the maximum value right over the top of the sphere. Again, it is similar to the near-field intensity behaviour for the p-incident wave (Fig. 2). The slight anisotropy along the x-axis (see Fig. 2 or equivalently, Fig. 6(c)) can be explained considering that the electric field vector originated from the p-polarized incident wave, vibrates not only along the z- but also along the x-axis. It can be taken into account in the quasi-electrostatic model by considering "a sphere in an electrostatic field" system with a dipole moment induced along the x-axis. As one can see, the quasi-electrostatic approximation can be considered as a limiting case of the non-global macroscopic theory, provided that not only the height but also the lateral dimensions of the sample are small compared with the wavelength.

A few remarks on the resolution ability of the c-mode NOM can be made. As we have stated above, the EM near-field over a sample can be thought as a (vector) sum of the incident field transmitted through the planar interface, "background", and the field due to the sample, "signal". In the constant height scan (as it is shown for example, in Fig. 2 for the p-polarized incident light) the calculated background near-field intensity can be reconstructed measuring the EM field intensity far from the sample, while the signal intensity is defined to be a result of the subtraction of the field intensity calculated near the sample and the background intensity. Fig. 5 presents calculated signal and background intensities together with the half width at half maximum (HWHM) of the signal, plotted versus height measured from the top of the semi-sphere. As one can see, the background field is attenuated slowly upon the distance from the sample compared with the signal, which attenuation constant is mostly due to the semi-sphere radius (not the wavelength). Note, that -10 dB attenuation takes place at a distance of about $1.6a$, and the presented dependence is one and the same for $ka \ll 1$. It clearly shows that the strong localization around a small sample is an important property of the optical near-field. In order to show schematically the c-mode NOM resolution issue we drew a "contingent noise level" curve which is supposed to be due to: intrinsic detector noise (for

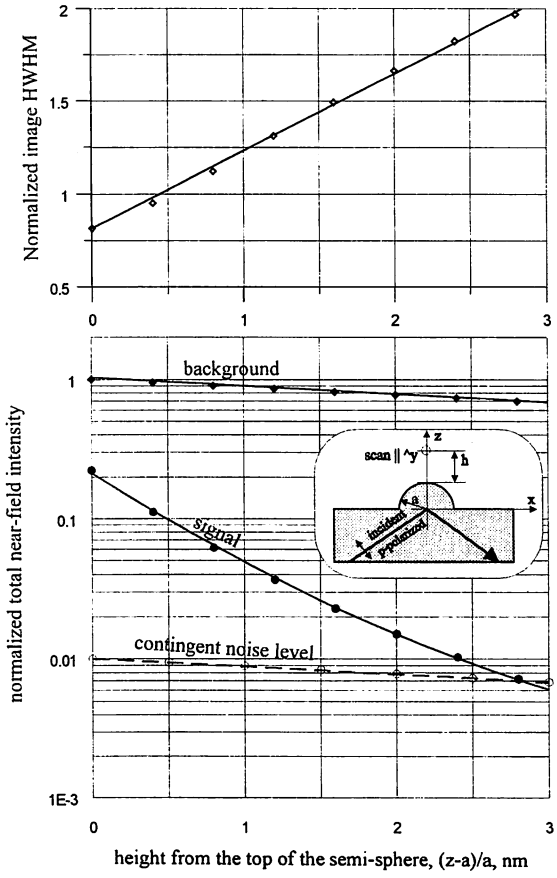

Fig. 5. Signal and background intensities of the total EM near-field over a semi-sphere of radius a on the planar interface (lower graph) and half width at half maximum of the signal (upper graph) dependences upon distance from the top of the semi-sphere. The incident light is chosen to be p-polarized, and the signal width is measured along the line ($x = 0$, $z = h$) as shown in the figure inset. Both signal and background intensities are normalized by the background intensity measured on the very top of the semi-sphere (0, 0, a), and HWHM is normalized by the semi-sphere radius, a. The distance from the sample is normalized by a, too. The contingent noise level is taken to be proportional to the background intensity.

example, dark-current noise of a photo-multiplier tube), and noise occurring as a result of the detector saturation by the background near-field intensity. The former noise intensity seems to be negligible under the typical experimental conditions. Of course, there are a variety of experimental means to extract the signal out of the background, but the noise is unavoidable and will restrict the resolution ability of the c-mode NOM. Crossing of the signal and the

noise level curves in Fig. 5 represents a point where the signal sinks under the noise. As it can be easily seen, the signal rapid attenuation with the distance from the sample presents the main limitation of the resolution. Spreading the signal width is of secondary importance for the resolution, as the upper graph of Fig. 5 shows. It should be noted, that the contingent noise level is drawn rather illustratively than realistically, and it reflects only its proportional dependence on the background intensity which saturates the detector. The real noise curve will depend on the experimental set-up, particularly, the detection circuit arrangement and probably can be taken into account only phenomenologically.

It is interesting to connect our results to the intuitive near-field theory recently proposed by Jang and Jhe, where particularly the sample was modelled by a small dielectric sphere on the planar surface illuminated by a plane evanescent wave [21]. As a result of Mie-scattering calculation, it was demonstrated that the total EM near-field intensity exhibits similar principle features as we have demonstrated in the present paper. The fact that the authors neglected the planar surface–sphere interaction, while we treated the surface and the semi-sphere self-consistently (via multiple reflections), lends us to the idea that the sample and the planar interface interact weakly in this configuration.

From now on, taking into consideration the coupling factor, we can analyse the following c-mode NOM configurations: (i) upward detection; (ii) full-angle detection; (iii) forward (backward) detection, as they are depicted in the inset of Fig. 1. The grey-scale images corresponding to each configura-

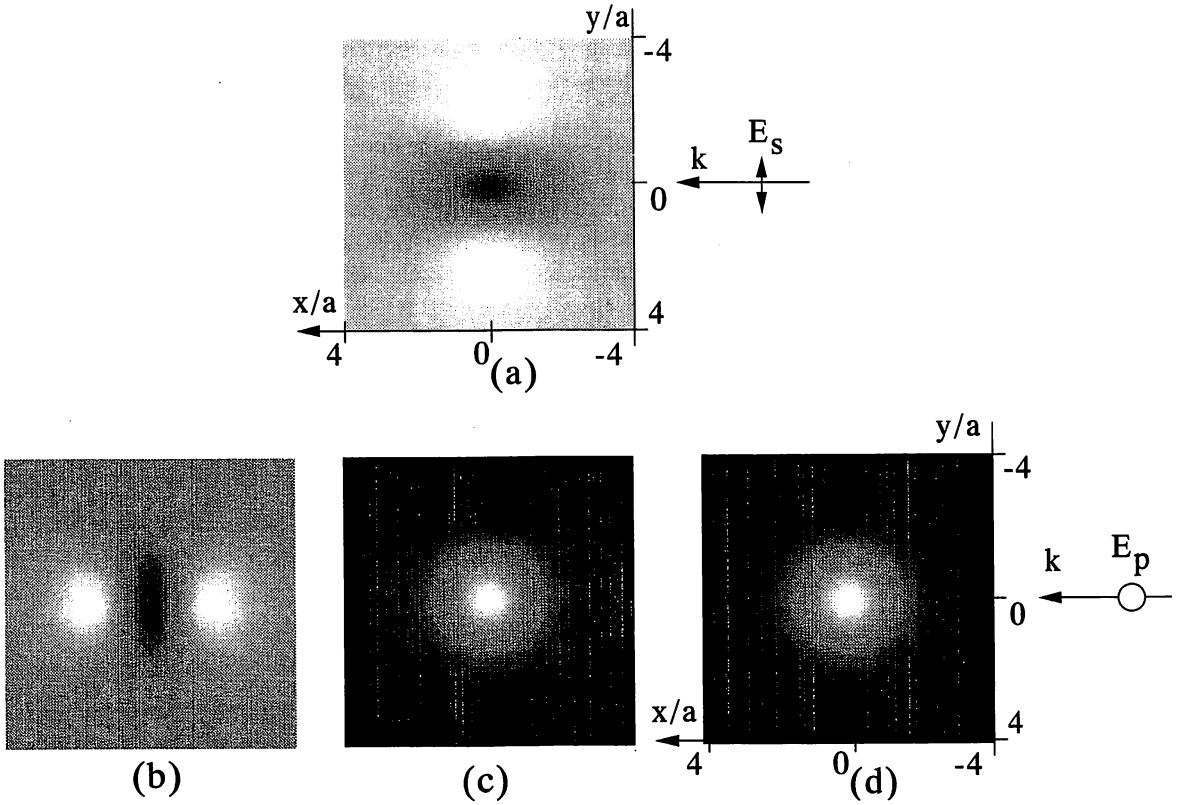

Fig. 6. Grey-scale images of intensities detected by the ideal probe plunged into the near-field over the semi-sphere calculated for the following c-mode NOM configurations and the incident wave polarization states: (a) for all configurations, and s-polarization; (b), (c), and (d) for p-polarization where (b) upward detection; (c) full-angle detection; (d) forward (backward) detection. Other parameters are the same as those for Fig. 2. Image relative intensities are chosen arbitrary for illustrative purpose.

tion are depicted in Figs. 6 (b), (c), and (d), respectively for p-polarized incident light, and in Fig. 6 (a), one and the same for all of these configurations for the s-polarized incident light.

(i) If c-mode NOM runs in its "upward detection" mode (see Fig. 1), only the E_y and E_x components of the electric near-field vector are coupled effectively into the fiber, but not E_z. (It holds, provided the cone angle θ of the tapered fiber collects the light scattered by the probe into a small angle; if it is not so, the corresponding image is a complicated convolution of all three components contribution. We address this problem to Ref. [14], and remark only that the collection angle $\theta = 20°$ seems to be critical for the "upward detection" assumption to hold.) The near-field generated by the s-polarized incident light consists of only E_y-component and hence is coupled to the fiber efficiently. But the corresponding image is not adequate. At the same time, the p-polarized incident wave generates a near-field which is coupled to the fiber only via its E_x-component. Also, it gives rise to a double-peak non-adequate image.

(ii) Actually, the c-mode NOM "full-angle detection" mode can be realized as it is shown in the inset of Fig. 1. A sample is placed on the semi-spherical glass prism and the light scattered by the probe is detected from below by a collection lens with large numerical aperture. In fact, the detection occurs approximately in half of the solid angle but it differs only by a constant factor (4, for intensity detection) from the full solid angle detection because scattering by the ideal probe is symmetric about the $z = 0$ plane. In this configuration the coupling factor does not ideally affect the image generation and the images come out as they are shown in Figs. 2 and 3, as three-dimensional plots and in Figs. 6 (c) and (a), respectively, as grey scale images. One can easily see that p-polarized incident light generates the EM near-field which follows the real surface profile rather faithfully. It is not so for the s-polarized incident light.

(iii) In the forward (backward) detection configuration, light scattered by the probe is detected in the forward (backward) direction in the x–z plane being collected by a collection lens. As it can be seen, the E_z- and E_y-components are well coupled to the detection circuit via scattering by the ideal probe, unlike the E_x-component. The E_y-component resulting from the s-polarized incident light produces a non-adequate image. On the contrary, the E_z electric near-field vector component originated from the p-polarized incident light is responsible for good confinement within the sample image.

If the size of the sample becomes larger in the lateral direction remaining flat, and exceeds the size determined by the reciprocal of the wave vector (of the order of $1/k$), the optical near-field loses its confinement. On the basis of the macroscopic non-global theory presented in this paper we propose the "full-angle detection" and the "forward-backward detection" configurations of c-mode NOM in conjunction with illumination by the p-polarized light which is advantageous for reproduction of the true surface topography, provided: (a) the sample is of the same dielectric as the substrate and is small in all three dimensions; (b) the probe is an ideal point-like weak-interacting electric dipole, as it is described in the Introduction.

4. Conclusion

We have presented a calculation of the scattered EM near-field intensity over a dielectric semi-sphere on a plane surface by applying perturbation theory via the optical extinction theorem. As a result, we have obtained analytical expressions for the near-field components which can be interpreted in terms of Fourier optics. The main numerical results calculated on the basis of our expressions can be summarised as follows:

– generally, the field over the sample turns out to be strongly localized within its radius, which agrees with recent experimental observation [22];

– in the particular case of a sample illuminated by a s-polarized wave the near-field is smeared in the direction of the incident wave propagation, unlike in the transverse direction, what induces strong anisotropy in the related image. The image appears to be inverted.

We found out, that our results are consistent with those obtained by Girard and Courjon on the basis of the microscopic self-consistent approach [23], which reveals an intimate relationship between the extinction theorem and the microscopic theory. The simple

quasi-electrostatic model presented in this paper allows us to clearly interpret our results on the near-field over a small semi-sphere. Qualitatively, the near-field may be thought of as a sum of the incident field and the field of a dipole at the origin. We also studied the influence of the coupling factor, i.e. the way how light scattered by an ideal probe plunged into the near-field is detected. On the basis of our analytical and numerical results we propose such a c-mode NOM configuration, i.e. that of "full-angles detection" or "forward (backward) detection" in conjunction with the p-polarized plane incident wave which is advantageous for detecting *true surface topography*, provided all constrains discussed in the paper are fulfilled.

Acknowledgements

We would like to express our gratitude to Prof. W. Jhe of the Seoul National University for stimulating discussions throughout this paper and careful reading the manuscript. This work was partially supported by the Korea-Japan Cooperative Science Program supported by the Korean Science & Engineering Foundation and Japan Society for Promotion of Science.

References

[1] See for example, Near-Field Optics, eds. D.W. Pohl and D. Courjon (Kluwer Academic Publishers, 1993); M. Ohtsu, J. Lightwave Technology 13 (1995) 1200.
[2] L. Novotny, D.W. Pohl and P. Regli, J. Opt. Soc. Am. A 11 (1994) 1768.
[3] E. Betzig and R.J. Chichester, Science 257 (1992) 189.
[4] R. Uma Maheswari, H. Kadano and M. Ohtsu, Optics Comm. submitted.
[5] D. Courjon, K. Sarayedinne and M. Spajer, Optics Comm. 71 (1989) 23.
[6] M. Naya, S. Mononobe, R. Uma Maheswari, T. Saiki and M. Ohtsu, Optics Comm. 124 (1996) 9.
[7] N.F. van Hulst, N.P. de Boer and B. Bolger, J. Microsc. 163 (1991) 117.
[8] S. Jiang, N. Tomita, H. Ohsawa and M. Ohtsu, Jap. J. Appl. Phys. 30 (1991) 2107.
[9] U.Ch. Fisher, U.T. Durig and D.W. Pohl, Appl. Phys. Lett. 52 (1988) 249.
[10] D. Courjon, C. Bainier and M. Spajer, J. Vac. Sci. Technol. B 10 (1992) 1.
[11] H. Chew, D.-S. Wang and M. Kerker, Appl. Optics 18 (1979) 2679.
[12] D. van Labeke and D. Barshiesi, J. Opt. Soc. Am. A 9 (1992) 5.
[13] D. Barshiesi and D. van Labeke, J. Mod. Optics 40 (1993) 1239.
[14] D. van Labeke and D. Barchiesi, J. Opt. Soc. Am. A 10 (1993) 2193.
[15] A. Sentenac and J.-J. Greffet, Ultramicrosc. 57 (1995) 246.
[16] E. Wolf, in: Coherence and Quantum Optics, eds. L. Mandel and E. Wolf (Plenum, New York, 1973) p. 339; and references therein.
[17] A. Madrazo and M. Nieto-Vesperinas, J. Opt. Soc. Am. A 12 (1995) 1298.
[18] G.S. Agarwal, Phys. Rev. B 15 (1977) 2371.
[19] J.W. Goodman, Introduction in Fourier Optics (McGraw-Hill, New York, 1968).
[20] J.D. Jackson, Classical Electrodynamics, second Edition (Wiley, 1975) Ch. 4, Sect. 4.4.
[21] K. Jang and W. Jhe, Optics Lett. 21 (1996) 236.
[22] T. Saiki, M. Ohtsu, K. Jang and W. Jhe, Optics Lett. to be published.
[23] C. Girard and D. Courjon, Phys. Rev. B 42 (1990) 9340.

TECHNICAL NOTE

Deducing structural variations of the apex of probes used in near-field optical microscopy through simultaneous measurement of shear force and evanescent intensity

R. Uma Maheswari, S. Mononobe, and M. Ohtsu

We propose a simple method employing the simultaneous detection of evanescent intensity and shear force to deduce variations in the near-field optical morphology of the apex of the probes used in near-field microscopy. Fabrication of our probes involves sharpening by chemical etching, metal coating, and removal of metal from the apex. We show that through the simultaneous measurement of shear force and evanescent intensity, it is possible to detect variations in the optical morphology of the very apex of the probes during near-field imaging by a scanning near-field optical microscope. © 1996 Optical Society of America

Key words: Near-field optical microscopy, shear force, evanescent intensity, simultaneous detection, near-field optical morphology of probe.

In a near-field optical microscope (NOM), first, a sharpened fiber probe fabricated either by chemical etching or by pulling a heated fiber was coated with metal to form a nanometer-sized aperture. Next, the apertured fiber probe was approached within a few nanometers from the sample and made to illuminate the sample. The light scattered from the sample is collected in either the transmission or the reflection geometry while the probe or the sample is moved in a raster fashion. The resulting two-dimensional (2-D) intensity distribution provides an image of the sample. For a detailed review of the NOM, see Refs. 1 and 2. Although this aperture-based NOM was employed successfully in the study of high-resolution observation of biological specimens,[3–5] the spectroscopy of quantum devices,[6–8] high-density memory,[9,10] etc., the evaluation of probes before their use has been limited to such methods as scanning electron microscope (SEM) observation. However, it is not always easy to obtain a clear perspective view of the apertured probe by the SEM because of its limited depth resolution. Furthermore, during actual scanning observations, especially the scanning of biospecimens, there is always a chance that some dirt or particle getting attached to the probe from the sample. Moreover, owing to high-power densities involved at the apex region of the probe, there is also heat-induced tip deformations.[11] There is no direct way of monitoring these changes that occur during actual scans because the scales involved are of a few nanometers. In this note, to evaluate the variations in the optical morphology of the probe while scanning is performed, we propose a method involving the simultaneous measurement of shear force and evanescent intensity.

A schematic view of the experimental system is shown in Fig. 1. The experimental system is the same as that of an illumination-mode NOM (Ref. 3) except for a slight modification of the sample mount. Light from an Ar^+ laser with a wavelength λ of 488 nm was passed through an acoustic-optic modulator and coupled into the apertured probe to illuminate the sample. The light scattered by the sample was collected by an objective lens (numerical aperture, 0.8) and detected through a photomultiplier tube. To perform 2-D scanning, we mounted the sample on an *xyz*-piezo stage. Furthermore, a shear force tech-

The authors are with Kanagawa Academy of Science and Technology, KSP East 408, 3-2-1, Sakado, Takatsu-Ku, Kawasaki-Shi, Kanagawa 213, Japan. M. Ohtsu is also with the Interdisciplinary Graduate School of Science and Engineering, Tokyo Institute of Technology, 4259 Nagatsuda, Midori-Ku, Yokohama, Kanagawa 226, Japan.

Received 4 March 1996; revised manuscript received 5 July 1996.

0003-6935/96/346740-04$10.00/0

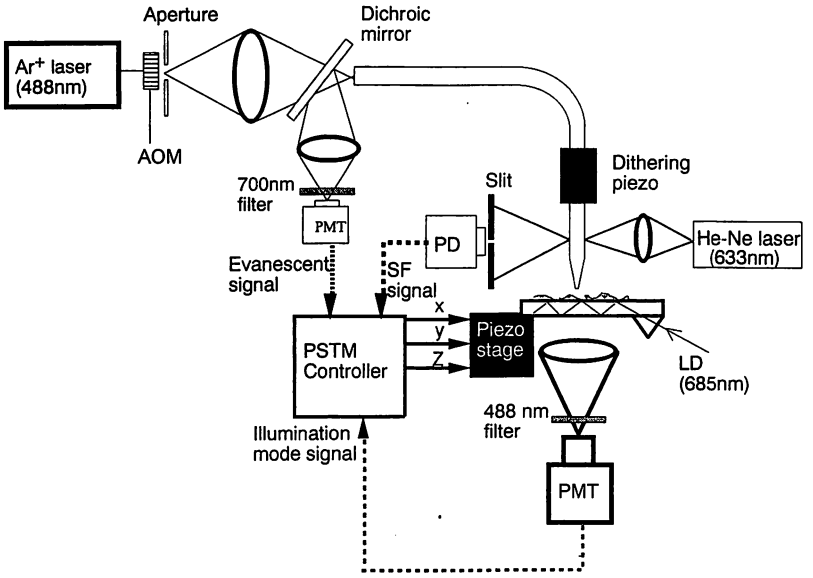

Fig. 1. Schematic view of the modified illumination-mode NOM experimental system operating under transmission geometry for the simultaneous generation of the evanescent field. AOM, acousto-optic modulator; PSTM, photon scanning tunneling microscope; PD, photodiode; LD, laser diode.

nique has been employed[12,13] to maintain the separation between the sample and the probe constant. This is done through dithering the fiber at its resonance frequency and detecting the vibrations with a He–Ne laser and a photodetector and slit.

Next, to detect simultaneously the evanescent intensity, we mounted the sample on a parallel plate that is optically bonded with a right-angled prism. Light from a laser diode (λ = 685 nm) was made incident at the prism at the critical angle, and the evanescent signal was generated on the surface of the sample. This evanescent signal was picked up by the same probe and detected through a photomultiplier tube. During signal detection, appropriate filters were employed to reduce the background. Here we should point out that the evanescent field is size dependent,[14,15] and for the case of the nonresonant sample, the field is also independent of wavelength.

In our case fabrication of the fiber probe involves, first, sharpening an optical fiber by a two-step selective chemical etching method[16] followed by coating these fibers with a gold film ~200 nm thick in a sputtering unit. Next, these fibers are coated with a resin film so that the apex part is devoid of resin, and finally gold from the apex part is removed by etching performed in a solution of potassium iodide and iodine.[17] Figure 2 shows the fabricated probe with a nanometric protrusion emerging from the metal-coated sharpened fiber. As can be seen from the figure, the diameter at the bottom of the protrusion is less than 40 nm and the length of the protrusion emerging from the metal film is less than 70 nm. The apex diameter is less than 10 nm. When this kind of probe is used, the problem of scattered light (especially strong for samples with large spatial variations), which reduces the signal-to-noise ratio encountered in evanescent signal detection, is considerably reduced.

The fiber probe with a nanometric protrusion was installed in the NOM to monitor the shear force and evanescent signals simultaneously. The sample used in this measurement was a biospecimen consisting of a protein called tubulin and was fixed on a glass substrate. The size of a single strand of tubulin as calibrated by the SEM is 25 nm. In our scanning experiments a scanning area is selected and before an actual 2-D scan is taken, the approach curves of both the force and the evanescent intensity are taken at a point that is the center of the intended 2-D scan. This process is repeated when the scan area is

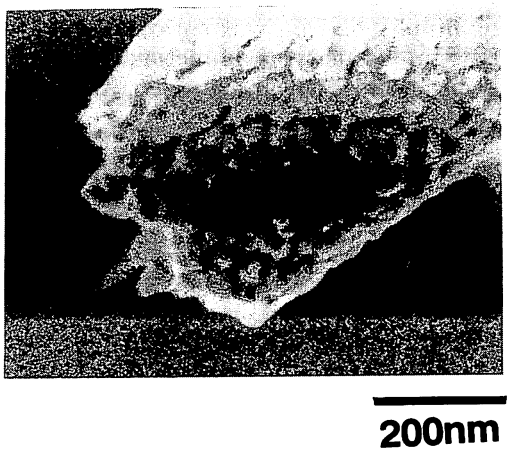

Fig. 2. SEM micrograph of a probe with a nanometric protrusion fabricated by chemically etching an optical fiber, coating the fiber with gold, and then removing the gold only from the apex region by etching in the KI–I_2 solution.

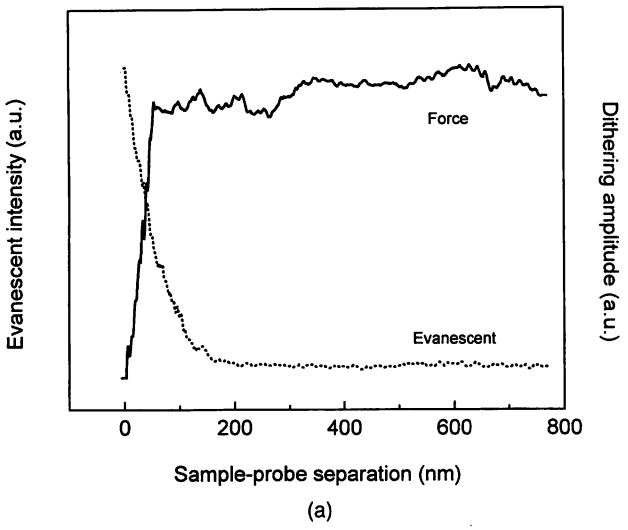

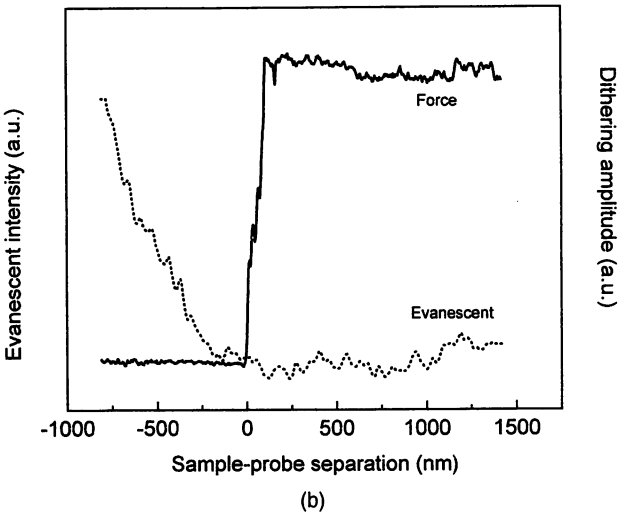

Fig. 3. Variation of dithering amplitude and evanescent intensity as a function of sample–probe separation (a) just after installation of the probe and (b) after a few raster scans of a biosample. Note the dramatic difference in the rise of evanescent intensity in (b).

changed. Figure 3(a) shows the variation of the dithering amplitude that was obtained and the evanescent signal intensity as a function of the sample–probe separation. As can be seen, the dithering amplitude decreases while the evanescent intensity increases with the decreasing sample–probe separation. Here zero has been defined as the point at which the dithering amplitude falls to zero. For both force and evanescent signals, it can be seen that the zero lies at almost the same point. So, for this case, with the shear force as a sample–probe separation measure, it is possible to operate the NOM in the proximity region. This is necessary for obtaining high-resolution images in the NOM.

Figure 3(b) shows a variation in the dithering amplitude and the evanescent signal intensity as a function of the sample–probe separation with the same fiber and for the same sample. This figure was obtained after a few 2-D raster scans of the sample were performed. During these scans the probe was assumed to be undamaged, because during the scans no drastic changes could be observed in the amount of light coming out of the nanometric protrusion of the fiber probe. However, the curves in Fig. 3(b) show a significant difference in position between the fall of amplitude in the dithering amplitude and the rise of evanescent intensity. Here, changing the position of the sample and repeating the approach scan, it has been found that the behavior of the approach curves of the dithering amplitude and the evanescent intensity are as in Fig. 3(b). Therefore this type of dramatic change in the behavior of the approach curves is at least not due to any change in the sample position. We believe that it is due to some dramatic changes in the optical morphology of the very apex of the probe during scanning. Although it is said that shear-force microscopy is equivalent to noncontact-force microscopy, it is not yet fully clear whether any actual contact is made with the surface during scanning or between which point the force actually operates because the tip is not ideally sharp. However, from our results one thing is quite clear; i.e., sometimes the optical morphology of the apex is drastically changed because of scanning.

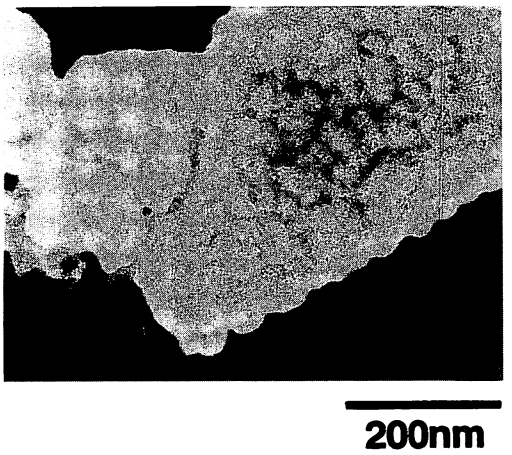

Fig. 4. SEM micrograph of a probe with a protruded tip with some dirt attached in the apex region.

Figure 4 shows a probe with dirt attached at the top. Actually, as a result of scanning the sample, a probe as shown in Fig. 2 must have resulted in one like that shown in Fig. 4. Especially, as in our case, biological samples are imaged; there is always a chance that the probe will pick up some dirt from the sample, resulting in very poor imaging. Because there are a large number of factors, e.g., scan parameters, light levels, sample–probe separation, involved in optimizing a NOM to obtain high-resolution images, the current simple technique of simultaneous detection of the evanescent intensity and the shear force would be helpful in deducing morphological variations of the very apex of the probe and hence in expediting the imaging process. The commonly used shear-force monitoring alone has disadvantages, such as the possibility of introducing artifacts

into the optical image from cross-talk problems and also the difficulty of operating in liquid.

Although we have discussed only probes fabricated by etching and protruding-type tips, the method itself could be applied to aperture-type probes fabricated by pulling and metal coating. Also, in the case of such probes, morphological irregularities can be checked by our method. Therefore our method is not only useful for deducing the regularity of near-field optical morphology in the probes during scanning, but it also could be used as a screening test of probes in the checking process before scanning. Furthermore, the experimental system proposed here can be used for conducting observations of biosamples in liquid by utilizing the evanescent intensity as a feedback signal to control sample–probe separation. The results of this research are published in a separate paper.[18]

References

1. D. W. Pohl and D. Courjon, eds., *Near-Field Optics*, NATO ASI Series E (Kluwer, Dordrecht, The Netherlands, 1993), Vol. 242.
2. M. Ohtsu, "Progress of high resolution photon scanning tunneling microscopy due to a nanometric fiber probe," J. Lightwave Technol. **13,** 1200–1221 (1995).
3. R. Uma Maheswari, H. Tatsumi, Y. Katayama, and M. Ohtsu, "Observation of subcellular nanostructure of single neurons with an illumination mode photon scanning tunneling microscope," Opt. Commun. **120,** 325–334 (1995).
4. M. Naya, S. Mononobe, R. Uma Maheswari, T. Saiki, and M. Ohtsu, "Imaging of biological samples by a collection-mode photon scanning tunneling microscope," Opt. Commun. **124,** 9–15 (1996).
5. E. Betzig and J. K. Trautman, "Near-field optics: microscopy, spectroscopy and surface modification beyond the diffraction limit," Science **257,** 189–195 (1992).
6. R. D. Grober, T. D. Harris, J. K. Trautman, E. Betzig, W. Wegscheider, L. Pfeiffer, and K. West, "Optical spectroscopy of a GaAs/AlGaAs quantum wire structure using near-field scanning optical microscopy," Appl. Phys. Lett. **64,** 1421–1423 (1994).
7. T. Saiki, S. Mononobe, M. Ohtsu, N. Saito, and J. Kusano, "Spatially resolved photoluminescence spectroscopy of lateral *p–n* junctions prepared by Si-doped GaAs using a photon scanning tunneling microscope," Appl. Phys. Lett. **67,** 2191–2193 (1995).
8. N. Toda, M. Kourogi, Y. Nagamune, Y. Arakawa, and M. Ohtsu, "Near-field optical properties of GaAs quantum dot structures measured by photon scanning tunnelling microscope," in *Technical Digest, Conference on Lasers and Electro-optics/Pacific Rim '95* (IEEE, New York, 1995), pp. 165–166.
9. E. Betzig, J. K. Trautman, R. Wolfe, E. M. Gyorgy, P. L. Fynn, M. H. Kryder, and C. H. Chang, "Near-field magneto-optics and high density data storage," Appl. Phys. Lett. **61,** 142–144 (1992).
10. S. Jiang, J. Ichihashi, H. Monobe, M. Fujihira, and M. Ohtsu, "Highly localized photochemical processes in LB films of photochromic material by using photon scanning tunneling optical microscope," Opt. Commun. **106,** 173–177 (1994).
11. A. H. La Rosa, B. I. Yakobson, and H. D. Hallen, "Origin and effects of thermal processes on near-field probes," Appl. Phys. Lett. **67,** 2597–2599 (1995).
12. E. Betzig, P. L. Finn, and J. S. Weiner, "Combined shear force and near-field scanning optical microscopy," Appl. Phys. Lett. **60,** 2484–2486 (1995).
13. M. Vaez-Iravani, R. Toledo-Crow, and Y. Chen, "Correlative imaging in scanning near-field optical microscopy," J. Vac. Sci. Technol. **A 11,** 742–747 (1993).
14. K. Jang and W. Jhe, "Nonglobal model for near-field scanning optical microscope using diffraction of the optical near field," Opt. Lett. **21,** 1–3 (1996).
15. T. Saiki, M. Ohtsu, K. Jang, and W. Jhe, "Direct observation of size-dependent feature of optical near field on a subwavelength spherical surface," Opt. Lett. **21,** 674–676 (1996).
16. T. Pangaribuan, S. Jiang, and M. Ohtsu, "Two-step etching method for fabrication of fiber probe for photon scanning tunneling microscope," Electron. Lett. **29,** 1978–1979 (1993).
17. S. Mononobe, M. Naya, R. Uma Maheswari, T. Saiki, and M. Ohtsu, "Fabrication technique of pencil-type fiber probes and nanometric apertures for photon scanning tunneling microscope," in *Proceedings of the EOS Topical Meeting on Near Field Optics, Brno, Czech Republic* (European Optical Society, Brno, 1995), Vol. 8, pp. 105–106.
18. R. Uma Maheswari, S. Mononobe, H. Tatsumi, Y. Katayami, and M. Ohtsu, "Observation of subcellular structures of neurons by an illumination mode near-field optical microscope under an optical feedback control," Opt. Rev. **3** (6) (1996).

ELSEVIER

15 October 1996

OPTICS COMMUNICATIONS

Optics Communications 131 (1996) 133–142

Full length article

Power spectral analysis for evaluating optical near-field images of 20 nm gold particles

R. Uma Maheswari [a], H. Kadono [a,b], M. Ohtsu [a,c]

[a] *Kanagawa Academy of Science and Technology, KSP East 408, 3-2-1 Sakado, Takatsu-Ku, Kawasaki-Shi, Kanagawa 213, Japan*
[b] *Department of Environmental Science and Human Engineering, Saitama University, 255 Shimookubo, Urawa, Saitama 338, Japan*
[c] *Interdisciplinary Graduate School of Science and Engineering, Tokyo Institute of Technology, 4259 Nagatsuta, Midori-Ku, Yokohama, Kanagawa 226, Japan*

Received 12 December 1995; revised version received 4 March 1996; accepted 28 March 1996

Abstract

We have demonstrated that the power spectral analysis could be employed as a potential tool for evaluation of near-field optical images of colloidal gold particles of size 20 nm fixed on a glass substrate. It has been found that the power spectral density of the near-field image resembles the Airy pattern due to a circular dot with the first minimum occurring at the spatial frequency 5.6×10^7 m^{-1}. This corresponds to an estimated particle diameter of 22 nm. From a comparison with the theoretical power spectral density of randomly distributed circular dots, the transfer function of the near-field optical microscope has been estimated. It has been found that the resolution estimated using -3 dB cutoff value obtained from the transfer function was 0.8 nm which is much higher than that determined by aperture size. The high resolving ability of the present microscopic system is believed to be due to the confinement of very high spatial frequency evanescent fields around the edges of the metal–glass fiber boundary at the apex of the apertured probe.

1. Introduction

Recently, the technique of near-field microscopy [1,2] has been applied to different fields such as probing single molecules [3–5], imaging biological specimens [6–8], spectroscopy of semiconductor devices [9–11] and high density optical storage [12,13]. This microscopic technique is known under different names such as Photon Scanning Tunneling Microscopy (PSTM) [14], Scanning Tunneling Optical Microscope (STOM) [15], Near-field Scanning Optical Microscope (NSOM) [16] and Scanning Near-filed Optical Microscope (SNOM) [17]. In this paper, we use the name SNOM as it has been popularly used emphasizing the analogy with other Scanning Probe Microscopes (SPM) (refer to the glossary of names and acronyms compiled by Pohl in Ref. [1]). Further, in this paper, we call the tunneling of the evanescent field from the sample to probe as *collection mode SNOM* [7,18,19] and vice-versa, i.e., the tunneling of the evanescent field from the probe to the sample as *illumination mode SNOM* [1] [8].

In spite of the very wide applications of near-field imaging listed above in various fields, only a few studies related to the detailed analysis of the images with respect to resolution and contrast of the obtained images and hence the transfer function of SNOM exists (e.g., Pieralli [20] describes an experi-

PII S0030-4018(96)00278-7

mental one-dimensional point spread function of SNOM with calculation based on imaging a random surface). This is because, in near-field microscopy, it is not straightforward to extend the same image evaluation parameters such as Rayleigh criterion [21] usually employed in the conventional diffraction-limited microscopy. In the actual case of a near-field, the imaging process involves a rather complex short range electromagnetic interaction between the probe and the sample. Further, the apertured probes employed in imaging have been mainly evaluated only by Scanning Electron Microscope (SEM) without a prior way of investigating its near-field properties. Therefore, in order to describe the performance of imaging by a SNOM system, we need a system function, in other words a transfer function, incorporating a criterion for evaluating resolution and contrast. Such parameters can also be obtained by performing power spectral analysis for describing the image characteristics.

The resolution could be defined as the highest -3 dB cutoff spatial Fourier frequency where the amplitude of the transfer function is attenuated to half its maximum value. An alternative way of defining the resolution could be the frequency at which the signal to noise ratio of the power spectral density (PSD) of the image is 0 dB. The contrast could be defined as the ratio of the PSD at the frequency corresponding to the size of the smallest feature in the sample to the PSD at the frequency corresponding to the surface variation of the substrate on which the sample lies.

In this communication, we present power spectral analysis of the near-field optical images of 20 nm gold particles. We will show that the two-dimensional power spectral analysis gives a direct estimate of the size of the gold particle which agrees very well with its nominal value. To our knowledge, an exact correspondence between the nominal size of 20 nm of the gold particle and the result of the power spectral analysis of the optical near-field image is the first to be reported. Section 2 gives a brief description of the experimental details on imaging gold particles. Section 3 presents the results of power spectral analysis of the near-field images of gold particles and discusses a comparison with a two-dimensional theoretical model and simulation results. Finally, Section 4 gives a summary.

2. Imaging of 20 nm gold particles

The illumination mode SNOM has been employed for imaging gold particles. The experimental arrangement used is the same as the one shown in the schematic of Fig. 3 of Ref. [8]. As mentioned in Section 1, in this mode, light (wavelength: 488 nm) from a nanometric aperture illuminates the sample and the scattered light from the sample is collected by an objective lens of numerical aperture 0.8 into a photo multiplier tube. For attaining higher signal to noise ratio, phase sensitive detection has been employed. Fabrication of nanometric aperture involves chemically etching an optical fiber with a high GeO_2 doped core [22,23] and metal coating. The chemical etching process involves a multi-step etching method [24] and the obtained fiber probe has a flattened apex. The coating of this fiber was performed in a vacuum evaporation unit. The coating layer consists of chromium of thickness 10 nm and gold of thickness 160 nm. This thickness of gold is sufficient to block light from the sides and the cladding facet of the fiber probe. The fabricated aperture has a diameter of less than 30 nm. Refer, respectively, to Figs. 1 and 2 of Ref. [8] for the results of etching and coating in the fabrication of the aperture.

As sample, we have employed randomly distributed gold particles because the diameter of a single particle has been accurately calibrated as 20 (± 0.5) nm by means of TEM. A drop of solution containing colloidal gold particles was dispersed onto a glass substrate and was allowed to dry at room temperature. The sample was mounted on a *XYZ*

[1] In a near-field microscope, the sample is illuminated (under total internal reflection) and the three-dimensionally confined evanescent field (see Ref. [7]) generated over the sample is scattered by a sharpened probe tip having a subwavelength radius of curvature at its top. From a phenomenological point of view (see Ref. [30]), this multiple scattering process involving short range electromagnetic interaction between the probe and the sample can be thought of as a tunneling of evanescent photons from the sample to probe. Further, it obeys the principle of reciprocity, i.e., the process is the same even when the positions of the sample and the probe are interchanged. In other words, the sample scatters the evanescent field generated by the sharpened probe tip.

piezo scanner with in-built sensors compensating for the effect of hysterisis and raster scanning was performed under constant sample–probe separation which was done through shear force detection technique [25,26].

Fig. 1(a) shows the SNOM image obtained under a sample–probe separation of less than 5 nm at which position, the slope corresponding to the tail of the force curve is small. In other words, the shear force feedback gain is low and the actual scanning can be considered to be almost done under free running condition. The scan area of this figure is 1.8×1.8 μm^2 with one pixel corresponding to approximately 7×7 nm^2. In this figure, the dark region A corresponds to gold particles formed as large clusters. A magnified view of region B in the clustered region A is shown in Fig. 1(b). Here, even within the clusters consisting of overlapping gold particles, dark regions, for example, the region indicated by the arrows corresponds to small clusters of gold particles. Fig. 1(c) shows a magnified view of region C away from the large cluster region A. As seen in this figure, some single gold particles, for example the region indicated by the arrow could be visualized.

3. Power spectral analysis

3.1. Experimental

Fig. 1 is the image of gold particles distributed randomly in space. Hence by analysing this image, one could determine information related to the size of a single gold particle and the degree of randomness of the particle distribution. In turn, with this information, the transfer function of our system could be determined. On the basis of the transfer function, resolution and contrast of the image could be obtained with the help of the definitions described in

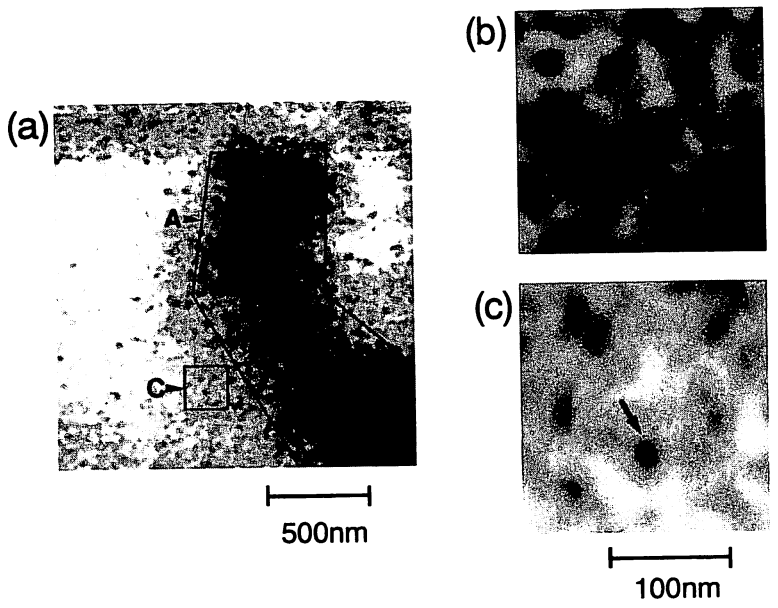

Fig. 1. (a) SNOM image of gold particles of diameter 20 nm over a scan area of 1.8×1.8 μm^2 with one pixel corresponding to an area of 7×7 nm^2. Here region A corresponds to gold particles formed as large clusters. Regions B and C respectively correspond to sections in the clustered and isolated gold particle region. (b) The magnified view of region B in the clustered region on the very right corner of region A. The arrows correspond to the small clusters consisting of two or more gold particles. (c) The magnified view of region C and corresponds to a section away from the large cluster region. The arrow indicates an isolated gold particle.

Section 1. In order to estimate the transfer function, we use power spectral analysis.

To perform power spectral analysis, the two-dimensional image shown in Fig. 1 has been Fourier transformed by using FFT algorithm. The resulting two-dimensional Fourier power spectral density (PSD) $F(\nu_x, \nu_y)$ is shown in Fig. 2. It has a very bright broad region at the center followed by a dark region. Around this dark region, a part of the bright region, indicated by eight arrows, could be seen. Here, due to the circular symmetry of the two-dimensional PSD, the spectral variation can be averaged along the angular direction (θ) of the polar coordinate system. From now onwards, we call this PSD averaged with respect to θ the averaged power spectral density (APSD). Fig. 3 shows the variation of APSD in a log–log scale.

Here, the PSD calculations have been done with software developed by us. Of course, it is much easier to do such calculations with Fourier transform routines available in commercial SPMs. However, they lack the flexibility in displaying spectral data and could not be used directly in our case. Actually, the Fourier spectral amplitudes at high frequencies are of very low strength compared to that of the low

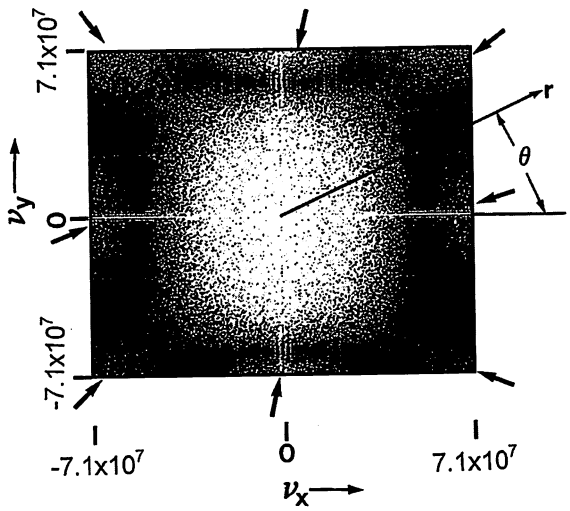

Fig. 2. Two-dimensional Fourier power spectral density $F(\nu_x, \nu_y)$ of the image shown in Fig. 1(a). The arrows indicate the bright regions at the rim of the figure. r and θ indicate the polar coordinates used for obtaining the APSD.

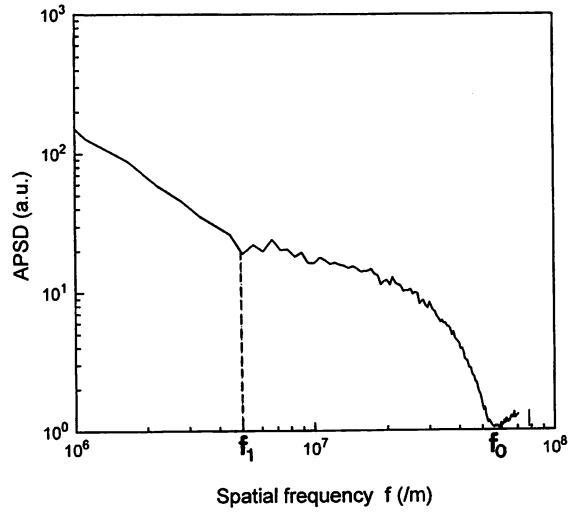

Fig. 3. The APSD as a functon of the spatial frequency f given in a log–log scale. Here averaging was done over the angular direction θ of Fig. 2. Here f_1 is the frequency below which the APSD is dominated by the effects due to random arrangement and clustering of the gold particle. For $f > f_1$, the APSD resembles that due to a single gold particle and has been used in the calculation of the transfer function. f_0 is the frequency at which the power spectral density becomes minimum.

frequency components and they could not be distinguished on a linear scale plot of the Fourier spectral data. The power spectral data must be displayed in a log–log scale in order to extract the information about minute features in the image or in other words to get a clear view of the high frequency components. Fig. 3 shows the variation of the APSD as a function of spatial frequency (f) in a log–log scale. The spectral variation clearly shows a minimum at the spatial frequency (f_0) 5.6×10^7 m^{-1}. It should be pointed out that the noise level of the present SNOM system is well below the lowest level of this figure and hence the minimum at f_0 in the APSD contains valuable information regarding the resolving ability of our SNOM system.

3.2. Theoretical and simulation results

We consider a simple model consisting of dots distributed randomly in space [27] to explain the presence of a minimum in the APSD of the experi-

mentally obtained near-field image of 20 nm gold particles. Such a random distribution could be represented as

$$u(x,y) = \sum_{n=0}^{N-1}\sum_{m=0}^{N-1} g(x-nd-\xi_{nm}, y-md-\eta_{nm}), \quad (1)$$

where $g(x, y)$ is the amplitude variation due to a single dot, n and m are the integers specifying each dot, d is the mean spacing between the dots, and ξ_{nm} and η_{nm} are the random displacements given to the center of the (n, m)th dot along the x and y directions, respectively. Here, consideration of a two-dimensional FFT model is possible because the observed image was obtained by keeping the sample–probe constant through the monitoring of the shear force. Further, especially on acquiring the image, the obtained image is a map of intensity as a function of x and y. Hence, only a two-dimensional FFT is possible in the experiment (and a three-dimensional FFT is just conceptual). Though there exists in the literature [28–30] theoretical calculations representing the sample as a sphere or a lattice of spheres, the discussion there is restricted only to the calculation of near-field intensity. There is no analysis of the obtained images and hence of the transfer function and of the resolution of the experimental system which has been conducted in this study. The Fourier transform of the random distribution of dots is given by

$$\begin{aligned} U(\nu,\mu) &= \int_{-\infty}^{\infty}\int_{-\infty}^{\infty} u(x,y)\exp[-i2\pi(\nu x+\mu y)]\,dx\,dy \\ &= G(\nu,\mu)\sum_{n=0}^{N-1}\sum_{m=0}^{N-1}\exp\{-i2\pi[(nd+\xi_{nm})\nu \\ &\quad +(md+\eta_{nm})\mu]\}. \end{aligned} \quad (2)$$

Here, $G(\nu, \mu)$ is the Fourier transform of the amplitude $g(x, y)$ of a single dot. Calculating the PSD $I(\nu, \mu)$,

$$\begin{aligned} I(\nu,\mu) &= |U(\nu,\mu)|^2 = |G(\nu,\mu)|^2 \\ &\quad \times \sum_{n}\sum_{n'}\sum_{m}\sum_{m'}\exp\{-i2\pi[(n-n')\nu d \\ &\quad +(m-m')\mu d]\} \\ &\quad \times\exp\{-i2\pi[(\xi_{nm}-\xi_{n'm'})\nu \\ &\quad +(\eta_{nm}-\eta_{n'm'})\mu]\}. \end{aligned} \quad (3)$$

An ensemble average of the PSD distribution is given by

$$\begin{aligned} \langle I(\nu,\mu)\rangle &= |G(\nu,\mu)|^2 \\ &\quad \times \sum_{n}\sum_{n'}\sum_{m}\sum_{m'}\exp\{-i2\pi[(n-n')\nu d \\ &\quad +(m-m')\mu d]\}\langle\exp\{-i2\pi[(\xi_{nm}-\xi_{n'm'})\nu \\ &\quad +(\eta_{nm}-\eta_{n'm'})\mu]\}\rangle, \end{aligned} \quad (4)$$

where $\langle..\rangle$ stands for the ensemble average and is operated over the random variables ξ and η.

We assume that the random displacements ξ and η are independent of each other and are stationary Gaussian random variables with mean value being zero. Further utilizing the property that the linear combination of Gaussian random variables is again a Gaussian random variable [31], the term $\langle..\rangle$ in Eq. (4) can be written as

$$\begin{aligned} &\langle\exp\{-i2\pi[(\xi_{nm}-\xi_{n'm'})\nu+(\eta_{nm}-\eta_{n'm'})\mu]\}\rangle \\ &\quad = \exp[-4\pi^2\sigma^2(\nu^2+\mu^2)(1-\delta_{nn'}\delta_{mm'})]. \end{aligned} \quad (5)$$

Here, σ^2 corresponds to the variance of the random displacements. $\delta_{nn'}$ and $\delta_{mm'}$ are the Kronecker deltas which take a value of unity for $n = n'$ and $m = m'$ and become zero otherwise.

Substituting Eq. (5), Eq. (4) becomes

$$\begin{aligned} \langle I(\nu,\mu)\rangle &= |G(\nu,\mu)|^2 \\ &\quad \times \sum_{n}\sum_{n'}\sum_{m}\sum_{m'}\exp\{-i2\pi[(n-n')\nu d \\ &\quad +(m-m')\mu d]\} \\ &\quad \times\exp[-4\pi^2\sigma^2(\nu^2+\mu^2) \\ &\quad \times(1-\delta_{nn'}\delta_{mm'})]. \end{aligned} \quad (6)$$

The multiple sum in Eq. (6) can be decomposed into

$$\begin{aligned} &\sum_{n}\sum_{n'}\sum_{m}\sum_{m'}[\ldots] \\ &= \Bigg(\sum_{\substack{n\\ n=n'}}\sum_{\substack{m\\ m=m'}} + \sum_{\substack{n\\ n=n'}}\sum_{m}\sum_{\substack{m'\\ m\neq m'}} \\ &\quad + \sum_{\substack{n\\ n\neq n'}}\sum_{n'}\sum_{\substack{m\\ m=m'}} + \sum_{n}\sum_{\substack{n'\\ n\neq n'}}\sum_{m}\sum_{\substack{m'\\ m\neq m'}}\Bigg) \end{aligned} \quad (7)$$

and taking into account the property of Kronecker delta, the ensemble averaged PSD can be evaluated as (see Appendix),

$$\langle I(\nu,\mu)\rangle = N^2|G(\nu,\mu)|^2\{1+\exp[-4\pi^2\sigma^2(\nu^2+\mu^2)] + [S^2(\nu,d)S^2(\mu,d)/N^2] \times\exp[-4\pi^2\sigma^2(\nu^2+\mu^2)]\}. \quad (8)$$

Here,

$$S^2(\nu,d) = [\sin^2(N\pi\nu d)/\sin^2(\pi\nu d)]. \quad (9)$$

Eq. (8) expresses the PSD distribution due to a random distribution of dots. It is given by the PSD $|G(\nu,\mu)|^2$ of a single dot and the line spectral components given by Eq. (9) which result from the regular arrangement of dots of mean spacing d. The exponential terms in Eq. (8) are the effect of random arrangement of the dots. When the variance of the fluctuation in the position of the dots becomes very large, i.e., when $\sigma^2 \to \infty$, Eq. (8) reduces to

$$\langle I(\nu,\mu)\rangle \approx N^2|G(\nu,\mu)|^2. \quad (10)$$

This implies that under very large fluctuations, the averaged PSD reduces to that due to a single dot. For a circular dot of diameter ρ, the amplitude variation due to a single dot can be expressed as

$$g(r) = \begin{cases} 1 & |r| \le \rho/2 \\ 0 & \text{otherwise} \end{cases} \quad (11)$$

where $r = \sqrt{x^2+y^2}$ and the APSD is the well known Airy pattern and is expressed in terms of a Bessel function of first order by

$$|G(\alpha)|^2 = [2J_1(2\pi\alpha\rho)/(2\pi\alpha\rho)]^2 \quad (12)$$

with

$$\alpha = \sqrt{\nu^2+\mu^2} \quad (13)$$

and the first zero occurs at the frequency

$$\alpha_0 = 1.22/\rho. \quad (14)$$

In addition to this theoretical analysis, we simulated a two-dimensional random dot array based on Eq. (1) using a computer and calculated its PSD by using the FFT algorithm. Fig. 4(a) shows the amplitude profile of the two-dimensional random distribution. Its PSD is shown in Fig. 4(b). The simulation has been done in a Helwett-Packard unix work station by starting from a regular dot array of 32×32 dots with the dot size (ρ) being 9/512 and the spacing (d) being 16/512 (total pixel size: 512×512). The variance of the fluctuations (σ^2) in the spacing was around $2d$. Due to the presence of random spatial fluctuations, as expected, only the Airy pattern due to a single dot is seen. Fig. 4(c) shows the APSD with the first minimum occurring at the value of 67 which is almost the same as that obtained from Eq. (14).

3.3. Comparison between experimental and theoretical results

Comparing the result of APSD from simulation in Fig. 4(c) with the experimental plot APSD in Fig. 3, the following facts could be drawn: First, in the low frequency region, i.e, for the frequencies below $f_1 = 5 \times 10^6$ m^{-1} of the experimental APSD and $f_1 = 20$ pixel^{-1} of the APSD from simulation, the APSDs vary in a monotonic fashion with the slope of the variation difference. The slope in Fig. 4(c) is determined by the random arrangement of dots given by the exponential terms of Eq. (8). However, for the case of experimental APSD in Fig. 3, the exponential terms arising from the random arrangement of gold particles and also the presence of clusters of gold particles of various sizes determine the slope (corresponding to the region A in Fig. 1(a) and darker regions like the ones indicated by arrows in Fig. 1(b)); Second, in the spatial frequency region beyond $f_1 = 5.0 \times 10^6$ of the experimental APSD and $f_1 = 20$ pixel^{-1} of the APSD from simulation, the APSD is largely determined by the PSD due to a single gold particle or a single circular dot as given by Eq. (12). In our following discussion, we consider only the spectrum beyond the frequency $f_1 = 5.0 \times 10^6$ m^{-1} determining the effect of a single particle.

From the APSD in the frequency range beyond f_1, the frequency f_0 at which the APSD becomes minimum is approximately around 5.6×10^7 m^{-1}. Substituting this value of frequency into Eq. (14), the diameter of a single gold particle could be estimated to be 22 nm. This estimated value is very close to the size of 20 (± 0.5) nm of a single gold particle. To our knowledge, such a direct and exact correspondence between the nominal size of the particle and

the estimated value from the power spectral analysis is reported for the first time.

Furthermore, based on the power spectral analysis, the transfer function of the SNOM system could be roughly estimated by considering the image as a convolution of the system function with a function describing the sample properties [32]. Its modulus transfer function (MTF) is given by

$$|H(\nu,\mu)| = \frac{I_{\exp}(\nu,\mu)}{\langle I(\nu,\mu)\rangle}. \quad (15)$$

Here, $I_{\exp}(\nu, \mu)$ is the experimental power spectrum given by Fig. 3 and $\langle I(\nu, \mu)\rangle$ is the theoretical power spectrum describing the sample properties given by Eqs. (8) and (12).

Here, it should be pointed out that for an accurate estimation of the transfer function, this ratio has to be calculated from Eqs. (8) and (12) and the experimental data obtained by averaging over many scans. In Fig. 1 showing a typical scanned image data of gold particles, a large number of particles could be seen. Therefore, for this case, spatially averaging the image can be considered to be equivalent to the average of many scans. In the present case, we could obtain many images of the gold particles similar to Fig. 1 by repeating the scanning at different areas of

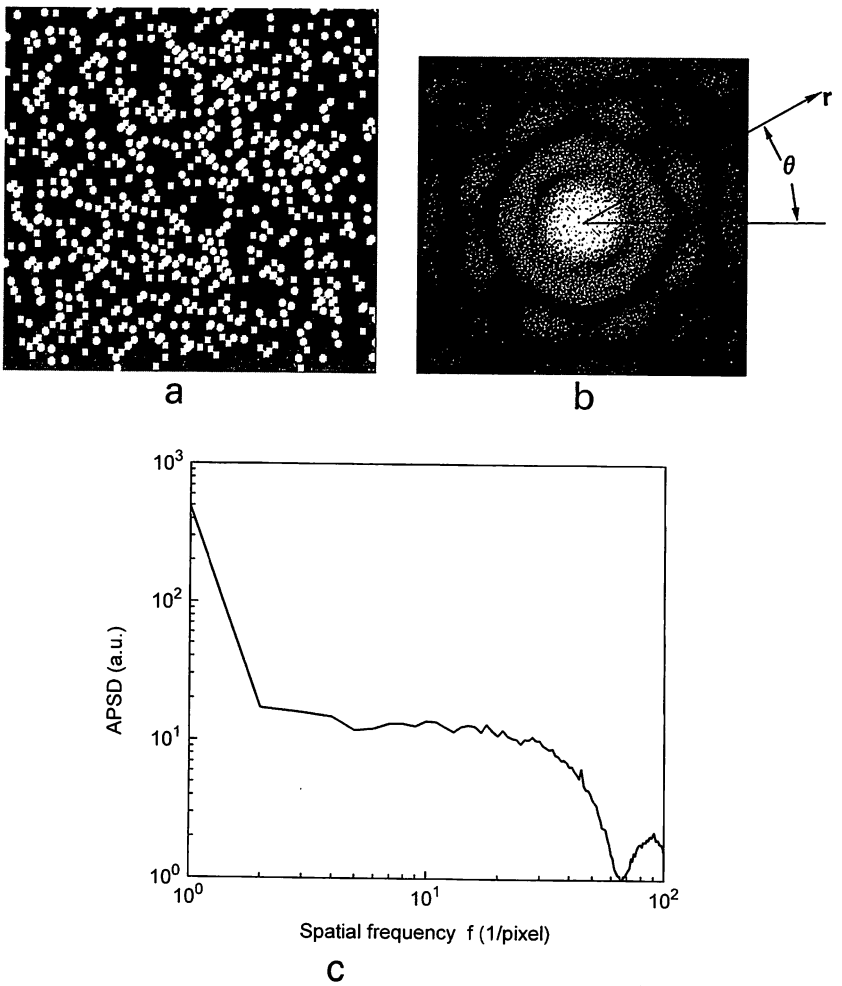

Fig. 4. (a) Two-dimensional distribution of randomly distributed circular dots simulated by computer, (b) its two-dimensional power spectral density, and (c) its APSD obtained by averaging (b) with respect to θ. Simulation parameters were $\rho = 9/512$, $d = 16/512$ and $\sigma^2 = 2d$.

the sample plate. Calculating the APSD of those images, we obtained curves similar to Fig. 3 with the minimum frequency occurring at the frequency f_0. The only difference was in the region $f < f_1$ due to the difference in the distribution of the particles and size of clusters of gold particles. Therefore, we have used the APSD given by Fig. 3 which was obtained by averaging the two-dimensional PSD of Fig. 1(a) over the angular direction θ of the polar coordinates (considering the region beyond f_1). For the theoretical power spectrum, Eq. (12) has been used.

The MTF has been estimated with the experimental APSD given in Fig. 3 and the theoretical APSD given by Eq. (12) with $\rho = 20$ nm. Here, Eq. (12) has been used for comparison instead of the APSD of Fig. 4(c) obtained from simulation. This is because the simulation is only approximate due to the resolution limitation in creating a circular dot pattern (limit of available computer memory) and does not converge to an exact Bessel function. Further, simulation has been done for verifying theoretical results. The estimated MTF has almost a linear variation in a log–log scale for the range $f \geq f_1$ and hence it can be expressed as

$$H(f/f_0) = 0.81(f/f_0)^{-0.16}, \qquad (16)$$

where H is normalized to unity at $f = f_1$. From this equation, the -3 dB cutoff frequency, giving a measure of resolution, could be determined to be 1.2×10^9 m^{-1} which corresponds approximately to a size of 0.8 nm. Though, the extrapolated value for the cutoff frequency of 1.2×10^9 m^{-1} is larger than the inverse of the pixel size, it gives an estimate of the resolution capability of the system. The finite size of the pixel introduces a low pass filtering effect. In our case, while determining the -3 dB cutoff frequency by extrapolating the estimated transfer function, we have used the spectral region where the effect due to pixel is negligible. Further, we would like to point out that this value of 1.2×10^9 is much higher than the cutoff frequency determined by the size of the aperture ($\approx 3.3 \times 10^7$ m^{-1}). Here, we should reminde again that the sample–probe separation during the scan of the image shown in Fig. 1 was much smaller than 5 nm, i.e., obtained under low shear force feedback gain. Further, repeating the scan over the same area where the image in Fig. 1 was obtained, only scratches could be found without any trace of gold particles. Due to the above facts, the resolution estimated based on power spectral analysis is solely due to the optical signal and not due to any shear force induced artifacts.

Such a high resolving ability of our SNOM system could be attributed to the boundary effect which has been observed earlier by us [8,33] and others [34]. This is related to the size dependent intensity distribution of the evanescent field on a subwavelength particle. Such a distribution has been proposed based on a phenomenological approach by Hori et al. [35]. Recently, based on Mie scattering approach, Jhe et al. [36] have reported a size dependent intensity distribution from an isolated sphere under the excitation of an evanescent field. Actually, such a phenomenon has been experimentally confirmed through power spectral analysis of near field images by Naya et al. [7] and near-field fluorescence observation from a dye-doped sphere by Saiki et al. [37]. Extending the same concept to our imaging of gold particles by the illumination mode SNOM, very high frequency evanescent fields would be generated at the metal–glass boundary present at the edges of the apex of the apertured probe. We believe this evanescent field was detected by being converted into propagation fields by the sample.

4. Summary

Colloidal gold particles of size 20 nm (± 0.5 nm) have been imaged with the illumination mode SNOM and the power spectral analysis has been carried out. The averaged power spectral density shows a minimum at the spatial frequency of 5.6×10^7 m^{-1} corresponding to an estimated particle size of 22 nm. To our knowledge, this is the first time, such a demonstration of direct and almost exact correspondence regarding the extension or size of a feature in the near-filed image has been presented. The resolution estimated using -3 dB cutoff value obtained from the estimated transfer function was 0.8 nm which is much higher than that determined by aperture diameter of the probe. Such a high resolving ability of the SNOM is attributed to the presence of high frequency evanescent fields confined around the

edges of the glass–metal boundary at the apex of the apertured fiber probe.

Acknowledgements

We would like to thank Dr. H. Tatsumi and Dr. Y. Katayama of Tokyo Medical and Dental University for providing us with the sample of gold particles. We would also like to thank Dr. M. Sano of Tokyo Institute of Technology for his critical reading of the manuscript and valuable suggestions on the power spectral analysis.

Appendix. Evaluation of Eq. (8)

Evaluating each term on the right hand side of the multiple sum of Eq. (7), the result becomes

$$\text{term } 1 = N^2, \tag{A1}$$

$$\text{term } 2 = N\left[\left|\sum_{m=0}^{N-1}\exp(-\mathrm{i}2\pi m\mu d)\right|^2 - N\right] = N\left\{\left[\sin^2(N\pi\mu d)/\sin^2(\pi\mu d)\right] - N\right\}, \tag{A2}$$

$$\text{term } 3 = N\left[\left|\sum_{n=0}^{N-1}\exp(-\mathrm{i}2\pi n\nu d)\right|^2 - N\right] = N\left\{\left[\sin^2(N\pi\nu d)/\sin^2(\pi\nu d)\right] - N\right\}, \tag{A3}$$

$$\text{term } 4 = \left[\left|\sum_{n=0}^{N-1}\exp(-\mathrm{i}2\pi n\nu d)\right|^2 - N\right] \times \left[\left|\sum_{m=0}^{N-1}\exp(-\mathrm{i}2\pi m\mu d)\right|^2 - N\right] = \left\{\left[\sin^2(N\pi\nu d)/\sin^2(\pi\nu d)\right] - N\right\} \times \left\{\left[\sin^2(N\pi\mu d)/\sin^2(\pi\mu d)\right] - N\right\}. \tag{A4}$$

Now, adding terms (A1) to (A4), the total sum in Eq. (6) reduces to Eq. (8).

References

[1] D.W. Pohl and D. Courjon, eds., Near-field optics, NATO ASI series E, Vol. 242 (Kluwer, Dordrecht, The Netherlands, 1993).
[2] M. Ohtsu, J. Lightwave Tech. 13 (1995) 1200.
[3] E. Betzig and J.K. Trautman, Science 257 (1992) 189.
[4] X.S. Xie and R.C. Dunn, Science 265 (1994) 361.
[5] W.P. Ambrose, P.M. Goodwin, J.C. Martin and R.A. Keller, Science 265 (1994) 364.
[6] E. Betzig and J.K. Trautman, Science 297 (1992) 189.
[7] M. Naya, S. Mononobe, R. Uma Maheswari, T. Saiki and M. Ohtsu, Optics Comm. 124 (1996) 9.
[8] R. Uma Maheswari, H. Tatsumi, Y. Katayama and M. Ohtsu, Optics Comm. 120 (1995) 325.
[9] T. Saiki, S. Mononobe, M. Ohtsu, N. Saito and J. Kusano, Appl. Phys. Lett. 67 (1995) 2191.
[10] N. Toda, M. Kourogi, Y. Nagamune, Y. Arakawa and M. Ohtsu, in: Conf. on Lasers and Electro-optics/Pacific Rim '95, Tech. Dig. p. 165.
[11] R.D. Grober, T.D. Harris, J.K. Trautman, E. Betzig, W. Wegscheider, L. Pfeiffer and K. West, Appl. Phys. Lett. 64 (1994) 1421.
[12] E. Betzig, J.K. Trautman, R. Wolfe, E.M. Gyorgy, P.L. Fynn, M.H. Kryder and C.H. Chang, Appl. Phys. Lett. 61 (1992) 142.
[13] S. Jiang, J. Ichihashi, H. Monobe, M. Fujihira and M. Ohtsu, Optics Comm. 106 (1994) 173.
[14] T.L. Ferrell, J.P. Goundonnet, R.C. Reddick, S.L. Sharp and R.J. Warmack, J. Vac. Sci. Technol. B 9 (1991) 525.
[15] D. Courjon, K. Sarayeddine and M. Spajer, Optics Comm. (1989) 23.
[16] E. Betzig, A. Lewis, A. Harootunian, M. Issacson and E. Kratschmer, Biophys. J. (1986) 269.
[17] D.W. Pohl, U.Ch. Fischer and U.T. Durig, Scanning Microscopy Technologies and Application, SPIE Vol. 897 (1988) 84.
[18] S. Jiang, N. Tomita, H. Ohsawa and M. Ohtsu, Jpn. J. Appl. Phys. 30 (1991) 2107.
[19] S. Jiang, H. Ohsawa, K. Yamada, T. Pangaribuan, M. Ohtsu, K. Imai and K. Ikai, Jpn. J. Appl. Phys. 31 (1992) 241.
[20] C. Pieralli, Optics Comm. 108 (1994) 203.
[21] M. Born and E. Wolf, Principles of Optics (Pergamon Press, Oxford, 1980).
[22] T. Pangaribuan and M. Ohtsu, Electron. Lett. 29 (1993) 1978.
[23] T. Pangaribuan, S. Jiang and M. Ohtsu, Scanning 16 (1994) 362.
[24] R. Uma Maheswari, S. Mononobe and M. Ohtsu, IEEE J. Lightwave Technol. 13, No. 12 (1995).
[25] E. Betzig, P.L. Finn and J.S. Weiner, Appl. Phys. Lett. 60 (1992) 2484.
[26] M. Vaez-Iravani, R. Toledo-Crow and Y. Chen, J. Vac. Sci. Technol. A 11 (1993) 742.
[27] R. Uma Maheswari, N. Takai and T. Asakura, J. Opt. Soc. Am. A 9 (1992) 1391.

[28] K. Jang and W. Jhe, Optics Lett. 21 (1996) 236.
[29] B. Labani, C. Girard, D. Courjon and D. Van Labeke, J. Opt. Soc. Am. B 7 (1990) 936.
[30] O. Keller, M. Xiao and S. Bozhvolnyi, Surface Science 280 (1992) 217.
[31] J.W. Goodman, Statistical Optics (Wiley, New York, 1985).
[32] J.W. Goodman, Fourier Optics (McGraw-Hill, New York, 1968).
[33] R. Uma Maheswari, H. Tatsumi, Y. Katayama and M. Ohtsu, in: Conf. on Lasers and Electro-optics/Pacific Rim '95, Tech. Dig. p. 125.
[34] M. Specht, J.D. Pedaring, W.M. Heckl and T.W. Hansch, Phys. Rev. Lett. 68 (1992) 476.
[35] H. Hori, in Near-field optics, NATO ASI series E, Vol. 242, eds. D.W. Pohl and D. Courjon (Kluwer, Dordrecht, The Netherlands, 1993) p. 105.
[36] W. Jhe, in: Conf. on Lasers and Electro-optics/Pacific Rim'95, Tech. Dig. p. 145.
[37] T. Saiki, M. Ohtsu, K. Jhang and W. Jhe, Optics Lett. 21, No. 9, May 1996.

Fabrication of a Fiber Probe with a Nanometric Protrusion for Near-Field Optical Microscopy by a Novel Technique of Three-Dimensional Nanophotolithography

Takuya Matsumoto and Motoichi Ohtsu, *Senior Member, IEEE*

Abstract—**A new technique based on photolithography has been developed to fabricate a fiber probe with a nanometric protruding tip for near field optical microscopy. As a first step, an optical fiber is sharpened by chemical etching and coated with metallic film. Next, it is coated with photoresist and its apex region is selectively exposed to an evanescent wave. Finally, the metallic film at the apex region is etched away. The foot diameter of the protrusion fabricated by this method is about 30 nm.**

I. Introduction

A NEAR-FIELD optical microscope (NOM) is a scanning probe optical microscope which has subwavelength resolution [1], [2]. The following two operation modes are widely used: 1) a nanometric sample is illuminated by light under total internal reflection condition to generate an evanescent field over the sample surface, and this field is scattered and collected by a probe (a sharpened fiber with a nanometric diameter apex). The detected intensity of the scattered light is displayed as a function of the position of the probe [3]–[5]; 2) a light is introduced into the probe to generate an evanescent field at the apex. This field illuminates the sample and the scattered light is deteced and displayed as a function of the position of the probe [6], [7]. In this paper, we call the former as collection mode NOM[1] and the latter as illumination mode NOM.

In particular, when employing the collection mode, the following factors should be taken into account to achieve high resolution [5], [8], [9]: The diameter of the apex should be small, and the probe should be kept as close to the sample surface as possible. One of the most promising methods of sharpening an optical fiber is a two step chemical etching method developed by Pangaribuan *et al.* [10], [11]. By this method, the diameter of the apex can be made as small as 3 nm with high reproducibility, with controlling the cladding diameter. Super high resolution NOM can be realized by using this probe fabrication method.

Manuscript received August 30, 1995; revised June 14, 1996.

The authors are with the Interdisciplinary Graduate School of Science and Engineering, Tokyo Institute of Technology, 4259 Nagatsuta, Midori-ku, Yokohama 226, Japan.

M. Ohtsu is also with the Kanagawa Academy of Science and Technology, KSP East 408, 3-2-1 Sakado, Takatsu-ku, Kawasaki, 213, Japan.

Publisher Item Identifier S 0733-8724(96)07658-X.

[1]There are a number of names used for near field optical microscope depending on the place of origin and mode of operation [1].

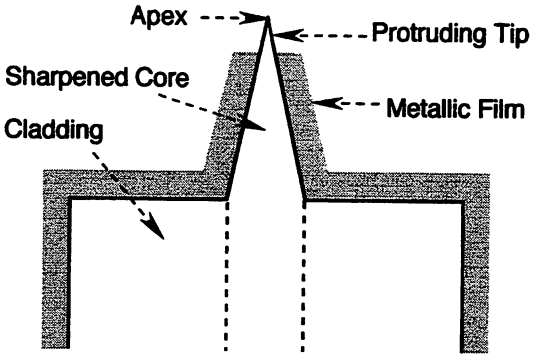

Fig. 1. Schematic illustration of a probe with a nanometric protruding tip.

However, the problem is that light with low spatial frequency components due to roughness of the sample (or the substrate on which the sample is located) is scattered and collected by the probe as a background noise. In order to suppress detecting such low spatial frequency components, it is necessary to coat the sharpened fiber with a metallic film leaving a nanometric protruding tip as shown in Fig. 1. This kind of probe is fabricated by coating the sharpened fiber with metal and then selectively removing the metallic film only from the apex region. Such a probe, to our best knowledge, has not been realized by other groups until now because of the technical difficulties of removing metallic film selectively from the apex.

In this paper, we report a method for realizing the probes with the nanometric protruding tip. This method is based on photolithography, which is popularly used for fabricating fine structures in semiconductor devices. In conventional photolithography, the minimum size of the fabricated structure is limited by the diffraction limit of light. However, in our method, nanometric fabrication beyond the diffraction limit is realized by using evanescent field for the exposure. In Section II, we describe the principle and the experimental method; Section III presents the experimental result, and finally, Section IV gives a summary.

II. Experimental

The fabrication process consists of the following six steps, as shown in Fig. 2.

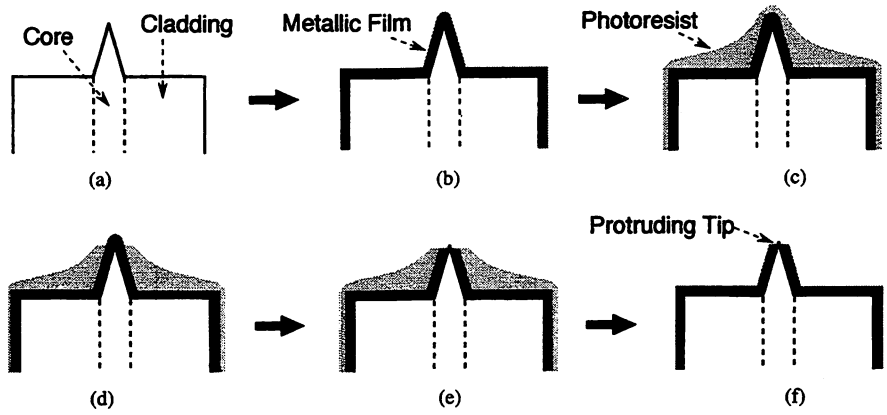

Fig. 2. Schematic illustration of the fabrication process of the probe with the nanometric protruding tip by three-dimensional (3-D) nanophotolithography: (a) sharpening an optical fiber, (b) coating metallic film, (c) coating photoresist, (d) exposing the apex region and development, (e) etching the metallic film, and (f) removal of photoresist.

a) sharpening an optical fiber by a chemical etching method;
b) coating the sharpened fiber with a metallic film;
c) coating the fiber with photoresist;
d) exposure of the apex region of the fiber and development;
e) etching the metallic film at the apex region, by which the apex of the sharpened fiber protrudes out from the metallic film;
f) removal of the photoresist.

The novelty of this process lies in the method of the exposure. In order to expose the nanometric area at the apex region selectively, evanescent waves generated over a prism surface are employed. That is, the fiber coated with photoresist is set above the prism surface as shown in Fig. 3 and laser light is incident into the prism at a total reflection angle to generate the evanescent wave over the prism surface. By the intrinsic feature of exponential decrease of evanescent wave intensity as a function of fiber-prism separation, the area at the apex region is selectively exposed and, thus, exposing a small area beyond the diffraction limit is realized.

The process of each step is as follows.

A. Etching an Optical Fiber

The core of an optical fiber is sharpened by a two-step etching method whereby an optical fiber (single mode fiber with 27 mol% GeO_2 doped SiO_2 core with a diameter of 2 μm and pure SiO_2 cladding with a diameter of 125 μm) is etched in an etching solution containing NH_4F (40% weight), HF (50% weight) and H_2O with the respective volume ratio of 1.7:1:1 for 60~ 80 min. In this process, the cladding diameter is controlled by controlling the etching time. In the present experiment, this control capability is important for the process of coating photoresist as will be described later. Second, the fiber is etched in an etching solution containing NH_4F, HF and H_2O with the respective volume ratio of 10:1:1 for 90 min to sharpen the core. We show SEM micrographs of the fibers etched by this method in Fig. 4. In this etching, the etching time of the first step is 73 min. (The temperature of the etching solution is 25.0 °C). As shown in Fig. 4(a), the cladding diameter is reduced from 125 μm to 23 μm, and as shown in Fig. 4(b), the apex diameter of the sharpened core is 3 nm.

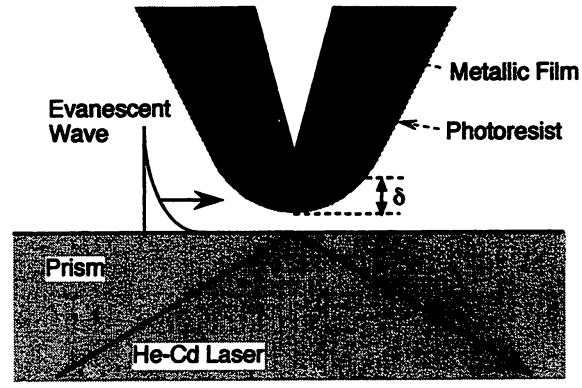

Fig. 3. Schematic explanation of the exposure method using the evanescent wave over a prism surface.

B. Coating Metallic Film

The sharpened fiber is coated with metal by using a filament type vacuum evaporation unit. In the present experiment, gold is employed as the coating material because it does not get easily oxidized (oxidation reduces the opacity of the metallic film), and the metallic film with small grain size is easily realized by the vacuum evaporation. The thickness of the gold film is about 100 nm.

C. Coating Photoresist

The metal coated fiber is coated with positive photoresist. In our experiment, Tokyo Okakogyo TSMR-V50 (Its viscosity is 60 mPa·s) is used as the photoresist because its dissolution speed of the unexposed part is sufficiently small (less than 10 nm/min.).

Furthermore, in order to realize high reproducibility of the exposure, the thickness of photoresist at the apex region (δ in Fig. 3) is maintained constant by coating the photoresist using a micro syringe as shown in Fig. 5. The coating method is as follows: 1) A droplet of photoresist is formed at the apex

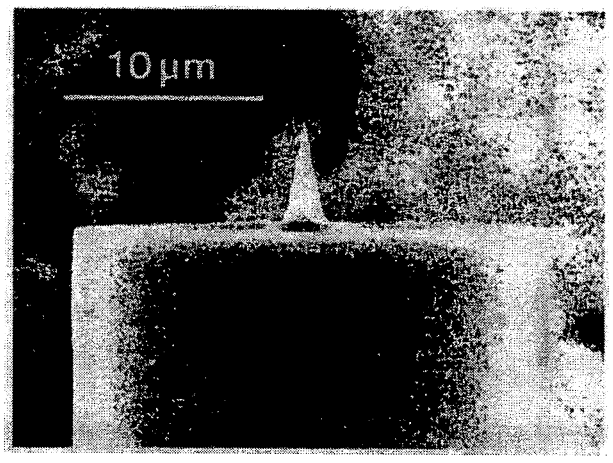

(a)

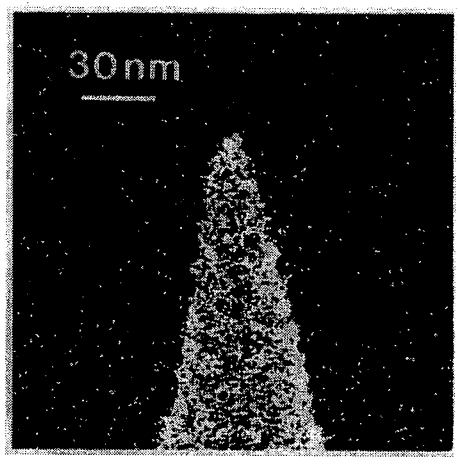

(b)

Fig. 4. SEM micrographs of a fiber etched by the two-step etching method for magnifications of (a) 3 K and (b) 350 K. In this micrographs, the fiber is coated with a gold film of 3 nm thickness for the observation in the SEM.

of the needle of the syringe; 2) The droplet is touched to the apex of the fiber; 3) The droplet is pulled up from the fiber. In this method, the thickness of the coated photoresist becomes thicker with increasing the cladding diameter as shown in Fig. 6. Here, the thickness of the photoresist at the apex region is 70 nm and 20 nm for the cladding diameter of 23 μm [Fig. 6(b)] and 18 μm [Fig. 6(c)], respectively, and this can be realized reproducibly as long as the viscosity of photoresist and the thickness of gold film are constant. In the case of 40 μm [Fig. 6(a)], although it is not straightforward to measure the thickness precisely, it is roughly estimated to be bigger than 70 nm by comparison with Fig. 6(b) and (c). In the present experiment, the cladding diameters are empirically adjusted to be 23 μm. This is because when the thickness of the photoresist is higher, the penetration depth of the evanescent wave is not enough for the apex of the metallic film to protrude out of the photoresist. On the other hand, when the photoresist film is too thin, photoresist around the exposed area gets easily peeled off in the process of etching the metallic film. Here, the two-step etching method is used to adjust the cladding diameter to the optimum value. In other words, the two-step etching method is

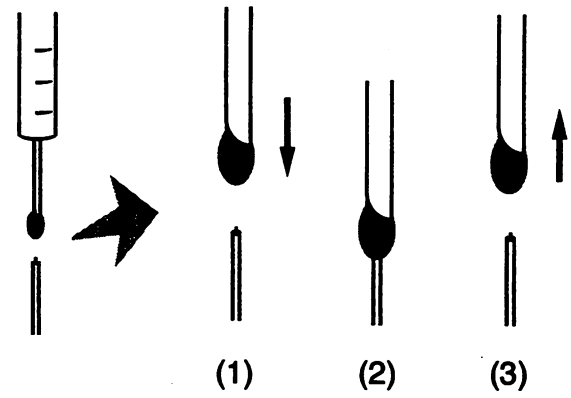

Fig. 5. Schematic explanation of coating photoresist.

indispensable to the present photolithography. The temperature and time of the prebaking are 80 °C and 20 min, respectively.

D. Exposure

The experimental apparatus for the exposure is shown in Fig. 7. Here, the fiber is exposed to the evanescent wave generated over the prism surface into which light from a He-Cd laser (wavelength =442 nm) is incident at the total reflection angle. The exposure time is controlled by using a shutter.

Precise control of the fiber-prism separation is necessary for attaining high reproducibility in the size of the exposed region. This is carried out by using shear force (lateral atomic force) between the prism and the apex of the fiber [12], [13]. Namely, the fiber is approached to the prism surface while dithering it laterally at its resonance frequency (probes fabricated by two-step etching method have sufficiently high resonance frequencies between 20 to 100 kHz). When the separation is as small as about 10 nm, the dithering amplitude decreases rapidly due to the atomic force as shown in Fig. 8. By using this change, a servo-control loop can be prepared to maintain constant separation by illuminating the fiber with an auxiliary laser light beam of 690 nm wavelength, to which the photoresist is insensitive. A diffraction pattern is then generated behind the fiber (see Fig. 7). By detecting this diffracted light intensity with a slit and a photodetector, the dithering amplitude can be monitored, and using this detected signal, the separation is kept to be around 5 nm with a servo-controller with a proportional amplifier and an integrator.

After the exposure, the fiber is dipped into developer (Tokyo Okakogyo NMD-3) to remove the exposed photoresist and baked at a temperature of 120 °C for 30 min (postbaking).

E. Etching the Metallic Film

The fiber is dipped into an etching solution to remove the metallic film from the apex in order to form the protruding tip. In our experiment, a solution containing KI, I_2, and H_2O with the respective volume ratio of 20:1:21 000 is used as the etching solution.

F. Removing Photoresist

The fiber is dipped into a remover of photoresist, which is a conventional process to remove the photoresist.

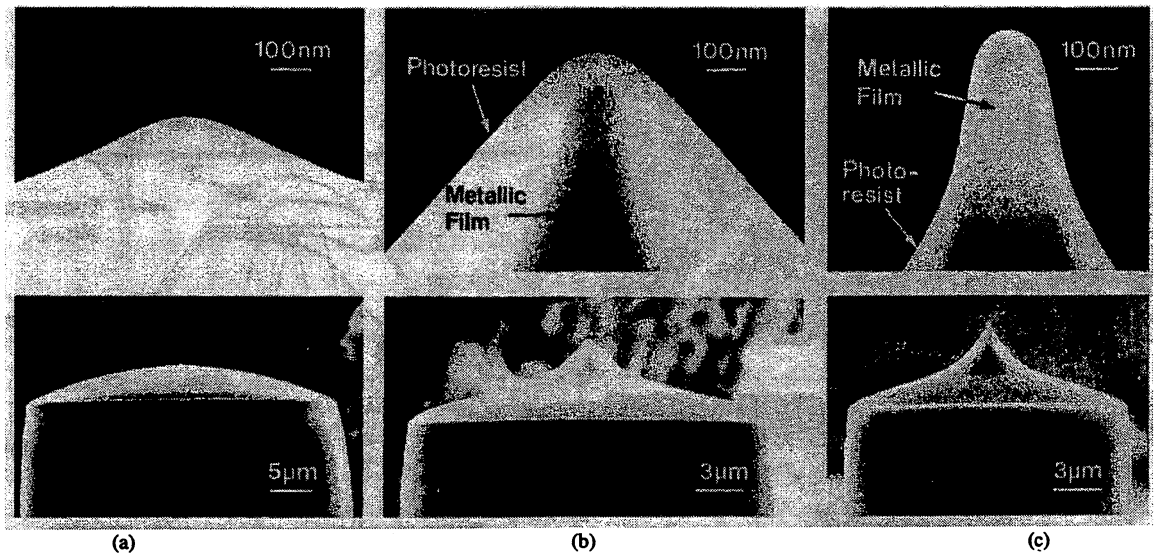

Fig. 6. SEM micrographs of fibers coated with photoresist for cladding diameters of (a) 40 μm, (b) 23 μm, and (c) 18 μm. Here, the viscosity of the cladding diameter is 60 mPa·s. Upper parts show the magnified pictures of the corresponding lower parts.

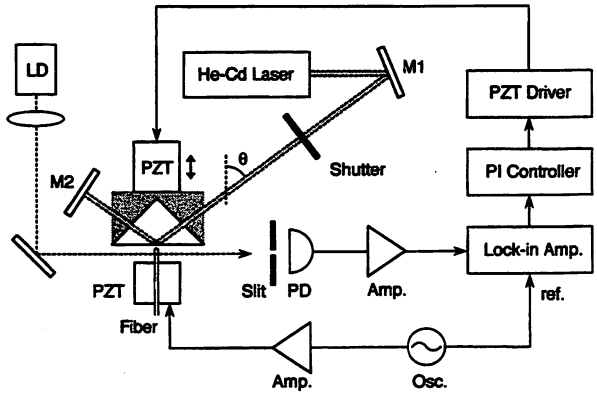

Fig. 7. Schematic explanation of the experimental apparatus used for the exposure.

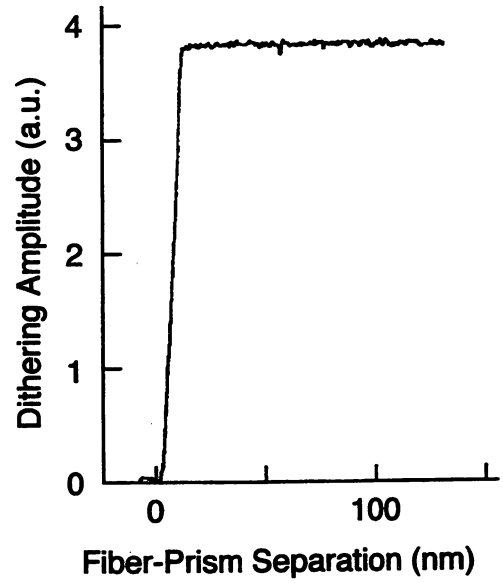

Fig. 8. Measured dithering amplitude of a fiber as a function of the fiber-prism separation.

III. Experimental Results and Discussions

Fig. 9 shows SEM micrographs of the apex regions of the fibers exposed with optical energies (the product of the exposure time and laser power) of (a) 0.08 mJ, (b) 0.12 mJ, (c) 0.16 mJ and (d) 0.33 mJ. Here, the fibers are exposed without using mirror $M2$ in Fig. 7, and the incident angle of the laser light is $\theta = 45°$. Fig. 10 gives a summary of the relation between the exposure energy and the profile of the exposed fiber shown in Fig. 9, which represents the intensity distribution of light inside the photoresist. Here, the curves a–d represent cross-sectional shapes of the exposed photoresist given by a–d in Fig. 9. As shown in this figure, the intensity distribution of light inside photoresist is not axially symmetrical. That is, the highest intensity area (i.e., strongly exposed area), is on the front side of the apex region with respect to the incident beam (indicated by X). It should be noted that there is another high intensity area which is on the rear side of the fiber with respect to the incident beam (indicated by Y). This high intensity area on the rear side is due to the scattering of the evanescent wave by the metallic film. To prove this, we show in Fig. 10 a SEM micrograph of the top view of the fiber exposed with the optical energy which corresponds to the condition identified by curve D in this figure. As shown in this micrograph, the width W of the strongly exposed area on the rear side is equal to that of the metallic film. Thus, the strongly exposed area on the rear side could be due to the metallic film which scatters the evanescent wave. In this SEM micrograph, an interference pattern can be seen at the front side of the fiber. This is due to the interference of the scattered evanescent wave in the photoresist because the interval of the fringe is equal to about 140 nm, which is half of the wavelength of the evanescent wave.

In Fig. 9, it is found that the optimum exposure corresponds to (b) because the profile of the exposed fiber is nearly axially symmetrical. However, the difference of the optical energy

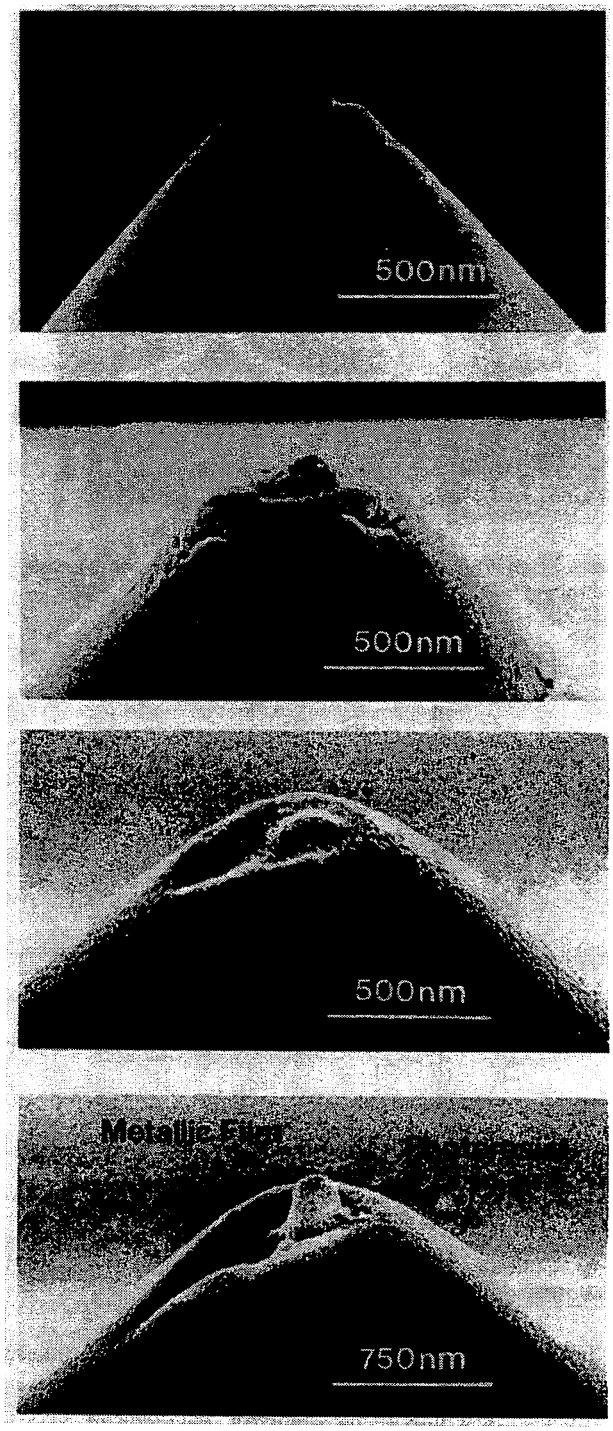

Fig. 9. SEM micrographs of the exposed fibers for exposure energies of (a) 0.08 mJ, (b) 0.12 mJ, (c) 0.16 mJ, (d) 0.33 mJ.

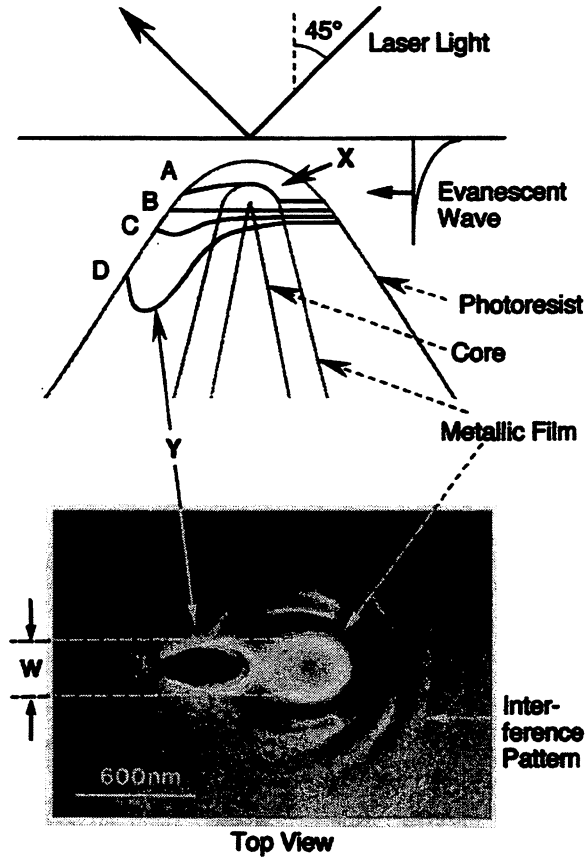

Fig. 10. Summary of the relation between the profile of the exposed fiber and the exposure power in Fig. 9(a) and (b). A SEM micrograph of the top view of the exposed fiber which corresponds to that of Fig. 9(c) and (d).

for exposure between (b) and (c) is so small that it is not straightforward to realize (b) with high reproducibility. In order to realize axially symmetric exposure, counter-propagating evanescent waves are used. That is, the laser light is introduced into the prism not only from one side but also from two sides to generate the counter-propagating evanescent waves by using mirror $M2$ in Fig. 7. When the optical energy for exposure is same as that of (a) in Fig. 9, axially symmetric exposure can be realized, as shown in Fig. 11. Here, the exposed depth D is 150 nm, which is sub-wavelength value. In this method, we expected that the counter-propagating evanescent waves interfere to produce a interference pattern over the prism surface. However, we did not see any such effects in our experiment, which may be due to the misalignment of the beams, i.e., slight difference of the incident angle between the beams from the laser and the mirror.

In Fig. 12, we show a SEM micrograph and its schematic explanation of the fiber after etching gold and removing photoresist. Here, the etching time of gold is 40 s. The foot diameter of the protrusion (d_f in Fig. 12) is about 30 nm. When the sample size is large (e.g., a few hundred nanometers), minor metal film irregularity may distort the optical image [14]. However, when the sample size is small (less than a few tens of nanometers), this irregularity will not distort the optical image since the high spatial frequency components of the optical near field over the sample are attenuated quickly in the vicinity of the apex of the protruding tip and do not reach the metallic film [5].

Although the foot diameter of the protrusion can be made as small as the apex diameter of the sharpened fiber in principle, the grain size of the metallic film limits the practical minimum size of the foot diameter of the protrusion. That is, the grain size of the metallic film formed by the vacuum evaporation is around 30 nm, which makes the minimum size of the foot diameter of the protrusion around 30 nm. However,

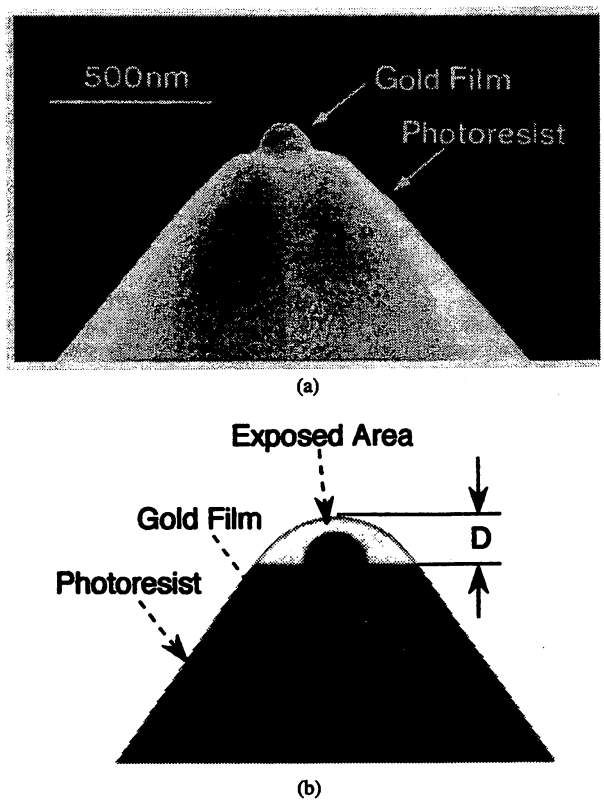

Fig. 11. (a) A SEM micrograph and (b) a schematic view of the fiber exposed by using the counter-propagating evanescent wave.

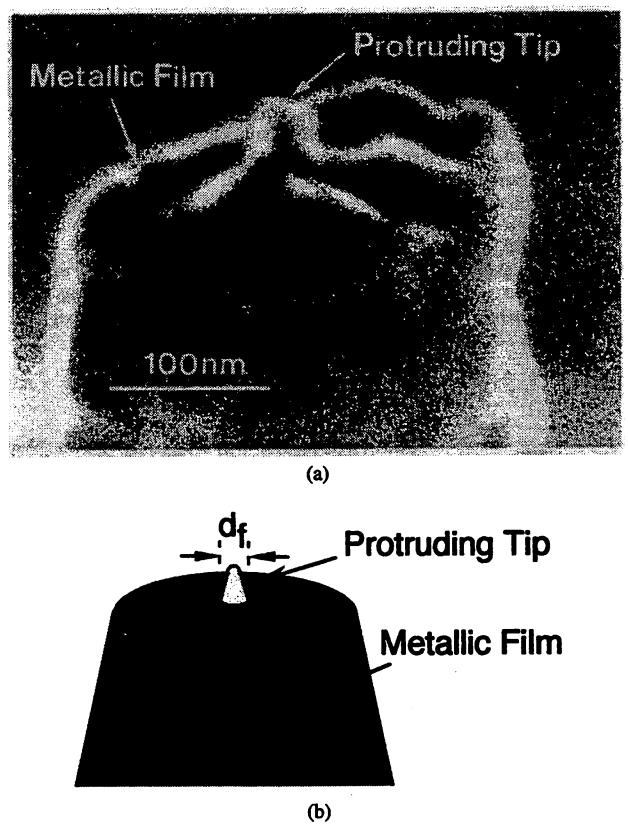

Fig. 12. (a) A SEM micrograph and (b) a schematic view of the probe with the nanometric protruding tip. Foot diameter of the protrusion (d_f) is about 30 nm.

by reducing the grain size, e.g., by using electron beam evaporation unit, a still smaller value for the foot diameter of the protrusion is expected.

Three probes having the protrusions with the foot diameter of about 30 nm could be fabricated from 10 fibers, i.e., the reproducibility of this fabrication process was about 30%, which was mainly caused by the reproducibility of coating the metallic film with proper thickness and small grain size. Higher reproducibility can be expected by improving the method of coating the metallic film.

IV. Summary

We proposed a technique based on photolithography in order to fabricate a probe with a nanometric protruding tip. An evanescent wave generated over a prism surface is employed to expose selectively a sub-wavelength area at the apex region of the fiber, and the probe having a protruding tip with a foot diameter of about 30 nm can be fabricated.

Finally, it could be claimed that the present photolithography, which realizes 3-D and nanometric fabrication, can be applied not only for the fabrication of the fiber probes with nanometric protrusions but also for fabrication of a wide variety of nanometric structures.

Acknowledgment

The authors would like to thank T. Sakaguchi (Tokyo Institute of Technology) for technical advice on photolithography and T. Saiki, R. U. Maheswari, S. Mononobe, M. Naya, H. Fukuda, R. Micheletto, K. Kurihara, T. Saito, and H. Ito (Ohtsu Photon Control Project of Kanagawa Academy of Science and Technology) for helpful discussions.

References

[1] W. Pohl and D. Courjon, Eds., *Near-Field Optics*. Dordrecht, The Netherlands: Kluwer Academic, 1993.

[2] M. Ohtsu, "Progress of high resolution photon scanning tunneling microscopy due to a nanometric fiber probes," *IEEE J. Lightwave Technol.*, vol. 13, pp. 1200–1221, 1995.

[3] D. Courjon, J. Vigoureux, M. Spajer, K. Sarayeddine, and S. Leblanc, "External and internal reflection near field microscopy: Experiments and result," *Appl. Opt.*, vol. 29, pp. 3734–3740, 1990.

[4] S. Jiang, H. Ohasawa, K. Yamada, T. Panagaribuan, M. Ohtsu, K. Imai, and A. Ikai, "Nanometric scale biosample observation using a photon scanning tunneling microscope," *Japan J. Appl. Phys.*, vol. 31, pp. 2282–2287, 1992.

[5] M. Naya, S. Mononobe, R. Uma Maheswari, T. Saiki, and M. Ohtsu, "Imaging of biological samples by a collection-mode photon scanning tunneling microscope with an apertured probe," *Opt. Commun.*, vol. 124, pp. 9–15, 1996.

[6] E. Betzig and J. K. Trautman, "Near-field optics: Microscopy, spectroscopy, and surface modification beyond the diffraction limit," *Science*, vol. 257, pp. 189–195, 1992.

[7] R. U. Maheswari, H. Tatsumi, Y. Katayama, and M. Ohtsu, "Observation of subcellular nanostructure of single neurons with an illumination mode photon scanning tunneling microscope," *Opt. Commun.*, vol. 120, pp. 325–334, 1995.

[8] K. Jang and W. Jhe, "Nonglobal model for a near-field scanning optical microscope using diffraction of the optical near field," *Opt. Lett.*, vol. 21, pp. 236–238, 1996.

[9] B. Labani, C. Girard, D. Courjon, and D. Van Labeke, "Optical interaction between a dielectric tip and nanometric lattice: Implications for near-field microscopy," *J. Optic. Soc. Am. B.*, vol. 7, pp. 939–943, 1990.

[10] T. Pangaribuan, S. Jiang, and M. Ohtsu, "Two-step etching method for fabrication of fiber probe for photon scanning tunneling microscope," *Electron. Lett.*, vol. 29, pp. 1978–1979, 1993.
[11] ——, "Highly controllable fabrication of fiber probe for photon scanning tunneling microscope," *Scanning*, vol. 16, pp. 362–367, 1994.
[12] R. Toledo-Crow, P. C. Yang, Y. Chen, and M. Vaez-Iravani, "Near-field differential scanning optical microscope with atomic force regulation," *Appl. Phys. Lett.*, vol. 60, pp. 2957–2959, 1992.
[13] E. Betzig, P. L. Finn, and J. S. Weiner, "Combined shear force and near-field scanning optical microscopy," *Appl. Phys. Lett.*, vol. 60, pp. 2484–2486, 1992.
[14] G. A. Valaskovic, M. Holton, and G. H. Morrison, "Image contrast of dielectric specimens in transmission mode near-field scanning optical microscopy: Imaging properties and tip artifacts," *J. Microscopy*, vol. 179, pp. 29–54, 1995.

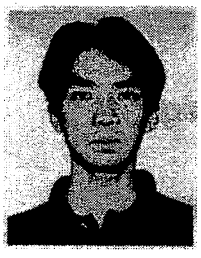

Takuya Matsumoto was born in Kanagawa, Japan, on February 17, 1970. He received the B.E. and M.E. degrees in electronics engineering in 1994 and 1996, respectively, from the Tokyo Institute of Technology, Tokyo, Japan, where he is presently in the graduate school program.

Mr. Matsumoto is a member of the Japan Society of Applied Physics.

Motoichi Ohtsu (M'88–SM'90) was born in Kanagawa, Japan, on October 5, 1950. He received the B.E., M.E., and D.E. degrees in electronics engineering from the Tokyo Institute of Technology, Tokyo, Japan in 1973, 1975, and 1978, respectively.

In 1978, he was appointed Research Associate and in 1982 became Associate Professor at the Tokyo Institute of Technology. From 1986 to 1987, while on leave from Tokyo Institute of Technology, he joined the Crawford Hill Laboratory, AT&T Bell Laboratories, Holdmel, NJ. In 1991, he became a Professor at the Tokyo Institute of Technology. Since April 1993, he has concurrently been the leader of the "PHOTON CONTROL" project of Kanagawa Academy of Science and Technology, Kawasaki, Japan. His main fields of interest are near-field optical microscopy and its applications to nano-scale photonics and quantum optics, and laser frequency control. He has written over 130 papers and received a number of patents. He is the author and coauthor of 13 books including two in English, *Highly Coherent Semiconductor Lasers* (Boston, MA: Artech House, 1992) and *Coherent Quantum Optics and Technology* (Dordrecht: Kluwer Academic, 1993). He has been a tutorial lecturer of the SPIE and OSA. He has been awarded eight prizes from academic institutions, including the Issac Koga Gold Medal of URSI in 1984, the Japan IBM Science Award in 1988, and two awards of the Japan Society of Applied Physics in 1982 and 1990.

Dr. Ohtsu is a member of the Institute of Electronics, Information and Communications Engineering of Japan, the Institute of Electrical Engineering of Japan, the Japan Society of Applied Physics, and the Optical Society of America.

Fabrication of a Pencil-Shaped Fiber Probe for Near-Field Optics by Selective Chemical Etching

Shuji Mononobe and Motoichi Ohtsu, *Senior Member, IEEE*

***Abstract*— We propose a novel method by chemical etching using hydrofluoric (HF) acid and a buffered HF solution (BHF) to fabricate a pencil-shaped fiber probe for near-field optics. We succeeded in producing such probes with high reproducibility using a dispersion-compensating fiber having the high GeO_2 doped core. The method involves tapering of the cladding, then sharpening of the core. The fabricated probe has a conical tip with a cone angle of 20° and an apex diameter of less than 10 nm.**

I. Introduction

NANOMETRIC probing technique of near-field optics [1], [2] has been applied to the observation of biological samples with nanometric resolution [3]–[5], spectroscopic study of semiconductor devices [6], [7], detection of fluorescent single molecules [8], and high density optical storage [9], [10]. In a near-field optical microscope (NOM) employing a probe tip, the apex size of the probe tip is one of the main factors deciding the resolution of the imaging.

To fabricate such tapered probes, there exist methods such as pulling of a fiber by a micropipette puller [11]. However, it is difficult to produce apex dimensions less than 50 nm by those methods. In this paper, we propose a novel method for fabrication of a tapered fiber having an apex diameter less than 10 nm with high reproducibility. From here on, the tapered fiber is called a pencil-shaped probe. In Section II, the method is described. Results and discussion are given in Section III. Section IV contains a summary.

II. Fabrication of a Pencil-Shaped Probe

The fabrication of the pencil-shaped probe is shown in Fig. 1. This method consists of four steps of tapering the cladding in step [A], hollowing the end of the taper in step [B], flattening the end of the taper in step [C], and sharpening the core in step [D]. In this figure, the notations HF acid and Oil/HF acid correspond to hydrofluoric (HF) acid and HF acid with a surface layer of oil, respectively. In our experiments, we use a buffered HF solution (BHF) with a volume ratio of ammonium fluoride solution [NH_4F sol.] (40 wt%): HF acid (50 wt%): water [H_2O] represented, respectively, as X:1:1. r_1 is the radius of the core, D_0 is the diameter of the fiber, α is the taper angle, δ_0 is the cladding thickness in the flat end generated by step [C], and θ_1 is the cone angle of the sharpened core. All steps are performed at 25 ± 0.2°C. Steps [B] and [D] are based on selective etching of a GeO_2 doped fiber. For the selective etching [12], refer to Appendix A. In step [A], meniscus etching [13] is used for tapering the fiber. In the following, we describe each step of the method:

Manuscript received September 18, 1995; revised June 3, 1996.

The authors are with the Kanagawa Academy of Science and Technology, KSP E-408, 3-2-1 Sakado,Takatsu-ku, Kawasaki 213 Japan.

M. Ohtsu is also with the Tokyo Institute of Technology, Midori-ku, Yokohama 226 Japan.

Publisher Item Identifier S 0733-8724(96)07655-4.

A. Tapering the Cladding

The cladding of a GeO_2 doped fiber is tapered by etching at the interface between oil and HF acid as shown by step [A] of Fig. 1. For tapering the cladding, the height of the meniscus formed at the interface around the fiber gets decreased as the cladding diameter is reduced [13]. Floated oil on the surface slows down the evaporation of the HF acid and determines the taper angle α. Using dimetylsilicone oil with a density of 0.935 g/cm^3, a tapered fiber is realized with an angle α of 20°.

B. Hollowing the End of the Taper

In HF acid, the tapered fiber end is hollowed as shown in step [B] of Fig. 1. Here, Oil/HF acid can also be used. However, the etching has to be done not at the interface but in the HF acid. This can be done with reproducibility.

C. Flattening the End of the Taper

The peaks on either side of the end of the taper are flattened by etching in X:1:1 (where $X \geq 1.7$). At $X = 1.7$, the flat end with the radius of $[r_1 + \delta_0]$ is realized as shown in step [C] of Fig. 1. In $X > 1.7$, both flattening the peaks and sharpening the core start at the same time. Therefore, the sharpened core with an apex diameter is realized on the flat end when the peaks are flattened.

D. Sharpening the Core

By etching in X:1:1 (where $X > 1.7$), the core is sharpened with the cone angle θ_1 and simultaneously, the cladding thickness of the flat end is decreased from δ_0. Here, the etching has to be stopped when the cladding thickness is zero.

Table I shows the etching solutions and the etching times for the fabrication of the pencil-shaped probe having $\alpha = 20°$ and $\theta_1 = 20°$. Here, for steps [C] and [D], the fiber is continuously etched in the same solution. These etching conditions are for the high GeO_2 doped fiber having parameters shown in Table II. The fiber was originally developed as a dispersion-compensating fiber (DCF) [14].

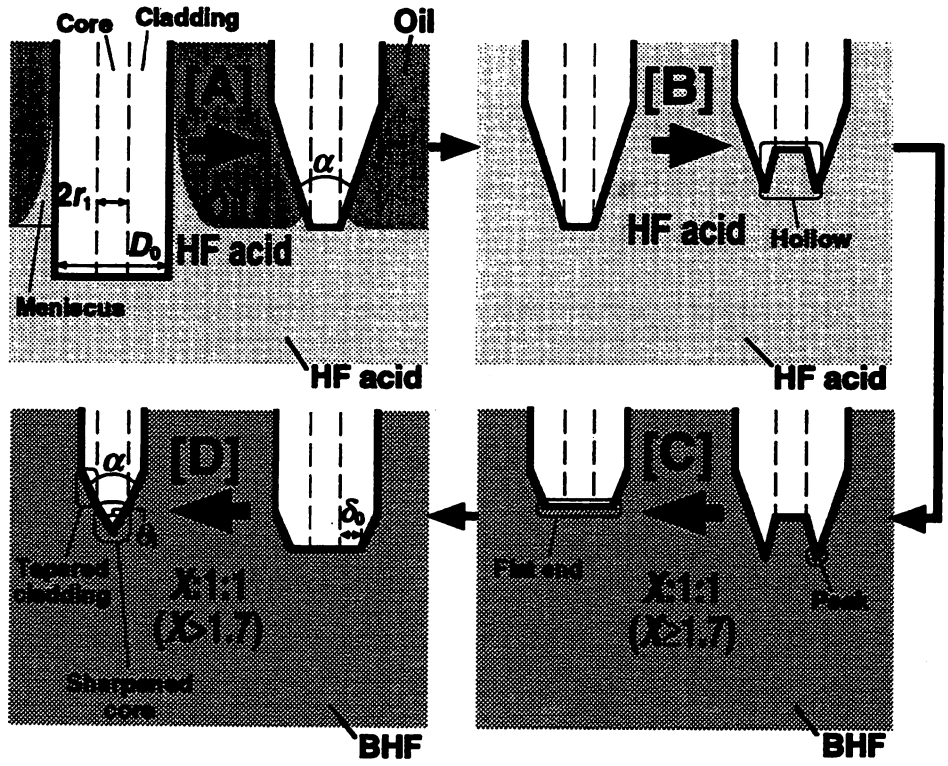

Fig. 1. Schematic illustration of a method to fabricate a pencil-shaped probe: Step [A] is tapering the cladding with a taper angle α by an etching solution of Oil/HF acid, Step [B] is hollowing the end of the taper by HF acid, Step [C] is flattening the peak at the end of the taper by a buffered HF solution (BHF) X:1:1 (where $X \geq 1.7$), Step [D] is sharpening the core with the cone angle θ_1 by BHF of X:1:1 (where $X > 1.7$). r_1 is a radius of the core, D_0 is the diameter of the fiber, α is the taper angle, and δ_0 is the cladding thickness of the flat end in the etched shape after step [C].

TABLE I
CONDITIONS FOR FABRICATING A PENCIL-SHAPED PROBE

Step	Etching solution [a]	Etching time
[A]	Dimethylsilicone oil [b] /HF acid (50wt%)	22 min
[B]	HF acid (50wt%)	2 min
[C] and [D]	NH_4F sol. (40wt%):HF acid (50wt%):H_2O=10:1:1	90 min

[a] 25°C (±0.2°C).
[b] Density of oil is 0.935 g/cm³.

TABLE II
PARAMETERS OF A HIGH GeO_2 DOPED FIBER USED FOR FABRICATING THE PENCIL-SHAPED PROBE

	Diameter	Material [c]	Index difference from pure SiO_2	Dissolution rate in 10:1:1	Dissolution rate in 50w% HF acid
Core	$2r_1$=2 μm	GeO_2-SiO_2	+2.5%	1 μm/hour [d]	1950 μm/hour [e]
Cladding	D_0=125 μm	SiO_2	0	6 μm/hour	170 μm/hour

[c] Silica glass was fabricated by vapor axial deposition.
[d, e] Estimated values (Refer to Appendix A.)

III. RESULTS AND DISCUSSION

The method shown in Fig. 1 was done by using conditions shown in Table I. Used fiber had the parameters shown in Table II. Fig. 2(a) shows a scanning electron micrograph (SEM) of the fabricated pencil-shaped probe. As seen, the probe has the sharpened core and the tapered cladding with a taper angle α of about 20°. Fig. 2(b) shows a magnified SEM micrograph of the apex region of the sharpened core. In this figure, the region indicated by C is the contamination due to bombardment of the electron beam and the region indicated by P is the tip coated by gold of about 3 nm thickness. This fiber has a cone angle θ_1 of 20° and the apex diameter d less than 10 nm which includes the coating thickness of gold film. By controlling X of BHF used in steps [C] and [D], we obtained various cone angles θ_1 of more than 20° with apex diameter less than 10 nm. Fig. 3 shows the dependence of the cone angle θ_1 on the volume ratio X of NH_4F solution.

Fig. 4 shows dependence of the apex diameter d on the etching time T_B in step [B]. Steps [C] and [D] were performed in 10:1:1. Here, the closed circles represent the experimental results. Solid line is least-square-fitted to these results. For an etching time of $T_B = 2$ min, the pencil-shaped probe having a cladding diameter of about 90 μm and an apex diameter of d less than 10 nm is fabricated. To determine theoretically the minimum etching time $T_{B\,min}$, we developed a model based on geometrical considerations. The model will be reported in a separate paper.

When a shear-force topographic technique [15] is employed for the near-field optical microscope, the cladding diameter D is one of the main parameters deciding the resonance frequency of dithering. Although the cladding diameter can be reduced by increasing the etching times in steps [B] and [C], there is another simple technique of control the cladding diameter. The technique is described in Appendix B.

The reproducibility of the meniscus etching [13] in step [A] depends on mechanical vibration of the whole system, degradation of the etching solution of Oil/HF acid, and organic contamination remaining on the etched fiber. However, the nanometric tip in the pencil-shaped probe is fabricated with

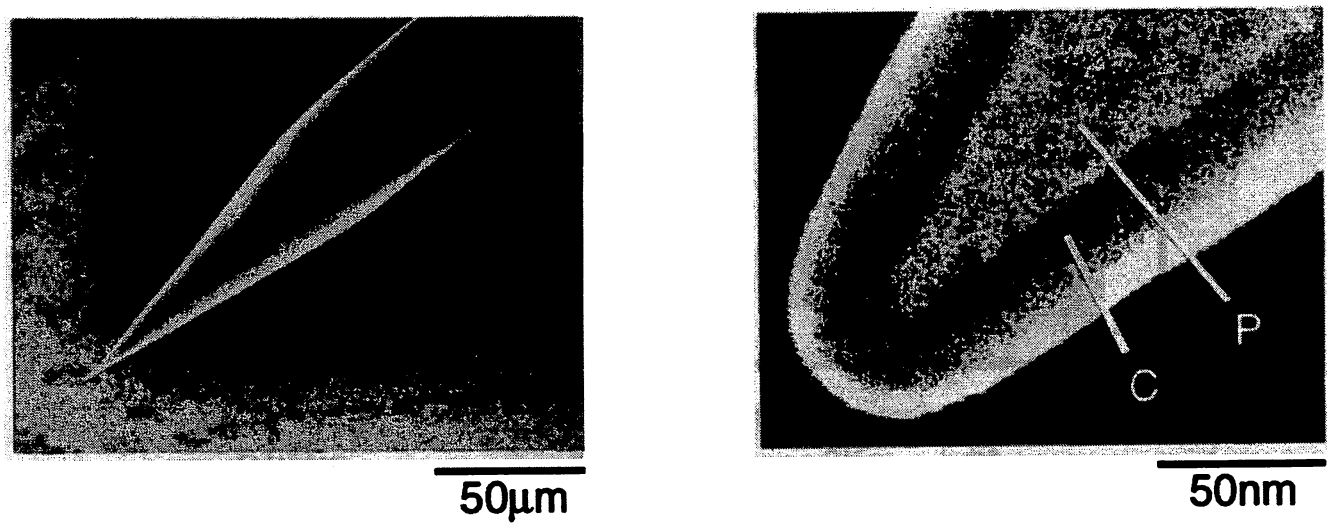

Fig. 2. (a) SEM micrograph of the fabricated pencil-shaped probe. Parameters of the fabrication is summarized in Table II. The taper angle α is 20°. (b) Magnified view of the top of pencil-shaped probe in (a). The layer indicated by C is the contamination due to bombardment of the electron beam. The region indicated by P is the fiber-probe coated by gold of about 3 nm. The cone angle θ_1 is 20°, and the apex diameter d is less than 10 nm including the gold film.

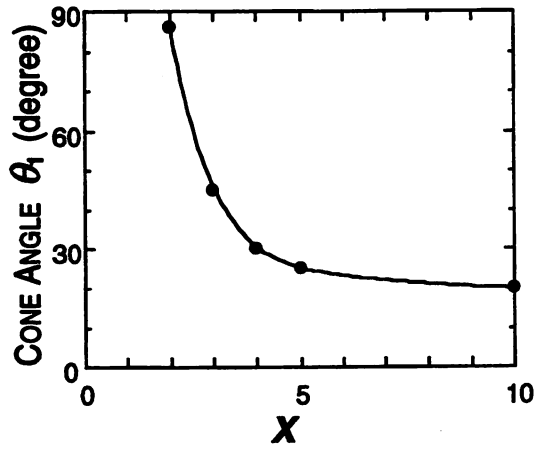

Fig. 3. Dependence of the cone angle θ_1 of the core of the pencil-shaped probe on X in step [D].

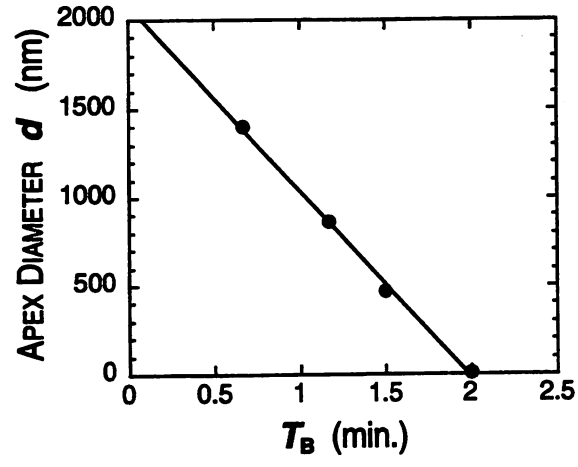

Fig. 4. Dependence of the apex diameter d of the pencil-shaped probe on the etching time T_B in step [B]. Closed circles represent the experimental results, and the solid line is least-square fitted to them. The minimum etching time $T_{B\,min}$ required for making apex diameter less than 10 nm is 2 min.

high reproducibility because the core is sharpened in step [D] based on the selective etching.

It should be pointed out that a metallized probe having silica tip protruding from the metal film was fabricated by coating and etching techniques [16] with the pencil-shaped probe. Here, the protrusion of the probe had the apex diameter less than 10 nm and the foot diameter about 30 nm. Using the protruded probe, we have succeeded in obtaining a nanometric optical image of a biological sample with a collection mode NOM or PSTM.[1] [5] We will discuss a method to fabricate the protruded probe [17] and an throughput characteristic of the probe elsewhere [18].

IV. Summary

We proposed a novel etching method for fabrication of a pencil-shaped fiber probe for near-field optical microscopy. The pencil-shaped probe was realized with high reproducibility by using a high GeO_2 doped fiber with an index difference of 2.5%. The probe was fabricated with the minimum cone angle of 20° and an apex diameter of less than 10 nm.

[1] For acronyms appearing here, refer to Pohl in [1].

Appendix A
Selective Chemical Etching and Etching Rates of a GeO_2 Doped Fiber

As shown in Fig. 5(a) and (b) where R_1 and R_2 represent the dissolution rates of the core and the cladding in a silica fiber, the fiber is hollowed when $R_1 > R_2$ and is sharpened when $R_1 < R_2$, respectively. In this figure, r_1 is the radius of the core, ϕ is the cone angle of the hollow, τ_1 is the etching time required for making the apex diameter zero, δ is the cladding thickness, and θ_1 is the cone angle of the sharpened core. Bright and dark shades are the original shapes and the etched shapes at (a) an etching time T (b) τ_1, respectively. Assuming that etching rates R_1 and R_2 are constant, the cone

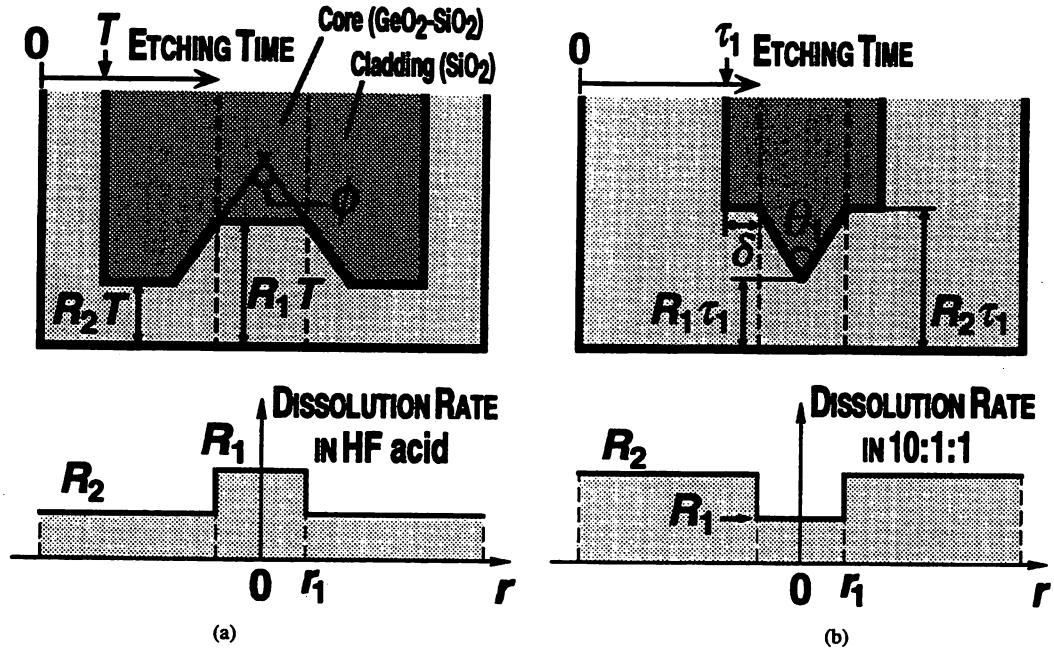

Fig. 5. Schematic explanation of selective etching of a GeO_2 doped fiber in (a) sharpening the core and (b) hollowing. The profiles show the etching rates of the fiber in (a) HF acid, (b) 10:1:1. R_1 and R_2 where $R_1 > R_2$ in (a) and $R_1 < R_2$ in (b) are the dissolution rates in the GeO_2 doped core and the pure silica cladding. r_1 is a radius of the core, ϕ [defined by (A1)] is the cone angle of the hollow, τ_1 [defined by (A4)] is the etching time required for making the apex diameter zero, δ is the cladding thickness, and θ_1 [defined by (A2)] is the cone angle of the sharpened core. Bright shades and dark shades are the original shapes and the etched shapes at (a) an etching time T (b) τ_1, respectively.

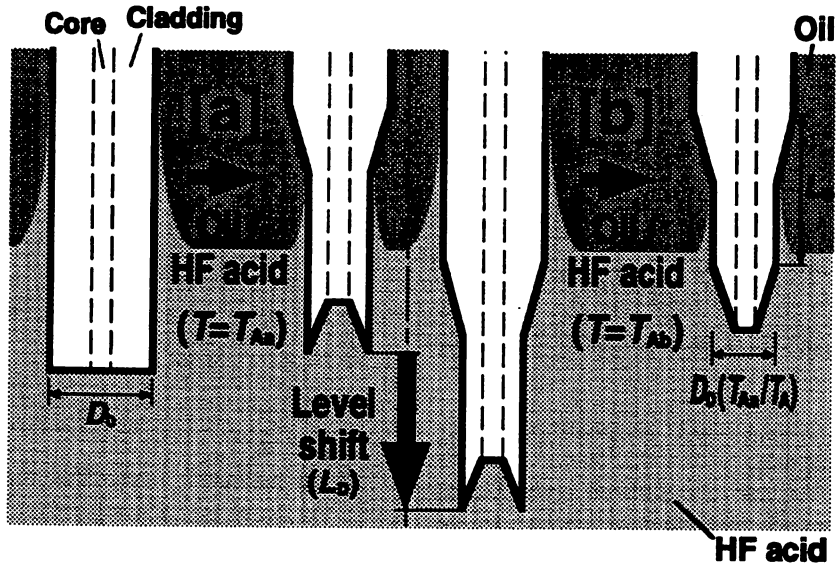

Fig. 6. Schematic illustration of the etching technique for controlling the cladding diameter of the pencil-shaped probe. This technique can be combined with the fabrication shown in Fig. 1 instead of step [A]. L_D is the lowering distance. The etching times for substep [a] and substep [b] are expressed by T_{Aa} and T_{Ab}. The sum of T_{Aa} and T_{Ab} is equal to the etching time T_A in step [A].

angle ϕ of the hollow is expressed as

$$\sin(\phi/2) = R_2/R_1 \quad (R_1 > R_2). \tag{A1}$$

The cone angle θ_1 and the apex diameter d of the sharpened core are expressed as

$$\sin(\theta_1/2) = R_1/R_2 \quad (R_1 < R_2). \tag{A2}$$

and

$$d = \begin{cases} 2r_1(1 - T/\tau_1) & (T \le \tau_1) \\ 0 & (T > \tau_1) \end{cases}. \tag{A3}$$

Since r_1 is equal to $[\{\cos(\theta_1/2)\}^{-1} - \tan(\theta_1/2)]R_1\tau_1$, τ_1 is expressed as

$$\tau_1 = (r_1/R_1)\sqrt{(R_1 + R_2)/(R_2 - R_1)} \tag{A4}$$

by using (A2).

When a GeO2 doped fiber is etched in a buffered HF solution (BHF) with a volume ratio of NH_4F solution (40 wt%): HF acid (50 wt%): H_2O = X:1:1 (where X is the variable), the fiber is hollowed in $X < 1.7$ and sharpened in $X > 1.7$. The ratio $[R_1/R_2]$ decreases with increasing X and

converges to a constant value at $X = 10$–30. At $X = 1.7$, the ratio is equal to unity. The cone angles θ_1 and ϕ take the minimum values at $X = 10$ and in only HF acid for which $X = 0$, respectively. The minimum cone angles are determined by the index difference which depends on the GeO_2 doping ratio [12].

We obtained a cone angle of $\theta_1 = 20°$ by etching the fiber having an index difference of 2.5% in $X = 10$ [12]. By substituting $\theta_1 = 20°$ and $R_2 = 6$ μm/h into (A2), we obtain $R_1 = 1\mu$m/h. By etching the fiber in HF acid (50 wt%), the hollowed fiber may have a smaller height of the hollow than that represented as $h_H = (R_1 - R_2)T$. This is considered to be due to the degradation of the etching solution resulting from the dissolved waste inside the hollow region. When the height of the hollow region is not much larger than the core diameter, R_1 and R_2 can be considered to have approximately constant values. By substituting $10°$ for ϕ and $R_2 = 170$ μm/h into (A1), we obtain $R_1 = 1950$ μm/h.

APPENDIX B
SIMPLE TECHNIQUE OF CONTROLLING CLADDING DIAMETER IN STEP [A]

To control the cladding diameter D, there is a level shift technique consisting of substep [a] tapering the cladding and [b] reducing the cladding as shown in Fig. 6. Here, the fiber diameter is D_0, and the etching times for substeps [a] and [b] are represented by T_{Aa} and T_{Ab}, respectively. In this technique, the fiber is only lowered down by a distance of L_D in Oil/HF acid for an etching time of T_{Aa}. The value of D is proportional to T_{Aa}. When in steps [B]–[D], we define the etching times by T_B, T_C, and T_D and denote the dissolution rates of the cladding as R_{2B}, R_{2C}, and R_{2D}, respectively, D is expressed

$$D = D_0\left(\frac{T_{Aa}}{T_{Aa}+T_{Ab}}\right) - 2[R_{2B}T_B + (R_{2C}T_C + R_{2D}T_D)] \tag{A5}$$

where $[T_{Aa}+T_{Ab}]$ is equal to the etching time T_A in step [A].

By this technique instead of step [A] shown in Fig. 1, we obtained the pencil-shaped probe with the reduced cladding diameter $D = 125(T_{Aa}/T_A) - 35$ [μm] for the condition shown in Table I. When $[T_{Aa}/T_A] = 0.6$, the probe shown in Fig. 2 was obtained with D of about 40 μm. Here, a lowering distance L_D was 1 mm.

ACKNOWLEDGMENT

The authors wish to thank S. Miyamoto (Fujikura Ltd.) for his discussion on fibers and also R. Uma Maheswari, T. Saiki, and M. Naya (KAST) for their useful suggestions and for applying fiber probes to a near-field optical microscope. Special thanks to R. Uma Maheswari for critically reading and commenting on the manuscript.

REFERENCES

[1] D. W. Pohl and D. Courjon, Eds., *Near Field Optics*, Dordrecht: Kluwer Academic, vol. 242 of NATO ASI Series E, 1993.

[2] M. Ohtsu, "Progress of high-resolution photon scanning tunneling microscopy due to a nanometric fiber probe," *J. Lightwave Technol.*, vol. 13, pp. 1200–1221, 1995.

[3] S. Jiang, H. Ohsawa, K. Yamada, T. Pangaribuan, M. Ohtsu, K. Imai, and A. Ikai, "Nanometric scale biosample observation using a photon scanning tunneling microscope," *Japan J. Appl. Phys.*, vol. 31, pp. 2282–2287, 1992.

[4] R. Uma Maheswari, H. Tatsumi, Y. Katayama, and M. Ohtsu, "Observation of subcellular nanostructure of single neurones with an illumination mode photon scanning tunneling microscope," *Opt. Commun.*, vol. 120, pp. 325–334, 1995.

[5] M. Naya, S. Mononobe, R. Uma Maheswari, T. Saiki, and M. Ohtsu, "Imaging of biological samples by a collection-mode photon scanning tunneling microscope," *Opt. Commun.*, vol. 124, pp. 9–15, 1996.

[6] R. D. Grober, T. D. Harris, J. K. Trautman, E. Bezig, W. Wegscheider, L. Pfeiffer, and K. West, "Optical spectroscopy of a GaAs/AlGaAs quantum wire structure using near-field scanning optical microscopy," *Appl. Phys. Lett.*, vol. 64, pp. 1421–1423, 1994.

[7] T. Saiki, S. Mononobe, M. Ohtsu, N. Saito, and J. Kusano, "Spatially resolved photoluminescence spectroscopy of lateral *p-n* junctions prepared by Si-doped GaAs using a photon scanning tunneling microscope," *Appl. Phys. Lett.*, vol. 67, pp. 2191–2193, 1995.

[8] E. Betzig and R. J. Chichester, "Single molecules observed by near-field scanning optical microscopy," *Science*, vol. 262, pp. 1422–1425, 1993.

[9] E. Bezig, J. K. Trautman, R. Wolfe, E. M. Gyorgy, P. L. Fynn, M. H. Kryder, and C.-H. Chang, "Near-field magneto-optics and high density data storage," *Appl. Phys. Lett.*, vol. 61, pp. 142–144, 1992.

[10] S. Jiang, J. Ichihashi, H. Monobe, M. Fujihira, and M. Ohtsu, "High localized photochemical processes in LB films of photochromic material by using a photon scanning tunneling microscope," *Opt. Commun.*, vol. 106, pp. 173–177, 1994.

[11] E. Betzig and J. K. Trautman, "Near-field optics: Microscopy, spectroscopy and surface modification beyond the diffraction limit," *Science*, vol. 257, pp. 189–195, 1992.

[12] T. Pangaribuan, S. Jiang, and M. Ohtsu, "High controllable fabrication of fiber probe for photon scanning tunneling microscope," *Scanning*, vol. 16, pp. 362–367, 1994.

[13] K. M. Takahashi, "Meniscus shapes on small diameter fibers," *J. Colloid Interface Sci.*, vol. 134, pp. 181–187, 1990.

[14] M. Onishi, H. Ishikawa, M. Shigematsu, H. Kanamori, and N. Nishimura, in *Proc. Conf. Optic. Fiber Communication*, 1994, vol. 4 of OSA Technical Digest Series, p. 224.

[15] E. Bezig, P. L. Finn, and J. S. Weiner, "Combined shear force and near-field scanning optical microscopy," *Appl. Phys. Lett.*, vol. 60, pp. 2484–2486, 1992.

[16] S. Mononobe, R. Uma Maheswari, T. Saiki, M. Naya, and M. Ohtsu, in *Proc. Conf. Near field Optics-3*, vol. 8 of EOS Topical Meeting Digests, 1995, pp. 105–106.

[17] S. Mononobe, T. Saiki, M. Naya, and M. Ohtsu, "Reproducible fabrication of a fiber probe with a nanometric protrusion for near-field optics," submitted to *Appl. Opt.*

[18] T. Saiki, S. Mononobe, M. Ohtsu, N. Saito, and J. Kusano, "Tailoring a high-transmission fiber probe for photon scanning tunneling microscope," *Appl. Phys. Lett.*, vol. 68, pp. 2612–2614, 1996.

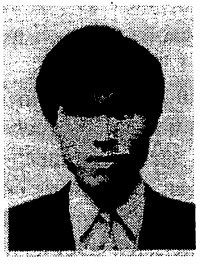

Shuji Mononobe was born in Osaka, Japan, in 1967. He received the B.S. and M.S. degrees from the University of Osaka Prefecture, Sakai, Japan, in 1991 and 1993, respectively.

Since April 1993, he has been with Kanagawa Academy of Science and Technology (KAST), Kawasaki, Japan, as a Researcher. His current research interests are fiber probes for near-field optics.

Mr. Mononobe is a member of the Japan Society of Applied Physics.

Motoichi Ohtsu (M'88–SM'90) for a photograph and biography, see this issue, p. 2230.

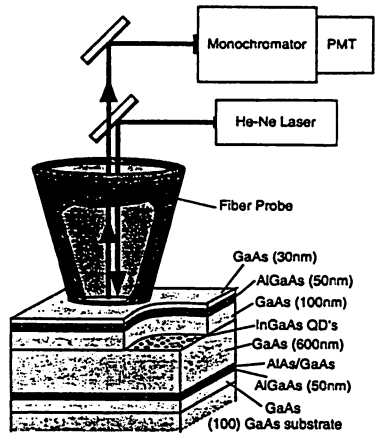

TuI2 Fig. 1. Schematic of experimental setup and quantum dots structure. The same aperture was used both for sample excitation and for signal collection.

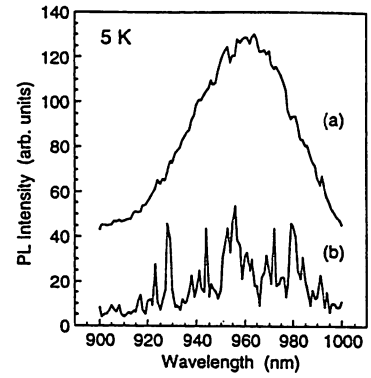

TuI2 Fig. 2. Photoluminescence spectra of quantum dots detected (a) in the far-field region and (b) in the near-field region.

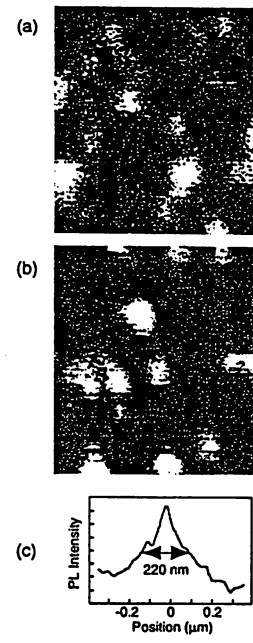

TuI2 Fig. 3. Wavelength-selected photoluminescence images of single quantum dots with the emission wavelengths of (a) 923 nm and (b) 928 nm. The spectral bandwidth of the detection is 1 nm. The image size is 3 × 3 μm.^{2} (c) Cross-section of a single spot image.

TuI2 1130

Near-field optical spectroscopy and imaging of single quantum dots

Toshiharu Saiki, Yoshitaka Yokoyama,* Kenichi Nishi,** Motoichi Ohtsu,*
Kanagawa Academy of Science and Technology, KSP East 408, 3-2-1 Sakado, Takatsu, Kawasaki, Kanagawa 213, JAPAN

Recently, there has been strong progress in the growth of semiconductor quantum dots (QD's) using the Stranski-Krastanow mode.[1] Single dot photoluminescence (PL) spectroscopy of the inhomogeneously broadened QD system has attracted much interest both in its fundamental properties and in its applications to opto-electronics. There exist, however, few experimental results on a single dot PL spectrum of high density (>10^{10} dots/cm^2) structure,[2,3] due to the poor spatial-resolving power of the conventional microscopic techniques.

One of the most powerful tools for the single dot spectroscopy is a near-field scanning optical microscope.[4,5] By using a highly sensitive near-field probe, we have successfully obtained sharp PL lines and clear images of single QD's, at cryogenic temperature, with the spatial resolution of $\lambda/5$ and in the weak excitation limit of $<5 \times 10^8$ excitons/s per dot.

Figure 1 shows a schematic of the QD sample structure and an experimental configuration. The $In_{0.5}Ga_{0.5}As$ self-assembled QD's were grown on (100) GaAs substrate by gas-source molecular beam epitaxy with a density of 2×10^{10} dots/cm^2. Typical dot diameter of around 30 nm and height of 15 nm were observed with atomic force microscope before the growth of cap layers of 180 nm. For the near-field optical excitation, QD sample on a scanning piezotube was illuminated with He-Ne laser light (633 nm) through a small aperture of a fiber probe. For the collection of PL signal, the same aperture was used, which was indispensable to avoid a decline of a spatial resolution due to the effect of a excited carrier diffusion. The collected light was focused into a 50-cm monochromator and detected by a cooled photomultiplier tube using a photon counting technique. Shear-force feedback was employed to control a tip-sample distance of less than 10 nm. The temperature of the sample was kept at 5 K in a cryostat.

Figure 2(a) shows a typical PL spectrum of inhomogeneously broadened QD's obtained by positioning the probe tip 2 μm above the sample surface and by detecting the PL signal from a large number of QD's. In the near-field region, on the other hand, sharp PL lines with the linewidths of 1~2 meV are clearly seen in Fig. 2(b). Since the measurement was performed in the weak excitation region, only the PL lines from the ground states are observed.

Through the wavelength-selected imaging, we also obtained the spatial distributions of the QD's having the same PL wavelengths of 923 nm and 928 nm as shown in Fig. 3(a) and (b). The smallest and the average sizes of the spot images, which correspond to the collection area of PL signal through the aperture, are 220 nm and 290 nm, respectively [Fig. 3(c)]. The number of the dots in this collection area is estimated as 15 from the dot density of this sample. This value is in good agreement with the number of main peaks observed in the spectrum of Fig. 2(b). Thus, we conclude that real single dot spectroscopy and imaging with $\lambda/5$ resolution is realized using near-field optical measurement, which can be widely applied to the single particle observation of the inhomogeneously broadened systems.

Interdisciplinary Graduate School of Science and Engineering, Tokyo Institute of Technology, Midori, Yokohama 226, JAPAN

**Opto-Electronics Research Laboratories, NEC Corporation, Miyukigaoka, Tsukuba, Ibaraki 305, JAPAN

1. K. Nishi, R. Mirin, D. Leonard, G. Medeiros-Ribeiro, P. M. Petroff, A. C. Gossard, J. Appl. Phys. 80, 3466 (1996).
2. J.-Y. Marzin, J.-M. Gérard, A. Izraël, D. Barrier, Phys. Rev. Let. 73, 716 (1994).
3. M. Grundmann, J. Christen, N. N. Ledentsov, J. Böhrer, D. Bimberg, S. S. Ruvimov, P. Werner, U. Richter, U. Gösele, J. Heydenreich, V. M. Ustinov, A. Yu. Egorov, A. E. Zhukov, A. E. Zhukov, P. S. Kop'ev, Zh. I. Alfelov, Phys. Rev. Lett. 74, 4043 (1995).
4. H. F. Ghaemi, B. B. Goldberg, C. Cates, P. D. Wang, C. M. Sotomayor Torres, M. Fritze, A. Nurmikko, Superlattices and Microstructures 17, 15 (1995).
5. Y. Toda, M. Kourogi, M. Ohtsu, Y. Nagamune, Y. Arakawa, Appl. Phys. Lett. 69, 827 (1996).

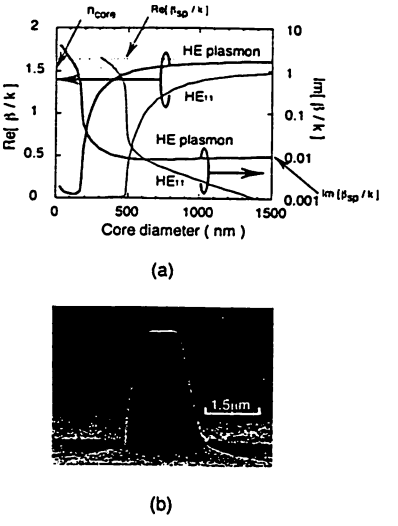

TuI3 Fig. 1. (a) Mode propagation constant as a function of a core diameter. Wavelength λ = 680 nm; refractive index of infinite Au cladding n_{Au} = 0.14 − i3.90; refractive index of dielectric core n_{core} = 1.53; propagation constant of surface plasmon β_{sp}/k = 1.66 − i0.01. (b) SEM image of a fabricated axially asymmetric fiber probe.

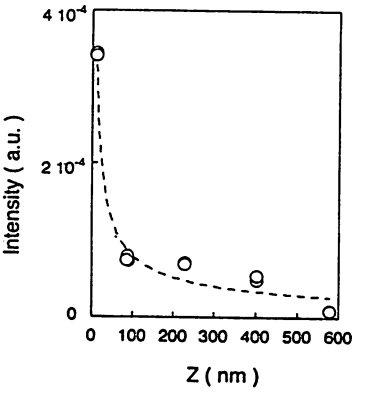

TuI3 Fig. 2. Measured near-field optical intensity as a function of the distance (z) from the aperture surface. Wavelength of the injected light λ = 680 nm.

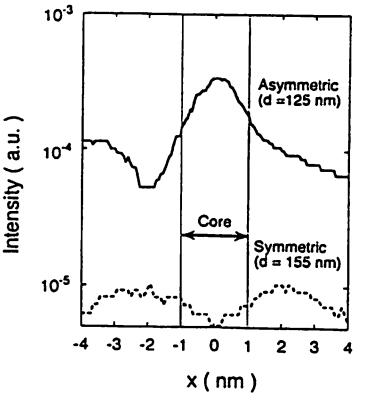

TuI3 Fig. 3. Measured near-field optical intensity profile across the aperture surface. The profile for the symmetric fiber probe is also shown for comparison.

Enhancing throughput over 30 times by an asymmetric fiber probe for near-field optics

Takashi Yatsui, Motonobu Kourogi,* Motoichi Ohtsu,* *Interdiscplinary Graduate School of Science and Engineering, Tokyo Institute of Technology, 4259 Nagatsuta, Midori-ku, Yokohama 226, JAPAN*

Near-field optical technique has improved drastically in its spatial resolution for nanometric imaging by using a sharpened fiber as a probe. We report here successful experimental results of drastically enhancing the throughput by breaking the axial symmetry of sharpened core of the fiber probe for further improvements in the spatially resolved spectroscopy and high-density optical storage/readout.

Since the throughput decreases rapidly with decreasing core diameter, some structural improvements of the fiber probe are required. First, we carried out mode analysis[1] for the gold coated core of the glass fiber. The results are summarized in Fig. 1(a). This figure shows that, in addition to an HE_{11} mode, there can exist an extremely low loss mode. It can be called "HE plasmon (HP) mode" because the value of its mode propagation constant approaches that of the surface plasmon in the limit of infinite core diameter. Because it is hardly excited in conventional fiber core, we propose here to break axial symmetry to introduce mode conversion capability to the sharpened metal coated core. To make the sharpened core asymmetric, the foot of the core was partly removed by a focused ion beam (FIB) after the core is tapered by chemical etching.[2] Then, the core was coated with 500-nm thick to block the leakage of the propagating far-field. Finally, the top of the metal coated core was removed by the FIB to form a subwavelength aperture [see Fig. 1(b)].

We measured the spatial intensity profile of the optical near-field generated on the aperture of the probe by injecting the light from the other end of the fiber. For this measurement, another conventional sharpened fiber probe was scanned over the aperture to scatter the optical near-field while maintaining their separation constant by shear-force feedback control. Figure 2 shows the measured result of relation between the separation and scattered optical near-field intensity for the asymmetric fiber probe (AFP) with the aperture of 125-nm diameter. The decay length as short as 50-nm and no background of the curve in this figure confirmed a selective generation capability of the near-field localized on the aperture while blocking the propagating far-field component.

The measured optical near-field intensity profile across the aperture is shown by Fig. 3. Compared with the profile for the symmetric fiber probe (SFP) with 155-nm diameter aperture (fabricated by the same process as AFP without removing the foot of the tapered core), that AFP shows a favourable bell-shape, which agrees with the theoretical profile of electric field of the HP mode. Comparison between the two curves shows that the maximal intensity of AFP is 33 times as high as that of SFP. Further, total power was found as high as 28 times. From these results, drastic enhancement of the throughput was confirmed.

Fabrication of sub-100-nm aperture is expected by the accuracy of the nano-fabrication process.

Kanagawa Academy of Science & Technology, 3-2-1 Sakado, Takatsu-ku, Kawasaki, Kanagawa 213 JAPAN

1. L. Novotony, C. Hafner. Physical Review E, 50, 4094 (1994).
2. T. Pangaribuan, *et al.* Jpn. Appl. Phys. Lett. 31, L1302 (1992).

WL2 1115

Fabrication of Si planar apertured array for high speed near-field optical storage and readout

M. B. Lee,* T. Nakano, T. Yatsui, M. Kourogi,** K. Tsutsui, N. Atoda,† M. Ohtsu,** *Interdisciplinary Graduate School of Science and Engineering, Tokyo Institute of Technology, 4259 Nagatsuta, Midori-ku, Yokohama 226, JAPAN*

An optical fiber probe with a sharp core tip fabricated by selective wet chemical etching[1] or by pipette pulling method[2,3] has been employed as an optical head writing-in or detecting the signal in high-density near-field optical storage. Such problems as the small photon number and low scanning speed, however, remain unsolved in these methods. We report here the fabrication of new Si planar apertured probe arrays especially aiming at the adaptibility of the probe to high-speed scanning. Since the probe has a flat side, the flying head technology, for example, used in magnetic hard disks can be applied to it for high data rate. Conventional lithography and etching for fabricating Si microstructures do not necessarily meet our requirements to obtain apertures less than 100 nm in size. The point here is how we can establish the fabrication method of nm-sized appertures (e.g., 10 nm) with high reproducibility. Schematic of the concept of our probe structure is illustrated in Fig. 1. Thermally oxidized SiO_2 film on Si(100) substrate was patterned in a 10 μm × 10 μm square array by photolithography. Following the removal of the patterned SiO_2 with buffered HF solution, anisotropic etching with 10 weight percents KOH aqueous solution at 80°C generated the inverted pyramidal shaped grooves which were faceted with {111} planes of Si. The substrate is again etched with the KOH solution from the back side until the aperture array appears. The apex angle of the pyramid was 70.5° and constant

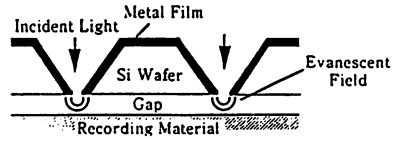

WL2 Fig. 1. Schematic structure of the Si apertured probe array.

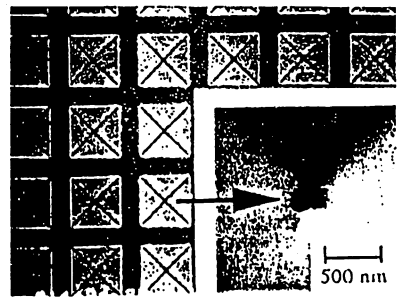

WL2 Fig. 2. SEM images of the grooves and one element of the aperture array.

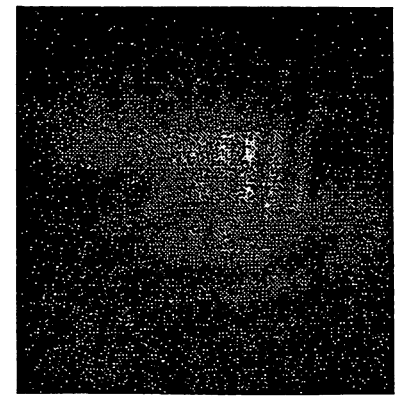

WL2 Fig. 3. NOM image (5 μm × 5 μm) of optical power distribution of the aperture.

due to the crystallography of Si. High reproducibility of the aperture size can be achieved in this process since the size distribution depends only on the deviation of original mask pattern size and flatness of etched Si surface. Etch stop layer such as a buried SiO_2 layer of SOI (silicon-on-insulator) wafer was useful to catch the time to stop etching, or the time was determined by preliminarily estimating the etch rate of Si in an ordinary wafer with 270 μm thickness. Finally, 100-nm-thick gold film was sputter-deposited from the patterned side to block the propagating far-field light. This yielded the array of aperture with about 200 nm in diameter which is in the subwavelength range. Figure 2 shows the scanning electron microscopic (SEM) images of the grooves and enlarged view of one element of the aperture array taken from the opposite side. Collection-mode near-field optical microscopy was used for characterization of the Si probe. The laser light (λ = 680 nm) was introduced from the patterned side of the sample which was located on a transparent stage subject to *xyz*-axis scanning. Evanescent light field emerging at the aperture was detected by a fiber probe with 70 nm aperture size, and the spatial profile of the light intensity was measured. The tip-sample separation was controlled by a shear force feedback. The constant height topographic image as well as near-field optical microscopic (NOM) image was displayed. Figure 3 shows the optical power distribution image from one element of the array. The contrast decayed rapidly with increasing the tip-sample separation, confirming the existence of little far-field light component and localization of the near field on the aperture. It is anticipated that we can also fabricate the aperture arrays with smaller dimensions by further improving present method.

*Also with National Institute for Advanced Interdisciplinary Research, 1-1-4 Higashi, Tsukuba, Ibaraki 305, JAPAN
**Also with "Photon Control" Project, Kanagawa Academy of Science and Technology, KSP East Room 408, 3-2-1 Sakado, Takatsu-ku, Kawasaki 213, JAPAN
†National Institute for Advanced Interdisciplinary Research, 1-1-4 Higashi, Tsukuba, Ibaraki 305, JAPAN

1. S. Jiang, J. Ichihashi, H. Monobe, M.

Fujihira, M. Ohtsu, Opt. Commun. 106, 173 (1994).
2. E. Betzig, J. K. Trautman, R. Wolfe, E. M. Gyorgy, P. L. Finn, M. H. Kryder, C.-H. Chang, Appl. Phys. Lett. 61, 142 (1992).
3. S. Hosaka, T. Shintani, M. Miyamoto, A. Hirotsune, M. Terao, M. Yoshida, K. Fujita, S. Kammer, Jpn. J. Appl. Phys. 35, 443 (1996).

ThK3 1145

Fabrication of functional probes for near-field optical microscopy

Kazuyoshi Kurihara, Motoichi Ohtsu,*
Kanagawa Academy of Science and Technology, KSP East, 3-2-1 Sakado, Takatsu-ku, Kawasaki-shi, Kanagawa-ken 213, JAPAN

Functional probes for near-field optical microscopy (NOM) are a key device for improving NOM in performance and applying NOM to chemistry and biology. Much effort has been made to fabricate the functional probes, but advances in the fabrication is not enough to make a great impact on NOM.[1]

We present a novel method to fabricate the functional probes by means of a capillary under a system of a conventional optical microscope and micro-manipulator. Functional materials are selectively fixed on the apex of optical fiber probes with a size of about a micron. Figure 1 shows a schematic of the fixation procedure. The capillary is used as a small beaker. The optical fiber probe is prepared with the SRC method.[2] The capillaries are prepared by pulling glass tubes with a puller for micro-electrodes.

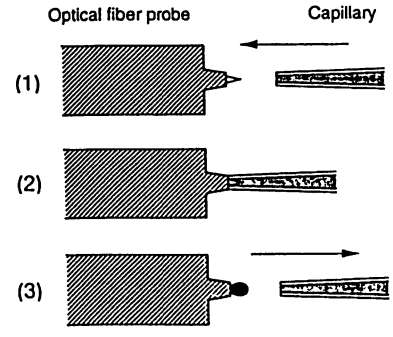

ThK3 Fig. 1. Schematic of fixation procedure under a system of a optical microscope and micro-manipulators.

The functional materials are dissolved in solvents and made low in viscosity to fill the top of capillaries. The capillary method[3] is applicable in fixing many kinds of functional materials.

In the SEM image of Fig. 2, poly(vinyl chloride) (PVC) film including fluorescein is fixed on the apex of the probe and gives a function of chemical sensor to the probe. The PVC film[4] is an attractive organic membrane which enables us to produce ion-selective membrane based on ion-exchange mechanism by dissolving ionophores with fluorescent indicators. The sensor size is from submicron to micron, depending on the fixation condition, especially depth of dipping the probe, diameter of the capillary and viscosity of the PVC film. The viscosity is adjusted with a solvent of Terahydrofuran (THF). In Fig. 2, typical fluorescence spectrum is shown when illuminating the probe with 488 nm of Ar-ion laser coupled to the fiber at a power of 0.2 mW. 70% of photobleaching is observed within 30 minutes.

In the SEM image of Fig. 3, polydiacetylene (PDA) 3ECMU is fixed on the apex of the probe. PDA is an organic polymer with large third-order nonlinear susceptibilities resulting from one-dimensional π-conjugated electrons. In near-field regions, optical processes of nonlinearity such as four-wave mixing and phase conjugation are not yet clear.[5] The nonlinear probes are direct tools to investigate nonlinearity in the near-field regions. In Fig. 3, fluorescence spectrum is shown when the probe is resonantly excited by 632.8 nm of He-Ne laser coupled to the fiber at a power of 2 mW. The probe with PDA is also used as light-emitting probes.

Figure 4 shows the probe with GaAs powder which is fixed on the glass surface of the optical fiber because of adsorption. Ethanol is used as solvent for GaAs powder which is prepared by crushing GaAs wafer in a mortar for about an hour. The apex of the probe is

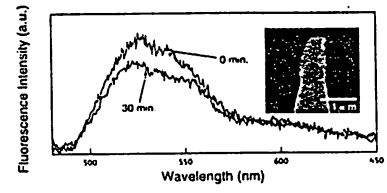

ThK3 Fig. 2. The SEM image and fluorescence spectrum of the probe with PVC film containing fluorescein.

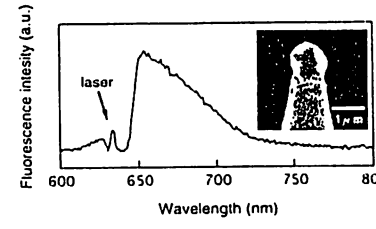

ThK3 Fig. 3. The SEM image and fluorescence spectrum of the probe with PDA 3ECMU.

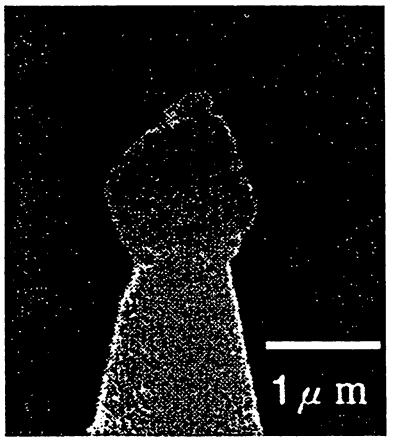

ThK3 Fig. 4. The SEM image of the probe with GaAs powder.

attached to accumulated GaAs powder at the top of the capillary because of ethanol evaporation. The probe with GaAs suggests that it is possible to fix powder on the apex of the optical fiber probes without adhesive agents.

Interdisciplinary Graduate School of Science and Engineering, Tokyo Institute of Technology, 4259 Nagatsuta-cho, Midori-ku, Yokohama-shi, Kanagawa-ken 226, JAPAN

1. H. Göttlich, *et al.*, Ultramicroscopy **61**, 145–153 (1995).
2. S. Mononobe, *et al.*, Appl. Opt. **36**, to be published (1997).
3. K. Kurihara, *et al.*, Proc. of OFS-11, 694–697 (1996).
4. M. Shortreed, *et al.*, Anal. Chem. **68**, 2656–2662 (1996).
5. S. I. Bozhevolnyi, *et al.*, Opt. Lett. **19**, 1601–1603 (1994).

P29

Fabrication of a triple tapered fiber probe for near-field optical spectroscopy in an ultraviolet region by selective etching of a multistep index fiber

Shuji Mononobe, Toshiharu Saiki, Motoichi Ohtsu,* *Kanagawa Academy of Science and Technology, Ohtsu Project, KSP E-408, 3-2-1 Sakado, Takatsu, Kawasaki 213, JAPAN*

Near-field optical microscopy (NOM) employing a metallized fiber probe[1,2] is applied to a spectroscopic study of semiconductor devices and other materials in a near infrared or visible region. However, it is difficult to employ tapered fiber probes having the GeO_2 doped core for spectroscopy in a ultraviolet region because of the optical absorption by GeO_2 at 363 nm. In this paper, we develop a triple tapered probe having the pure silica core for near-field optical spectroscopy in a near ultraviolet region.

Figure 1(a) shows an illustration of a metallized triple tapered probe. Here, λ, α, β, γ, d_1, d_2, and L are the optical wavelength in the fiber, the three cone angles of the triple taper, the two base diameters of the cones with α and β, and the length from the portion with the cross sectional diameter of λ to the apex. The light entering in the taper having a cone angle is strongly absorbed by metal from the portion with the diameter of λ to the apex.[3] To improve the throughput for the optical near field, one has to decrease the length

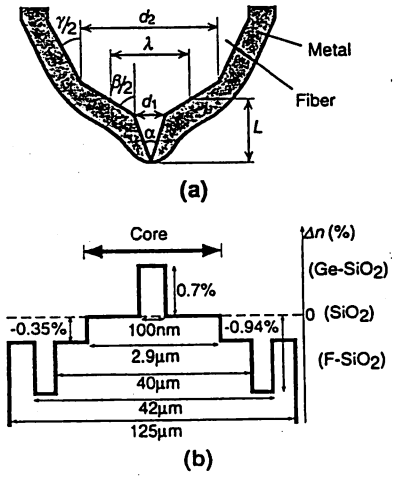

P29 **Fig. 1.** (a) Schematic illustration of triple tapered fiber. Here, α, β, γ, λ, d_1, d_2, and L are the three cone angles of the triple tapered probe, the wavelength in the fiber, the two base diameters of the cones with α and β, the length from the cross sectional diameter of λ to the apex. (b) Multistep index fiber used for fabrication of the triple tapered probe. The core consists of two sections made of pure silica and of GeO_2 doped silica. The pure silica section has a 900 times larger area than the GeO_2 doped section. The cladding is made of F doped silica.

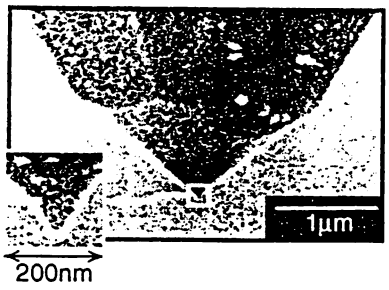

P29 Fig. 2. Scanning electron micrograph of the fabricated triple tapered fiber.

P29 Fig. 3. Photoluminescence image of polysilanes excited by a laser with a wavelength of 350 nm by near-field optical microscope.

L. In the triple tapered probe, by increasing β, we can decrease the length, L, and enhance the throughput. Further, we can obtain a highly resolved image by the tip having a zero apex diameter and the cone angle of α which is smaller than β.

We fabricated the probe by selective etching[4] of a multistep index fiber as schematically shown in Fig. 1(b). Here, the core is mostly made of the pure silicate. The fiber is consecutively etched in buffered hydrogen fluoride solutions with volume ratios of NH_4F solution (40 wt %): HF acid (50 wt %): H_2O being 0.6:1:1, 1.7:1:1, and 10:1:1 for 40, 20, and 10 min. Figure 2 shows scanning electron micrographs of the triple tapered fiber and the magnified top region. The triple tapered cone has an apex diameter of less than 10 nm. The values of d_1, d_2, α, β, and γ are 100 nm, 2 μm, 60°, 120°, and 60°, respectively.

We coated the triple tapered fiber with aluminum film having a thickness of 150 nm by vacuum evaporation. The aluminized probe had a throughput of 10^{-4} at 633 nm wavelength which is as high as that[3] of the single tapered probe[1] having a cone angle of 20° and a protruding tip[2] emerged from a gold film with a foot diameter of 100 nm. With a highly sensitive NOM employing the probe, we succeeded in obtaining a photoluminescence image of polysilanes excited by an Ar^+ laser with a wavelength of 350 nm.

In conclusion, we fabricated a triple tapered fiber probe for near-field optical microscopy. The probe had a shape of a triple tapered conical tip having angles of 60°, 120°, and 60° and an apex diameter of less than 10 nm. Employing the probe, we obtained a photoluminescence image of polysilanes excited by a laser with a wavelength of 350 nm.

The authors would like to thank T. Gozen (Mitsubishi Cable Ind.) for his discussion on an optical fiber.

*(also with) Tokyo Institute of Technology, Yokohama 226, JAPAN

1. S. Mononobe, *et al.*, EOS Topical Meeting **8**, 105 (1995).
2. S. Mononobe, *et al.*, Appl. Opt. **36**(7) (1997).
3. T. Saiki, *et al.*, Appl. Phys. Lett. **68**, 2612 (1996).
4. S. Mononobe, *et al.*, J. Lightwave Technol. **14**, 2231 (1996); ibid. **15**, 162 (1997).

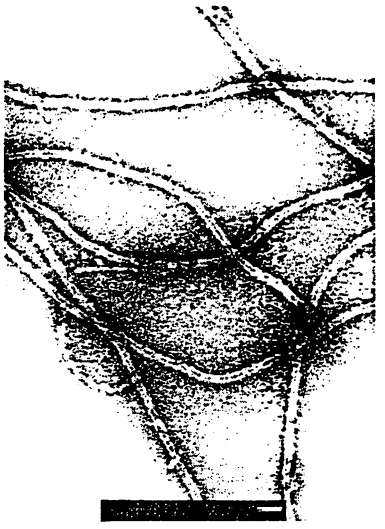

ThR2 Fig. 1. TEM image of a microtubule. (Small bar = 100 nm)

ThR2 1600

Application of the near-field optical microscope to the imaging of non-labelled microtubules and comparison with other techniques

J. D. White, A. Zvyagin,* A Uchida,** S. Hisanaga,** H. tatsumi,†‡ Y. Katayama,† M. Ohtsu,* *Photon Control Project, Kanagawa Academy of Science and Technology, 3-2-1 Sakado, Takatsu-ku, Kawasaki, Kanagawa 213, JAPAN*

Cellular structures have characteristic diameters ranging from 5 nm (DNA) to 1 μm (mitochondrion). A vast array of optical [differential interference contrast (DIC), dark field], and non-optical [TEM, atomic force] imaging techniques, each having their respective strengths and weaknesses, have proven useful in imaging these basic elements of God's work in the later periods of creation and in analyzing their interactions with each other. This paper will report on and compare these microscopes, focusing on the near-field optical (NOM), and the shear force microscope.

Microtubules (MTs), formed from the polymerization of tubulin, were chosen for this study due to their importance in the cytoskeleton (which maintains cell shape) and in the elongation of the neuronal process, as well as the existence of a number of unanswered questions regarding their assembly/disassembly and resulting dynamic instability. At these 30 nm diameters, micron long structures fall midway in the size range for intracellular structures, they are ideal for the comparison of imaging techniques.

Tubulin, along with the microtubule associated proteins (MAPs), was purified from porcine brains. 10 μM tubulin with MAPs, along with 0.5 nM of GTP in a PEM (0.1 M Pipes, pH 6.8, 1mM $MgCl_2$, 1mM EGTA) solution were incubated for 30 minutes to allow microtubule assembly and disassembly to reach a steady state condition.

After fixation with 1% glutaraldehyde, some solution was placed on a TEM grid and negatively stained with 2% uranyl acetate (Fig. 1). The remaining solution was dropped on a carefully cleaned parallel plate glass slide coated with polylysine. After a few minutes the excess solution was wisked away and observed with DIC, shear force (Fig. 2), and near-field optical (Fig. 3) microscopes.

ThR2 Fig. 2. Microtubules seen using a homemade shear force microscope. The scan area is 4 μm by 4 μm.

TEM provides the most detailed structural information (although what one sees is the Uranium shadow not the MT itself). In both DIC and dark field images MTs are clearly visible but appear to be about 300 nm in diameter as resolution is diffraction limited. In the NOM image (Fig. 3), the MT appears to have a diameter (FWHM) of 40 nm, slightly larger than the 25–30 nm diameter under TEM, which is to be expected due to the convolution of the finite sized probe tip with the MT. In this shear force image (Fig. 2), the MTs have an apparent diameter of 70 nm (height ~16 nm). In other shear force images, MTs have apparent diameters ranging from 50–90 nm, dependent primarily on the probe tip, slightly smaller than the 70–100 nm previously reported using SFM.[2]

NOM is seen to offer the advantages of sub-wavelength resolution while retaining the non-intrusive advantages of

ThR2 **Fig. 3.** NOM image of the microtubule seen in the lower left hand corner of Fig. 2 obtained using the same homemade microscope with a chemically etched fiber probe.[1] The scan area is 800 nm by 600 nm. The effect of aliasing, which makes this MT appear to be doubled, will be discussed at the conference.

an optical technique (i.e., no vacuum or staining needed). When coupled with shear force microscopy, NOM uniquely provides a cheap and attractive method of imaging subcellular structures with vertical as well as lateral resolution.

In summary, non-labelled MTs have been observed with a variety of microscopes and the images compared. An NOM image of microtubules as narrow as 40 nm (FWHM) was obtained for the first time.

*Interdisciplinary Graduate School of Science and Engineering, Tokyo Institute of Technology, Nagatsuta, Midori-ku, Yokohama, Kanagawa 226, JAPAN
**Laboratory of Cell and Developmental Biology, Faculty of Biosciences, Tokyo Institute of Technology, Nagatsuta, Midori-ku, Yokohama, Kanagawa 226, JAPAN
†Department of Autonomic Physiology, Medical Research Institute, Tokyo Medical and Dental University, 2-3-10 Kandasurugadai, Chiyodaku, Tokyo 101, JAPAN
‡"The Intelligence and its Origin," PRESTO Japan Science and Technology Corporation, JAPAN

1. S. Mononobe, *et al.*, Appl. Opt. **36** (1997).
2. W. Vater, *et al.*, J. Cell Sci. **108**, 1063–1069 (1995).

FJ2 1115

Direct observation of surface plasmon interference using a near-field optical microscope

Makoto Ashino, Yoh Yamamoto, Motoichi Ohtsu,* *Knagawa Academy of Science and Technology, KSP East, 3-2-1 Sakado, Takatsu-ku, Kawasaki 213, JAPAN*

Surface plasmon polaritons (SPPs), coupled modes of electromagnetic waves, and collective excitations of charges on conductive surfaces, is excellent in spatial coherence. The potential of SPPs for photonic devices has been widely discussed[1] with special interests in these sensitivity to chemical and physical changes of surfaces.[2] Our main focus is, however, to apply these highly coherence to nanometer scale novel devices. As the first step, we have tried to control SPPs on flat surfaces, and directly observed counter 2 SPPs interference on metal films on glass plates by means of near-field optical microscope (NOM) technique.

Figure 1 shows the experimental setup, where the sharpened tapered fiber probe with 50-100 nm aperture[3] was scanned over the surface keeping the constant distance at about 10 nm by shear-force feedback control. In Kretschmann configuration of ATR method,

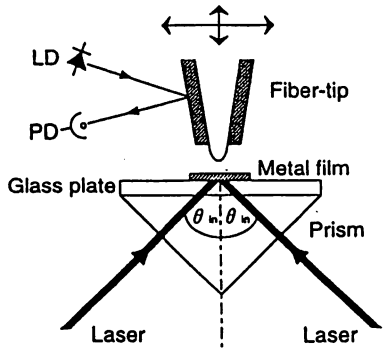

FJ2 Fig. 1. Experimental setup of counter 2 surface plasmons interference using a near-field optical microscope. Both of two incident laser beam were non-focused and *p*-polarized, and entered in the same opposite angle θ_{in} to the metal thin film.

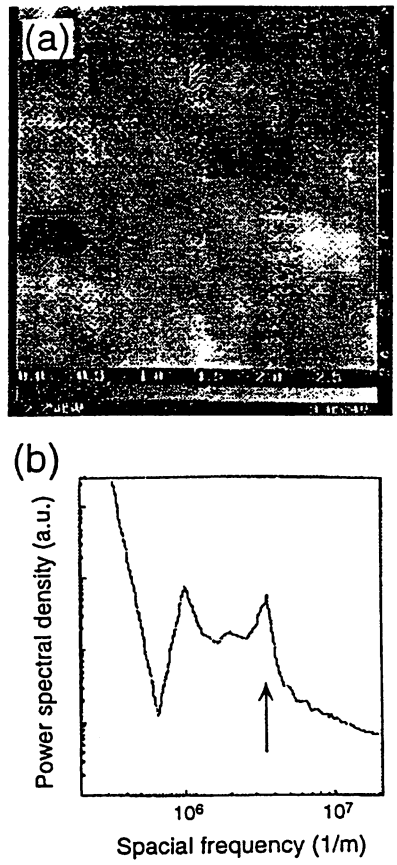

FJ2 Fig. 2. Observation of counter 2 surface plasmons interference on a gold thin film. (a) Near-field optical microscope image (scanned area 3.0 μm × 3.0 μm), (b) power spectrum of the former scanning image. The peak pointed by an arrow corresponds to the cycle of interference pattern of 2 surface plasmons.

counter 2 SPPs were exited over 48 nm thick gold film by incoming 2 p-polarized He-Ne laser lights (~1 mw, 632.8 nm) from opposite sites at the same angle. Photons picked up by scanning probe were transferred through the optical fiber to a photomultiplier tube, and 2D distributed image shown in Fig. 2(a) was obtained. The 2 SPPs propagated in transverse opposite directions. The longitudinal lines present spatial variation of near-field caused by those interferences. Fig. 2(b) is the result of power spectral analysis of Fig. 2(a). The peak pointed out by an arrow is attributed to the 277 nm-pitch interference corrugation, and it corresponds to half the wave length of SPPs because it is approximately equal to that of incident light from the prism site. The obtained wave length ~554 nm, which is much shorter than the theoretical value (~605 nm),[4] may depend on the condition of its surface and interface. This result shows the possibility of realization of the near-field spatial variation with less than 100 nm-pitch by the excitation of SPPs with higher energy.

The interference of SPPs also occurs by reflection at the edge. We present a clear NOM image of SPPs' interference

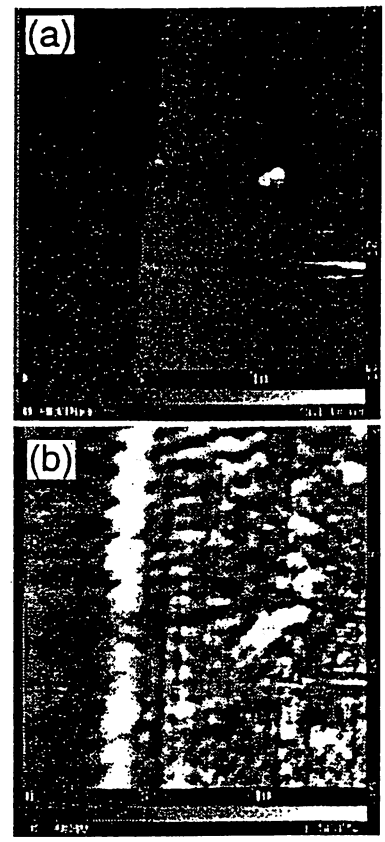

FJ2 Fig. 3. Observation of interference between incident and reflective surface plasmons at the edge of a silver thin film. (a) Shear force image of the silver film edge (scanned area 15 μm × 15 μm), (b) near-field optical microscope image of the same area.

near a 50 nm thick silver film's edge made by e-beam lithography. Only one 632.8 nm light excited a SPP near the edge, whose topographic image is shown in Fig. 3(a). The SPPs propagated perpendicularly to the edge from right hand, and in NOM image [Fig. 3(b)] parallel lines show the interference fringe. Since the reflectivity of SPPs at the edge is not so high, the visibility of that in Fig. 3(b) is lower than in Fig. 2(a). However, the suitable selection of a reflector might make it possible to attain the high reflectivity of SPPs and to confine those in smaller areas than the light wave length.

*(also with) Tokyo Institute of Technology, 4259, Nagatsuta-cho, Midori-ku, Yokohama 226, JAPAN

1. V. M. Agranovich, D. L. Mills, eds., Surface polaritons North-Holland, Amsterdam (1982).
2. H. Knobloch, *et al.*, Appl. Phys. Lett. 69, 2336 (1996); I. I. Smolyaninov *et al.*, Phys. Rev. Lett. 77, 3877 (1996).
3. S. Mononobe, *et al.*, Appl. Opt. 36(7) (1997).
4. H. Raether, Surface Plasmons on Smooth and Rough Surface and on Grating, Springer-Verlag, Berlin (1988).

FV2 1600

Near-field optical microscope image formation: theoretical and experimental study

A. Zvyagin, J. D. White,* M. Ohtsu,*
Interdisciplinary Graduate School of Science and Engineering, Tokyo Institute of Technology, Nagatsuta, Midori-ku, Yokohama, Kanagawa 226, JAPAN

The near-field optical microscope (NOM) is a device utilizing a scanning technique which exploits such a unique property of the optical near-field as the spatial localization. Due to its ability to achieve subwavelength resolution without harming a sample, it has found application in such diverse fields as biology, material science and optical storage. The rapid growth in applications has been accompanied by much theoretical work aiming to clarify the image formation mechanism. This paper reports on the first successful quantitative comparison between theory and experiment.

The NOM can be operated in a number of different modes. In the collection mode NOM (*c*-mode NOM), a nanometric sample on the flat substrate is illuminated under the TIR condition. A sharpened fiber tip, immersed in this highly localized optical field, acts as a probe. By coating the fiber by metal, except at the apex, most far-field light is excluded.[1] The image is created by detecting the optical field intensity as the fiber is moved laterally.

We have developed a macroscopic classical theory of the *c*-mode NOM which models the optical near-field over the sample as a spetrum of plane, mostly evanescent waves and the fiber tip apex as a nanometer sized dielectric sphere.[2] This model predicts that the probe and the sample interact weakly and that the intensity picked up by the probe is proportional to the near-field intensity. By applying the optical extinction theorem, the near-field intensity over the sample has been calculated.

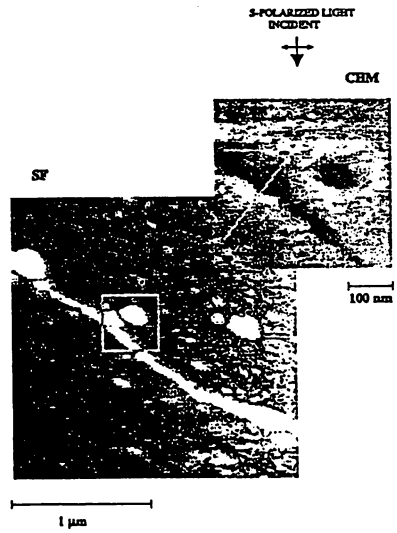

FV2 Fig. 1. Image of microtubule (long) and a protein aggregate (round). (SF: Topography of the 2 μm × 2 μm scan area obtained using shear force microscopy; CHM: Magnified optical image of the highlighted region taken under constant height mode. Note the inversion of the optical image and the edge enhancement effect.)

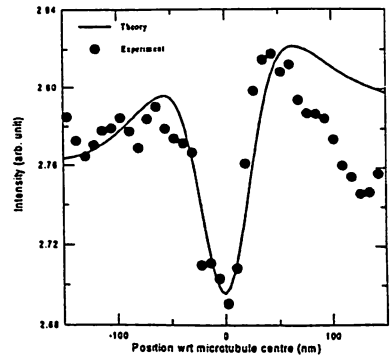

FV2 Fig. 2. Comparison of light intensity observed in passing over a microtubule in constant height mode with theoretical calculations based on the optical extinction theory. The experimental data is taken along the line shown in Fig. 1 (CHM).

In order to verify these theoretical predictions, experimental observations were also carried out. A biological specimen, microtubule (MT), was chosen due to its well identified nanometric size (25–30 nm in diameter and microns in length), and importance, biologically. In addition, it is convenient for the investigation of directional and polarization effects as the direction of illumination can be varied with respect to the axis of the MT.

For the initial scan of an area, we employed the shear-force technique to maintain *constant separation* between the fiber tip and the sample (~5 nm), in order to obtain a topographical image of the sample (Fig. 1, SF). Areas of interest were then investigated more closely and optical images taken under at a *constant height* of approximately 30 nm (Fig. 1, CHM), using *s*-polarized incident light (LD, 680 nm). The illumination direction is shown in Fig. 1. Relative to the topography, the optical image appears inverted and exhibits the edge enhancement effect in agreement with theory. The results of a more careful comparison is shown in Fig. 2 where the observed light intensity across the microtubule compared with the results of the optical extinction theory based calculations[2] in which the MT is represented by a 30 nm diameter half-cylinder. For the first time, good agreement between calculations and the experiment is seen for both the MT diameter and in the observed asymmetry of the edge effect (intensity is lower in the direction closest to the light source).

Photon Control Project, Kanagawa Academy of Science and Technology, 3-2-1 Sakado, Takatsu-ku, Kawasaki, Kanagawa 213, JAPAN

1. S. Mononobe, *et al.*, Appl. Opt. 36 (1997).
2. A. Zvyagin, M. Ohtsu, Opt. Comm. 133, 328 (1997).
3. B. Hecht, *et al.*, J. Appl. Phys. (to be published).

4. R. Uma Maheswari, S. Mononobe, M. Ohtsu, Appl. Opt. 35, 34 (1996).

FV3 1615

Near field optical imaging of an atomic sapphire step and nanometric lithium niobate crystals under the absence of shear force feedback

R. Uma Maheswari, S. Takehara,* S. Mononobe, G. H. Lee,** M. Yoshimoto,** H. Koinuma,** M. Ohtsu,* *Kanagawa Academy of Science and Technology, KSP East 408, 3-2-1, Sakado, Takatsu Ku, Kawasaki, Kanagawa Ken, JAPAN*

Near-field microscopy (NOM) has been getting a lot of attention for its application over a variety of fields such as biological imaging, spectroscopic diagnostics of novel semiconductor devices, etc.[1] In such applications, the resolution capability of the NOM has to be improved to the nanometer level. In this study, we use collection mode NOM in which the sample is illuminated under total internal reflection and the evanescent field generated on the sample surface is scattered by a nanometric probe. For characterizing the vertical resolution, a sapphire staircase consisting of monoatomic layers grown epitaxially has been used. The height of the step as measured by atomic force microscope (AFM) is 1 to 4 nm and width of step is 250 nm. In order to characterize lateral resolution, nanocrystals of $LiNbO_3$ grown on the sapphire staircase have been used. The average size of a $LiNbO_3$ nanocrystal based on AFM is 80 × 40 nm^2.

Figure 1 shows the experimental system of a c-mode NOM and a micrograph of the nanometric probe used. Light from LD (685 nm) is made to incident the prism at the angle of total internal reflection. Sapphire sample is mounted on the prism surface with a sandwich of index

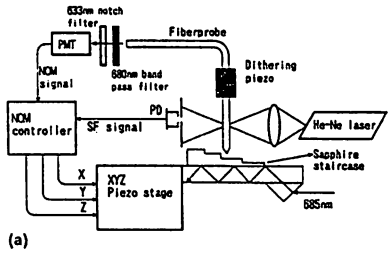

(a)

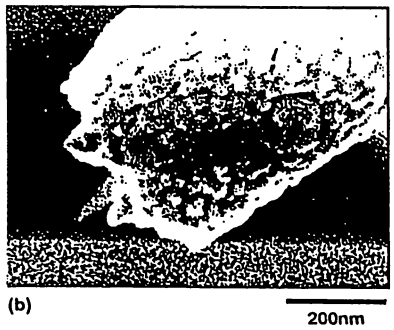

(b) 200nm

FV3 Fig. 1. Schematic diagram of the collection mode NOM (a) with the nanometric protruding tip (b).

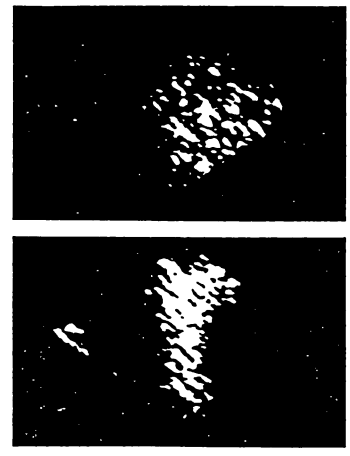

(a)

(b)

FV3 Fig. 2. Constant height images of a single step of the atomic sapphire staircase under a probe height of (a) ~100 nm and (b) ~5 nm.

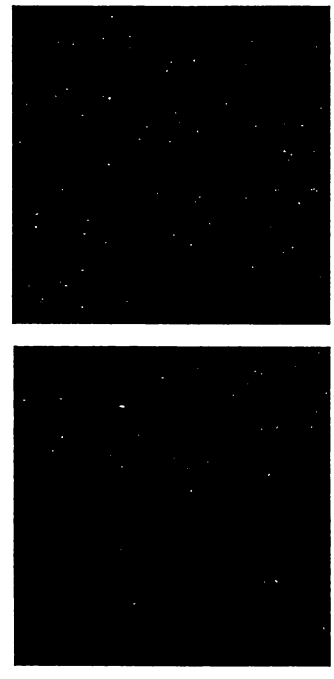

(a)

(b)

FV3 Fig. 3. Constant intensity image of the nanocrystals of $LiNbO_3$ on sapphire surface under a sample-probe separation of ~10 nm under the polarization of (a) s- and (b) p-.

matching oil. The evanescent field generated on the sample surface is scattered by a probe having a nanometric dielectric protrusion.[2] Here, the shear force feedback for sample-probe separation control[3,4] was not used to avoid the effect of artifact and only its detection scheme has been included to calibrate sample-probe separation.

Images have been obtained under constant intensity mode by keeping the evanescent intensity constant and constant height mode by keeping the height of the probe constant. Figure 2(a) and (b) show respectively, the images obtained under constant height mode approximately at a height of 100 nm and 5 nm. The step could be visualized only by approaching the probe as close to the step height. This dependence of contrast is due to the intrinsic feature of size dependent localization of the optical near field.[5] Figure 3 shows the image of nanocrystals of $LiNbO_3$ grown on the sapphire surface obtained almost at a separation of around 10 nm. The smallest particle has got a lateral dimension of 30 nm × 40 nm indicating the very high lateral and vertical resolution capability of our NOM without shear force feedback for the first time.

*Interdisciplinary Graduate School of Science and Engineering, Tokyo Institute of Technology, 4259 Nagatsuta, Midori ku, Yokohama, Kanagawa 226, JAPAN
**Materials and Structure Laboratories, Tokyo Institute of Technology, 4259 Nagatsuta, Midori ku, Yokohama, Kanagawa 226, JAPAN

1. M. Ohtsu, J. Lightwave Technology 13, 2000 (1995).
2. S. Mononobe, *et al.*, Appl. Opt. 36(3) (1997).
3. B. Hecht, *et al.*, J. Appl. Phys. 11 (1996).
4. R. Uma Maheswari, *et al.*, Appl. Opt. 35, 6740 (1996).
5. T. Saiki, *et al.*, Opt. Lett. 21, 674 (1996).

Record of the 16th Electronic Materials Symposium, Minoo, July 9-11,1997

Diagnosing Electronic/Photonic Devices and Materials by Near-field Optical Technique

Motoichi OHTSU

Graduate School, Tokyo Institute of Technology
4259 Nagatsuta, Midori-ku, Yokohama 226, Japan
(also with Kanagawa Academy of Science and Technology,
KSP East Rm. 408, 3-2-1 Sakado, Takatsu-ku, Kawasaki 213, Japan)

A single-particle spectroscopy has been successfully realized owing to the development of new type of microscope and to the progress of sample fabrication technique. Near-field optical microscope(NOM)[1] is one of the powerful tools to obtain the individual spectra of inhomogeneously broadened systems. Since a fiber probe of NOM also works as a tip of the atomic-force microscope, one can acquire an accurate correspondence between the local optical response and the geometrical structure of the sample. We demonstrate here the spatially resolved photoluminescence (PL) spectroscopy of InGaAs quantum dots (QD's) and polisilanes(PS's). Experiments on diagnosing other electronic/photonic devices and materials are also reviewed.

(1) The $In_{0.5}Ga_{0.5}As$ self-assembled QD's were grown (Stranski-Krastanow mode) on (100) GaAs substrate by gas-source molecular beam epitaxy with a density of 2 x 10^{10} dots/cm^2[2]. Typical dot diameter of around 30 nm and height of 15 nm were observed with atomic force microscope before the growth of cap layers of 180 nm thick. For the near-field optical excitation, QD sample on a scanning piezo-tube was illuminated with He-Ne laser light (λ =633 nm) through a small aperture of a fiber probe. For the collection of PL signal, the same aperture was used, which was indispensable to avoid a decline of a spatial resolution due to the effect of an excited carrier diffusion. The collected light was focused into a 50 -cm monochromator and detected by a cooled photomultiplier tube using photon counting technique. Shear-force feedback was employed to control a tip-sample distance of less than 10 nm. The temperature of the sample was kept at 5K in a cryostat. Figure 1(a) shows a typical PL spectrum of inhomogeneously broadened QD's obtained by positioning the probe tip of 2 μ m above the sample surface and by detecting the PL signal from a large number of QD's. In the near-field region, on the other hand, sharp PL lines with the linewidths of 1 - 2 meV are clearly seen in Fig.1(b). Since the measurement was performed in the weak excitation region, only the PL lines from the ground states are observed. Through the wavelength-selected imaging, we also obtained the spatial distribution of the QD's having the same PL wavelengths of 923 nm and 928 nm as shown in Figs. 2(a) and (b). The smallest and the average size of the spot images, which correspond to the collection area of PL signal through the

aperture, are 220 nm and 290 nm, respectively[Fig.2(c)]. The number of the dots in this collection area is estimated as 15 from the dot density of this sample. This value is in good agreement with the number of main peaks observed in the spectrum of Fig.1(b). Thus, we conclude that real single dot spectroscopy and imaging with λ /5 resolution is realized using NOM measurement, which can be widely applied to the single particle observation of the inhomogeneously broadened systems.

(2) Polisilanes(PS's) are s-conjugated polymers, which can be regarded as ultimate quantum wires made of Si. PS's are expected to be applied to the ultraviolet light-emitting device due to their wide electronic band gap and the high quantum efficiency. The optical properties of PS's can be controlled by changing the conformation of the Si backbones and the shape of molecules. Here, NOM enables us to investigate the optical response of the single PS quantum wire corresponding to its geometrical structure. Figure 3 shows a schematic of an experimental configuration. A dilute solution of polydihexylsilanes(PDHS's) with trans-planar-type conformation is prepared as a sample. At room temperature, PDHS has the absorption and PL peak at the wavelength of 370 nm and 380 nm, respectively. For the optical excitation, 351 nm line of Ar laser is coupled into the fiber probe. The PS molecules dispersed on the silica substrate are illuminated by the near-field light through the aperture of the tip. PL from the excited PS molecules is collected by an objective lens or spherical lens. In two-dimensional optical imaging, the collected signal is detected by photomultiplier tube through the bandpass filters. A monochromator with cooled CCD is employed for the spectroscopic analysis of the PL signal. In order to achieve a high sensitivity and high resolution simultaneously, the shape of the fiber tip is tailored using a chemical etching technique[3]. By shortening the length of the optical loss region due to the evanescent propagation and metal-cladding absorption, we have successfully obtained high transmission coefficient[4]. Moreover, the protrusion part at the apex functions as the localized light source for the super-resolution imaging. Figure 4 shows a schematic and scanning electron microscope images of the apex part of the chemically etched probe. In Fig.5, PL spectra from an aggregate structure of PS's are acquired every 3 second by CCD camera using a rather large aperture with 100-nm excitation. The peak wavelength of 380 nm and spectral width of 9 nm are obtained. These values are not so different from the result of the far-field spectroscopy of PS thin film. Under the high-power excitation at room temperature, the spectrum is rapidly bleached in some tens seconds. To avoid this photobleaching, the excitation power should be as low as possible. PL image of a thin aggregate part is also obtained under the low excitation condition (- 0.5 nW) as show in Fig.6. From the shear-force image, the thickness of the aggregate is evaluated as about 20 nm. A clear contrast and high resolution PL imaging is attained. The maximum photocounts of 400 cps is in good

agreement with numerical estimation using parameters of absorption coefficients, quantum efficiency and so on. For the realization of single PS molecule spectroscopy in ultraviolet region, the improvement of signal detection efficiency and the measurement in low-temperature circumstances are in progress. The modification of the emission properties due to the tip-sample interaction will be discussed in terms of quantum optics[5].

(3) As other promising application of NOM to diagnosing diagnosing electronic/photonic devices and materials, we have carried out spatially resolved Raman spectroscopy of Si, and near-field optically induced resistance change in the Al wires on a Si integrated circuit for searching a sub-wavelength void in the Al wires.

Acknowledgments; M. Ohtsu thanks Drs.,T. Saiki(KAST), K. Nishi(NEC), S. Koshihara(TIT) for their collaborations.

References

[1] M. Ohtsu, J. Lightwave Technol., **13**, 1200 (1995)
[2] K. Nishi, et.al., Appl. Phys., **80**, 3466 (1996)
[3] S. Mononobe and M. Ohtsu, J. Lightwave Technol., **14**, 2231 (1996)
[4] T. Saiki et.al., Appl. Phys. Lett., **68**, 2612 (1996)
[5] T. Saiki, et.al., Opt. Lett., **21**, 674(1996)

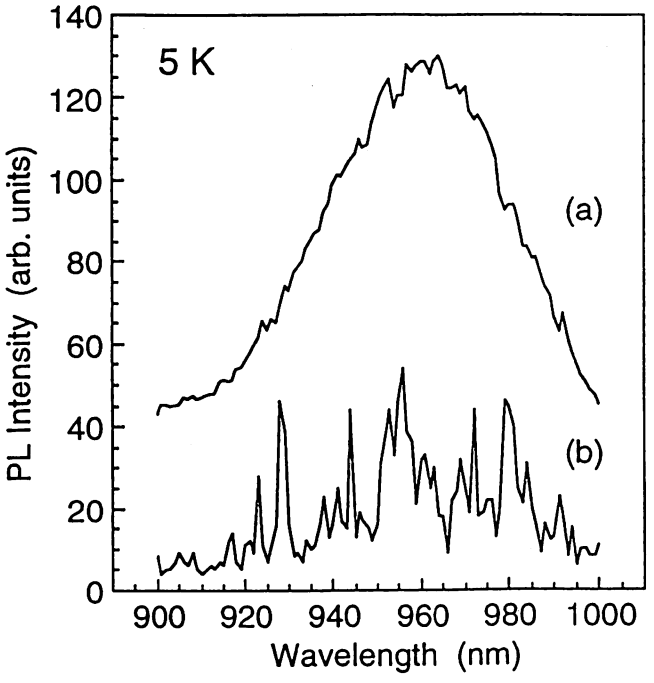

Fig. 1
PL spectra of QD's detected
(a) in the far-field region and
(b) in the near-field region.

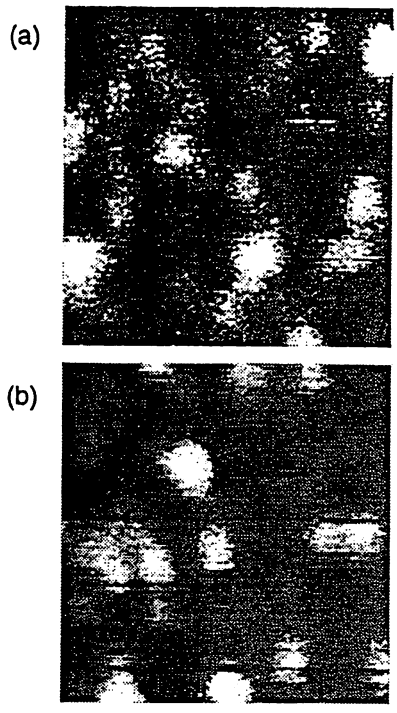

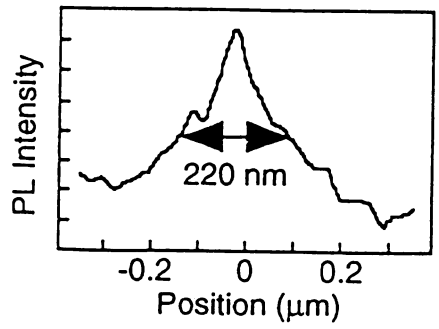

Fig.2
Wavelength-selected PL images of single QD's with the emission wavelengths of (a) 923 nm and (b) 928 nm. The spectral bandwidth of the detection is 1 nm. The image size is 3 x 3 μ m^2. (c) Cross-section of a single spot image.

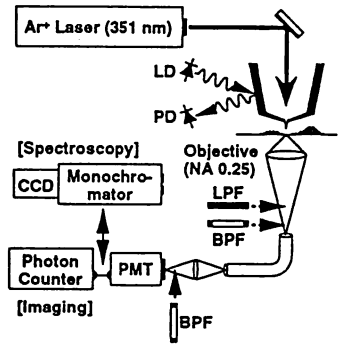

Fig. 3
Experimental setup of PL spectroscopy of PS's.

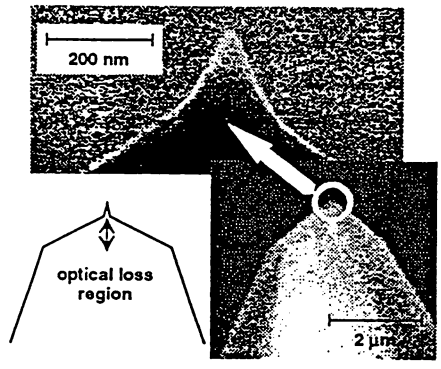

Fig. 4
Triple-tapered probe.

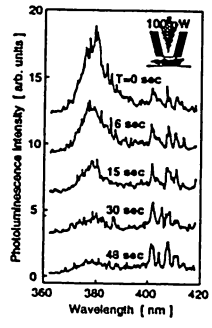

Fig.5
PL spectra of PS's.

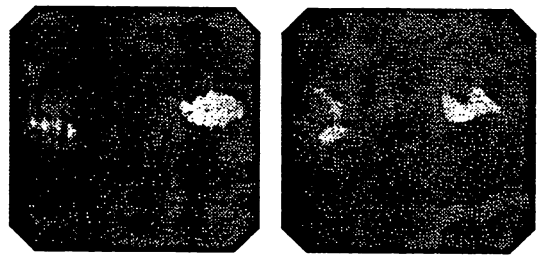

Fig.6
Shear-force image(a) and PL image(b).

8A-1-1

NEAR FIELD OPTICAL TECHNIQUES TO NANO/ATOM PHOTONIC

Motoichi OHTSU
Graduate School, Tokyo Institute of Technology
4259 Nagatsuta, Midori-ku, Yokohama 226, Japan
(also with Kanagawa Academy of Science and Technology,
KSP East Rm. 408, 3-2-1 Sakado, Takatsu-ku, Kawasaki 213, Japan)

Near-field optical microscope(NOM)[1] is one of the powerful tools to obtain the individual spectra of inhomogeneously broadened systems. Related near field optical techniques can also be used for microprocesses and nanotechnology. We demonstrate results of our recent works listed below.

(1) Spatially resolved photoluminescence (PL) spectroscopy of InGaAs quantum dots (QD's)[2] at 5K:

Sharp PL lines with the linewidths of 1 - 2 meV are clearly seen. Since the measurement was performed in the weak excitation region, only the PL lines from the ground states are observed. Through the wavelength-selected imaging, we also obtained the spatial distribution of the QD's. The smallest and the average size of the spot images, which correspond to the collection area of PL signal through the aperture, are 220 nm and 290 nm, respectively. The number of the dots in this collection area is estimated as 15 from the dot density of this sample. This value is in good agreement with the number of main peaks observed in the spectrum. Thus, we conclude that real single dot spectroscopy and imaging with $\lambda/5$ resolution is realized using NOM measurement.

(2) Spatially resolved PL spectroscopy of s-conjugated polymers of polisilanes(PS's) quantum wire at ultraviolet region:

In order to achieve a high sensitivity and high resolution simultaneously, the shape of the fiber tip is tailored using a chemical etching technique[3,4]. Moreover, the protrusion part at the apex functions as the localized light source for the super-resolution imaging. The thickness of the aggregate is evaluated as about 20 nm. A clear contrast and high resolution PL imaging is attained. The maximum photocounts of 400 cps is in good agreement with numerical estimation using parameters of absorption coefficients, quantum efficiency and so on. For the realization of single PS molecule spectroscopy in ultraviolet region,

the improvement of signal detection efficiency and the measurement in low-temperature circumstances are in progress. The modification of the emission properties due to the tip-sample interaction will be discussed in terms of quantum optics[5].

(3) Ultrahigh density optical storage/read out by near-field optical technology:

In order to realize this future memory system, we have discussed essential problems to be solved. From this discussion, we have proposed a Si planar apertured probe array for high throughput and compatible with high scan speed with nanometric gap control. This is an application of microprocesses and nanotechnology, which can be called as nano-photonics.

(4) Manipulating gaseous atoms by near-field optics :

Toward the novel technology, being called as atom photonics, atom manipulation and guidance by optical near-field on a hollow fiber was carried out[6]. Possibility of atom-level deposition was also discussed.

Acknowledgments

M. Ohtsu thanks Drs.,T. Saiki, Ito (KAST), K. Nishi(NEC), S. Koshihara(TIT), and Prof. W. Jhe(SNU) for their collaborations.

References

[1] M. Ohtsu, J. Lightwave Technol., **13**, 1200 (1995)
[2] K. Nishi, et.al., Appl. Phys., **80**, 3466 (1996)
[3] S. Mononobe and M. Ohtsu, J. Lightwave Technol., **14**, 2231 (1996)
[4] T. Saiki et.al., Appl. Phys. Lett., **68**, 2612 (1996)
[5] T. Saiki, et.al., Opt. Lett., **21**, 674(1996)
[6] H. Ito, et.al., Phys. Rev. Lett., **76,** 4500 (1996)

Near-field Optical Technology for Nano/Atom Photonics

M. Ohtsu

Interdisciplinary Graduate School of Science and Engineering, Tokyo Institute of Technology, 4259 Nagatsuta, Midori-ku, Yokohama 226, JAPAN
(also with Kanagawa Academy of Science and Technology, KSP-East, Rm408, 3-2-1 Sakado, Takatsu-ku, Kawasaki 213, JAPAN)

In the workshop, requirements on near-field probe fabrication technology were presented to realize a new field of nano/atom photonics. As an example, fabrication of planar probe array for high density optical storage was demonstrated and related problems were presented for nano photonics. On atom photonics, progress of atom guidance by optical near-field was reviewed to realize an atomic-level deposition in forming the crystal surface. Among these topics, this post-workshop report will focus on technical problems that have to be solved for realizing high density optical memory by optical near-field.

Experiments on the heat-mode[1] and the photo-mode[2] write/read-out(W/R) by optical near-field have revealed 1Tb/inch^2-class high density optical memory, where the limit on density is determined by the size of the optical near-field probe tip. However, there are a lot of problems to be solved to realize a practical optical memory, being compatible with the future commercial products which can be mass produced by industry. The
problems are categorized to four. They are:

[I] Software

(1)What is the expected application software. For example, does it provide the information on personal health care, library data base, motion picture, weather forecasting, and so on? The form of the memory(, e.g., read-only, erasable, etc.,) strongly depends on these applications.

[II] System

(1)Fast driving mechanism should be developed, e.g., by following a flying head technology of hard disk drive.

(2)Technique of precisely controlling the gap between the W/R head and the storage medium should be developed. The gap should be as narrow as 10 - 50nm.

(3) Accurate tracking or tracking-less drive should be developed to scan the W/R head.

(4)In the case of the removable memory, the W/R head should also be removable with the disk. In this case, a low-cost W/R head with a reliable packaging should be developed, e.g., using a LED as a light source instead of using a LD.

(5)Ultrasensitive photon detection technique should be developed.

[III] Devices

(1)A probe with high throughput should be developed in order to realize a fast driving head.

(2) Interface devices connecting light source, probe, and detector should be developed.

(3) Flying head, actuator, and so on, should be developed for fast driven and scanning.

[IV] Storage media

(1)It is essential to search for sensitive interaction mechanisms between the nano-particle and the optical near-field.

(2) Novel media with small grain/domain size should be found.

(3) Heat diffusion mechanism in nanometric volume should be studied.

(4) An ultra-thin protection layer for storage media should be developed.

Among the problems listed above, we have considered the problems on the devices. Since we have developed a precise and reproducible probe fabrication technique based on selective chemical etching of a fiber[3,4], the detected light power by our probe, originated due to reflection from the surface of the storage medium, has become as high as 1 μ W. In this case, the data transmission rate for read-out, limited by the shot noise associated with the detected photon number, is estimated to be as high as or even higher than 100 Mb/s assuming that the contrast of the memory is 0.3 , the quantum efficiency of the photo-detector is 0.3, bit-error-rate is 10^{-9} (@PCM mode), and the optical frequency is 600 THz(Fig.1)

It is promising to have such a high data transmission rate in order to realize a fast read-out. However, the problem is how to scan the read-out head. If one uses a single probe tip to read-out the memory with the pit spacing of 10 nm, the scanning speed has to be as high as 1 m/s to realize the 100Mb/s data transmission rate. On the other hand, if the two-dimensional probe array with 100 x 100 elements is used, the scanning speed can be

reduced to 100 μ m/s, which can be easily realized by a conventional driving technology.

However, probe array with two-dimensional sharpened tip elements cannot be practical because the fluctuations in the tip lengths cannot be reduced to 10 nm by the existing micro/nano fabrication process. In order to avoid this difficulty, we have proposed a planar apertured probe array fabricated by a silicon planar process(Fig.2). Advantages of this probe array are; (1) suitable for flying head technique of the hard disk drive, (2) precise gap control is possible by following the hard disk technique, (3) parallel information processing is possible, and more advantageously, the tracking-less read-out is possible[5], and (4) compatible with integration of a slab waveguide and an array of photo-detectors.

Fabrication process includes oxidation, photolithography, removing SiO_2, anisotropic etching to form V-grooves and windows, and deposition of Au film. Figure 3 shows a SEM image of the fabricated probe array. Among the fabricated several arrays, the smallest aperture size was 80 nm[6]. It should be noted that the fluctuations of the size of each aperture in the array is not essential for tracking-less read-out. Instead, the separation between the adjacent aperture must be regulated, which can be assured by carefully designing a mask pattern for the photolithography in the present fabrication process.

Spatial distribution of the optical near-field intensity generated on the aperture was measured by scanning a conventional sharp fiber probe tip on the planar aperture. As is shown by Fig. 4, a clear Gaussian profile of distribution was observed, from which a reliable operation of the probe array was confirmed. It was also confirmed semi-quantitatively that the throughput of this aperture is as high as, or even higher than that of our high throughput probe[7]. For further increase of the throughput, an array using a ball lens was proposed and fabricated (Fig.5) [5].

As a future outlook, it is expected that the conventional technology for optical disk and hard disk will be combined with the near-field optical technology to realize a 1Tb/inch^2-class high density near-field optical memory. This is because the driving mechanism is similar to that for the hard disk memory and a large amount of technology/know-how have been accumulated for conventional optical disk.

In summary, problems on software, system, devices, and storage

media were presented to realize a high density near-field optical memory. Shot noise-limited data transmission rate, as high as 100 Mb/s, was estimated. Planar apertured probe array was proposed for tracking-less and high-speed read-out. Fabrication of Si planar apertured probe array with the smallest aperture size of 80 nm was demonstrated. Possibility of increasing the throughput via the use of a ball lens was also demonstrated

We acknowledge Prof. K. Tsutui and Dr. M. Kourogi(TIT), Drs. S. Mononobe and R. Uma Maheswari (KAST), Drs. M.B.Lee and N. Atoda (NAIR) for their collaborations and discussions.

[References]

[1] E. Betzig, et.al., Appl. Phys. Lett., vol.61 (1992) p.142

[2] S.Jiang, et.al. Opt. Commun., vol.106 (1994) p.173

[3] M. Ohtsu, J. Lightwave Technol., vol.13 (1995) p.1200

[4] S. Mononobe, et.al., J. Lightwave Technol., vol.14 (1996) p.2231

[5] M. Kougori, et.al., Tech. Digest, The 6th Workshop on Near-field Optics, July 3, 1997, Osaka, Japan, p.73(in Japanese)

[6] M.B. Lee, et.al., Technical Digest, The Pacific Rim Conference on Lasers and Electro-Optics (CLEO/PR'97), July 14-18, Makuhari, Japan, paper number WL2, p.91

[7] T. Saiki,et.al., Appl. Phys. Lett., vol.68 (1996) p.2612

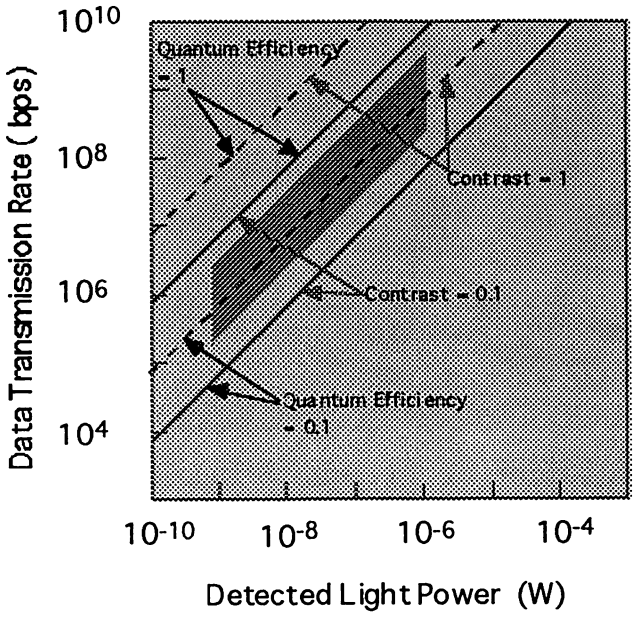

Fig.1
Relation between the detected light power and the data transmission rate, which is limited by the shot noise. Shadowed area represents that the relation between power and rate to be realized by the present experimental condition. Contrast: ratio between the light reflected from the stored and non-stored part of the surface of the storage medium.

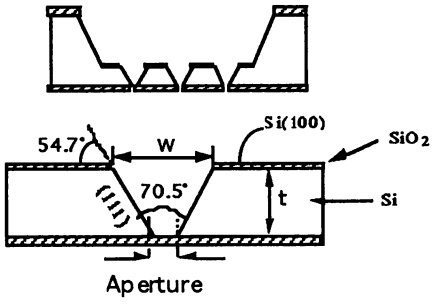

Fig.2
Cross sectional profile of a planar apertured probe array.

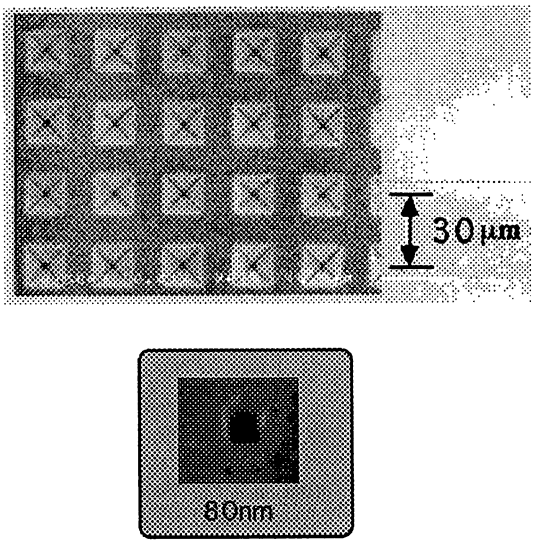

Fig.3
SEM image of the fabricated planar apertured probe array(upper) and that of the smallest size aperture(lower).

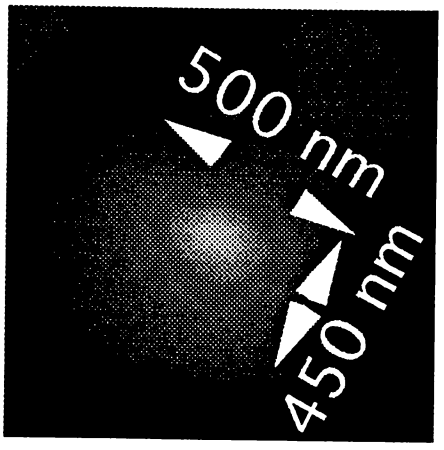

Fig.4
Measured spatial distribution of the optical near-field intensity on the aperture .

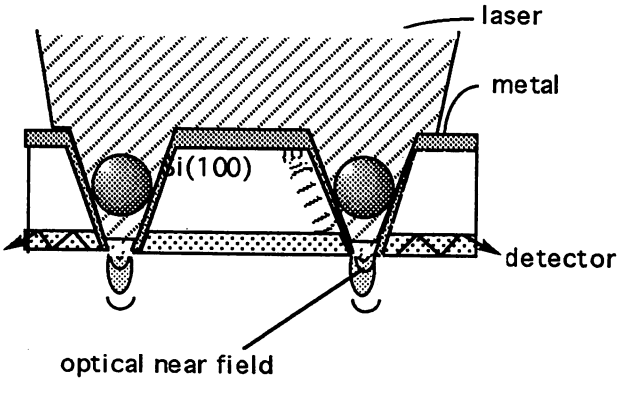

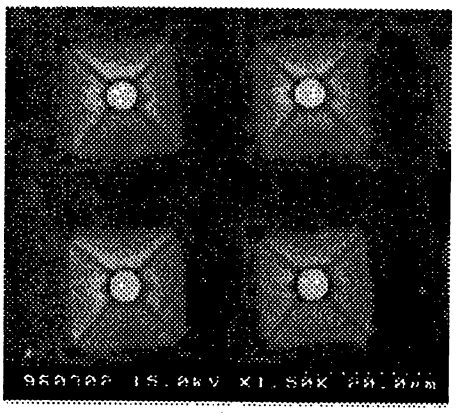

Fig.5
A schematic of the cross sectional profile of a planar apertured probe array with ball lenses and the SEM image of the fabricated array.

Application of the near field optical microscope to the imaging of non-labelled microtubules

J. D. White*, A. Zvyagin**, M. Ohtsu*,**

*Photon Control Project, Kanagawa Academy of Science and Technology,
3-2-1 Sakado, Takatsu-ku, Kawasaki, 213 Japan
Tel: 81-44-819-2071; Fax: 81-44-819-2072; Email: whitejd@ksp.or.jp

**Interdisciplinary Graduate School of Science and Engineering,
Tokyo Institute of Technology, Nagatsuta, Yokohama, 226 Japan
Tel: 81-44-924-5476; Fax: 81-45-921-1204; Email: zvyagin@ae.titech.jp

Cellular structures have characteristic diameters ranging from 5 nm (DNA) to 1 μm (mitochondrion). A vast array of optical [differential interference contrast (DIC), dark field], and non-optical [TEM, atomic force] imaging techniques, each having their respective strengths and weaknesses, have proven useful in imaging these basic elements of God's work in the later periods of creation and in analysing their interactions with each other. We report on and compare these microscopes, focusing on the near-field optical (NOM) [1], and shear force microscopes.

Microtubules (MTs), formed from the polymerisation of tubulin, were chosen for this study due to their importance in the cytoskeleton and in the elongation of the neuronal process. As these 30 nm diameter, micron long structures fall midway in the size range for intracellular structures, they are ideal for the comparison of imaging techniques.

Tubulin along with microtubule associated proteins (MAPs) was purified from porcine brains. After 30 minutes of incubation (to allow microtubule assembly and disassembly to reach a steady state condition), the microtubules were fixed with glutaraldehyde. Some solution was placed on a TEM grid and negatively stained with uranyl acetate. The remaining solution was dropped on a leaned, polylysine coated, parallel plate glass slide. After wicking away the excess, these samples were observed with DIC, shear force, and NOM microscopes.

TEM provides the most detailed structural information (although what one sees is the Uranium shadow not the MT itself). In both DIC and dark field images MTs are clearly visible but appear to be about 300 nm in diameter as resolution is diffraction limited. In the NOM image, the MT appears to has a diameter (FWHM) of 40 nm, slightly larger than the 25-30 nm diameter under TEM (due to the convolution of the finite sized probe tip with the MT). In shear force images, the MTs have an apparent diameters of 50-90 nm (height ~16 nm). The exact size depends on the probe.

NOM is seen to offer the advantages of sub-wavelength resolution while retaining the non-intrusive advantages of an optical technique (i.e. no vacuum or staining needed). When coupled with shear force microscopy, NOM uniquely provides a cheap and attractive method of imaging subcellular structures with vertical as well as lateral resolution. Operation under liquid conditions has recently been shown to be feasible [2].

Acknowledgements
We wish to thank A. Uchida and Dr. S. Hisanaga of Tokyo Institute of Technology for their assistance in the preparation of tubulin. We also extend our thanks to Dr. H. Tatsumi of Tokyo Medical and Dental University for many helpful discussions.

1. Motoichi Ohtsu, J. Light. Tech. **13**, 1200-1221 (1995).
2. R. Uma Maheswari et al., Optical Review **3**, 463-467 (1996).

NEAR-FIELD ULTRAVIOLET PHOTOLUMINESCENCE STUDY OF ONE-DIMENSIONAL ELECTRONIC STRUCTURES OF POLISILANES

M. Ohtsu[1,2], T. Saiki[2], S. Mononobe[2], S. Koshihara[1], K. Ebihara[1], K. Obata[3], T. Miyazawa[3], M. Kira[3,4], M. Yoshimoto[1], T. Maeda[1], T. Ohnishi[1], K. Yoshida[1], and H. Koinuma[1]

1) Tokyo Institute of Technology, 4259 Nagatsuta, Midori, Yokohama 226, Japan,
2) Kanagawa Academy of Science and Technology, 3) RIKEN, 4) Tohoku Univ.

Recently, a single-particle spectroscopy has been successfully realized owing to the development of new type of microscopes and to the progress of sample fabrication technique. Near-field optical microscope (NOM) [1] is one of the powerful tools to obtain the individual spectra of inhomogeneously broadened systems, such as single molecules and self-assembled quantum dots. Since a fiber probe of NOM also works as a tip of the atomic-force microscope, we can acquire an accurate correspondence between the local optical response and the geometrical structure of the sample.

Polysilanes (PS's) are s-conjugated polymers, which can be regarded as ultimate quantum wires made of Si. PS's are expected to be applied to the ultraviolet light-emitting device due to their wide electronic band gap and the high quantum efficiency. The optical properties of PS's can be controlled by changing the conformation of the Si backbones and the shape of molecules. Here, NOM enables us to investigate the optical response of the single PS quantum wire corresponding its geometrical structure. In this paper, we report the near-field photoluminescence study of aggregate structures of PS's by applying the ultraviolet spectroscopy technique.

Figure 1 shows a schematic of an experimental configuration. A dilute solution of polydihexylsilanes (PDHS's) with trans-planar-type conformation is prepared as a sample. At room temperature, PDHS has the absorption and photoluminescence peak at the wavelength of 370 nm and 380 nm, respectively. For the optical excitation, 351-nm line of Ar^+ laser is coupled into the fiber probe. The PS molecules dispersed on the silica substrate are illuminated by the near-field light through the aperture of the tip. Photoluminescence (PL) from the excited PS molecules is collected by an objective lens or spherical lens. In two-dimensional optical imaging, the collected signal is detected by photomultiplier tube through the bandpass filters. A monochromator with cooled CCD is employed for the spectroscopic analysis of the PL signal. In order to achieve a high sensitivity and high resolution simultaneously, the shape of the fiber tip is tailored using a chemical etching technique [2]. By shortening the length of the optical loss region due to the evanescent propagation and metal-cladding absorption, we have successfully obtained high transmission coefficients [3]. Moreover, the protrusion part at the apex functions as the localized light source for the super-resolution imaging. Figure 2 shows a schematic and scanning electron microscope images of the apex part of the chemical-etched probe.

In Fig. 3, PL spectra from an aggregate structure of PS's are acquired every 3 seconds by CCD camera using a rather large aperture with 100-nW excitation. The peak wavelength of 380 nm and spectral width of 9 nm are obtained. These values are not so different from the result of the far-field spectroscopy of PS thin film. Under the high-power excitation at room temperature, the spectrum is rapidly bleached in some tens seconds. To avoid this photobleaching, the excitation power should be as low as possible.

PL image of a thin aggregate part is also obtained under the low excitation condition (~0.5 nW) as shown in Fig. 4. From the shear-force image, the thickness of the aggregate is evaluated as about 20 nm. A clear contrast and high resolution luminescence imaging is attained. The maximum photocounts of 400 cps is in good agreement with the numerical estimation using parameters of absorption coefficients, quantum efficiency and so on.

For the realization of single PS molecule spectroscopy in ultraviolet region, the improvement of signal detection efficiency and the measurement in low-temperature circumstances are in progress. The modification of the emission properties due to the tip-sample interaction will be discussed in terms of quantum optics [4].

References

[1] M. Ohtsu, J. Lightwave Technol. **13**, 1200 (1995).
[2] S. Mononobe and M. Ohtsu, J. Lightwave Technol. **14**, to be published in Oct. 1996.
[3] T. Saiki, S. Mononobe, M. Ohtsu, N. Saito, and J. Kusano, Appl. Phys. Lett. **68**, 2612 (1996).
[4] T. Saiki, M. Ohtsu, K. Jang, and W. Jhe, Opt. Lett. **21**, 674 (1996).

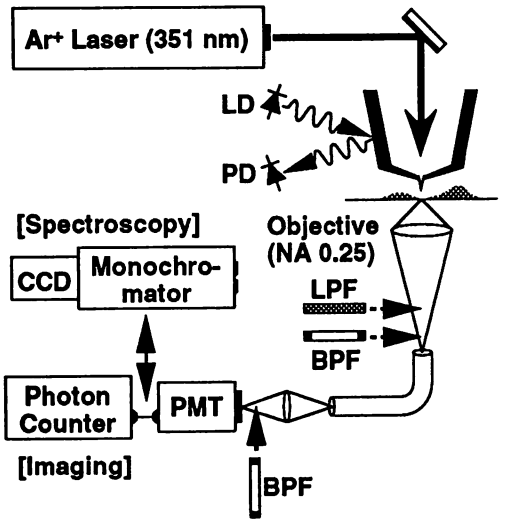

FIG. 1 Experimental setup.

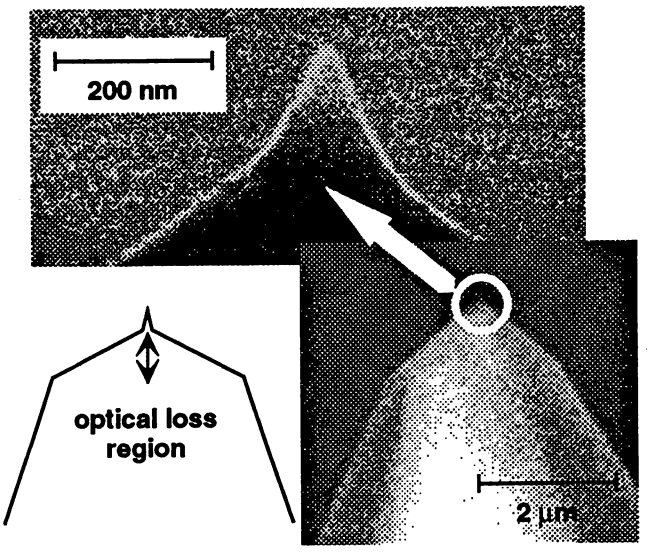

FIG. 2 Triple-tapered probe.

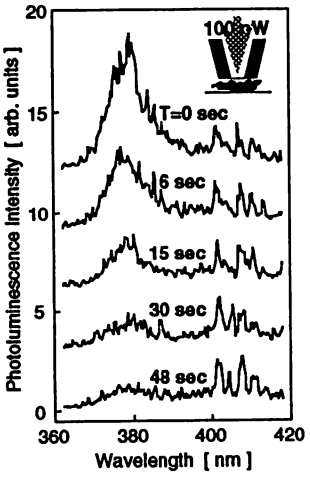

FIG. 3 PL spectra.

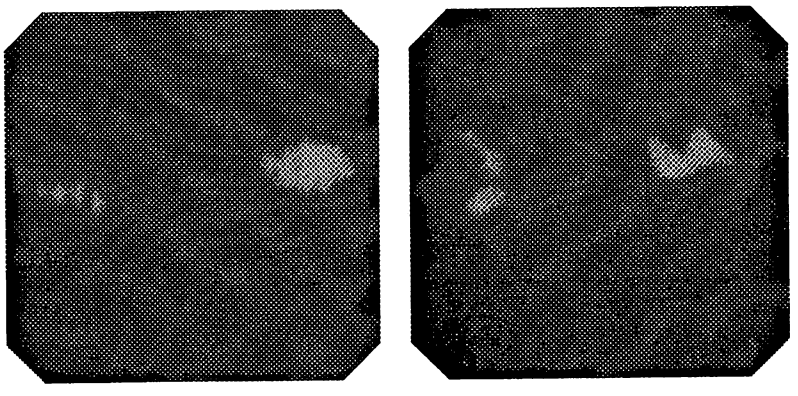

FIG. 4 Shear-force image (a) and PL image (b).

NEAR-FIELD OPTICAL IMAGES OF ATOMIC STEP ON AN α-Al_2O_3 PLATE AND NANOMETRIC $LiNbO_3$ CRYSTALS WITHOUT SHEAR FORCE FEEDBACK

M. Ohtsu[1,2], R. Uma Maheswari[2], R. Micheletto[2], S. Takehara[1] and S. Mononobe[2]

1) Graduate School, Tokyo Institute of Tecnology, 4259 Nagatsuta, Midori-ku, Yokohama 226, JAPAN
2) Kanagawa Academy of Science and Technology, KSP East 408, 3-2-1 Sakado, Takatsu ku, Kawasaki 213, JAPAN

We have developed a metal coated protruded fiber probe with an apex diameter of several nm and a foot diameter of 40 nm (see Fig.1). By using it or its modified version, we have obtained the optical image of gold particles and carried out the spatial Fourier analysis to determine the transfer function of the microscope. The high frequency cutoff was estimated from the transfer function to give the measure of resolution as high as 0.8nm[1].

In the present study, we demonstrate the high resolution capability of our collection-mode near-field microscope (NOM) using the protruded fiber probe by using a nanometric reference sample. The collection-mode NOM experiments[2] have been conducted using without shear force feedback control to avoid artifacts[3] The sample is fixed homogeneously on a substrate and its topography is calibrated by other complementary methods such as contact mode AFM. The samples used are (1) an atomic step on an ultra-flat, semitransparent sapphire (α-Al_2O_3) plate and (2) nanometric $LiNbO_3$ particles grown on the α-Al_2O_3 plate.

(1) Atomic-steps on an α-Al_2O_3 plate: The atomic step was fabricated by using advanced surface processing technology of oxide materials[4]. Theoretical analysis based on molecular dynamics shows that Al and O atoms on the stabilized top surface form a mono atomic layered step with a step height of 0.2 nm. The width of the step can be varied from 20 to 1000 nm. Figures 2 (a) and (b) show the near-field optical images of the step obtained under constant intensity feedback, i.e., by utilizing the rapid decay of the evanescent field, and under constant height (i.e.free running) operations, respectively. A clear image of the 2.5 nm step could be seen in Fig.2(a) which was obtained by optimizing the gain and the bandwidth of the optical feedback loop. Based on our results in Fig.2, it has been found that the contrast of the image decreases rapidly with increasing sample-probe separation and disappears for a separation larger than 10 nm. This clear dependence of the contrast of the imge on the sample-probe separation originates from the size dependent decay length of the evanescent field. In other words, for obtaining good contrast images of the step, the sample-probe separation has to be controlled to be several nm to pick up the high spatial Fourier frequency components of the evanescent fields which has a nanometric decay length. During the imaging of Fig.2, an s-polarized laser beam (λ= 685 nm) was used and it was incident normal to the step.

(2) Nanometric $LiNbO_3$ particles on the α-Al_2O_3 plate: Nanometric $LiNbO_3$ particles grown epitaxially on the α-Al_2O_3 plate were used for demonstrating the high 3D resolution of our NOM system. The particles are of cubic shape with a maximum size of 100 nm x 40 nm x 40 nm where the size is limited by lattice mis-matching. Figures 3(a) and (b) show the near-field optical images obtained under optical feedback for the s- and the p- polarized incident lights, respecticvely. Here, the experimental system used is the same as that in Ref.2 and the scan area is 175x150nm^2. The bright spots corresponding to the the nanometric particles could be seen with very good contrast. Particles as small as 20 nm as indicated by arrows could be seen

confirming the high resolution capability of the system. These high contrast images of the particles could only be obtained for separations smaller than the size of the particles and contrast of the image decreased rapidly with increasing sample-probe separation as for the case of Fig.2 Study of nonlinear response in these $LiNbO_3$ particles is in progress. Such an investigation would help in developing novel nonlinear optical devices without any requirement for phase matching.

The authors thank Prof. Yoshimoto for supplying α-Al_2O_3 plate and $LiNbO_3$ particles.

References

1)R. Uma Maheswari, et al., Opt. Commun., 131 (1996) 2612.
2)M. Naya, et al., Opt. Commun., 124 (1996) 9.
3)B. Hecht. et al., submitted to J. Appl. Phys.
4) M. Yoshimoto, et al., Appl.Phys.Lett., 67 (1996) 2615.

Fig. 1

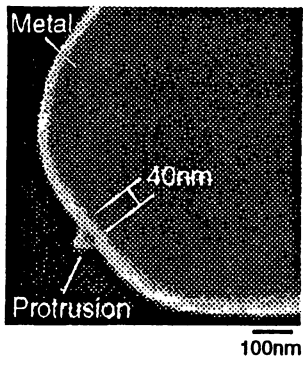

a

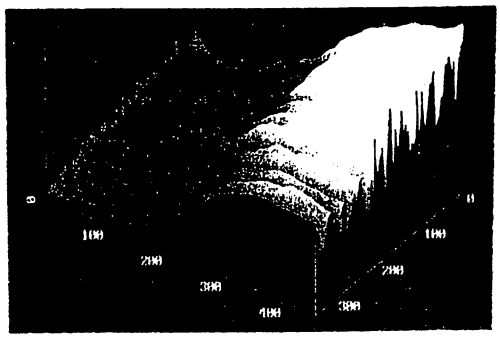

b

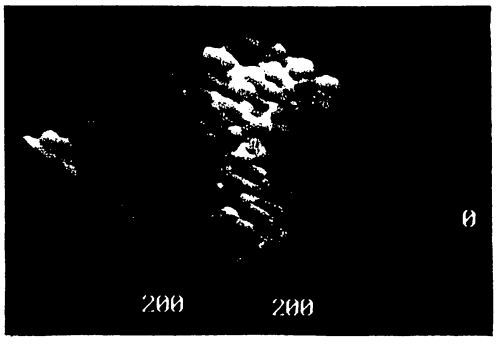

Fig. 2

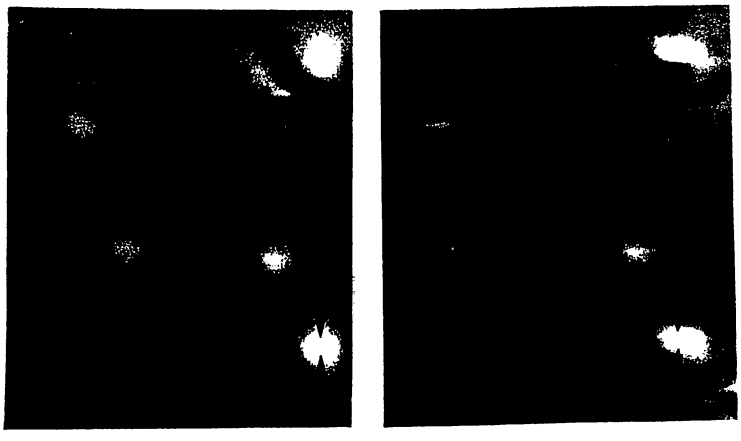

Fig. 3

ENHANCING THROUGHPUT OVER 100 TIMES BY AN ASYMMETRIC FIBER PROBE FOR NEAR-FIELD OPTICAL MICROSCOPE

M. Ohtsu[1,2], T. Yatsui[1], M. Kougori[1,2], S. Mononobe[2], T. Saiki[2], M.B. Lee[1,3], K. Tsutsui[1], and N. Atoda[3]

1) Graduate School, Tokyo Inst. of Tech., 4259 Nagatsuta, Midori-ku, Yokohama 226, JAPAN
2) Kanagawa Academy of Sci. and Tech. 3) National Inst. for Advanced Inter. Res.

We have sharpened the fiber core reproducibly by the selective chemical etching process in order to realize the apex diameter as small as several nm[1]. Further, by applying nanometric photo-lithograpy[2] and selective resin coating method[3], a protruded fiber probe with the foot diameter of 30 nm was realized. By using this protruded fiber probe or its modified version, we have obtained high resolution images of flagellar filaments of salmonella of 25 nm diameter[4] and atomic-steps of a sapphire substrate[5]. Further, spatial Fourier analysis was carried out to determine the transfer function of the microscope, and its high frequency cutoff was estimated to give the measure of resolution as high as 0.8 nm[6]. Through these works, it was confirmed that our protruded fiber probes can be used for high-resolution nanometric imaging.

On the other hand, for local spectroscopy and fabrication, higher throughput of the probe is required. To meet this requirement, we have developed a two-step etching for enhancing the throughput by 10 times[7]. By using it, we have carried out PL, EL and photocurrent spectroscopy of a planar GaAs pn junction at the room temperature[8,9], and PL spectroscopy of a GaAs quantum dot at the liquid helium temperature[10]. In the present paper, we report successful experimental results of drastically enhancing throughput by breaking the axial symmetry of the sharpened core of the fiber probe.

Since the throughput decreases drastically with decreasing core diameter, some structural improvements of the fiber probe are required. One of the solutions is to make the fiber core asymmetric. This will improve the matching efficiency between the guided modes of the fiber and the guided modes of the metal coated tapered core. We used the focused ion beam(FIB) technique to remove a part of the foot of the sharpened core to make it axially asymmetric. After this FIB process, a gold film was coated and an aperture was fabricated on the top. Figure 1 shows its SEM micrograph.

The asymmetric probes with various aperture diameters were fabricated and their throughputs were measured. Figure 2 shows the result, where the light power on the aperture normalized to the input light power into the fiber is plotted as a function of the aperture diameter. By comparison with those of the axially symmetric fibers, drastic enhancement of the throughput can be seen. It is as large as 200 for s aperture diameter smaller than 100 nm. A second conventional fiber probe with almost an equal aperture diameter was used to measure the spatial profile of the light power on the aperture with the help of the shear force technique to control the separation between the two probes. The result showed that the propagating light components were sufficiently suppressed and evanescent light was effectively

generated.

The large enhancement in throughput by the asymmetric fiber probe can make it possible to realize a high-speed optical storage and read-out, and also high speed imaging. For realizing such a high speed operation, we are now fabricating a two-dimensional flat array of the probes using silicon planar process. Their details will be presented at the session.

References

1) T. Pangaribuan, et al., Jpn. J. Appl. Phys., 31 (1992) L1302
2) T. Matsumoto, et al., IEEE J. Lightwave Technol., 14 (1996) in press
3) S. Mononobe, et al., Appl. Opt., to be published
4) M. Naya, et al., Opt. Commun., 124 (1996) 9
5) R. Micheletto, et al., Tech. Digest , the 1st Asia-Pacific Near-field Optics Workshop, Seoul, August 1996, p.54
6) R. UmaMaheswari, et al., Opt. Commun., 131 (1996) 133
7) T. Saiki, et al., Appl. Phys. Lett., 68 (1996) 2612
8) T. Saiki, et al. Appl. Phys. Lett., 67 (1995) 2191
9) T. Saiki, et al., Appl. Phys. Lett., 69 (1996) 644
10) Y. Toda, et al., Appl. Phys. Lett., 69 (1996) 827

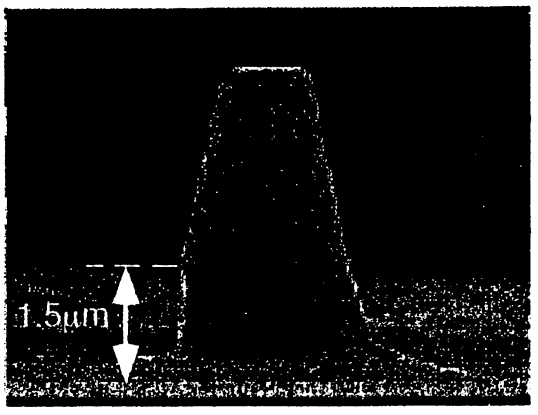

Fig. 1

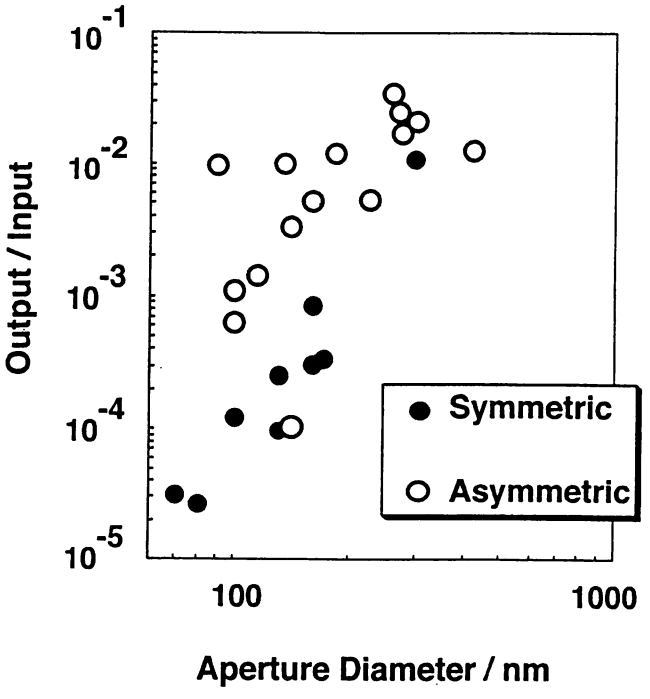

Fig. 2

[I-3] REVIEW PAPERS

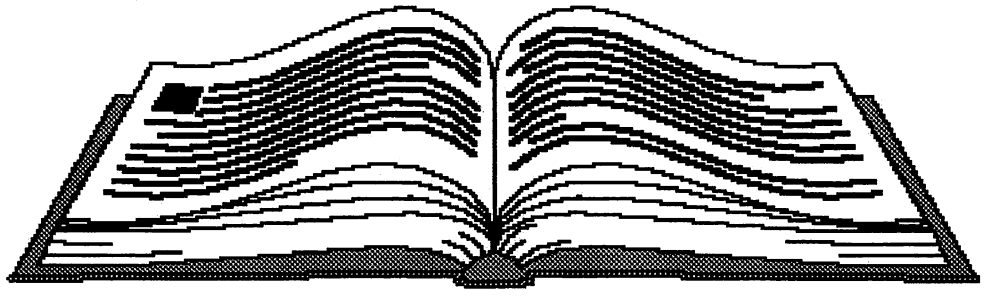

近接場光学顕微鏡の開発の現状と将来

大津元一*

1. まえがき

従来の多様な計測，加工に用いられている光は自由空間または波長に比べ大きな領域を伝搬している．この光を用いる限り，これらの応用システムの空間的特性は光の回折効果により決定される．たとえば，光学顕微鏡では試料により散乱された光をレンズで集め，結像させようとすると，光がわずかに広がり，像がぼける．そのぼけの大きさは光の波長程度であるので，光学顕微鏡では光の波長以下の寸法の試料は観察できない．さらに，レーザの光を集光して加工に使おうとすると，その加工精度も回折効果により制限される．以上のように，従来は光波長以下の寸法の超微細な光応用システムは皆無であった．

しかし，物質表面にしみ出たエバネッセント光(evanescent light：これはまた近接場光とも呼ばれている)は回折の効果を持たないので，これを利用すると超微細な光応用システムが可能となる．たとえば，回折限界を越える分解能を持つ光学顕微鏡が可能となる．これは，近接場光学顕微鏡(near field optical microscope：NOM)と呼ばれる．研究者によっては，これをSNOM，NSOM，PSTMなどとと略称している場合もあるが，これらは必ずしもエバネッセント光の物理的特性を反映したものではないので，最も基本的な略称であるNOMを使うのがよい．エバネッセント光は物質表面に近接した領域にある場であることからNOMおよび関連する光学現象に関する研究分野は近接場光学(near field optics)と呼ばれる．NOMの原理と提案は60年前にさかのぼる[1]が，その実験は1980年代に入ってから開始された[2]．しかし，ここ数年この研究開発が急激に活発化している．その理由は近接場光学の基礎となる科学技術，さらに応用可能分野がきわめて広い分野，特に将来の科学技術に関わる分野と密接に関わっているからである．

NOMはプローブ顕微鏡の一種であるが，走査トンネル顕微鏡(STM)，原子間力顕微鏡(AFM)と異なり，光学スペクトルを測定することができること，多様な環境下で使用できることが顕著な利点である[3~5]．ここでは，近接場光学に基づく超微細光計測器としてのNOMについて記し，さらに微細加工技術の一つである超高密度光記録，および極限技術である原子操作について触れる．

2. 顕微鏡の原理と構成

物体に光を照射すると，その表面で光は反射，透過し，伝搬していく．そのとき，同時に物体表面にはエバネッセント光が発生している．エバネッセント光は，光照射により物体中に生じた分極の間の局所的相互作用を光として表現したものに他ならないので，上記の反射光，透過光と異なり，遠方へ伝搬せず，分極近傍に局在している．たとえば，照射する光の波長よりずっと小さい半径aを持つ誘電体球表面に発生するエバネッセント光のパワーのしみ出し厚みはa程度であり，光波長には依存しない[6,7]．

図1にNOMの基本的構成を示す．この図中，先端の鋭いプローブを試料表面付近で走査しながらこのエバネッセント光を散乱して伝搬光に変換し，そのパワーを検出してプローブの位置の関数として図示すれば，試料表面の三次元的像が表示できる．このとき，像の分解能はプローブ先端の鋭さによって決まるので，通常の光学顕微鏡とは異なり光の回折限界を越えることができる．

NOM装置の中で基本となる素子はプローブである．従来，ガラス性のマイクロピペットを加熱して引き延ばしたもの，光ファイバを加熱して引き延ばしたもの[8]，さらには微小球を用いるものなどがプローブとして用いられてきた．最近では製作の際の高い再現性，先端曲率半径を10 nm以下に

* 東京工業大学 大学院 総合理工学研究科，神奈川科学技術アカデミー
(Motoichi Ohtsu)

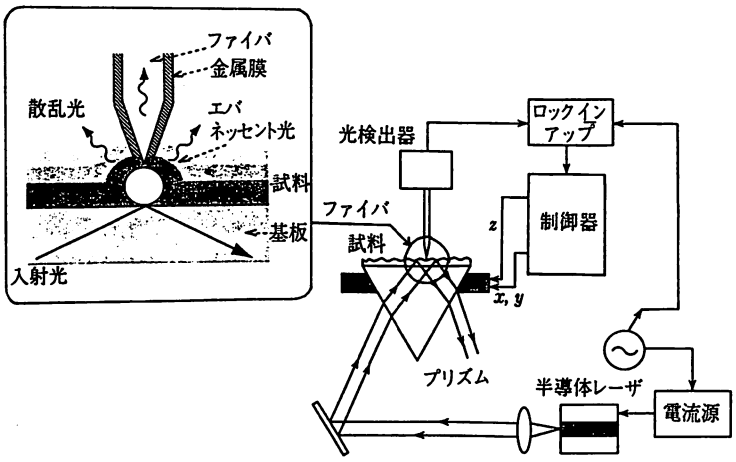

図 1　近接場光学顕微鏡 (NOM) の基本的構成 (試料表面のエバネッセント光をプローブでピックアップし，集める方式．C モードと呼ばれている．内挿図は試料とプローブの部分の拡大図)

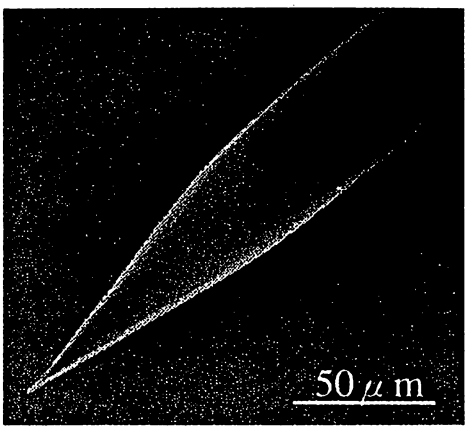

(a) 全体図

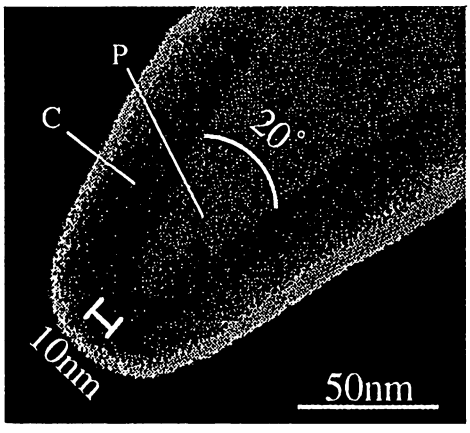

(b) 先端部の拡大図

図 2　ペンシル形プローブの電子顕微鏡写真 (C と記した部分は電子顕微鏡による観測時に付着した汚れ．P と記した部分が金属膜の蒸着された先鋭化光ファイバ)

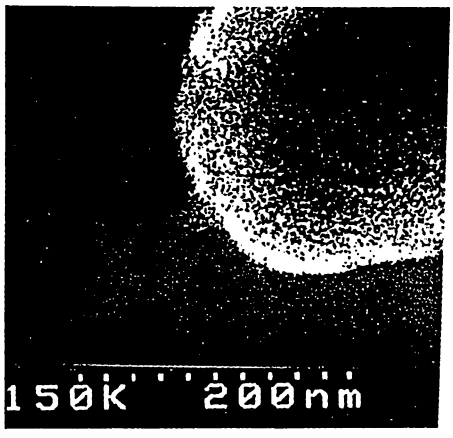

図 3　先端部から金の薄膜を除去しファイバ先端部が露出したプローブの断面説明図の電子顕微鏡写真 (根元は金の薄膜が蒸着されている)

すること，高い集光効率を得ること，などを目指して，光伝送用のファイバを緩衝フッ酸溶液で選択化学エッチングする方法が開発されている[9]．NH_4F の体積比を調節することによりコア部のみを先鋭化すること，さらには二段階エッチングによりクラッド部を細径化すること[10]，四段階エッチングによりクラッド部の角のないペンシル形にすること[11]，などが可能となった．先端形状の電子顕微鏡写真を図 2 に示すが，10 nm 以内の先端曲率半径が実現している．また，先鋭角の最小値は 15 度になる．

先鋭化したプローブの根元に金属膜をコーティングし，先端部分の金属膜をヨウ化カリウム溶液により除去してファイバ先端部を露出させ，開口を形成することができる．先端部の電子顕微鏡写真を図 3 に示すが，開口径 30 nm が実現している．

図 1 のように光を試料裏面から全反射角で入射させ，発生したエバネッセント光をプローブでピックアップする方法の他に，図 4 に示すようにプローブ先端にエバネッセント光をしみ出させ，これを試料により散乱光に変換して測定する方法などがある．なお図 1 は C モード (Collection mode)，

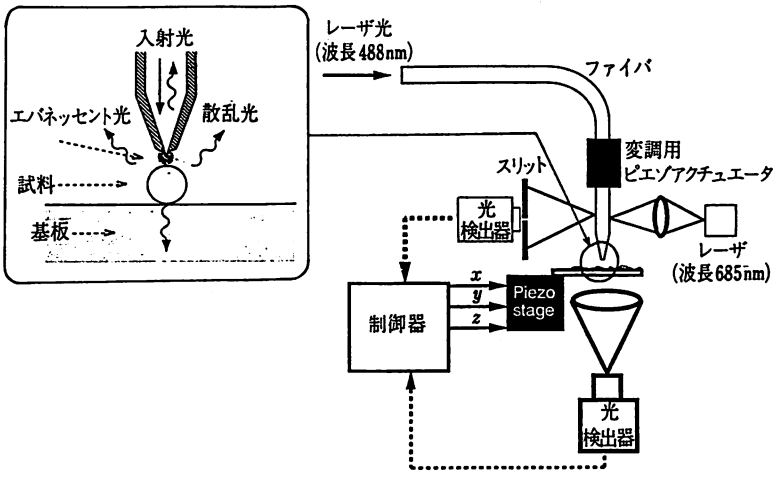

図 4　近接場光学顕微鏡（NOM）の基本的構成（プローブ先端からしみ出すエバネッセント光で試料を証明する方式．Iモードと呼ばれている．内挿図は試料とプローブの部分の拡大図）

図4はIモード(Illumination mode)と呼ばれる．Cモードでは高い分解能の画像計測が可能であり，また入射光の偏光状態を調節することが容易である．一方，試料基板としては透明または半透明である必要がある．Iモードでは基板は不透明でもよいが，試料に入射するエバネッセント光の偏光状態を調節することは困難である．Iモードは加工などに使われている．両モードとも信号処理，プローブ駆動には他の走査プローブ顕微鏡と同様の装置が使用できる．ただし，試料・プローブ間の距離制御には独自の方法が取られている．Cモードではプローブを通して検出するエバネッセント光パワーが一定になるようにプローブ位置を自動制御する．Iモードの場合には感度の点でこれが困難なので，プローブと試料との間のせん断応力を測定し，それが一定になるようにプローブ位置を自動制御する[12]．この方法を使うとプローブと試料との間隔を制御することができるのみでなく，NOM像と同時に原子間力顕微鏡(AFM)像が測定できる利点を有する．ただし，試料表面においてせん段応力の等力面とエバネッセント光の等パワー面の分布は異なるので，画像計測時の信号クロストークの問題，さらには，せん断応力は生体微粒子などの柔らかい試料表面の損傷，水中での動作困難性などの問題を持っている．最近ではIモードでもせん断応力を使わずに第二の光源を用い，そのエバネッセント光パワー測定によりプローブ位置を制御する方法が開発された[13]．

検出される光パワーは数pW～数nWなので低雑音の測定環境を準備する必要がある．一辺1μm以下の視野で像を観測するために，試料を基板に固定する際には注意が必要である．すなわち，試料固定時に散乱光発生源を作らないこと，などである．生体試料の基板への固定にはAFM像観察用試料の固定法と同様の方法を用いることができるが，そのときは試料とプローブとの間の水分子の存在，誘電体試料表面の帯電荷などに注意する必要がある．

3．ナノメータ計測

NOMの分解能を評価するために金の微粒子を標準試料として用い，その画像を空間フーリエ周波数解析することによりNOMのシステム関数が推定され，その高域遮断周波数より，NOMの分解能の目安として0.8 nmが得られている[14]．

さらに，バクテリオファージT4[15]，神経軸窄内の毛細管の束[16]などが観測されている．また，図5に示すのは直径25 nmのサルモネラ菌の鞭毛の測定例である[17]．さらに，水中での細胞試料の測定も行われている[13]．一方，光エレクトロニクス用微小デバイスの評価にも使われている．図6はプロトン交換$LiTaO_3$導波路のY分岐における導波

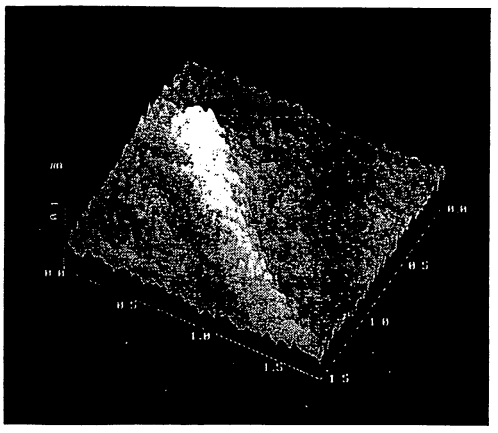

図 5　サルモネラ菌の直径 25 nm の鞭毛の観測像
(画像の寸法は 480 nm×480 nm)

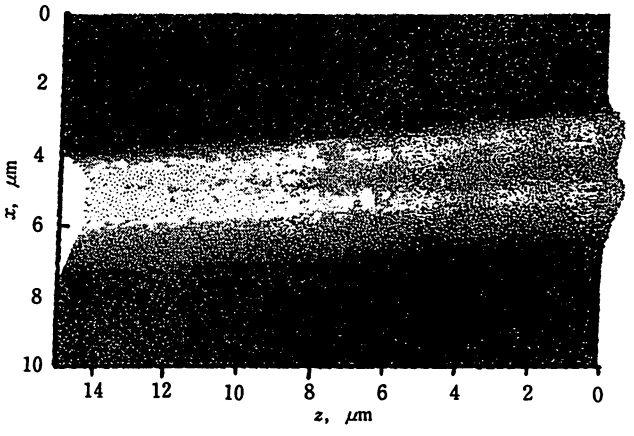

図 6　プロトン交換 $LiTaO_3$ 製の Y 分岐光導波路の導波モードの観察像 (画像の寸法は 10 μm×15 μm)

モード形状の測定結果であるが，これより波長以下の寸法をもつ散乱源の同定，ビーム伝搬法による計算結果との比較などが行われ，光導波路の新しい非破壊・高分解能評価法が提示されている[18]．

他の走査プローブ顕微鏡と異なり，NOM では入射光により励起された試料からの蛍光を局所的に測定することが可能である．ただしこの場合，光子計数法などの微弱光検出技術を組み合わせる必要がある．さらに NOM の特長として，入射光の波長を掃引することにより試料の局所的光学スペクトルが観測可能である．これにより，試料形状のみでなく，試料構造，特に生体試料の場合には局所的な化学種の同定が可能となる．今までに応力下のルビーの蛍光スペクトル[19]，ダイアモンドのラマンスペクトル[20]，さらには単一色素分子からの蛍光スペクトル[21]が測定されており，またプローブが近づいたときの蛍光クエンチングが検出されている[22]．

一方，半導体の量子ドットが基板上に二次元アレイ状に成長されている場合，従来の方法では空間的分解能が不十分なので個々のドットからの発光を分離測定することができないが，NOM ではそれが可能になる[23]．なお，熱によるスペクトルの広がりや量子効率の低下を避けるために極低温(液

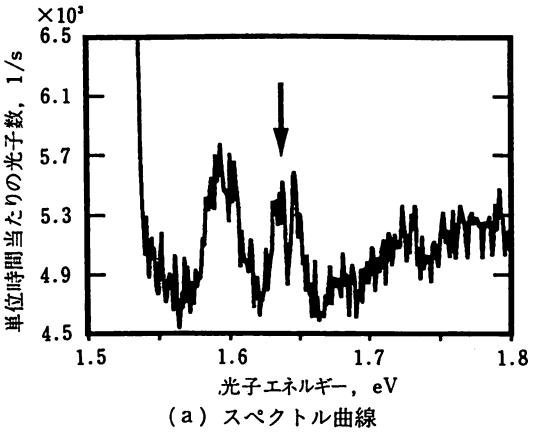

(a) スペクトル曲線

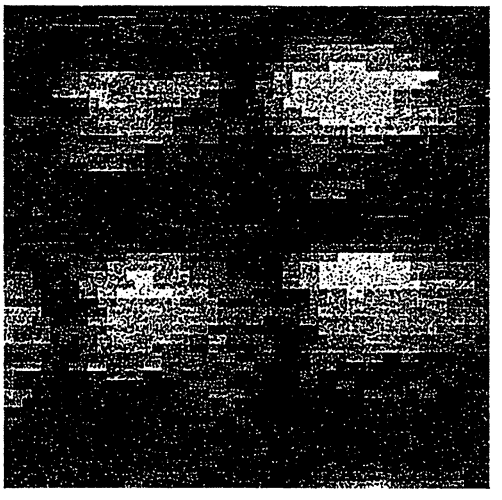

(b) フォトルミネッセンス光強度の空間分布
(この図の一辺は 2 μm)

図 7　基板上に間隔 1 μm で二次元アレイ状に成長した直径 200 μm，厚さ 20 nm の GaAs 量子ドットからのフォトルミネッセンスを温度 18 K で測定した結果

体ヘリウム温度)で動作するNOM装置が必要となる．すなわち，プローブを走査するためのピエゾ・アクチュエータの熱膨張などに注意し，熱ドリフトの少ない装置を組み立てて使う．その他の装置構成は図4と同様である．発光スペクトル強度は弱いので光子計数器を用いる．図7(a)，(b)には，各々発光スペクトル，発光強度分布の測定結果を示すが，従来の遠視野の場合と異なり，スペクトルの不均一広がりが除去でき，幅の狭い数本のスペクトルが分離されて観測されている．特に矢印を施したスペクトル成分は量子ドットからの発光であると推定されている．

また，関連する実験としては単一量子井戸の励起子スペクトルの測定などがある[24]．

4. ナノメータ加工機・操作機としての使用

ナノメータ加工の一例として，プローブからエバネッセント光をしみ出させ，その光パワーを用いて光メモリ材料に記録する試みが報告されている．記録寸法はプローブ先端寸法によって決まるので，従来の光記録とは異なり，回折限界を越えた記録が可能になる．光磁気メモリ材料のCo/Ptにアルゴンレーザを用いて熱モードで記録し，記録寸法約100 nm，記録密度45 Gb/inch^{2}を得ている[25]．これは従来の光メモリの記録密度の100の値に相当する．読み出しもNOMを用いている．記録装置寸法を小型化するために同じ記録を半導体レーザにより行う試みも報告されている[26]．なお，この方法では光の偏光を利用しているが，光波長以下の微小開口からのエバネッセント光の偏光状態は入射光の偏光を保存しないので，今後の高密度化には不利である．この点を解決するために，下記のようにフォトクロミック材料であるジアゾベンゼン誘導体のLB膜(60層)を記録媒体として用い，フォトンモードによる記録，再生，消去が試みられている[27]．

(1) 記録

NOM用プローブ先端にエバネッセント光をしみ出させ，プローブとメモリ用媒体との距離を光波長以下(すなわち近接場の領域)に保ったまま掃引する．このとき，エバネッセント光のエネルギー

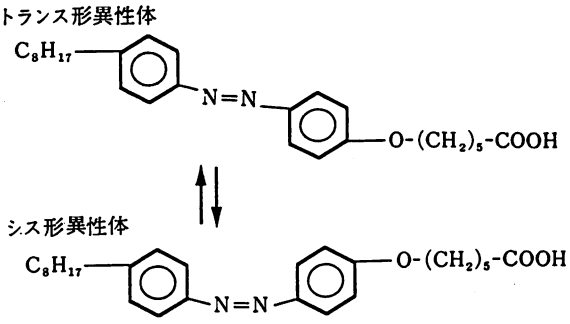

(a) 記録媒体の分子構造

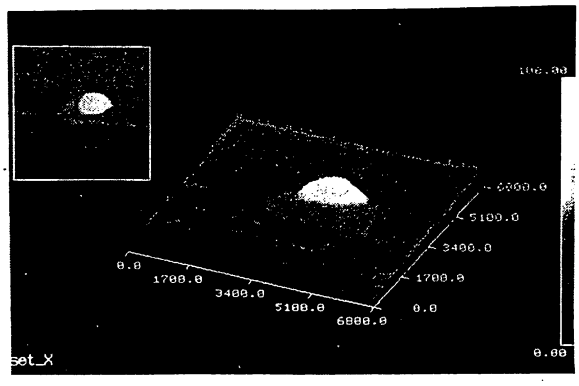

(b) 光記録されたピットの再生像
(写真中の円形の明部)〔直径は約100 nm．図の一辺は700 nmに相当〕

図8　フォトンモード光記録の結果

により媒体表面の構造を変化させる．図8(a)に示すように，波長350 nmの紫外光により記録媒体をトランス形異性体からシス形異性体へと変化させることにより記録を行う．上記の紫外光は出力パワー60 mWのアルゴンレーザから得，実際の記録の際のエバネッセント光パワーは約30 nWである．

(2) 再生

上記の記録過程での構造変化を顕微鏡としてのNOMで測定する．再生にも同じ光源を使うことができるが，出力パワーを減少させる必要がある．波長350 nmにおける吸光度はトランス形異性体では0.31，シス形異性体では0.16であること，すなわちその差が0.15と大きく異なることを利用し，再生には同じ装置をNOMとして用い，記録媒体の透過率の面内での局所変化を測定することにより行う．図8(b)には再生結果の例を示す．円形スポットがシス形異性体に構造変化している箇所であり，記録されたピットに相当する．

なお，この図では円形スポットの直径は約100 nmであり，記録時の光波長以下の値になっている．これらの直径の値は周囲温度揺らぎによる記録中のプローブ位置の横方向揺らぎにも依存する．今後，プローブ位置揺らぎを抑圧する制御を施すことにより，より小さい直径が期待される．

（3）消去

光照射により記録とは逆方向の構造変化を誘起し，消去する．このためには，記録より長波長の光を照射し，トランス形異性体へと変化させる．

ここで示した近接場光学による光記録・再生方式はまだ研究開発の初期段階であるが，記録できるピット径は最終的にはプローブ先端曲率半径により制限される値まで小さくすることが期待され，数nmとなり得る．この意味で本方法は超高密度の光記録実現のための有望な方法といえる．さらに進展させるには下記の基本的な問題を解決する必要がある．

① 高感度プローブの開発
② プローブの高速走査機構とそのためのデバイス開発
③ 高感度記録媒体の開発
④ 関連するソフトウェアの開発

また，ここで示したフォトンモードの光記録は見方を変えれば局所的な光化学反応の実験と考えることができる．したがって，熱モードによる方法もあわせて考えると，光記録のみならず，将来はその他のナノメータ加工，すなわちレーザトリミング，レーザアニーリングなどへの発展も期待できる．従来のレーザ光を利用した微細加工の代表例はレーザマスクリペアであり，最小加工線幅0.7 μm，修正位置精度0.1 μm程度がすでに実現しており，64 MbのDRAM用のマスク修正などに用いられているが，これ以上の高分解能化は従来方法ではかなり困難と考えられている．本節で紹介した方法は，この問題を打破する新技術となり得る．特に，256 MbのDRAM以降のフォトマスク修正が可能となれば，将来のULSI製造プロセスでも大きなインパクトが期待できる．

ところで，極限的な微細加工の方向を示す研究として，最近では三次元構造をもつエバネッセント光を用いた原子操作が活発になっている．たとえば，中空ファイバ中にしみ出したエバネッセント光による原子誘導路[28]，プローブ先端にしみ出すエバネッセント光により真空中に浮遊する原子を一つずつ捕獲する方法[29,30]などが提案されている．最近では，上記の原子誘導路の実験が初めて成功し，同位体分離への応用も示された[31]．以上の原子操作により捕獲された原子を冷却結晶基板の上に一つずつ固定して単原子レベルの結晶成長や光メモリの作製を行うなどの応用が期待される．

5. 今後の展望とまとめ

NOMは，単に光の波長以下の寸法の物体像やその構造を観察する超微細光計測システムとしてのみでなく，新しい微小物質を作り出す加工機，操作機としての機能を持っている．この特徴こそが微小半導体デバイス，光メモリ，さらにはバイオテクノロジー，マイクロマシンなどの広い分野で最近注目を集めている理由である．また，その動作原理の基礎も奥深く，従来の光学ではカバーしきらない内容も含まれる．すなわち，NOMを扱う「近接場光学」，「ナノ・フォトニクス」の基礎と応用は極めて多岐にわたる．

今後は，測定の時定数を減少させ，高速測定を可能にすることが望まれる．これは，プローブの感度にかかっており，そのようなプローブの作成にはマイクロシーニングなどのデバイス技術の導入が必要である．また，測定対象を広げるために，物理，化学，機械，熱などの各種の量を光に変換する機能性プローブの開発が待たれる．今後は，システムの改良により原理的には原子レベルの分解能が可能である．

また，熱耐性の高いプローブが実現すれば，高温プロセスとしての半導体の単原子レベルでの結晶成長が可能となる．また光機能デバイスについては，光波長以下の寸法を持つナノ光論理素子などの実現，それによる光情報処理，光通信システムの超高速化，大容量化が期待できる．

「近接場光学」，「ナノ・フォトニクス」の内容は光エレクトロニクス，ナノ加工の研究開発に関し，従来は日本がリードしており，日本の研究素地が充実しているので，日本の得意な分野であるといえる．ここ1，2年の間にこれらに関する大型プロ

ジェクトが発足している．この中で，わが国の大学関係では文部省科学研究費補助金・重点領域研究が発足し，また通産省工業技術院・融合領域研究所ではテラバイト級の記録容量を目指す「次世代光基盤研究」プロジェクトが産官学の共同研究を開始した．世界をリードする研究開発をわが国の気鋭の若手研究者が推進していただけること望んでいる．

参考文献

1) E.H. Synge：Phil. Mag., 6 (1928) p.356.
2) D.W. Pohl and D. Courjon：Near Field Optics, Kluwer (1993).
3) M. Ohtsu：IEEE J. Lightwave Technol., 13,7 (1995) p.1200.
4) 大津元一：応用物理，65,1 (1996) p.2.
5) M. Ohtsu and H. Hori：Near Field Nano-Optics, Pleunm, NY (1997).
6) K. Jang and W. Jhe：Opt. Lett., 21,4 (1996) p.236.
7) T. Saiki, M. Optsu, K. Jang and W. Jhe：Oot. Lett., 21,9 (1996) p.674.
8) U. Durig, D. Pohl and F. Rohner：IBM J. Res. Dev., 30 (1986) p.478.
9) T. Pangaribuan, K. Yamada, S. Jiang, H. Ohsawa and M. Ohtsu：Jpn. J. Appl. Phys., 31, 9 A (1992) L 1302.
10) T. Pangaribuan, S. Jiang and M. Ohtsu：Electron. Lett., 29,22 (1993) p.1978.
11) S. Mononobe and M. Ohtsu：IEEE J. Lightwave Technol., 14, 10 (1996) p, 2231.
12) E. Betzig, P.L. Finn and J.S. Weiner：Appl. Phys. Lett., 60,20 (1992) p.2484.
13) R. Uma maheswari, S. Mononobe, H. Tatsumi, Y. Katayama and M. Ohtsu：Opt. Rev., 3, 6 B (1996) p, 463.
14) R. Uma Maheswari, H.Kadono and M. Ohtsu：Opt. Commun., 131, 5 (1996) p, 133.
15) S. Jiang, H. Ohsawa, K. Yamada, T. Pangaribuan, M. Ohtsu, K. Imai and A. Ikai：Jpn. J. Appl. Phys., 31,7 (1992) p.2282
16) R. Uma Maheswari, H. Tatsumi, Y.Katayama and M. Ohtsu：Opt. Commun., 120 (1995) p.325.
17) M. Naya, S. Mononobe, R. Uma Maheswari, T. Saiki and M. Ohtsu：Opt. Commun., 124 (1996) p.9.
18) Y. Toda and M. Ohtsu：IEEE Photonics Technol. Lett., 7,1 (1995) p.84.
19) P.J. Moyer, C.L. Jahncke, M.A. Paesler, R.C. Reddic and R.J. Warmack：Phys. Lett. A, 145,6 (1990) p.343.
20) D.P. Tsai, A Othonos, M. Moskvits and D. Uttamacha ndani：Appl. Phys. Lett., 64, 14 (1994) p.1768.
21) W.P. Ambrone, P.M. Goodwin, J.C. Martin and R. A. Keller：Phys. Rev. Lett., 72,1, (1994) p.160.
22) X.S. Xie and R.C. Dunn：Science, 265 (1994) p.361.
23) Y. Toda, M. Kourogi, M. Ohtsu,Y. Nagamune and Y. Arakawa：Appl. Phys. Lett, 69,5 (1996) p.827.
24) H.F. Hess, E. Betzig, T.D. Harris, D. Pfeiffer, and K. West：Science, 264 (1994) p.1740.
25) E. Betzig, J.K. Traitman, R. Wolfe, E.M. Gyorgy, P.L. Finn, M.H. Kryder and C.-H. Chang：Appl. Phys. Lett., 61,2 (1992) p.142.
26) S. Hosaka, T. Shintani, M. Miyamoto, A. Hirotsune, M. Terao, M. Yoshida, K. Fujita and S. Kammer：Jpn. J. Appl.Phys., 35, 1 B (1996) p.443.
27) S. Jiang, J. Ichihashi, H. Monobe, M. Fujihira and M. Ohtsu：Opt. Commun., 106 (1994) p.173.
28) M.A. 01'Shanii, Yu.B. Ovchinnikov and V.S. Letokhov：Opt. Commun., 98 (1993) p.77.
29) 大津元一：フォトンSTM (V) 一単原子レベル結晶成長，第51回応用物理学会学術講演会，1990年 (平成2年) 秋季，講演番号27 aL 79.
30) M. Ohtsu, S. Jiang, T. Pangaribuan and M. Kozuma：Near Field Optics (ed. by D.W. Pohl and D. Courjon), Kluwer, Dordrecht, (1992) p.131.
31) H. Ito. T. N akata, K. Sakaki, M. Ohtsu, K.I. Lee and W. Jhe：Phys. Rev. Lett., 76,24 (1996) p.4500.

◆M&BE最前線（Vol.8, No1, 1997）

近接場光学顕微鏡による半導体試料の分光観察

神奈川科学技術アカデミー
斎木　敏治，大津　元一

§1　はじめに

光を用いた極微構造の観察手段として，光学顕微鏡の性能は日々向上を続け，その分解能は，ほぼ回折限界にまで達している．しかし，最近の微細加工技術の進歩を背景に，現在われわれは，光の波長に制限されない空間的な光操作が可能になっている．このような技術の応用として，走査型プローブ顕微鏡の１つである近接場光学顕微鏡がここ数年で急速に普及し，大きな成果を上げつつある［１，２］．図１にその動作原理を示す．観察試料，あるいは必要な分解能に応じてプローブの種類，光の照射・検出方法はさまざまである．ここでは，最も頻繁に用いられている，微小開口型プローブによる測定方法について簡単に説明する．鋭く尖らせた光ファイバに遮光のための金属膜をほどこし，先端部分に光の波長よりも小さな開口を作製する．ファイバ中に導入され，微小開口を通過した直後の光は，２種類の成分から構成されている．１つは伝搬光成分であり，そのスポット径は開口径と同程度にコリメートされている．もう１つは，遠方まで伝搬しないエバネッセント光成分であり，開口近傍に局在している．したがって，微小開口を観察試料に対して，開口径以下の距離（ニアフィールド）まで接近させ，２次元走査をおこなうことにより，波長に制限されない分解能をもつ画像計測が可能となる．

近接場光学顕微鏡を生体試料，有機分子，半導体デバイスなどの観察に応用する際，光を用いる特長を生かし，形状のみならず分光的な情報も強く要求されることがしばしばある．しかし，観察領域が微小であるため，高分解能とのトレードオフとして，十分な感度が得られないことが多く，深刻な問題となっている．この大きな困難を克服するためには，高い励起効率，検出効率を得るためのプローブ設計が緊急の課題である．本稿では，高感度を達成するためのプローブ作製の方法をまず述べる．続いて，このようなプローブを用いておこなった横方向ｐ－ｎ接合の多角的評価，低温における単一量子ドットの発光スペクトル測定，および有機ポリシランの紫外分光の結果を順に紹介する．

§2　高感度プローブの設計と作製［3］

われわれのグループでは図２に示すように，化学エッチングにより先鋭化をおこ

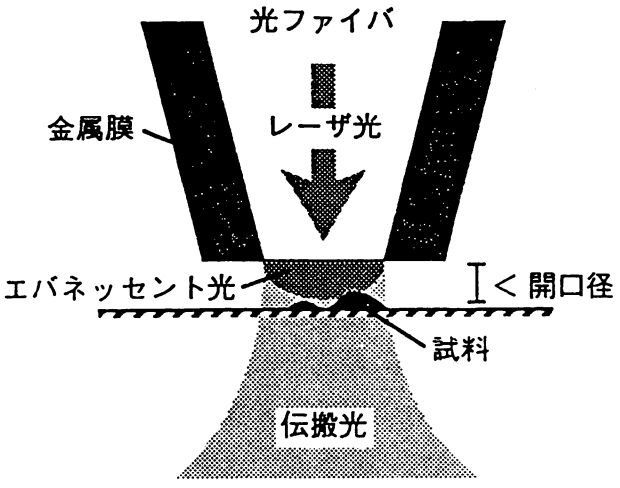

図１：近接場光学顕微鏡の原理.

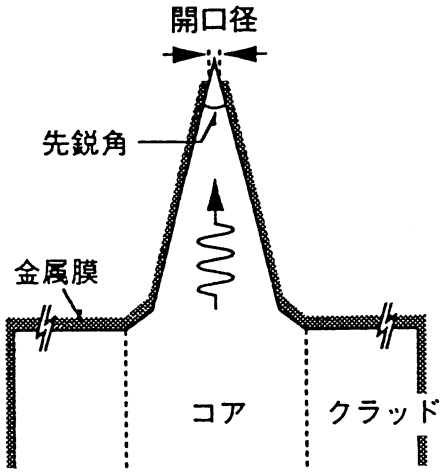

図２：先鋭化ファイバプローブ.

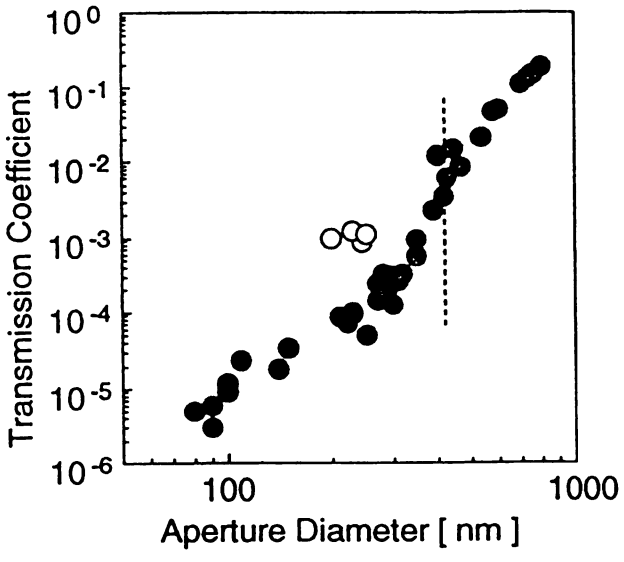

図３：伝達効率の開口径依存性.

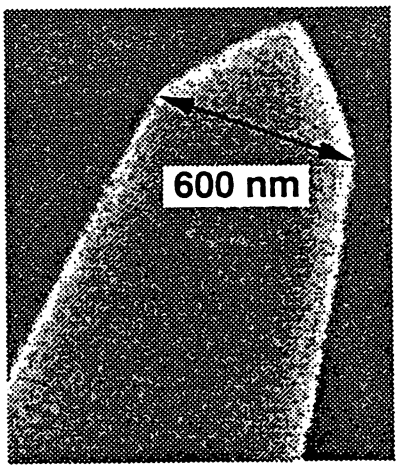

図４：高効率２段型プローブの電子顕微鏡像.

なった光ファイバ［4，5］に金属膜（本測定では金を用いた）をほどこすことによって微小開口を作製している．開口部に達するまでの光の伝搬部分は，金属をクラッドとする導波路とみなすことができる．ここで，先端までの光の伝達効率（開口から漏れだす光量のファイバへの入射光量に対する比）は，導波モードのカットオフ径やクラッド金属の吸収強度によって決定される．そこで，これらの影響を定量的に評価するため，さまざまな開口径をもつプローブを準備し，それらの伝達効率を測定した結果を図３に●で示す．光源としては，Ｈｅ－Ｎｅレーザ（波長６３３ｎｍ）を使用している．開口径４００ｎｍ付近を境界として，伝達効率が急激に低下していることがわかる．この結果は，金属クラッド導波路のカットオフ，および金属吸収などによる光減衰が，この領域から強く起こり始めていることを示唆している．そこでこの結果をもとに，実験上の操作性も考慮して，プローブ形状の最適化をおこなった．図４に実際に作製したプローブ（金属蒸着前）の電子顕微鏡像を示す．２段型の形状にすることにより，光減衰の大きな，コアの細い領域が極力短くなるように工夫してある．このようなプローブに対して伝達効率を評価した結果を図３に○で示す．従来の先端角の小さな１段型プローブ（●）に比べ，効率が１桁以上向上していることがわかる．この２段型プローブは特に，半導体試料の観測において局所励起・局所検出を同時におこなう際に大きな威力を発揮する．

§３　横方向ｐ－ｎ接合の多角的評価［6，7］

横方向ｐ－ｎ接合は，基板面と垂直な方向に光を放射する面発光レーザとして機能することが期待されている．試料形状を模式的に図５（ａ）に示す．半絶縁性ＧａＡｓ（１１１）Ａ基板に対し，パタニングをほどこした後，選択エッチングをおこない，（３１１）Ａ斜面を作製する．この基板の上に，ＳｉドープＧａＡｓを１μｍの厚さにＭＢＥ成長させる．Ｓｉは成長基板の面方位により，その伝導型，キャリア濃度が大きく変化する．この試料においては，（１１１）Ａ面上でアクセプタ，（３１１）Ａ斜面上ではドナーとしてはたらくため，それぞれの面はｐ型，ｎ型の伝導特性を示す．

この試料に対し，ｐからｎへの遷移領域の位置，幅，および伝導型の変化のようすを調べるため，空間分解発光スペクトル測定をおこなった．実験配置の概略を図６（ａ）に示す．プローブとしては，§２で述べた高感度プローブを使用した．開口径は２００ｎｍであり，伝達効率として5×10^{-2}が得られている．励起光源としては，Ｈｅ－Ｎｅレーザ（波長６３３ｎｍ）を用い，０．５ｍＷをファイバ端から導入する．プローブ先端を試料に対し近接場領域まで接近させ，微小開口を通して漏れ出た光を照射する．励起領域は横方向に対しては開口径の２００ｎｍ，深さ方向に関しても，吸収係数から約２００ｎｍと見積もられ，十分に局所的な励起が

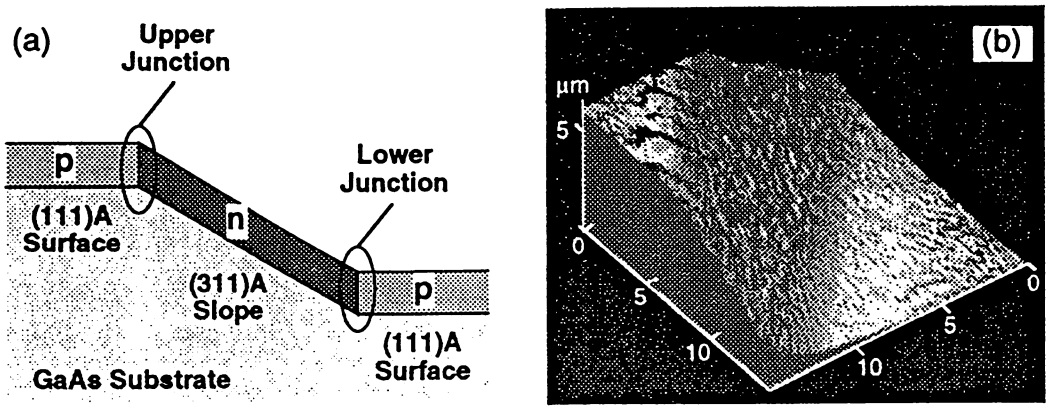

図５：横方向ｐ－ｎ接合の構造模式図（ａ）と斜面近傍の
シアフォース像（ｂ）．

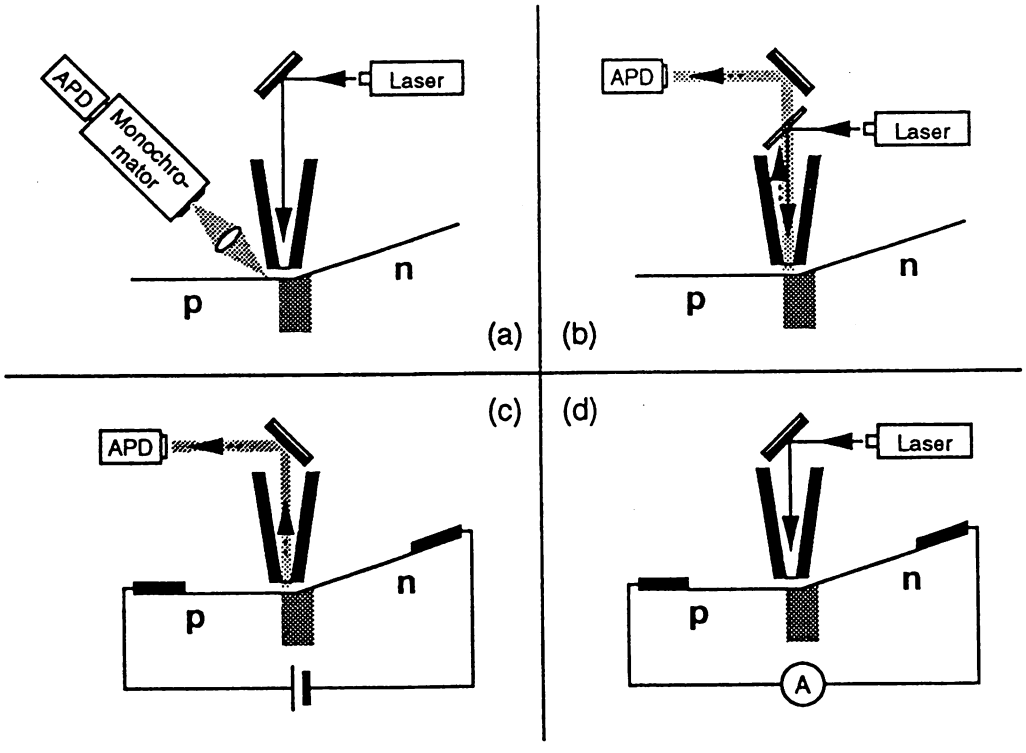

図６：発光スペクトル（ａ），発光強度像（ｂ），電流注入
発光像（ｃ），光電流像（ｄ）の測定配置図．

おこなわれている．試料からの発光を外部でＮＡ０．４の対物レンズによって集光し，分光器へ導く．光検出は，高感度アバランシェフォトダイオード（ＡＰＤ）を用い，フォトンカウンティングによってその強度を測定する．また，プローブ先端はシアフォース顕微鏡の針としての役割を兼ねており，共振周波数で振動させたプローブ先端に半導体レーザ光を照射し，その振幅をモニターしながら距離の制御をおこなっている．レーザとしては，その波長がＧａＡｓの吸収端からはずれた１．５５μｍのものを使用する．

図５（ｂ）にシアフォース顕微鏡によって斜面近傍の形状観察をおこなった結果を示す．斜面の高さ，幅はそれぞれ１０μｍ，６μｍ程度である．頂上付近から斜面にかけて大きな凹凸がみられるが，これは斜面作製過程におけるエッチングによって生じたものと考えられる．

斜面近傍の特徴的な位置での発光スペクトルを図７に示す．ＧａＡｓ層の面方位を反映したピーク波長の変化は，伝導型およびキャリア濃度の移り変わりのようすを明瞭に表わしている．（１１１）Ａ面上（図７Ａ，Ｅ），および（３１１）Ａ斜面上（図７Ｃ）でそれぞれｐ型，ｎ型となっていることが確認された．また接合部分においてはその中間のピーク波長を示していることがわかる．そこでさらに，遷移領域における伝導型，キャリア濃度の詳細な変化を追うために，発光スペクトルのピーク波長，全発光強度を斜面近傍の位置の関数としてプロットしたのが図８である．この結果から上接合と下接合では，遷移領域（図中，網掛け部分）の構造が大きく異なることがわかる．下接合においては，断面の形状からわかるように非常に緩やかに（１１１）Ａ平面から斜面に移行しており，これを反映して５～６μｍ程度の広い領域で遷移が起こっていることがわかる．それに対し，上接合における面方位の移り変わりは非常に急激であり，これに対応して遷移領域の幅は１μｍ程度の狭いものとなっている．

ｐ－ｎ接合試料に対し，電極を装着することにより，発光素子，光検出素子としての動作を確認し，活性領域の高分解能観察をおこなうことも可能となる．図６（ｃ）の配置により，電流注入による発光を局所的に検出する．また，図６（ｄ）に示すように微小開口を通して，活性領域に光照射することにより，光電流観測をおこなう．下接合近傍において，シアフォース像，フォトルミネッセンス像（図６（ｂ）の配置），電流注入発光像，光電流像を同一箇所にて測定した結果を図９に示す．プローブの走査範囲は，４μｍ×６μｍである．電流注入発光と光電流信号がほぼ同位置に観測されており，これらから活性領域の位置，幅が正確に評価される．この領域でフォトルミネッセンス強度が逆に弱くなっているのは，光生成されたキャリアが内部電場によって発光に寄与しない方向にドリフトするためであると考えられる．また，このような狭い活性領域をもつｐ－ｎ接合は，微小開口近傍の

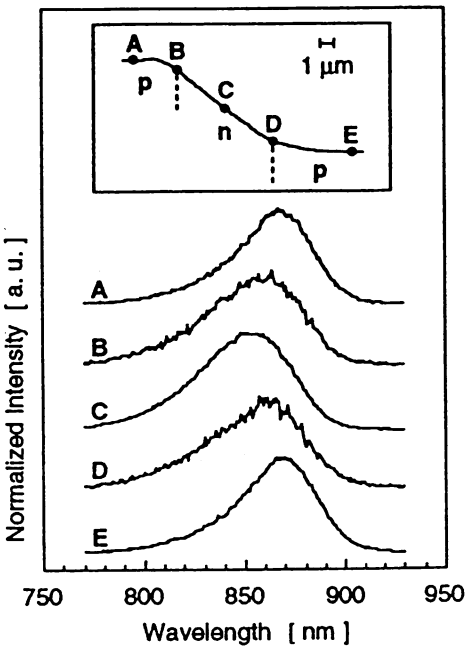

図７：斜面近傍の発光スペクトル.

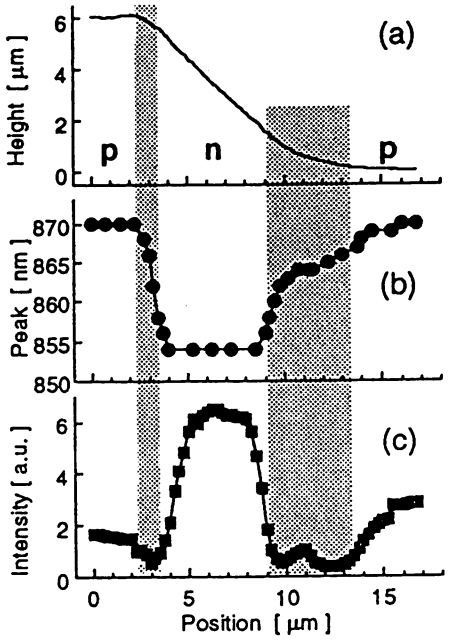

図８：斜面近傍の断面形状（ａ），発光のピーク波長（ｂ），および全発光強度（ｃ）.

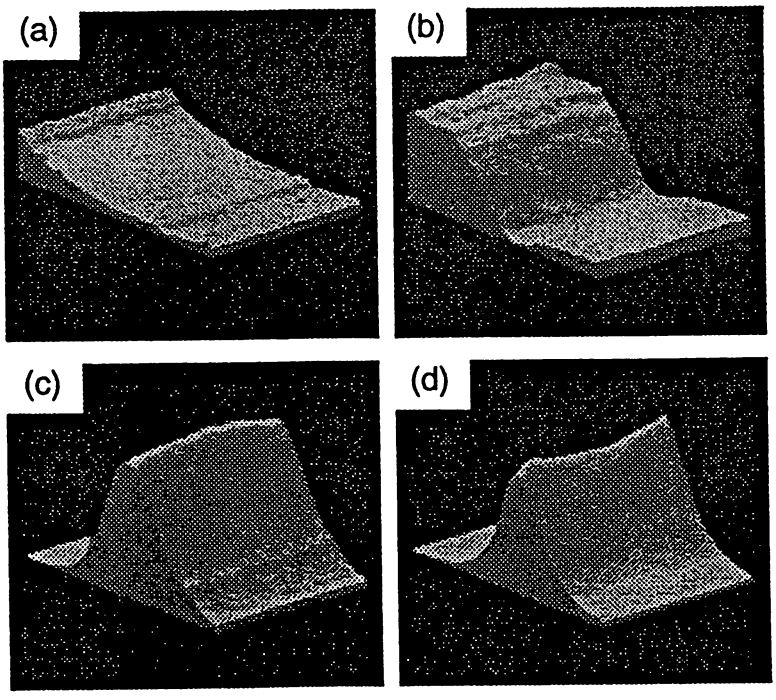

図９：下接合におけるシアフォース像（ａ），フォトルミネッセンス像（ｂ），電流注入発光像（ｃ），光電流像（ｄ）.

光強度分布を観察するための，光検出器としての働きを持つ．これにより，エバネッセント光の空間ひろがり，あるいは高屈折率媒質との相互作用による伝搬光への変換など，重要な情報が得られている．

§4　自己形成単一量子ドットの発光スペクトル測定

不均一ひろがりをもつ粒子系に対してその観測粒子数を制限し，個々のスペクトルを抽出する手段として，近接場光学顕微鏡が盛んに利用され始めている．単一分子，量子井戸，量子ドットなどがその代表的な応用例である．量子ドットに関しては，フォノンボトルネックの観点から均一ひろがりに対する強い関心が集まっており，さまざまな測定手段によるアプローチがなされている．特に自己形成量子ドットの場合，その成長方法の特徴から，ドットの低密度化には制限があるので，励起領域をできるかぎり絞ることによる測定側からの歩み寄りが重要である．ここでは低温において得られた自己形成量子ドット分光測定の結果を示す．

試料としては，図１０に示すようにＧａＡｓ基板上に成長させたＩｎＧａＡｓ量子ドットを用いる．ドット1つのサイズは直径３０ｎｍ，高さ１５ｎｍ程度である．ドット密度は$2\times10^{10}\,cm^{-2}$であり，直径３００ｎｍの円中に約１５個のドットが存在することに相当する．測定はすべてクライオスタットの中でおこない，試料温度は５Ｋに保たれている．励起光源としてＨｅ－Ｎｅレーザを用いることにより，ＧａＡｓ層においても光吸収が起こり，ドット部へのキャリアの供給をおこなっている．プローブとしては十分な感度を得る目的で，５００ｎｍ程度の開口を用いている．発光領域はキャリアの拡散のために～μｍ程度広がるので，集光もまた微小開口を通しておこなうことにより，検出領域を制限する必要がある．

図１１に得られた発光スペクトルの一例を示す．一番上のスペクトルはプローブを１μｍ程度試料から離すことにより得られたファーフィールド領域でのスペクトルである．多数のドットを同時に観測しているという状況を反映して，スペクトル形状はなめらかであり，不均一ひろがりの情報だけを与えている．一方，下の４つのスペクトルは，プローブをニアフィールド領域まで近づけて測定した結果である．スペクトル形状は励起強度によらず，飽和が生じる前の線形な発光領域での測定であると考えられる．いずれのスペクトルにも再現性良く確認される細かなピーク構造があり，単一のドットからの発光が分離して観測されていることを示唆する．個々のスペクトル幅としては，１～２ｍｅＶが得られている．さらに，検出するピーク波長（９２８ｎｍと９５１ｎｍ）を固定し，プローブを走査することにより得られた画像を図１２（ｂ），（ｃ）に示す．走査範囲は，３μｍ×３μｍである．２つの検出波長に対し，全く異なった発光画像が得られている．図中の1つ1つのスポットが（分光器の分解能の範囲で）同じ発光波長をもつドットの分布のようすを示し

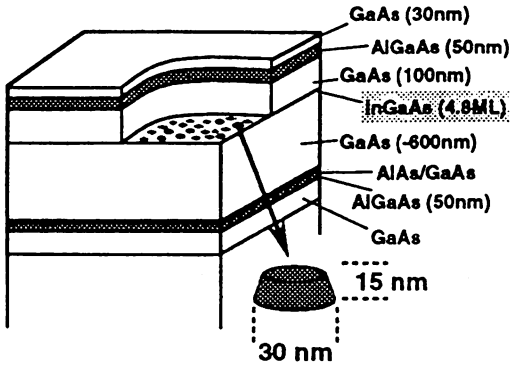

図１０：ＩｎＧａＡｓ自己形成量子ドット.

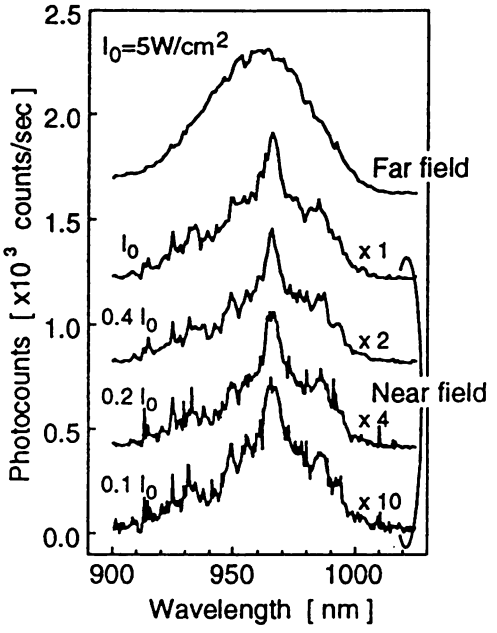

図１１：量子ドット発光スペクトル.

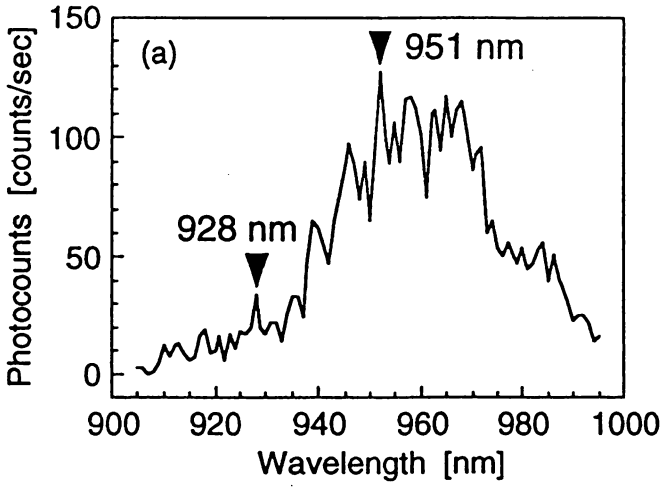

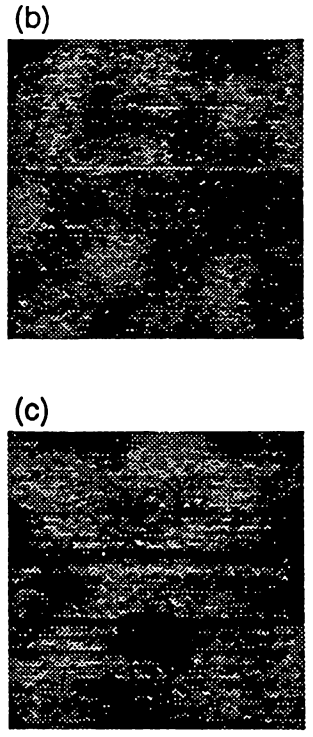

図１２：量子ドットからの発光スペクトル（ａ）と検出波長を９２８ｎｍ（ｂ），および９５１ｎｍ（ｃ）に固定して得られた発光画像.

ている．ドットの実際のサイズが３０ｎｍに対して，画像上でのスポットサイズが３００ｎｍ程度となっており，この大きさが本測定の分解能であると解釈される．

§５　有機ポリシランの紫外発光観察

ポリシランはＳｉ原子を主鎖とする擬一次元半導体であり，バンドギャップが３～４ｅＶに存在するため紫外発光素子として大きな期待が寄せられている．しかも側鎖のアルキル基の種類により主鎖の骨格構造を変えることが可能であるため，それにともなう電子状態の変化が基礎物性，デバイス化の両方の面で非常に興味深い．ただし，主鎖の構造，および長さの違いに起因する発光特性の変化は，それらの不均一性を取り除いた空間分解分光によってはじめて明確な議論が可能になる．

試料としては，十分に薄めたポリジヘキシルシラン（ＰＤＨＳ）を石英基板上に分散させたものを用いている．観察位置により，大小のドメイン構造から単一分子構造まで選択が可能である．測定配置を図１３に示す．励起用光源としては，ＰＤＨＳの吸収のピークにあたるアルゴンレーザの３５１ｎｍラインを使用する．プローブは，紫外光のロスの小さい，純粋石英をコアとするファイバを用い，高分解能と高感度を同時に達成するために，３段型プローブを準備した．微小開口を通して励起光を照射し，試料からのフォトルミネッセンスを検出する．測定はすべて室温でおこなっている．

５００ｎｍ程度の高さをもつＰＤＨＳ凝集構造に対し，開口を通じた１００ｎＷの強い光照射下での発光スペクトルの時間変化を追った結果を図１４に示す．室温大気中の測定であることと強励起であることのために，１分間程度で退色が起こっていることが確認された．続いて，この退色現象を避けるため，０．５ｎＷ程度の弱励起下において，発光画像の計測をおこなった結果を図１５に示す．走査範囲は１μｍ×１μｍである．高さ２０ｎｍ程度の微小な凝集構造からの発光像が得られている．ただし，この画像で得られた最大の検出光子数は，４００ｃｐｓである．今後，単一分子の画像，スペクトル計測を達成するためには，集光・検出系の改良をおこない，感度の向上を図る必要がある．

§６　おわりに

近接場光学顕微鏡を用いた半導体試料の分光，特に発光観測について主な結果を紹介した．このような分光観察への応用を試みる場合，感度の低さが最も大きな障害となる．しかし，必要な分解能に応じて，開口径を調整することにより，十分な感度が得られることもしばしばある．このように，分解能と感度の兼ね合いを，開口径によってコントロールすることが可能である点は，近接場光学顕微鏡の大きな特長であるといえる．もちろん今後，感度の向上を目指し，プローブの改善を図る

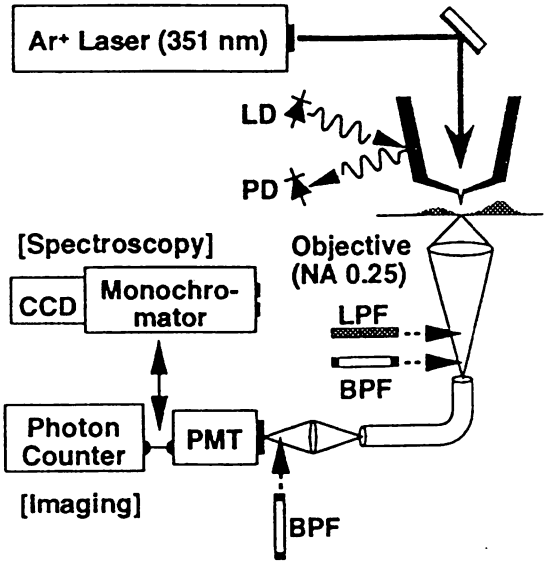

図１３：ポリシラン発光測定配置.

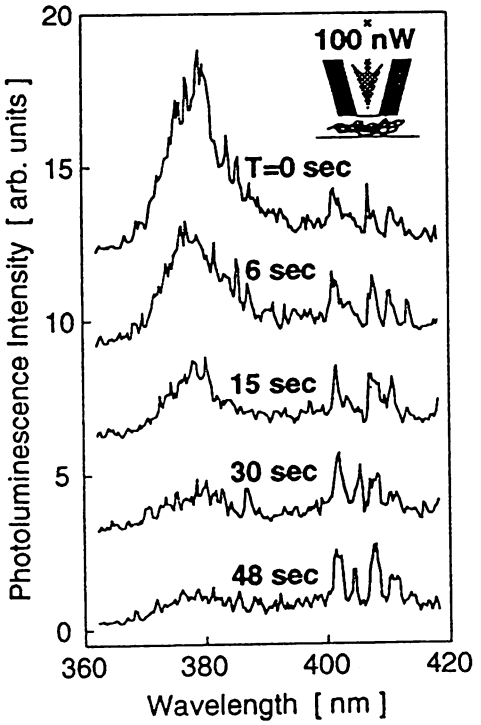

図１４：ＰＤＨＳ凝集構造からの発光スペクトル.

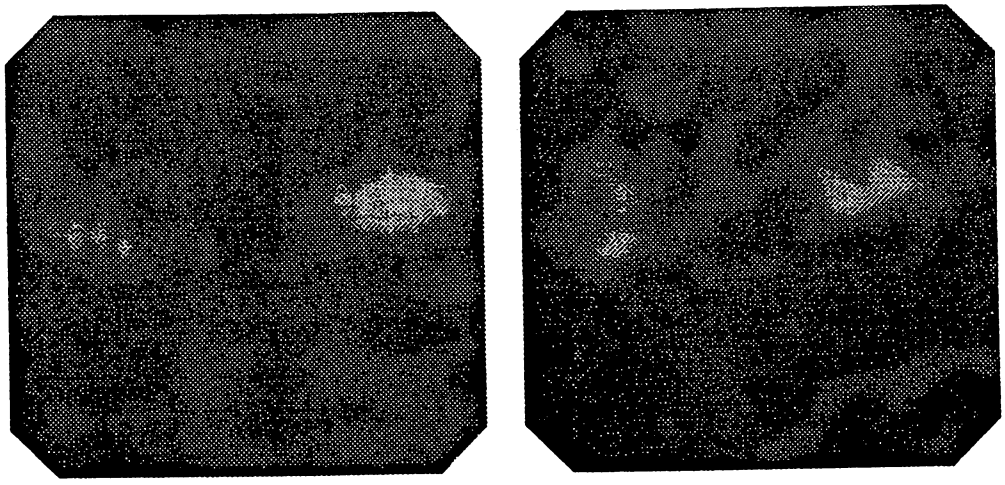

(a)　　(b)

図１５：ＰＤＨＳ凝集構造のシアフォース像（ａ）と発光像（ｂ）.

ことが最優先の課題である．先端形状の工夫，プラズモンモードの利用などがその候補と考えている．これらの実現により，非線形分光技術，時間分解分光技術なども不自由なく導入することができるであろう．

また，先鋭化をおこなったファイバを単なる観察のためのプローブとしてではなく，光学応答の制御のために利用することが新たな発展の方向であると考えられる［8］．プローブの微小物質への接近は，局所的な環境屈折率の変化をもたらす．その結果，たとえば，発光物質に対しては，輻射寿命の変化や励起エネルギー移動を誘起する．また，鋭い共鳴構造をもつ物質に対しては，その共鳴エネルギーシフトをもたらし，さまざまな興味深い現象を発現させるであろう．

このような，分解能・感度など，システムの向上に合わせ，観察から制御へという新たな展開により，近接場光学の分野がさらに活発化し，研究分野の裾野が広がることを期待する．

謝辞

本研究を遂行するにあたり，ＮＨＫ放送技研・斎藤信雄氏（横方向ｐ－ｎ接合），ＮＥＣ光エレ研・西研一氏，東工大・横山吉隆氏（量子ドット），東工大・腰原伸也助教授，蝦原健三氏（ポリシラン）のご協力をいただきました．また，ファイバプローブ作製全般に関して，神奈川科学技術アカデミー・物部秀二氏にお手伝いいただきました．これらの方々に深く感謝致します．

参考文献

［1］ M. Ohtsu, J. Lightwave Technol. 13, 1200 (1995).
［2］ H. Heinzelmann and D. W. Pohl, Appl. Phys. A 59, 89 (1994).
［3］ T. Saiki, S. Mononobe, M. Ohtsu, N. Saito, and J. Kusano, Appl. Phys. Lett. 68, 2612 (1996).
［4］ T. Pangaribuan, S. Jiang, and M. Ohtsu, Scanning 16, 362 (1994).
［5］ S. Mononobe and M. Ohtsu, J. Lightwave Technol. 14, 2231 (1996).
［6］ T. Saiki, S. Mononobe, M. Ohtsu, N. Saito, and J. Kusano, Appl. Phys. Lett. 67, 2191 (1995).
［7］ T. Saiki, N. Saito, J. Kusano, and M. Ohtsu, Appl. Phys. Lett. 69, 644 (1996).
［8］ T. Saiki, M. Ohtsu, K. Jang, and W. Jhe, Opt. Lett. 21, 674 (1996).

原子を導く光のトンネル

――エバネッセント光による原子の制御――

伊藤治彦
大津元一

光が波として伝わってゆくことは誰でも知っている．しかし，光にはもう一つ，ある場所にとどまって動かない「エバネッセント光」という形がある．このエバネッセント光を利用すると原子を導く“光のトンネル”をつくることができる．

「伝搬光」と「エバネッセント光」

光は波長の短い電磁波の一種であって，真空中であればおよそ30万km/sもの速さで伝搬してゆく．光通信をはじめとする現代の高度な光技術は，このような伝搬光の高速性，直進性に依拠したものが多い．一方，最近，「エバネッセント光」と呼ばれる伝搬しない光が注目を集めている．エバネッセント光は波長よりも小さな領域に局在する光の場である．ここでは，エバネッセント光を利用した原子の高精度な制御の方法について紹介する．これは将来，究極の微細加工技術に発展する可能性を秘めている．

全反射とエバネッセント光

障害物のない自由な空間では，光は1秒間当たり10^{14}回も振動する電磁波として伝搬する．しかし，光の形態はこのような伝搬光だけではない．屈折率が変化する境界面に光がさしかかると，光の反射や屈折といった現象が起こるが，境界面上では光の状態は不確定で，伝搬しない光の成分――エバネッセント光――も存在する．

エバネッセント光が生じる典型的な場合は，屈折率が変化する境界面で全反射を起こすときである．図1に示すように，空気中に置かれたガラスに入射した光線が端面から出ようとする場合を考えよう．全反射は，光が屈折率の大きいガラスから屈折率の小さい空気に進入しようとするときに起こる．入射角がある臨界値より大きくなると，屈折光が存在しなくなる現象である．この場合，ガラス内には反射光が伝搬するが，ガラスの外の空気側には光が伝搬してゆかない．しかし，入射光と反射光とをつじつまが合うように反射面でうまくつないでやるためには，空気側にも光の場がしみ出していることが必要となる．この光の場がエバネッセント光（“だんだん消えてゆく”光という意味）と呼ばれるものである．エバネッセント光も伝搬光と同様に，非常に高い周波数で振動する電磁界からできている．

中空光ファイバーで原子を導く

原子を自在に操ることができれば，結晶成長を原子レベルで

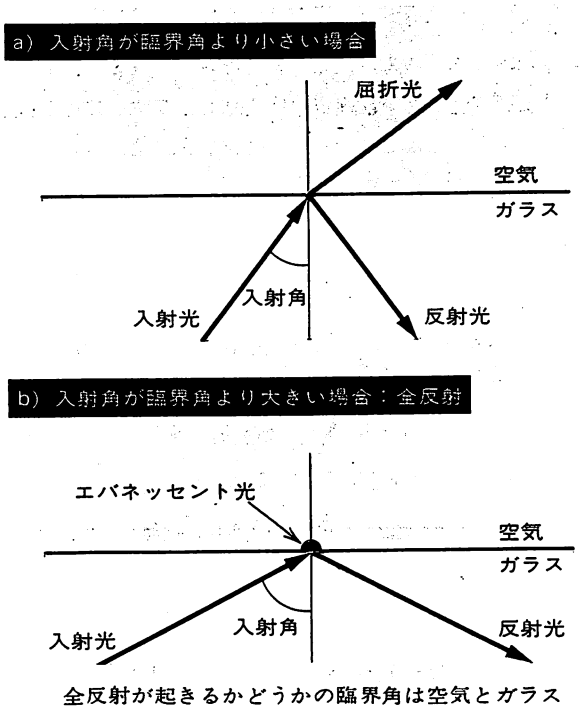

全反射が起きるかどうかの臨界角は空気とガラスの屈折率の比で決まる．

図1　光の反射と屈折

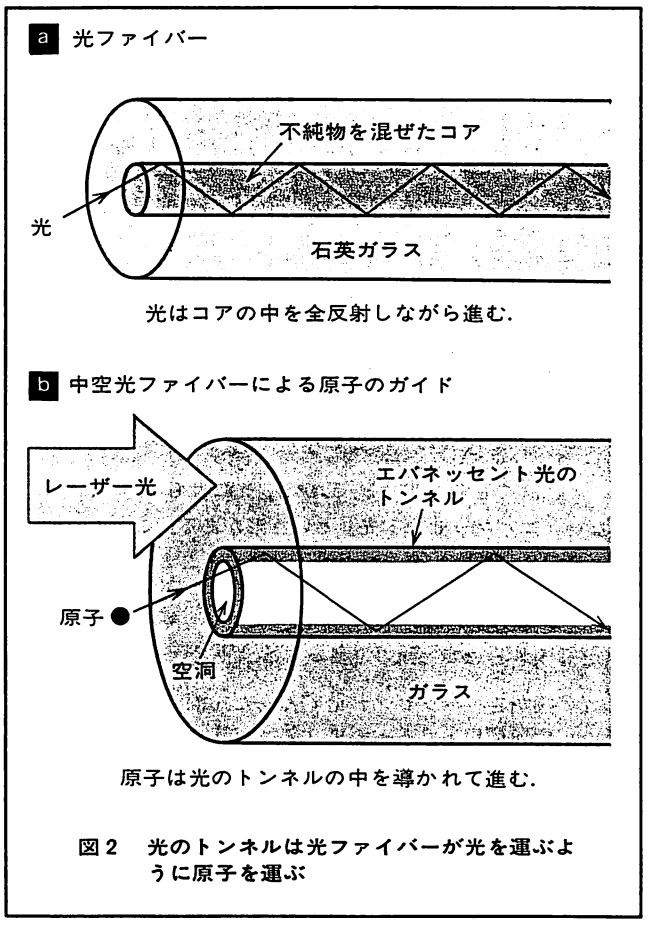

図2　光のトンネルは光ファイバーが光を運ぶように原子を運ぶ

制御したり，量子力学の基礎理論の検証実験や表面の化学的性質の探求などに新たな道を開くことになる．これまで，原子を狭い空間に閉じ込めたり，極低温に冷却したりするには伝搬光が使われてきた．しかし，エバネッセント光には，伝搬光とは著しく異なる次のような性質がある．

1）物質の表面に局在する．

2）電界の振幅（光の強度）が表面からの距離に比例して指数関数的に減少する．

3）物質の大きさや形状によって分布の仕方が決まる．

このため，これらの特徴を活用すれば，伝搬光を使うよりもはるかに精度の高い原子の制御が可能となる．その端緒として，我々は気体原子の運動を一次元的に制御する「光のトンネル」をつくり上げた．これは，従来の伝搬光を用いた原子の制御とは一線を画するものである．

ガラス平面からしみ出したエバネッセント光がある条件のもとで原子を反射する鏡のように振る舞うことは，近年の一連の研究によって明らかにされてきた．光のトンネルは，この性質を立体的に拡張したものである．光のトンネルは光ファイバーと似た構造をもち(図2)，光ファイバーが光を任意の位置に運んでゆくのと同じような形で原子を運ぶことを可能にする．

光通信に使われる光ファイバーは石英ガラスでできており，中心部分にゲルマニウムなどの不純物を混ぜることによって光を閉じ込めて伝える小さな領域（コア）が設けられている（図2a)．光はこのコアの中を全反射を繰返しながら損失なく導かれてゆく．一方，光のトンネルをつくるには，図2bのような，中心部分が空洞になった光ファイバーが使われる．空洞が原子を閉じ込めて運ぶコアとなるべき部分であり，その中で光の全反射に相当することを原子に行わせる必要がある．ガラスと原子の間には強いファンデルワールス力が働き，原子がガラスに衝突するとくっついてしまうことが多い．したがって空洞の壁に衝突する前に原子を跳ね返さないと，原子は空洞をうまく通り抜けることができない．ここで，原子を反射するための斥力をつくるのがエバネッセント光の役目なのである．

図2bのように，中空光ファイバーの空洞のまわりのガラスの部分にレーザー光を入射し,伝搬させる.このときファイバーの内壁では全反射が起こっており，伝搬光は空洞内には入ってゆかない．しかし，ごく表面付近ではエバネッセント光が空洞

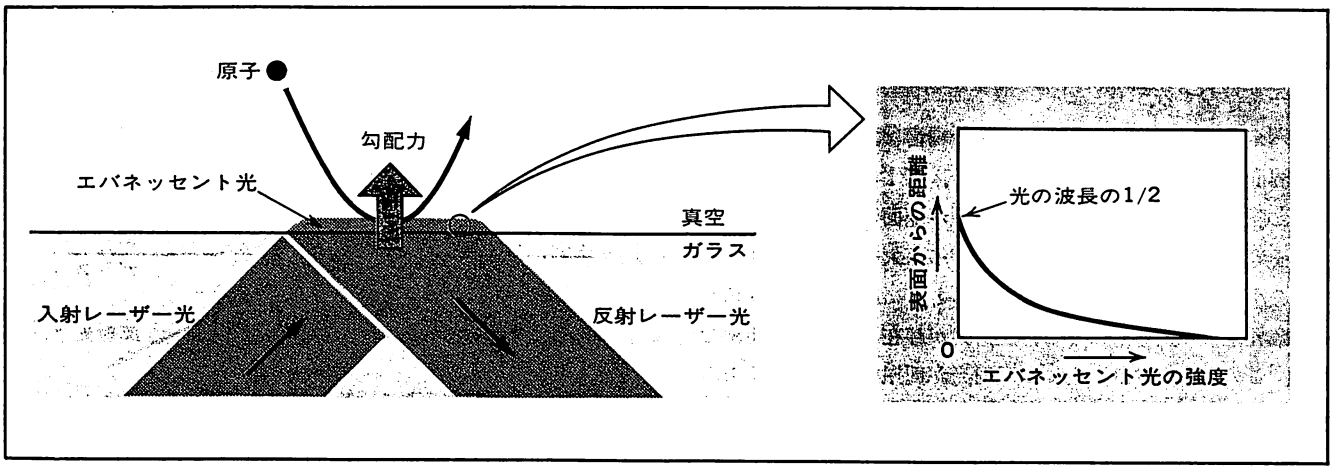

図3　エバネッセント光による原子の反射

内にしみ出しているのである．このエバネッセント光が空洞の壁面を取り巻いて原子を反射し，導く光のトンネルとなる．

原子を反射する光の鏡

原子は中性であって電界や磁界からほとんど力を受けない．それなのに，なぜエバネッセント光は原子を反射することができるのだろうか．それは，光と原子の相互作用によって生じる共鳴的な力の一つである「勾配力」のおかげである．勾配力は，光の強度が空間的に変化する場合に光が原子に及ぼす力で，光強度の変化が大きいほど強い．図3に示すように，エバネッセント光の強度は，ガラス表面から離れると指数関数的に減少するため，非常に強い勾配力を生み出す．ただし，勾配力によって原子を反射するには条件がある．その条件とは，エバネッセント光をつくるレーザー光（以下でガイド光と呼ぶ）の周波数を原子の共鳴周波数よりも少し高くすることである．

エバネッセント光が原子に及ぼす勾配力の向きは，光の周波数と原子の共鳴周波数（後述する誘起双極子の固有周波数）との兼ね合いによって二つの場合に分かれる．光の周波数が原子の共鳴周波数よりも低いときには光強度が強くなる向き（引力）に，高いときには弱くなる向き（斥力）に働く．その由来は正しくは量子力学で説明されるべきものであるが，以下に示すように，古典力学の範囲内でもおおよそのことは理解できる．

図4に示すように，光の場の中では原子は光電界によって分極を起こし，電気双極子を形成する．この誘起双極子にふたたび光電界が作用して力が生じる．光電界の向きと誘起双極子の向きの関係には二通りの場合がある．図4aのように，光電界の振動の周波数が誘起双極子の振動の固有周波数（原子の共鳴周波数）よりも小さいときには両者は向きを揃えて振動するが，大きいときには光電界の振動に双極子の振動が追従できず，図4bのように反対の向きで振動する．エバネッセント光は，壁に近いほうが光強度（光電界）が強いから，向きを揃えて振動する場合には双極子に作用する正味の力（正負二つの電荷に作用する力の差．正電荷には光電界と同じ向きに，負電荷には逆向きに力が作用する）は原子をエバネッセント光のほうへ引き込む向きに，反対の向きで振動する場合には原子をエバネッセント光からはじく向きに作用する．こうして原子の共鳴周波数を境にして原子に働く勾配力の向きが反転することになる．図5に，勾配力の大きさと向きの周波数変化を理論計算によって求めた結果を示した．

ルビジウム原子を導く

原子を跳ね返す勾配力の大きさは，光強度とその変化の勾配および誘起双極子の大きさに比例する．大きな誘起双極子が形成される原子としてナトリウムやルビジウムなどのアルカリ金属原子がある．これらの原子の共鳴周波数は可視領域から赤外

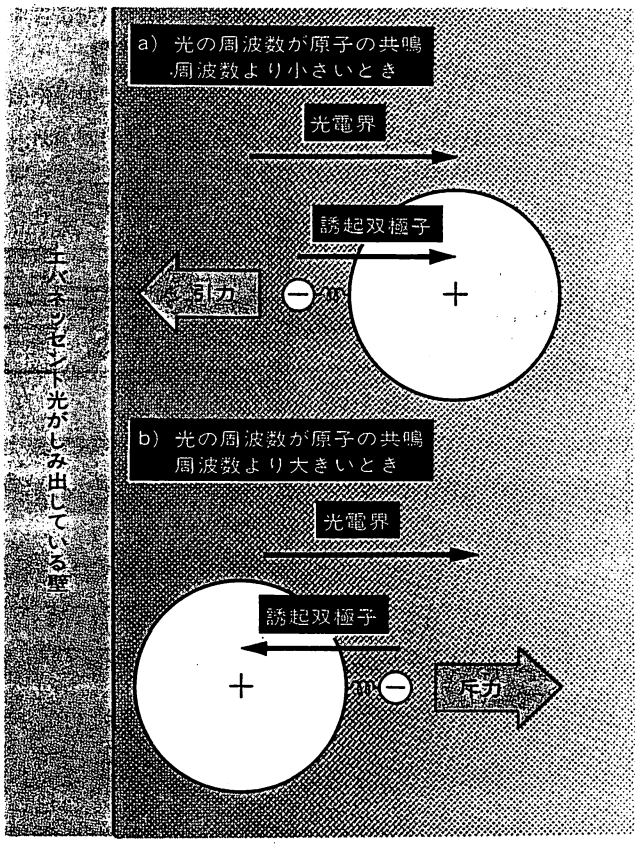

振動する光電界が右を向いている瞬間を示した．
背景の色の濃さは光電界の強さを示している．

図4　誘起双極子に作用する勾配力の向き

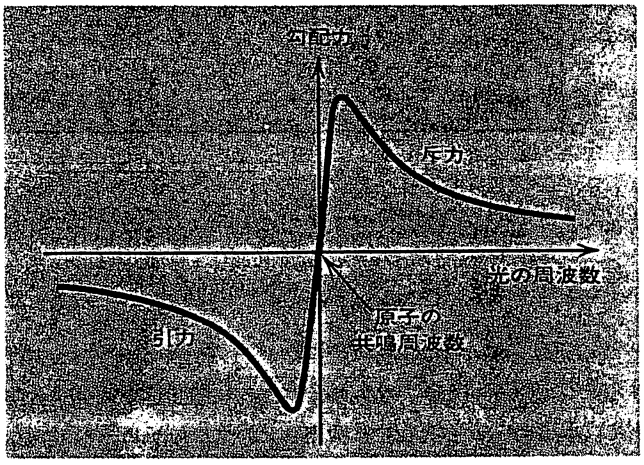

図5　勾配力の周波数による変化

にかけての波長に当たり，色素レーザーやチタンサファイヤレーザーなどの波長可変レーザーを用いて同調することができる．中でもルビジウム原子の共鳴周波数は波長にすると780 nmであって，市販の半導体レーザーの発振波長に適合し，都合がよい．そこで，我々は，光トンネルの実際例として，空洞直径が1 μm程度の非常に小さな中空の光ファイバーを用いてルビ

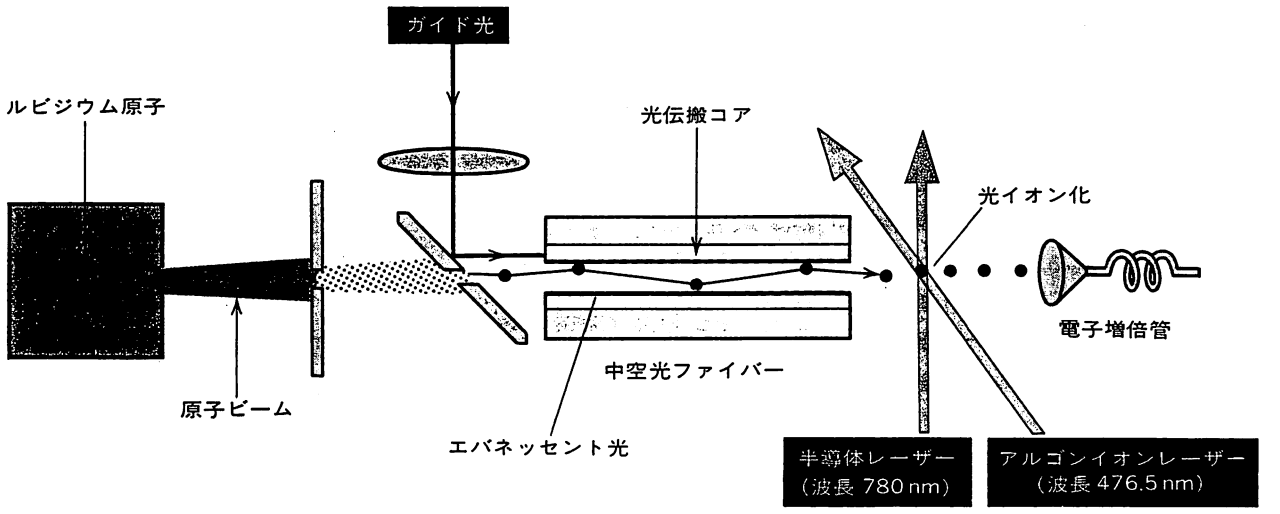

図6　ルビジウム原子を導く実験

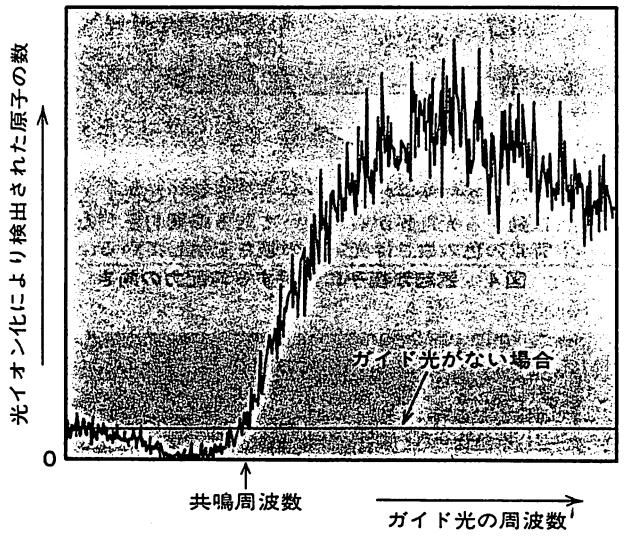

図7　中空光ファイバーから出てくるルビジウム原子の数はガイド光の周波数によって変化する

ジウム原子を導く実験を行った．

図6に実験系を示す．金属ルビジウムを閉じ込めた小部屋を熱して小さな穴から真空中に噴出させ，細い原子ビームをつくる．200°C程度に熱した場合，ルビジウム原子は平均の進行速度300 m/sで中空ファイバー内に飛び込み，空洞の部分を進んでゆく．他方，原子は横方向にもおよそ1 m/s程度の速度をもっており，やがては中空ファイバーの内壁に衝突してしまう．この横方向の速度に打ち勝つエバネッセント光をつくるためには，十分な強度をもつガイド光を中空ファイバー中に伝搬させる必要がある．そこで，我々は，写真1のような光伝搬コア(空洞をとりまく薄いドーナツ部分）をもつ中空ファイバーを用いた．この中空ファイバーを用いると，光のエネルギーが薄い光伝搬コアの領域に集中して強いエバネッセント光をつくることが可能となる．

中空ファイバーに導かれて出てきた原子を検出するには，原子を光イオン化し，生じたイオンを電子増倍管を用いて捕らえるという方法をとった．期待される原子の数は1秒間当たりせいぜい数万個と少ない上に300 m/sという速さで通り抜けてしまうからである．光イオン化は，図6に示すように，2種類のレーザー光を用いて2段階で行った．まず，半導体レーザーによってルビジウム原子を基底状態から励起状態に移し，次いでアルゴンイオンレーザーを照射して最外殻の電子をはぎ取る．半導体レーザーを用いると，ルビジウム原子のみを励起できるため，高真空中でも残存しているほかの原子と区別して検出することができる．

図7に中空径1.4 μm，長さ3 cmの光ファイバー(直径が1.4 cmで長さが300 mのトンネルに相当する）で導いたルビジウム原子を検出した結果を示す．横軸は光の周波数を，縦軸は光イオン化により検出されたルビジウム原子の数を表す．ガイド光の周波数が共鳴周波数より大きいとき，導かれた原子の数が大幅に増加しており，光のトンネルが機能しているのがわかる．逆に，ガイド光の周波数が共鳴周波数より小さい場合は，導かれて出てくる原子の数は減少している．これは，エバネッセント光が引力をつくり，原子を積極的に引込んでガラス上に吸着したためと考えられる．このように，勾配力の向きの周波数変化を反映して，共鳴周波数を境に原子の導かれ方が大きく変化する．

光のトンネルの応用

中空の光ファイバー内につくった光のトンネルによって，原

子の運動を上下および左右方向に1 μm に近い精度で，かつ，長い距離にわたって制御できることがわかった．また，導かれて出てくる原子の数は，ガイド光の周波数および強度を調整することによって変えることができる．さらに，光ファイバーは曲げて使うことが可能であるから，原子の位置制御にも優れている．光のトンネルによる原子の制御のこのような特徴を利用して，ナノメートルスケールの微小構造物を作製するといった新しいタイプの物質形成を行うことが考えられる．図8のように，原子を導いて適当な基板上に吹き付け，結晶成長を行うのである．現在よく使われる分子線エピタキシー（分子を基板に蒸着する方法）では，結晶成長は層を積み重ねるようにしか行えないのに対して，この方法ではドット状に噴出する原子を用いて局所的加工を行えるという大きな利点がある．

技術的に重要な応用をもう一つ挙げよう．原子の導かれ方が周波数によって大きく変化することを利用して，同位体分離を行うことができる．たとえば，天然のルビジウムには質量数85と87の二つの同位体がおよそ7対3の割合で含まれている．質量の相違により，両者の共鳴周波数は異なる．この差に着目してガイド光の周波数を選んでやると，一方の同位体のみが中空ファイバーを通過して出てくるようになる．このように，光の

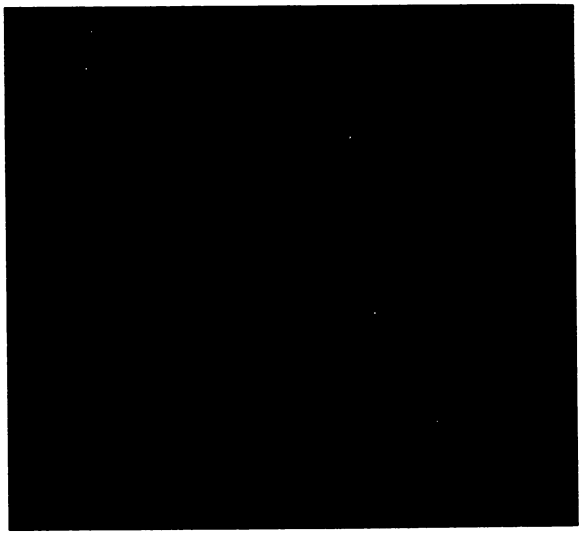

黒くみえる中央部分が空洞である．空洞の直径が1 μm 程度のものは空洞の所在が見にくいので，ここでは直径7 μm のものを示した．白く光っている部分がレーザー光が伝搬するコア．

写真1　中空光ファイバーの断面写真

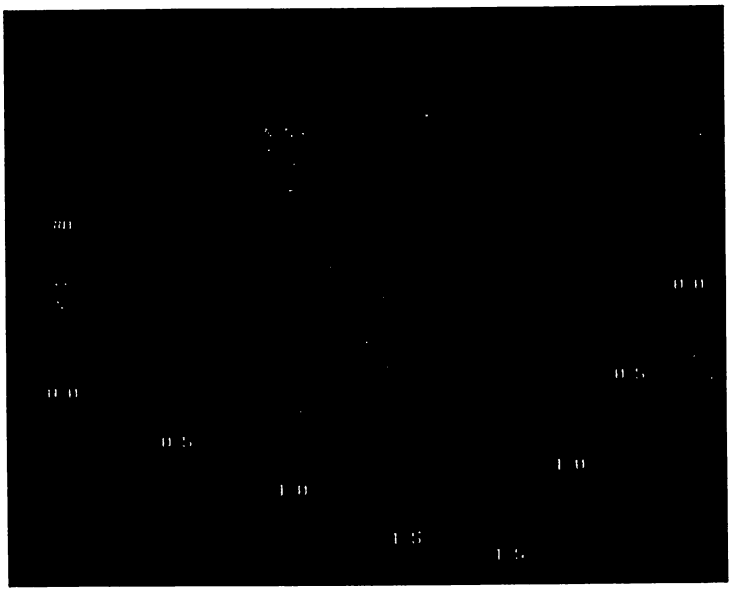

中央付近の直径は30 nm.

写真2　エバネッセント光を用いた近接場光学顕微鏡によるサルモネラ菌べん毛の拡大像

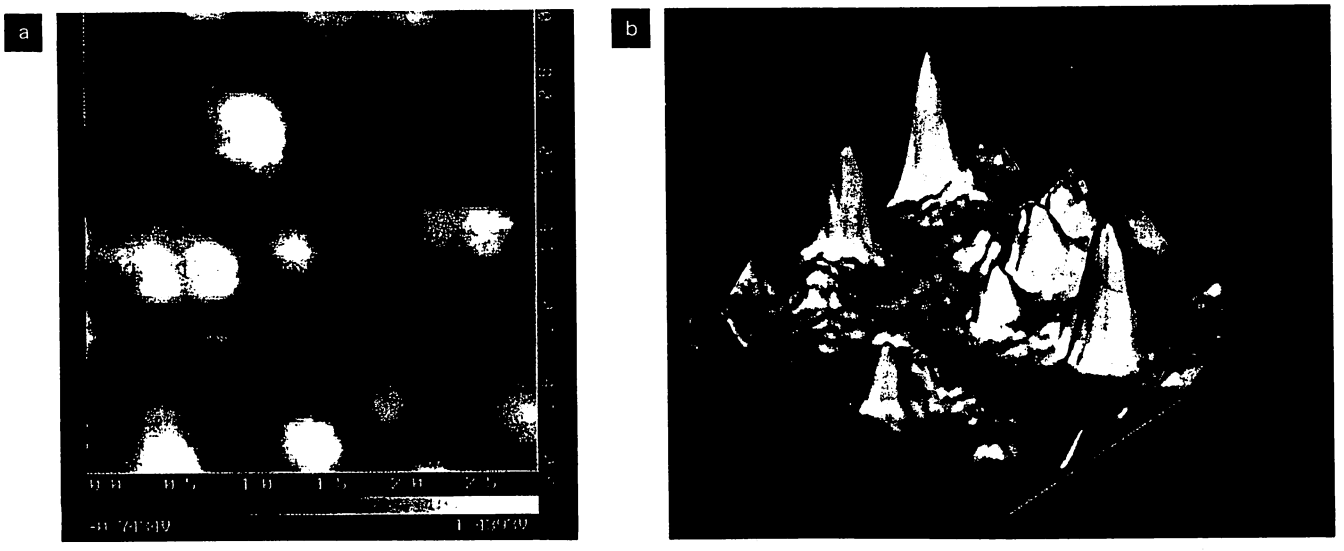

走査範囲は3 μm×3 μm．約1800個の量子ドット（ナノメートルスケールの微小構造物の一例）から特定のサイズの量子ドットのみを選択して表示することができる．a）は二次元で，b）は三次元で表示したもの．

写真3　InGaAs 単一量子ドットの走査近接場光学顕微鏡によるホトルミネセンス分布像

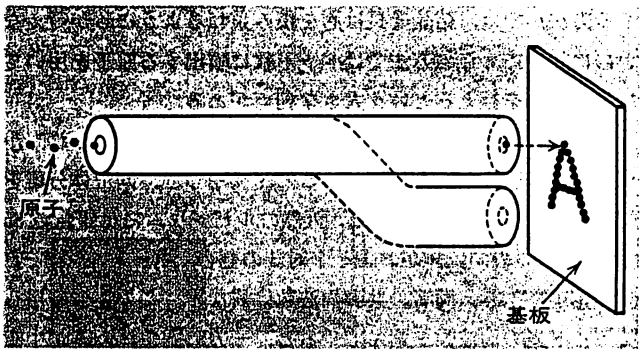

図8　光のトンネルを用いた物質形成

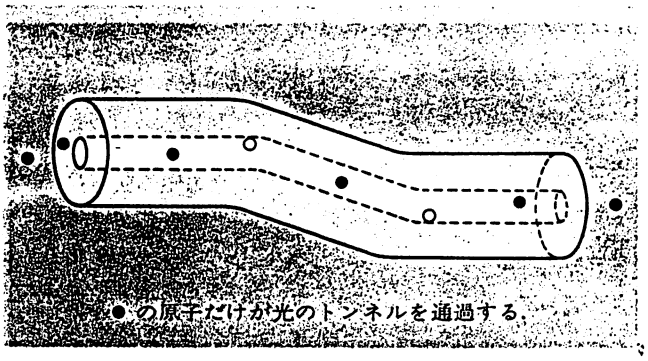

図9　光のトンネルを用いた原子のフィルター

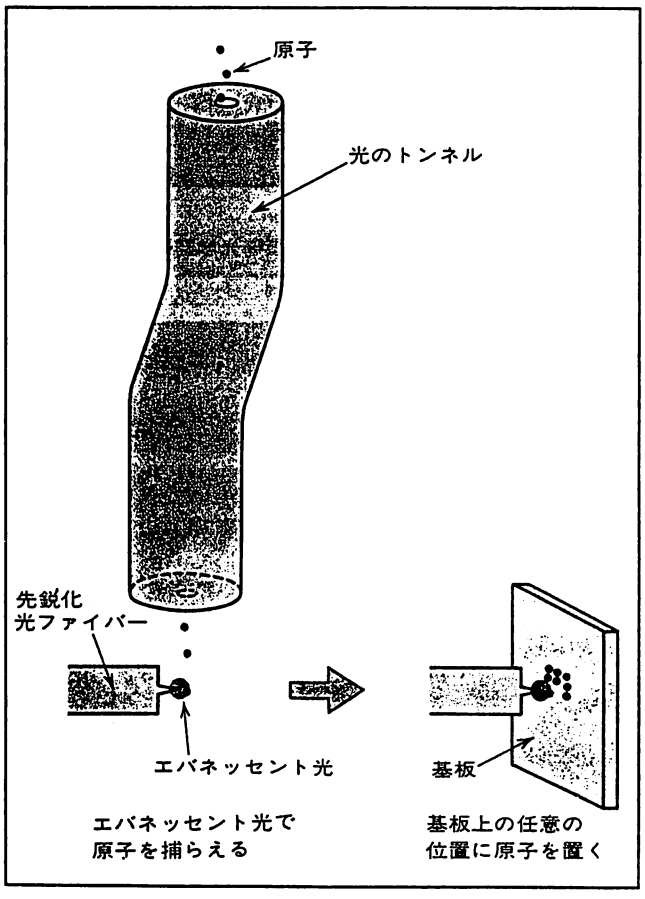

図10　先鋭化光ファイバーによる単一原子操作と
原子レベルの構造の作製

トンネルは原子を選択するフィルターとして活用することができる(図9)．これはまた，原子の純度がきわめて高い高品質の結晶成長が行えることを意味する．

このほかにも，量子力学の基礎にかかわる実験に応用したり，原子を集めて閉じ込めるためのトラップとして利用したりすることが考えられている．

回折限界を超えて

ここで，原子の制御以外へのエバネッセント光の利用についても触れておこう．伝搬光にはその波長で決まる「回折限界」が存在する．光を物体に当てたときに，その物体の裏側に回り込んで光が伝搬する現象が回折である．回り込みの際の光の広がり具合は，物体の大きさや位置と光源との兼ね合いで決まるが，波長以下の寸法にはならない．このことは逆に，もしも物体の寸法が波長以下の場合には，その物体を観察するために伝搬光をいくら小さく絞ろうとしても波長程度には必ずぼけてしまい，その物体を識別できないことを意味する．これが従来の伝搬光を用いた光学顕微鏡の分解能を決めている．

ところが，伝搬光でないエバネッセント光は回折の影響を受けない．エバネッセント光のしみ出しの大きさは，ちょうどそれがしみ出す物体の寸法程度である．したがって，エバネッセント光を生じさせる物体の大きさを小さくすればするほど分布領域の狭いエバネッセント光が得られる．このようなエバネッセント光を用いれば光学顕微鏡の分解能を著しく向上させることができる．現在，可視光をしみ出させて得たエバネッセント光によって1 nm程度の分解能を得る新しい光学顕微鏡の開発が進められている．これにより観察したサルモネラ菌の像を写真2に示した．

また，エバネッセント光を光源とすることにより，ごく微小な部分についての分光学的測定を行うことも可能である．この一例として半導体材料表面の分析例を写真3に示した．

原子ホトニクスに向けて

レーザー光を用いて原子の運動を制御する研究分野は原子光学と呼ばれており，活発な研究が行われている．従来の伝搬光を主体とした制御では，回折限界のため波長以下の精度で原子を操作することは難しかったが，エバネッセント光を用いれば，この限界を克服することができ，原理的に単一原子の操作を行うことも不可能ではない．実際，先端を1 nmの程度にまで尖らせた先鋭化光ファイバー（写真4）を利用することが検討されている．先端以外を光が通らないようにマスクしておくと，伝搬光は波長以下の領域には伝わらないため，先鋭化光ファイバーからは伝搬光が出てこない．しかし，エバネッセント光ならその先端からしみ出すことができるのである．このエバネッセント光の周波数を調整すれば，1個の原子をファイバーの先

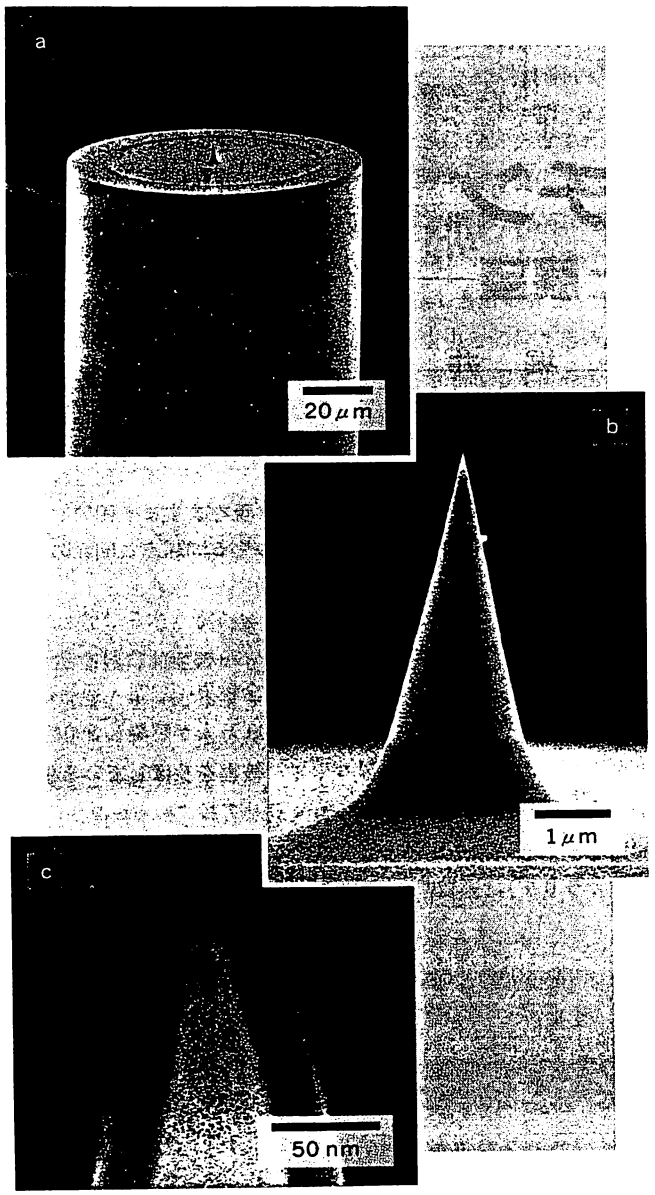

a）は全体像．b）は尖らせた部分の拡大像．c）はさらにその先端を拡大したもので，表面に電子顕微鏡観察時に付着した汚染物の層がある．

写真4　先端を鋭く尖らせた光ファイバーの電子顕微鏡写真

端付近で捕まえたり放したりすることが可能となる．さらに，図10のように，先鋭化光ファイバーで捕まえた原子を基板上に運ぶことによって原子レベルの構造をつくることも夢ではない．

筆者らの研究室では，ここで述べてきたような，伝搬光にはないエバネッセント光の優れた特徴を活かした高精度な原子操作技術の開発と，それを利用した原子レベルでの物質形成技術の確立を目指している．これらが基盤となり，近い将来「原子ホトニクス」とでもいうべき，光を用いた新しい物質科学の創造につながることを期待している．

表面科学 Vol. 18, No. 1, pp. 55-57, 1997

実験ノウハウ

近接場光学顕微鏡でどこまで高分解能像が得られるか？(2)

大津 元一*, **

*東京工業大学大学院総合理工学研究科 〒226 横浜市緑区長津田 4259
**神奈川科学技術アカデミー フォトン制御プロジェクト 〒213 川崎市高津区坂戸3-2-1, KSP東棟 408号

(1996年3月11日受理)

Realizing Ultrahigh Resolution in a Near-field Optical Microscope

Motoichi OHTSU*, **

*Interdisciplinary Graduate School of Science and Engineering, Tokyo Institute of Technology
4259 Nagatsuta, Midori-ku, Yokohama 226
**"Photon Control" Project, Kanagawa Academy of Science and Technology
KSP East Rm. 408, 3-2-1 Sakado, Takatsu-ku, Kawasaki 213

(Received March 11, 1996)

前回は近接場光学顕微鏡の原理と構成を中心に述べた。今回は具体的な画像計測の例を提示する。システム関数推定結果より，0.8 nmの分解能が得られたこと，さらに原理的には原子レベルの分解能が期待できることを示す。特に生体試料，フォトニクス用材料，素子の測定評価を中心に記し，空気中，水中，極低温中など，特殊環境下での測定が可能であることを示す。さらに形状計測のみでなく，分光計測が可能であることを示す。

4. 画像計測

4.1 基本的特性

前回の図2 (a) でも示したように，エバネッセント場の物質寸法依存のパワー局在は近接場光学顕微鏡 (NOM) の動作原理の一つであるが，これに関する実験結果が得られている[1]。また，Cモードにて超平坦サファイア基板上の段差2 nmの原子層レベルのステップが観測されている[2]。その像を図1に示す。ここではプローブ位置制御にはせん断応力を使わない点が優れている。

さらに具体的に分解能を推定するために，20 nm直径の金微粒子像をIモードにて測定し，その結果より顕微鏡のシステム関数が推定されている。その関数の－3dB遮断・空間フーリエ周波数より，分解能が0.8 nmと推定されている[3]。これらの高い分解能は先端直径が1 nm程度の小さなプローブを使い，さらにそれを試料表面に1 nm程度まで近づけることにより実現している。試料表面までの距離の測定はエバネッセント場の測定の際の雑音の大きさにより制限されるが，その雑音の基本要因は光のショット雑音である。この雑音の大きさに対応する縦分解能は3×10^{-3}nmであると推定されており[4]，この値と本節の実験結果からNOMは原理的には原子レベルの分解能を実現しうると考えられる。

4.2 生体試料の計測

光学顕微鏡の主要な適用分野は生体試料観測である。そのためにはNOMに期待される性能は高い分解能を保ちながら水中で観測できること，蛍光を測定できること，などである。次の結果が得られている。

(a) サルモネラ菌の直線状の鞭毛：Cモードで空気中にて測定されている。その像の直径は30 nmであるが，電子顕微鏡による値（25 nm）と大差ない。水中でも測定されている。この場合せん断応力を使う必要がないので安定なプローブ走査ができ，空気中の値と大差ない直径が得られ，高い分解能が確保されている[5]。

(b) ニューロンの軸索内部の毛細管の束：Iモードの

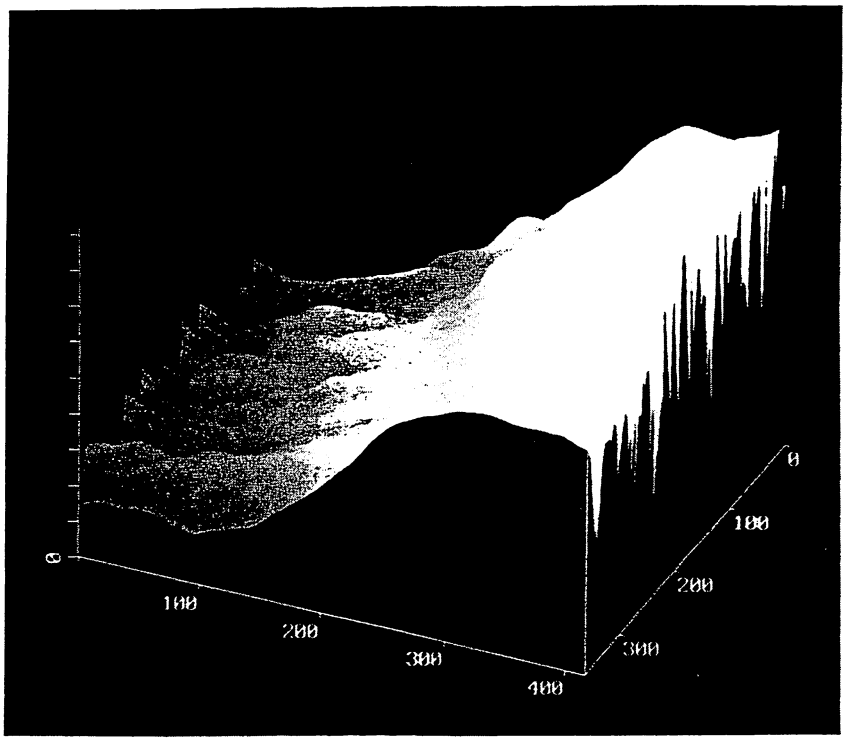

図1 Cモードにて測定した超平坦サファイア基板上の段差2 nmの原子層レベルのステップの像。底面の一辺は400 nm。

NOMにより空気中で測定されている。毛細管の直径は26 nmであった。電子顕微鏡ではこれらの毛細管を軸窄から取り出して測定し，直径25 nmが得られている。このことはNOMでは軸窄から取り出さずに，電子顕微鏡と同等の寸法の毛細管像が得られることを意味している[6]。

(c) 色素分子をドープした生体試料からの蛍光：Iモードで測定されている。

4.3 フォトニクス用材料，素子の評価

従来の光エレクトロニクス素子は光波長以上の寸法を有するので，NOMにとっては大きな試料である。しかしその表面の微小な構造変化などの計測や評価にはNOMは有効である。

(a) 光導波路：Y分岐のLiTaO$_3$導波路の導波モードの観測，光波長以下の寸法の微小散乱光源の同定，さらには導波損失の測定などが行われている[7]。

(b) 半導体量子ドット：発光の量子効率を上げるために液体ヘリウム温度で測定されている。このために極低温で動作するNOMが開発されている。図2に液体ヘリウム温度付近での発光スペクトルの測定結果を示すが，従来の遠視野の場合と異なり，不均一ひろがりが除去でき，幅の狭い数本のスペクトルが分離されて観測されている[8]。特に矢印を施したスペクトル成分は内挿図と比較すると量子ドットからの発光であると推定されている。

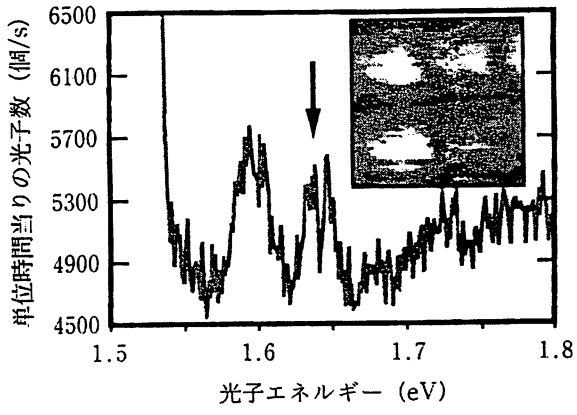

図2 GaAs量子ドットのフォトルミネッセンスのスペクトル測定結果。温度18 K。内装図はスペクトル曲線中の矢印の位置でのフォトルミネッセンス強度の空間分布。この図の一辺は2 μm。

なお，関連する実験として温度2Kにおける GaAs/AlGaAsの厚さ2.3 nmの単一量子井戸の励起子スペクトルの測定[9]，キャリヤ緩和の位置依存性の評価[10]などが行われている。

(c) 面発光素子：段差加工を施したGaAs基板上にSiをドープしたGaAs層をMBE成長させることにより形成された横方向pn接合のフォトルミネッセンス分光が行われている（図3）[11]。このほか，エレクトロルミネッセンス，光励起電流の空間分布も測定され，pn接合面の傾

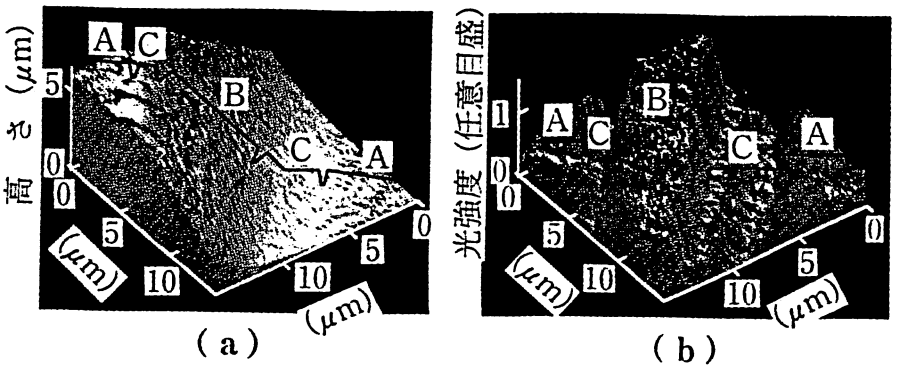

図3 段差加工を施したGaAs面発光素子の測定結果。A, B, Cは各々p形, n形, および遷移領域。(a) せん断応力により同時測定した形状。(b) フォトルミネッセンス強度分布。矢印の位置は遷移領域中での局所的な発光強度の大きい箇所を示す。

きなどが評価されている。

4.4 その他の試料の計測

(a) 色素分子の蛍光測定： 励起領域に数個の色素分子しか存在しないような低密度の試料を準備し，単一色素分子からの蛍光測定が行われている[12]。さらに単一色素分子の退色過程，可逆的な蛍光強度変化，プローブ周辺の金属膜の影響による消光現象などが観測されている[13]。

(b) 固体の光学スペクトル： 応力下でのルビーの蛍光スペクトル[14]，ダイヤモンドのラマンスペクトル[15]などが報告されている。さらには金属膜上の表面プラズモン波動が検出されている[16]。

5. ま と め

NOMはすでに1 nmを打破する高い分解能が実現し，原理的には原子レベルの分解能に達することも可能である。またその動作環境は空気中，水中，極低温など，広範囲にわたる。さらに形状測定のみでなく，分光測定が可能であるところが利点である。この特徴を生かし，他の走査プローブ顕微鏡では得られなかった微小物質に関する多様な情報の取得が可能になる。さらにまた本稿では割愛したが，Iモードのプローブ先端にしみ出すエバネッセント光エネルギー密度を高めて，物質表面の加工，さらには超高密度光記録などが行われている。

文 献

1) T. Saiki, S. Mononobe and M. Ohtsu: Proc. Quantum Electron. and Laser Sci. (Opt. Soc. Am., 1995) p.84
2) R.ミケレット, 物部秀二, 大津元一, 吉本 護, 大西剛, 前田辰郎, 鯉沼秀臣: 第43回応用物理学関係連合講演会, 26aZM 11 (1996).
3) R. Uma Maheswari, H. Kadota and M. Ohtsu: Opt. Commun. **131**, 133 (1996).
4) M. Ohtsu: J. Lightwave Technol. **13**, 1200 (1995).
5) M. Naya, R. Uma Maheswari, R. Micheletto, S. Mononobe and M. Ohtsu: Proc. Int. Conf. Near Field Optics and Related Technol. (Euro. Opt. Soc., 1995) p.105.
6) R. Uma Maheswari, H. Tatsumi, Y. Katayama and M. Ohtsu: Opt. Commun. **120**, 325 (1995).
7) Y. Toda and M. Ohtsu: IEEE Photonics Technol. Lett. **7**, 84 (1995).
8) Y. Toda, M. Kourogi, Y. Nagamune, Y. Arakawa and M. Ohtsu: Proc. Conf. Lasers and Electro-Opt./Pacific Rim '95 (Opt. Soc. Am., 1995) p.165.
9) H.F. Hess, E. Betzig, T.D. Harris, L.N. Pfeiffer and K.W. West: Science **264**, 1740 (1994).
10) S. Smith, B.G. Orr, R. Kopelman and T. Norris: Proc. Quantum Electron. and Laser Sci. (Opt. Soc. Am., 1995) p.85.
11) T. Saiki, S. Mononobe, M. Ohtsu, N. Saito and J. Kusano: Appl. Phys. Lett. **67**, 2191 (1995).
12) E. Betzig and R.J. Chichester: Science, **262**, 1422 (1993).
13) X.S. Xie and R.C. Dunn: Science **265**, 361 (1994).
14) P.J. Moyer, C.L. Jahncke, M.A. Paesler, R.C. Reddick and J. Warmack: Phys. Lett. A **145**, 343 (1990).
15) D.P. Tsai, A. Othonos, M. Woskvits and D. Uttamachandani: Appl. Phys. Lett. **64**, 1768 (1994).
16) P. Dawson, F. de Fornel and J.-P. Gourdonet: Phys. Rev. Lett. **72**, 2927 (1994).

近接場光学顕微鏡の現状と将来

東工大・総合理工
神奈川科学技術アカデミー
大津元一

1. まえがき

従来取り扱われている光は自由空間または波長にくらべ大きな領域を伝搬している。この光を用いた光学顕微鏡の分解能は回折効果により決定される。すなわち，試料により散乱された光をレンズで集め，結像させようとすると光がわずかに広がり，像がぼけてしまう。そのぼけの大きさは光の波長程度であるので，光学顕微鏡では光の波長以下の寸法の試料は観察できない。同様にレーザの光を集光して加工に使おうとすると，その加工精度も回折効果により制限される。

しかし物質表面にしみ出たエバネッセント光を用いると回折限界を越える分解能をもつ光学顕微鏡が可能となる。これは近接場光学顕微鏡（Near-field Optical Microscope: NOM）と呼ばれる。エバネッセント光は物質表面に近接した領域にある場であることからNOMおよび関連する光学現象に関する研究分野は近接場光学（Near Field Optics）と呼ばれる。NOMの原理と提案は60年前にさかのぼるが[1]，その実験は1980年代に入ってから開始された[2]。しかしここ数年その研究開発が急激に活発化している。その理由は近接場光学の基礎となる科学技術，さらに応用可能分野がきわめて広い分野，特に将来の科学技術に関わる分野と密接に関わっているからである。

NOMはプローブ顕微鏡の一種であるが，STM，AFMと異なり，光学スペクトルを測定することができること，多様な周囲環境化で使用できることが圧倒的な利点である[3),4)]。本稿では微細加工技術の一つである超高密度光記録，および極限技術である原子操作の試みも含めた将来について述べる。

2. 顕微鏡の原理と構成

図1にNOMの基本的構成を示す。物体に光を照射するとその表面で光は反射，透過し，伝搬していく。そのとき同時に物体表面にはエバネッセント光が発生している。エバネッセント光は光照射により物体中に生じた分極の間の局所的相互作用を光として表現したものに他ならないので，上記の反射光，透過光と異なり，遠方へ伝搬せず，分極近傍に局在している。

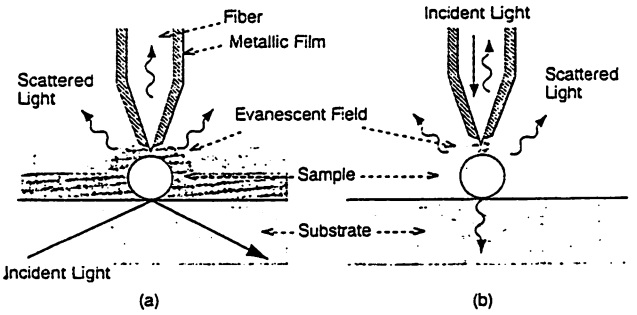

図1　近接場光学顕微鏡(NOM)の基本的構成
(a)試料表面のエバネッセント光をプローブでピックアップし，集める方式。
(b)プローブ先端からしみ出すエバネッセント光で試料を照明する方式。

図1(a)において，先端の鋭いプローブを試料表面付近で走査しながらこのエバネッセント光を散乱して伝搬光に変換し，そのパワーを検出してプローブの位置の関数として図示すれば試料表面の三次元的像が表示できる。このとき像の分解能はプローブ先端の鋭さによって決まるので，通常の光学顕微鏡とは異なり光の回折限界を越えることができる。

NOM装置の中で基本となる素子はプローブである。従来，ガラス性のマイクロピペットを加熱して引き延ばたもの[5]，光ファイバを加熱して引き延ばしたもの[6]，さらには微小球を用いるもの[7]，などがプローブとして用いられてきた。我々は製作の際の高い再現性，先端曲率半径を10nm以下にすること，高い集光効率を得ること，などを目指して，光伝送用のファイバを緩衝フッ酸溶液で選択化学エッ

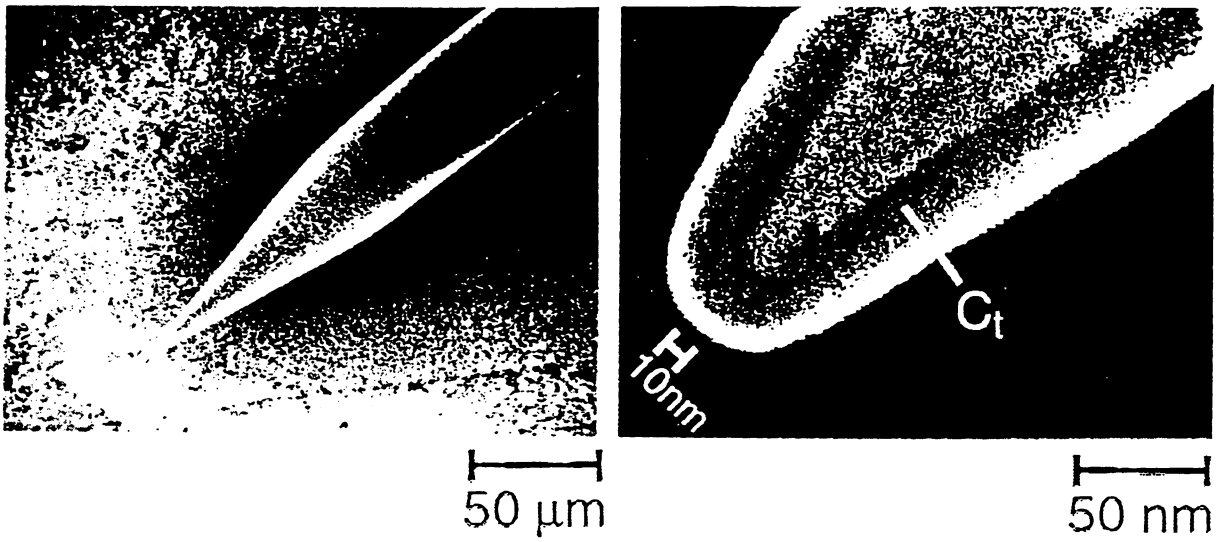

図2

(a) ペンシル形プローブの電子顕微鏡写真。(b) 先端部の拡大図[10,11]。最外部は電子顕微鏡による観測時に付着した汚れ(Ctと示した部分)。内部が金属膜の蒸着された先鋭化光ファイバ。

チングした[8]。NH_4F の体積比を調節することによりコア部のみを先鋭化すること，さらには二段階エッチングによりクラッド部を細径化すること[9]，四段階エッチングによりクラッド部の角のないペンシル形にすること[10),11]，などが可能となった。先端形状の電子顕微鏡写真を図2に示すが，10nm以内の先端曲率半径が実現している。また，先鋭角の最小値は15度になる。

先鋭化したプローブの根元に金属膜をコーテイングし，先端部分の金属膜をヨウ化カリウム溶液により除去してファイバ先端部を露出させ，開口を形成することができる。先端部の電子顕微鏡写真を図3に示すが，開口径30nmが実現している[11]。

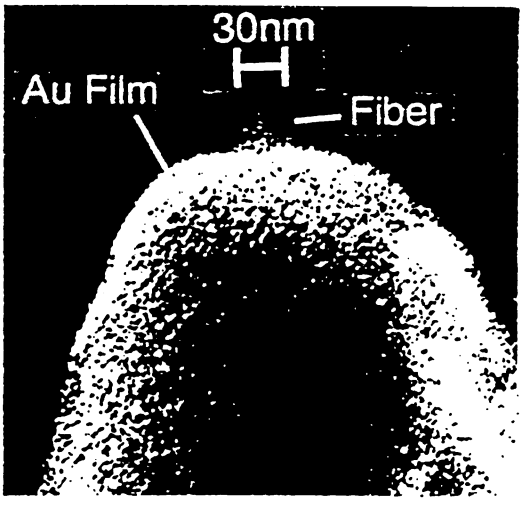

図3 先端部から金の薄膜を除去しファイバ先端部が露出したプローブの断面説明図の電子顕微鏡写真[11]。根元は金の薄膜が蒸着されている。

図1(a)のように光を試料裏面から全反射角で入射させ，発生したエバネッセント光をプローブでピックアップする方法の他に，プローブ先端にエバネッセント光をしみ出させ，これを試料により散乱光に変換して測定する方法などがある（図1(b)）。この場合，NOMの装置で重要なのはプローブの位置制御である。そのためにプローブと試料との間のせん断応力をモニターする方法が考案されている[12]。この他に上記の二段階エッチングによりクラッド部が細径化されたプローブをわずかに傾けて試料に近づけ，試料との間の原子間力によるたわみをモニターしてプローブ位置を制御する方法もある[13]。これらの方法を使うとプローブと試料との間隔を制御することができるのみでなく，NOM像と同時に原子間力顕微鏡（AFM）像が測定できる利点を有する。ただし，試料表面においてせん断応力の等力面とエバネッセント光の等パワー面の分布は異なるので，画像計測時の信号クロストークの問題，さらには，せん断応力は生体微粒子などの軟らかい試料表面の損傷，水中での動作困難性などの問題を持っている。

検出される光パワーは数pW～数nWなので低雑音の測定環境を準備する必要がある。NOM独自の雑音源は光検出の際のショット雑音である。我々の測定例では，フーリエ周波数10Hz以上ではショッ

ト雑音が支配的であり，対応する縦方向分解能は3pm／$\sqrt{Hz}$であった。10 Hz以下では音響振動の影響により雑音レベルが大きく，フーリエ周波数1 Hzでは対応する縦分解能は0.1nmであった。

上記の光パワー直接検出方式の他に共振形プローブを用いたヘテロダイン検出法も提案されているが[14]，その場合には微小開口をもつQ値の高い微小共振器を作成することが課題である。

一辺1 μm以下の視野で像を観測するために，試料を基板に固定する際には注意が必要である。すなわち，試料固定時に散乱光発生源を作らないこと，などである。生体試料の基板への固定にはAFM像観察用試料の特長の一つは大気中での観察が可能なことであるが，そのときは試料とプローブとの間の水分子の存在，誘電体試料表面の帯電荷などに注意する必要がある。

3. ナノメータ計測

NOMの分解能を評価するために各種の微粒子（たとえば誘電体のラテックス球[15]，バクテリオファージT4[16]などが）観測されている。さらに図4に示すのは直径25nmのサルモネラ菌の鞭毛の測定例である。これらの一連の測定結果より分解能は数nm以内に達していると評価されている。今後，システム性能の向上によりさらに高分解能化が進むであろう。

一方，光エレクトロニクス用微小デバイスの評価にも使われている。図5はプロトン交換$LiTaO_3$導

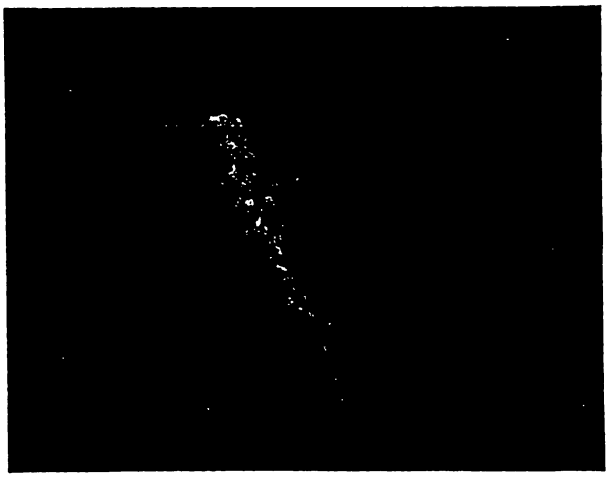

図4　サルモネラ菌の直径25nmの鞭毛の観測像。画像の寸法は480nm×480nm。

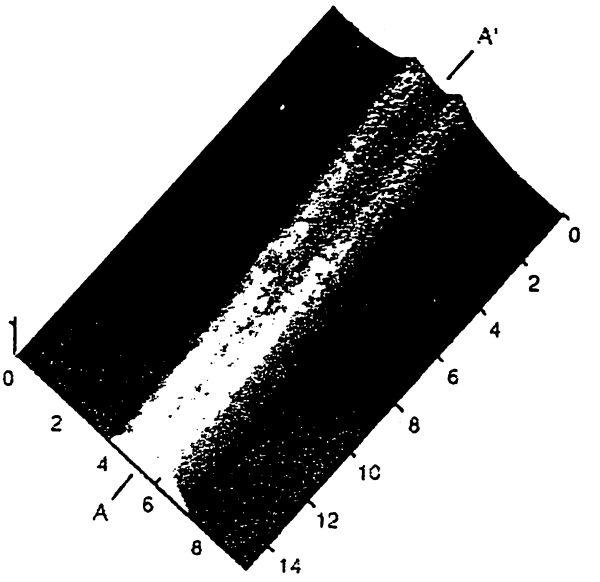

図5　プロトン交換$LiTaO_3$製のY分岐光導波路の導波モードの観測像[17,18]。画像の寸法は10 μm×15 μm。

波路の導波モード形状の測定結果であるが，これより波長以下の寸法をもつ散乱源の同定，ビーム伝搬法による計算結果との比較などが行われ，光導波路の新しい非破壊・高分解能評価法が提示されている[17,18]。一方，半導体の量子細線の形状測定なども試みられている[19]。

他の走査プローブ顕微鏡と異なり，NOMでは入射光により励起された試料からの蛍光を局所的に測定することが可能である。ただしこの場合，光子計数法などの微弱光検出技術を組み合わせる必要がある。一例として，図6に色素がドープされた微小ラテックス球からの蛍光像を示す[20]。

さらにNOMの特長として入射光の波長を掃引することにより試料の局所的光学スペクトルが観測可能である。これにより試料形状のみでなく，試料構造，特に生体試料の場合には局所的な化学種の同定が可能となる。今までに応力下のルビーの蛍光スペクトル[21]，ダイアモンドのラマンスペクトル[22]，さらには単一色素分子からの蛍光スペクトル[23]が測定されており，またプローブが近づいたときの蛍光クエンチングが検出されている[24]。これは量子電気力学に関連する現象として興味深い。また，上記の半導体量子細線の蛍光スペクトルが低温にて測定されている[19]。これらの分光実験では空間的分解能は100nm程度であり，まだ予備実験の段階といえる。最近は分解能は低いが，低温技術，超短光パルスに

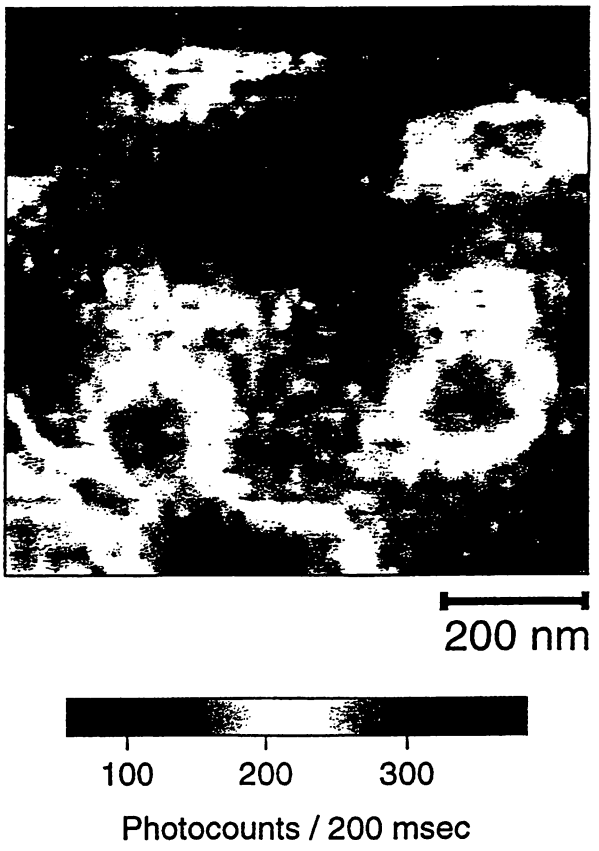

図6 色素ドープされた直径100nmの複数個のラテックス球からの蛍光測定結果[20]。図下部の色表示は測定時間(200ms)中に測定されたフォトン数を表す。

よる励起[25]，などの技術を組み合わせる分光法の開発が盛んになっている。

4. ナノメータ加工機・操作機としての使用

ナノメータ加工の一例として，プローブからエバネッセント光をしみ出させ，その光パワーを用いて光メモリ材料に記録する試みが報告されている。記録寸法はプローブ先端寸法によって決まるので，従来の光記録とは異なり，回折限界を越えた記録が可能になる。光磁気メモリ材料のCo／Ptにアルゴンレーザを用いて熱モードで記録し，記録寸法約100nm，記録密度45Gb／inch^{2}を得ている[26]。これは従来の光メモリの記録密度の10倍の値に相当する。読み出しもNOMを用いている。記録装置寸法を小型化するために同じ記録を半導体レーザにより行う試みも報告されている[27]。なおこの方法では光の偏光を利用しているが，光波長以下の微小開口からのエバネッセント光の偏光状態は入射光の偏光を保存しないので今後の高密度化には不利である。この点を解決するためにフォトンモードによる記録が試みられている[28]。フォトンモードによる記録，再生の原理は次のとおりである：

［記録］NOM用プローブ先端にエバネッセント光をしみ出させ，プローブとメモリ用媒体との距離を光波長以下（すなわち近接場の領域）に保ったまま掃引する。このときエバネッセント光のエネルギーにより媒体表面の構造を変化させる。

［再生］上記の記録過程での構造変化を顕微鏡としてのNOMで測定する。

フォトクロミック材料であるジアゾベンゼン誘導体のLB膜（60層）が記録媒体として使われている[28]。図7に示すように波長350nmの紫外光により記録媒体をトランス形異性体からシス形異性体へと変化させることにより記録を行なう。上記の紫外光は出力パワー60mWのアルゴンレーザから得た。なお，実際の記録の際のエバネッセント光パワーは約30nWであった。

再生にも同じ光源を用いたが，出力パワーを0.6mWまで減少させている。波長350nmにおける吸光度はトランス形異性体では0.31，シス形異性体では0.16であること，すなわちその差が0.15と大きく異なることを利用し，再生には同じ装置をNOMとして用い，記録媒体の透過率の面内での局所変化を測定することにより行った。このときエバネッセント光パワーを約0.3nWに減少させて記録媒体の透過率を測定した。図8には再生結果の例を示す。円形スポットがシス形異性体に構造変化している箇所であり，記録されたピットに相当する。

なお，この図では円形スポットの直径は約100nmであり，記録時の光波長以下の値になっている。これらの直径の値は周囲温度揺らぎによる記

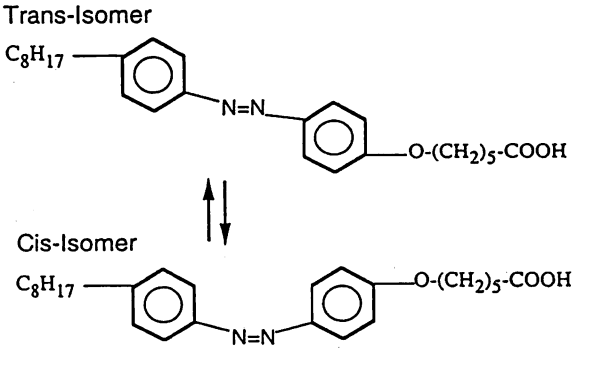

図7 記録媒体の分子構造

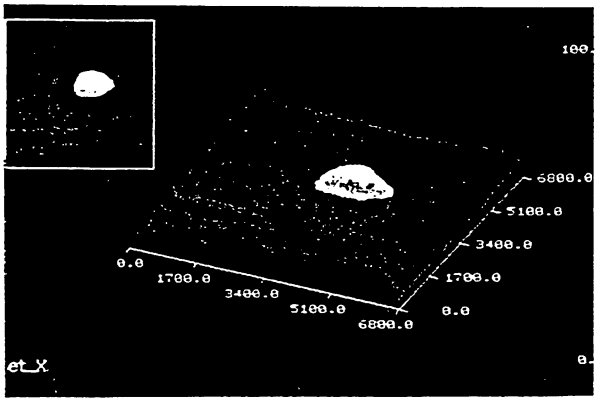

図8 光記録されたピットの再生像(写真中の円形の明部)。直径は約100nm。図の一辺は700nmに相当。

録中のプローブ位置の横方向揺らぎにも依存することがわかった。今後，プローブ位置揺らぎを抑圧する制御を施すことにより，より小さい直径が期待される。

ここで示した近接場光学による光記録・再生方式はまだ研究開発の初期段階であり，さらに進展させるには下記の基本的な問題を解決する必要がある。

(1) 最適記録媒体の探索
(2) プローブへの入力可能レーザ光パワーの上限とプローブ熱破壊限界の推定
(3) 再生の際の光検出雑音の評価と記録密度上限，再生速度上限の推定

しかし記録できるピット径は最終的にはプローブ先端曲率半径により制限される値まで小さくすることが期待され，数nmとなり得る。この意味で本方法は超高密度の光記録実現のための有望な方法といえる。

また，ここで示したフォトンモードの光記録は見方を変えれば局所的な光化学反応の実験と考えることができる。従って熱モードによる方法もあわせ考えると光記録のみならず，将来はその他のナノメータ加工，すなわちレーザトリミング，レーザアニーリングなどへの発展も期待できる。従来のレーザ光を利用した微細加工の代表例はレーザマスクリペアであり，最小加工線幅0.7μm，修正位置精度0.1μm程度がすでに実現しており，64MbのDRAM用のマスク修正などに用いられているが，これ以上の高分解能化は従来方法ではかなり困難と考えられている。本節でご紹介した方法はこの問題を打破する新技術となり得る。特に256MbのDRAM以降のフォトマスク修正が可能となれば，将来のULSI製造プロセスでも大きなインパクトが期待できる。

ところで極限的な微細加工の方向を示す研究として，最近では三次元構造をもつエバネッセント光を用いた原子操作が活発になっている。たとえば，直径数μmの微小リング共振器から共振器外周にしみ出すエバネッセント光による原子の周回[29]，さらに中空ファイバ中にしみ出したエバネッセント光による原子誘導路[30]，さらには凹状先端をもつファイバからのエバネッセント光中による原子の捕獲[31]，などの提案がなされている。我々もすでにプローブ先端にしみ出すエバネッセント光により真空中に浮遊する原子を一つづつ捕獲する方法を提案している[32),33]。最近では上記の原子誘導路の実験が初めて成功し，同位体分離への応用も示された[34]。

以上の原子操作は捕獲された原子を冷却結晶基板の上に一つづつ固定して単原子レベルの結晶成長や光メモリの作製を行うなどの応用が期待される。

5. おわりに

NOMは単に光の波長以下の寸法の物体像やその構造を観察する測定器としてのみでなく，新しい微小物質を作り出す加工機，操作機としての機能を持っている。この特徴こそが微小半導体デバイス，光メモリ，さらにはバイオテクノロジー，マイクロマシンなどの広い分野で最近注目を集めている理由である。また，その動作原理の基礎も奥深く，従来の光学ではカバーしきらない内容も含まれる。すなわちNOMを扱う「近接場光学」，「ナノ・フォトニクス」の基礎と応用は極めて多岐にわたる。

最近はNOM装置の市販品も現れ，ユーザ数も増えている。研究人口も増加し，既に過去三回の国際会議が開催されている[35),36]。第四回目は来春イスラエルのエルサレム市で開催されることが決まっている。また，日本でも研究人口が活発化し，学会レベルでも近接場研究グループが発足している。
今後は新しい光学，フォトニクスの分野として発展することを期待したい。

謝　辞

サルモネラ菌の鞭毛試料をご提供頂いた，帝京大学理工学部・相沢慎一先生，また試料固定法に関しご教示いただいたNTT境界領域研究所・梅村茂博

士に感謝します。

実験結果の写真をご提供頂いた神奈川科学技術アカデミー，物部秀二氏（図2，3），納谷昌之氏（図4），斎木敏治氏（図6）に感謝します。

〔参考文献〕

1) E.H.Synge: A Suggested Method for Extending Microscopic Resolution into Ultra-microscopic Resolution, Phil. Mag., 6, (1928) 356
2) E.Betzig and J. K. Trautman: Near-Field Optics: Microscopy, Spectroscopy, and Surface Modification, Science, 257, (1992) 189
3) M. Ohtsu: Progress of High-Resolution Photon Scanning Tunneling Microscopy Due to a Nanometric Fiber Probe, IEEE J. Lightwave Technology, 13, 7, 1200 (1995)
4) 大津元一：フォトン走査トンネル顕微鏡技術，応用物理，65, 1 (1996) 2
5) E. Betzig, M. Issacson, H. Barshatzky, A. Lewis and K. Lin: Near-field scanning optical microscopy (NSOM), SPIE, 897, (1988) 91
6) U. Durig, D. Pohl and F. Rohner: Near-field optical scanning microscopy with tunnel-distance regulation, IBM J. Res. Dev.,30, (1986) 478
7) 片岡俊彦，高田和政，遠藤勝義，井上晴行，森勇蔵，稲垣耕司：走査型近接場光学顕微鏡（SNOM）の開発IV，第41回応用物理学関係連合講演会，1994年（平成6年）春季，講演番号28aC4
8) T. Pangaribuan, K. Yamada, S. Jiang, H. Ohsawa and M. Ohtsu: Reproducible Fabrication Technique of Nanometric Tip Diameter Fiber Probe for Photon Scanning Tunneling Microscope, Jpn. J. Appl. Phys.,31 (1992) L1302
9) T. Pangaribuan, S. Jiang and M. Ohtsu: Two-step etching method for fabrication of fibre probe for photon scanning tunneling microscope, Electron. Lett., 29, (1993) 1978-1979
10) 物部秀二，R.ウママヘスワリ，斎木敏治，納谷昌之，大津元一：フォトン走査トンネル顕微鏡用ペンシル形ファイバプローブの作成，第41回応用物理学関係連合講演会，1994年（平成6年）春季，講演番号28p D1
11) 物部秀二，納谷昌之，R. ウママヘスワリ，斎木敏治，大津元一：フォトン走査トンネル顕微鏡用ペンシル形ファイバープローブと微小開口の作製法，第13回光波センシング技術研究会，1994年6月，講演番号LST13-13
12) E. Betzig, P.L. Finn and J.S. Weiner: Combined shear force and near-field scanning optical microscopy, Appl. Phys. Lett., 60, (1992) 2484
13) 今井一宏，興梠元伸，蒋曙東，大津元一：AFM同時動作可能なフォトン走査トンネル顕微鏡，第41回応用物理学関係連合講演会，1994年（平成6年）春季，講演番号28pD4
14) S. Jiang, K. Nakagawa and M. Ohtsu: Reflection-Resonance-Type Photon Scanning Tunneling Microscope, Jpn. J. Appl. Phys., 33, (1994) L55
15) S. Jiang, N. Tomita, H. Ohsawa and M. Ohtsu: A Photon Scanning Tunneling Microscope Using an AlGaAs Laser, Jpn. J. Appl. Phys., 30, (1991) 2107
16) S. Jiang, H. Ohsawa, K. Yamada, T. Pangaribuan, M. Ohtsu, K. Imai and A. Ikai: Nanometric Scale Biosample Observation Using a Photon Scanning Tunneling Microscope, Jpn. J. Appl. Phys., 31, (1992) 2282
17) 戸田泰則，大津元一：フォトン走査トンネル顕微鏡による$LiTaO_3$導波路の導波モード観測，第41回応用物理学関係連合講演会，1994年（平成6年）春季，講演番号30pG12
18) 戸田泰則，大津元一：フォトン走査トンネル顕微鏡による光導波路の高分解能評価，第13回光波センシング技術研究会，1994年6月，講演番号LST13-15
19) R. D. Grober, T. D. Harris, J. K. Trautman, E. Betzig, W. Wegscheider, L. Pfeiffer and K. West: Optical spectroscopy of GaAs/AlGaAs quantum wire structure using near-field scanning optical microscopy, Appl. Phys. Lett., 64 (1994) 1421
20) 斎木敏治，納谷昌之，R.ウママヘスワリ，物部秀二，大津元一：先鋭化光ファイバ・プローブの分光への応用，日本物理学会第49回年会，1994年3月，講演番号29aD2

21) P. J. Moyer, C. L. Jahncke, M. A. Paesler, R.C.Reddic and R.J. Warmack: Spectroscopy in the Evanescent Field with an Analytical Photon Scanning Tunneling Microscopy, Phys. Lett.A, 145, (1990) 343
22) D.P. Tsai, A. Othonos, M. Moskvits and D. Uttamachandani: Raman spectroscopy using a fiber optic probe with subwavelength aperture, Appl. Phys. Lett., 64, (1994) 1768
23) W.P. Ambrose, P. M. Goodwin, J. C. Martin and R.A. Keller: Single Molecule Detection and Photochemistry on a Surface Using Near-Field Optical Excitation, Phys. Rev. Lett., 72, (1994) 160
24) R. C. Dunn, G. R. Holton and X. S. Xie: Fluorescence spectroscopy on a single molecule basis with a near-field spectrometer, Tech. Digest of Int. Quantum Electron. Conf. 94, May 1994, Anaheim, 2
25) S. Smith, B. G. Orr, R. Kopelman, T. Norris: Femtosecond near-field scanning optical microscope, Tech. Digest of Conference on Lasers and Electro-Optics, May 1994, Anaheim, 147
26) E. Betzig, J. K. Trautman, R. Wolfe, E. M. Gyorgy, P.L. Finn, M.H. Kryder and C.-H. Chang: Near-field magneto-optics and high density data storage, Appl. Phys. Lett., 61, (1992) 142
27) 新谷俊通，中村公夫，丸山洋治，保坂純男，井村亮：半導体レーザを用いたSNOMの試作，第41回応用物理学関係連合講演会，1994年(平成6年) 春季，講演番号31aMC7
28) S. Jiang, J. Ichihashi, H. Monobe, M. Fujihira and M. Ohtsu: Highly localized photochemical processes in LB films of photochromatic material by using a photon scanning tunneling microscope, Opt.Commun., 106 (1994) 173
29) H. Mabuchi and H. J. Kimble: Atom galleries for whispering atoms: binding atoms in stable orbits around an optical resonator, Opt. Lett., 19, (1994) 749
30) M. A. Ol'Shanii, Yu. B. Ovchinnikov and V.S. Letokhov: Laser guiding of atoms in a hollow optical fiber, Opt. Commun., 98 (1993) 77
31) J. P. Dowling and J. Gea-Balacloche: Atomic quantum dot, Tech. Digest of Int. Quantum Electron. Conf.94, May 1994, Anaheim, 185
32) 大津元一：フォトンSTM (V) —単原子レベル結晶成長，第51回応用物理学会学術講演会，1990年 (平成2年) 秋季，講演番号27aL79
33) H. Hori, S. Jiang, M. Ohtsu and H. Ohsawa: A Nanometer-Resolution Photon Scanning Tunneling Microscope and Proposal of Single Atom Manipulation, Tech. Digest of the 18th Int. Quantum Electron. Conf., June 1992, Vienna, 48
34) H. Ito, T. Nakata, K. Sakaki, M. Ohtsu, K.I. Lee and W. Jhe: Laser Spectroscopy of Atoms Guided by Evanesecnt Waves in Micron-Sized Hollow Optical Fibers, Phys. Rev. Lett., 76, (1996)450
35) 大津元一，堀裕和：近視野光学ワークショップ報告，応用物理，62,(1993) 292
36) 大津元一：第2回近接場光学国際会議報告，応用物理，63, (1994) 77

表面科学 Vol. 17, No. 12, pp. 771-774, 1996

実験ノウハウ

近接場光学顕微鏡でどこまで高分解能像が得られるか？（1）

大津元一*,**

*東京工業大学大学院総合理工学研究科 〒226 横浜市緑区長津田4259
**神奈川科学技術アカデミー・フォトン制御プロジェクト 〒213 川崎市高津区坂戸3-2-1，KSP東棟408号

（1996年5月8日受理）

Realizing Ultrahigh Resolution in a Near-Field Optical Microscope

Motoichi OHTSU*,**

* Interdisciplinary Graduate School of Science and Engineering
Tokyo Institute of Technology, 4259 Nagatsuta, Midori-ku, Yokohama 226
** "Photon Control" Project, Kanagawa Academy of Science and Technology
KSP East Rm. 408, 3-2-1 Sakado, Takatsu-ku, Kawasaki 213

(Received May 8, 1996)

エバネッセント場を利用した近接場光学顕微鏡の原理，基本構成について概説する。特にエバネッセント場のもつ二つの基本的性質（物質寸法依存のパワー局在，プローブ・試料の寸法に関する共鳴）について述べ，これをもとに分解能はプローブ先端の寸法が決めることなどについて指摘する。微小なプローブを作成する技術，プローブ位置を制御する方法などを述べる。

1. まえがき

近接場光学顕微鏡（Near-field Optical Microscope: NOM）は光の回折限界を超える高い分解能をもつ顕微鏡であり，エバネッセント場（Evanescent field）と呼ばれる光を使う。これは物質表面にごく近い領域（近接場領域:表面から光波長以下の距離）に存在する光のうちの非伝搬成分である。本稿ではその原理，実験について述べる[1]。

2. 近接場光学顕微鏡の原理

NOMの提案は60年以上前にさかのぼるが[2]，その実現は1980年代に入ってからである[3]。その構成を図1(a)，(b)に示す。(a)ではプローブ球がエバネッセント場を散乱し，その光を光検出器に集めるのでCollection mode(Cモード)と呼ぶ。一方，(b)では試料球をエバネッセント場で照明するのでIllumination mode(Iモード)と呼ぶ。

プローブとしてはガラスファイバ中心のコア部を先鋭化し，その根元に金属膜を蒸着したものを用いる。即ちプローブは円錐形である。この場合，金属膜の位置でのコアの直径とコア先端曲率直径とによって決まる範囲内の寸法を持つエバネッセント場が散乱（Cモード）または発生（Iモード）する。すなわちエバネッセント場の検出効率は空間フーリエ周波数軸上では帯域通過特性を示し，その高域遮断周波数はコア先端寸法によって決まる。これが分解能の基本的決定要因である。

この原理について説明するために，ここで注目するエバネセント場の性質は次の二つである[4]。

(1) 物質寸法依存のパワー局在（図2(a)）：微小物質表面にしみ出すエバネッセント場の分布は物質寸法と同程度の厚みをもつ。この性質により回折限界を越える分解能を有するNOMが実現する。すなわち分解能はプローブの寸法によって決まる。

(2) プローブ，試料の寸法に関する共鳴（図2(b)）：試料物質表面のエバネッセント場は非伝搬光なので，それを微小なプローブで散乱し，伝搬光に変換してそのパワ

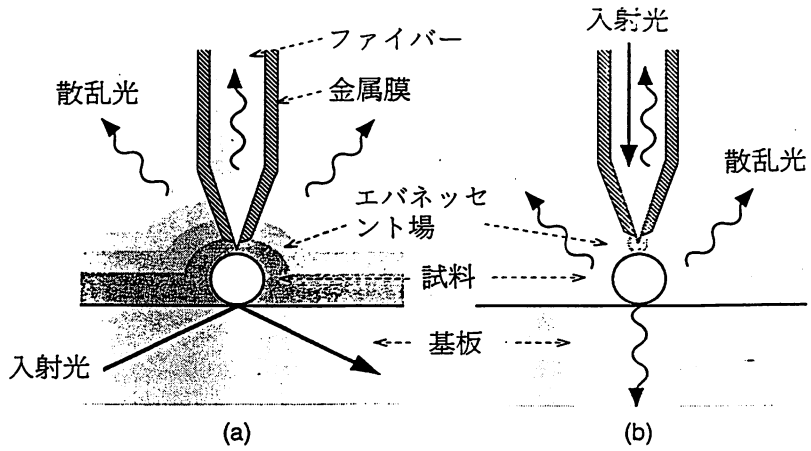

図1 NOMの構成。(a) Cモード，(b) Iモード

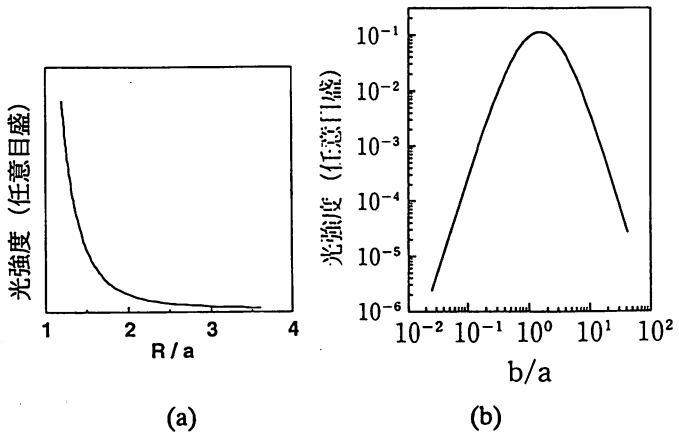

図2 エバネッセント場の二つの性質を表す計算結果。(a) 物質寸法依存のパワー局在。a: エバネッセント場を発生する誘電体球の半径。R: 誘電体球中心からの距離。(b) プローブ，試料をともに球形と仮定した場合，その寸法に関する共鳴。a，bプローブ，試料の半径。

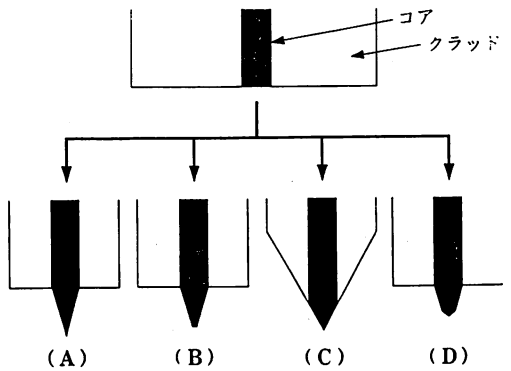

図3 選択化学エッチングにより先鋭化されたコアを持つファイバの断面形状。(A) 小クラッド径型，(B) 先端平坦型，(C) ペンシル型，(D) 二重先鋭型

ーを測定する。その際，散乱光を検出する効率は試料，プローブ両者の寸法が互いに等しいときに最高となる。この性質によれば，微小球試料表面のエバネッセント場を散乱させ，その光強度を最高感度で測定するには，試料と同じ寸法のプローブを使うことが最良であることがわかる。従って高い分解能を最高感度で得るための技術的方策は小さなプローブを実現することである。

なお，CモードとIモードの実際上の比較はおおむね次のとおりである：Cモードでは入射光の偏光状態が制御できるなどの利点があり，高い分解能の像を得るのに適している。Iモードでは試料用基板が不透明な場合にも適用できる。さらに，ガラスファイバプローブ先端からしみ出すエバネッセント光のエネルギーを利用して，加工などが可能である。

3. プ ロ ー ブ

3.1 作成技術

ガラスファイバやガラス毛細管を加熱して引っ張り，次に金属膜を蒸着して先端部に微小開口を形成し，これをプローブとして使う技術が開発されている[5]。この方法にくらべさらに微小化し，かつ再現性を上げる方法として緩衝フッ酸溶液による選択化学エッチングによるガラスファイバの先鋭化法が開発された[6,7]。先鋭化の後に金属膜を蒸着し，先端部のみから蒸着膜を除去して先鋭化ファイバの先端部のみを露出させる。この方法により小さなプローブを高い再現性で実現できるが，この円錐状の露出先端部が図1のプローブに対応する。

まず，体積比が$NH_4F : HF : H_2O = X : 1 : 1$なる溶液中にガラスファイバを約1時間浸すとコアが選択的に先鋭化され，クラッドの端面は除去される。ここで$X > 5$ではコアの先鋭角はXの値によらずコア中のGeO_2濃度によっ

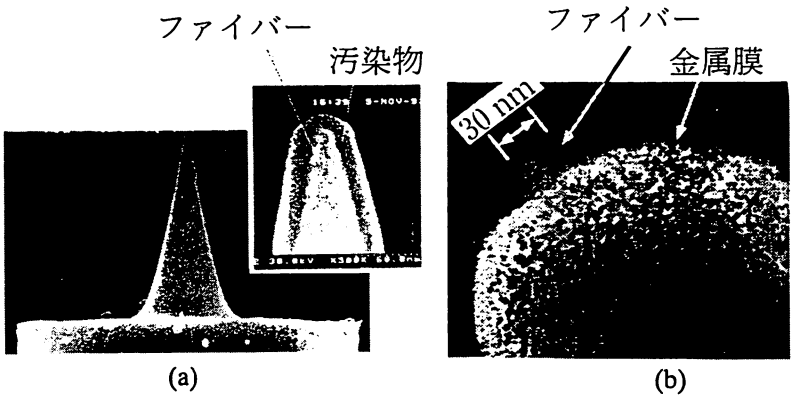

図4 (a) 小クラッド径型ファイバの電子顕微鏡写真。右上図は先端の拡大写真（写真の横幅は1.6 μm）。ファイバには厚さ7 nmの金属膜が蒸着。その表面には電子顕微鏡観察のための電子ビーム照射時に付着した汚染物層がある。(b) 先鋭化コア先端部の金属膜を除去した後の電子顕微鏡写真。

て決まる。このことは先鋭角がエッチング溶液の組成のばらつきによらず，高い再現性で作成できることを示している。

上記の基本的なエッチング過程を修正すると，図3および次に示す多様な先端形状のファイバが得られる。

(A) 小クラッド径型[8]：先端の電子顕微鏡を図4(a) に示す。先端曲率直径は3 nmと推定されている。クラッド直径は8 μm程度まで小さくなっている（当初の値は125 μm。）先端曲率半径が小さいので高分解能計測に適する。同時にクラッド径も小さいので，プローブ位置制御のためにせん断応力を利用する際，この応力に敏感となり，高分解能を得るためにさらに好都合である。

(B) 先端平坦型[8]：プローブ先端が平坦なので柔らかい試料表面を損傷することがなく，生体試料観測に適している。また平坦な先端に光機能微粒子などを固定するのに用いられている。

(C) ペンシル型[9]：先端曲率半径が小さいので高分解能計測に適する。また，クラッド外周に角がなくなっているので金属膜を均一に蒸着するのに適しており，この点が高分解能を得るためにさらに好都合である。

(D) 二重先鋭型[10]：ファイバのコア根元と先端の間での光の伝送効率が高いので，微弱な蛍光などの高感度測定に適している。

次に，先鋭化したファイバのコア先端部を除いて根元を金属膜を蒸着することにより，エバネッセント場の低空間フーリエ周波数成分の散乱（Cモードの場合），発生（Iモードの場合）を防ぎ，高い分解能を得る。金属膜蒸着後，エッチングにより金属膜表面を除去し，コア先端のみを突出させる。その結果の電子顕微鏡写真を図4(b) に示す。この図では突出したコアの根元の直径は約30 nmである。

3.2 位置制御技術

第2節の2つの性質によると高い分解能・感度を得るためには微小プローブを製作するのみでなく，プローブ・試料間距離を試料（又はプローブ先端）の寸法程度まで近づける必要がある。これを行うために特にIモードでは従来は，20 nm程度以内の距離で顕著に現れるせん断応力（原子間力の一形態）を測定し，それを制御信号として使う方法が用いられている[11, 12]。しかし最近の議論では高分解能測定の場合，原子間力の等力面とエバネッセント場の等パワー面とは異なること，さらに原子間力によるプローブ位置制御信号が光測定信号に混入するクロストークの現象，などがあることが指摘されている。すなわち，高分解能を得る目的のためにはせん断応力の利用は必ずしも有利ではない。この問題を解決するためにエバネッセント場のパワーの急激な空間変化を測定し，それを制御信号に使う純光学的制御法が考案されている。

要するに微小なプローブを作ることのみでなく，試料表面に数nm以内まで近づけることが重要で，これが実現すると1 nm以内の分解能が十分可能である。

文 献

1) 大津元一：応用物理 **65**, 2 (1996).
2) E.H. Synge: Phil. Mag. **6**, 356 (1928).
3) D.W. Pohl: "Near Field Optics" (Kluwer, Dordrecht, 1993) p.1.
4) K. Jang and W. Jhe: Opt. Lett. **21**, 236 (1996).
5) K. Liberman, S. Harush, A. Lewis and R. Kopelman: Science **247**, 59 (1990).
6) T. Pangaribuan, K. Yamada, S. Jiang, H. Ohsawa and M. Ohtsu: Jpn. J. Appl. Phys. **31**, L1302 (1992).
7) T. Pangaribuan, S. Jiang and M. Ohtsu: Scanning **16**, 362

(1994).
8) R. Uma Maheswari, S. Mononobe and M. Ohtsu: J. Lightwave Technol. **13**, 2308 (1995).
9) S. Mononobe, M. Naya, R. Uma Maheswari, T. Saiki and M. Ohtsu: Proc. Int. Conf. Near Field Optics and Related Technol. (Euro. Opt. Soc. 1995) p.105.
10) T. Saiki, S. Mononobe and M. Ohtsu, N. Saito and J. Kusano: Appl. Phys. Lett. **68**, 2612 (1996).
11) E. Betzig, P.L. Finn and J.S. Weiner: Appl. Phys. Lett. **60**, 2484 (1992).
12) R. Toledo-Cow, P.C. Yang, Y. Chen and M. Vaez-Iravani: Appl. Phys. Lett. **64**, 2957 (1992).

電子情報通信学会誌 Vol.79 No.11 pp.1160-1164 1996年11月

特集

6. 夢のメモリデバイス

6-4

近接場光学による超高密度光メモリ

大津元一

大津元一：正員 東京工業大学大学院総合理工学研究科 E-mail ohtsu@ae.titech.ac.jp

Ultra-High Density Optical Storage by Near-Field Optical Technique. By Motoichi OHTSU, Member (Interdisciplinary Graduate School of Science and Engineering, Tokyo Institute of Technology, Yokohama-shi, 226 Japan).

ABSTRACT

従来の光記録再生方式では光の回折が記録再生密度の上限を決めている．本稿ではこれを打破するために提案されている近接場光学の手法について述べる．まず原理について説明し，次に熱モードおよび光子モード記録の現状について概説する．すなわち，45 Gbit/in^2 程度の記録密度が得られていることを示す．本手法を実用化するために解決すべき課題として，高感度なプローブおよび記録媒体の開発，プローブの高速走査技術の開発，などについて述べる．

キーワード：光記録，近接場，ファイバ，走査

1. まえがき

従来の光記録再生方式では，光の回折の性質のために1ビット当りの記録再生の最小寸法は光波長程度（約0.5 μm）となる．短波長の光を使えばこの寸法は更に減少するので，最近では短波長の半導体レーザデバイスの開発が活発であるが，それを用いても光の回折限界による記録密度は数10 Gbit/in^2（1ビットの記録寸法数百nm）が上限である[1]．現在1 Gbit/in^{2}が既に実現しており，技術の急速な進歩を考えると近い将来上記の理論限界に達すると考えられ，大幅な技術革新が必要とされる．

但し光の回折限界は絶対的な制限ではない．すなわち，従来の方式では光を電磁場の波としてとらえ，利用していたのでこの制限が課されていたが，形態の異なる光を使えばこの制限はなくなる．その一例として光波長以下の寸法の空間での制御された電磁相互作用を媒介する場として光をとらえ，利用することが可能で，そのような光の場はエバネッセント場（Evanescent field）とよばれる．これは物質表面にごく近い領域（近接場領域：表面から光波長以下の距離）に存在する光のうちの非伝搬成分である．このような光技術分野は，近接場光学とよばれており，更に筆者らはその応用分野をナノ・ホトニクスとよんでいる[2]．

2. 光記録と再生の原理

（1） 光記録（図1(a)）：光ファイバを先鋭化した後，不透明な金属膜を蒸着し，ファイバ先端部の金属膜を除去して光波長の値よりずっと小さい開口を作る．これをプローブと称する．ファイバ後端から光を入射すると通常の波としての光はプローブから出射しないが，エバネッセント場はしみ出る．その光パワーはプローブ表面から遠ざかるにつれ減少するが，その減少の度合を表す「しみ出しの厚み」はプローブ先端寸法と同程度であり，光波長には依存しないことがわかっている[2]．この光の単位断面積当りのパワー密度は100 W/cm^{2}に達する可能性がある．従って，光記録媒体の表面をこのプローブに近づければ，エバネッセント場により誘起される温度上昇または光化学反応を利用して記録ができる（各々熱モード記録，光子モード記録である）．

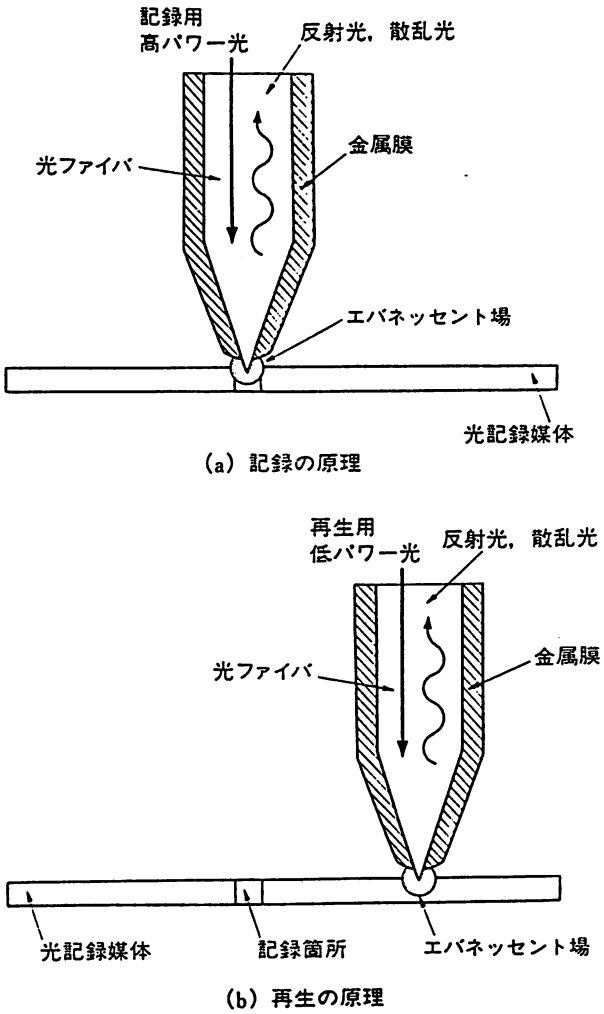

図1　近接場光学の手法による光メモリの原理

（2）　再生（図1(b)）：記録後の媒体表面にこのプローブからのエバネッセント場を再び照射し，媒体表面で散乱される光パワーを測定したり，反射される光パワーの偏光変化を測定すれば，光メモリの再生が可能となる．

以上の記録，再生の空間的分解能は散乱されるエバネッセント場の体積，従ってプローブ先端の寸法によって決まるので，光の回折限界を越える超高密度メモリが実現し，原理的には1 Tbit/in^{2}の記録密度が可能である．このとき，散乱によりプローブ表面のエバネッセント場が最も効率良く光記録媒体に移乗するのは光記録媒体の粒径等の構造の寸法がプローブ先端の寸法に等しい場合であることがわかっている[2]．従って記録，再生にはプローブ先端寸法と同程度の粒径をもつ光記録媒体を，プローブ先端寸法と同程度までプローブに近づけ，その状態でプローブを走査する必要がある．

3.　技術の現状

（1）　熱モード記録：光磁気記録媒体であるCo/Ptにアルゴンレーザを用いて媒体表面を局所的にキュリー点温度（約400°C）以上に加熱して記録し，ピットの直径約100 nm，記録密度1 in^{2}当り45 Gbitを得ている[3]．なお，2.に示したように光記録材料の粒径に等しい寸法の先端をもつプローブを用いることが最も効率が良いが，従来の試みではプローブ先端の大きさより材料の粒径の方が小さく，従って記録ピットの大きさは材料の粒径によって決まっている．再生にはエバネッセント場の偏光状態の変化を測定している．

上記に比べ加熱温度が低くてもよい（約200°C）相変化形（非晶質と結晶との間の相変化）の記録再生も試みられている．GeSbTe膜を媒体として用い，再生は反射率の局所変化を測定することにより行っている[1]．上記と同程度の記録再生結果が得られている．

（2）　光子モード記録：ジアゾベンゼン誘導体のホトクロミック材料の薄膜を記録媒体とし，波長350 nmの紫外光のエバネッセント場を局所的に照射して光化学反応を誘起し，トランス形異性体からシス形異性体へと変化させることにより記録を行う．再生にはトランス形と

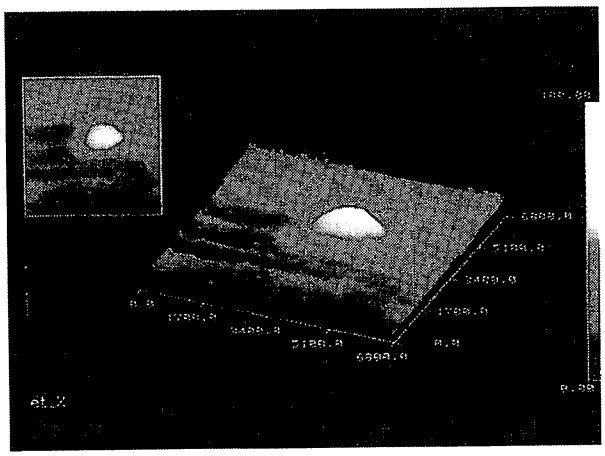

図2　記録再生の結果　　中央の黄色い円形（直径約50 nm）は記録後のシス形異性体，周囲の赤部はトランス形．

シス形の異性体の吸光度が上記波長の光に対し互いに異なることを利用し，記録媒体の光透過率の局所変化を測定することにより行う．この後可視光を照射することによりメモリを消去することも可能である．図2に示すようにこの場合でも(1)と同様の寸法の記録ピットが実現している．更にこの記録再生方式のために，吸光度の非常に大きなホトクロミック材料の開発も進められている[4]．これらの材料を用いた場合，その記録時間は(1)に比べ長いが，光と物質との共鳴相互作用を利用しているため，将来分子レベルの記録が実現する場合にはピコ秒程度の短い応答時間となることが期待される．

4. 課題と展望

現存のプローブや記録材料などを用いて超低速で記録再生のデモンストレーションをする時代は既に終ったといえる．今後は本技術を実用化することが課題である．これに関し，解決すべき課題を指摘するために，図3に掲げる．この図は再生速度の各種パラメータ依存性の推定結果である．横軸は再生の場合の検出光パワー，縦軸は符号誤り率 1×10^{-9} を維持するための再生速度である．この他のパラメータはデュティ比（非記録表面に対する記録部分からの反射光量の割合），光検出器の量子効率である．再生速度として10～100 Mbit/s（図中の破線A，Bで挟まれた領域）を確保するための課題を以下に列挙する．

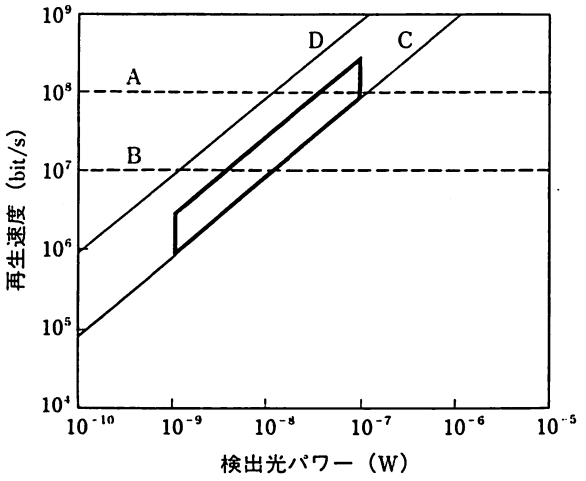

図3 必要な検出光パワーと再生速度との関係 再生時の符号誤り率は 1×10^{-9}．破線A，Bはそれぞれ再生速度100 Mbit/s，10 Mbit/sを表す．実線C，Dは光検出器の量子効率を0.3，光記録媒体のデュティ比をそれぞれ0.1，1.0と仮定した場合の計算結果．太線で囲んだ領域は実現可能と考えられる．

（1） 高感度プローブの開発：図3の横軸の検出光パワーはエバネッセント場の発生効率に依存している．従って高感度プローブの設計と作成技術のためのナノメータ加工技術の開発が重要である．その方法として緩衝ふっ酸溶液による選択化学エッチングにより光ファイバを先鋭化し，その後金属膜を蒸着し，先端部から蒸着膜を除去して先鋭化ファイバコアの先端部のみを露出させる方法が開発された[2]．この方法により小さなプローブを高い再現性で実現できると共に，この基本的なエッチング過程を修正すると，多様な先端形状のファイバが再現性良く得られる．この先端の電子顕微鏡の例を図4(a)，(b)に示す．先端曲率直径は3 nmと推定されている．

図4(a)，(b)のプローブは高分解能を得るために使われるが，図4(c)に示す二重先鋭型は高感度を得るために使う．そのために先端部の曲率半径が大きくなっている．この場合，エバネッセント場の発生効率は図4(a)，(b)のものに比べ10～100倍大きい．これを用いれば図3の横軸の検出光パワー値として1～100 nWが期待される．

（2） 高感度記録媒体の開発：3.の実験結果は従来の光記録媒体を流用しており，図3中のデュティ比は既に0.1程度が得られている．しかし今後は磁区や粒径の減少，キュリー温度や相転移温度の減少，光化学反応感度の増加，により大きなデュティ比を短い記録時間で実現する必要がある．更に，媒体表面の10～50 nm上空をプローブを走査するために，媒体表面の平たん度の向上，ナノメータ程度の薄い保護膜の開発，などナノメータ材料の開発が重要である．ひいては，近接場光学の特長を十分に引き出すために，媒質と光との間のどのような光化学反応を使うかを検討する必要があろう．

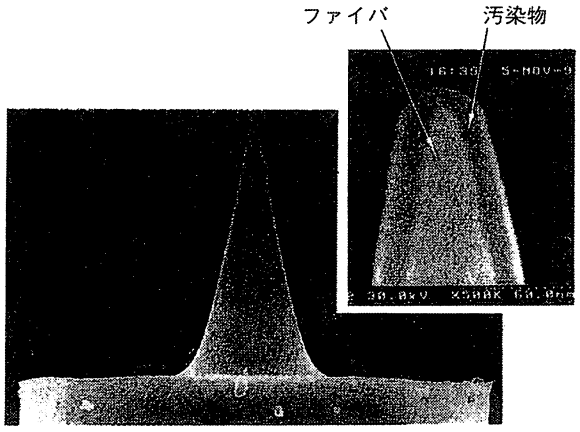

(a)

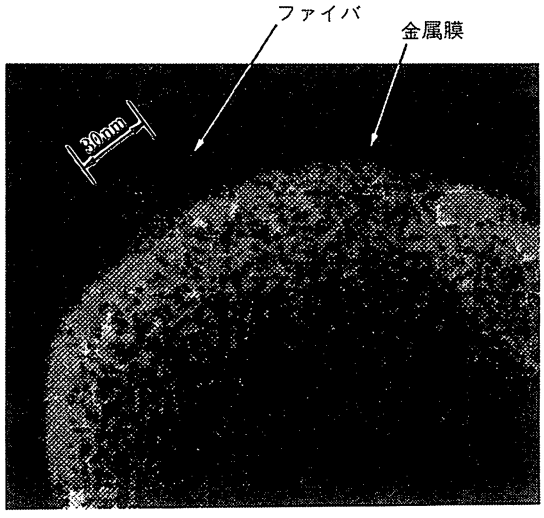

(b)

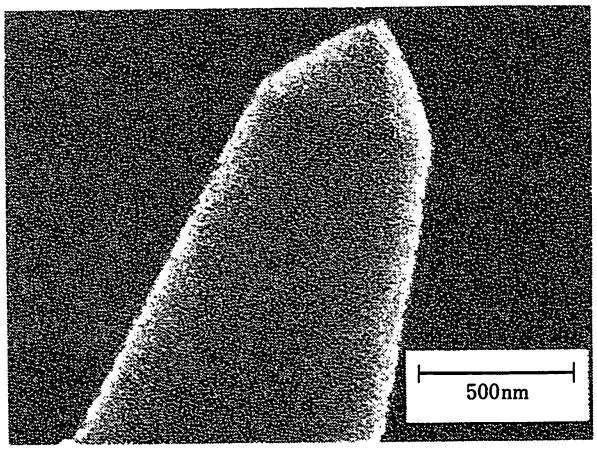

(c)

図4　各種のファイバプローブの形状　(a) クラッド直径を8 μm まで減少させた先鋭化ファイバの電子顕微鏡写真．右上図は先端部拡大写真（写真の横幅は1.6 μm）．ファイバには厚さ7 nm の金属膜が蒸着されており，その表面には電子顕微鏡観察のための電子ビーム照射時に付着した汚染物層がある．(b) 金属膜を蒸着後，先鋭化コア先端部のみから金属膜を除去した後の電子顕微鏡写真．(c) 高感度化のための二重先鋭化ファイバの先端部の電子顕微鏡写真．

（3）　プローブの高速走査：光検出器の量子効率は0.1以上を実現することが可能なので，上記（1），（2）の課題解決により図3中の太枠で囲んだ領域が実現でき，従って10～100 Mbit/s の再生速度が期待できる．しかし，そのような高速度を実現するためには実際にプローブを高速走査しなければならない．3.の実験ではプローブと記録媒体表面との間の距離を一定に保つためにアクチュエータを用いて自動制御を施しながら，超低速でプローブを走査している．この方式は高速走査の実現には隔たりが大きく，これを開発するためには例えばハードディスクの再生ヘッドの走査のように空気の流体力学的特性を利用するような高速走査方式の開発が必要となる．その際に微小な浮上ヘッドとプローブを一体化するようなマイクロマシン技術の開発が必要となる[5],[6]．更に安定な走査のためにトラッキング技術の開発が不可欠である．

（4）　その他：本稿で述べた記録方式では，その記録密度の上限は1 Tbit/in^2 に達するが，そのような大きな値の場合には従来の記録再生方式を踏襲するのではなく，超高密度固有の新しい記録再生方式の考案が必要となろう．また，このような超高密度の光メモリの動作形態，使用形態などを検討する必要がある．更には，例えばナノメータ寸法の記録媒体表面の欠陥などによる誤再生を防ぐなど，新しいソフトウェア技術の開発が望まれる．

5.　ま　と　め

メモリの超高密度化を光で行う際には従来方式では限界に近づきつつあるので，本稿のような新方式が提案され研究開発が進んでいる．解決すべき課題は多いが，幸いなことにこの方式に興味をもつ技術者の数がここ1,2年の間に国内外を通じ急増している．このような状況の急展開をみるに，今年が超高密度光記録の発展にとってのターニングポイントになるように思える．

謝辞　今後の課題に関し，数値的な検討に御

協力頂いた興梠元伸博士（東京工業大学）に感謝する．

文　献

（1） 保坂純男，“エバネッセント光による高密度光記録，” 光技術コンタクト，vol.33，no.12，pp.672-679，Dec. 1995.

（2） 大津元一，“フォトン走査トンネル顕微鏡技術，” 応用物理，vol.65，no.1，pp.2-12，Jan. 1996.

（3） E. Betzig, J. Trautman, R. Wolfe, E.W. Gyorgy, P.L. Finn, M.H. Krder, and C.-H. Chang, “Near-field magneto-optics and high density data storage,” Appl. Phys. Lett., vol.61, no.2, pp.142-144, July 1992.

（4） 入江正浩，“フォトクロミック有機材料，” 高分子，vol.43，no.8，pp.544-548，Aug. 1994.

（5） W. Tang, V. Temesvary, R. Miller, A. Dasai, Y.-C. Tai, and D.K. Miu, “Silicon Micromachined Electromagnetic Microactuators,” IEEE Trans. Magnetics, vol.31, no.6, pp.2964-2966, Nov. 1995.

（6） T. Hirano, S. Kanemaru, H. Tanoue and J. Ito, “Emission Characteristics of Ion-Implanted Silicon Emitter Tips,” Jpn. J. Appl. Phys., vol.34, no.12B, pp.6907-6911, Dec. 1995.

大津　元一（正員）

昭48東工大・工・電子卒．昭53同大学院博士課程了．同年同大学奉職．以来，光エレクトロニクスの研究に従事．現在，同大学院総合理工学研究科教授．（財）神奈川科学技術アカデミー・プロジェクトリーダ兼任．工博．昭63日本IBM科学賞，平2応用物理学会賞など受賞．

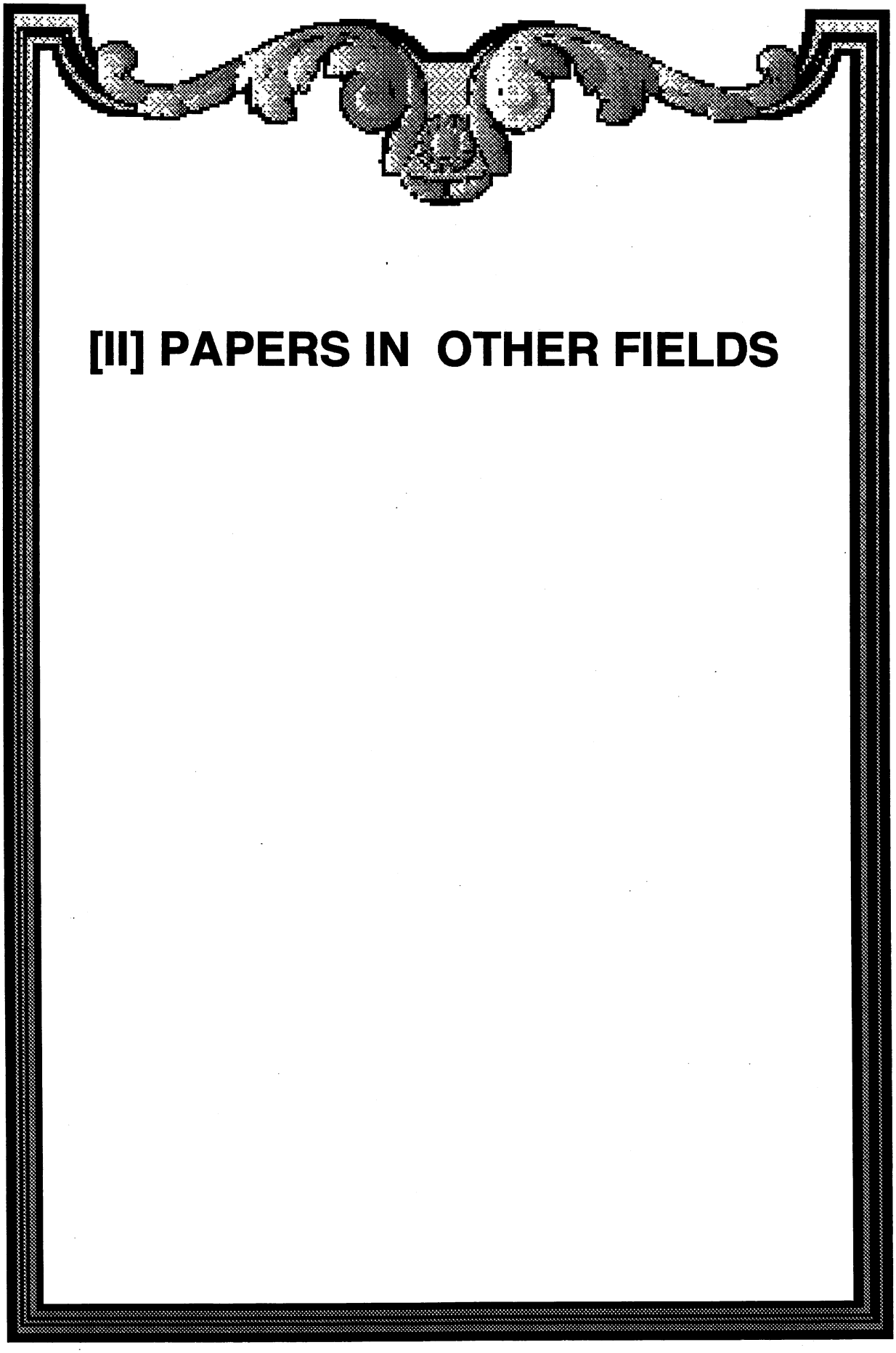

[II] PAPERS IN OTHER FIELDS

ELSEVIER

1 May 1997

Optics Communications 137 (1997) 295–298

OPTICS COMMUNICATIONS

Tunable UV CW generation by frequency tripling of a Ti:sapphire laser

Shuji Sayama [a], Motoichi Ohtsu [a,b]

[a] *Interdisciplinary Graduate School of Science and Engineering, Tokyo Institute of Technology, 4259 Nagatsuta-cho, Midori-ku, Yokohama 226, Japan*

[b] *Kanagawa Academy of Science and Technology, KSP East Room 408, 3-2-1 Sakado, Takatsu-ku, Kawasaki 213, Japan*

Received 7 June 1996; revised 28 October 1996; accepted 10 December 1996

Abstract

We developed a tunable ultraviolet continuous-wave light source by frequency tripling of a Ti:sapphire laser. The third harmonic was generated in a BBO crystal by sum-frequency mixing between the fundamental wave and the second harmonic which was generated in a LBO crystal placed in an external built-up cavity. The third harmonic power of 8 nW was obtained at 252 nm wavelength with an input fundamental power of 500 mW. The tuning range of the third harmonic was from 252 nm to 267 nm.

Nonlinear optical frequency conversion is a useful technique for generating radiation of ultraviolet (UV) frequency. Although its conversion efficiency has been relatively low, it was demonstrated recently that the efficiency can be improved by using a nonlinear crystal placed in an enhancement cavity [1,2]. This suggested that the tunable UV continuous-wave (CW) radiation can be generated by frequency up-conversion of a tunable CW fundamental light source. The employment of a laser diode (LD) as a fundamental light source offers the possibility of a compact, efficient and low-cost tunable UV CW light source. Some demonstrations of tunable UV generations with LD relied on the second harmonic generation (SHG) by a nonlinear crystal placed in a built-up cavity [3,4]. It has been reported that the UV CW radiation was generated by frequency quadrupling of a high power CW LD-pumped solid-state laser, i.e. one nonlinear crystal in a built-up cavity generated the SHG, which was further frequency-doubled by another nonlinear crystal [5].

In this paper we report the generation of tunable UV CW light near 252 nm by frequency tripling of a tunable CW Ti:sapphire laser which can be replaced by a LD. This wavelength is appropriate for laser-induced fluorescence detection of silicon (Si). The allowed transition, $^3P_0$–$^3P_1$ (transition wavelength is 252.487 nm) can be used for laser cooling of the Si atoms [6]. Recently, cooling and nanometer-scale deposition of aluminum (Al) atoms have been demonstrated by using a frequency doubled ring dye laser source [7]. Laser spectroscopy has been also reported on the rubidium (Rb) atoms which were guided by an evanescent wave in a small hollow-core optical fiber [8,9]. These show that our UV light source is applicable on the cooling, nanometer-scale deposition and atomic wave guide of Si.

A schematic of the experimental setup is shown in Fig. 1. The third harmonic generation (THG) was conducted by two successive stages. The first stage was frequency doubling of the fundamental wave in a LiB_3O_5 (LBO) crystal placed in an external built-up cavity. The second stage was sum-frequency generation between the fundamental wave and the SHG in a β-BaB_2O_4 (BBO) crystal. Then, the generated third harmonic (TH) was tuned by tuning the fundamental wavelength while rotating the LBO crystal and the BBO crystal to maintain phase matching. A fundamental light source was a tunable CW Ti:sapphire laser (Coherent 899-21) whose frequency was stabilized to a reference cavity. A Ti:sapphire output beam was mode-matched with an external built-up cavity by using a plano-convex lens L1 ($f = 400$ mm) followed by a half-wave

PII S0030-4018(96)00799-7

plate ($\lambda/2$). The cavity was a bow-type ring cavity, consisting of two flat mirrors M1, M2 and two curved mirrors M3, M4 (curvature radius $R = 100$ mm). Total round-trip loss in the cavity was estimated to be about 2%; therefore, the input coupling mirror M1 for the fundamental wave had reflection of 98% at 750 nm. The input coupling mirror was selected to impedance match the built-up cavity. Reflectivities of the mirrors M2–M4 are higher than 99.3% at 750 nm. We chose a LBO crystal that was cut at an angle $\theta = 90°$, $\phi = 37°$ with respect to the optical axis. It permitted type I phase matching at 750 nm wavelength fundamental beam [10]. Both crystal facets were antireflection (AR)-coated for the fundamental wave at 750 nm and for the SHG at 375 nm. The crystal length was 7 mm. The crystal was installed at the center between the two curved mirrors M3 and M4, where the beam waist of the cavity was located. The generated second harmonic (SH) in the crystal passed through the curved mirror M4. Under this condition, the beam waist was estimated to be 25 μm. This suggested that the second harmonic conversion coefficient should be about 6.3×10^{-5} W^{-1} [11]. To maintain the cavity resonant to the fundamental frequency, the cavity length was controlled with the flat mirror M2 directly mounted on a piezo-electric transducer (FZT) by a feedback loop. The feedback loop derives its error signal from the beam reflected back from the input coupler M1 using the polarization technique [12].

The built-up factor (P_c/P_i) of the cavity was estimated to be about 50, where P_c and P_i are the intracavity and the incident power, respectively. The output mirror M4 allowed the power transmission for the SHG to be more than 85% with AR-coated at 375 nm wavelength. The SH power was estimated to be 14.3 mW for the fundamental power of 500 mW at 750 nm. In the experiment, the intracavity fundamental power P_c was measured to be 15.7 W; therefore the observed spatial mode-matching factor was 61%. The highest SHG power obtained was 11.8 mW,

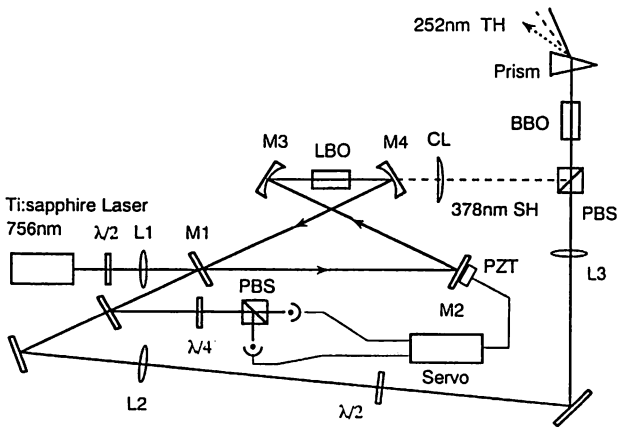

Fig. 1. Schematic experimental setup for frequency tripling of the Ti:sapphire laser. PBS, polarization beam splitter; PZT, piezo-electric transducer; $\lambda/2$, half-wave plate; $\lambda/4$, quarter-wave plate.

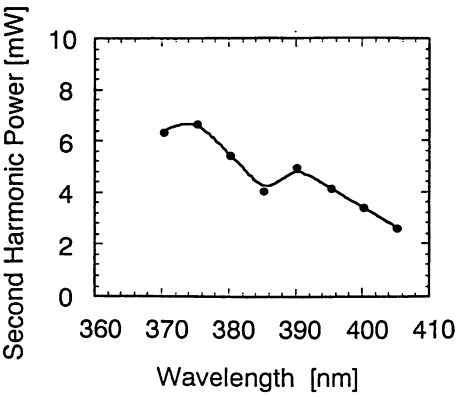

Fig. 2. The tuning curve of the SH obtained by frequency doubling of the Ti:sapphire laser emission in a LBO crystal in the external built-up cavity.

which was smaller than the estimated value because of the surface reflection loss of the prism and the transmission loss of the UV-pass filter being used. The tuning curve of the SHG is shown in Fig. 2. We tuned the SH wavelength by tuning the fundamental wavelength while rotating the LBO crystal placed in the external build-up cavity. The SH was tuned from 370 nm to 405 nm, which was limited by the tuning range of our Ti:sapphire laser, i.e. from 740 nm to 810 nm with 500 mW. The SH power decreased with increasing wavelength because of the wavelength-dependence of the reflectivities of the cavity mirrors and increase in inaccuracy of the crystal rotation for the phase matching. The SH power decreased abruptly at 385 nm because the output mirror M4 transmission reduced near 385 nm. The surface of the mirror was AR-coated for the SHG and highreflection (HR)-coated for the fundamental wave. Transmission of a mirror possesses an interference dip at a half of the fundamental wavelength (generation of this dip has been called the half-wave hole effect [13]). The SH power was high enough for sum-frequency mixing between the fundamental wave and the SHG. The SH frequency could be tuned for 500 MHz by varying the cavity length and the frequency tuning of the Ti:sapphire laser. The field spectral linewidth of the SH light was estimated to be 1 MHz by the linewidth of the Ti:sapphire laser.

The TH was generated by frequency mixing between the fundamental wave and its SH. We employed a BBO crystal that was cut at an angle $\phi = 30°$, $\theta = 61.7°$ with respect to the optical axis, that permitted type II phase matching of 750 nm and 375 nm wavelength fundamental beams [14,15]. The crystal length was 7 mm. Usually, both BBO crystal facets were coated to protect the crystal against hydroscopical damage. Since this protection coating reduced the transmission for UV light, we applied AR-coatings for the fundamental wavelength at 750 nm, the SH wavelength at 375 nm and the TH wavelength at 250 nm to both surfaces of the crystal, which appeared also to be effective to protect the surface of the crystal

against hydroscopic damage. Both surfaces of the crystal had a transmission of 99.8% at 750 nm, 99.6% at 375 nm and 90% at 250 nm. The fundamental beam was focused by two plano-convex lenses (L2 and L3; focal length $f = 600$ mm, 80 mm) at the center of the BBO crystal after the beam reflected back from the cavity and passed through a half-wave plate ($\lambda/2$) (see Fig. 1). The SH output beam from the cavity was an astigmatical beam because the SH beam from the LBO crystal had different divergence angles in the vertical and horizontal directions due to the small acceptable angle and the walk-off effect, and passed out of the cavity through the curved mirror M4. In order to overcome this difficulty a fused silica cylindrical lens CL ($f = 100$ mm) was used to compensate for the astigmatism and to focus the SH beam into the center of the BBO crystal. We employed an AR-coated polarization beam splitter (PBS) to superpose the fundamental beam and the SH beam. The PBS was advantageous compared with the double-coated dichroic mirror whose surface was HR-coated for the fundamental wave and AR-coated for the SHG. This is because the half-wave hole effect did not occur on the surface of the PBS. The generated TH beam was separated from the fundamental beam and the SH beam by the fused silica prism which was chosen to reduce the surface reflection of the THG. This beam was detected by a solar blind calibrated photomultiplier (Hamamatsu C1053) with cut-off wavelength at 320 nm.

When the power of the fundamental light source was 600 mW at 756 nm, the SH power at 378 nm was about 5 mW, and the fundamental power which reflected back from the cavity was about 300 mW, and then the 3.3 nW THG was measured at 252 nm. Part of the TH power was dissipated by the surface reflection loss and transmission loss in the fused silica prism. By accounting for these losses of the TH, the generated TH power is estimated to be 8 nW. The conversion coefficient of sum-frequency mixing between the fundamental wave at 756 nm and the SH at 378 nm in the BBO crystal was calculated to be about 6.2×10^{-6} W^{-1}. With the fundamental power of 300 mW at 756 nm wavelength and the SH power of 5 mW, the TH power at 252 nm wavelength was estimated to be about 9.3 nW. The tuning curve of the THG is shown in Fig. 3. The TH was tuned from 252 nm to 267 nm which was limited mainly by the tuning capability of our Ti:sapphire laser. The TH power decreased with increasing wavelength because of the tuning characteristic of the SHG shown in Fig. 2. In order to increase the TH power and to achieve a LD based UV tunable system, it is possible to improve our experimental setup in the following way: First, the BBO crystal is placed in an external built-up cavity which is designed for the fundamental wave to be resonant. Secondly, the curved mirrors for making the circulating beam astigmatic are replaced by flat mirrors and biconvex lenses. These improvements are now in progress by the authors.

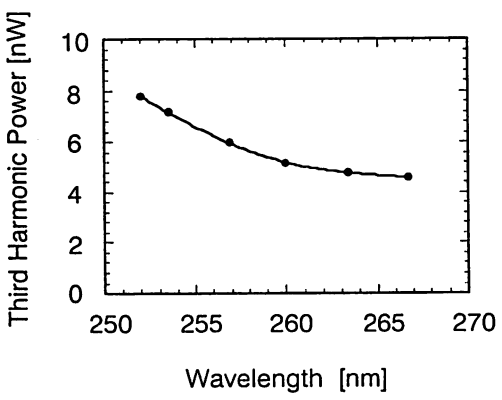

Fig. 3. The tuning curve of the TH obtained by sum-frequency mixing between the Ti:sapphire laser emission and its SH in a BBO crystal.

In summary, frequency tripling of a tunable CW Ti:sapphire laser was demonstrated. It was accomplished by frequency doubling of the fundamental wave in the LBO crystal placed in an external enhancement cavity and sum-frequency mixing between the fundamental wave and the SHG in the BBO crystal. As a result, a 8 nW tunable UV CW light source was obtained at 252 nm wavelength and the tunable range of 252–267 nm with 6 nW of average power. To our knowledge, this is the first time a THG using a CW Ti:sapphire laser as a fundamental source was obtained.

Acknowledgements

We gratefully acknowledge fruitful discussions on frequency doubling in LBO with Mr. Fukuda of the Kanagawa Academy of Science and Technology.

References

[1] Y. Taira, Jpn. J. Appl. Phys. 31 (1992) L682.
[2] S. Bourzeix, M.D. Plimmer, F. Nez, L. Julien and F. Biraben, Optics Comm. 99 (1993) 89.
[3] K. Hayasaka, M. Watanabe, H. Imajo, R. Ohmukai and S. Urabe, Appl. Optics 33 (1994) 89.
[4] C. Oh, S. Kim, Y. Song, Y. Kim and P. Kim, Jpn. J. Appl. Phys. 33 (1994) 1634.
[5] L.Y. Liu, M. Oka, W. Wiechmann and S. Kubota, Optics Lett. 19 (1994) 189.
[6] See e.g. A.N. Zaidel', V.K. Prokof'ev, S.M. Raiskii, V.A. Slavnyi and E.Ya. Shreider, Tables of Spectral Lines (IFI/Plenum Data Corporation, 1970).
[7] R.W. McGowan, D.M. Giltner and S.A. Lee, Optics Lett. 24 (1995) 2535.
[8] H. Ito, T. Nakata, K. Sakaki, M. Ohtsu, K.I. Lee and W. Jhe, Phys. Rev. Lett. 76 (1996) 4500.
[9] M.J. Renn, D. Montgomery, O. Vdovin, D.Z. Anderson, C.E. Wieman and E.A. Cornell, Phys. Rev. Lett. 75 (1995) 3253.

[10] C. Chen, Y. Wu, A. Jiang, B. Wu, G. You, R. Li and S. Lin, J. Opt. Soc. Am. B 6 (1989) 616.
[11] G.D. Boyd and D.A. Kleinmann, J. Appl. Phys. 39 (1968) 3597.
[12] T.W. Hänsch and B. Couillaud, Optics Comm. 35 (1980) 441.
[13] See e.g. O.S. Heavens, Optical Properties of Thin Solid Films (Butterworths, 1955).
[14] C. Chen, Y. Wu, A. Jiang, B. Wu and G. You, Scientia Sinica XXVIII (1985) 235.
[15] D. Eimerl, L. Davis, S. Velsko, E.K. Graham and A. Zalkin, J. Appl. Phys. 62 (1987) 1968.

Jpn. J. Appl. Phys. Vol. 35 (1996) pp. 6090–6094
Part 1, No. 12A, December 1996

Accurate Frequency Control of External-Cavity Laser Diode by Sideband Locking Technique

Takashi FUJII*, Takuya NAYUKI, Koshichi NEMOTO, Mikio KOZUMA[1], Motonobu KOUROGI[1] and Motoichi OHTSU[1]

Electrophysics Department, Komae Research Laboratory, Central Research Institute of Electric Power Industry, 11-1 Iwado Kita 2-chome, Komae-shi, Tokyo 201

[1]*Interdisciplinary Graduate School of Science and Engineering, Tokyo Institute of Technology, 4259 Nagatsuta, Midori-ku, Yokohama, Kanagawa 226*

(Received May 9, 1996; revised manuscript received August 26, 1996; accepted for publication September 9, 1996)

We developed a new, simple laser diode (LD) system in which the laser frequency can be tuned continuously and stabilized at a desired value. The frequency of the 780 nm LD which had no additional antireflection coating on the output facet was varied continuously over a range of 22 GHz by scanning the grating angle and the drive current simultaneously. The LD frequency was offset locked by locking of the frequency of one of the sidebands to a Fabry-Perot interferometer which was locked to a frequency-stabilized He–Ne laser. The sidebands were generated by passing the laser beam through a traveling-wave EO-modulator. By varying the modulation frequency of the EO-modulator, the laser frequency was varied smoothly in a range of 200 MHz, and was stabilized at a frequency which differed by 500 MHz from the resonance frequency of the Fabry-Perot interferometer.

KEYWORDS: laser diode, continuous frequency tuning, frequency locking, Fabry-Perot interferometer, sideband, EO-modulator, external cavity

1. Introduction

A laser diode (LD) has several merits such as small size, high efficiency and long operating life. Moreover, a LD is attractive as a tunable laser for application in various fields such as spectroscopy, lidar and laser isotope separation, because the frequency of the LD can be controlled easily by varying the operation current. For example, injection seeding of high-power tunable lasers such as dye lasers and Ti: sapphire lasers[1–3] using a LD is very useful for line narrowing and frequency control. For application of these tunable lasers to laser isotope separation, it is necessary to stabilize the laser frequency at a desired value and tune the frequency over a range of about 30 GHz without mode hopping. Although the laser frequency can be stabilized by locking it to the resonance frequency of an atom or molecule,[4–8] or to discrete values depending on the free spectral range (FSR) of a Fabry-Perot interferometer (FPI),[9–12] stabilization has been achieved only at particular frequencies. For application to laser isotope separation, the laser frequency must be tuned precisely to various atomic absorption bands, the frequencies of which are close to those of other isotopes. However, it is difficult to use the absorption bands of the target isotope as the frequency reference in the case of radioactive atoms such as uranium, because of difficulties in handling of the frequency reference cells. The frequency-offset locking technique has been studied as a possible means of stabilizing the LDs at frequencies other than these discrete frequency references. Using this technique, a slave LD is offset locked to the master LD which is stabilized relative to an external reference using a heterodyne phase-locked loop.[13–15] Moreover, techniques in which an optical frequency comb[16,17] or a frequency translation optical ring circuit[18] is used as a frequency reference have been studied as possible means of realizing wide-range offset-frequency locking.

Here we describe a new, simple LD system in which the laser frequency can be tuned continuously and stabilized at a desired value. This system incorporates only one LD and does not require a heterodyne phase-locked loop.[19] The frequency of the LD is controlled by locking the frequency of one of the sidebands generated by passing the laser beam through a traveling-wave EO-modulator (TWEOM) to a FPI, the FSR of which is actively stabilized.[9,20] The frequency can be tuned precisely by varying the modulation frequency of the TWEOM. In this work, we describe this technique and frequency stabilization and tunability results for a 780-nm-band LD obtained using this technique.

2. Experimental Setup

Figure 1 shows the concept of frequency control using the sideband locking technique. The sidebands are generated by passing the laser beam through a TWEOM. Since the difference between the frequencies of the carrier and the sideband is dependent on the modulation frequency of the TWEOM, it can be precisely controlled by varying the modulation frequency. As shown in Fig. 1, the carrier frequency can be stabilized in the frequency region between the resonance frequencies of the FPI by locking one of the sidebands to a resonance frequency of the FPI. Moreover, the carrier frequency can be varied smoothly by controlling the frequency difference between the carrier and the sideband. In order to cover all frequencies between the resonance frequencies, the modulation frequency of the TWEOM must be varied from DC to half of the FSR. Since the resonance frequencies of the FPI are used as discrete frequency references at equal intervals, the laser frequency can be stabilized at a desired value using this method.

Figure 2 shows the experimental setup for frequency control using the sideband locking technique. The FSR and finesse of the FPI were 2 GHz and 300,[21] respec-

*E-mail address: fujii@criepi.denken.or.jp

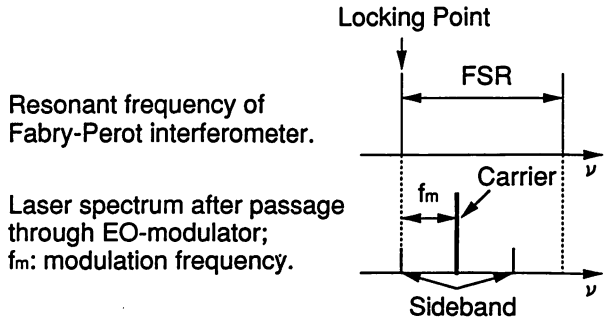

Fig. 1. Concept of frequency control by locking sideband to resonant frequency of FPI.

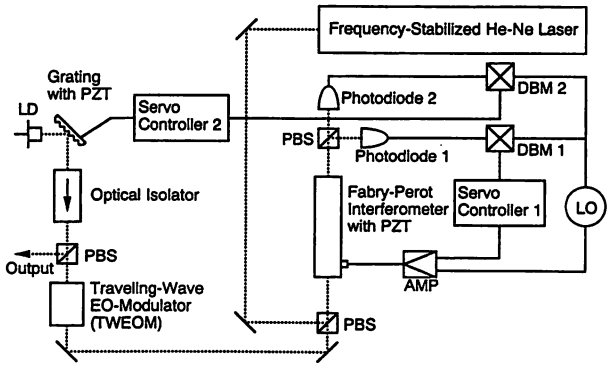

Fig. 2. Experimental setup of LD system using sideband locking technique for frequency control. PBS: polarizing beam splitter; DBM: double-balanced mixer; LO: local oscillator; AMP: amplifier.

tively. The cavity length of the FPI was piezoelectrically modulated at a frequency of 20 kHz using a local oscillator to produce error signals. Using the error signals, the FSR of the FPI and the laser frequencies of the LD were stabilized. The output beam from a frequency-stabilized He–Ne laser (Melles Griot: 05-STP-901) was injected into the FPI, and the light transmitted through the FPI was detected using photodiode 1. The error signal from one of the double-balanced mixers (DBM1) was fed to the piezoelectric transducer (PZT) mounted on the mirror of the FPI via servo controller 1 and an amplifier. Since the cavity length of the FPI was controlled so as to allow transmission of the maximum power of the He–Ne laser beam by electrical negative feedback using servo controller 1, the FSR of the FPI was stabilized against fluctuations due to factors such as temperature variation.[9,20]

A 780 nm LD (Hitachi, HIL7851G) was used as the laser source. A Littrow-type external cavity, the characteristics of which are described in detail in §3, was used to suppress the linewidth and control the laser frequency by optical feedback. The LD output beam was divided using a polarized beam splitter (PBS). One beam was used as the output beam and the other was fed into the electrical negative feedback loop. The sidebands were generated by passing the laser beam through the TWEOM. For stabilization of the carrier frequency at all frequencies in the range of 2 GHz between the FPI resonance frequencies, a TWEOM with a modulation frequency range from DC to 1 GHz was used. The laser beam was passed through the FPI, and one of the sidebands was locked to the resonant peak of the FPI. The error signal from the second double-balanced mixer (DBM2) was fed to the PZT mounted on the diffraction grating of the external cavity through servo controller 2. The carrier frequency was controlled by varying the diffraction grating angle of the external cavity using the electrical negative feedback from servo controller 2. Servo controllers 1 and 2 consisted of integrators and proportional amplifiers. In this experiment, although the error signal was obtained by modulating the cavity length of the FPI, the main output laser beam was not modulated because the time response of servo controller 2 was sufficiently slow to suppress the influence of the modulation of the FPI.

3. Frequency Tunability of External-Cavity LD without Antireflection (AR) Coating on the Output Facet

Before carrying out the frequency-locking experiment, we investigated the continuous frequency tunability of the external-cavity LD. The output facet of the LD used in this system was not coated with additional antireflector. Usually, the output facet of a LD to which an external cavity is applied is coated with an antireflector in order to realize wide-range continuous frequency tuning.[22,23] However, the application of an AR coating to the output facet of a LD is difficult and requires special equipment. Moreover, during the AR coating procedure, breakdown of the LD may occur because the LD facet is exposed. Recently, it was reported that the laser frequency of a commercial 670 nm LD without AR coating was tuned continuously over a range of 18 GHz by incorporating a grating feedback external cavity.[24] In this LD frequency control method, the diode drive current was controlled along with the external-cavity length. However, since an electrical negative feedback system was used to control the current, additional apparatus such as a lock-in amplifier and a local oscillator were required. In our work, to achieve continuous frequency tuning of the LD, we used a simpler method which does not involve electrical negative feedback control but only simultaneous scanning of the diode drive current and the diffraction grating angle of the external cavity at an appropriate rate.[25]

The optimum conditions for wide-range continuous frequency tuning of an external-cavity LD, the output facet of which is not AR coated, can be determined by considering a combination of two cavities. One is a short cavity with an optical length of L_1, which is defined by the two facets of the LD. The other is a long cavity with an optical length of L_2, which is defined by the output facet of the LD and the diffraction grating used to obtain optical feedback in the external cavity. For continuous frequency tuning, L_1 and L_2, which can be varied by varying the injection current and the diffraction grating angle, respectively, must be varied simultaneously.

The arrangement of the external cavity with respect to the LD is shown in Fig. 3. The output beam of the LD was collimated using a lens, and the beam propagation direction was controlled using a long-focal-length lens so

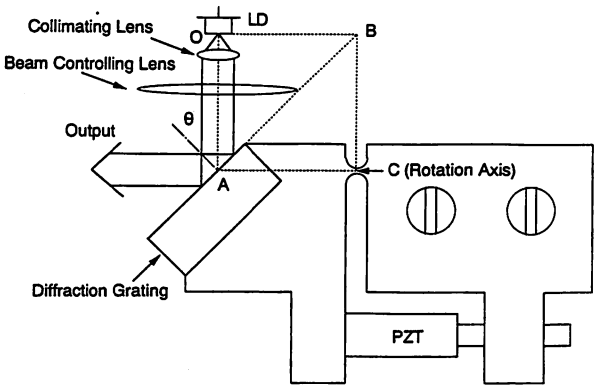

Fig. 3. Configuration of external-cavity LD.

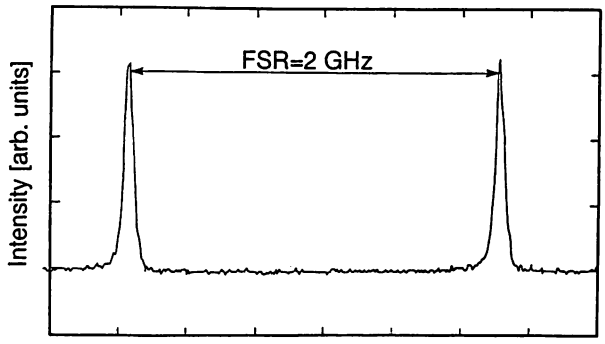

Fig. 4. Lasing spectrum of external-cavity LD measured by scanning FPI.

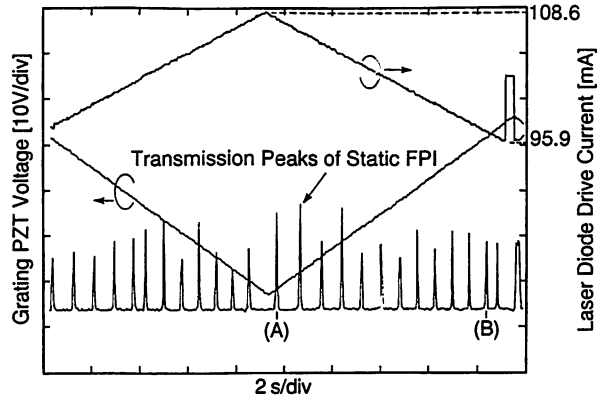

Fig. 5. Signal from photodiode used to detect external-cavity LD beam after passing through a static FPI. Here, the LD frequency was varied by simultaneously scanning the diffraction grating angle at the LD external cavity and the drive current.

that the feedback beam diffracted from the grating could return to the LD. The 1800 grooves/mm grating was mounted at a distance of 24 mm from the LD and was used as an optical feedback source. The angle of incidence θ of the laser beam with respect to the diffraction grating was 44.6°, which was the Littrow angle. The first-order diffracted beam from the grating returned to the LD as the feedback light, and the zero-order beam was used as the laser output. θ was determined using the equation

$$2\sin\theta = \frac{\lambda}{d}, \tag{1}$$

where d is the grating spacing and λ is the output wavelength of the LD. The rotation axis C of the diffraction grating was determined as a vertex of the rectangle OACB in Fig. 3. OA is the optical axis of the LD output beam, and AB is the extrapolated line from the surface of the diffraction grating. By using the point C as the rotation axis of the diffraction grating, the frequencies of the external-cavity-longitudinal modes and the frequency of the diffracted beam from the grating can be scanned at the same speed. Therefore, mode hopping between external-cavity-longitudinal modes is suppressed during frequency tuning.[26,27]

Figure 4 shows the lasing spectra of the external-cavity LD measured by scanning the FPI shown in Fig. 2. The external-cavity LD has a single longitudinal mode. First, we measured the continuous frequency tunability by varying either the diffraction grating angle of the external cavity or the injection current and observing the shift of the frequencies transmitted by the scanning FPI. Mode hopping was observed after the frequency was varied by 1.25 GHz or 1.5 GHz when the diffraction grating angle or the injection current, respectively, was varied.

Next, we performed wide-band continuous frequency tuning by varying the diffraction grating angle and the injection current simultaneously. The continuous frequency tuning range was measured using the FPI, the cavity length of which was fixed, when the voltage applied to the PZT mounted on the diffraction grating of the external cavity was varied by 39 V, while the drive current was varied from 95.9 mA to 108.6 mA. Figure 5 shows the variation of the voltage applied to the PZT and the drive current, and the transmission peaks of the static FPI. We observe that, for the twelve peaks between (A) and (B), the interval between successive peaks, which represent the resonance of FPI, decreased linearly with frequency from the beginning of the scan (A) until the twelfth peak (B). After the peak at (B), the rate of decrease changed discontinuously due to mode hopping. The continuous decrease resulted from the nonlinearity of the PZT. Therefore, the continuous frequency tuning range is calculated to be more than 22 GHz because the FSR of the FPI was 2 GHz. A tuning range of 22 GHz without mode hopping is quite large for a LD without an AR coating on the output facet. The frequency-tuning range between two points at which mode hopping occurs must be determined in order to evaluate the full continuous frequency tuning range. However, in this measurement, mode hopping was observed only once during a half-cycle of the variation of the drive current and the voltage applied to the PZT, because the voltage applied to the PZT was limited by the performance of the function generator used to drive the PZT. Therefore, a wider range of continuous frequency tunability can be achieved by increasing the variation of the PZT voltage and the injection current.

The dependence of the continuous frequency tuning range on the bias current and the variation ratio of the drive current to the voltage applied to the PZT was measured by observing the shift of the frequencies transmit-

ted by the scanning FPI. The variation of the PZT voltage was fixed between −18 V and +18 V. The continuous frequency tuning range was measured when the bias current was 99.2 mA, 100.2 mA or 101.2 mA, with a current variation of 6 mA, 12 mA, 18 mA or 24 mA for each bias current. Although no dependence of the continuous frequency tuning range on the bias current was observed in these three cases, a strong dependence on the current variation was observed. The maximum continuous frequency tuning range of more than 22 GHz, measured using the static FPI, was obtained when the current variation was 12 mA, but the continuous frequency tuning range was only about 3 GHz when the current variation was 6 mA or 24 mA.

4. Frequency Control Using Sideband Locking Technique

Next, we studied the characteristics of the frequency control system using sideband locking, as shown in Fig. 2. First, we stabilized the cavity length of the FPI by locking its resonance frequency to the frequency-stabilized He–Ne laser. The stability of the FSR of the FPI was evaluated using the error signal from DBM 1. The stability was 600 kHz over four seconds, which was estimated from the tracking characteristic of the cavity length to the He–Ne laser frequency.

Secondly, we stabilized the LD frequency by locking it to the FSR-stabilized FPI. Before locking the sideband to the FSR-stabilized FPI, we locked the carrier of the LD to the FSR-stabilized FPI and measured the stability of the LD carrier frequency in order to evaluate the frequency stabilization characteristics of the feedback loop without sideband locking. In this experiment, the TWEOM shown in Fig. 2 was removed so that no sidebands were generated, and the carrier was injected directly into the FPI. Figure 6 shows the frequency-locking characteristics of the external-cavity LD locked to the resonance frequency of the FPI. First, the frequency of the LD was scanned slowly without frequency locking. The single longitudinal mode of the external-cavity LD and its first derivative were obtained clearly, as shown in Fig. 6. Then the laser frequency was locked to the resonant peak of the FPI. The stability of the LD carrier frequency was 10 MHz over 40 s, which was estimated from the tracking characteristic of the carrier frequency to the FPI. In this experiment, the servo controller consisted of only the proportional amplifier and the integrator.

Frequency locking of the external-cavity LD sideband generated by passing the laser beam through the TWEOM to the FSR-stabilized FPI was carried out. Figure 7 shows the first derivative of the external-cavity LD spectrum, in which sidebands are generated. The first derivatives of the sidebands were observed clearly. We locked one of the sidebands to the FSR-stabilized FPI. Figure 8 shows the variation of the PZT voltage used to control the diffraction grating angle of the LD external cavity, when one of the sidebands was locked to the stabilized FPI and the modulation frequency of the TWEOM was varied from 300 MHz to 500 MHz. The PZT voltage varied with the modulation frequency of the

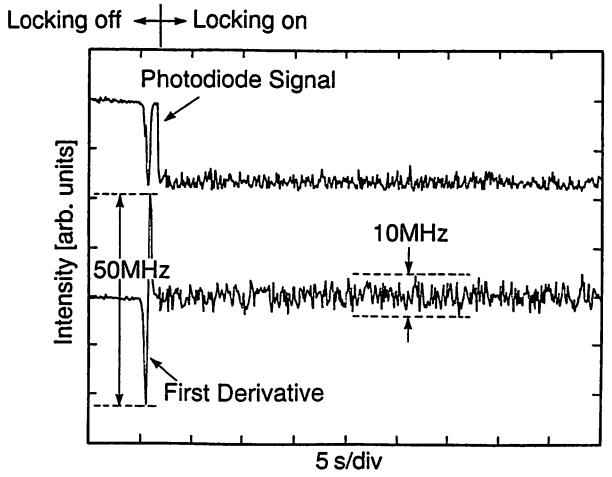

Fig. 6. Photodiode signal and first derivative of LD spectrum transmitted through FPI before and after the LD frequency is locked to the stabilized FPI.

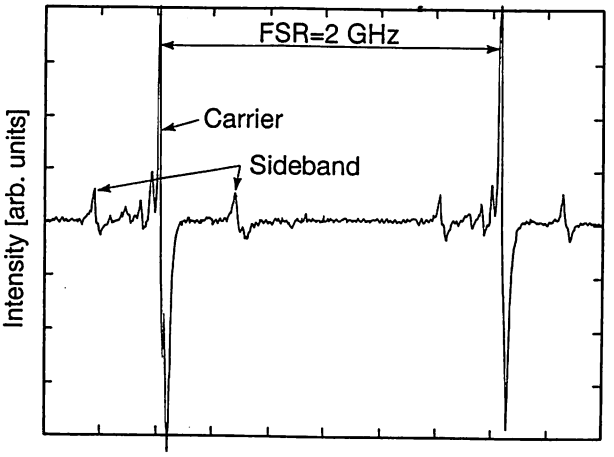

Fig. 7. First derivative of external-cavity LD spectrum in which sidebands are generated after passage of the LD beam through TWEOM.

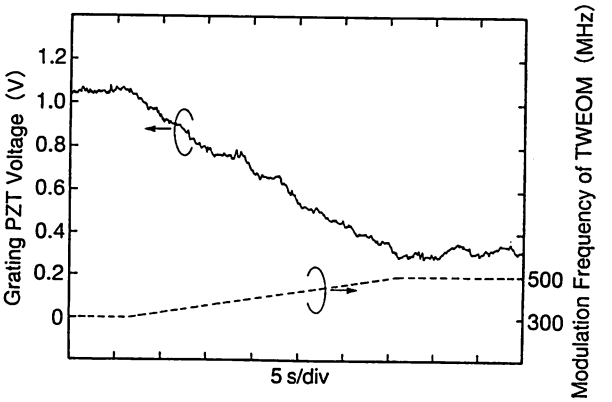

Fig. 8. Correlation of voltage applied to PZT at diffraction grating of LD external cavity to modulation frequency of TWEOM. Here, one of the sidebands was locked to the stabilized FPI.

TWEOM. In this experiment, since one of the sidebands was locked and the carrier frequency was controlled by the electrical negative feedback to the PZT voltage, the variation of the PZT voltage shows the variation of the

carrier frequency. Therefore, Fig. 8 shows that the frequency of the carrier stabilized at 300 MHz dissociated from the FPI resonance frequency was varied smoothly by 200 MHz, and was stabilized again at 500 MHz dissociated from the FPI resonance frequency.

These results show that the frequency of the LD system we developed was tuned continuously and controlled precisely by locking of the frequency to a discrete stable frequency standard. Therefore, the laser frequency can be stabilized at a desired value, in the frequency range in which the LD oscillates without mode hopping, using this system.

5. Conclusions

We developed a new LD system in which the laser frequency can be tuned continuously over a wide range, and stabilized at the desired value by locking of one of the sidebands generated by passing the laser beam through a TWEOM to a FSR-stabilized FPI, i.e., a discrete stable frequency standard. The frequency of a 780 nm LD without additional AR coating on its output facet was varied continuously over a range of 22 GHz by scanning the LD drive current and the diffraction grating angle of the external cavity simultaneously at an appropriate rate. The carrier frequency of the LD was varied smoothly over a range of 200 MHz by locking of one of the sidebands, and was stabilized at 500 MHz dissociated from the FPI resonance frequency. These results show that, using the developed LD system, the laser frequency can be tuned continuously over a range of 22 GHz, and stabilized at a desired value in the frequency range in which the LD oscillates without mode hopping. This technique can also be used to control the frequency of dye lasers, tunable solid-state lasers and other tunable lasers, and is promising for application to laser isotope separation, high-resolution spectroscopy and lidar.

Acknowledgements

We thank Dr. S. Sasaki and Dr. S. Yokoyama of CRIEPI for their continuous encouragement during the course of this work. We also thank K. Okuda of Photonics Corp. for the fabrication of the servo controllers and technical assistance.

1) M. R. H. Knowles and C. E. Webb: Opt. Commun. **89** (1992) 493.
2) C. E. Hamilton: Opt. Lett. **17** (1992) 728.
3) T. D. Raymond and A. V. Smith: Opt. Lett. **16** (1991) 33.
4) T. Yanagawa, S. Saito, S. Machida, Y. Yamamoto and Y. Noguchi: Appl. Phys. Lett. **47** (1985) 1036.
5) A. Weis and S. Derler: Appl. Opt. **27** (1988) 2662.
6) M. Nakagawa, T. Sato and M. Shimba: Electron. Lett. **25** (1989) 430.
7) Y. Sakai, I. Yokohama, F. Kano and S. Sudo: IEEE Photon. Technol. Lett. **4** (1992) 96.
8) M. Kozuma, M. Kourogi, M. Ohtsu and H. Hori: Appl. Phys. Lett. **61** (1992) 1895.
9) H. Tsuchida, M. Ohtsu and T. Tako: Jpn. J. Appl. Phys. **20** (1981) L403.
10) R. W. P. Drever, J. L. Hall, F. V. Kowalski, J. Hough, G. M. Ford, A. J. Munley and H. Ward: Appl. Phys. B **31** (1983) 97.
11) B. Glance, O. Scaramucci, T. L. Koch and J. Stone: Electron. Lett. **25** (1989) 1193.
12) R. P. Hackel and B. E. Warner: Proc. SPIE **1859** (1993) 120.
13) K. Kuboki and M. Ohtsu: IEEE J. Quantum Electron. **23** (1987) 388.
14) K. Kuboki and M. Ohtsu: IEEE J. Quantum Electron. **25** (1989) 2084.
15) O. Ishida and H. Toba: J. Lightwave Technol. **9** (1991) 1344.
16) M. W. Maeda and L. G. Kazovsky: Photon. Technol. Lett. **1** (1989) 455.
17) M. Kourogi, K. Nakagawa and M. Ohtsu: IEEE J. Quantum Electron. **29** (1993) 2693.
18) K. Shimizu, Y. Sakai, T. Horiguchi and Y. Koyamada: IEEE J. Quantum Electron. **31** (1995) 1038.
19) T. Fujii, T. Nayuki, K. Nemoto, M. Kourogi and M. Ohtsu: Tech. Dig. Pacific Rim Conf. Lasers and Electro-Optics, Chiba, 1995, p. 215, FO5.
20) R. L. Barger, J. B. West and T. C. English: Appl. Phys. Lett. **27** (1975) 31.
21) Value quoted to us by the supplier. We have not independently confirmed this value.
22) M. G. Boshier, D. Berkeland, E. A. Hinds and V. Sandoghdar: Opt. Commun. **85** (1991) 355.
23) M. Weidemuller, C. Gabbanini, J. Hare, M. Gross and S. Haroche: Opt. Commun. **101** (1993) 342.
24) S. N. Atutov, E. Mariotti, M. Meucci, P. Bicchi, C. Marinelli and L. Moi: Opt. Commun. **107** (1994) 83.
25) T. Nayuki, T. Fujii, K. Nemoto, M. Kourogi and M. Ohtsu: Ext. Abstr. 42nd Spring Meeting of the Japan Society of Applied Physics and Related Societies, Kanagawa, March, 1995, 28p-ZQ-1 [in Japanese].
26) M. de Labachelerie, C. Latrasse, P. Kamssu and P. Cerez: J. Phys. III **2** (1992) 1557.
27) F. Favre, D. Le Guen, J. C. Simon and B. Landousies: Electron. Lett. **22** (1986) 795.

A Coupled-Cavity Monolithic Optical Frequency Comb Generator

M. Kourogi, T. Enami, and M. Ohtsu, *Senior Member, IEEE*

***Abstract*— We have designed a monolithic optical frequency comb generator (M-OFC-G) that uses an external coupled cavity for the 1.5-μm region. The comb envelope was observed with a span of 6.3 THz and the total cavity transmission has been 16%. With an additional etalon inside the external coupled cavity, the comb envelope spanned 7 THz while the transmission dropped to 9%. We also demonstrated the possibility of increasing the power of selected sidebands by using a coupled cavity at the output port of the M-OFC-G. We observed an increase of the power of the selected sidebands within a range of 5.6 THz.**

AN optical frequency comb (OFC) generator (OFC-G) (or a Fabry–Perot electrooptic modulator) is known as a modulator which can generate ultrashort optical pulse and high-order sidebands from a single-mode laser input. It consists of an electrooptic phase modulator installed in an optical cavity. To create high-order sidebands the electrooptic phase modulator is driven with an integer multiple of the cavity free-spectral-range (FSR) [1]–[9]. Since the generated sidebands are separated by the modulation frequency, they can be used as an OFC in precision control, sweep, and counting of large optical frequency differences. In order to ensure that a large fraction of the optical power transferred to high-order sidebands, a high-finesse optical cavity and a high efficient modulator is required. To meet this requirement, we have constructed a monolithic optical frequency comb generator (M-OFC-G) [7]–[9] that is simultaneously used as the electrooptic modulator. However, use of a high-finesse cavity and a highly efficient modulator reduces the coupling efficiency of the laser to the OFC cavity and then reduces the total power of the generated sidebands, even if the relative power transferred to the high-order sidebands is increased. This reduction can be understood by considering that the output light from the OFC generator forms an optical pulse train whose peak power is limited to the input laser power [1]. When the finesse of the optical cavity and/or the modulation index is increased, the pulse-width is decreased without an increase of the peak power. Therefore, the total power of the sidebands, which is equal to the average power, becomes small.

Manuscript received January 29, 1996; revised August 5, 1996.

M. Kourogi and M. Ohtsu are with the Interdisciplinary Graduate School of Science and Engineering, Tokyo Institute of Technology, Midori-ku, Yokohama, Kanagawa 226, Japan, and also with the Kanagawa Academy of Science & Technology, Takatsu-ku, Kawasaki, Kanagawa 213 Japan.

T. Enami was with the Interdisciplinary Graduate School of Science and Engineering, Tokyo Institute of Technology, Midori-ku, Yokohama, Kanagawa 226 Japan. He is now with Ricoh, Ltd., Tuzuki-ku, Yokohama, Kanagawa 224, Japan.

Publisher Item Identifier S 1041-1135(96)08800-3.

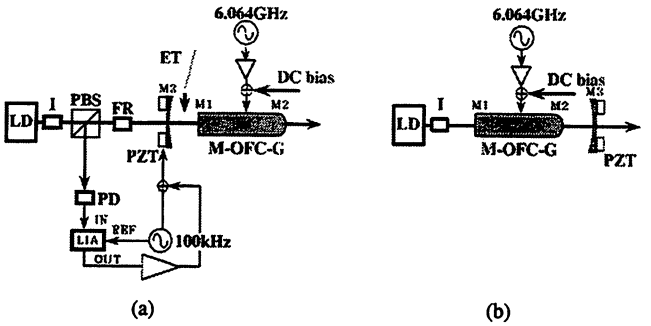

Fig. 1. Scheme of the experimental setups (a) and (b). LD: laser diode; I: isolator; FR: Faraday rotator; PBS: polarizing beam splitter; PZT: piezoelectric transducer; ET: etalon; PD: photodiode;LIA: lock-in-amplifier.

To solve this problem, we used a new type of M-OFC-G with an external coupled cavity (CC) to realize highly efficient OFC generation. Furthermore, we propose a novel highly efficient frequency shifter based on this scheme. The CC setup has been previously studied by Morimoto *et al.* [3] and Bell *et al.* [6], but without the monolithic comb generator.

Here, we report on two types of CC M-OFC-G that have the CC placed in different positions [Fig. 1(a) and (b)]. The light source was a 1.5-μm DFB laser and the incident light power onto the CC M-OFC-G was 5 mW. The M-OFC-G was fabricated by using an electrooptic modulator with high reflection coatings on both ends ($LiNbO_3$ crystal $1\times1.2\times23$ mm^3; modulation frequency 6.064 GHz = 2× FSR; modulation index 0.11π rad; M1: radius of curvature ∞, reflectivity 99.6%; M2: radius of curvature 50 mm, reflectivity 99.6%).

Without the modulation frequency switched on, the finesse of the M-OFC-G was 410 and the transmission on resonance was 30%. When the modulator was driven, and one of the resonant fringes of the monolithic cavity was tuned to the laser frequency by adjusting the dc bias voltage on the crystal, the cavity transmission became 0.3%. In the experimental setup that is shown in Fig. 1(a), a mirror (M3: radius of curvature 42 mm, reflectivity 99.3%) was placed in front of M1 to form a CC. M3 was mounted on a piezoelectric transducer (PZT) at a distance of 15 mm from M1. The finesse of the CC was 240, when the modulator was switched on and one of the resonant fringes of the monolithic cavity was adjusted to the laser frequency. To lock the external CC to the laser, an error signal was created by modulating the PZT and detecting the first derivative of the reflected light. As a result, the incident light will be transmitted by the CC while it becomes highly

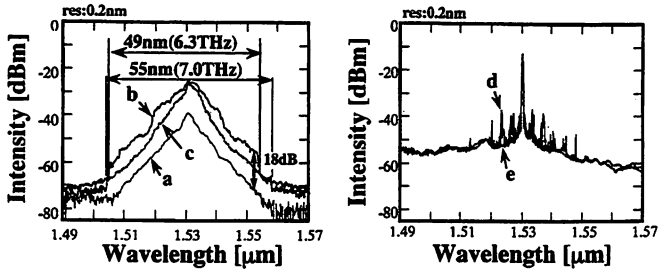

Fig. 2. The spectral profiles measured with the experimental setup (a). Curve *a*: transmitted light without the silica etalon and M3. Curves *b* and *d*: transmitted and reflected light with the CC (at the input port of the M-OFC-G) and without the silica etalon installed. Curves *c* and *e*: transmitted and reflected light with the CC (at the input port of the M-OFC-G) and the silica etalon installed.

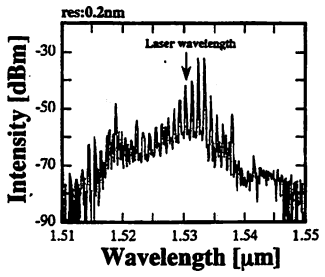

Fig. 3. Spectral profile of the transmitted light measured with the experimental setup (b).

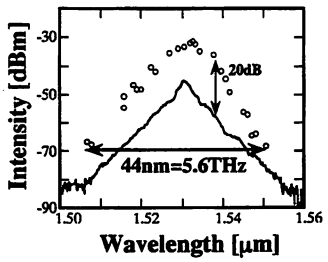

Fig. 4. Power spectrum of the sidebands transmitted through the experimental setup (b). Open circles: transmitted light. Solid curve: copy of curve *a* of Fig. 2(a) where the level was normalized to a single side-band power per monochromator resolution bandwidth.

reflective for the sidebands generated by the M-OFC-G. In this way, the total transmission of the setup was increased 18 dB, i.e., from 0.3% to 16%. The spectra labeled *a* and *b* of Fig. 2(a) show the measured profiles of the transmitted light without and with M3. Because our monochromator had a resolution of 0.2 nm only, we could not resolve the generated sidebands, only the envelopes of the spectral profile. The increase in intensity of the comb envelope was observed with a span of 6.3 THz. Since some of the sidebands are also resonant with the external CC, one finds regions in the comb envelope where the increase in intensity (curve *b* over curve *a*) is not quite 18 dB. These sidebands are observed in the light that is reflected from M3. A spectral profile of the reflected light is shown in Fig. 2(b) and is labeled *d*.

In order to suppress the leaking out of the sidebands through the CC, it is necessary to reduced the number of modes of the CC that match with the sidebands created by the M-OFC-G. One method to realize this is to increase the finesse and the FSR of the coupled cavity. Another way is to suppress the matching of resonant modes with the sidebands by tuning the CC with a silica plate etalon. Curve *e* in Fig. 2(b) shows the spectral profile of the reflected light with the silica plate etalon (thickness: 150 μm) installed in the CC. In this case, the resultant finesse of the CC decreased to about 170. From the reflected light, whose spectra is shown as curve *e* in Fig. 2(b), we found that the outleaking of sidebands was indeed efficiently suppressed. The resulting comb envelope was observed with a span of 7 THz. It is labeled *c* in Fig. 2(a). The drop in output power of certain regions of the spectrum is decreased except for the stepwise discontinuity at both ends, which is due to the material dispersion of the electrooptic crystal [8]. The total transmission was 9% which was somewhat lower than without the silica etalon because of the extra losses in the CC.

Referring to curve *d* of Fig. 2(b) it should be noted that the CC can also be used as a filter for the enhanced extraction of certain sidebands from the monolithic cavity. If only one sideband with large power is needed, e.g., to shift the frequency of the input, it is effective to take out only the sideband needed, leaving as much power as possible inside the M-OFC-G. However, in the setup shown in Fig. 1(a), it was difficult to extract an arbitrary sideband because the CC needs to be locked to the incident laser. To allow us the selection of extracted sidebands, we removed the external cavity from the input port of the M-OFC-G and installed it at the output port. Fig. 1(b) shows this setup where M3 was placed in behind M2 at a distance of 13 mm. The spectral profile of the transmitted light is shown in Fig. 3. Some enhanced sidebands are now clearly visible in the spectrum. By adjusting the bias voltage at the PZT on which M3 was mounted an appropriate set of sidebands may be selected. In Fig. 4, open circles represent the peak level of the sideband extracted through the CC for various values of the bias voltage on the PZT. It should be noted that in this situation only one sideband can be recorded by the monochromator within its resolution bandwidth. This is because the side-band frequency and the FSR CC cannot match twice within the resolution of 0.2 nm. For the comparison of the absolute power of the enhanced sidebands, we plotted curve *a* of Fig. 2(a) again in Fig. 3. Here the level was normalized to a single side-band power, i.e., it was decreased by 6 dB because without the CC there are four instead of one sidebands within the resolution bandwidth of the monochromator. We found that the peak levels of the sidebands transmitted through the CC were several (~20) decibels larger than the levels of the sidebands without the CC within a range of 5.6 THz. In this experiment, we could not control the exact order of the selected sideband. However, a control system can be realized if a high-resolution monochromator or a super cavity is employed. If a CC with a higher finesse and larger FSR is used, it will be possible to concentrate the optical power into a single sideband that will then be a CW light source.

Furthermore, if two stable CC's are installed at the input and the output port of the M-OFC-G the power of the selected sideband may be increased. In this case the M-OFC-

G will become a highly efficient frequency shifter for a wide frequency range.

In summary, we constructed a monolithic optical frequency comb generator operated in the 1.5 μm region that is coupled to an external cavity. The intensity envelope of the comb was observed with a span of 6.3 THz and the total cavity transmission has been 16%. With an additional silica etalon installed in the external cavity the span increased to 7 THz. In addition we discussed the possibility to realize a THz laser frequency shifter.

The authors would like to thank Professor Kobayashi and Dr. Morimoto of the Osaka University for helpful comments.

REFERENCES

[1] T. Kobayashi, T. Sueta, Y. Cho, and Y. Matsuo, "High-repetition-rate optical pulse generator using a fabry-perot electro-optic modulator," *Appl. Phys. Lett.*, vol. 21, no. 8, pp. 341–343, 1972.

[2] M. Kourogi, K. Nakagawa, and M. Ohtsu, "Wide-span optical frequency comb generator for accurate optical frequency difference measurement," *IEEE J. Quantum Electron.*, vol. 29, no. 10, pp. 2693–2701, 1993.

[3] A. Morimoto, A. Shibagaki, and T. Kobayashi, "Efficient ultrashort pulse generation using a modified fabry-perot modulator," in *Proc. CLEO'93, 1993}, paper number CThS84.*

[4] H. Keang-Po and J. M. Kahn, "Optical frequency comb generator using phase modulation in amplified circulating loop," *IEEE Photon. Technol. Lett.*, vol. 5, no. 6, pp. 721–725, 1993.

[5] L. R. Brothers, D. Lee, and N. C. Wong, "Terahertz optical frequency comb generation and phase locking of an optical parametric oscillator at 665 GHz," *Opt. Lett.*, vol. 19, no. 4, pp. 245–247, 1994.

[6] A. S. Bell, G. M. Mcfalane, E. Riis, and A. I. Ferguson, "An efficient optical frequency comb generator," *Opt. Lett.*, vol. 20, no. 1, pp. 1435–1439, 1995.

[7] M. Kourogi, T. Enami, and M. Ohtsu, "A monolithic optical frequency comb generator," *IEEE Photon. Technol. Lett.*, vol. 6, no. 2, pp. 214–217, 1994.

[8] M. Kourogi, W. Bambang, Y. Takeuchi, and M. Ohtsu, "The limits of optical frequency comb generation due to the material dispersion," *IEEE J. Quantum Electron.*, vol. 31, no. 12, pp. 2120–2126, 1995.

[9] M. Kourogi, B. Widiyatmoko, and M. Ohtsu, "3.17 THz frequency-difference measurement between lasers using two optical frequency combs," *IEEE Photon. Technol. Lett.*, vol. 8, no. 4, pp. 560–562, 1996.

An Optical Frequency Synthesizer Using a Waveguide-Type Optical Frequency Comb Generator at 1.5-μm Wavelength

T. Saitoh, M. Kourogi, and M. Ohtsu, *Senior Member, IEEE*

***Abstract*— An optical frequency synthesizer was developed at 1.5-μm wavelength region by utilizing a diode laser whose frequency was locked to an absorption line (P-branch, J = 23) of acetylene, a frequency tunable laser, and a waveguide-type optical frequency comb generator. This synthesizer has the frequency tunable range of 1.3 THz around 1.54-μm wavelength and absolute frequency stability of $\sigma = 4.5 \times 10^{-10}$ at 1 s integration time.**

HETERODYNE optical communication and precise measurements of physical constants could require a highly accurate optical frequency synthesizer (OFS) with the capabilities of frequency setting and tuning in the range of several THz. For example, in the development of wavelength division multiplexing (WDM) systems, an OFS whose frequency can be locked to frequencies with an accuracy of several MHz and is tunable in the range of over 1 THz, is required. A frequency reference diode laser has been developed by locking its frequency to an absorption line of atom or molecule gas [1]. However, it has not been possible to vary the locked frequency for a wide range. In the case of a commercially available frequency tunable laser, its frequency can be tuned over a span of several tens of nm. However, it has only a frequency accuracy larger than 10 GHz because it has no frequency reference. Recently, an optical frequency comb generator (OFCG) was developed [2]–[6]. The OFCG is composed of an optical phase modulator within an optical resonator and can generate many modulation sidebands with the span as wide as several THz. Since the generated modulation sidebands have the same frequency stability and accuracy as that of the frequency reference diode laser, it can be used as a reliable local oscillator.

In this letter, we report the OFS that is realized by frequency-offset-locking between a frequency locked reference laser and a frequency tunable laser using a waveguide-type optical frequency comb generator (WG-OFCG) as a local oscillator [7]–[10].

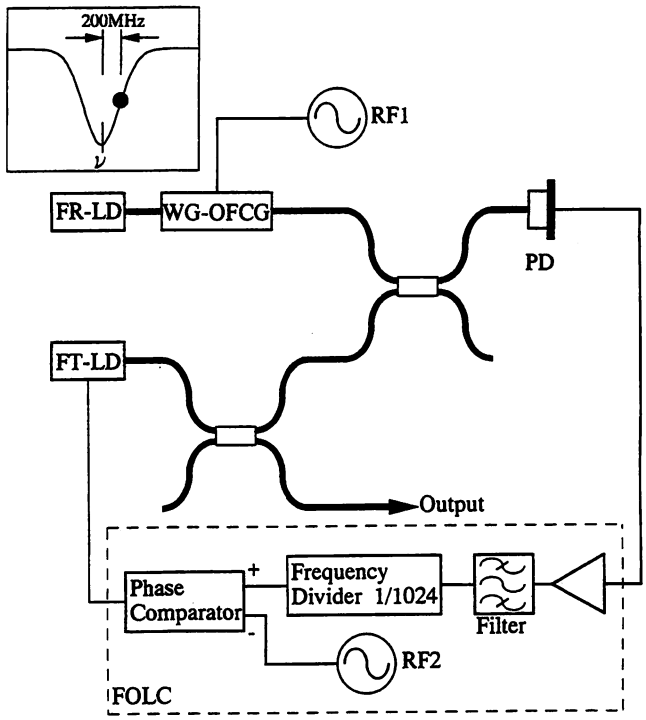

Fig. 1. Schematic explanation of an optical frequency synthesizer. FR-LD: frequency reference laser; FT-LD: frequency tunable laser; WG-OFCG; waveguide-type optical frequency comb generator; FOLC: frequency offset locking circuit; PD: photodiode; RF1 and RF2: RF synthesizers. The inset shows the profile of absorption line of acetylene and frequency locking point of the FR-LD. ν is the center frequency of the absorption line.

Fig. 1 shows the structure of the fabricated OFS, which is composed of a frequency reference laser (FR-LD), a WG-OFCG, a frequency tunable laser (FT-LD) and a frequency offset locking loop.

A distributed feedback laser diode was used as the FR-LD. Frequency stabilization and field spectral linewidth narrowing of the FR-LD were carried out by using the absorption line (P-branch, J = 23) of acetylene gas as a frequency reference. The center frequency of this absorption line was measured to be 194.7426 THz [11]. The inset of this figure shows the frequency locked point of the FR-LD, which was a $\nu + 200$ MHz, where a ν is the center frequency of the absorption line. The laser frequency and the power of the

Manuscript received March 21, 1996; revised July 29, 1996.

T. Saitoh is with the Kanagawa Academy of Science and Technology, KSP East Building, Room 408, 3-2-1 Sakado, Takatsu-ku, Kawasaki, Kanagawa 213, Japan. He is also with the Anritsu Corporation, 1800 Onna, Atsugi, Kanagawa 243, Japan.

M. Kourogi and M. Ohtsu are with the Kanagawa Academy of Science and Technology, KSP East Building, Room 408, 3-2-1 Sakado, Takatsu-ku, Kawasaki, Kanagawa 213, Japan. They are also with the Interdisciplinary Graduate School of Science and Engineering, Tokyo Institute of Technology, 4259 Nagatuta, Midori-ku, Yokohama, Kanagawa 226, Japan.

Publisher Item Identifier S 1041-1135(96)08133-5.

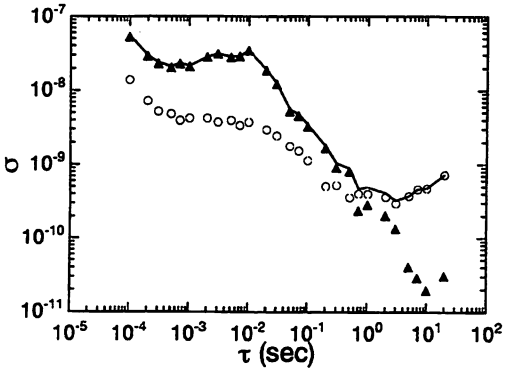

Fig. 2. Frequency stability represented by square root of the Allan variance σ^2. Open circles are frequency stability of the FR-LD. Closed triangles are frequency stability of the heterodyne signal between the 175th modulation sideband and the FT-LD. The solid curve is the frequency stability of the optical frequency synthesizer.

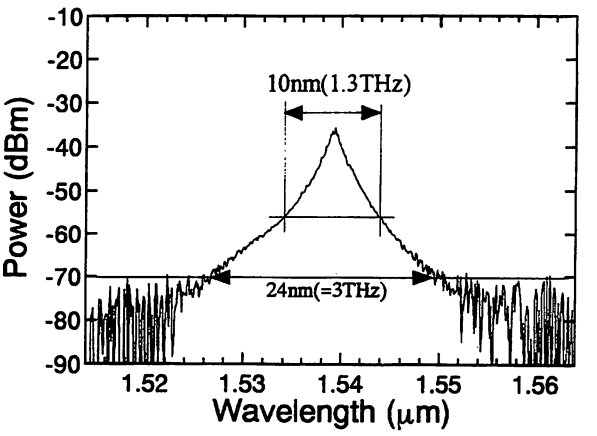

Fig. 3. Envelope spectrum of the OFC of the FR-LD generated by the WG-OFCG. This spectrum was measured by an optical spectrum analyzer with resolution bandwidth of 0.1 nm.

FR-LD were 194.7428 THz and 5 mW, respectively. Open circles in Fig. 2 show the square root of Allan variance σ^2 representing the frequency stability of the FR-LD estimated from the heterodyne frequency stability between the two independently constructed FR-LD's. From these results, the frequency stability of the FR-LD was estimated to be $\sigma = 4 \times 10^{-10}$ at the integration time τ of 1 s. The field spectral linewidth and the sidemode suppression ratio (SMSR) of the FR-LD were 500 kHz and 15 dB which was measured by a delayed self heterodyne method.

For the FT-LD, an external cavity configuration with a grating was employed using a Fabry–Perot cavity-type diode laser. Wavelength of the FT-LD could be varied for the range of 1.52–1.56 μm by rotating the grating. By using a piezoelectric transducer (PZT) on which the grating was mounted, the frequency of the FT-LD could be tuned in the range of 60 GHz without any mode-hoppings and phase-jumps. The linewidth and power of the FT-LD were 100 kHz and 1 mW, respectively.

The WG-OFCG was used for generating a series of modulation sidebands which is called an optical frequency comb (OFC). This OFC was generated by using quasirectangular modulation whose power and fundamental frequency were 0.2 W and 3.74 GHz, respectively [12]. Fig. 3 shows an envelope of the OFC of the FR-LD measured by an optical spectrum analyzer with resolution bandwidth of 0.1 nm. For the heterodyne detection between the modulation sideband (500 kHz linewidth) and FT-LD (100 kHz linewidth) with detection bandwidth of 100 MHz, the shot noise limited power of the sideband is estimated to be −70 dBm from Eq. (4) in [2]. As shown in Fig. 3, the modulation sidebands in wavelength span as wide as 24 nm that corresponds to 3 THz, and can be heterodyne detected in theory.

A heterodyne signal between a modulation sideband and the FT-LD was detected by a photodiode, amplified and frequency-divided by 1/1024 by a frequency divider. The phase of this frequency-divided heterodyne signal was compared to with that of a reference oscillator (RF2) whose frequency was 0.1–10 MHz. This provides a feedback signal used to control the PZT of the FT-LD. The frequency offset locking range was 0.1–1.0 GHz. The upper and lower limits of locking range were restricted by the band-width of the photodiode and $1/f$ noise.

Closed triangles in Fig. 2 show the frequency stability of the heterodyne signal between the FT-LD (195.3970 THz) and the 175th modulation sideband (195.3975 THz) under frequency offset locking. Here, the frequency difference between the FR-LD and the FT-LD was 0.655 THz, and the heterodyne frequency was 520 MHz. The frequency offset locking was effective in the range of $\tau \geq 1 \times 10^{-2}$ s which was limited by the bandwidth of the PZT (= 100 Hz). The frequency stability of the heterodyne signal was $\sigma = 2 \times 10^{-10}$ at $\tau = 1$ s.

The frequency fluctuation of the FT-LD under frequency offset locking is expressed as

$$\delta f_{\mathrm{FT}}^2 = \delta f_{\mathrm{FR}}^2 + (n \cdot \delta f_{\mathrm{RF1}})^2 + \delta f_{\mathrm{he}}^2$$
$$\sigma_x = \delta f_x / f_x \qquad (x = \mathrm{FR, FT, RF1 \text{ and } he}) \tag{1}$$

where δf_{FR}, δf_{RF1} and δf_{he} are frequency fluctuations of the FR-LD, RF1 and the heterodyne signal between the n-th modulation sideband and the FT-LD, respectively. σ_x is the square root of Allan variance. The fluctuation of the frequency offset locking circuit including the RF2 and the frequency divider is included in the δf_{he}. Absolute frequency stability of the FT-LD was estimated from (1) and the nominal valued of δf_{RF1} supplied by the manufacture (i.e., $\delta f_{\mathrm{RF1}} = 1.0\tau^{-1/2}$ (Hz)). The solid curve in Fig. 2 shows this estimated result for which n and the frequency difference between FR-LD and FT-LD were 175 and 0.655 THz, respectively. Since the laser output from the FT-LD is used as the output of the present OFS system, frequency stability of the OFS, i.e., the frequency stability of the FT-LD under frequency offset locking, was estimated to be $\sigma = 4.5 \times 10^{-10}$ at $\tau = 1$ s. The OFS can tune its frequency with the absolute frequency stability of 4.5×10^{-10} in the range of 1.3 THz. In this range, the frequency stability of the OFS was almost constant and independent of n. The frequency stability of the frequency offset locking is determined by the signal-to-noise ratio (S/N) of its heterodyne signal, which is in proportion to sideband power. So, the frequency stability decreases with increasing n. However, since the FR-LD has a SMSR of only 15 dB the S/N

of the heterodyne signal is limited to 15 dB and the frequency stability becomes almost constant and independent of n in the range of $-175 \leq n \leq 175$. In the range of $|n| > 175$, stable frequency offset locking cannot be carried out because S/N is too low.

In summary, an optical frequency synthesizer was developed at 1.5-μm wavelength region by utilizing a frequency stabilized laser whose frequency is locked to an absorption line (P-branch, $J = 23$) of acetylene, a frequency tunable laser, and a WG-OFCG. This optical frequency synthesizer has performances of wavelength tunable range of 1.54 ± 0.005 μm (± 0.655 THz) and absolute frequency stability $\sigma = 4.5 \times 10^{-10}$ at $\tau = 1$ s.

REFERENCES

[1] T. Yanagawa, S. Saito, and Y. Yamamoto, "Frequency stabilization of 1.5-μm InGaAsP distributed feedback laser to NH_3 absorption lines," *Appl. Phys. Lett.*, vol. 45, pp. 826–828, Oct. 1984.

[2] M. Kourogi, K. Nakagawa, and M. Ohtsu, "Wide-span optical frequency comb generator for accurate optical frequency difference measurement," *IEEE J. Quantum Electron.*, vol. 29, no. 10, pp. 2693–2701, Oct. 1993.

[3] N. C. Wong, D. Lee, and L. R. Brothers, "Optical frequency counting based on parametric oscillation," in *Tech. Dig. Int. Symp. Atomic Frequency Standards and Coherent Quantum Electron.*, Nara, Japan, Aug. 1993, pp. 14–17.

[4] L. R. Brothers, D. Lee, and N. C. Wong, "Terahertz optical frequency comb genearation and phase locking an optical parametric oscillator at 665 GHz," *Opt. Lett.*, vol. 19, no. 4, pp. 245–247, Feb. 1994.

[5] M. Kourogi, T. Enami, and M. Ohtsu, "A monolithic optical frequency comb generator," *IEEE Photon. Technol. Lett.*, vol. 6, no. 2, pp. 214–217, Feb. 1994.

[6] M. Kourogi and M. Ohtsu, "Frequency difference measurement by optical frequency comb generator," in *Proc. Conf. Lasers Electro-Opt.*, Baltimore, MD, May 1995, paper CTuI7pp. 91–92.

[7] T. Saitoh, M. Kourogi, and M. Ohtsu, "Waveguide type optical frequency comb generator," *IEEE Photon. Technol. Lett.*, vol. 7, no. 2, pp. 197–199, Feb. 1995.

[8] T. Saitoh, E. Durand, M. Kourogi, and M. Ohtsu, "Waveguide type optical frequency comb generator," *Proc. SPIE*, vol. 2378, 1995, p. 212.

[9] E. Durand, T. Saitoh, M. Kourogi, and M. Ohtsu, "0. 4 THz frequency offset locking between two optical frequency combs," *IEEE Photon. Technol. Lett.*, vol. 8, no. 1, pp. 163–165, Jan. 1996.

[10] T. Saitoh, E. Durand, M. Kourogi, and M. Ohtsu, "Proposal of a multiplex optical frequency comb generation system," *IEEE Photon. Technol. Lett.*, vol. 8, pp. 287–289, Feb. 1996.

[11] S. Kinugawa and H. Sasada, "Wavenumber measurement of the 1.5-μm band of acetylene by semiconductor laser spectrometer," *Jpn. J. Appl. Phys.*, vol. 29, no. 3, p. 611, 1990.

[12] T. Saitoh, E. Durand, M. Kourogi, and M. Ohtsu, "Expansion of span-width of an optical frequency comb using a higher harmonic wave modulation," *IEEE Photon. Technol. Lett.*, vol. 8, pp. 1379–1381, Oct. 1996.

Expansion of Span-Width of an Optical Frequency Comb Using a Higher Harmonic Wave Modulation

T. Saitoh, M. Kourogi, and M. Ohtsu, *Senior Member, IEEE*

Abstract—**We propose a novel method for expanding the span-width of an optical frequency comb that utilizes modulation by a superposition of higher harmonic waves. Based on the calculations, it was found that in the terms up to third-order harmonic wave, the optimum superposition is the one whose power ratio between the fundamental and the third-order harmonic waves is 1:1. The validity of this method was experimentally confirmed at 1.5-μm wavelength region. By this optimum modulation with a wave power of 1.0 W, the span-width of OFC was increased to 72 nm (= 9.1 THz).**

A MEASUREMENT of a frequency difference between two lasers is an important technique for the optical communication and development of the optical synthesizer [1], [2]. Although the heterodyne detection has been conventionally for the measurement of the frequency difference, the maximum frequency difference is limited by the bandwidth of the heterodyne receiver, which is about 10 GHz. In order to overcome this difficulty, an optical frequency comb (OFC) generator was developed for the measurement of the frequency difference of several THz [3]–[7]. The first OFC generator was composed of a microwave cavity and an optical phase modulator installed into an optical resonator with two discrete mirrors. The second was a bulk-type whose optical resonator was monolithically fabricated by high reflection coating on the two end facets of a phase modulation crystal [8]. Its modified versions were a type that had one or two external mirrors for enhancing sidebands powers [9] and a type that used a waveguide-type phase modulator [10], [11], in order to increase the efficiency of generating sidebands. The waveguide-type OFC generator modulates the phase of optical wave by a copropagating microwave that propagates through a microstrip line formed on the waveguide. Therefore, it requires the microwave whose frequency is integral multiple that of the free spectral range (FSR) of the optical resonator. By utilizing this requirement, this letter reports an expansion of the span-width of the OFC by changing the modulation wave-form from sinusoidal to quasirectangular.

Manuscript received December 12, 1995; revised May 24, 1996.

T. Saitoh is with the Kanagawa Academy of Science and Technology, KSP East Building, Room 408, 3-2-1 Sakado, Takatsu-ku, Kawasaki, Kanagawa 213, Japan. He is also with the Anritsu Corporation, 1800 Onna, Atsugi, Kanagawa 243, Japan.

M. Kourogi and M. Ohtsu are with the Kanagawa Academy of Science and Technology, KSP East Building, Room 408, 3-2-1 Sakado, Takatsu-ku, Kawasaki, Kanagawa 213, Japan. They are also with the Interdisciplinary Graduate School of Science and Engineering, Tokyo Institute of Technology, 4259 Nagatuta, Midori-ku, Yokohama, Kanagawa 226, Japan.

Publisher Item Identifier S 1041-1135(96)07423-X.

Since the OFC generator behaves as a high speed shutter by modulating the resonance frequency of the optical resonator, its output becomes a pulse train whose repetition frequency is twice the modulation frequency. The resonance frequency $f_{p\text{-}\sin}$ and the pulse width $w_{p\text{-}\sin}$ can be described as

$$f_{p\text{-}\sin} = f_0 + \frac{m}{2\pi}\mathrm{FSR}\cdot\sin(2\pi f_m t), \tag{1}$$

$$w_{p\text{-}\sin} = \frac{1}{m\cdot F\cdot f_m} \tag{2}$$

where f_0 is the unmodulated resonance frequency of the optical resonator, m is the modulation index, f_m is the sinusoidal modulation frequency, F and FSR are respectively the finesse and the free spectral range of the optical resonator. The attenuation factor of sideband power $\Delta_{\sin}$ in the unit of THz^{-1} is, thus, described as

$$\Delta_{\sin} = \exp\left(\frac{-\pi}{m\cdot F\cdot f_m}\right). \tag{3}$$

This equation shows that the pulse-width will be narrowed and the span-width of generated sidebands will be increased if one can increase f_m, F and/or m. However, increasing the modulation frequency reduces the modulation index by a factor of -0.3 dB/GHz. The finesse of the waveguide-type OFC generator used for this study is 30, which is, to our knowledge, the highest for the case of a waveguide-type resonator. The maximum microwave power for the waveguide-type OFC generator is about 1 W that is limited by the heat resistance of the waveguide. The modulation index is in proportion to the square root of the microwave power, which is 2π at the microwave power and frequency of 1 W and 10 GHz, respectively. However, by changing the modulation wave-form sinusoidal to rectangular, the span-width of OFC can be increased even by the same values of m, F and FSR.

If a rectangular wave is approximately expressed as the Fourier-expanded terms up to the $2n-1$th order, the instantaneous resonance frequency $f_{p\text{-rec}}$ of the optical resonator and the pulse-width $w_{p\text{-rec}}$ under the rectangular modulation are given by

$$\begin{aligned} f_{p\text{-rec}} = f_0 + \frac{m}{2\pi}\mathrm{FSR} \\ \times\left\{\sin(2\pi f_m t) + \frac{1}{3}\sin(2\pi\cdot 3 f_m t)\right. \\ + \frac{1}{5}\sin(2\pi\cdot 5 f_m t)\cdots \\ \left. + \frac{1}{2n-1}\sin(2\pi\cdot(2n-1) f_m t)\right\} \end{aligned} \tag{4}$$

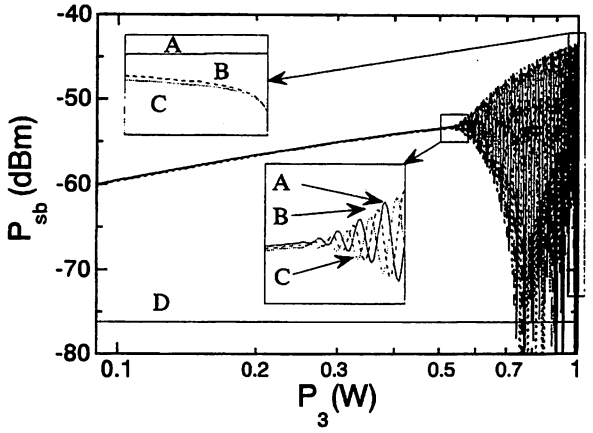

Fig. 1. Dependence of a sideband power P_{sb} on a power of third-order harmonic wave P_3. Here, the sum of P_3 and the fundamental wave power P_1 was kept to be 1 W. Curves A, B and C are sideband powers of 330th, 331th, and 332th orders, respectively. Line D represents 330th sideband power obtained only under the fundamental wave modulation, that is $P_1 = 1$ W and $P_3 = 0$ W.

$$w_{p\text{-rec}} = \frac{1}{n \cdot m \cdot F \cdot f_m}. \tag{5}$$

The attenuation factor of sideband power Δ_{rec} (THz^{-1}) under the rectangular modulation is expressed as

$$\Delta_{rec} = \exp\left(\frac{-\pi}{n \cdot m \cdot F \cdot f_m}\right). \tag{6}$$

Comparison with (3) confirms a drastic decrease of the attenuation, which is due to the factor of $1/n$ in (6).

For the cases of $n = 2$, we calculated a dependence of the sideband powers P_{sb} on the powers of the fundamental and the third-order harmonic waves P_1 and P_3, respectively. The sideband powers were calculated from the Fourier analysis of transmitted light of the waveguide-type OFC generator. The total power of the rectangular wave, that is $P_1 + P_3$, was fixed to be 1 W. Fig. 1 shows the calculated results, in which curves A, B, and C represent calculated sideband powers of 330th-, 331th-, and 332th orders, respectively. Line D in this figure represents the sideband power of 330th-order modulated only by the fundamental wave, that is $P_1 = 1$ W and $P_3 = 0$ W. The curves A-C show that the sideband powers vary drastically after a monotonous increase up to $P_3 = 0.5$ W. At only the third-order harmonic wave modulation, that is $P_1 = 0$ W and $P_3 = 1$ W, only curve A whose order is multiple of three remains while the curves B and C disappear. From (4), the modulation amplitude ratio between the fundamental and the third-order harmonic waves is 1:1/3 at the rectangular modulation. So, the wave-form at P_1:P_3 = 1:1/9, i.e., for which $P_1 = 0.9$ W and $P_3 = 0.1$ W, is the best approximation to the rectangular modulation. However, as shown in Fig. 1, since the wave-form at $P_3 = 0.5$, i.e., for which $P_1 = P_3$, can generate sidebands whose powers are large and almost independent of P_3. This wave-form composed of the fundamental and the third higher harmonic waves is found to be the optimum wave-form for the generation of the sidebands especially for the heterodyne detection.

We have carried out an experiment to confirm sideband generation utilizing the optimum wave-form modulation. The frequency of the fundamental wave was 3.74 GHz, which is twice the FSR. The higher harmonic waves were generated by using output saturation of a low-power amplifier. The low power amplifier had bandwidth, gain and maximum output of 4 GHz, 15 dB and 15 dBm, respectively. This low-power amplifier was made to saturate at the microwave power of 12 dBm. The power ratio between the fundamental and the third-order harmonic waves for the optimum wave-form was controlled by the source voltage of the low power amplifier. The modulation wave was applied to the waveguide-type OFC generator after being amplified by a traveling wave tube (TWT) amplifier with a bandwidth of 20 GHz. From the bandwidth of the TWT amplifier, one can apply up to the fifth-order harmonic wave to the waveguide-type OFC generator. Fig. 2 shows the spectrum of the microwave applied to the waveguide-type OFC generator. The total microwave power was 1.0 W.

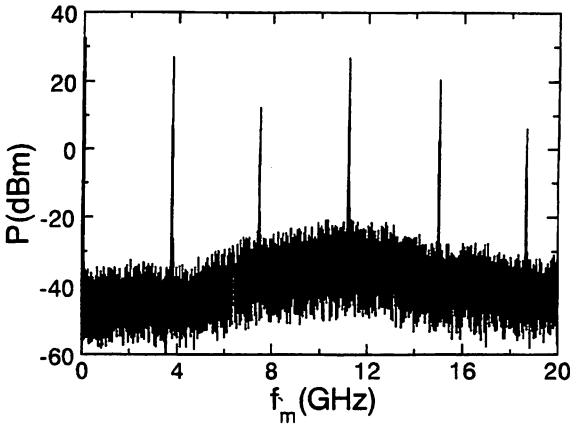

Fig. 2. Microwave spectrum of modulation wave applied to a waveguide-type OFC generator. The fundamental frequency is 3.74 GHz. This modulation wave has terms up to fifth-order harmonic wave because a TWT amplifier has a bandwidth of 20 GHz. Total power of this modulation wave is 1.0 W.

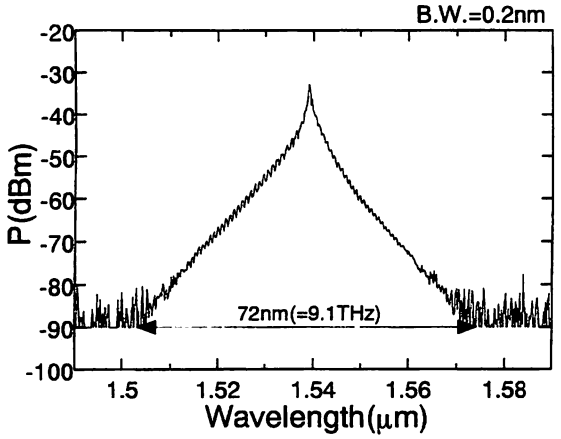

Fig. 3. Envelope spectrum of the OFC generated by the optimum wave-form modulation whose fundamental frequency and total microwave power are 3.74 GHz and 1.0 W, respectively. This OFC was measured by an optical spectrum analyzer with the resolution bandwidth of 0.2 nm.

Fig. 3 shows the envelope spectrum of the OFC generated by the optimum wave-form modulation. A diode laser used here had the wavelength, linewidth and power of 1.54 μm, 1 MHz and 5 dBm, respectively. For the heterodyne detection

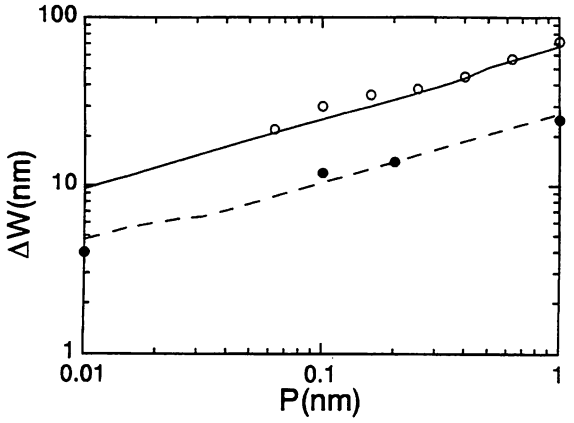

Fig. 4. Calculated and measured results of the relation between the modulation wave power P and the span-width ΔW of OFC whose sidebands have power higher than −90 dBm. The open and filled circles are the measured results for the optimum wave-form and conventional sinusoidal modulations, respectively. The solid and broken curves are the calculated results for the optimum wave-form and the conventional sinusoidal modulations, respectively.

between the sideband (100 kHz linewidth) and a slave laser (10 mW-power and 100 kHz linewidth) with detection bandwidth of 10 MHz, the shot noise limited power of the sideband is estimated to be −90 dBm from [5, eq. (4)]. Therefore, it is estimated from Fig. 3 that the span-width of OFC that can be used for the heterodyne detection is 72 nm (= 9.1 THz). This value, to our knowledges, is the widest span-width of an OFC. There are about 2500 sidebands in this span.

Fig. 4 shows the relations between the total microwave power and the span-width of the OFC under the optimum wave-form and the conventional sinusoidal modulation. From this figure, it is found that the optimum wave-form modulation can generate the OFC whose span-width is three times that of the conventional sinusoidal modulation. The solid and broken curves are results that are calculated by Fourier-transforming the time varying output intensity of the waveguide-type OFC generator into a frequency domain under the condition of the optimum wave-form and the conventional sinusoidal modulations, respectively.

In summary, we proposed a novel method for increasing the span-width of the OFC that utilized superposition of higher harmonic waves. In the terms up to third-order harmonic wave, theoretical analysis found that the optimum wave-form is realized when power ratio between fundamental and third higher harmonic waves was 1:1. The validity of this method was experimentally confirmed at 1.5-μm wavelength region. By this optimum wave-form modulation with 1.0 W total microwave power, the span-width of OFC was increased to 72 nm (= 9.1 THz).

REFERENCES

[1] K. Kuboki and M. Ohtsu, "A synthesized method to improve coherence in semiconductor lasers by electrical feedback," *IEEE J. Quantum Electron.*, vol. 25, no. 10, pp. 2084–2090, Oct. 1989.

[2] O. Ishida and H. Toba, "Lightwave synthesizer with lock-in-detected frequency references," *J. Lightwave Technol.*, vol. 9, no. 10, pp. 1344–1352, Oct. 1991.

[3] M. Kourogi, N. Nakagawa, C. H. Shin, M. Teshima, and M. Ohtsu, "Accurate frequency measurement system for 1.5 μm wavelength laser diodes," in *Proc. Conf. Lasers and Electro-Opt.*, Baltimore, May 1991, Paper CThR57.

[4] M. Kourogi and M. Ohtsu, "A highly accurate frequency counting system for 1.5 μm wavelength semiconductor lasers," *Proc. SPIE Frequency-Stabilized Lasers and Their Applications*, Boston, MA, vol. 1837, Nov. 1992, pp. 205–215.

[5] M. Kourogi, K. Nakagawa, and M. Ohtsu, "Wide-span optical frequency comb generator for accurate optical frequency difference measurement," *IEEE J. Quantum Electron.*, vol. 29, pp. 2693–2701, Oct. 1993.

[6] N. C. Wong, D. Lee, and L. R. Brothers, "Optical frequency counting based on parametric oscillation," in *Tech. Dig. Int. Symp. Atomic Frequency Standards and Coherent Quantum Electron.*, Nara, Japan, Aug. 1993, pp. 14–17.

[7] L. R. Brothers, D. Lee, and N. C. Wong, "Terahertz optical frequency comb genearation and phase locking an optical parametric oscillator at 665 GHz," in *Opt. Lett.*, vol. 19, no. 4, pp. 245–247, Feb. 1994.

[8] M. Kourogi, T. Enami, and M. Ohtsu, "A monolithic optical frequency comb generator," *IEEE Photon. Technol. Lett.*, vol. 6, no. 2, pp. 214–217, Feb. 1994.

[9] M. Kourogi and M. Ohtsu, "Frequency difference measurement by optical frequency comb generator," in *Proc. Conf. Lasers and Electro-Opt.*, Baltimore, MD, May 1995. Paper CTuI7.

[10] T. Saitoh, M. Kourogi, and M. Ohtsu, "Waveguide type optical frequency comb generator," *IEEE Photon. Technol. Lett.*, vol. 7, pp. 197–199, Feb. 1995.

[11] T. Saitoh, E. Durand, M. Kourogi, and M. Ohtsu, "Waveguide type optical frequency comb generator," in *Proc. SPIE 2378*, vol. 212, 1995.

ThA1 900

47THz span optical frequency comb generation by self-phase modulation in an optical fiber

Kazuhiro Imai, Motonobu Kourogi,* Motoichi Ohtsu,* *Interdisciplinary Graduate School of Science and Engineering, Tokyo Institute of Technology, Midori-ku, Yokohama 226, JAPAN*

An optical frequency comb generator (OFCG) is a highly efficient modulator[3] which generates equally spaced sidebands beyond a span of several tera-Hertz and it has been applied for difference frequency measurements.[1] To extend the OFC span as high as the carrier frequency and to realize the absolute frequency measurement by an optical-frequency-to-radio-frequency division method,[4] we applied self-phase modulation (SPM) in an optical fiber to the output of an OFCG. SPM also generates equally spaced sidebands as a result of coherent four-wave mixing among the sidebands. Therefore the frequency intervals of the sidebands are also expected to be as accurate as a frequency of a microwave oscillator used in the OFCG.

The output of a cw laser diode (λ = 1.54 μm, 2 mW) was transformed into pulse train whose repetition rate was twice the modulation frequency 6 GHz by a coupled-cavity OFCG.[2] Because the laser output was low, the output of the OFCG was amplified the average power to 30 mW by an optical fiber amplifier, and then introduced to a 1 km dispersion flattened fiber (DFF) (anomalous dispersion, 0.12 ps/km/nm at 1550 nm, mode field diameter 6.1 μm at 1550 nm, loss 0.23 dB/km at 1550 nm).[5]

Figure 1, curve *A*, is the spectral profile of the output of the OFCG. After the amplification, the spectral profile was affected by the gain profile of the amplifier shown in curve *B*, and sidebands in the shorter wavelength side were more efficiently amplified. After it propagated in the DFF, the span of the OFC was extended to 47 THz shown in Figure 2

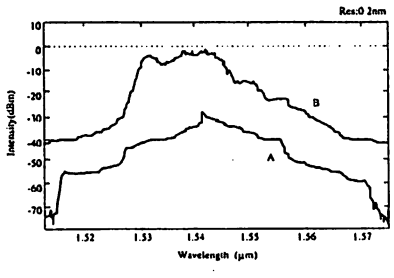

ThA1 Fig. 1. Spectral envelopes of OFC. *A*: original OFC. *B*: amplified OFC.

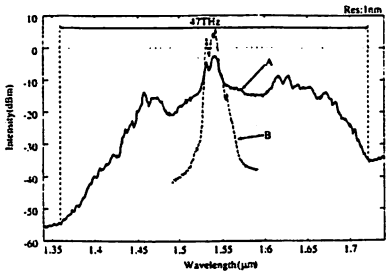

ThA1 Fig. 2. Spectral envelopes of OFC. A: OFC after passing through the DFF. B: before passing through the DFF.

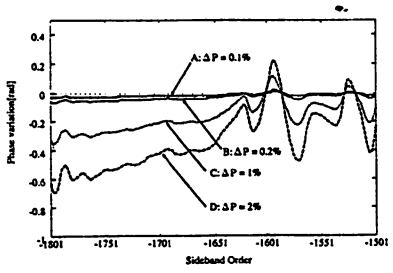

ThA1 Fig. 3. Phase variations as a function of the order of odd-sideband. Curves *A* ~ *D* are for the input average power fluctuation ΔP of 0.1%, 0.2%, 1% and 2%, respectively.

curve A. However, the spectral profile was asymmetric, and the power of sidebands in the longer wavelength side were increased. Therefore the center frequency of the spectrum was shifted to the longer wavelength side. This shift is considered to be the effect of stimulated Raman scattering. The OFC includes more than 7700 sidebands and the span 47 THz is already as large as a quarter of an absolute frequency of 1.65 μm. By this large span, we expect to determine the absolute frequency by using the OFC and two difference-frequency dividing stages.[4]

We estimated phase stability of the OFC generated by SPM about the input average power by numerical simulations. In Figure 3 curves *A* ~ *D* are phase variations of odd sidebands when the input average power fluctuations ΔP are 0.1%, 0.2%, 1%, and 2%, respectively. Though the magnitude of the phase variation depends on the order of the sideband, they are proportional to ΔP for each sideband, and the maximum phase variation was less than 0.5 radian per 1% of input average power fluctuation. If one reduced the power fluctuation to lower than 1% for the measurement time of 1 second, the uncertainty of the measurement is less than 0.1 Hertz. Thus, accuracy of 10^{-14} can be expected for the 10 THz difference frequency measurement from the carrier frequency.

*Kanagawa Academy of Science & Technology, Takatsu-ku, Kawasaki, Kanagawa 213, JAPAN

1. M. Kourogi, *et al.*, IEEE J. Quantum Electron. 29, 2693–2701 (1993).
2. M. Kourogi, *et al.*, IEEE Photon. Technol. Lett. 8, 1698–1700 (1996).
3. T. Kobayashi, *et al.*, Appl. Phys. Lett. 21, 341–343 (1972).
4. H. R. Telle, *et al.*, Opt. Lett. 15, 532–534 (1990).
5. Y. Kubo, *et al.*, ECOC 21, 505–508 (1990).